UNIVERSITY OF CALIFORNIA SAN DIEGO

Fe-S Clusters as Targets for Drug Discovery: Studies of the Interaction Between NEET Protein MiNT and Caged Xanthones

A Dissertation submitted in partial satisfaction of the requirements
for the degree Doctor of Philosophy

in

Chemistry

by

Gary Edward Arevalo

Committee in charge:

Professor Emmanuel A. Theodorakis, Chair
Professor Joseph M. O'Connor, Co-Chair
Professor Thomas J. Bussey
Professor Kamil Godula
Professor Thomas C. Hermann
Professor Patricia A. Jennings
Professor JoAnn Trejo

2022

The Dissertation of Gary Edward Arevalo is approved, and it is acceptable in quality and form for publication on microfilm and electronically.

University of California San Diego

2022

DEDICATION

For mom and all my mentors.

TABLE OF CONTENTS

LIST OF FIGURES

LIST OF TABLES

LIST OF ABBREVIATIONS

Ac_2O	Acetic anhydride
ACN/CH_3CN	Acetonitrile
$AlCl_3$	Aluminum chloride
BME	2-Mercaptoethanol
CD	Circular dichroism
$CDCl_3$	Deuterochloroform
CD_3OD	Tetradeuteromethanol
C_5D_5N/pyridine-*d*5	Pentadeuteropyridine
$CO(CH_3)_2$	Acetone
DCM/CH_2Cl_2	Dichloromethane
DIPEA	*N*-Ethyldiisopropylamine
DMAP	4-(Dimethylamino)pyridine
DMF	*N,N*-Dimethylformamide
DMSO	Dimethyl sulfoxide
DMSO-*d*6	Hexadeuterodimethyl sulfoxide
DNase	Deoxyribonuclease
E. coli	*Escherichia coli*
epi-GBA	*epi*-Gambogic acid
eq.	Molar equivalents
Et_2O	Diethyl ether
EtOAc	Ethyl acetate
Fe-S	Iron-sulfur

GBA	Gambogic acid
GBA•pyr	Gambogic acid pyridinium salt
g	Gram(s)
h	Hour(s)
HBr	Hydrobromic acid
HCl	Hydrochloric acid
H_2O	Water
HOAc	Acetic acid
HATU	(1-[bis(dimethylamino)methylene]-1H-1,2,3-triazolo[4,5-b]pyridinium 3-oxide hexafluorophosphate
HRMS	High resolution mass spectrometry
Hz	Hertz
IBC	Inflammatory breast cancer
IEX	Ion-exchange chromatography
IPTG	Isopropyl β-D-1-thiogalactopyranoside
K_2CO_3	Potassium carbonate
kDa	Kilodaltons
KOH	Potassium hydroxide
LB	Luria-Bertani medium
MeI	Methyl iodide
MeOH	Methanol
mg	Milligram(s)
$MgCl_2$	Magnesium chloride

MHz	Megahertz
MiNT/CISD3	Mitochondrial inner NEET protein
mL	Milliliter(s)
mmol	millimole
mNT/CISD1	mitoNEET protein
mol	mole
NaCl	Sodium chloride
NAF-1/CISD2	Nutrient-deprivation autophagy factor-1
$NaHCO_3$	Sodium bicarbonate
n-BuLi	*n*-Butyllithium
NMR	Nuclear magnetic resonance
$Pd(PPh_3)_4$	Tetrakis(triphenylphosphine)palladium(0)
$POCl_3$	Phosphoryl chloride
ppm	Parts per million
pyr	Pyridine
r.t.	Room temperature
R_f	Retention factor
ROS	Reactive oxygen species
RPA	rhodamine B-[(1,10-phenanthrolin-5-yl aminocarbonyl]
rpm	Revolutions per minute
r.t.	Room temperature
SDS	Sodium dodecyl sulfate
SEC	Size exclusion chromatography

THF	Tetrahydrofuran
TLC	Thin-layer chromatography
TMS	Tetramethylsilane
TNBC	Triple negative breast cancer
Trizma/Tris	Tris(hydroxymethyl)aminomethane
UV/Vis	Ultraviolet/visible
μL	Microliter(s)
μmol	Micromole(s)
$ZnCl_2$	Zinc chloride

ACKNOWLEDGEMENTS

First and foremost, I would like to acknowledge my advisor, Professor Emmanuel A. Theodorakis, for making this work possible. Undoubtedly, his guidance, mentorship, and generosity have shaped me into a better scientist and person. I have grown in every way under his tutelage, and I cannot thank him enough for helping me achieve my dream.

I would also like to acknowledge Professor Patricia A. Jennings for allowing me to work in her lab in pursuit of this dissertation, for her kindness and mentorship, and for all the fruitful discussions about NEET proteins; I performed all the biochemical and biophysical work in her lab. I would also like to thank our collaborators, Henri-Baptiste Margault (Silberman Institute, HUJI) and Professor Rachel Nechushtai (Silberman Institute, HUJI) and Professor Maria Theodoraki (Arcadia University) for the testing of compounds in biological assays and production of biological data used for this dissertation, as well as for their valuable insight during group meetings. I also acknowledge the UCSD Mass Spectrometry facility for all mass spectrometry work, Dr. Nicole Avakyan for help and support with the CD spectrometer, and Professor Arnold Rheingold for X-ray crystallographic data. Many thanks to my dissertation committee for their invaluable support: Professors Thomas J. Bussey, Kamil Godula, Thomas C. Hermann, Patricia A. Jennings, Joseph M. O'Connor, Emmanuel A. Theodorakis, and JoAnn Trejo.

A special thank you goes out to all my lab mates: Dr. Dominique T. Capraro, who taught me more biochemistry and biophysics than I could have imagined, and whose mentorship, friendship, infectious laughter, and positive attitude made the lab such a great place to work; Maryam Ranjbar for help and support with protein expression and purification; Tiange (Grace) Tau for always being willing to lend a hand and for the many helpful collaborations/discussions; Hsuan Lin for enthusiastically continuing this work; and Shrinav Bhakta for general lab support.

I am also forever thankful to the Alfred P. Sloan Foundation for a graduate fellowship and the UCSD Sloan Program for helping me make it through grad school. Thank you to my sloaner crew (Dr. Nancy Ronquillo, Dr. Sean Bearden, and Sinai Cota) whose support means so much to me and whose friendship will last a lifetime. I would also like to acknowledge my Sloan mentor, Professor Vicki Grassian, for her mentorship and support over the years, as well as Shana Slebioda and Drs. Kim Barrett and April Bjornson who run the program. I also thank the Chemistry & Biochemistry department staff for all their administrative support during my time as a graduate student: Asmaa Khatib, Erica Lennard, Jeff Rances, and especially, Amy Tran.

Last (but certainly not least!), I would like to thank my mother, Odilia, whom I dedicate this dissertation to and who gives me strength every single day; and my sister, Vilma, for being such an amazing person—I love you both so much. Thank you to all my friends (you all know who you are!), and a ***huge*** thank you to all my past and present mentors (UCSD, UC Davis, Materia, Inc, and Cal State LA), because every single one of you helped me get to this point.

It truly does take a village!

Chapter 1, in part, is currently being prepared for submission for publication of the material, Arevalo, G. E.; Frank, M. K.; Decker, K. S.; Theodoraki, M. A.; Theodorakis, E. A. The dissertation author was the primary researcher and author of this material.

Chapter 2, in part, is currently being prepared for submission for publication of the material. Arevalo, G. E.; Capraro, D. T.; Lin, H. H.; Jennings, P. A.; Theodorakis, E. A. The dissertation author was the primary researcher and author of this material.

Chapter 3, in part, is currently being prepared for submission for publication of the material. Arevalo, G. E.; Capraro, D. T.; Lin, H. H.; Jennings, P. A.; Theodorakis, E. A. The dissertation author was the primary researcher and author of this material.

VITA

2011	Bachelor of Science, University of California Davis
2011-2015	Research Associate, Materia, Inc.
2017	Master of Science, California State University, Los Angeles
2017-2022	Teaching Assistant, University of California San Diego
2022	Doctor of Philosophy, University of California San Diego

PUBLICATIONS

Arevalo, G. E.; Frank, M. K.; Decker, K. S.; Theodoraki, M. A.; Theodorakis, E. A. Gambogic acid: multi-gram scale isolation, stereochemical erosion toward *epi*-gambogic acid, and biological profile **2022** (manuscript in preparation).

Arevalo, G. E.*; Capraro, D.*; Margault, H. B.*; Ranjbar, M.; Lin, H.; Jennings, P. A.; Nechushtai, R.; Theodorakis, E. A. Caged xanthones modulate the Fe-S clusters of the NEET protein MiNT **2022** (manuscript in preparation).

Arevalo, G. E.; Cagan, D. A.; Monsour, C. G.; Garcia, A. C.; McCurdy, A.; Selke, M. A photoprotective effect by cation-pi interaction? Quenching of singlet oxygen by an indole cation-pi model system. *Photochem Photobiol* **2020**, *96*, 1200-1207.

Arevalo, G. E. The Influence of Cation-Pi Interactions on Singlet Oxygen Reaction Rates. *CSU Los Angeles Academic Press,* August **2017** (master's thesis).

MacDonald, J. P.; Badillo, J. J.; Arevalo, G. E.; Garcia-Silva, A.; Franz, A. K. Catalytic stereoselective synthesis of diverse oxindoles and spirooxindoles from isatins. *ACS Comb Sci* **2012**, *14*, 285-293.

Badillo, J. J.; Arevalo, G. E.; Fettinger, J. C.; Franz, A. K. Titanium-Catalyzed Stereoselective synthesis of spirooxindole oxazolines. *Org Lett* **2011**, *13*, 418-421.

FIELD OF STUDY

Major Field: Chemistry

Studies in Organic Chemistry & Biochemistry
Professors Emmanuel A. Theodorakis and Patricia A. Jennings

ABSTRACT OF THE DISSERTATION

Fe-S Clusters as Targets for Drug Discovery: Studies of the Interaction Between NEET Protein MiNT and Caged Xanthones

by

Gary Edward Arevalo

Doctor of Philosophy in Chemistry

University of California San Diego, 2022

Professor Emmanuel A. Theodorakis, Chair
Professor Joseph M. O'Connor, Co-Chair

According to the World Health Organization, almost 10 million people worldwide died of cancer in 2020, a number that is expected to rise to over 16 million annually by 2040. As a result, there is a pressing need for drugs that effectively eliminate cancer in new and innovative ways. This dissertation addresses this challenge by first discussing an improved method for the extraction and purification of gambogic acid (GBA), a highly cytotoxic compound that is part of a family of synthetic and natural products collectively known as caged *Garcinia* xanthones (CGXs) . We next identify novel CGXs with improved cytotoxicity in several breast cancer cell lines. Lastly, we identified novel drug leads for proteins that have not been previously identified as amenable to

pharmaceutical modulation. Specifically, we developed an in vitro model that identified new CGXs that can bind to the surface of the mitochondrial NEET protein MiNT and modulate the release of its Fe-S clusters. We identified an improved method for the expression and purification of MiNT, and by utilizing various spectroscopic methods, we measured binding constants of CGXs to MiNT and determined that they have a stabilizing effect on its Fe-S clusters as seen in spectroscopic measurements of their decay. In addition, we identified structural changes of MiNT that occur due to binding of xanthone ligands and their contribution to the stability of MiNT Fe-S clusters. Taken together, our results demonstrate that CGXs are highly cytotoxic in numerous cancer cell lines, and that one of their protein targets, the Fe-S protein MiNT, is a novel promising target for anticancer pharmaceutical development, specifically with CGXs.

Chapter 1

Gram-Scale Extraction & Synthesis of Caged Xanthones

1.1 Introduction

Gambogic acid (GBA) is a complex, poly-prenylated natural product that is part of the caged *Garcinia* xanthone (CGX) family known for its unique chemical structure and myriad of biological activities.[1-122] Aside from its striking chemical architecture, GBA has been shown to have a potent antitumor profile as evidenced by its ability to inhibit cancer cell growth, invasion, metastasis and angiogenesis in various cell-based assays.[123] Although the biological mode of action of GBA is still under study, recent proteomic studies have shown that GBA targets or affects the expression of several proteins that are involved in cancer growth and development.[110,124] Moreover, pharmacological and toxicity studies in animal models have shown that GBA has minimal effects on cardiovascular and respiratory functions suggesting a favorable safety profile

and acceptable therapeutic index.[109] In fact, GBA has entered clinical trials in China for the treatment of colon, non-small cell lung, and renal cancers.[34] Albeit promising, these studies have identified certain challenges in developing GBA as a drug that may stem from its limited stability and suboptimal pharmacokinetics.[125] In principle, these challenges can be overcome by evaluating analogs, conjugates, and delivery systems for GBA.[126] However, these studies have been hindered by the limited availability of this natural product.

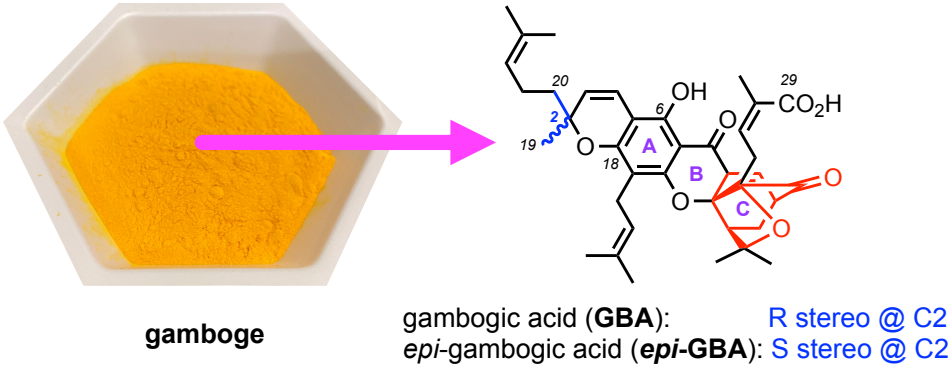

Figure 1.1: Chemical structures of gambogic acid (GBA) and its C2 epimer *epi*-gambogic acid (*epi*-GBA) available from natural gamboge (yellow powder). The cage motif of these compounds and related CGXs is shown in red.

At present, gambogic acid is obtained from gamboge via extraction as its pyridinium salt followed by acidification. This approach is not streamlined and results in GBA that is expensive and primarily available in milligram amounts. More importantly, commercially available GBA is typically contaminated with various amounts of its C2 epimer, a compound known as *epi*-gambogic acid (*epi*-GBA, Figure 1.1). In continuation of our studies on the chemistry and biology of CGXs, we present an efficient method to isolate GBA from readily available gamboge as a single isomer in greater than 97% purity. We also show that GBA can undergo a thermal isomerization to *epi*-GBA via a process that involves formation of an *ortho*-quinone methide intermediate and results in a nearly 6:4 ratio of the two compounds. This stereochemical erosion

at the C2 stereocenter hints to inherent stability issues of this natural product. Nonetheless, we found that both GBA and *epi*-GBA show similar cytotoxicity effects in MDA-MB-231 breast cancer cells suggesting that the ubiquitous C2 isomerization does not significantly impact the bioactivity of this natural product. Moreover, we demonstrate that GBA can be converted to novel amide derivatives with improved cytotoxicity relative to GBA.

1.2 A Brief History of Gamboge

Tropical trees of the genus *Garcinia*, grown mainly in Southeast Asia, Brazil and India, are widely known not only for their high value as sources of food, but also for their impact in arts and sciences.[109] For instance gamboge, the yellow resin from *Garcinia* spp., has been used as a colorant for various artifacts and paintings around the world.[127] Also known as "rongthong" (gold resin) gamboge has been used in Eastern ethnomedicine for its anti-infective and anti-parasitic properties.[128] Efforts to isolate the bioactive constituents of gamboge led to the identification of gambogic acid (GBA, Figure 1.1), an unusual polyprenylated metabolite structurally defined by a tricyclic xanthone backbone (A-B-C ring system) of which the C ring has been converted into a cage structure.[1] The seemingly inconspicuous xanthone motif is further decorated by peripheral substitutions and oxidations to produce an ever-growing family of natural products collectively referred to as caged *Garcinia* xanthones (CGXs).

1.3 Chemical Composition of Gamboge

Although GBA has been extensively studied in biological systems, it remains an expensive natural product, likely due to the difficulty of its isolation and purification. Extracts of gamboge

resin are typically composed of ~30% water-soluble components and ~70% water-insoluble components, which can be extracted with organic solvents such as DCM or MeOH. The average composition of the water insoluble components is typically 30% GBA, 25% *epi*-GBA, and various amounts of other non-identified compounds. This composition was consistent across three different sources of gamboge that we analyzed spectroscopically (Figure 1.2).

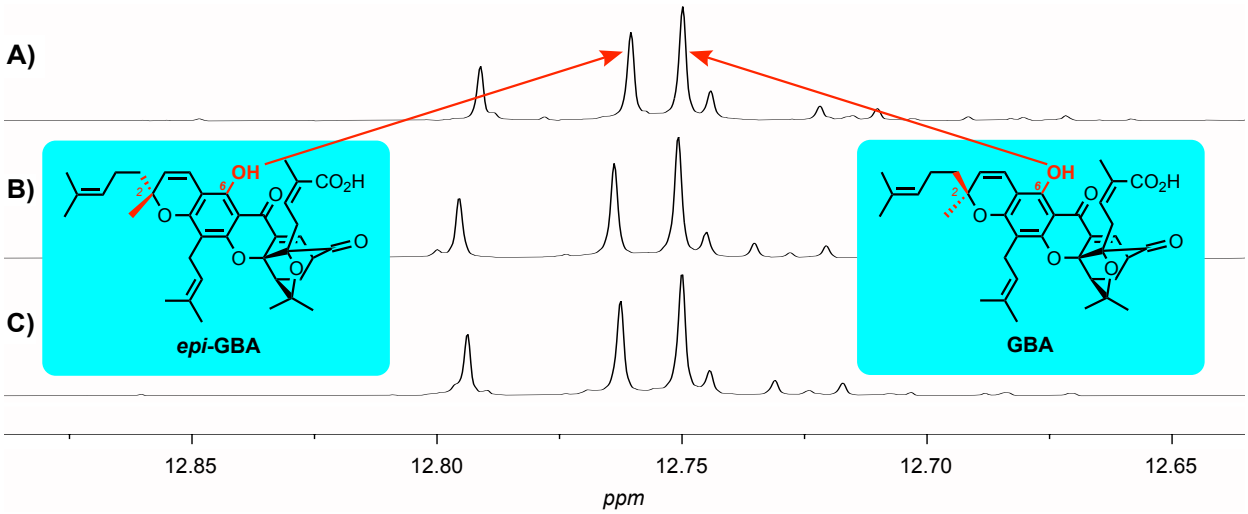

Figure 1.2: Various sources of gamboge. Partial ^{1}H NMR spectra of three different sources of gamboge resin showing the different signals of the C6 hydroxy group of the various components present in gamboge. A) gamboge sourced from Metropolitan Music Company B) gamboge from WoodFinishing Enterprises and C) gamboge from Kremer Pigmente. The representative C6 hydroxy group of GBA appears at 12.75 ppm and that of *epi*-GBA at 12.76 ppm in $CDCl_3$.

1.4 Multigram-Scale Extraction & Purification of GBA

To obtain pure GBA (as a single epimer), gamboge resin in its powder form was first mixed with 300 mL of MeOH (Figure 1.3). The resulting mixture was stirred for 10 minutes and filtered to remove all insoluble components. The off-white solids were washed twice with 100 mL of MeOH, and the filtrate was concentrated to dryness. Overall, 500 mL of MeOH per 100 grams of gamboge were utilized. After extraction and concentration, 70-73 grams of crude gamboge extract were obtained as an amorphous, orange solid. Although MeOH is a nucleophilic solvent known to

yield conjugate addition products of GBA, the high solubility of gamboge in MeOH and easier filtration when using this solvent allowed us to quickly extract and concentrate the extract to dryness in our workflow, which prevented possible chemical modification of GBA by the solvent as determined by ^{1}H NMR spectroscopy.

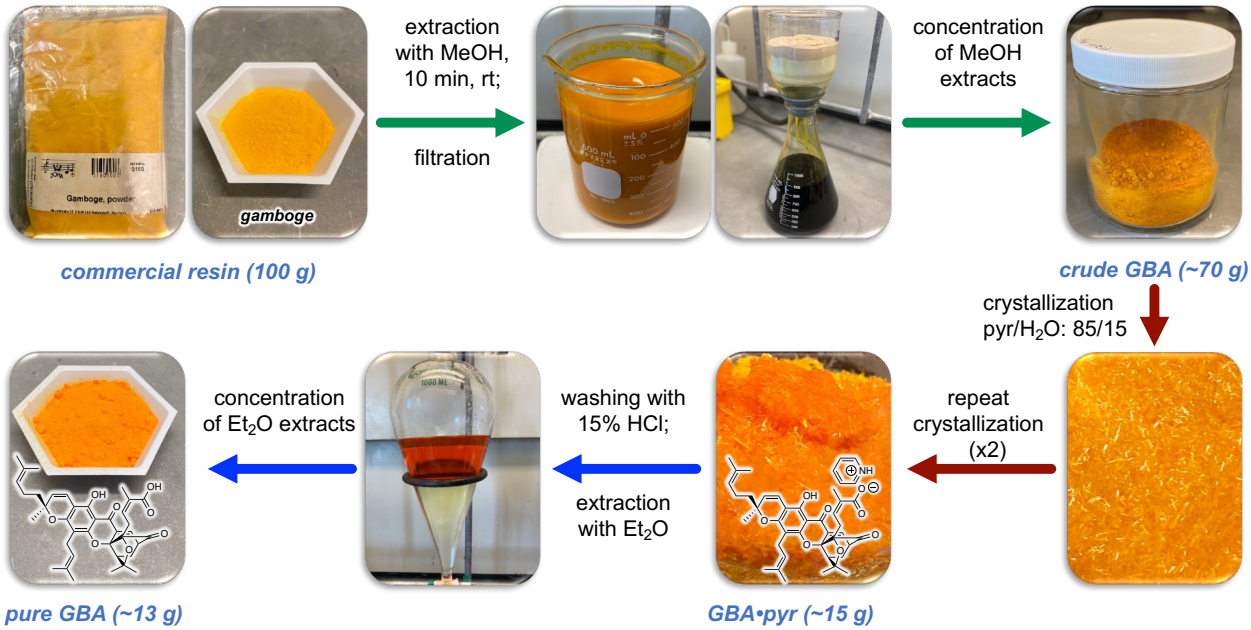

Figure 1.3: Workflow for the isolation of GBA from commercially available gamboge resin. Step 1 (green) involves extraction, filtration, and concentration of crude GBA. Step 2 (red) involves (re)crystallization and isolation of gambogic acid as its pyridinium salt (GBA•pyr). Step 3 (blue) involves neutralization of the pyridinium salt of gambogic acid followed by extraction/concentration to yield pure GBA.

Previous studies have indicated that prolonged exposure of GBA to hydroxylated solvents like MeOH give rise to conjugate addition products (i.e., Michael addition of MeOH to the α,β-unsaturated carbonyl moiety of GBA).[129] We therefore explored the possibility of extracting gamboge with non-nucleophilic solvents like acetone, ACN, DCM, and Et_2O. We found, however, that these solvents were not as effective at extracting GBA from gamboge as MeOH (Table 1.1). We performed test extractions with various solvents, and out of 25 g of gamboge, 7 g of extract

were obtained when using Et_2O. Acetone, ACN, and DCM yielded 12.6-13.8 g of extract from gamboge resin. When utilizing DCM as the extraction solvent, however, the insoluble gum was difficult to remove by filtration compared to all other solvents as swelling of the insoluble materials was observed, which severely hindered filtration using various techniques. When utilizing MeOH as the extraction solvent, the maximum amount of extract was obtained, and we therefore utilized it as part of our purification workflow as show above.

Table 1.1: Extraction of gamboge with various solvents identified MeOH as the best solvent for multigram-scale extraction of gamboge.

Solvent	Amount Solvent Utilized (mL)	Amount Crude GBA Obtained (g)
Acetone	300	13.8
ACN	500	12.6
Diethyl Ether	450	7
DCM	500	13.7
MeOH	200	18

After concentration of the methanolic extract, the amorphous orange solid was dissolved in 125 mL of a mixture containing 20% water in pyridine and heated at 60 ºC until completely dissolved (~10 min). After removal from heat, formation of orange crystals was quickly observed in the solution, which was allowed to sit overnight at room temperature to ensure complete crystallization of GBA as a pyridinium salt (GBA•pyr, Figure 1.4A). The orange crystals were then filtered and dried to yield 22.9 g, which after spectroscopic evaluation, was determined to be composed of 76% GBA•pyr, 18% *epi*-GBA•pyr, and 6% of a non-identified compound (Figure 1.4C). GBA•pyr was then recrystallized by dissolving in 63 mL of 20% water in pyridine at 60 ºC (~10 min) and allowing the solution to cool at room temperature overnight. The enriched crystals were then filtered and dried to yield 15.8 g of GBA•pyr in 89% purity (Figure 1.4D). A third

recrystallization under identical conditions as the second yielded 14.9 g of 97% GBA•pyr and 3% *epi*-GBA•pyr as bright orange crystals. These crystals were then dissolved in Et_2O (200 mL) and washed with 15% aqueous HCl (200 mL). The phases were partitioned, and the organic phase was concentrated to dryness to yield 13.3 g composed of 97% GBA and 3% of *epi*-GBA as confirmed by ^{1}H NMR spectroscopy (Figure 1.4E).

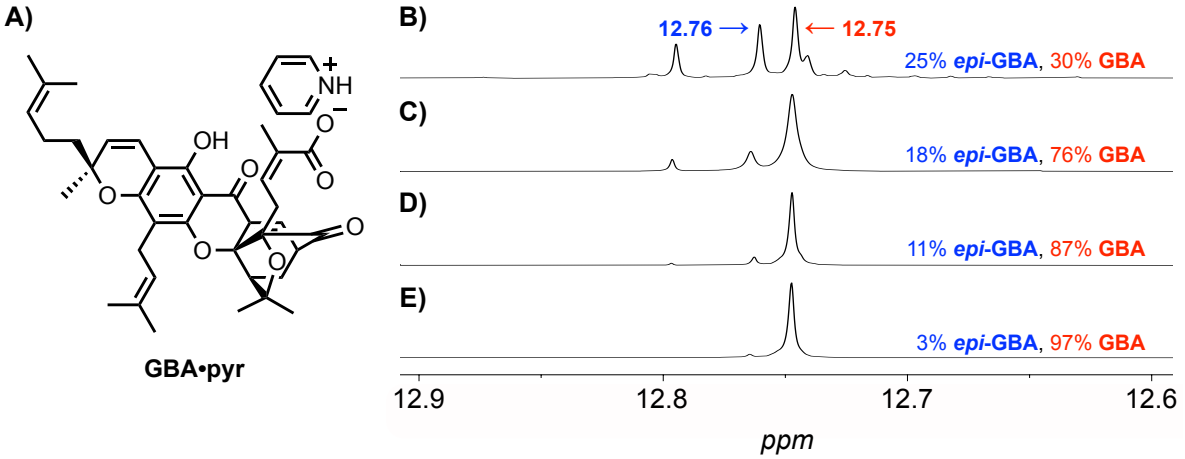

Figure 1.4: Profiling the purification of GBA from gamboge. A) Chemical structure of GBA•pyr, the pyridinium salt of GBA B) partial ^{1}H NMR spectrum showing the representative C6 hydroxy groups of the various components in crude gamboge extract and C-E) spectra of GBA during and after several rounds of pyr/water crystallizations, which result in ≥ 97% pure GBA. Spectra C-E are of acidified samples of GBA•pyr for ^{1}H NMR analysis.

Overall, our improved method for the extraction and purification of GBA from gamboge is reproducible, easy, and cost-effective, yielding multigram quantities of GBA in 97% purity as confirmed by ^{1}H NMR spectroscopy. It should be noted that we did not observe further improvement in purity with more crystallizations than what we utilized for our purification workflow. Considering only reagents, we estimate that the cost of extracting and purifying GBA from commercially available gamboge using our method is marginal when compared to the cost of commercially available pure GBA (i.e., Sigma-Aldrich).

1.5 Epimerization Studies of GBA

Among the many unique chemical features of GBA is its benzopyran moiety, also known in this case as a 2,2-dialkyl chromene. The chromene system is a common motif found in numerous bioactive synthetic and natural products, including Likonide B, Cannabichromenic acid, Mahanimbine, and Panduratin B, which all possess chirality at C2 (Figure 1.5). In GBA, the C2 quaternary center in the benzopyran ring gives rise to two epimers: GBA having the (R) stereochemical configuration, and *epi*-GBA having the (S) configuration (Figure 1.1).

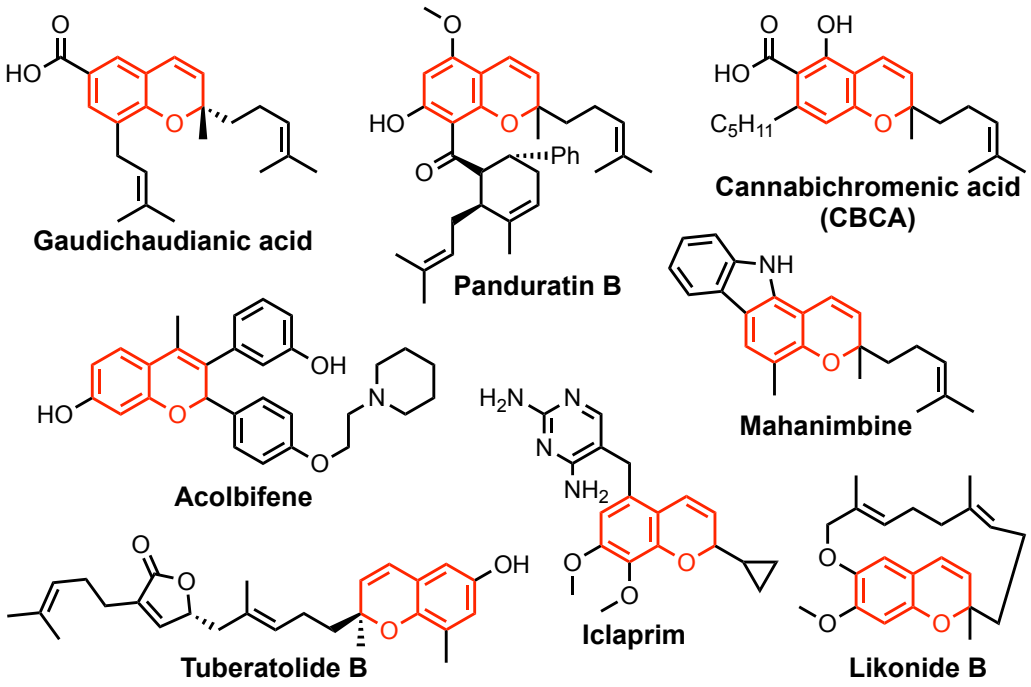

Figure 1.5: Chemical structures of chromene-containing bioactive compounds.

Puzzled by the presence of *epi*-GBA in all fractions, we wondered whether GBA could isomerize to *epi*-GBA, and if this is due to an in-situ isomerization of the C2 stereocenter that is located on the chromene ring system. In addition, we also wondered how readily this isomerization can occur. It is known that isomerization of 2,2-dialkyl chromenes can occur under photochemical

and thermal conditions, such as that observed by Kolc and Becker during their study of the spectroscopic and photochromic properties of spiropyran (Figure 1.6).[130] However, it is not known whether a similar isomerization can occur in the chromene system of GBA. This observation led us to consider the thermal stability of GBA and its potential to isomerize at C2 into *epi*-GBA under heat conditions, especially during heating in pyridine/water to form GBA•pyr crystals, a key step in our multigram scale isolation and purification of GBA discussed earlier.

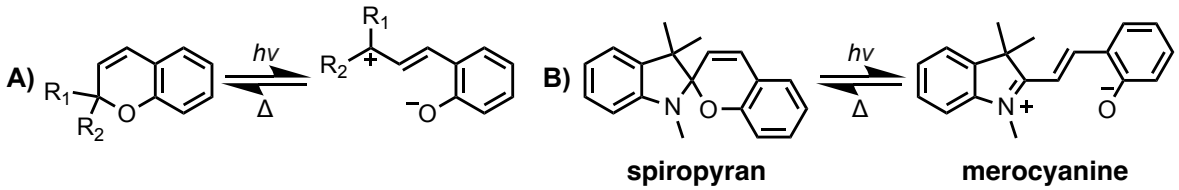

Figure 1.6: A) Proposed mechanism of reversible photochromic and thermal ring-opening of chromenes and B) reversible ring-opening of spiropyran to merocyanine.

To determine if GBA undergoes a thermal ring-opening that results in epimerization to *epi*-GBA, we heated solutions of GBA in various deuterated solvents that enabled us to monitor epimerization by ^{1}H NMR spectroscopy. Our initial studies on the epimerization of GBA in $CDCl_3$ showed that GBA, in fact, epimerizes to *epi*-GBA under heat conditions. We tested several solvents to determine the influence of the solvent on the epimerization, and our results showed that GBA epimerizes faster in DMSO-*d*6 and C_5D_5N than it does in $CDCl_3$ (Figure 1.7). After four hours of heating at 100 ºC, solutions of GBA in DMSO-*d*6 and pyridine-*d*5 resulted in a ratio of GBA:*epi*-GBA of 58:42 and 61:39, respectively. Under the same conditions, in $CDCl_3$, the ratio of GBA:*epi*-GBA was observed to be 73:27. Although DMSO is the most polar of the three solvents we tested, the epimerization occurs similarly in both DMSO and pyridine, which have a polarity approximately equal to chloroform.[131] Heating GBA in $CDCl_3$ at higher temperatures,

however, achieved the same epimerization ratio observed in DMSO and in pyridine at a comparable rate.

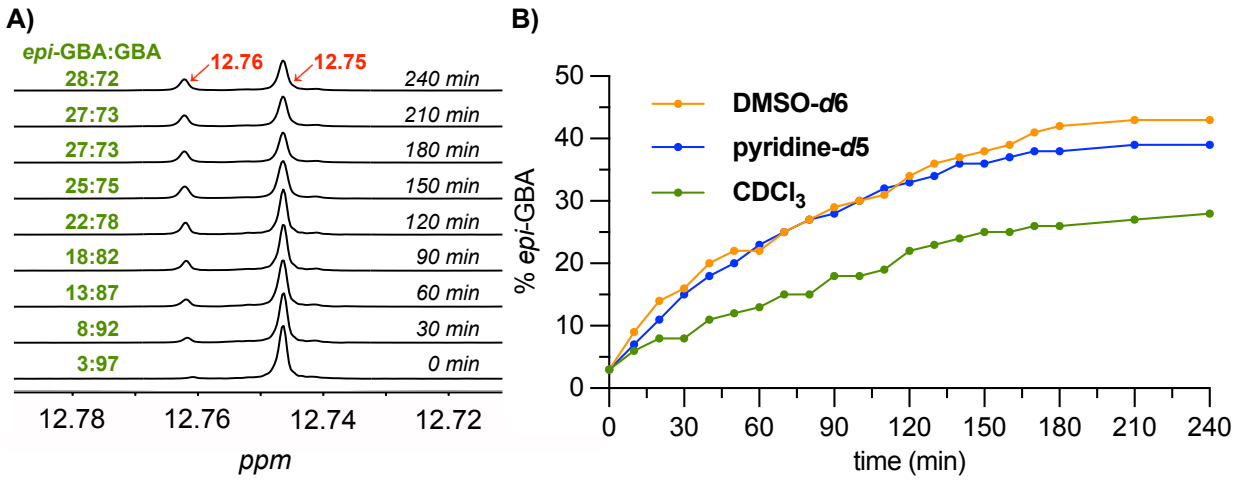

Figure 1.7: Solvent effect on the epimerization of GBA to *epi*-GBA. A) Solvent studies on the epimerization of GBA at 100 ºC and B) ^{1}H NMR of the phenolic moiety of GBA in $CDCl_3$ representing the epimerization of GBA to *epi*-GBA at C2.

To further probe the epimerization of GBA, we settled on DMSO-*d*6 as our model solvent due to its high boiling point and ability to fully epimerize GBA in a reasonable timeframe. Since GBA is a Bronsted acid, we wondered whether the carboxylic acid moiety is responsible for and/or contributes to the epimerization rate considering that the calculated value for the pK_a of the carboxyl proton is 4.58 (determined using ACD/PhysChem Suite 2021). Since the phenolic beta-hydroxy moiety is also acidic, with a calculated pK_a value of 8.90, we wondered whether this proton could also facilitate the epimerization. To test our hypothesis, we first replaced the carboxylic acid moiety of GBA with an amide moiety, such as the thiomorpholine moiety seen in **1** and heated a solution of **1** in DMSO-*d*6 at 100 ºC for four hours. Eliminating the carboxylic acid moiety caused an insignificant change in the epimerization of GBA: the epimerization of **1** was

nearly identical to that of GBA where the final ratio of GBA:*epi*-GBA was observed to be 58:42 and the final ratio of **1**:*epi*-**1** was observed to be 59:41 (Figure 1.8).

Since almost no change in the epimerization of GBA was observed when converting the carboxylic acid to ester **1**, we wondered whether eliminating both acidic protons—the carboxylic and phenolic protons—would hinder the epimerization of GBA. Therefore, we synthesized compound **2** where both acidic protons have been replaced with a methyl group. We determined that under the same conditions as GBA and **1**, **2** epimerizes at a much slower rate. In the case of **2**, the ratio of **2**:*epi*-**2** after four hours of heating at 100 ºC was observed to be 89:11 by ^{1}H NMR, a remarkable difference compared to **GBA** and **1**.

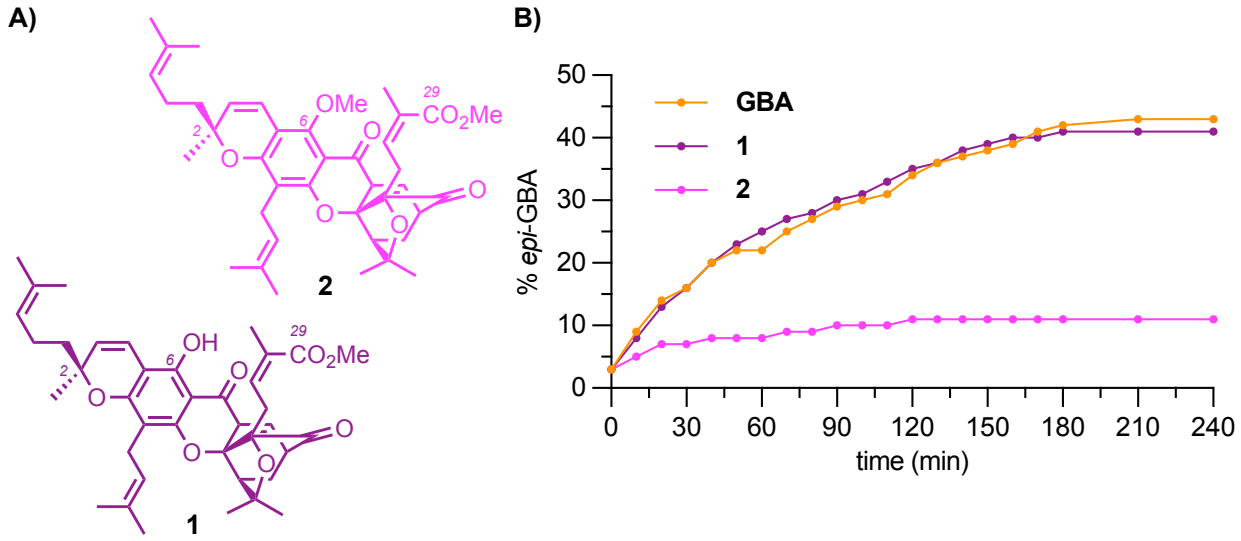

Figure 1.8: Evaluation of the effect of acidic protons on the epimerization of GBA. A) Chemical structure of compounds **1** and **2** and B) a graphical representation of the epimerization of GBA, **1**, and **2** in DMSO-*d*6 at 100 ºC over 4 h.

1.6 Proposed Epimerization Mechanism of GBA to *epi*-GBA

Our initial studies on the epimerization of GBA to *epi*-GBA lead us to believe that the epimerization was likely occurring by an acid-facilitated process. We envisioned a mechanism

where the chromene oxygen is first protonated, which causes the C-O bond between the chromene oxygen and C2 to break. This, in turn, could cause formation of a carbocation, which is especially stabilized by its tertiary and allylic character. This mechanism was corroborated when we observed little epimerization of **2** under the same conditions as GBA and **1**. However, upon heating of **2** in DMSO-*d*6 at 150 ºC for 30 minutes, a 52:48 epimerization ratio of **2** to *epi*-**2** was observed. Consequently, we propose a different mechanism previously observed in simpler chromene systems.

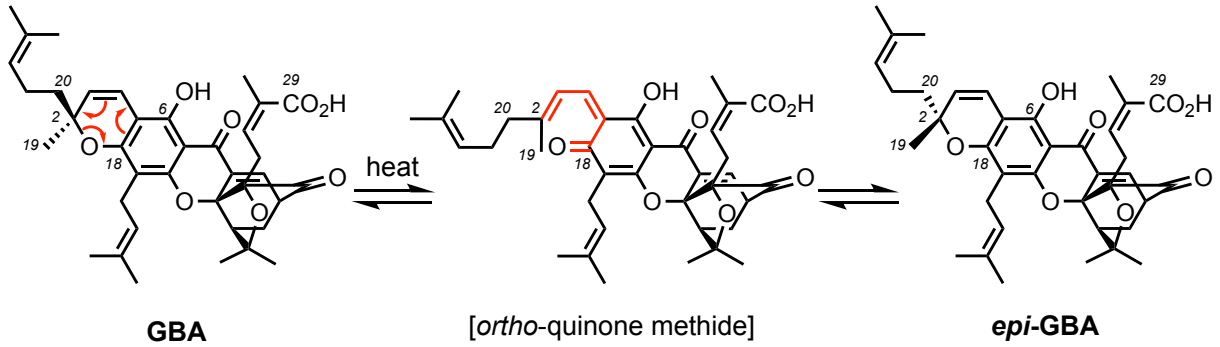

Figure 1.9: Proposed oxa-6π electrocyclic thermal isomerization mechanism of GBA to *epi*-GBA.

Due to our observation of the epimerization of **2**, we propose that the epimerization of GBA likely occurs through the formation of an ortho-quinone methide, which is subsequently converted to *epi*-GBA via a thermal oxa-6π electrocyclic mechanism (Figure 1.9).[132] Our studies demonstrate that the epimerization of GBA to *epi*-GBA occurs at a significantly higher rate at mild temperatures when acid is present. At elevated temperatures (150 ºC or higher), the epimerization occurs readily without a Bronsted acid. Although we cannot preclude the possibility that both mechanisms occur simultaneously with or without acid, it is highly likely that under acid-free conditions, the pericyclic mechanism predominates.

1.7 Biological Evaluation of GBA & *epi*-GBA

Inspired by several accounts of different bioactivities between several natural product isomers, we set out to determine if there is a difference in the biological activity of pure GBA and a mixture of GBA and *epi*-GBA.[31, 133] GBA was isolated according to our protocol mentioned previously, and a clean mixture of GBA and *epi*-GBA was prepared by heating 1 g of GBA in 10 mL of $CHCl_3$. Our previous studies on the epimerization of GBA showed that 100 ºC is an ideal temperature to study GBA spectroscopically. However, GBA can be heated to 120 ºC, which ensures a faster isomerization without affecting the final ratio of GBA and *epi*-GBA observed at lower temperatures (Figure 1.10). After heating, $CHCl_3$ is removed under reduced pressure to afford a 60:40 mixture of GBA:*epi*-GBA as an orange, amorphous solid in quantitative yield.

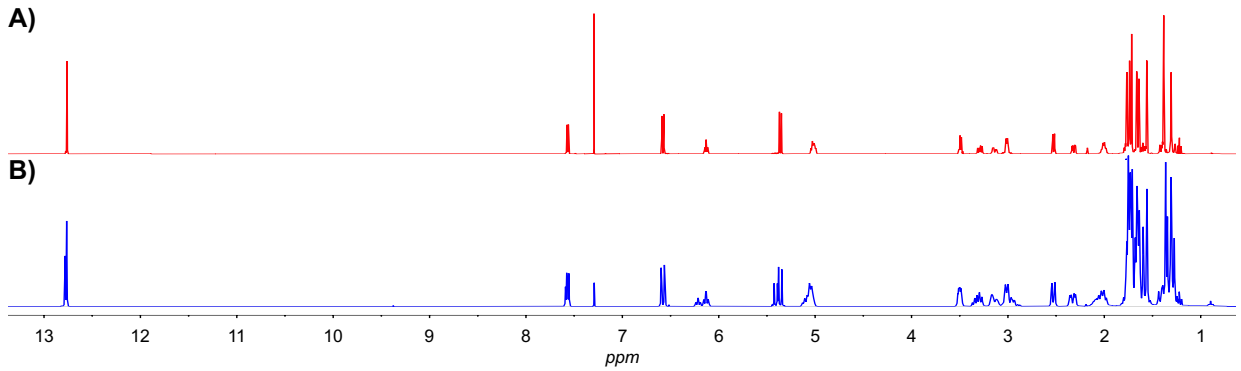

Figure 1.10: Comparison of pure GBA and as a mixture of epimers by ^{1}H NMR spectroscopy. A) GBA as one epimer and B) a 60:40 mixture of GBA:*epi*-GBA (equilibrated GBA) prepared on a 1 g scale. Equilibrated GBA can be readily prepared by heating pure GBA in chloroform at 120 ºC using a sealed vessel.

Our lab previously established that GBA is bioactive in the triple negative breast cancer cell line MDA-MB-231.[123] Therefore, in order to determine if there is a difference in bioactivity between pure GBA (> 97%), a mixture of GBA:*epi*-GBA (60:40), and GBA•pyr, our collaborators, Maria Theodoraki and coworkers, obtained brightfield microscopy images of MDA-MB-231 cells

treated with each 1 μM of each compound after 24h (Figure 1.11). The images demonstrated that all three compounds are cytotoxic, showing clear and evident cell death in cells treated with 1 μM GBA, its pyridinium salt, and a mixture of epimers compared to the control, cells were treated with 50 μM of our compound delivery solvent, DMSO.

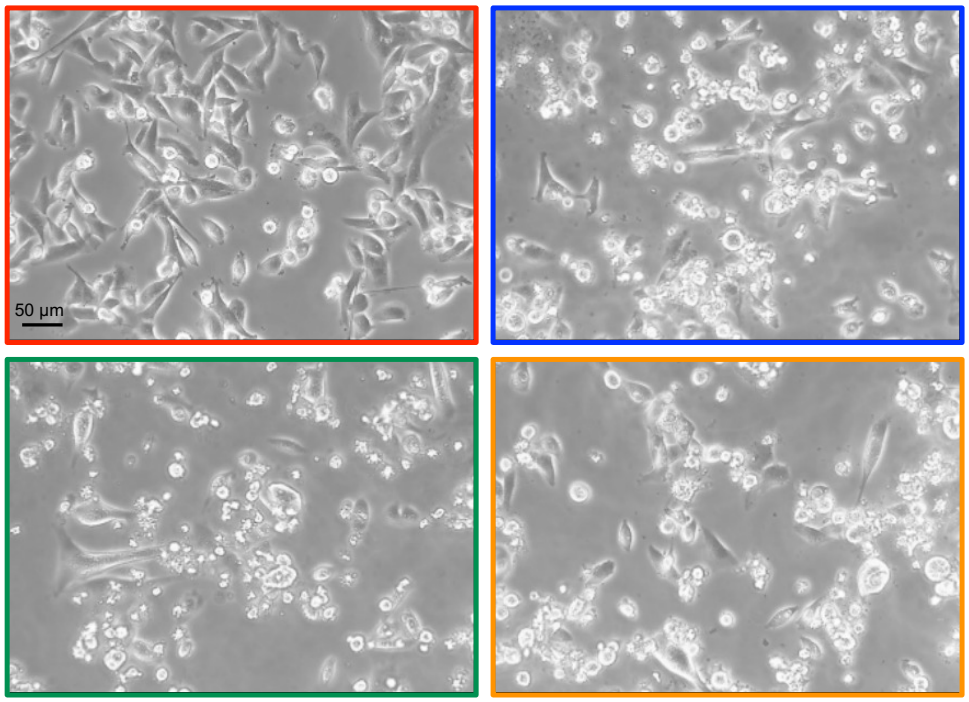

Figure 1.11: Images of MDA-MB-231 TNBC cells after 24 h incubation with 50 μM DMSO (red) and 1 μM each of GBA (blue), GBA:*epi*-GBA (green), and GBA•pyr (orange). Images were obtained using a brightfield microscope at 20x objective.

Inspired by this result, we conducted further ATP viability assays using MDA-MB-231 cells that were treated with each compound at concentrations of 0.2, 0.5, 1, 5, 10, and 20 μM (Figure 1.12) and incubated for 24 h. At 20 μM treatment with each compound, nearly no cell viability is observed. At 5 and 10 μM, a similar viability was observed for all three compounds, which was between 1-3%. A similar trend was observed at 1, 0.5, and 0.25 μM where all three compounds showed similar cytotoxicity of 12-14%, 38-39%, and 81-91%, respectively.

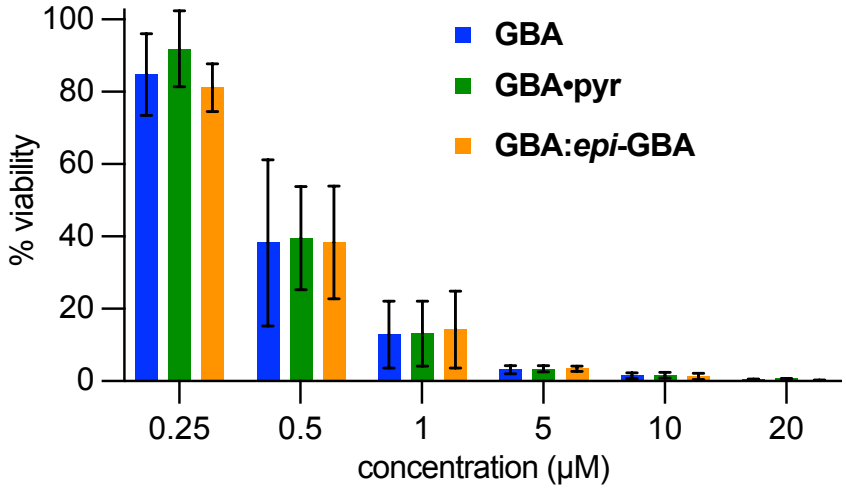

Figure 1.12: ATP assay portraying percent viability of MDA-MB-231 cells treated with each compound at various concentrations after 24 h exposure. Statistical analysis using ANOVA single factor was performed to determine statistically significant differences between each GBA form.

Given the effect of gambogic acid formulations on the morphology and viability of the MDA-MB-231 cell line (Figures 1.11 and 1.12), we further investigated the kinetics of induction of apoptosis. To that end, activation of the executioner caspases 3/7 was studied after 3, 6, 12, and 24 h of treatment with 1 μM of each GBA formulation (Figure 1.13A). All three formulations led to a similar increase in the activity of executioner caspases 3/7 with maximum activity reached after 12 h of exposure to 1 μM of each formulation, indicating similar performance in induction of cell death via apoptosis.

Activation of the executioner caspases leads to proteolytic cleavage of effector proteins and degradation of cellular components. A well-known substrate targeted by activated caspases is poly (ADP-ribose) polymerase-1 (PARP-1), and its proteolytic processing by caspases 3/7 generates a catalytic fragment with 89 kDa size (cPARP) that is considered a molecular hallmark of apoptosis. With this in mind, we sought to verify the induction of the apoptotic pathway by western blot detection of cleaved PARP (Figure 1.13B). Treatment of MDA-MB-231 breast cancer cells with 1 μM of the equilibrated mixture, GBA•pyr or >97% GBA for 24 h was sufficient to

allow detection of the cleaved large fragment (89 kDa) of human PARP asserting apoptotic cell death.

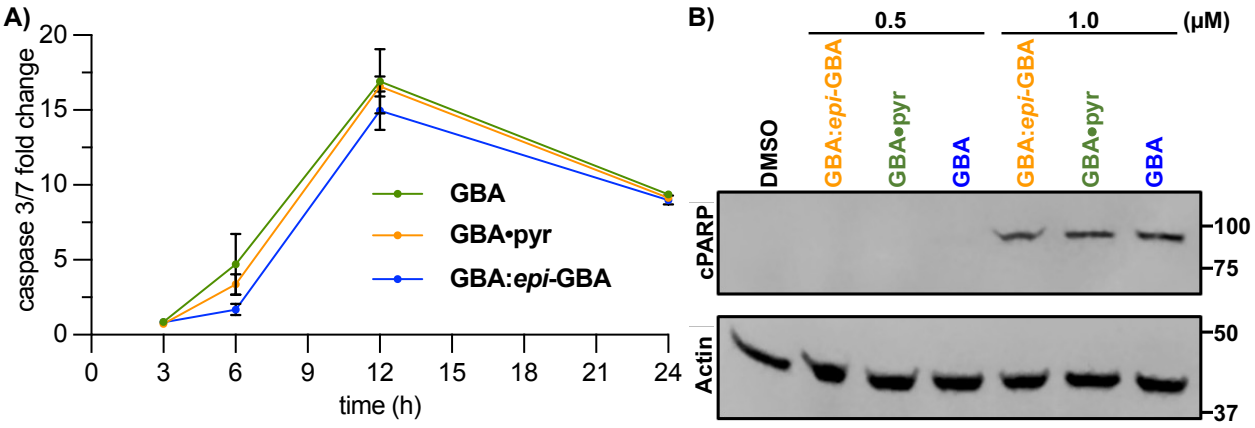

Figure 1.13: Kinetics of induction of apoptosis in MDA-MB-231 cells by GBA formulations. A) Time course analysis of caspases 3/7 activity in MBA-MB-231 cells upon incubation with 1 μM of various GBA formulations. Data presented are mean ± SD (n=3) B) Detection of cleaved PARP (cPARP) via western blot analysis. MDA-MB-231 cells treated with 0.5 and 1.0 μM of GBA formulations were lysed after 24 h; 20 μg of total protein was used for gel electrophoresis. After transfer, the membrane was probed with anti-cPARP; actin was used as a loading control.

From our experimental result, we concluded that there is no statistical difference in the bioactivity of GBA, its pyridinium salt or a roughly equal mixture of GBA:*epi*-GBA in our MDA-MB-231 TNBC cell assay. However, these results do not preclude the possibility of a difference in bioactivity in other in vitro or in vivo models. Therefore, we highly encourage a thorough examination of the quality of GBA from any source prior to biological studies, and we recommend our purification method for multigram quantities of high quality GBA at an affordable rate.

1.8 Synthesis & Biological Evaluation of Synthetic CGX MAD28

Previous work in our lab demonstrated that MAD28, a synthetic derivative of GBA, is bioactive against triple negative (TNBC) and inflammatory breast (IBC) cancer cells.[14, 123] In

collaboration with the Jennings (UCSD) and Nechushtai (HUJI) labs, we identified MAD28 as a selective binder to NEET proteins, which are proteins known to be overexpressed in IBC and TNBC.[134] Binding of MAD28 to NEET protein mitoNEET, for example, causes the protein to release iron within cancer cells, which leads to ROS damage and eventually cell death. This was observed in the selective cytotoxicity of MAD28 on the TNBC cell line MDA-MB-231 over normal human breast MCF-10A control cells. One of the most promising aspect this work is that accumulation of MAD28 in TNBC and IBC cells is selective, which was shown to be, in part, the result of NEET protein upregulation in cancer cells.[135]

Due to promising results obtained from our previous studies of the interaction between MAD28 and NEET proteins, we hypothesized that targeting a newly identified and yet undrugged NEET protein isoform MiNT with caged xanthones will afford an additional pathway in the search for a treatment of cancers like TNBC and IBC, which is the topic of chapters 2 and 3.

To elucidate the binding profile of MAD28 to NEET protein MiNT, the synthesis of MAD28 must be optimized to efficiently produce high quantities of MAD28 for biological studies. Structurally, MAD28 does not contain the chromene or carboxyl moieties of GBA, however, it does contain the cage and xanthone backbone (Figure 1.14 in red). Since we can easily obtain multigram quantities of GBA, its direct derivatization to MAD28 would be ideal. However, because of the chemical complexity of GBA, we determined that a more chemically feasible option is to synthesize MAD28 from inexpensive and commercially available building blocks. Our strategy would incorporate optimized chemistry previously developed in our laboratory, including the synthesis of the cage motif in MAD28 from an O-allylated xanthone backbone that undergoes a Claisen rearrangement followed by a Diels-Alder reaction (Figure 1.14 in blue).

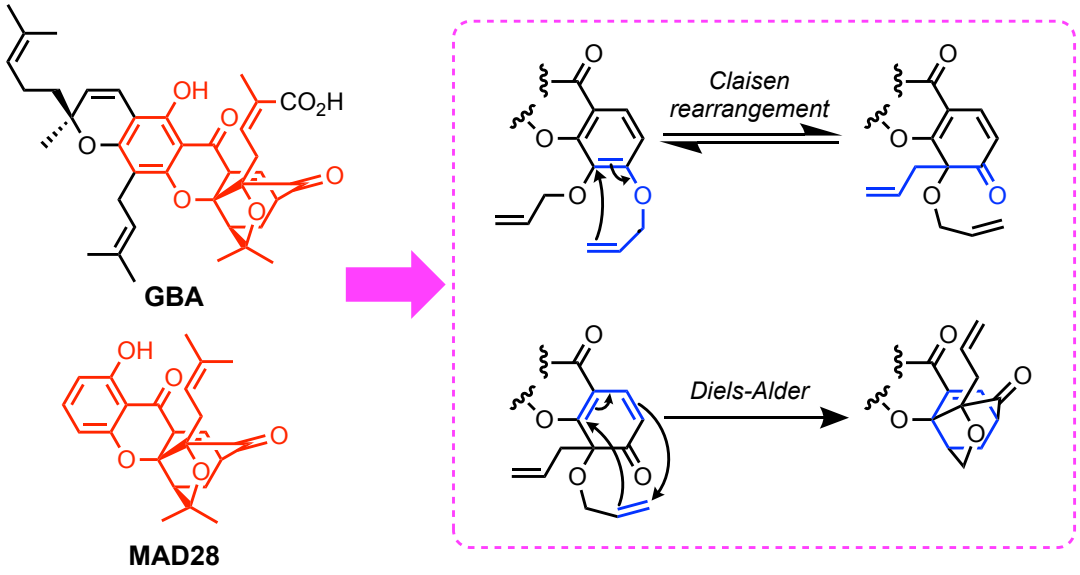

Figure 1.14: Mechanism for the formation for the cage moiety of caged xanthones. GBA and MAD28 have a common core structure, a cage and xanthone backbone (red). Both GBA and MAD28 can be synthesized from an O-allylated xanthone, which undergoes a Claisen rearrangement followed by a Diels-Alder reaction (blue).

Our MAD28 synthetic strategy began with the synthesis of acid chloride **3**, obtained in quantitative yields by treating 2,6-dimethoxybenzoic acid with oxalyl chloride in DCM at room temperature (not shown). **3** is then treated with 1,2,3-trimethoxybenzene to generate **4** via a Friedel-Crafts acylation reaction utilizing $AlCl_3$ as the Lewis acid (Figure 1.15). Since this reaction is exothermic, it is initially performed at 0 ºC and is allowed to slowly warm to room temperature. Once complete, the Lewis acid was quenched, and the solution was concentrated to dryness. To avoid utilizing column chromatography and further increase the efficiency of our synthetic strategy, we opted to recrystallize **4** in MeOH, which afforded 15 g of 4 in > 99% purity as confirmed by ^{1}H NMR, and 80% yield. In addition, the connectivity of the hydroxy group of **4** was dubious as it was not known whether the acid chloride or 1,2,3-trimethoxybenzene underwear demethylation during the reaction. Our purification strategy allowed us to obtain X-ray quality crystals of **4**, which we used to confirm that it is 1,2,3-trimethoxybenzene that undergoes demethylation to produce **4** (appendix Tables 1.2-1.6).

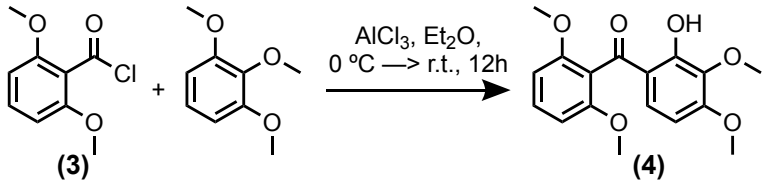

Figure 1.15: Synthesis of **4** via a Friedel-Crafts acylation reaction.

Previous strategies for the subsequent step, formation of **5**, were challenging as the base-induced cyclization was difficult to reproduce. The cyclization of **4** to **5** was previously achieved by heating **4** in a mixture of MeOH/H_2O to reflux temperatures under basic conditions for three days. Despite vigorous refluxing for prolonged periods of time and testing of various MeOH/H_2O solvent combinations, we could only obtain **5** in modest yields (40%). We determined that MeOH is not necessary for the reaction, which was likely utilized previously due to the poor solubility of **4** in water. **5** can in fact be synthesized by using only water as the solvent since heating under basic conditions to 120 ºC for 12 hours in a pressure vessel fully solubilizes **4** and allows the cyclization to readily occur (Figure 1.16). Our strategy reproducibly afforded 14 g of **5** with > 99% purity and quantitative yields, and utilized recrystallization as the purification method, which further obviated the need for column chromatography. The high efficiency, low reaction time, and environmentally friendly synthesis of **5** was largely possible by conducting the reaction in a heated pressure vessel instead of refluxing at ambient pressure for three days.

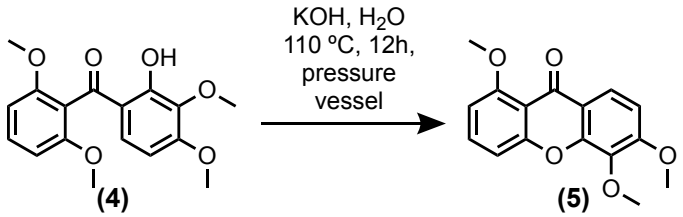

Figure 1.16: Synthesis of xanthone **5** via an intramolecular cyclization of **4**.

Deprotection of **5** under acidic conditions to afford xanthone **6** was also previously challenging as the reaction would yield a mixture of mono-, di-, and fully deprotected xanthones, which afforded **6** in only modest yields (42%) after purification. Our strategy for the synthesis of **6** involved the heating of **5** under acidic conditions and further utilization of a pressure vessel to perform the reaction (Figure 1.17). As the reaction mixture was allowed to cool, **6** precipitated from the acidic solution as a glittery gold solid, which was filtered and dried without further purification to afford **6** (10 g, 87% yield) in > 99% purity as confirmed by ^{1}H NMR spectroscopy.

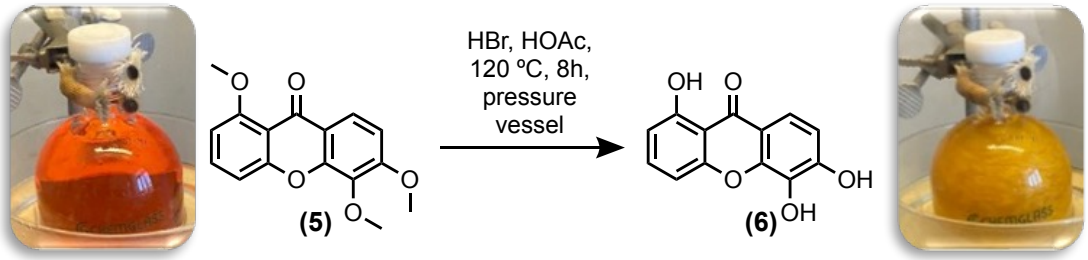

Figure 1.17: Synthesis of trihydroxy xanthone **6** via deprotection of trimethyl xanthone **5**. An image of the dissolution of **5** after heating (left) and of a cooled pressure vessel after the reaction is complete (right), which highlights the precipitation of **6** as a gold solid that can be easily isolated via filtration.

A complex aspect of our MAD28 synthetic strategy is a palladium-catalyzed O-allylation of **6** using diallyl carbonate **7** to form **9**. Pd-catalyzed O-allylations are notoriously challenging and typically successful only on a small scale. Our strategy, however, reproducibly afforded diallyl xanthone **9** in multigram quantities (Figure 1.18). Previous attempts to generate **9** often led to mixed results, with mono-allylation and O-prenylation observed as competing side reactions. We determined, however, that the purity of the palladium catalyst, $PdPPh_4$, is highly variable depending on the source, likely due to its air-sensitive nature, and that for the reaction to work effectively with minimal side products, the palladium complex must be a bright yellow color,

which typically signifies high catalyst purity. We found that the highest quality of $Pd(PPh_3)_4$ can be obtained from Strem Chemicals, Inc.

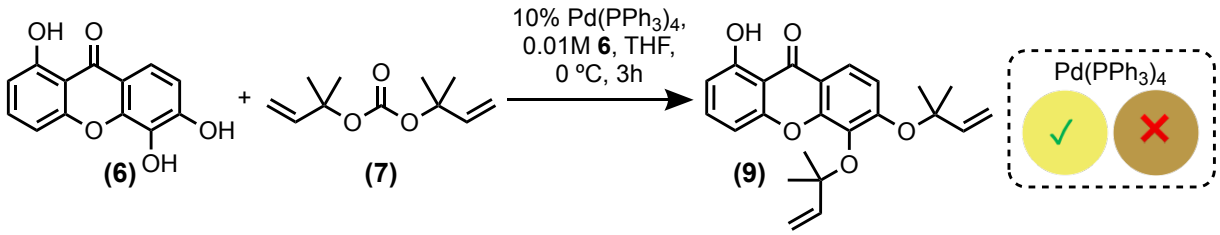

Figure 1.18: Palladium-catalyzed double O-allylation of xanthone **6** and the various colors of $Pd(PPh_3)_4$, which in pure form bright yellow (left circle) and brown when impure (right circle).

Despite utilizing high purity $Pd(PPh_3)_4$, the reaction initially yielded a mixture of mono- and di-O-allylated products. We subsequently determined that the reaction is heavily concentration-dependent, and that to consistently produce di-allylated compound **9** with few or no side products, the reaction must be conducted at a concentration of 0.01 M based on **6**. The reaction is initially translucent and green, but at higher concentrations of **6**, we observed the formation of an unidentified precipitate, which we speculate is a metal chelate of the palladium catalyst that cannot perform O-allylation. We ultimately obtained 1.2 g of **9** in > 99% purity and 65% yield. Since **9** is a viscous and labile yellow liquid, we purified **9** using column chromatography, which is the only instance we employ this purification technique in our synthetic strategy of MAD28.

A drawback of our palladium-catalyzed O-allylation is that the reaction utilizes an excess of **7** (10 mol eq.). Fortunately, **7** was easily synthesized by first reacting 1,1'-carbonyldiimidazole with 2-methyl-3-buten-2-ol in DCM at room temperature to afford **8**, which was subsequently reacted with deprotonated 2-methyl-3-buten-2-ol at lower temperatures to afford 13 g of **7** as a colorless liquid with > 99% purity and 85% yield after purification (Figure 1.19). The purification

of **7** was efficiently achieved by utilizing vacuum distillation at 30 ºC, which had not been previously attempted with this substrate due to its lability.

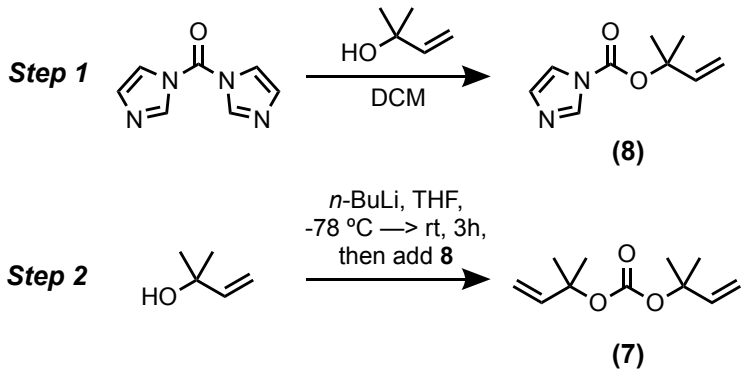

Figure 1.19: Diallyl carbonate **7** is synthesized in a two-step process that begins with 2-methyl-3-buten-2-ol and 1,1'-carbonyldiimidazole.

The final step of our MAD28 synthesis employed a thermal rearrangement of **9** involving a Claisen rearrangement followed by a Diels-Alder reaction. To generate the cage moiety of MAD28, **9** was heated in DMF at 100 ºC for three hours (Figure 1.20). Although the reaction is faster at 120 ºC, we observed approximately 10% formation of *neo*-MAD28 at or above this temperature. To mitigate formation of the *neo* product, we opted to perform the reaction at 100 ºC. MAD28 was isolated as a yellow crystalline solid in > 99% purity by first dissolving MAD28 in DCM (50 mg/mL) then adding five times the quantity of hexanes by volume above the DCM layer without mixing the two solvents and allowing the crystallization to occur slowly overnight.

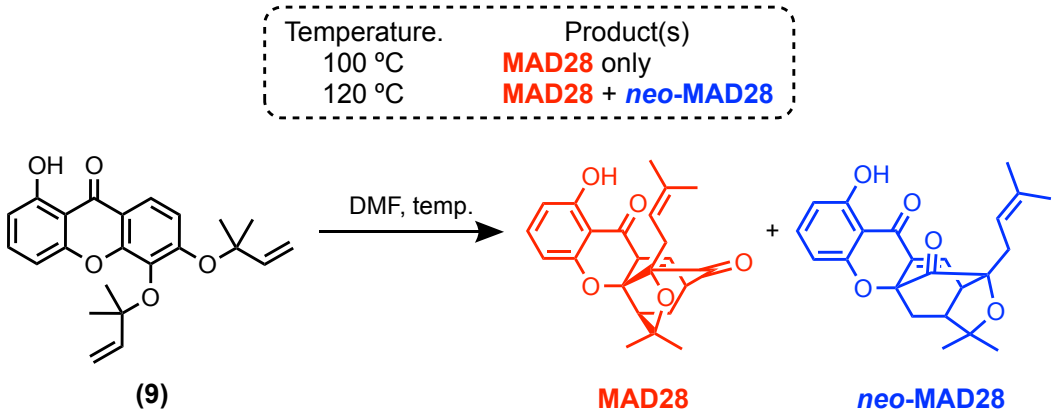

Figure 1.20: Formation of the cage moiety of MAD28. The final step in our synthesis of MAD28 involves a Claisen rearrangement followed by a Diels-Alder reaction, which affords MAD28 and *neo*-MAD 28 in a 9:1 ratio, respectively when performed at 120 ºC. At 100 ºC, the reaction affords only MAD28.

1.9 Synthesis of Biologically Active CGX Natural Product Forbesione

Forbesione is a bioactive natural product that has a similar chemical structure to GBA, notably the cage and xanthone backbone, and is a hydroxylated version of MAD28. Previous studies in our lab identified forbesione as a potent and selective cytotoxic agent in TNBC and IBC cell lines. Unlike GBA, however, a broad understanding of its bioactivity has not been achieved as forbesione is found in significantly lower quantities in nature compared to GBA. As a result, the extraction of forbesione is not an easy or practical option for obtaining high quantities for biological evaluation. To solve the issue of supply, we optimized a method for the synthesis of forbesione that utilizes similar chemical strategies in our synthesis of MAD28.

The total synthesis of forbesione, first achieved by Tisdale et al., afforded 60 mg of pure product.[136, 137] Although this strategy yielded more forbesione than its extraction from natural sources likely would, obtaining larger quantities of forbesione remained an issue. This is likely a result of the difficulty in achieving efficient and selective O-allylated products, which in this case

are necessary precursors for the tandem Claisen/Diels-Alder rearrangement that affords the cage motif.

To form xanthone **10**, we initially employed the strategy we utilized to for xanthone **6** (Figure 1.21A). Under the same conditions, however, the analogous starting materials, 1,2,3-trimethoxybenzene and 2,4,6-trimethoxybenzoyl chloride, proved to be poor substrates for the Friedel-Crafts reaction as it afforded the *para*-methoxy analogue of **4** in only 20% yield. In addition, the cyclization and deprotection steps proved to be low-yielding, especially the deprotection step as it yielded a mono-methylated product and **10** in equal amounts (not shown). Therefore, we opted to employ the strategy previously developed by Tisdale et al. for the synthesis of **10**, which utilized a zinc chloride mediated condensation of 1,3,5-trihydroxybenzene with 2,3,4-trihydroxybenzoic acid in $POCl_3$ (Figure 1.21B).[136] Although this strategy utilizes $POCl_3$, we isolated 5 g of **10** as a brown solid in 60% yield. Efforts to circumvent $POCl_3$ are ongoing.

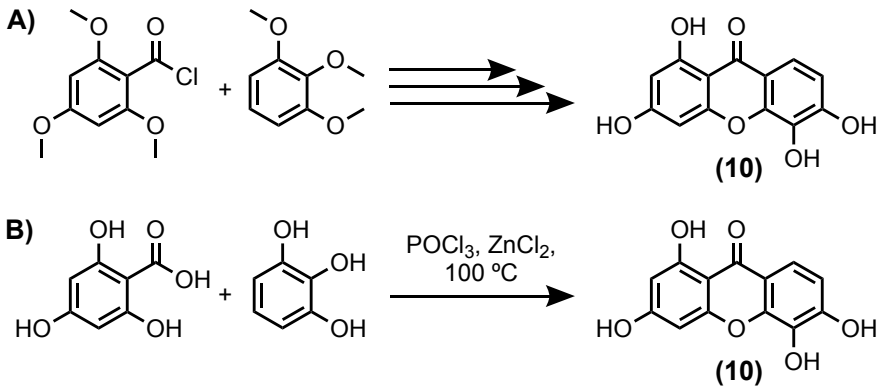

Figure 1.21: A) General scheme for the synthesis of tetrahydroxy xanthone **10** utilizing the multi-step synthetic strategy for **6** B) A one-pot zinc-mediated Friedel-Crafts acylation between 2,3,4-trihydroxybenzoic acid and 1,3,5-trihydroxybenzene followed by cyclization utilizing $POCl_3$ as the solvent/dehydrating agent yields **10**. Although not ideal, B is a higher-yielding synthetic strategy than A.

Tisdale et al. achieved O-allylation of xanthone **10** in a two-step process that employed a copper-catalyzed propargylation of the C3, C5, and C6 hydroxy groups of **10** with 2-chloro-2-

methylbutyne under basic conditions, which afforded tri-propargyl **11** in 25% yield (Figure 1.22A).[136] A subsequent Lindlar hydrogenation of **11** yielded the O-allylated precursor **12**. Our approach to **12**, however, utilized a one-step palladium-catalyzed O-allylation of **10** with carbonate **7** (Figure 1.22B), which afforded gram quantities of **12** in 63% yield. A drawback of our approach is that, like the O-allylation of MAD28 precursor **9**, the O-allylation of **10** must be performed at low concentrations of xanthone (0.01M) to be reproducible. In addition, an excess of carbonate **7** (10 mol eq.) is still required to drive the allylation reaction forward, although synthesizing gram quantities of **7** is easily achievable as discussed previously.

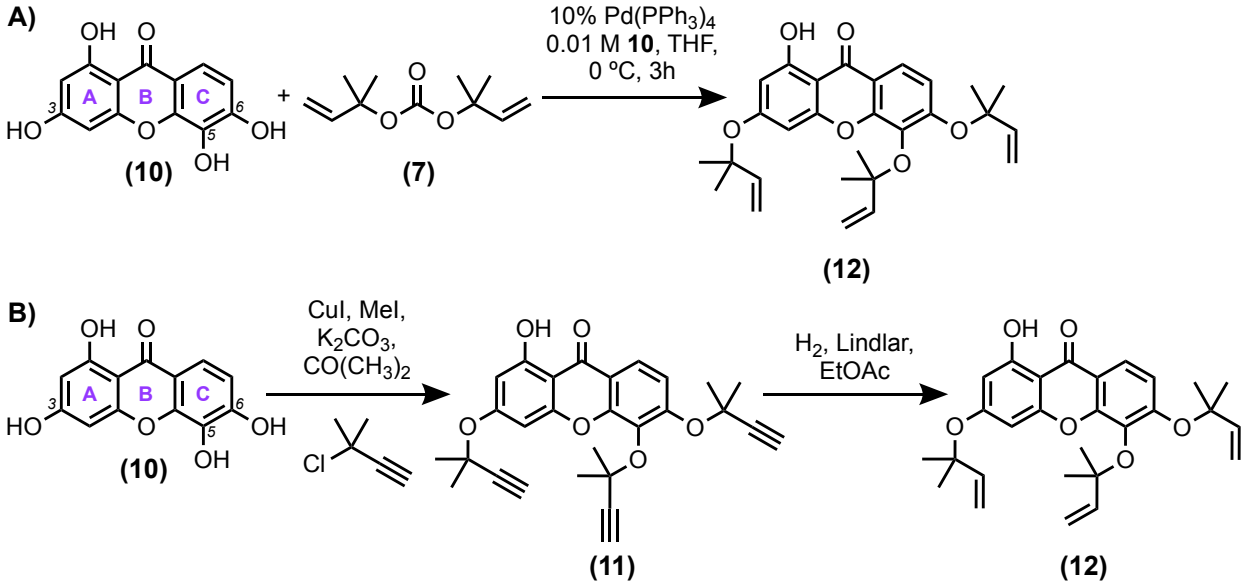

Figure 1.22: One-pot formation of triallyl xanthone **12**. A) Synthesis of forbesione-precursor **12** by Tisdale et al. O-allylation of **10** was previously achieved via tri-propargylation to yield **11**, which was hydrogenated to form tri-O-allylated forbesione precursor **12** and B) our approach to **12** is a one-step palladium-catalyzed O-allylation.

The final step in our synthesis of forbesione involved a tandem Claisen/Diels-Alder/Claisen rearrangement by heating **12** to 120 ºC in DMF for two hours (Figure 1.23). We found that heating at 100 ºC made the reaction slower without changing the ratio of forbesione to

iso-forbesione. To mitigate the formation of *iso*-forbesione, Tisdale at al. previously acetylated the C1 hydroxy group of **12** to create steric hindrance around C2 and mitigate its prenylation resulting from a Claisen rearrangement, which after deprotection, yielded forbesione exclusively. We did not employ this strategy, however, as the crystallinity/solubility of forbesione and *iso*-forbesione differ sufficiently in the DCM/hexanes crystallization we employed for MAD28 such that the two isomers can be efficiently resolved by this method. In addition, generation of *iso*-forbesione was also of interest to as its biological activity is largely unknown. Overall, our synthetic strategy afforded 310 mg and 200 mg of forbesione and *iso*-forbesione, respectively, which can be synthesized on a multigram scale.

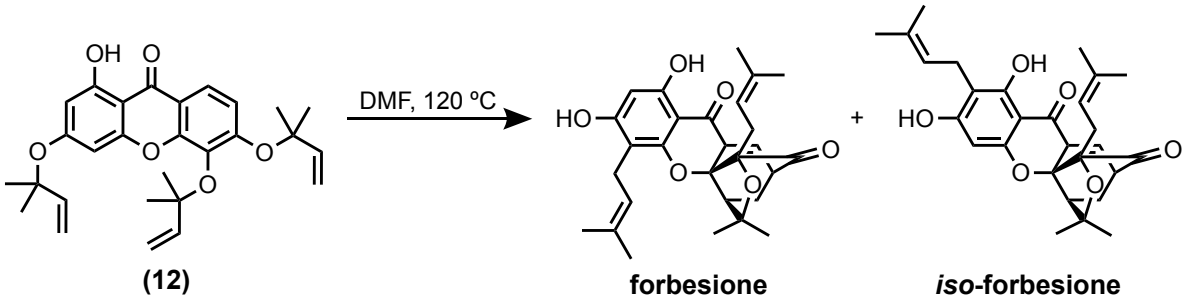

Figure 1.23: Compound **12** undergoes a thermal Claisen/Diels-Alder/Claisen rearrangement to afford forbesione and *iso*-forbesione in a 6:4 ratio, respectively.

Future studies of forbesione and of our CGXs library of compounds will be geared at further probing the biology of our compounds. Therefore, to perform studies such as "protein stapling" or in vivo azide-alkyne cycloaddition reactions, we developed a method to synthesize alkyne analogues of our CGXs. As an example, *p*-toluenesulfonyl chloride was reacted with 4-pentyn-1-ol to produce. sulfonate ester **13** in 79% yield. We then utilized the ester to synthesize **14**, which is an alkyne derivative of acetylforbesione (Figure 1.24). Studies are ongoing to determined novel protein targets of our CGXs through protein stapling.

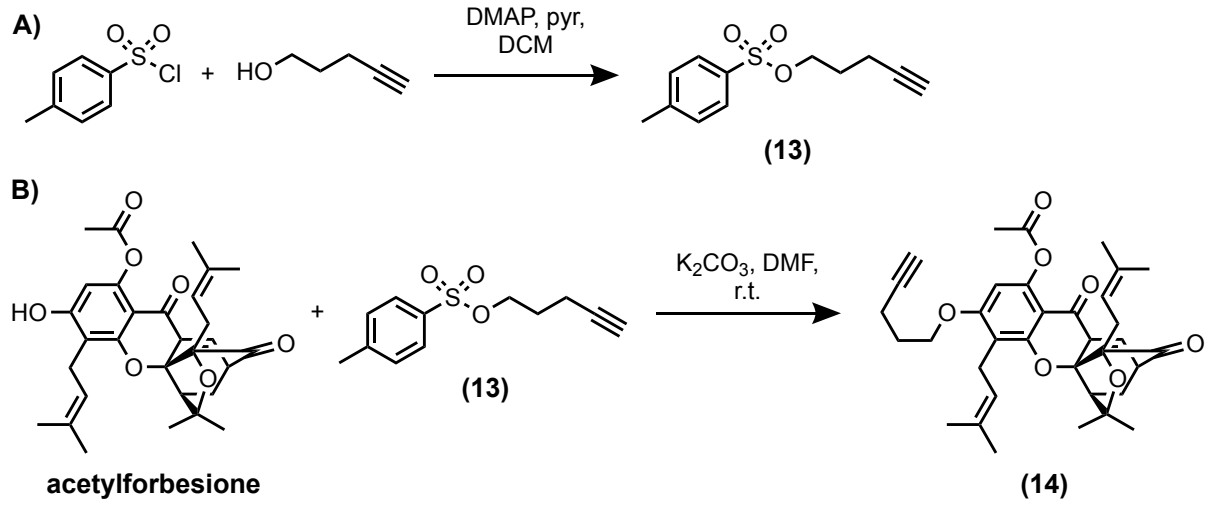

Figure 1.24: The synthesis of alkyne analogues of CGXs for biological studies. *p*-toluenesulfonyl chloride is reacted with 4-pentyn-1-ol to yield **13**, which was utilized for the synthesis of **14**, a CGX alkyne analogue for biological evaluation.

1.10 Synthesis & Biological Evaluation of Novel Amide Derivatives of GBA

Our previous attempts to improve the cytotoxicity of GBA led us to determine that converting the carboxylic acid group of GBA into an amide (Figure 1.25) yielded derivatives with improved cytotoxicity in cell-based assays. We identified DAP19, a GBA amide derivative containing a morpholino moiety to be particularly inhibiting on cell growth. When triple-negative breast cancer cell line MDA-MB-231 was treated with 0.5 μM of DAP19, for example, after 24 h we observed a relative cell growth of 4.5% compared to our control. In contrast, GBA, which is a known cytotoxic natural product (and our benchmark compound in this study), showed a relative cell growth of 58% under the same concentration (Figure 1.26).

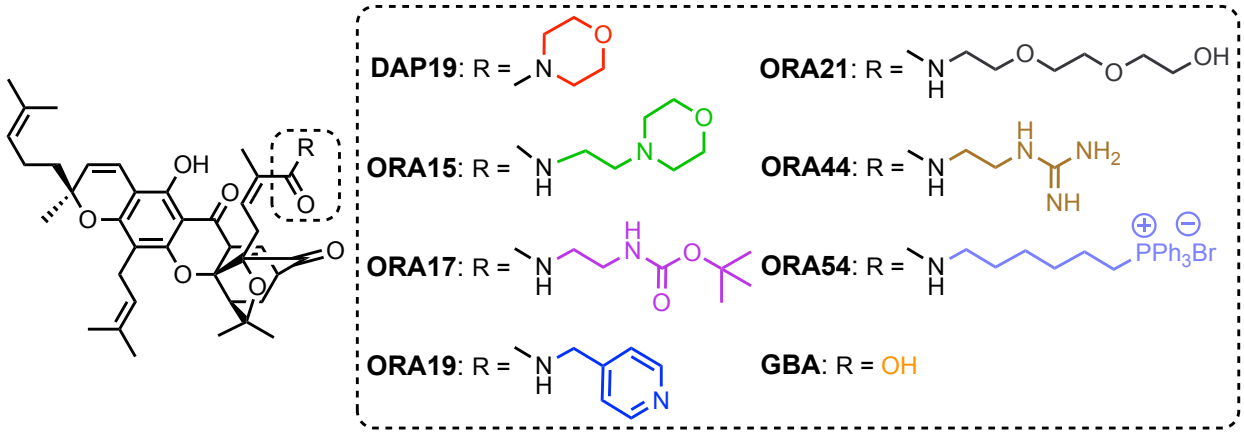

Figure 1.25: Chemical structure of amide derivatives of GBA synthesized previously in our lab, which were tested for bioactivity in the triple-negative breast cancer cell line MDA-MB-231. The most cytotoxic compound here, DAP19, served as the inspiration for the synthesis of novel GBA analogues.

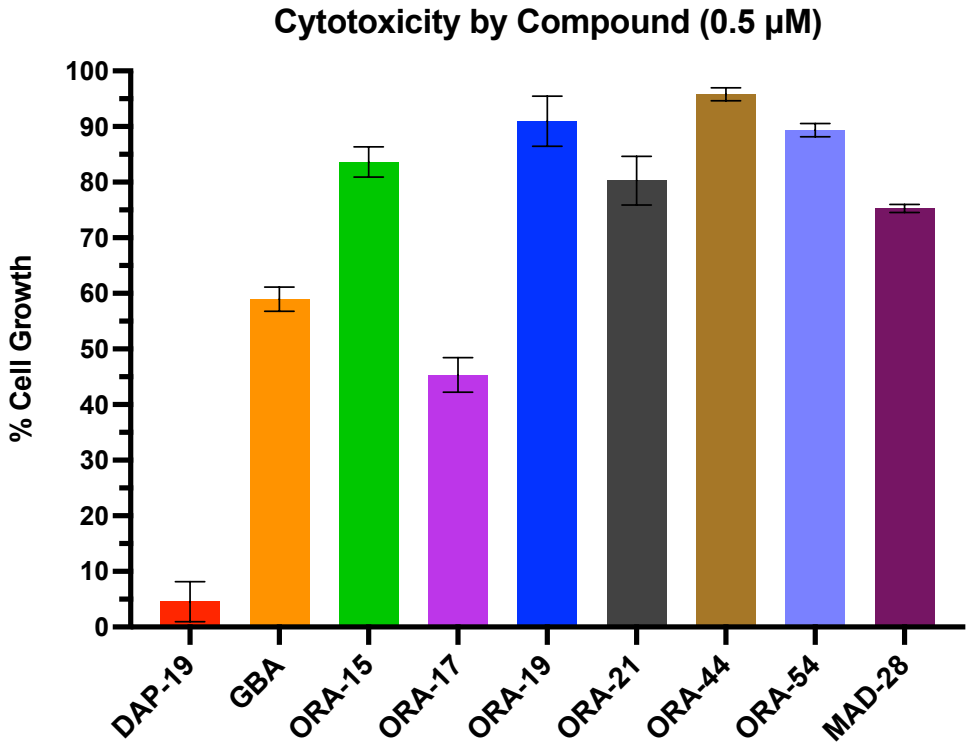

Figure 1.26: Bioactivity of GBA amide derivatives in breast cancer cell line MDA-MB-231. MDA-MB-231 cells was treated with several derivatives of GBA at a concentration of 0.5 µM. DAP19 was identified as the most cytotoxic followed by ORA-17.

When replacing the morpholino moiety with a group containing an ethyl linked to a *tert*-butyl carbamate moiety, we observed a relative breast cancer cell growth of 45%, which is a mild

improvement in cytotoxicity compared to GBA. All other derivatives, however, had a significantly lower inhibitory effect on growth, affording a relative cell growth between 75-93%. Although our less cytotoxic derivatives have potentially higher solubility, our studies suggest that converting the carboxylic acid moiety of GBA to amide groups bigger than morpholine reduces its cytotoxicity.

We wondered whether the inhibitory/cytotoxic effect of DAP19 was consistent across several breast cancer cell lines, including BT-474, an invasive ductal carcinoma cell line; MCF-7, MDA-MB 468, and SKBR-3, all metastatic adenocarcinoma breast tissue; as well as MDA-MB-231, triple-negative breast cancer tissue (Figure1.27). When each breast cancer cell line was treated with DAP19 at a concentration of 5 μM, nearly complete cell death was observed across all cell lines. At a concentration of 2 μM, DAP19 was most effective in the breast cancer cell lines MDA-MB-231 and SKBR-3 with a cell death of 87% and 81%, respectively. This pattern was similarly observed at a concentration of 1 μM of DAP19 with a cell death of 80% and 47% for MDA-MB-231 and SKBR-3, respectively.

In contrast, at a concentration of 0.5 μM, cell growth was observed across all breast cancer cell lines except MDA-MB 468, which showed a 2% cell death. Unsurprisingly, at a 0.25 μM concentration, the lowest concentration we tested, cell growth was observed across all cell lines. At this concentration, there was no inhibition of cell growth observed in MDA-MB-231, which is a stark contrast to when this cell line is treated with 1 μM or higher of DAP19. The lowest percentage of cell growth at 0.25 μM DAP19 was observed in the BT-474 cell line.

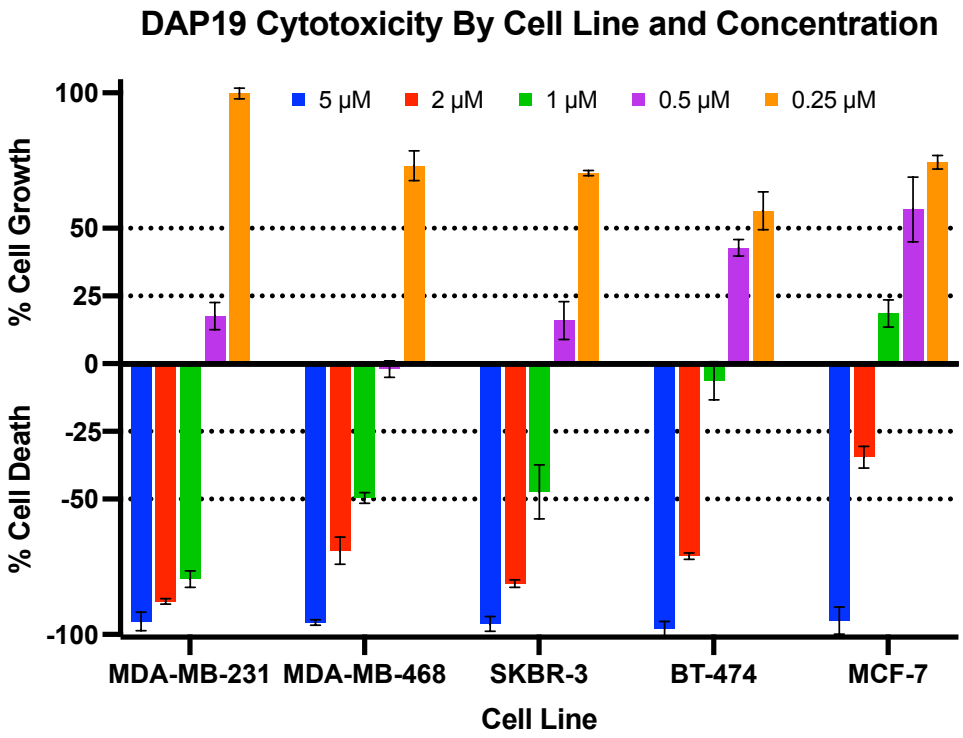

Figure 1.27: Bioactivity of DAP19 in various breast cancer cell lines. DAP19 was assessed for its broad-spectrum potential. Several breast cancer cell lines were treated with DAP19 at various concentrations.

Inspired by our findings on the cytotoxicity of DAP19, we constructed a library of several amide derivatives containing similar moieties to DAP19 that are biologically relevant in known pharmaceuticals. This includes replacing the morpholino group with substituents having various polarities, hydrogen bonding capabilities, and increased size at the site where the oxygen atom in the morpholino moiety resides. Some examples include a trifluoromethyl (compound **115**), dimethyl (compound **118**), 1-methylpiperazinyl (compound **130**), thiomorpholinyl (compound **135**), and various other substituents (Figure 1.28).

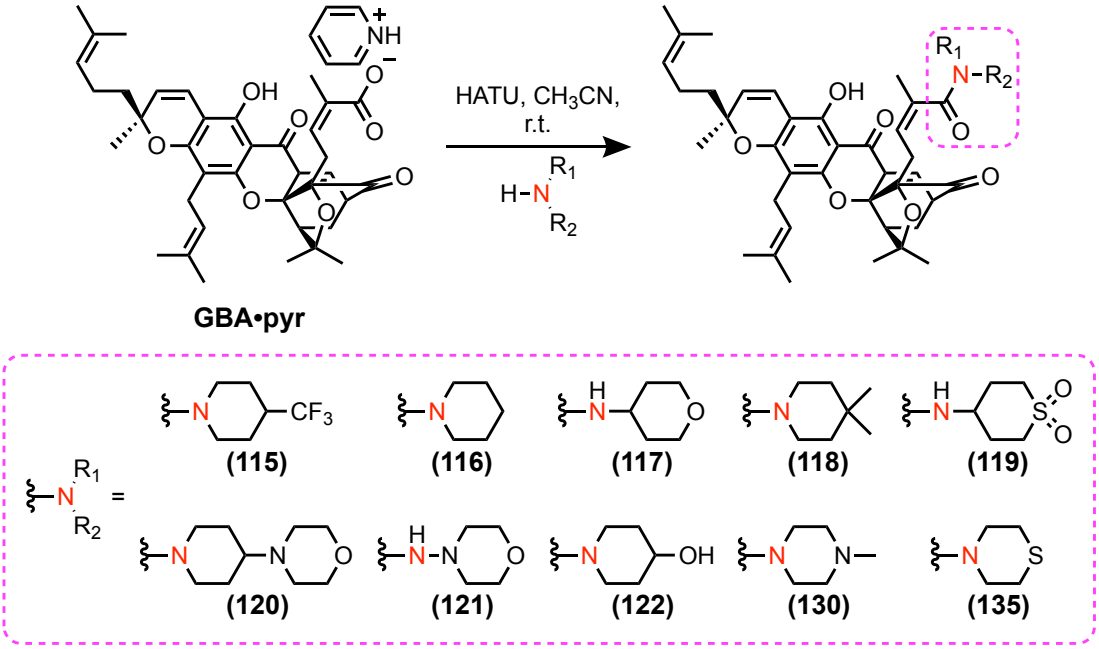

Figure 1.28: Synthesis of novel amide derivatives of GBA. The reaction between GBA and various amines via amide coupling reagent HATU affords compounds **115**-**122**, **130**, and **135**.

Working with collaborators (HUJI), we were able to determine the cytotoxicity of several of our compounds, including GBA, **118**, and **130**. There results showed that all three compounds are cytotoxic. Notably, **118** (Figure 1.30) and **130** (Figure 1.31) were cytotoxic in a dose-dependent manner, whereas GBA (Figure 1.29) was not. In addition, all three compounds showed a high selectivity for cancer cells over normal cells. Both **118** and **130** showed high cytotoxicity, especially at higher concentrations. The most cytotoxic compound, however, is **130**, which also has a higher cytotoxicity relative to DAP19. This indicates that modifications to the morpholino ring can improve cytotoxicity. Work is ongoing to determine the mode of action of these compounds, and specifically how they target NEET proteins.

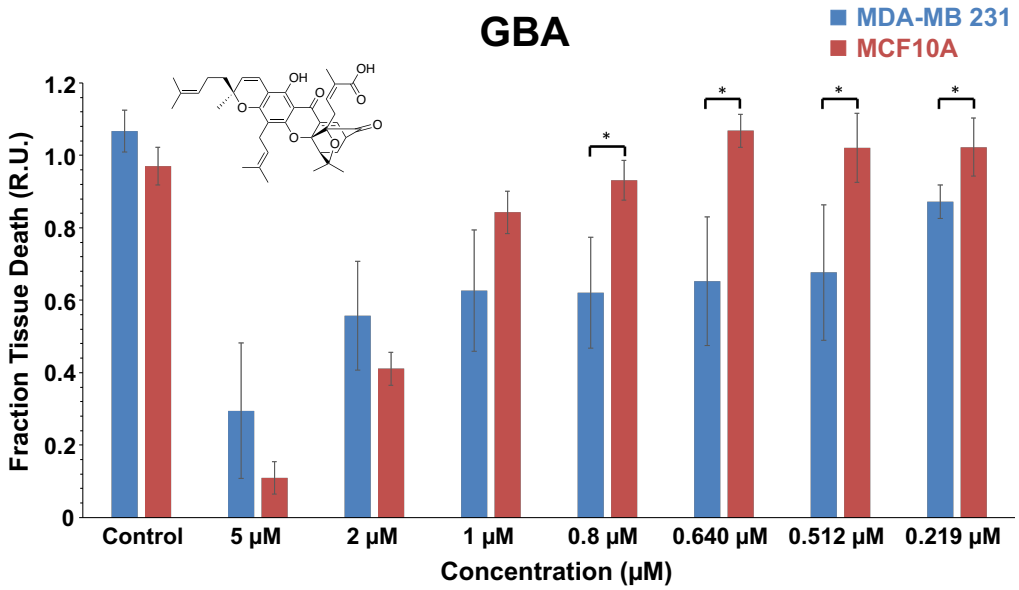

Figure 1.29: Cytotoxicity of GBA on breast cancer cell line MDA-MB-231 vs. normal human breast cell line MCF-10A. Effect of GBA on the viability of cancer cells (MDA-MB-231 in blue) and normal cells (MCF-10A in red) after 24h treatment at various concentrations (5 µM, 2 µM, 1 µM, 0.8 µM, 0.640 µM, 0.512 µM, 0.219 µM) and untreated cells (control). *P < 0.01, **P < 0.001, **P < 0.0001 compared to MCF-10 cells on the same condition; Student's t-test. Cytotoxicity was measured in relative units (R.U.). This figure was obtained with permission from H. B. Margault and R. Nechushtai (HUJI).

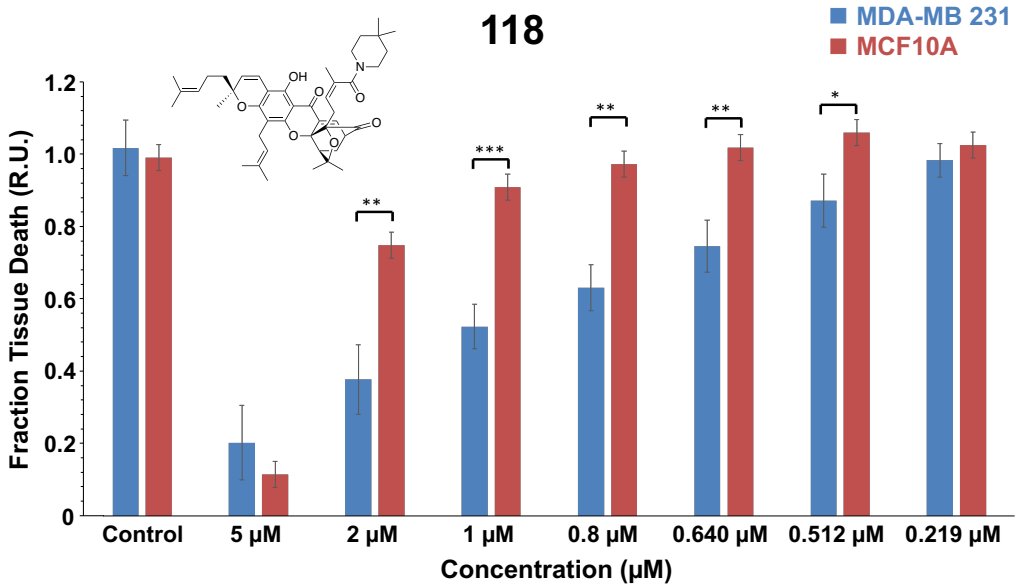

Figure 1.30: Cytotoxicity of **118** on breast cancer cell line MDA-MB-231 vs. normal human breast cell line MCF-10A. Effect of **118** on the viability of cancer cells (MDA-MB-231 in blue) and normal cells (MCF-10A in red) after 24h treatment at various concentrations (5 µM, 2 µM, 1 µM, 0.8 µM, 0.640 µM, 0.512 µM, 0.219 µM) and untreated cells (control). *P < 0.01, **P < 0.001, **P < 0.0001 compared to MCF-10 cells on the same condition; Student's t-test. This figure was obtained with permission from H. B. Margault and R. Nechushtai (HUJI).

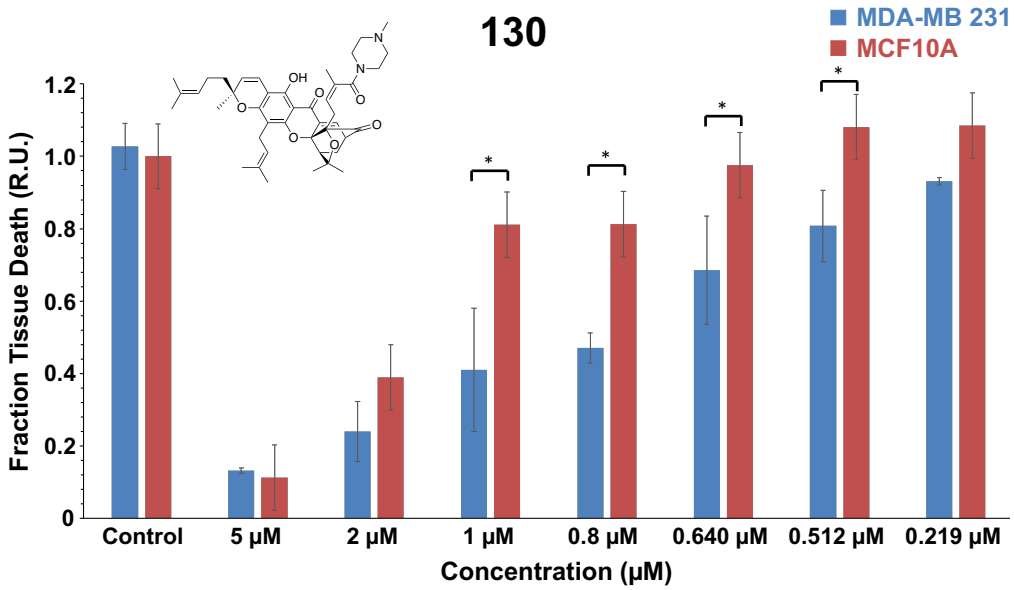

Figure 1.31: Cytotoxicity of **130** on breast cancer cell line MDA-MB-231 vs. normal human breast cell line MCF-10A. Effect of **130** on the viability of cancer cells (MDA-MB-231 in blue) and normal cells (MCF-10A in red) after 24h treatment at various concentrations (5 µM, 2 µM, 1 µM, 0.8 µM, 0.640 µM, 0.512 µM, 0.219 µM) and untreated cells (control). *P < 0.01, **P < 0.001, **P < 0.0001 compared to MCF-10 cells on the same condition; Student's t-test. This figure was obtained with permission from H. B. Margault and R. Nechushtai (HUJI).

1.11 Appendix

Experimental Procedures & Spectroscopic Data

Commercially available reagents were obtained from Acros, AKSci, Alfa Aesar, Chem Science, Combi-Blocks, Matrix Scientific, Sigma Aldrich, Synthonix, or TCI and used without further purification. All anhydrous solvents were dispensed from a solvent purification system that passes the solvent through two columns of dry neutral alumina. Anhydrous ACN was purchased from Alfa Aesar. GBA was extracted from gamboge resin obtained from Kremer Pigmente, WoodFinishing Enterprises or Metropolitan Music Corporation.

All reactions were performed in oven-dried and argon- purged glassware (including 20 mL vials fitted with caps) equipped with Teflon-coated magnetic stirbars. All ^{1}H spectra were recorded at ambient temperature using a JEOL ECA 500 spectrometer (400 or 500 MHz). All ^{13}C spectra were recorded at ambient temperature using a Varian VX-500 spectrometer (125 MHz) equipped with a Xsens two-channel cold probe. The ^{1}H spectral data is reported as follows: chemical shift in parts per million (ppm) downfield from tetramethylsilane on the δ scale, multiplicity (s, singlet; d, doublet; t, triplet; q, quartet; s, septet; m, multiplet; dd, doublet of doublets; dt, doublets of triplets; td, triplet of doublets; and b, broadened), coupling constants (Hz), and integration. ^{13}C NMR chemical shifts are reported in ppm from tetramethylsilane with the solvent reference employed as the internal standard (deuterochloroform, $CDCl_3$, at 77.3 ppm).

Compounds were analyzed for HRMS on an Agilent Technologies 6230 TOF Mass Spectrometer (Santa Clara, CA) using electrospray in the positive ion mode at > 60,000 resolution and using typical ESI source values, which resulted in mass accuracies < 1ppm. The jet stream source was operated under positive ionization mode with the following parameters: VCap: 3500 V; fragmentor voltage: 175 V; nozzle voltage: 500 V; drying gas temperature: 325 °C, sheath gas

temperature: 325 °C, drying gas flow rate: 7.0 L/min; sheath gas flow rate: 10 L/min; nebulizer pressure: 40 psi.

When indicated, the progress of reactions was monitored by analytical thin layer chromatography using glass plates pre-coated with SiliCycle, Inc. 250 μm F254 silica gel and visualized with UV light (254 nm). Flash chromatography was performed on SiliCycle, Inc. SiliaFlash P60 40-63 μm (230-400 mesh size) 60 Å grade silica gel. All chromatography solvents were acquired from Fisher Scientific and used as is.

Commercial Sources of Gamboge Resin

Commercially available gamboge was purchased from Kremer Pigments (https://www.kremer-pigmente.com/ Lot No: 37050), Metropolitan Music (https://www.metmusic.com/ Lot No: 27320), and WoodFinishing Enterprises (https://woodfinishingenterprises.com/ Lot No: 14-1720).

Isomerization Studies of GBA to *epi*-GBA

GBA (10 mg) was dissolved in $CDCl_3$ (0.6 mL) and the resulting orange solution was placed in an NMR tube. The tube was sealed and placed in a heating bath at respective temperatures (80, 100, 120, and 150 ºC). ^1H NMR spectra were recorded at predetermined times.

Cell Culture and Compound Assays

The MDA-MB-231 cell line was obtained from ATCC (HTB-26) and was cultured in RPMI 1640 media (Gibco 21-870-092) supplemented with 10% heat inactivated FBS (Gibco, 10438-026), 2mM L-Glutamine (Gibco, 25030-081), and 100 U/mL penicillin, 100 μg/mL

streptomycin (Gibco, 15140-122). The cell cultures were maintained at 37℃ in a humidified atmosphere with 5% CO_2 and subcultured using trypsin (Gibco, 25300-054) after reaching 80% confluency. The three formulations of **GBA** (equilibrated **GBA**, **GBA•pyr**, or >97% **GBA**) were dissolved in DMSO to a stock concentration of 10 mM. For microscopy studies, the cells were treated at 70% confluency with 1 μM of each formulation or DMSO for 24 h.

ATP Assay

Cell viability was assessed by ATP quantification of metabolically active cells using a CellTiter-Glo 3D kit (Promega, G9682) in multiwell plates according to the manufacturer's instructions. Briefly, MDA-MB-231 cells at a density of 10^4/well were seeded in opaque 96-well tissue culture plates and allowed to adhere overnight. The three formulations of gambogic acid (equilibrated **GBA**, **GBA•pyr** or >97% **GBA**) were then added to final concentrations of 0.25, 0.5, 1, 5, 10 and 20 μM in quadruplicates. DMSO was used as a control and all treatments were performed for 24 h at 37 ºC. After one hour of equilibration at room temperature, CellTiter-Glo 3D reagent at a 1:1 ratio was added to each well. The plates were mixed on a plate shaker for 10 min and end-point luminescence values were recorded with a FilterMax F-5 multimode microplate reader. Percent viability was calculated as (RLU post-treatment/RLU of DMSO)*100.

Caspase 3/7 Activity

Initiation of apoptosis via induction of caspase 3/7 activity was measured as above using the Caspase-Glo 3/7 kit (Promega, G8981). Cells in triplicates were treated with 1 μM of >97% **GBA**, **GBA•pyr** or equilibrated **GBA** for 3, 6, 12, and 24 h. Wells with media only were used as blanks, and wells with untreated cells only were used as controls for background luminescence

measurements. Relative light units (RLU) were recorded one hour after the addition of the Caspase-Glo 3/7 reagent at a 1:1 ratio and fold change was calculated at each time point using the following equation: Fold change = (treatment RLU - blank RLU) / negative control RLU.

Western Blotting

MDA-MB-231 cells treated with DMSO or gambogic acid formulations (>97% **GBA**, **GBA•pyr** or equilibrated **GBA**) at 0.5 and 1 μM for 24 h were lysed using RIPA buffer (ThermoFisher, 89901). Total protein extract was quantified using a BCA protein assay kit (ThermoFisher, 23225), and 20 μg of protein were loaded and analyzed on a 4-12% Bis-Tris Mini Protein Gel. Following gel electrophoresis, the proteins were transferred to a PVDF membrane using an iBlot2 dry blotting system. Membranes were blocked with 5% dry fat-free milk in TTBS and incubated with primary antibodies overnight at 4 ºC. The primary antibodies used were anti-PARP (Cell Signaling Technology, 9546) and anti-GAPDH (Invitrogen, MA5-15738). Secondary antibodies conjugated to IRDye 680RD or IRDye 800CW (LI-COR Biosciences) were used to visualize the proteins of interest on a LI-COR Odyssey FC Imaging system, which were quantified using Image Studio software.

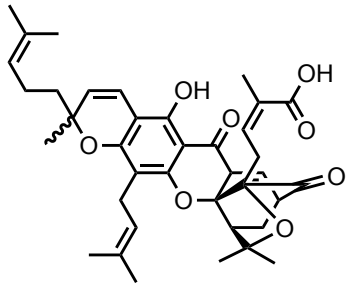

GBA + *epi*-GBA
(mixture of epimers)

4-(8-hydroxy-2,2,11-trimethyl-13-(3-methylbut-2-en-1-yl)-11-(4-methylpent-3-en-1-yl)-4,7-dioxo-1,2,5,7-tetrahydro-11*H*-1,5-methanofuro[3,2-*g*]pyrano[3,2-*b*]xanthen-3a(4*H*)-yl)-2-methylbut-2-enoic acid (GBA + *epi*-GBA, mixture of epimers): To a 500 mL beaker was added gamboge powder (100 g) and 300 mL of MeOH. The mixture was stirred for 10 minutes at room temperature and subsequently filtered. The solids obtained were washed with MeOH (200 mL, x2), the organic filtrates were combined, and concentrated under reduced pressure. The resulting crude orange extract was then dried under high vacuum for 6 h. Next, the crude extract was combined with 200 mL of 15% deionized water in pyridine (v:v). The mixture was heated to 60 ºC until all the solids were dissolved (~10 min). The resulting dark red solution was allowed to sit overnight at room temperature. The orange crystals formed were then collected by filtration and subsequently dissolved in 200 mL of Et_2O, which was washed with 200 mL of 15% HCl (v:v). The organic phase was partitioned and concentrated to dryness to afford a mixture of GBA:*epi*-GBA as an amorphous orange solid (23 g, ~4:1 ratio of GBA:*epi*-GBA).

^{1}H NMR (500 MHz, $CDCl_3$) δ 12.77 (d, J = 7.6 Hz, 1H), 7.55 (d, J = 6.7 Hz, 1H), 6.58 (d, J = 10.1 Hz, 1H), 6.18 – 6.02 (m, 1H), 5.45 – 5.28 (m, 1H), 5.19 – 4.94 (m, 2H), 3.48 (s, 1H), 3.33 – 3.27 (m, 1H), 3.13 (d, J = 10.4 Hz, 1H), 3.02 – 2.84 (m, 2H), 2.52 (d, J = 9.1 Hz, 1H), 2.32 (d, J = 13.2 Hz, 1H), 2.11 – 1.97 (m, 2H), 1.85 – 1.69 (m, 10H), 1.69 – 1.59 (m, 7H), 1.58 (s, 1H), 1.54 (s, 2H), 1.41 – 1.36 (m, 3H), 1.34 (s, 1H), 1.29 (s, 3H), 1.25 (s, 1H).

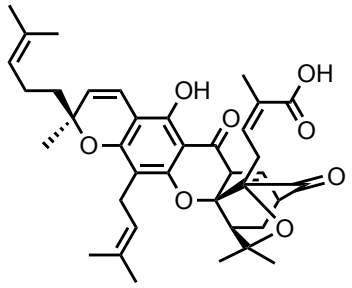

GBA

4-(8-hydroxy-2,2,11-trimethyl-13-(3-methylbut-2-en-1-yl)-11-(4-methylpent-3-en-1-yl)-4,7-dioxo-1,2,5,7-tetrahydro-11*H*-1,5-methanofuro[3,2-*g*]pyrano[3,2-*b*]xanthen-3a(4*H*)-yl)-2-methylbut-2-enoic acid (GBA): High purity GBA purified in the same way as previously mentioned. After the first crystallization, the orange powder was combined with 60 mL of 15% deionized water in pyridine (v:v) and stirred at 60 ºC until completely dissolved (~15 min). The dark red solution was allowed to sit overnight, and the resulting orange crystals were filtered and recrystallization once more under the same conditions. The resulting orange crystals were then collected by filtration, dried under reduced pressure then dissolved in 200 mL of Et_2O, which was washed with 200 mL of 15% HCl (v:v). The organic phase was partitioned and concentrated to dryness to afford GBA as an amorphous orange solid (13 g, > 97% pure).

^{1}H NMR (500 MHz, $CDCl_3$) δ 12.73 (s, 1H), 7.53 (d, *J* = 6.9 Hz, 1H), 6.55 (d, *J* = 10.1 Hz, 1H), 6.10 (t, *J* = 8.1 Hz, 1H), 5.34 (d, *J* = 10.1 Hz, 1H), 5.07 – 4.97 (m, 2H), 3.47 (dd, *J* = 6.6, 4.1 Hz, 1H), 3.28 (dd, *J* = 14.6, 8.2 Hz, 1H), 3.11 (dd, *J* = 14.6, 5.1 Hz, 1H), 2.97 (d, *J* = 7.4 Hz, 2H), 2.50 (d, *J* = 9.3 Hz, 1H), 2.30 (dd, *J* = 13.4, 4.7 Hz, 1H), 1.99 (h, *J* = 9.5, 9.0 Hz, 2H), 1.76 – 1.71 (m, 4H), 1.70 (s, 3H), 1.68 (s, 3H), 1.63 (s, 3H), 1.61 (s, 3H), 1.59 – 1.54 (m, 1H), 1.53 (s, 3H), 1.40 – 1.35 (m, 1H), 1.34 (s, 3H), 1.28 (s, 3H), 1.24 (s, 1H). ^{13}C NMR (125 MHz, $CDCl_3$) δ 203.39, 178.84, 171.66, 161.47, 157.53, 157.32, 138.39, 135.29, 133.34, 131.77, 131.48, 127.57, 124.42, 123.85, 122.24, 115.87, 107.54, 102.69, 100.40, 90.91, 83.87, 83.80, 81.26, 48.98, 46.78, 41.97, 29.85, 29.70, 29.25, 28.88, 27.68, 25.66, 25.17, 22.73, 21.59, 20.73, 18.07, 17.62.

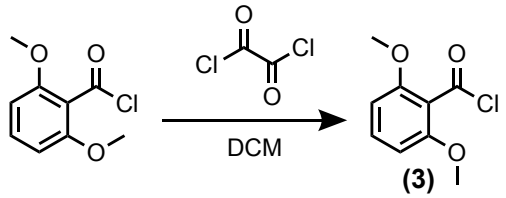

2,6-dimethoxybenzoyl chloride (3): To an oven-dried 250 mL round-bottom flask equipped with a magnetic stirbar was added anhydrous DCM (123.2 mL), 2,6-dimethoxybenzoic acid (5.00 g, 27.45 mmol, 1 eq.), and oxalyl chloride (11.7 mL, 137.23 mmol, 5 eq.). The mixture was allowed to stir at room temperature for 12 h. Next, the mixture was concentrated under reduced pressure and kept under an inert atmosphere argon. The resulting solid was dried under high vacuum for 24 hours to afford **3** as an off-white solid, which was utilized without further purification.

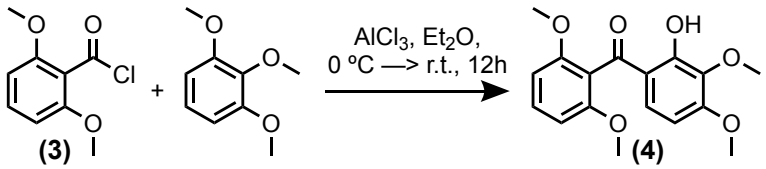

(2,6-dimethoxyphenyl)(2-hydroxy-3,4-dimethoxyphenyl)methanone (4): To a 250 mL round bottom flask containing **3** (5.507 g, 27.45 mmol, 1 eq.) and a magnetic stirbar under an inert atmosphere of argon was added 1,2,3-trimethoxybenzene (4.848 g, 28.82 mmol, 1.05 eq.), and anhydrous Et_2O (150 mL). When all the contents in solution were completely dissolved, the mixture was cooled to 0 ºC and $AlCl_3$ (10.98 g, 82.35 mmol, 3 eq.) was added in two equal portions. The mixture turned a bright yellow color and formation of a yellow solid was observed. The mixture was allowed to warm to room temperature and was stirred for 10 hours. Next, the mixture was transferred to a 1 L separatory funnel and ethyl EtOAc (200 mL) and 2M aqueous HCl (200 mL) was added. The aqueous phase was removed, and the organic phase was washed with deionized water (200 mL) and saturated brine (200 mL). The organic phase was collected, treated with sodium sulfate, filtered, and concentrated under reduced pressure. The resulting solid was

placed in a 100 mL beaker and 75 mL of MeOH were added. The solution was vigorously boiled until the solids were completely dissolved. The solution was then slowly cooled to room temperature and yellow crystals began to form. The crystals were filtered and dried under reduced pressure to afford **4** as a yellow, crystalline solid (7.4 g, > 99% pure, 85% yield).

^{1}H NMR (500 MHz, $CDCl_3$) δ 12.41 (s, 1H), 7.36 (t, *J* = 8.2 Hz, 1H), 7.08 – 7.02 (m, 1H), 6.62 (d, *J* = 8.2 Hz, 2H), 6.38 (d, *J* = 8.8 Hz, 1H), 3.94 (s, 3H), 3.90 (s, 3H), 3.74 (s, 6H).

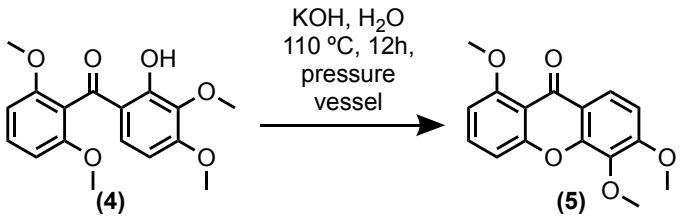

1,5,6-trimethoxy-9*H*-xanthen-9-one (5): To a 350 mL pressure vessel equipped with a magnetic stirbar was added **4** (15.0 g, 47.12 mmol, 1 eq.), KOH (26.44 g, 471.21 mmol, 10 eq.), and deionized water (170 mL). The pressure vessel was sealed, and the mixture was stirred until all the contents were dissolved and turned a bright yellow color. Next, the pressure vessel was heated to 110 ºC for 24 h. The vessel was then allowed to cool to room temperature and the resulting yellow slurry was filtered and the solids were washed with deionized water (50 mL, x4) until they were off-white in color. The solids were subsequently dried under reduced pressure and recrystallized in MeOH to afford **5** as a white, crystalline solid (13.067 g, > 99% pure, 97% yield).

^{1}H NMR (300 MHz, $CDCl_3$) δ 8.05 (d, J = 9.0 Hz, 1H), 7.59 (t, J = 8.4 Hz, 1H), 7.14 (d, J = 8.4 Hz, 1H), 6.97 (d, J = 9.1 Hz, 1H), 6.80 (d, J = 8.2 Hz, 1H), 4.02 (s, 6H), 4.00 (s, 3H).

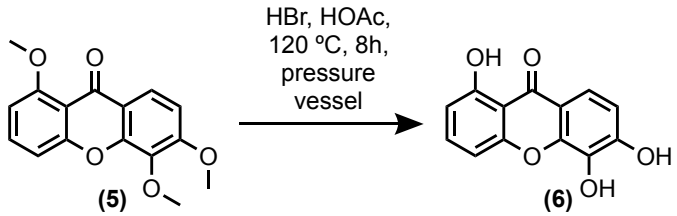

1,5,6-trihydroxy-9H-xanthen-9-one (6): To a 350 mL pressure vessel equipped with a magnetic stirbar was added 48% aqueous hydrobromic acid (66 mL), acetic acid (210 mL), and **5** (7.0 g, 24.45 mmol, 1 eq.). The mixture was heated to 120 ºC and stirred at this temperature for 24 hours. The solution was allowed to cool to room temperature and formation of a gold solid was observed. The solid was filtered, washed with deionized water (100 mL, x2), and dried under reduced pressure to afford **6** as a brilliant gold solid (5.2 g, > 99% pure, 87% yield).

^{1}H NMR (500 MHz, CD_3OD) δ 7.66 – 7.59 (m, 2H), 7.04 (d, J = 8.3 Hz, 1H), 6.92 (d, J = 8.7 Hz, 1H), 6.73 (d, J = 8.2 Hz, 1H).

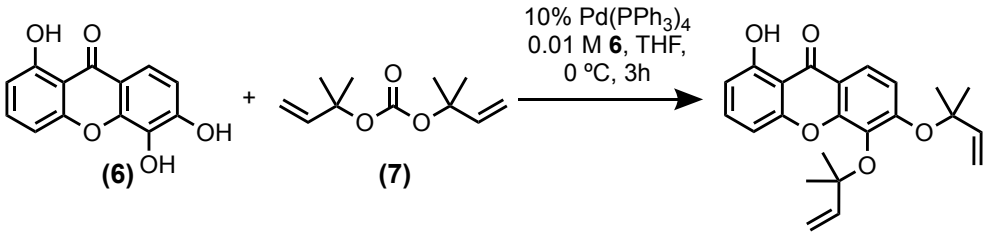

(9)

1-hydroxy-5,6-bis((2-methylbut-3-en-2-yl)oxy)-9*H*-xanthen-9-one (9): To an oven-dried 250 mL round-bottom flask equipped with a magnetic stirbar kept under an inert atmosphere of argon was added **6** (500 mg, 2.05 mmol, 1 eq.), anhydrous THF (200 mL), and carbonate **7** (4.06 g, 20.5 mmol, 10 eq.). Next was added high purity tetrakis(triphenylphosphine)-palladium(0) (237 mg, 0.2 mmol, 0.1 eq.) and the resulting mixture was allowed to stir at room temperature. Within five minutes, the solution turned a dark green color, which was allowed to stir for a total of three hours. The resulting yellow/green mixture was then concentrated to dryness under reduced pressure and immediately purified by silica gel column chromatography with a gradient eluent of 0% to 10% EtOAc in hexanes to afford **9** as a pale-yellow liquid that coeluted with carbonate **7**. The isolated mixture of **7** and **9** was then dried under reduced pressure to afford **9** as a viscous yellow liquid (563 mg, > 90% pure, 65% yield).

^{1}H NMR (500 MHz, $CDCl_3$) δ 12.75 (s, 1H), 7.86 (d, *J* = 9.0 Hz, 1H), 7.55 (t, *J* = 8.3 Hz, 1H), 7.14 (d, *J* = 8.8 Hz, 1H), 6.93 (d, *J* = 8.4 Hz, 1H), 6.78 (d, *J* = 8.2 Hz, 1H), 6.22 (ddd, *J* = 36.1, 17.6, 10.9 Hz, 2H), 5.25 – 5.17 (m, 3H), 5.03 (d, *J* = 10.7 Hz, 1H), 1.58 (s, 6H), 1.58 (s, 6H).

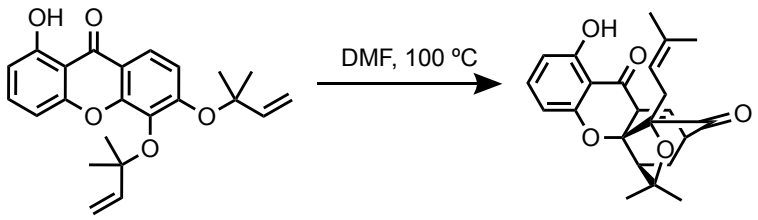

(9) **MAD28**

8-hydroxy-2,2-dimethyl-3a-(3-methylbut-2-en-1-yl)-1,2-dihydro-1,5-methanofuro[2,3-*d*]xanthene-4,7(3a*H*,5*H*)-dione (MAD28): To an oven-dried 25 mL round-bottom flask equipped with a magnetic stirbar was added **9** (500 mg, 1.31 mmol, 1eq.) and anhydrous DMF (26 mL). The flask was equipped with a reflux condenser and the resulting solution was stirred at 100 ºC until completion as determined by TLC (40% EtOAc in hexanes). The mixture was then cooled to room temperature and concentrated to dryness under reduced pressure. The residue was purified via silica gel column chromatography using a gradient eluent of 0 to 20% EtOAc in hexanes, and the resulting yellow solid was recrystallized in a 1:5 DCM:hexanes system to afford MAD28 as a yellow, crystalline solid (280 mg, > 99% pure, 56% yield).

^{1}H NMR (500 MHz, $CDCl_3$) δ 12.09 (s, 1H), 7.49 (d, *J* = 6.9 Hz, 1H), 7.40 (t, *J* = 8.3 Hz, 1H), 6.57 – 6.49 (m, 2H), 4.43 – 4.38 (m, 1H), 3.55 – 3.51 (m, 1H), 2.63 (d, *J* = 9.9 Hz, 2H), 2.46 (d, *J* = 9.7 Hz, 1H), 2.36 (dd, *J* = 13.7, 4.6 Hz, 1H), 1.70 (s, 3H), 1.37 (s, 3H), 1.30 (s, 3H), 1.01 (s, 3H).

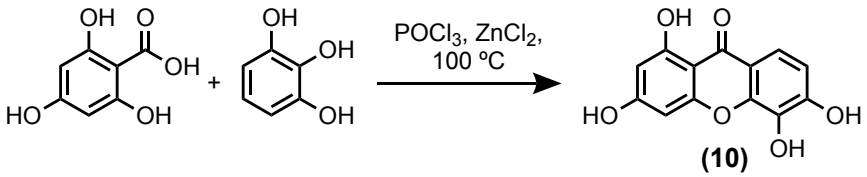

1,3,5,6-tetrahydroxy-9*H*-xanthen-9-one (10): To an oven-dried 100 mL pressure vessel equipped with a magnetic stirbar kept under an inert atmosphere of argon was added 1,3,5-trihydroxybenzene (2.5 g, 19.82 mmol, 1 eq.), 2,3,4-trihydroxybenzoic acid (3.54 g, 20.82 mmol, 1.05 eq.), and phosphoryl chloride (50 mL). Next was added portion-wise anhydrous zinc chloride (13.51 g, 99.12 mmol, 5 eq.) and the vessel was appropriately sealed. The mixture was subsequently stirred overnight at 100 ºC. After 1 hour of heating, the mixture began to turn dark red. Next, the vessel was allowed to cool to room temperature, and in increments of ~5 mL, was carefully quenched by pouring into a 500 mL beaker containing 200 mL of crushed ice. The mixture was then poured into a 1L separatory funnel and EtOAc (300 mL), and deionized water (200 mL) were added. The organic phase was partitioned and washed with deionized water (100 mL, x3) and dried over sodium sulfate. The mixture was then filtered and concentrated to dryness under reduced pressure to yield an orange/red solid. The solid was dried under high vacuum and then dissolved in EtOAc (150 mL). The red solution was then passed through a plug of silica and the resulting brown solution was concentrated under reduced pressure to afford **10** as a brown, amorphous solid (5.3 g, > 99% pure, 60% yield).

^{1}H NMR (300 MHz, CD_3OD) δ 7.58 (d, J = 8.8 Hz, 1H), 6.88 (d, J = 8.8 Hz, 1H), 6.44 (d, J = 2.2 Hz, 1H), 6.17 (d, J = 2.2 Hz, 1H).

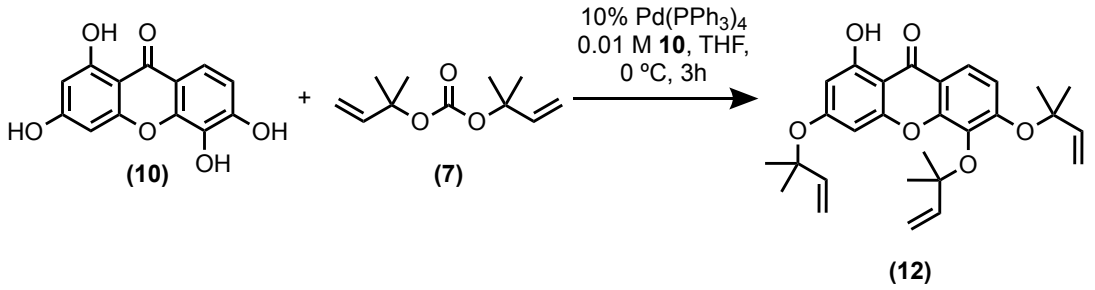

1-hydroxy-3,5,6-tris((2-methylbut-3-en-2-yl)oxy)-9*H*-xanthen-9-one (12): To an oven-dried 500 mL round-bottom flask equipped with a magnetic stirbar kept under an inert atmosphere of argon was added **10** (1 g, 3.84 mmol, 1 eq.), anhydrous THF (384 mL), and carbonate **7** (7.6 g, 38.4 mmol, 10 eq.). Next was added high purity tetrakis(triphenylphosphine)-palladium(0) (444 mg, 0.38 mmol, 0.1 eq.) and the resulting mixture was allowed to stir at room temperature. Within five minutes, the solution turned a dark green color, which was allowed to stir for a total of three hours. The resulting yellow/green mixture was then concentrated to dryness under reduced pressure and immediately purified by silica gel column chromatography using a gradient eluent of 0% to 20% EtOAc in hexanes to afford **12** as a yellow liquid coeluting with carbonate **7**. The isolated mixture of **7** and **12** was then dried under reduced pressure to afford **12** as a viscous yellow liquid (1.2 g, 94% pure, 63% yield).

^{1}H NMR (500 MHz, $CDCl_3$) δ 12.81 (s, 1H), 7.80 (d, J = 8.9 Hz, 1H), 7.09 (d, J = 9.0 Hz, 1H), 6.53 (d, J = 2.2 Hz, 1H), 6.42 (d, J = 2.3 Hz, 1H), 6.26 – 6.13 (m, 3H), 5.30 – 5.16 (m, 5H), 5.02 (dd, J = 10.9, 1.0 Hz, 1H), 1.57 (s, 6H), 1.57 (s, 6H), 1.55 (s, 6H).

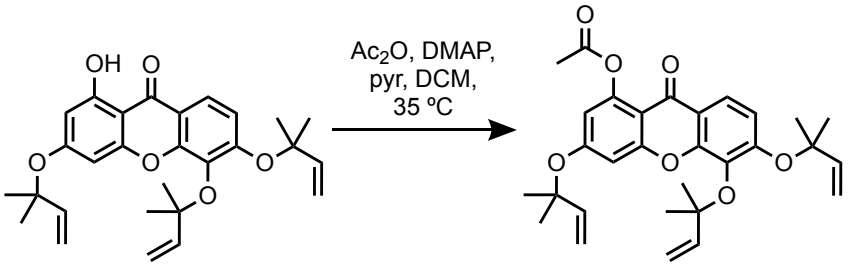

(11) **(12b)**

3,5,6-tris((2-methylbut-3-en-2-yl)oxy)-9-oxo-9*H*-xanthen-1-yl acetate (12b): To an oven-dried 50 mL round-bottom flask equipped with a magnetic stirbar was added **12** (600 mg, 1.29 mmol, 1 eq.) and anhydrous DCM (25 mL). Next was added pyridine (2.6 mL, 32.3 mmol, 25 eq.), 4-(dimethylamino)pyridine (16 mg, 0.13 mmol, 0.1 eq.), and acetic anhydride (3 mL, 32.3 mmol, 25 eq.). The mixture was heated to 35 ºC and stirred overnight. The reaction mixture was then quenched with saturated aqueous $NaHCO_3$ and partitioned with DCM. The organic phase was washed with brine, dried over sodium sulfate, filtered, and concentrated to dryness under reduced pressure. The resulting mixture was subsequently purified by silica gel column chromatography using a gradient eluent of 0% to 20% EtOAc in hexanes to afford **12b** as a clear, viscous liquid (536 mg, > 99% pure, 82% yield).

^{1}H NMR (500 MHz, $CDCl_3$) δ 7.78 (d, J = 9.0 Hz, 1H), 7.04 (d, J = 9.0 Hz, 1H), 6.96 (d, J = 2.4 Hz, 1H), 6.58 (d, J = 2.4 Hz, 1H), 6.24 (dd, J = 17.5, 10.8 Hz, 1H), 6.19 (dd, J = 10.9, 2.9 Hz, 1H), 6.15 (dd, J = 10.9, 3.0 Hz, 1H), 5.30 (d, J = 17.7 Hz, 1H), 5.27 (d, J = 10.9 Hz, 1H), 5.20 (d, J = 3.8 Hz, 1H), 5.17 (d, J = 4.1 Hz, 1H), 5.16 (d, J = 3.2 Hz, 1H), 5.02 (d, J = 10.8 Hz, 1H), 2.46 (s, 3H), 1.58 (s, 6H), 1.54 (s, 8H), 1.54 (s, 6H).

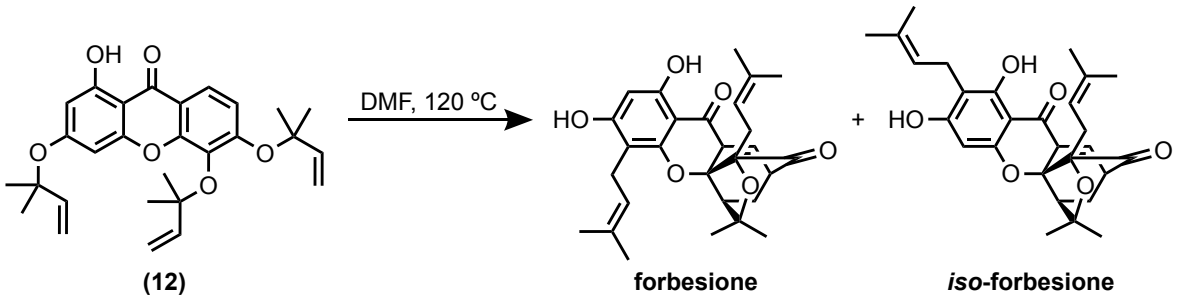

(12) **forbesione** ***iso*-forbesione**

8,10-dihydroxy-2,2-dimethyl-3a,11-bis(3-methylbut-2-en-1-yl)-1,2-dihydro-1,5-methanofuro[2,3-*d*]xanthene-4,7(3a*H*,5*H*)-dione (forbesione) and **8,10-dihydroxy-2,2-dimethyl-3a,9-bis(3-methylbut-2-en-1-yl)-1,2-dihydro-1,5-methanofuro[2,3-*d*]xanthene-4,7(3a*H*,5*H*)-dione (*iso*-forbesione)**: To an oven-dried 50 mL pressure vessel equipped with a magnetic stirbar was added **12** (500 mg, 1.08 mmol, 1eq.) and anhydrous DMF (22 mL). The vessel was sealed and stirred in a preheated oil bath at 120 ºC for two hours. The mixture was then cooled to room temperature and concentrated to dryness under reduced pressure. The resulting yellow residue was purified by silica gel column chromatography using a gradient eluent of 0 to 20% EtOAc in hexanes to afford a mixture of forbesione and *iso*-forbesione (425 mg, 60% forbesione and 40% *iso*-forbesione). The resulting yellow solid was then crystallized in a 1:5 DCM:hexanes system and formation of forbesione crystals were observed after 18h. The crystals were filtered, washed with hexanes (5 mL, x2), and dried under reduced pressure to afford forbesione as a yellow, crystalline solid (170 mg, > 99% pure, 34% yield). The resulting mother liquid was concentrated to dryness under reduced pressure and crystalized in a 1:5 EtOAc:hexanes system and formation of *iso*-forbesione crystals were observed after 18h. The crystals were filtered, washed with hexanes (5 mL, x2), and dried under reduced pressure to afford *iso*-forbesione as a yellow, crystalline solid (67 mg, 95% pure, 13% yield).

Forbesione: ^{1}H NMR (500 MHz, $CDCl_3$) δ 12.60 (s, 1H), 7.46 (d, *J* = 6.9 Hz, 1H), 6.05 (s, 1H), 6.04 (s, 1H), 5.26 – 5.22 (m, 1H), 4.42 (s, 1H), 3.52 – 3.49 (m, 1H), 3.43 (t, *J* = 6.7 Hz, 2H), 2.56 (d, *J* = 10.1 Hz, 2H), 2.48 (d, *J* = 9.5 Hz, 1H), 2.34 (dd, *J* = 13.6, 4.7 Hz, 1H), 1.81 (s, 3H), 1.76 (s, 3H), 1.68 (s, 3H), 1.37 (s, 3H), 1.29 (s, 3H), 1.04 (s, 3H).

***iso*-Forbesione**: ^{1}H NMR (500 MHz, $CDCl_3$) δ 12.83 (s, 1H), 7.41 (d, *J* = 7.0 Hz, 1H), 6.22 (s, 1H), 6.03 (s, 1H), 5.24 (t, *J* = 7.1 Hz, 1H), 4.44 (t, *J* = 7.7 Hz, 1H), 3.50 – 3.47 (m, 1H), 3.38 (s, 1H), 3.37 (s, 1H), 2.61 (s, 1H), 2.59 (s, 1H), 2.40 (d, *J* = 9.5 Hz, 1H), 2.32 (dd, *J* = 13.6, 4.5 Hz, 1H), 1.83 (s, 3H), 1.77 (s, 3H), 1.67 (s, 3H), 1.39 (s, 3H), 1.29 (s, 3H), 1.11 (s, 3H).

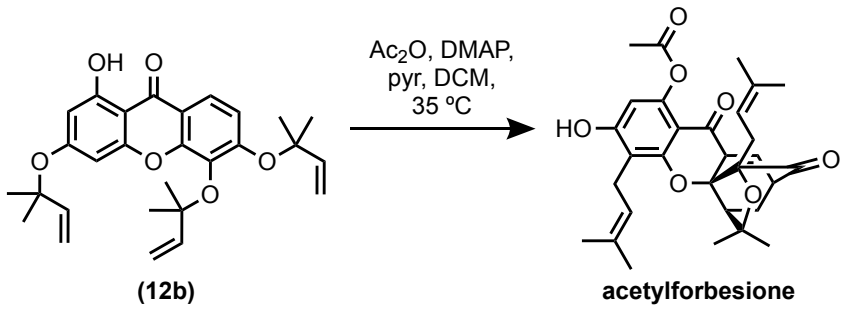

(12b) **acetylforbesione**

10-hydroxy-2,2-dimethyl-3a,11-bis(3-methylbut-2-en-1-yl)-4,7-dioxo-1,2,3a,4,5,7-hexahydro-1,5-methanofuro[2,3-*d*]xanthen-8-yl acetate (acetylforbesione): To an oven-dried 50 mL pressure vessel equipped with a magnetic stirbar was added **12b** (500 mg, 1 mmol, 1eq.) and anhydrous DMF (20 mL). The vessel was sealed and stirred in a preheated oil bath at 120 ºC for two hours. The mixture was then cooled to room temperature and concentrated to dryness under reduced pressure. The resulting yellow residue was purified by silica gel column chromatography using a gradient eluent of 0 to 20% EtOAc in hexanes to afford acetylforbesione as a yellow solid (258 mg, 93% acetylforbesione and 7% *iso*-acetylforbesione, 48% yield).

^{1}H NMR (300 MHz, $CDCl_3$) δ 7.34 (d, J = 6.9 Hz, 1H), 6.57 (s, 1H), 6.24 (s, 1H), 5.27 (t, J = 7.0 Hz, 1H), 4.51 – 4.40 (m, 1H), 3.56 – 3.41 (m, 3H), 2.60 – 2.43 (m, 3H), 2.38 (s, 3H), 2.30 (dd, J = 13.6, 4.8 Hz, 1H), 1.81 (s, 3H), 1.76 (s, 3H), 1.67 (s, 3H), 1.61 (s, 1H), 1.38 (s, 3H), 1.27 (t, J = 3.6 Hz, 6H), 1.05 (s, 3H).

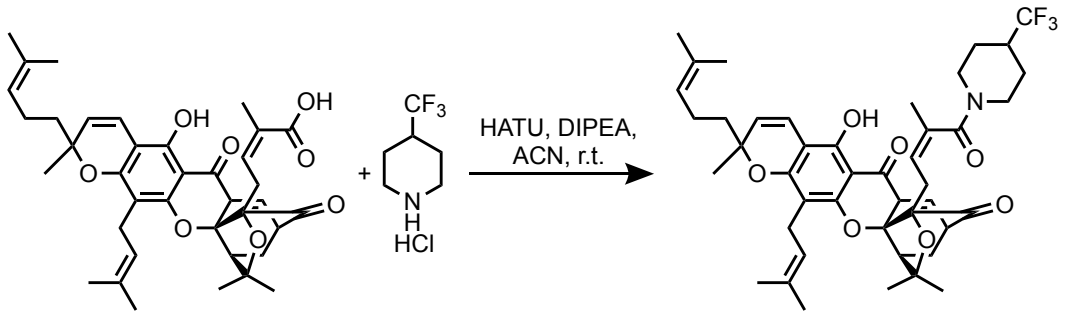

GBA (115)

8-hydroxy-2,2,11-trimethyl-3a-(3-methyl-4-oxo-4-(4-(trifluoromethyl)piperidin-1-yl)but-2-en-1-yl)-13-(3-methylbut-2-en-1-yl)-11-(4-methylpent-3-en-1-yl)-1,2-dihydro-11*H*-1,5-methanofuro[3,2-*g*]pyrano[3,2-*b*]xanthene-4,7(3a*H*,5*H*)-dione (115): To an oven-dried 20 mL scintillation vial equipped with a magnetic stirbar kept under an inert atmosphere of argon was added gambogic acid (100 mg, 0.16 mmol, 1 eq.), HATU (67 mg, 0.17 mmol, 1.1 eq.), and anhydrous ACN (2.5 mL). To the mixture was then added N-ethyldiisopropylamine (68 μL, 0.4 mmol, 2.5 eq.) and the resulting mixture was allowed to stir at room temperature for 10 minutes. Next, was added 4-(trifluoromethyl)piperidine hydrochloride (30 mg, 0.16 mmol, 1 eq.) and the reaction was allowed to stir at room temperature until complete as determined by TLC (product R_f = 0.3, 40% EtOAc in hexanes). The reaction mixture was then diluted with EtOAc (10 mL) and washed with deionized water (5 mL, x2) and saturated brine (5 mL, x2). The organic phase was then treated with magnesium sulfate, filtered, and concentrated under reduced pressure. The resulting crude mixture was then purified by silica gel column chromatography using a gradient eluent of 20% to 40% EtOAc in hexanes to afford **115** as an orange solid (105 mg, 86% yield).

^{1}H NMR (500 MHz, $CDCl_3$) δ 12.86 (m, 1H), 7.52 (m, 1H), 6.67 (d, J = 10.1 Hz, 1H), 5.43 (m, 2H), 5.06 (m, 2H), 4.59 (t, J = 12.8 Hz, 1H), 3.67 (m, 1H), 3.42 (s, 1H), 3.27 (m, 2H), 2.84-2.69 (m, 1H), 2.51-2.02 (m, 8H), 1.86 (d, J = 13.3 Hz, 1H), 1.81-1.73 (m, 8H), 1.66 (d, J = 11.3 Hz, 9H), 1.58 (s, 2H), 1.55 (s, 2H), 1.43 (s, 3H), 1.36 (s, 3H), 1.24 (s, 3H). ^{13}C NMR (125 MHz,

$CDCl_3$) δ 174.98, 165.74, 153.76, 131.43, 129.51, 127.96, 127.70, 120.95, 120.75, 119.76, 118.57, 118.43, 118.16, 98.77, 79.62, 78.91, 77.44, 44.92, 40.79, 38.06, 35.64, 26.12, 25.41, 25.29, 24.81, 23.89, 21.79, 21.72, 21.43, 20.25, 18.76, 17.75, 16.78, 14.20, 13.67. HRMS: Exact mass calculated for $[C_{44}H_{53}F_3NO_7]^+$, 764.3763. Found 764.3769.

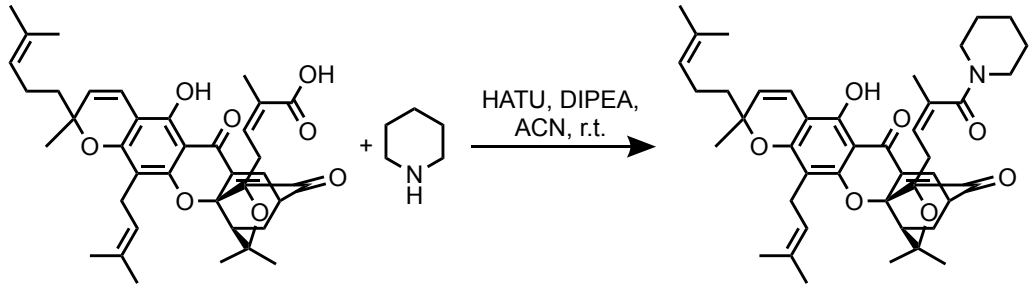

GBA **(116)**

8-hydroxy-2,2,11-trimethyl-3a-(3-methyl-4-oxo-4-(piperidin-1-yl)but-2-en-1-yl)-13-(3-methylbut-2-en-1-yl)-11-(4-methylpent-3-en-1-yl)-1,2-dihydro-11*H*-1,5-methanofuro[3,2-*g*]pyrano[3,2-*b*]xanthene-4,7(3a*H*,5*H*)-dione (116): To an oven-dried 20 mL scintillation vial equipped with a magnetic stirbar kept under an inert atmosphere of argon was added gambogic acid (100 mg, 0.16 mmol, 1 eq.), HATU (67 mg, 0.17 mmol, 1.1 eq.), and anhydrous ACN (2.5 mL). To the mixture was then added N-ethyldiisopropylamine (41 μL, 0.24 mmol, 1.5 eq.) and the resulting mixture was allowed to stir at room temperature for 10 minutes. Next, was added piperidine (16 μL, 0.16 mmol, 1 eq.) and the reaction was allowed to stir at room temperature until complete as determined by TLC (product R_f = 0.2, 40% EtOAc in hexanes). The reaction mixture was then diluted with EtOAc (10 mL) and washed with deionized water (5 mL, x2) and saturated brine (5 mL, x2). The organic phase was then treated with magnesium sulfate, filtered, and concentrated under reduced pressure. The resulting crude mixture was then purified by silica gel column chromatography using a gradient eluent of 20% to 40% EtOAc in hexanes to afford **116** as an orange solid (90 mg, 81% yield).

^{1}H NMR (500 MHz, $CDCl_3$) δ 12.88 (s, 1H), 7.53 (d, *J* = 6.8 Hz, 1H), 6.68 (d, *J* = 10.2 Hz, 1H), 5.44 (d, *J* = 10.1 Hz, 1H), 5.40 (t, *J* = 6.5 Hz, 1H), 5.08 (q, *J* = 8.2 Hz, 2H), 3.56 – 3.48 (m, 1H), 3.43 (t, *J* = 5.8 Hz, 1H), 3.38 – 3.32 (m, 1H), 3.31 – 3.23 (m, 2H), 3.15 – 3.07 (m, 2H), 2.50 (d, *J* = 9.4 Hz, 1H), 2.42 (dd, *J* = 16.1, 6.3 Hz, 1H), 2.29 (dd, *J* = 13.5, 4.8 Hz, 1H), 2.22 (dd, *J* = 16.1,

7.7 Hz, 1H), 2.14 – 2.01 (m, 2H), 1.82 – 1.72 (m, 7H), 1.69 – 1.64 (m, 9H), 1.59 (s, 1H), 1.56 (s, 4H), 1.50 – 1.42 (m, 5H), 1.40 – 1.29 (m, 4H), 1.25 (s, 3H). ^{13}C NMR (125 MHz, $CDCl_3$) δ 199.46, 175.08, 165.47, 157.64, 153.73, 153.63, 131.60, 129.94, 129.07, 127.95, 127.65, 120.64, 119.77, 118.20, 117.49, 111.90, 103.66, 98.67, 96.50, 87.02, 79.55, 78.89, 77.38, 44.94, 43.06, 42.92, 38.08, 37.74, 26.13, 25.41, 24.79, 23.95, 22.80, 21.80, 21.72, 21.52, 21.42, 20.61, 18.78, 17.75, 16.88, 14.21, 13.68. HRMS: Exact mass calculated for $[C_{43}H_{54}NO_7]^+$, 696.3891. Found 696.3895.

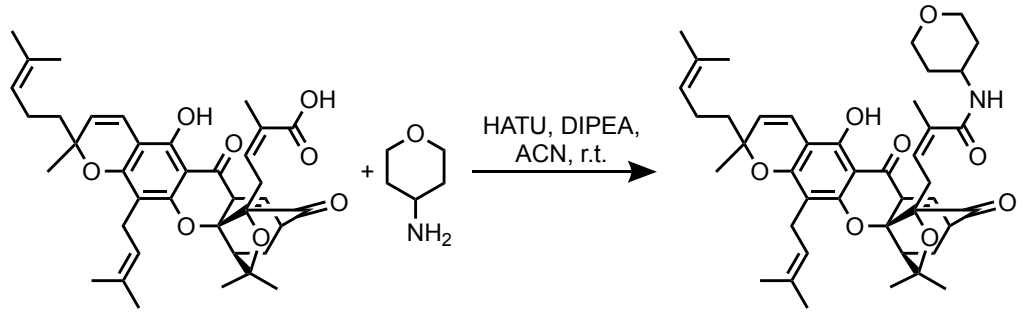

4-(8-hydroxy-2,2,11-trimethyl-13-(3-methylbut-2-en-1-yl)-11-(4-methylpent-3-en-1-yl)-4,7-dioxo-1,2,5,7-tetrahydro-11H-1,5-methanofuro[3,2-g]pyrano[3,2-b]xanthen-3a(4H)-yl)-2-methyl-N-(tetrahydro-2H-pyran-4-yl)but-2-enamide (117): To an oven-dried 20 mL scintillation vial equipped with a magnetic stirbar kept under an inert atmosphere of argon was added gambogic acid (100 mg, 0.16 mmol, 1 eq.), HATU (67 mg, 0.17 mmol, 1.1 eq.), and anhydrous ACN (2.5 mL). To the mixture was then added N-ethyldiisopropylamine (41 μL, 0.24 mmol, 1.5 eq.) and the resulting mixture was allowed to stir at room temperature for 10 minutes. Next, was added 4-aminotetrahydropyran (16 μL, 0.16 mmol, 1 eq.) and the reaction was allowed to stir at room temperature until complete as determined by TLC (product R_f = 0.4, 40% EtOAc in DCM). The reaction mixture was then diluted with EtOAc (10 mL) and washed with deionized water (5 mL, x2) and saturated brine (5 mL, x2). The organic phase was then treated with magnesium sulfate, filtered, and concentrated under reduced pressure. The resulting crude mixture was then purified by silica gel column chromatography using a gradient eluent of 20% to 40% EtOAc in DCM to afford **117** as an orange solid (62 mg, 55% yield).

^{1}H NMR (500 MHz, $CDCl_3$) δ 12.84 (s, 1H), 7.55 (d, J = 6.9 Hz, 1H), 6.85 (d, J = 7.6 Hz, 1H), 6.68 (d, J = 10.1 Hz, 1H), 5.46 (d, J = 10.1 Hz, 1H), 5.21 (t, J = 8.4 Hz, 1H), 5.11 – 4.97 (m, 2H), 4.00 – 3.90 (m, 3H), 3.46 (t, J = 10.7 Hz, 3H), 3.31 (dd, J = 14.6, 7.9 Hz, 1H), 3.16 (d, J = 17.9 Hz, 1H), 2.73 (dd, J = 15.2, 9.3 Hz, 1H), 2.54 (d, J = 9.4 Hz, 1H), 2.31 (dd, J = 13.5, 4.6 Hz, 1H),

2.20 (dd, J = 15.4, 7.9 Hz, 1H), 2.16 (s, 1H), 2.10 – 1.99 (m, 2H), 1.89 (t, J = 14.1 Hz, 2H), 1.79 (s, 4H), 1.72 (s, 3H), 1.68 (s, 3H), 1.63 (d, J = 7.1 Hz, 7H), 1.57 – 1.45 (m, 5H), 1.43 (s, 2H), 1.40 (dd, J = 9.8, 3.5 Hz, 1H), 1.30 (s, 3H). ^{13}C NMR (125 MHz, $CDCl_3$) δ 204.12, 178.98, 168.50, 162.14, 157.98, 157.34, 136.53, 135.93, 133.37, 132.22, 132.11, 125.16, 123.91, 122.18, 116.03, 108.03, 103.11, 100.59, 91.35, 84.49, 83.73, 81.81, 67.21, 67.11, 49.23, 47.05, 45.90, 42.31, 33.26, 32.95, 30.22, 29.34, 29.24, 28.15, 25.98, 25.94, 25.41, 22.97, 21.82, 21.44, 18.39, 17.91. HRMS: Exact mass calculated for $[C_{43}H_{53}NO_8]^+$, 712.3844. Found 712.3838.

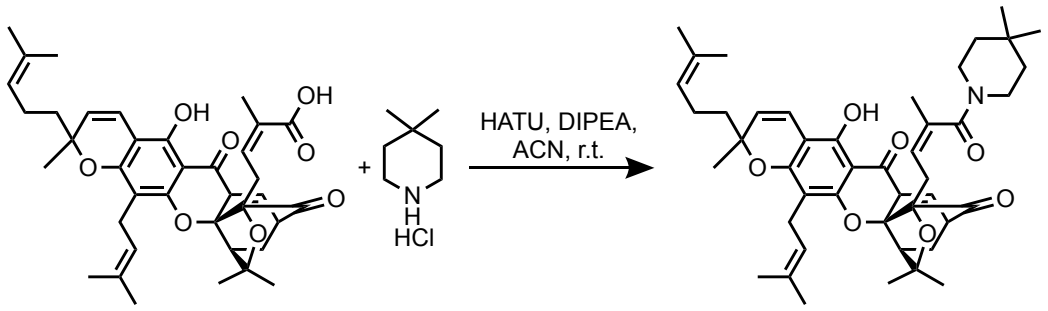

GBA (118)

3a-(4-(4,4-dimethylpiperidin-1-yl)-3-methyl-4-oxobut-2-en-1-yl)-8-hydroxy-2,2,11-trimethyl-13-(3-methylbut-2-en-1-yl)-11-(4-methylpent-3-en-1-yl)-1,2-dihydro-11*H*-1,5-methanofuro[3,2-*g*]pyrano[3,2-*b*]xanthene-4,7(3a*H*,5*H*)-dione (118): To an oven-dried 20 mL scintillation vial equipped with a magnetic stirbar kept under an inert atmosphere of argon was added gambogic acid (100 mg, 0.16 mmol, 1 eq.), HATU (67 mg, 0.17 mmol, 1.1 eq.), and anhydrous ACN (2.5 mL). To the mixture was then added N-ethyldiisopropylamine (68 μL, 0.4 mmol, 2.5 eq.) and the resulting mixture was allowed to stir at room temperature for 10 minutes. Next, was added 4,4-dimethylpiperidine hydrochloride (24 mg, 0.16 mmol, 1 eq.). The reaction was allowed to stir at room temperature until complete as determined by TLC (product R_f = 0.2, 40% EtOAc in hexanes). The resulting yellow solution was diluted with EtOAc (10 mL) and washed with deionized water (5 mL, x2) and saturated brine (5 mL, x2). The organic phase was then treated with magnesium sulfate, filtered, and concentrated under reduced pressure. The resulting yellow solid was then purified by silica gel column chromatography using a gradient eluent of 20% to 40% EtOAc in hexanes to afford **118** as an orange solid (91 mg, 79% yield).

^{1}H NMR (500 MHz, $CDCl_3$) δ 12.87 (s, 1H), 7.52 (d, *J* = 6.9 Hz, 1H), 6.66 (d, *J* = 10.1 Hz, 1H), 5.43 (d, *J* = 10.2 Hz, 1H), 5.36 (t, *J* = 7.0 Hz, 1H), 5.09 – 5.03 (m, 2H), 3.65 – 3.54 (m, 1H), 3.42 (dd, *J* = 6.8, 4.4 Hz, 1H), 3.33 – 3.23 (m, 3H), 3.15 – 3.05 (m, 2H), 2.48 (d, *J* = 9.3 Hz, 1H), 2.42 (dd, 1H), 2.28 (dd, *J* = 13.5, 4.7 Hz, 1H), 2.22 (dd, *J* = 15.7, 7.3 Hz, 1H), 2.03 (h, *J* = 7.9 Hz, 2H),

1.80 – 1.75 (m, 1H), 1.73 (s, 3H), 1.72 (d, J = 1.4 Hz, 3H), 1.67 (s, 3H), 1.64 (s, 6H), 1.64 – 1.55 (m, 7H), 1.55 (s, 3H), 1.43 (s, 3H), 1.41 – 1.27 (m, 2H), 1.24 (s, 4H), 1.09 (s, 2H), 0.91 (s, 3H), 0.91 (s, 3H). ^{13}C NMR (125 MHz, $CDCl_3$) δ 203.50, 179.10, 169.53, 161.77, 157.83, 157.69, 135.61, 134.02, 133.14, 131.98, 131.70, 124.72, 123.88, 122.32, 121.74, 116.00, 107.76, 102.82, 100.57, 91.10, 83.56, 83.04, 81.44, 49.08, 47.14, 42.66, 42.16, 39.55, 38.13, 37.48, 30.19, 29.46, 29.25, 28.87, 28.53, 27.94, 26.99, 25.83, 25.76, 25.53, 22.80, 21.81, 20.94, 18.24, 17.72, 0.10. HRMS: Exact mass calculated for $[C_{45}H_{58}NO_7]^+$, 724.4208. Found 724.4204.

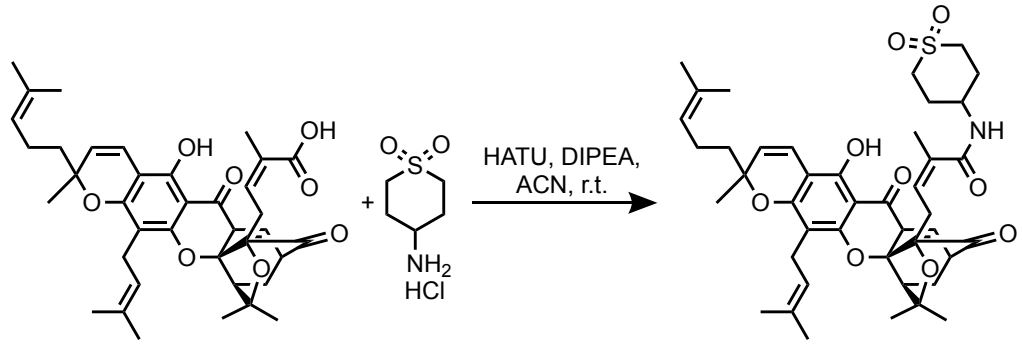

GBA **(119)**

***N*-(1,1-dioxidotetrahydro-2*H*-thiopyran-4-yl)-4-(8-hydroxy-2,2,11-trimethyl-13-(3-methylbut-2-en-1-yl)-11-(4-methylpent-3-en-1-yl)-4,7-dioxo-1,2,5,7-tetrahydro-11*H*-1,5-methanofuro[3,2-*g*]pyrano[3,2-*b*]xanthen-3a(4*H*)-yl)-2-methylbut-2-enamide (119):** To an oven-dried 20 mL scintillation vial equipped with a magnetic stirbar kept under an inert atmosphere of argon was added gambogic acid (100 mg, 0.16 mmol, 1 eq.), HATU (67 mg, 0.17 mmol, 1.1 eq.), and anhydrous ACN (2.5 mL). To the mixture was then added N-ethyldiisopropylamine (68 μL, 0.4 mmol, 2.5 eq.) and the resulting mixture was allowed to stir at room temperature for 10 minutes. Next, was added 4-aminotetrahydro-2*H*-thiopyran 1,1-dioxide hydrochloride (30 mg, 0.16 mmol, 1 eq.) and the reaction was allowed to stir at room temperature until complete as determined by TLC (product R_f = 0.4, 40% EtOAc in DCM). The reaction mixture was then diluted with EtOAc (10 mL) and washed with deionized water (5 mL, x2) and saturated brine (5 mL, x2). The organic phase was then treated with magnesium sulfate, filtered, and concentrated under reduced pressure. The resulting crude mixture was then purified by silica gel column chromatography using a gradient eluent of 20% to 40% EtOAc in DCM to afford **119** as an orange solid (78 mg, 64% yield).

^{1}H NMR (500 MHz, $CDCl_3$) δ 11.88 (d, *J* = 4.3 Hz, 1H), 7.52 (d, *J* = 7.1 Hz, 1H), 6.69 – 6.61 (m, 1H), 5.89 (dt, *J* = 12.0, 6.1 Hz, 1H), 5.47 (dd, *J* = 13.4, 10.1 Hz, 1H), 5.12 – 5.03 (m, 1H), 4.98 (d,

J = 6.6 Hz, 1H), 4.16 – 4.11 (m, 1H), 3.98 (dd, *J* = 4.0, 1.8 Hz, 1H), 3.32 (dd, *J* = 14.6, 8.8 Hz, 1H), 3.23 – 3.16 (m, 2H), 3.15 – 3.07 (m, 6H), 2.99 – 2.91 (m, 3H), 2.81 (d, *J* = 7.2 Hz, 1H), 2.56 (td, *J* = 9.5, 8.5, 4.3 Hz, 2H), 2.48 (q, *J* = 6.6, 6.0 Hz, 2H), 2.37 (d, *J* = 17.0 Hz, 3H), 1.94 (s, 3H), 1.72 (s, 3H), 1.66 (d, *J* = 7.0 Hz, 6H), 1.42 (s, 1H), 1.37 – 1.32 (m, 5H), 1.19 (s, 3H). ^{13}C NMR (125 MHz, $CDCl_3$) δ 209.89, 169.06, 161.84, 156.72, 155.33, 136.39, 132.26, 131.66, 125.64, 123.89, 122.74, 116.00, 109.00, 103.33, 101.99, 89.40, 87.16, 83.52, 81.49, 50.76, 49.74, 49.60, 49.32, 48.82, 45.38, 44.39, 43.40, 42.03, 30.43, 30.04, 30.02, 30.00, 29.93, 29.73, 29.32, 28.56, 28.14, 27.89, 27.39, 25.95, 25.93, 25.91, 25.89, 23.12, 22.87, 21.68, 20.94, 20.91, 18.34, 18.31, 17.92, 17.87. HRMS: Exact mass calculated for $[C_{43}H_{54}NO_9S]^+$, 760.3514. Found 760.3517.

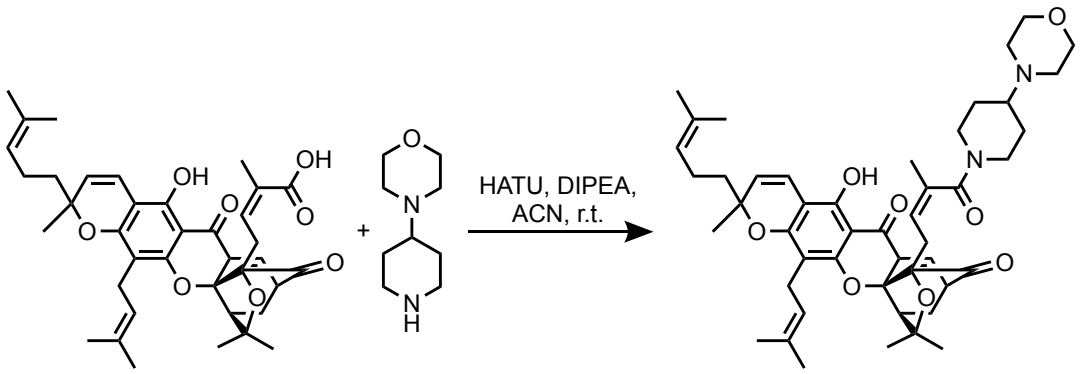

GBA (120)

8-hydroxy-2,2,11-trimethyl-3a-(3-methyl-4-(4-morpholinopiperidin-1-yl)-4-oxobut-2-en-1-yl)-13-(3-methylbut-2-en-1-yl)-11-(4-methylpent-3-en-1-yl)-1,2-dihydro-11*H*-1,5-methanofuro[3,2-*g*]pyrano[3,2-*b*]xanthene-4,7(3a*H*,5*H*)-dione (120): To an oven-dried 20 mL scintillation vial equipped with a magnetic stirbar kept under an inert atmosphere of argon was added gambogic acid (100 mg, 0.16 mmol, 1 eq.), HATU (67 mg, 0.17 mmol, 1.1 eq.), and anhydrous ACN (2.5 mL). To the mixture was then added N-ethyldiisopropylamine (41 μL, 0.24 mmol, 1.5 eq.) and the resulting mixture was allowed to stir at room temperature for 10 minutes. Next, was added 4-morpholinopiperidine (27 mg, 0.16 mmol, 1 eq.) and the reaction was allowed to stir at room temperature until complete as determined by TLC (product R_f = 0.5, 10% MeOH in DCM). The reaction mixture was then diluted with EtOAc (10 mL) and washed with deionized water (5 mL, x2) and saturated brine (5 mL, x2). The organic phase was then treated with magnesium sulfate, filtered, and concentrated under reduced pressure. The resulting crude mixture was then purified by silica gel column chromatography using a gradient eluent of 0% to 10% MeOH in DCM to afford **120** as an orange solid (80 mg, 64% yield).

^{1}H NMR (500 MHz, $CDCl_3$) δ 12.88 (d, *J* = 9.1 Hz, 1H), 7.53 (d, *J* = 6.6 Hz, 1H), 6.68 (d, *J* = 9.9 Hz, 1H), 5.59 – 5.22 (m, 3H), 5.07 (s, 2H), 4.46 (dd, *J* = 35.3, 12.2 Hz, 1H), 3.71 (s, 4H), 3.58 (s, 1H), 3.44 (s, 1H), 3.28 (s, 2H), 2.77 (dt, *J* = 33.8, 10.3 Hz, 1H), 2.68 – 2.55 (m, 1H), 2.51 (s, 6H),

2.30 (d, J = 9.1 Hz, 4H), 2.05 (d, J = 7.4 Hz, 2H), 1.80 (s, 2H), 1.74 (s, 3H), 1.72 (s, 3H), 1.69 – 1.64 (m, 8H), 1.61 – 1.54 (m, 4H), 1.44 (s, 3H), 1.39 – 1.31 (m, 3H), 1.25 (s, 3H). ^{13}C NMR (125 MHz, $CDCl_3$) δ 203.76, 179.22, 169.55, 161.92, 157.95, 157.72, 135.76, 134.03, 133.25, 132.16, 131.86, 124.91, 123.96, 122.37, 122.12, 116.10, 107.86, 102.93, 100.71, 91.19, 83.73, 83.15, 81.61, 67.50, 62.27, 61.98, 50.08, 49.97, 49.19, 47.21, 45.40, 45.10, 42.27, 42.07, 40.31, 40.09, 30.30, 29.49, 29.32, 29.04, 28.16, 27.46, 26.01, 25.93, 25.61, 22.98, 21.97, 21.11, 21.06, 18.41, 17.89. HRMS: Exact mass calculated for $[C_{47}H_{61}N_2O_8]^+$, 781.4422. Found 781.4415.

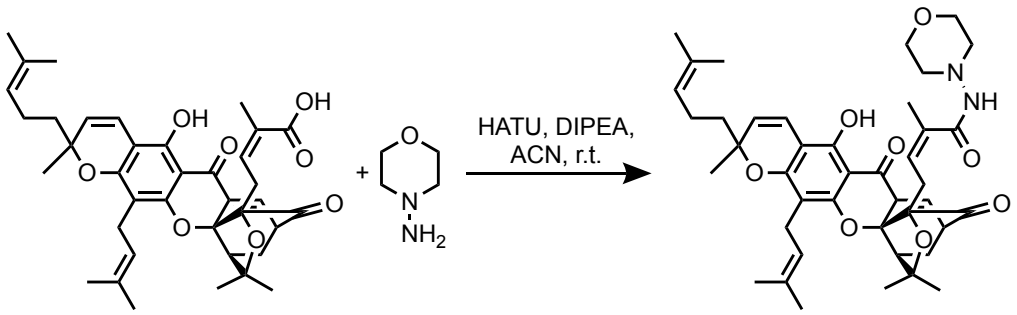

GBA (121)

4-(8-hydroxy-2,2,11-trimethyl-13-(3-methylbut-2-en-1-yl)-11-(4-methylpent-3-en-1-yl)-4,7-dioxo-1,2,5,7-tetrahydro-11*H*-1,5-methanofuro[3,2-*g*]pyrano[3,2-*b*]xanthen-3a(4*H*)-yl)-2-methyl-*N*-morpholinobut-2-enamide (121): To an oven-dried 20 mL scintillation vial equipped with a magnetic stirbar kept under an inert atmosphere of argon was added gambogic acid (100 mg, 0.16 mmol, 1 eq.), HATU (67 mg, 0.17 mmol, 1.1 eq.), and anhydrous ACN (2.5 mL). To the mixture was then added N-ethyldiisopropylamine (41 μL, 0.24 mmol, 1.5 eq.) and the resulting mixture was allowed to stir at room temperature for 10 minutes. Next, was added 4-aminomorpholine (15 μL, 0.16 mmol, 1 eq.) and the reaction was allowed to stir at room temperature until complete as determined by TLC (product R_f = 0.2 40% EtOAc in DCM). The reaction mixture was then diluted with EtOAc (10 mL) and washed with deionized water (5 mL, x2) and saturated brine (5 mL, x2). The organic phase was then treated with magnesium sulfate, filtered, and concentrated under reduced pressure. The resulting crude mixture was then purified by silica gel column chromatography using a gradient eluent of 20% to 40% EtOAc in DCM to afford **121** as an orange solid (68 mg, 60% yield).

^{1}H NMR (500 MHz, $CDCl_3$) δ 12.84 (s, 1H), 7.75 (s, 1H), 7.57 (d, *J* = 6.8 Hz, 1H), 6.69 (d, *J* = 9.9 Hz, 1H), 5.47 (d, *J* = 9.8 Hz, 1H), 5.26 (t, *J* = 8.4 Hz, 1H), 5.09 – 4.99 (m, 2H), 3.83 (s, 4H), 3.53 – 3.47 (m, 1H), 3.35 – 3.30 (m, 1H), 3.16 (d, *J* = 14.7 Hz, 1H), 2.86 (s, 4H), 2.71 (dd, *J* = 15.1, 9.3 Hz, 1H), 2.56 (d, *J* = 9.4 Hz, 1H), 2.33 (dd, *J* = 13.4, 4.5 Hz, 1H), 2.18 (dd, *J* = 15.4, 7.6

Hz, 1H), 2.07 – 2.00 (m, 2H), 1.81 (s, 3H), 1.73 (s, 3H), 1.71 (s, 3H), 1.68 – 1.63 (m, 8H), 1.56 (s, 3H), 1.45 (s, 3H), 1.33 (s, 3H), 1.26 (t, J = 6.7 Hz, 1H). ^{13}C NMR (125 MHz, $CDCl_3$) δ 204.07, 178.89, 166.57, 162.19, 157.99, 157.25, 135.94, 135.30, 133.33, 132.23, 132.18, 125.22, 124.15, 123.90, 122.13, 115.99, 108.01, 103.17, 100.57, 91.35, 84.68, 83.63, 81.88, 66.67, 56.15, 49.22, 47.04, 42.31, 30.26, 29.46, 29.32, 28.18, 25.98, 25.94, 25.41, 22.97, 21.81, 21.43, 18.39, 17.92. HRMS: Exact mass calculated for $[C_{42}H_{53}N_2O_8]^+$, 713.3796. Found 713.3793.

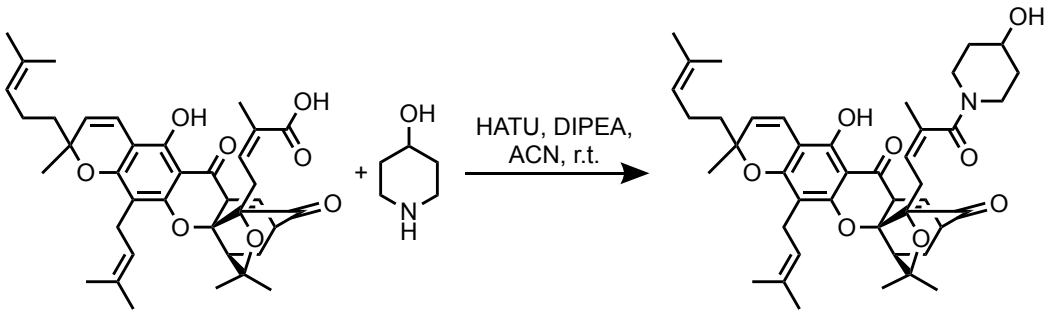

GBA (122)

8-hydroxy-3a-(4-(4-hydroxypiperidin-1-yl)-3-methyl-4-oxobut-2-en-1-yl)-2,2,11-trimethyl-13-(3-methylbut-2-en-1-yl)-11-(4-methylpent-3-en-1-yl)-1,2-dihydro-11H-1,5-methanofuro[3,2-g]pyrano[3,2-b]xanthene-4,7(3aH,5H)-dione (122): To an oven-dried 20 mL scintillation vial equipped with a magnetic stirbar kept under an inert atmosphere of argon was added gambogic acid (100 mg, 0.16 mmol, 1 eq.), HATU (67 mg, 0.17 mmol, 1.1 eq.), and anhydrous ACN (2.5 mL). To the mixture was then added N-ethyldiisopropylamine (41 μL, 0.24 mmol, 1.5 eq.) and the resulting mixture was allowed to stir at room temperature for 10 minutes. Next, was added 4-hydroxypiperidine (16 mg, 0.16 mmol, 1 eq.) and the reaction was allowed to stir at room temperature until complete as determined by TLC (product R_f = 0.1 40% EtOAc in DCM). The reaction mixture was then diluted with EtOAc (10 mL) and washed with deionized water (5 mL, x2) and saturated brine (5 mL, x2). The organic phase was then treated with magnesium sulfate, filtered, and concentrated under reduced pressure. The resulting crude mixture was then purified by silica gel column chromatography using a gradient eluent of 20% to 40% EtOAc in DCM to afford **122** as an orange solid (97 mg, 85% yield).

^{1}H NMR (500 MHz, $CDCl_3$) δ 12.84 (d, J = 39.6 Hz, 1H), 7.55 (t, J = 7.8 Hz, 1H), 6.68 (d, J = 10.1 Hz, 1H), 5.54 – 5.35 (m, 2H), 5.07 (s, 2H), 3.81 (d, J = 40.0 Hz, 1H), 3.49 (d, J = 14.1 Hz, 1H), 3.45 – 3.41 (m, 1H), 3.36 – 3.20 (m, 2H), 3.19 – 2.85 (m, 2H), 2.51 (d, J = 9.2 Hz, 1H), 2.48 – 2.38 (m, 1H), 2.30 (d, J = 13.6 Hz, 1H), 2.25 – 2.15 (m, 1H), 2.10 – 2.00 (m, 2H), 1.88 – 1.79

(m, 2H), 1.74 (s, 7H), 1.68 (s, 5H), 1.66 (s, 6H), 1.60 (s, 1H), 1.56 (s, 2H), 1.45 (s, 3H), 1.38 (s, 1H), 1.37 – 1.29 (m, 2H), 1.26 (s, 4H). ^{13}C NMR (125 MHz, $CDCl_3$) δ 203.83, 179.26, 169.91, 162.19, 157.95, 136.34, 135.90, 133.93, 133.57, 133.15, 132.20, 125.00, 123.98, 122.32, 116.05, 108.00, 107.95, 102.98, 100.69, 91.28, 84.04, 83.01, 81.78, 68.06, 67.42, 49.10, 47.35, 43.87, 43.28, 42.32, 38.83, 38.21, 35.81, 35.09, 34.57, 34.02, 30.35, 29.65, 29.03, 28.25, 25.95, 25.44, 23.00, 21.97, 20.97, 18.43, 17.91. HRMS: Exact mass calculated for $[C_{43}H_{54}NO_8]^+$, 712.3844. Found 712.3838.

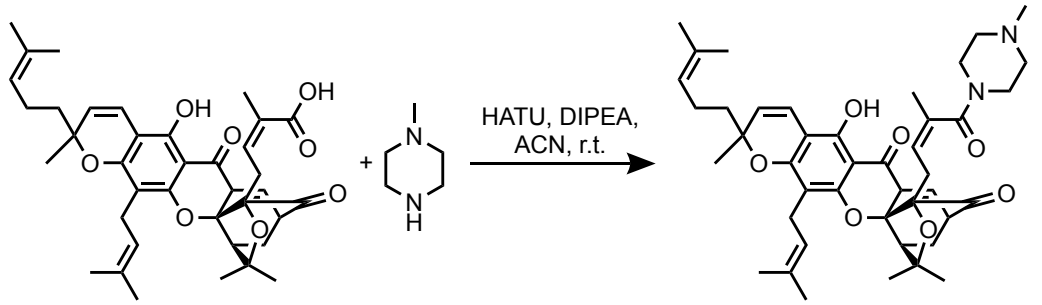

GBA (130)

8-hydroxy-2,2,11-trimethyl-3a-(3-methyl-4-(4-methylpiperazin-1-yl)-4-oxobut-2-en-1-yl)-13-(3-methylbut-2-en-1-yl)-11-(4-methylpent-3-en-1-yl)-1,2-dihydro-11*H*-1,5-methanofuro[3,2-*g*]pyrano[3,2-*b*]xanthene-4,7(3a*H*,5*H*)-dione (130): To an oven-dried 20 mL scintillation vial equipped with a magnetic stirbar kept under an inert atmosphere of argon was added gambogic acid (100 mg, 0.16 mmol, 1 eq.), HATU (67 mg, 0.17 mmol, 1.1 eq.), and anhydrous ACN (2.5 mL). To the mixture was then added N-ethyldiisopropylamine (41 μL, 0.24 mmol, 1.5 eq.) and the resulting mixture was allowed to stir at room temperature for 10 minutes. Next, was added 4-methylpiperazine (18 μL, 0.16 mmol, 1 eq.) and the reaction was allowed to stir at room temperature until complete as determined by TLC (product R_f = 0.6, 10% MeOH in DCM). The reaction mixture was then diluted with EtOAc (10 mL) and washed with deionized water (5 mL, x2) and saturated brine (5 mL, x2). The organic phase was then treated with magnesium sulfate, filtered, and concentrated under reduced pressure. The resulting crude mixture was then purified by silica gel column chromatography using a gradient eluent of 0% to 10% MeOH in DCM to afford **130** as an orange solid (73 mg, 64% yield).

^{1}H NMR (500 MHz, $CDCl_3$) δ 12.88 (s, 1H), 7.54 (d, *J* = 6.9 Hz, 1H), 6.68 (d, *J* = 10.1 Hz, 1H), 5.49 – 5.41 (m, 2H), 5.12 – 5.04 (m, 2H), 3.63 (s, 1H), 3.48 – 3.40 (m, 2H), 3.33 – 3.20 (m, 4H), 2.80 (s, 1H), 2.51 (d, *J* = 9.3 Hz, 1H), 2.41 (dd, *J* = 15.7, 6.6 Hz, 1H), 2.38 – 2.26 (m, 3H), 2.26 – 2.17 (m, 6H), 2.15 – 2.02 (m, 3H), 1.74 (s, 6H), 1.69 (s, 3H), 1.67 – 1.60 (m, 7H), 1.56 (s, 2H),

1.44 (s, 2H), 1.39 – 1.33 (m, 2H), 1.26 (s, 3H). ^{13}C NMR (125 MHz, $CDCl_3$) δ 203.75, 179.14, 169.82, 161.89, 157.93, 157.76, 135.79, 133.49, 133.23, 132.13, 131.86, 124.86, 123.96, 122.46, 122.38, 116.09, 107.87, 102.92, 100.65, 91.24, 83.83, 83.02, 81.60, 55.83, 54.86, 49.12, 47.25, 46.25, 46.02, 42.27, 40.97, 30.33, 29.68, 29.00, 28.14, 25.99, 25.92, 25.61, 22.97, 21.95, 21.04, 18.40, 17.87. HRMS: Exact mass calculated for $[C_{43}H_{55}N_2O_7]^+$, 711.4004. Found 711.4002.

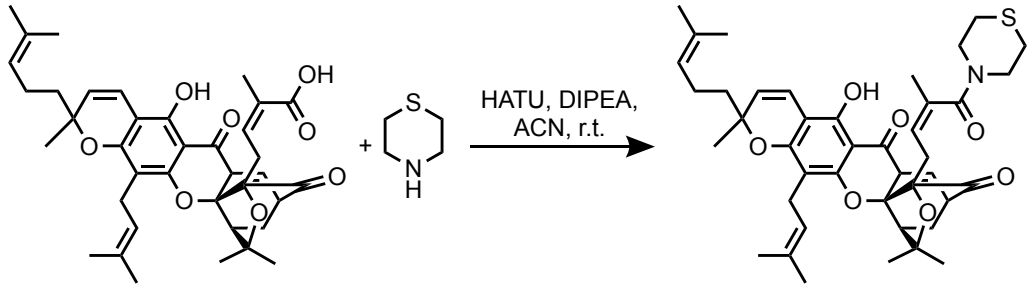

GBA **(135)**

8-hydroxy-2,2,11-trimethyl-3a-(3-methyl-4-oxo-4-thiomorpholinobut-2-en-1-yl)-13-(3-methylbut-2-en-1-yl)-11-(4-methylpent-3-en-1-yl)-1,2-dihydro-11*H*-1,5-methanofuro[3,2-*g*]pyrano[3,2-*b*]xanthene-4,7(3a*H*,5*H*)-dione (135): To an oven-dried 20 mL scintillation vial equipped with a magnetic stirbar kept under an inert atmosphere of argon was added gambogic acid pyridinium salt (100 mg, 0.14 mmol, 1 eq.), HATU (59 mg, 0.16 mmol, 1.1 eq.), and anhydrous ACN (2.5 mL). To the mixture was then added N-ethyldiisopropylamine (36 µL, 0.21 mmol, 1.5 eq.) and the resulting mixture was allowed to stir at room temperature for 10 minutes. Next, was added thiomorpholine (14 µL, 0.14 mmol, 1 eq.) and the reaction was allowed to stir at room temperature until complete as determined by TLC (product R_f = 0.3, 40% EtOAc in hexanes). The reaction mixture was then diluted with EtOAc (10 mL) and washed with deionized water (5 mL, x2) and saturated brine (5 mL, x2). The organic phase was then treated with magnesium sulfate, filtered, and concentrated under reduced pressure. The resulting crude mixture was then purified by silica gel column chromatography using a gradient eluent of 20% to 40% EtOAc in hexanes to afford **135** as an orange solid (86 mg, 86% yield).

^{1}H NMR (500 MHz, $CDCl_3$) δ 12.87 (s, 1H), 7.54 (d, *J* = 6.8 Hz, 1H), 6.68 (d, *J* = 10.1 Hz, 1H), 5.45 (d, *J* = 10.1 Hz, 1H), 5.39 (td, *J* = 7.1, 1.6 Hz, 1H), 5.11 – 5.03 (m, 2H), 3.89 (s, 1H), 3.66 (s, 1H), 3.52 – 3.41 (m, 3H), 3.34 – 3.23 (m, 2H), 2.61 – 2.52 (m, 2H), 2.51 (d, *J* = 9.4 Hz, 1H), 2.50 – 2.43 (m, 2H), 2.40 (ddd, *J* = 15.8, 7.0, 1.6 Hz, 1H), 2.30 (dd, *J* = 13.5, 4.7 Hz, 1H), 2.23 (ddd, *J*

= 15.8, 7.4, 1.5 Hz, 1H), 2.05 (h, *J* = 7.9 Hz, 2H), 1.82 – 1.77 (m, 1H), 1.75 (s, 3H), 1.73 (d, *J* = 1.5 Hz, 3H), 1.68 (s, 3H), 1.66 (d, *J* = 1.4 Hz, 6H), 1.65 – 1.55 (m, 4H), 1.44 (s, 3H), 1.39 – 1.34 (m, 1H), 1.26 (s, 3H). ^{13}C NMR (125 MHz, $CDCl_3$) δ 203.74, 179.23, 170.12, 161.95, 158.01, 157.77, 135.75, 133.69, 133.38, 132.17, 131.94, 124.94, 124.02, 122.63, 122.45, 116.12, 107.89, 102.99, 100.73, 91.24, 83.84, 83.16, 81.69, 77.55, 77.30, 77.05, 49.22, 48.70, 47.27, 43.40, 42.33, 30.36, 29.66, 29.05, 28.62, 28.18, 27.74, 26.01, 25.93, 25.65, 23.00, 21.99, 21.13, 18.43, 17.89. HRMS: Exact mass calculated for $[C_{42}H_{51}NO_7S]^+$, 714.3459. Found 714.3456.

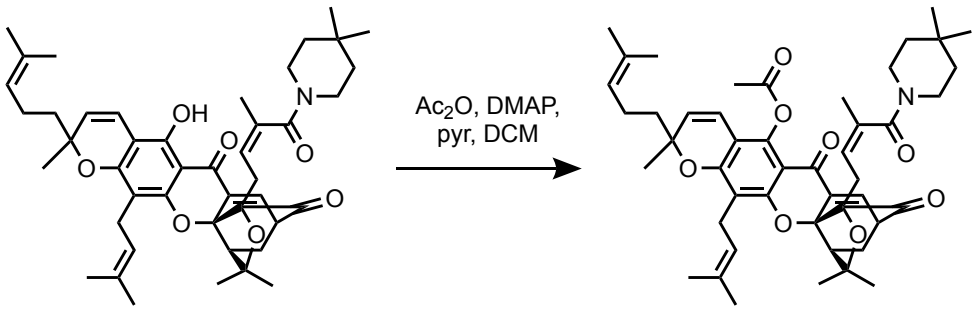

(118) (143)

3a-(4-(4,4-dimethylpiperidin-1-yl)-3-methyl-4-oxobut-2-en-1-yl)-2,2,11-trimethyl-13-(3-methylbut-2-en-1-yl)-11-(4-methylpent-3-en-1-yl)-4,7-dioxo-1,2,3a,4,5,7-hexahydro-11*H*-1,5-methanofuro[3,2-*g*]pyrano[3,2-*b*]xanthen-8-yl acetate (143): To a 20 mL scintillation vial equipped with a magnetic stirbar kept under an inert atmosphere of argon was added 3a-(4-(4,4-dimethylpiperidin-1-yl)-3-methyl-4-oxobut-2-en-1-yl)-8-hydroxy-2,2,11-trimethyl-13-(3-methylbut-2-en-1-yl)-11-(4-methylpent-3-en-1-yl)-1,2-dihydro-11*H*-1,5-methanofuro[3,2-*g*]pyrano[3,2-*b*]xanthene-4,7(3a*H*,5*H*)-dione (100 mg, 0.14 mmol, 1 eq.) and anhydrous DCM (2.5 mL). Next were added pyridine (280 μL, 3.46 mmol, 25 eq.), 4-(dimethylamino)pyridine (2 mg, 0.01 mmol, 0.1 eq.), and acetic anhydride (327 μL, 3.46 mmol, 25 eq.). The reaction was allowed to stir at room temperature until complete as determined by TLC (product R_f = 0.2, 40% EtOAc in hexanes). The reaction mixture was then quenched with saturated sodium bicarbonate and partitioned with DCM. The organic phase was washed with brine, dried over magnesium sulfate, filtered, and concentrated under reduced pressure. The resulting crude mixture was purified by silica gel column chromatography using a gradient eluent of 20% to 40% EtOAc in hexanes to afford **143** as a pale yellow, amorphous solid (30 mg, 28% yield).

^{1}H NMR (500 MHz, $CDCl_3$) δ 7.41 (d, *J* = 6.9 Hz, 1H), 6.42 (d, *J* = 10.2 Hz, 1H), 5.59 (d, *J* = 10.2 Hz, 1H), 5.30 (s, 1H), 5.11 (t, *J* = 6.6 Hz, 1H), 5.04 (t, *J* = 7.1 Hz, 1H), 3.57 (s, 1H), 3.44 – 3.29 (m, 4H), 3.11 (s, 2H), 2.49 (d, *J* = 9.3 Hz, 2H), 2.42 (s, 3H), 2.26 (dd, *J* = 13.5, 4.7 Hz, 1H), 2.24

– 2.17 (m, 1H), 2.03 (q, J = 7.6 Hz, 2H), 1.81 – 1.76 (m, 1H), 1.75 (s, 3H), 1.73 (s, 3H), 1.66 (s, 3H), 1.66 – 1.64 (m, 7H), 1.63 – 1.59 (m, 1H), 1.55 (s, 3H), 1.46 (s, 3H), 1.36 – 1.30 (m, 1H), 1.29 – 1.26 (m, 2H), 1.24 (s, 3H), 1.24 – 1.09 (m, 3H), 0.92 (s, 3H), 0.92 (s, 3H). ^{13}C NMR (125 MHz, $CDCl_3$) δ 169.52, 159.60, 158.87, 144.63, 134.79, 134.56, 132.22, 132.14, 128.85, 123.68, 121.56, 115.82, 114.45, 109.84, 91.26, 83.42, 83.15, 81.10, 49.08, 47.06, 42.70, 42.07, 39.52, 38.11, 37.49, 30.18, 29.46, 29.27, 28.91, 27.87, 25.81, 25.74, 25.68, 22.74, 22.36, 21.17, 20.97, 18.28, 17.73. HRMS: Exact mass calculated for $[C_{47}H_{60}NO_8]^+$, 766.4313. Found 766.4306.

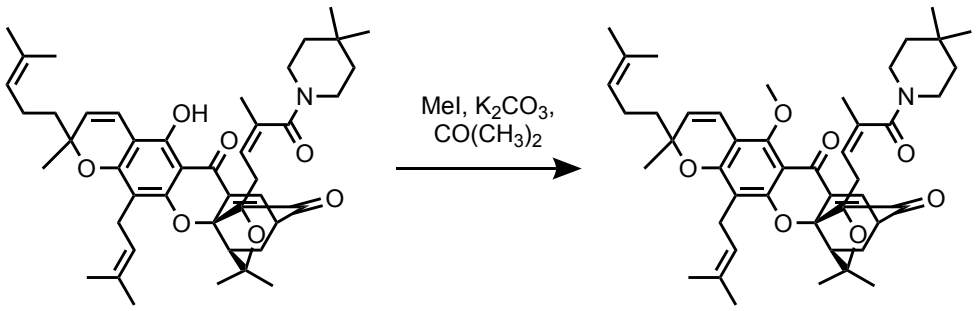

(118) (149)

3a-(4-(4,4-dimethylpiperidin-1-yl)-3-methyl-4-oxobut-2-en-1-yl)-8-methoxy-2,2,11-trimethyl-13-(3-methylbut-2-en-1-yl)-11-(4-methylpent-3-en-1-yl)-1,2-dihydro-11*H*-1,5-methanofuro[3,2-*g*]pyrano[3,2-*b*]xanthene-4,7(3a*H*,5*H*)-dione (149): To a 20 mL scintillation vial equipped with a magnetic stirbar was added 3a-(4-(4,4-dimethylpiperidin-1-yl)-3-methyl-4-oxobut-2-en-1-yl)-8-hydroxy-2,2,11-trimethyl-13-(3-methylbut-2-en-1-yl)-11-(4-methylpent-3-en-1-yl)-1,2-dihydro-11*H*-1,5-methanofuro[3,2-*g*]pyrano[3,2-*b*]xanthene-4,7(3a*H*,5*H*)-dione (50 mg, 0.07 mmol, 1eq.), acetone (1.5 mL), potassium carbonate (38 mg, 0.28 mmol, 4 eq), and methyl iodide (172 µL, 2.76 mmol, 40 eq.). The reaction was allowed to stir at 35 ºC until complete as determined by TLC (product R_f = 0.2, 40% EtOAc in hexanes). Next, the solution was cooled to room temperature and washed with water (5 mL, x2). The mixture was then partitioned, concentrated under reduced pressure, and purified by silica gel column chromatography using a gradient eluent of 20% to 40% EtOAc in hexanes to afford **149** as a pale yellow, amorphous solid (13 mg, 25% yield).

^{1}H NMR (500 MHz, $CDCl_3$) δ 7.43 (d, *J* = 6.8 Hz, 1H), 6.67 (d, *J* = 10.2 Hz, 1H), 5.55 (d, *J* = 10.2 Hz, 1H), 5.34 (t, *J* = 6.2 Hz, 1H), 5.12 (t, *J* = 6.8 Hz, 1H), 5.06 (t, *J* = 7.1 Hz, 1H), 3.82 (s, 3H), 3.59 (s, 1H), 3.39 (dd, *J* = 6.8, 4.4 Hz, 1H), 3.37 – 3.29 (m, 3H), 3.18 – 3.11 (m, 2H), 2.53 – 2.45 (m, 2H), 2.27 (dd, *J* = 13.4, 4.6 Hz, 1H), 2.21 (dd, *J* = 16.2, 6.9 Hz, 1H), 2.04 (q, *J* = 7.8 Hz, 2H), 1.76 (s, 3H), 1.73 (s, 3H), 1.67 (s, 3H), 1.65 (s, 6H), 1.63 – 1.59 (m, 4H), 1.55 (s, 3H), 1.45 (s,

3H), 1.25 (s, 6H), 0.93 (s, 6H). ^{13}C NMR (125 MHz, $CDCl_3$) δ 204.12, 174.78, 169.56, 159.84, 159.33, 155.51, 135.58, 134.02, 133.98, 132.01, 131.97, 127.51, 123.85, 121.95, 121.86, 116.75, 112.81, 110.22, 107.41, 91.01, 83.46, 83.19, 80.73, 62.22, 49.03, 47.06, 42.76, 42.12, 39.54, 38.15, 37.48, 30.21, 29.81, 29.56, 29.27, 28.91, 27.83, 25.84, 25.82, 25.75, 22.76, 22.30, 20.99, 18.28, 17.71. HRMS: Exact mass calculated for $[C_{46}H_{60}NO_7]^+$, 738.4364. Found 738.4366.

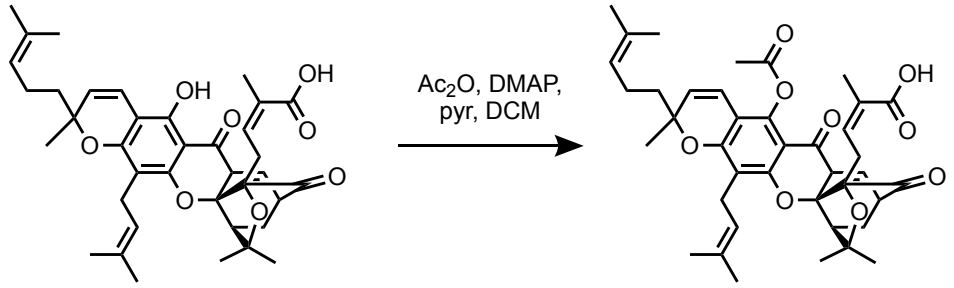

GBA (142)

4-(8-acetoxy-2,2,11-trimethyl-13-(3-methylbut-2-en-1-yl)-11-(4-methylpent-3-en-1-yl)-4,7-dioxo-1,2,5,7-tetrahydro-11*H*-1,5-methanofuro[3,2-*g*]pyrano[3,2-*b*]xanthen-3a(4*H*)-yl)-2-methylbut-2-enoic acid (142): To a 20 mL scintillation vial equipped with a magnetic stir bar was added gambogic acid (100 mg, 0.16 mmol, 1 eq.) and anhydrous DCM (3 mL). Next were added pyridine (322 µL, 3.98 mmol, 25 eq.), 4-(dimethylamino)pyridine (2 mg, 0.02 mmol, 0.1 eq.), and acetic anhydride (376 µL, 3.98 mmol, 25 eq.). The reaction was allowed to stir at room temperature until complete as determined by TLC (product R_f = 0.2, 40% EtOAc in hexanes). The reaction mixture was then quenched with saturated sodium bicarbonate and partitioned with DCM. The organic phase was washed with brine, dried over magnesium sulfate, filtered, and concentrated under reduced pressure. The resulting crude mixture was purified by silica gel column chromatography using a gradient eluent of 20% to 40% EtOAc in hexanes to afford **142** as a yellow, amorphous solid (16 mg, 15% yield).

^{1}H NMR (500 MHz, $CDCl_3$) δ 7.46 (d, *J* = 6.9 Hz, 1H), 6.38 (d, *J* = 10.0 Hz, 1H), 6.16 (s, 1H), 5.58 (d, *J* = 10.1 Hz, 1H), 5.12 – 4.96 (m, 2H), 3.47 – 3.36 (m, 2H), 3.17 (s, 1H), 2.52 (d, *J* = 9.3 Hz, 1H), 2.41 (s, 3H), 2.28 (dd, *J* = 13.4, 4.7 Hz, 1H), 2.04 – 1.95 (m, 2H), 1.87 – 1.71 (m, 8H), 1.69 (s, 3H), 1.65 (s, 3H), 1.64 (s, 3H), 1.54 (s, 3H), 1.43 (s, 3H), 1.39 – 1.31 (m, 2H), 1.29 (s, 3H), 1.27 – 1.18 (m, 2H). ^{13}C NMR (125 MHz, $CDCl_3$) δ 203.86, 174.14, 159.23, 158.77, 144.27, 134.55, 132.18, 132.09, 129.09, 127.68, 123.72, 121.52, 115.64, 114.58, 110.04, 105.62, 91.39,

83.99, 81.17, 49.13, 46.74, 41.94, 29.91, 29.80, 29.18, 28.92, 27.86, 25.75, 25.22, 22.89, 22.79, 22.16, 21.21, 20.94, 18.20. HRMS: Exact mass calculated for $[C_{40}H_{47}O_9]^+$, 671.3215. Found 671.3215.

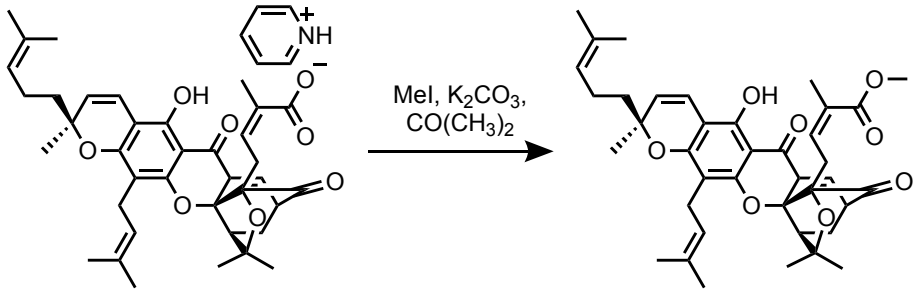

GBA•pyr **(1)**

Methyl-4-(8-hydroxy-2,2,11-trimethyl-13-(3-methylbut-2-en-1-yl)-11-(4-methylpent-3-en-1-yl)-4,7-dioxo-1,2,5,7-tetrahydro-11*H*-1,5-methanofuro[3,2-*g*]pyrano[3,2-*b*]xanthen-3a(4*H*)-yl)-2-methylbut-2-enoate (1): To a 20 mL scintillation vial equipped with a magnetic stirbar was added Gambogic acid pyridinium salt (100 mg, 0.14 mmol, 1eq.), acetone (3 mL), potassium carbonate (78 mg, 0.57 mmol, 4 eq.), and methyl iodide (176 μL, 2.83 mmol, 20 eq.). The reaction was allowed to stir at room temperature until complete as determined by TLC (product R_f = 0.6, 40% EtOAc in hexanes). Next, the mixture was diluted with EtOAc and washed with water (5 mL, x2). The organic phase was partitioned, dried over magnesium sulfate, filtered, and concentrated under reduced pressure. The resulting crude mixture was then purified by silica gel column chromatography using a gradient eluent of 30% to 40% EtOAc in hexanes to afford **1** as an orange, amorphous solid (60 mg, 67% yield).

^{1}H NMR (500 MHz, $CDCl_3$) δ 12.85 (s, 1H), 7.54 (d, *J* = 6.9 Hz, 1H), 6.68 (d, *J* = 10.1 Hz, 1H), 5.94 (td, *J* = 7.4, 1.4 Hz, 1H), 5.44 (d, *J* = 10.1 Hz, 1H), 5.09 – 5.00 (m, 2H), 3.48 (dd, *J* = 6.9, 4.5 Hz, 1H), 3.43 (s, 3H), 3.31 (dd, *J* = 14.6, 8.1 Hz, 1H), 3.15 (dd, *J* = 14.6, 5.3 Hz, 1H), 2.99 (qdd, *J* = 16.4, 7.4, 1.4 Hz, 2H), 2.52 (d, *J* = 9.3 Hz, 1H), 2.31 (dd, *J* = 13.4, 4.7 Hz, 1H), 2.06 – 2.01 (m, 2H), 1.81 – 1.76 (m, 1H), 1.74 (s, 3H), 1.69 (s, 3H), 1.67 (s, 3H), 1.65 (s, 3H), 1.64 (s, 3H), 1.63 – 1.59 (m, 1H), 1.55 (s, 3H), 1.44 (s, 3H), 1.44 – 1.32 (m, 2H), 1.29 (s, 3H). ^{13}C NMR (126 MHz, $CDCl_3$) δ 203.68, 179.12, 167.44, 161.40, 157.65, 136.17, 135.13, 133.65, 131.99, 131.65,

127.89, 124.58, 123.85, 122.27, 116.00, 107.61, 102.56, 100.54, 90.99, 83.97, 83.81, 81.37, 60.51, 51.21, 49.14, 46.92, 42.15, 31.69, 29.98, 29.22, 28.93, 28.12, 25.78, 25.75, 25.19, 22.83, 22.76, 21.70, 20.96, 18.18, 17.72, 14.30, 14.23. HRMS: Exact mass calculated for $[C_{39}H_{47}O_8]^+$, 643.3265. Found 643.3261.

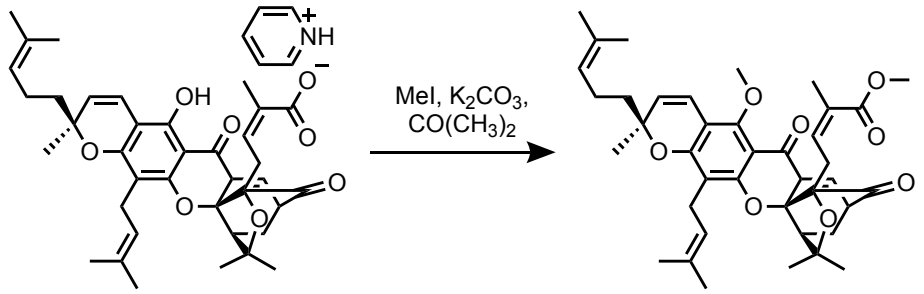

GBA•pyr **(2)**

Methyl-4-(8-methoxy-2,2,11-trimethyl-13-(3-methylbut-2-en-1-yl)-11-(4-methylpent-3-en-1-yl)-4,7-dioxo-1,2,5,7-tetrahydro-11*H*-1,5-methanofuro[3,2-*g*]pyrano[3,2-*b*]xanthen-3a(4*H*)-yl)-2-methylbut-2-enoate (2): To a 20 mL scintillation vial equipped with a magnetic stirbar was added gambogic acid pyridinium salt (300 mg, 0.42 mmol, 1eq.), acetone (4.7 mL), potassium carbonate (293 mg, 2.12 mmol, 5 eq.), and methyl iodide (1.3 mL, 21.2 mmol, 50 eq.). The mixture was allowed to stir for six days (product R_f = 0.5, 40% EtOAc in hexanes). The mixture was then filtered and concentrated under reduced pressure. The resulting crude mixture was then purified by silica gel column chromatography using a gradient eluent of 30% to 40% EtOAc in hexanes to afford **2** as a yellow, amorphous solid (163 mg, 59% yield).

^{1}H NMR (500 MHz, $CDCl_3$) δ 7.42 (d, *J* = 6.9 Hz, 1H), 6.65 (d, *J* = 10.1 Hz, 1H), 5.94 (td, *J* = 7.2, 1.6 Hz, 1H), 5.53 (d, *J* = 10.2 Hz, 1H), 5.12 – 5.06 (m, 1H), 5.06 – 4.99 (m, 1H), 3.80 (s, 3H), 3.48 – 3.33 (m, 5H), 3.23 (dd, *J* = 14.6, 5.4 Hz, 1H), 3.02 – 2.90 (m, 2H), 2.50 (d, *J* = 9.3 Hz, 1H), 2.28 (dd, *J* = 13.4, 4.7 Hz, 1H), 2.01 (q, *J* = 7.9 Hz, 2H), 1.74 (s, 3H), 1.68 (s, 3H), 1.67 (s, 3H), 1.64 (s, 6H), 1.58 (s, 2H), 1.53 (s, 3H), 1.43 (s, 3H), 1.38 (dd, *J* = 13.4, 9.5 Hz, 1H), 1.28 (s, 3H). ^{13}C NMR (125 MHz, $CDCl_3$) δ 204.22, 174.74, 167.45, 159.77, 158.89, 155.35, 136.36, 135.91, 133.72, 132.02, 131.94, 127.62, 127.32, 123.80, 121.92, 116.73, 112.69, 109.91, 107.44, 90.98, 83.89, 83.70, 80.65, 62.21, 51.12, 49.07, 46.83, 42.13, 30.00, 29.43, 28.99, 27.99, 25.78, 25.75, 25.54, 22.75, 22.21, 20.94, 18.24, 17.70. HRMS: Exact mass calculated for $[C_{40}H_{49}O_8]^+$, 657.3422. Found 657.3426.

(13)

Pent-4-yn-1-yl 4-methylbenzenesulfonate (13): To an oven-dried 100 mL round-bottom flask equipped with a magnetic stirbar was added anhydrous DCM (25 mL) and 4-pentyn-1-ol (1.5 g, 17.83 mmol, 1 eq.). The mixture was cooled to 0 ºC and pyridine (1.44 mL, 19.61 mmol, 1 eq.), 4-(dimethylamino)pyridine (436 mg, 3.57 mmol, 0.2 eq.), and *p*-toluenesulfonyl chloride (3.74 g, 19.61 mmol, 1.1 eq.) were added. The reaction mixture was allowed to warm to room temperature and stirred overnight (product *Rf* = 0.6, 40% EtOAc in hexanes). Next, deionized water (10 mL) was added, and the organic and aqueous phases were partitioned. The aqueous phase was extracted with DCM (20mL, x3) and the combined organic phases were washed with saturated brine (10 mL). The organic phase was separated, treated with magnesium sulfate, filtered, and concentrated under reduced pressure. The resulting mixture was then purified by silica gel column chromatography using a gradient eluent of 0% to 40% EtOAc in hexanes to afford **13** as a clear liquid (3.37 g, 79% yield).

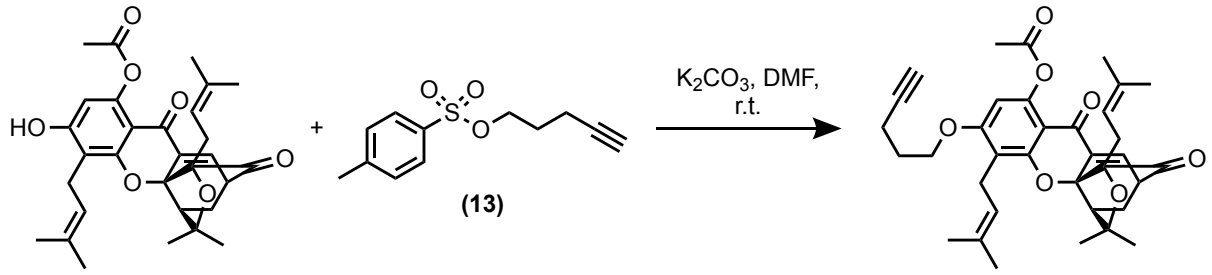

10-(but-3-yn-1-yloxy)-2,2-dimethyl-3a,11-bis(3-methylbut-2-en-1-yl)-4,7-dioxo-1,2,3a,4,5,7-hexahydro-1,5-methanofuro[2,3-*d*]xanthen-8-yl acetate (14): To an oven-dried 10 mL round-bottom flask equipped with a magnetic stirbar was added 70% acetylforbesione (250 mg, 0.49 mmol, 1eq.), DCM (5 mL) and **13** (235 mg, 0.99 mmol, 2 eq.). The reaction mixture was allowed to stir at room temperature overnight. The mixture was then diluted with DCM (20 mL) and washed with deionized water (20 mL, x2). The organic and aqueous phases were partitioned, and the aqueous phase was washed with DCM (20 mL, x2). The organic phases were combined, washed with brine (20 mL), partitioned, dried over sodium sulfate, filtered, and concentrated under reduced pressure. The resulting mixture was subsequently purified by silica gel column chromatography using a gradient eluent of 20% to 40% EtOAc in hexanes (R_f = 0.5, 40% EtOAc in hexanes) to afford **14** as a white solid (165 mg, 66% yield).

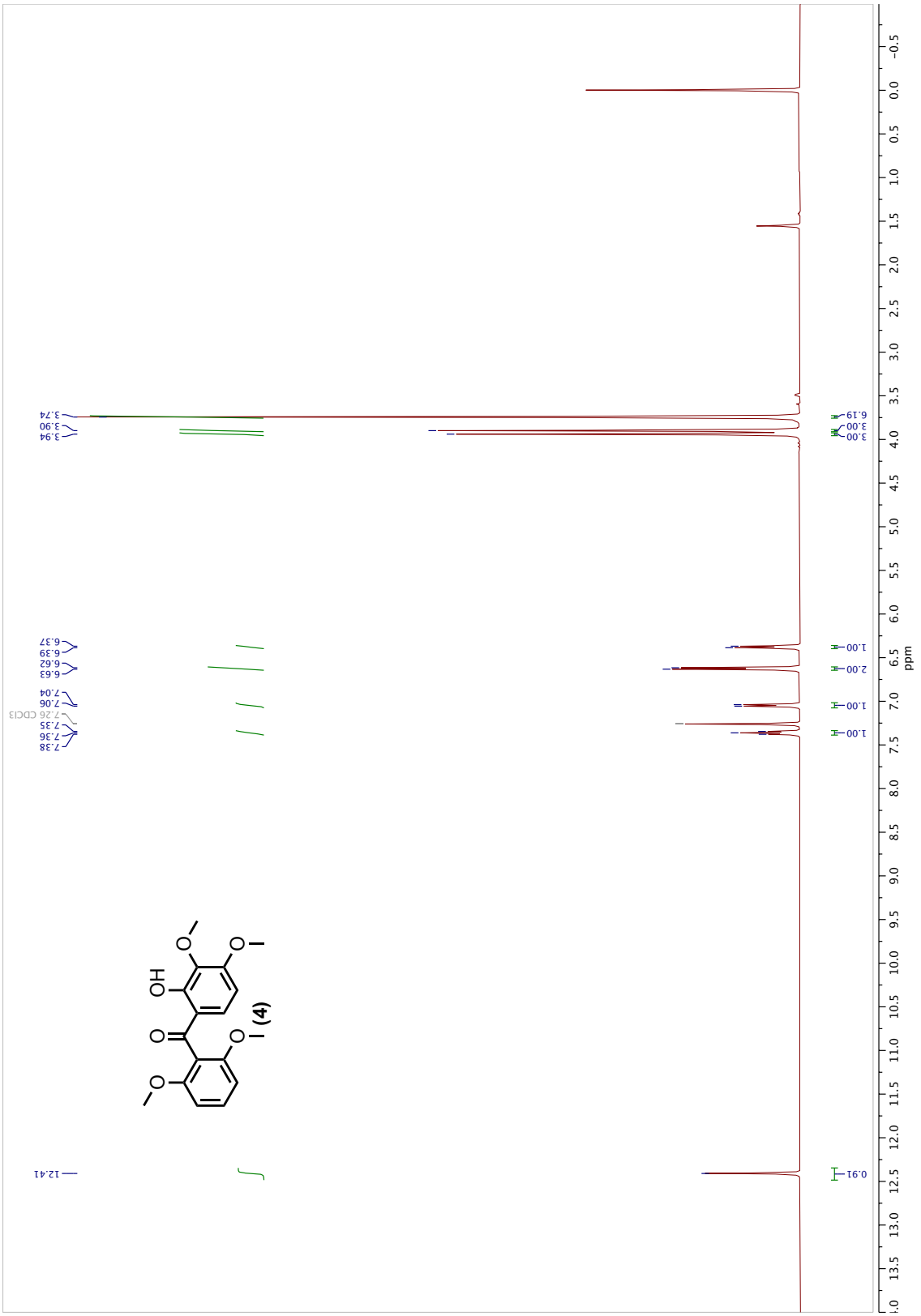
(4)
ppm

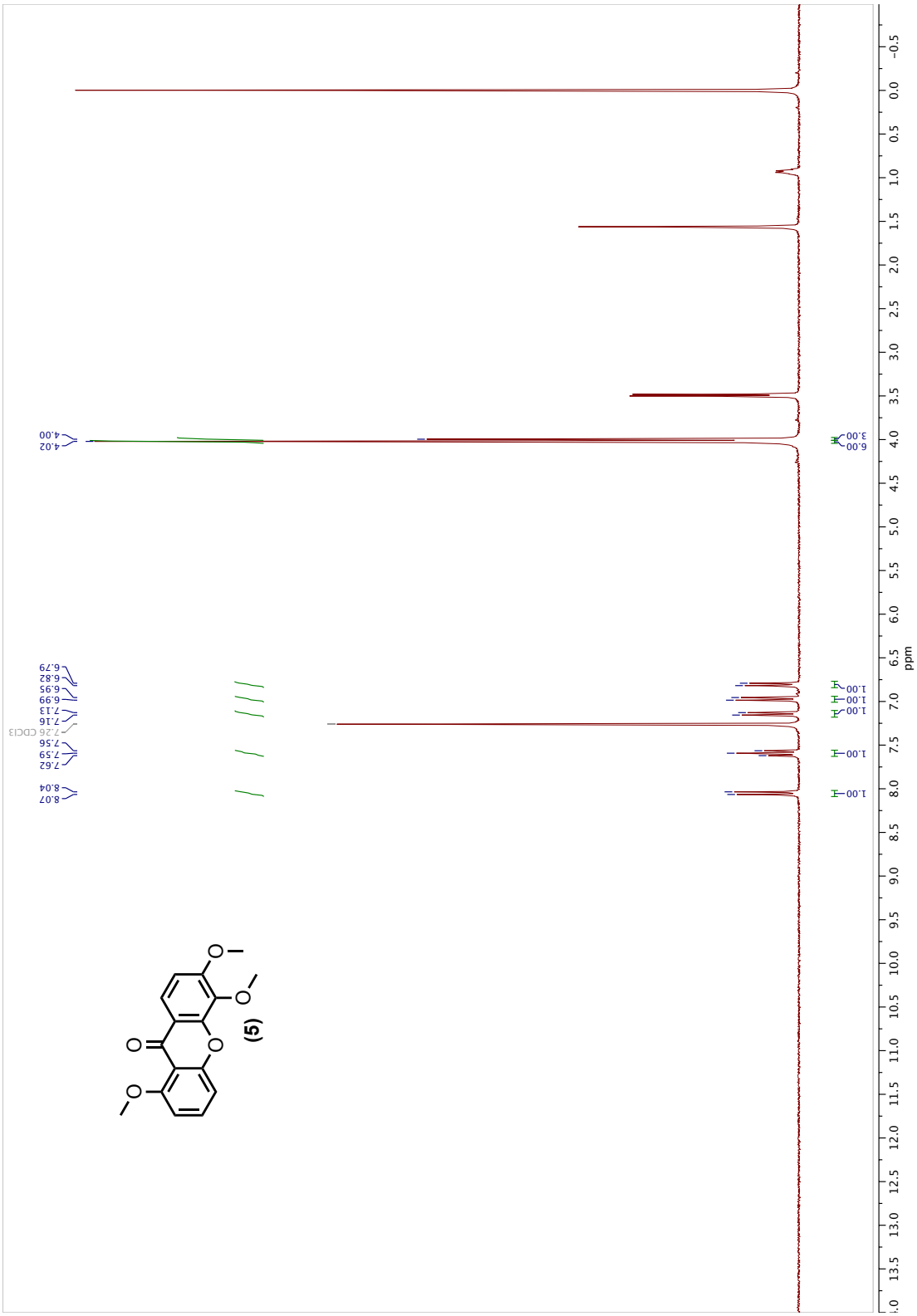
8.07
8.04
7.62
7.59
7.56
7.26 CDCl3
7.16
7.13
6.99
6.95
6.82
6.79
4.02
4.00
1.00
1.00
1.00
1.00
6.00
3.00
ppm
(5)

7.65
7.64
7.63
7.61
7.59
7.04
7.03
6.93
6.91
6.74
6.73
3.31 CD3OD
2.00
1.00
1.00
1.00
ppm
OH
HO
O
O
OH
(9)

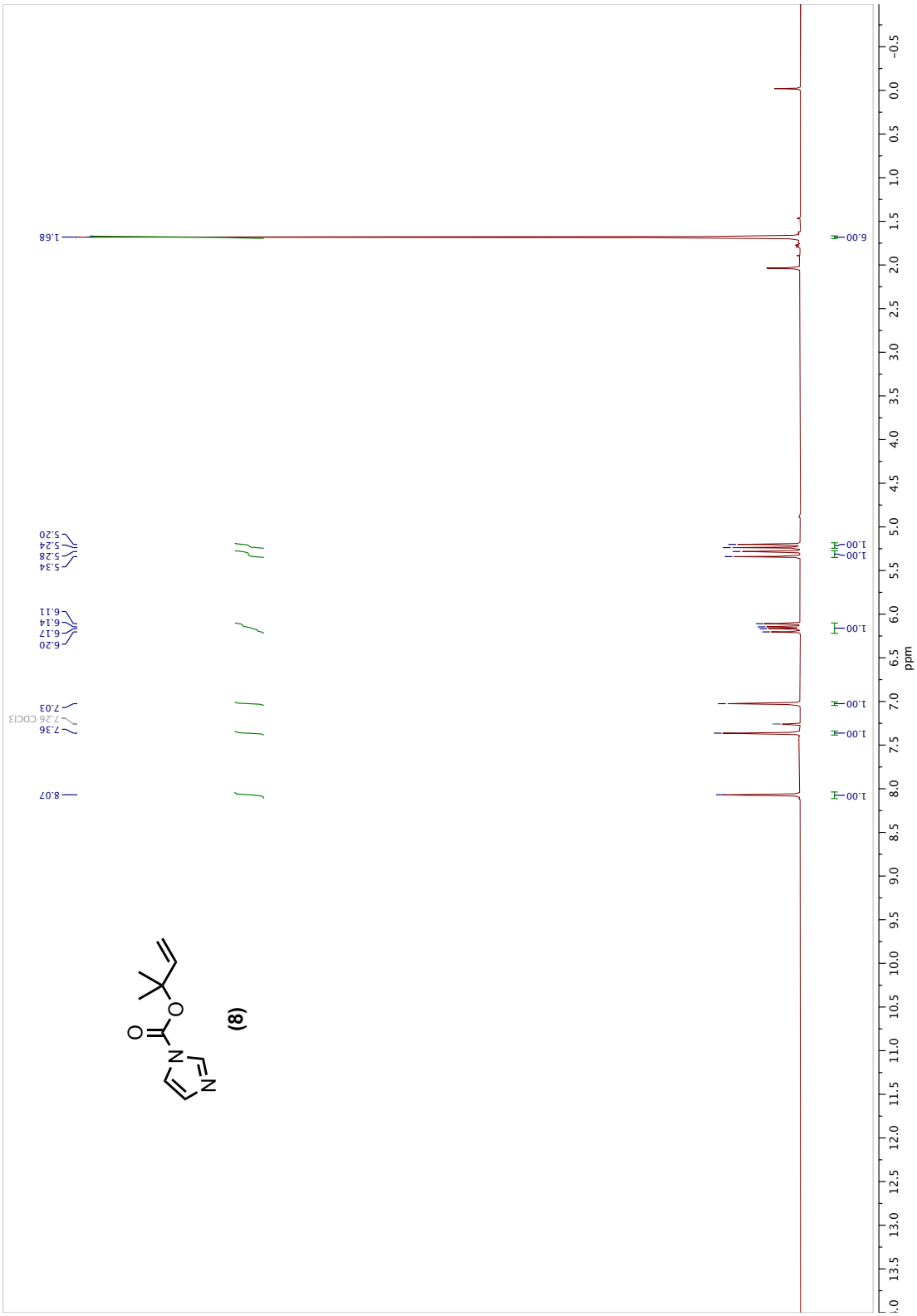
1.68
5.34
5.28
5.24
5.20
6.20
6.17
6.14
6.11
7.03
7.26 CDCl3
7.36
8.07
6.00
1.00
1.00
1.00
1.00
1.00
1.00
ppm

(8)

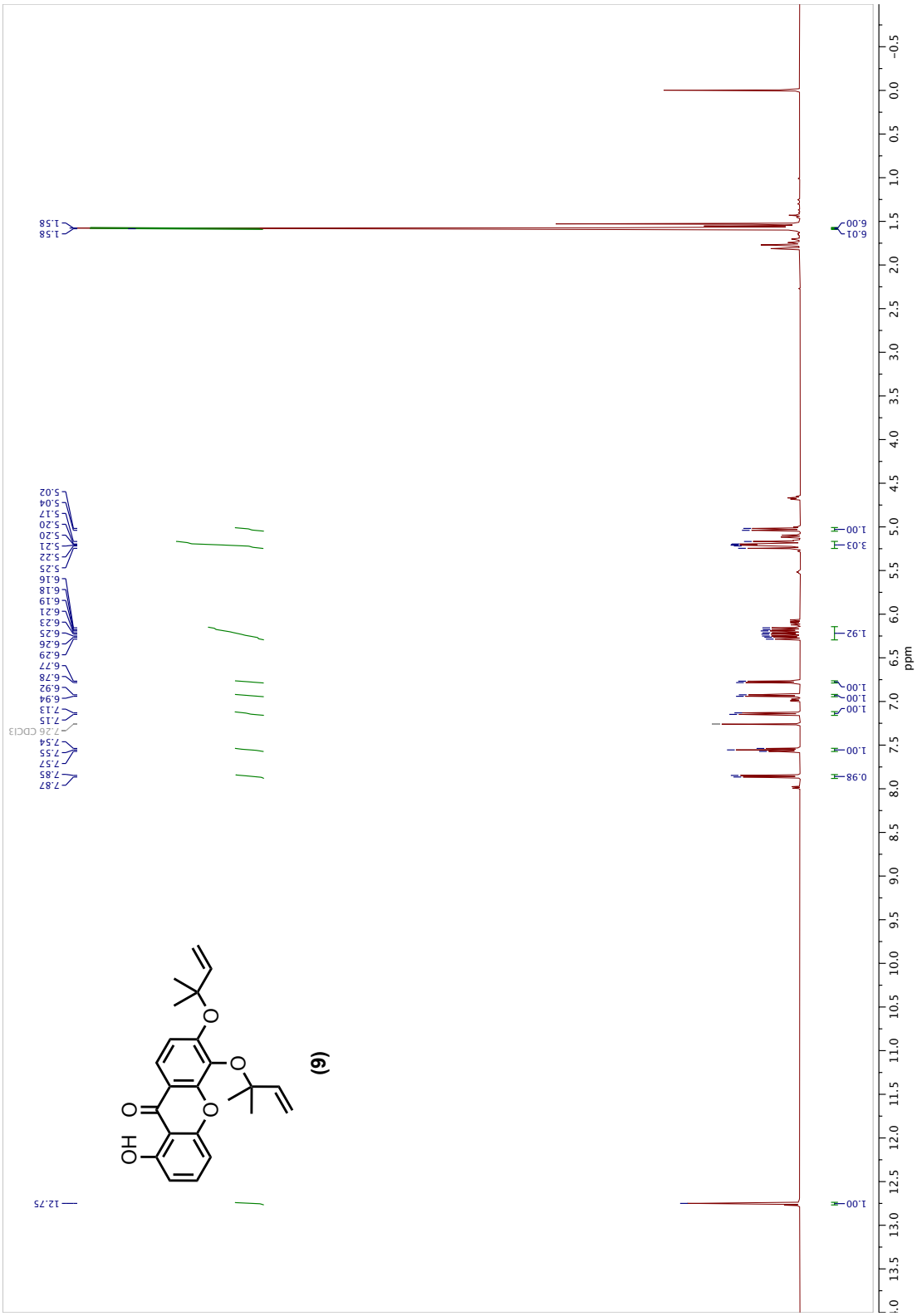
(9)
HO
O
O
O
O
ppm

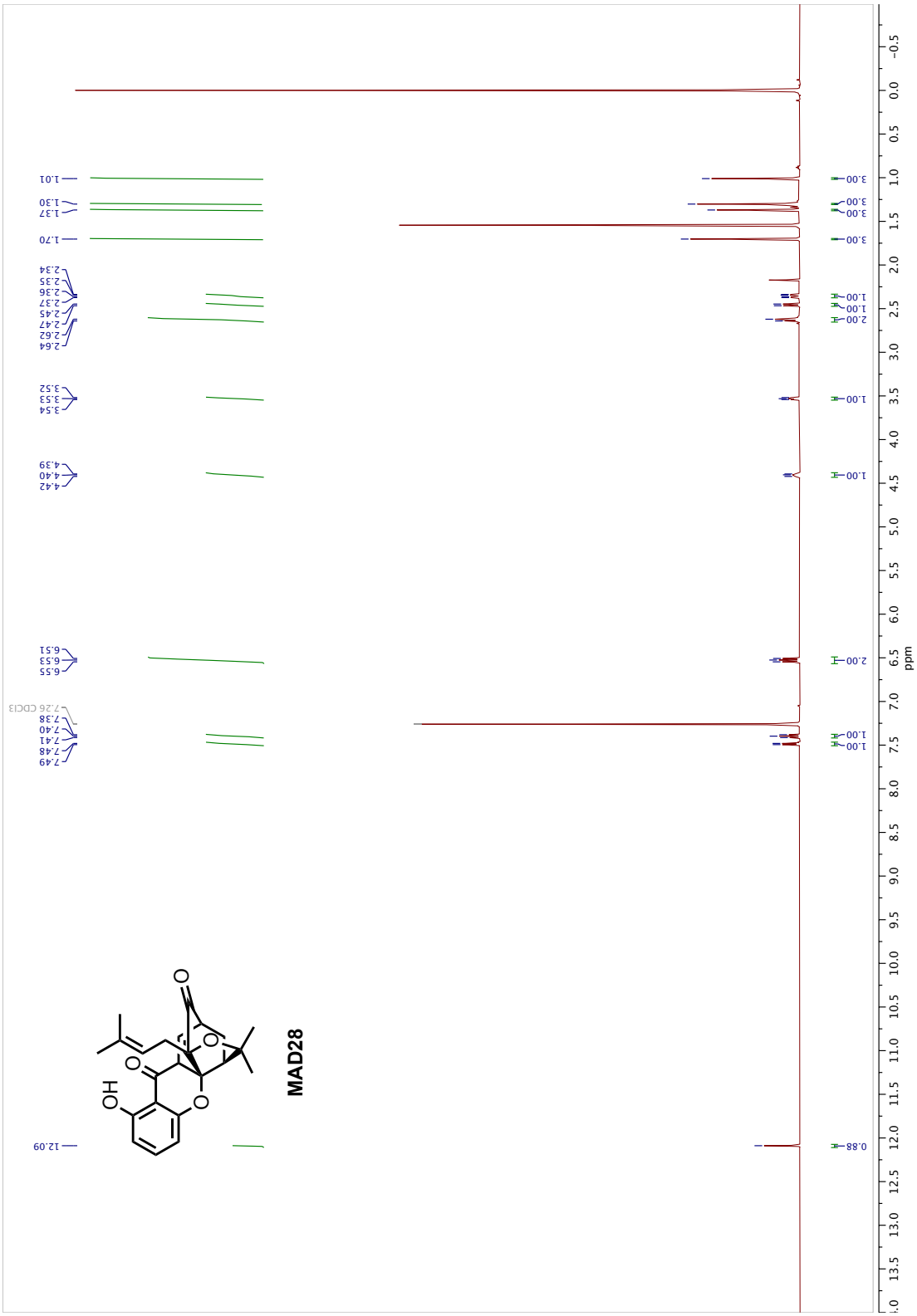
MAD28
ppm

OH
OH
O
O
OH
OH
(10)
7.59
7.56
6.89
6.86
6.44
6.43
6.17
6.17
3.31 CD3OD
1.00
1.00
1.00
1.00
ppm

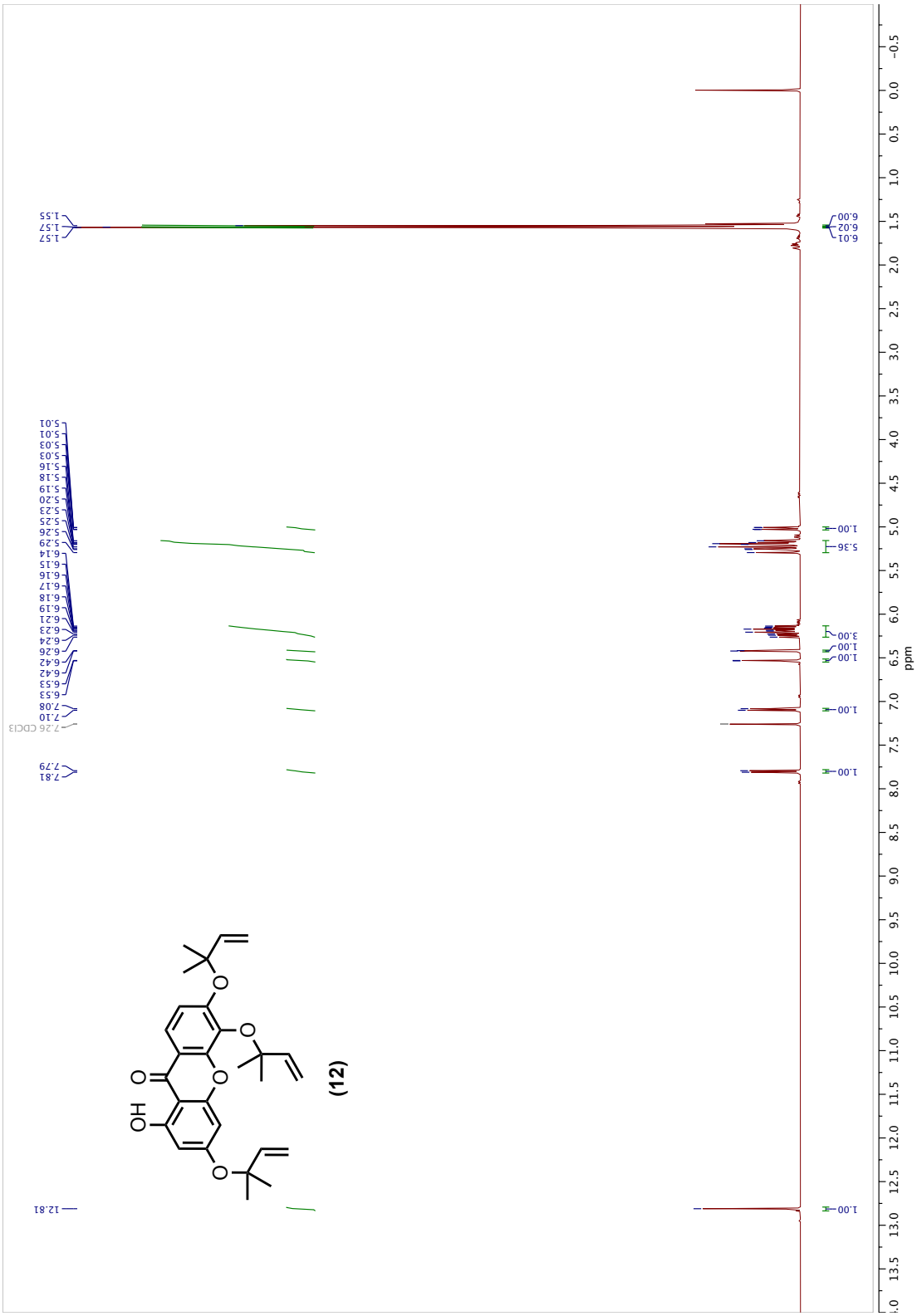
(12)
OH
O
O
O
O
O
ppm
1.55
1.57
6.01
6.02
6.00
5.29
1.00
5.36
3.00
1.00
1.00
7.08
1.00
7.79
1.00
12.81

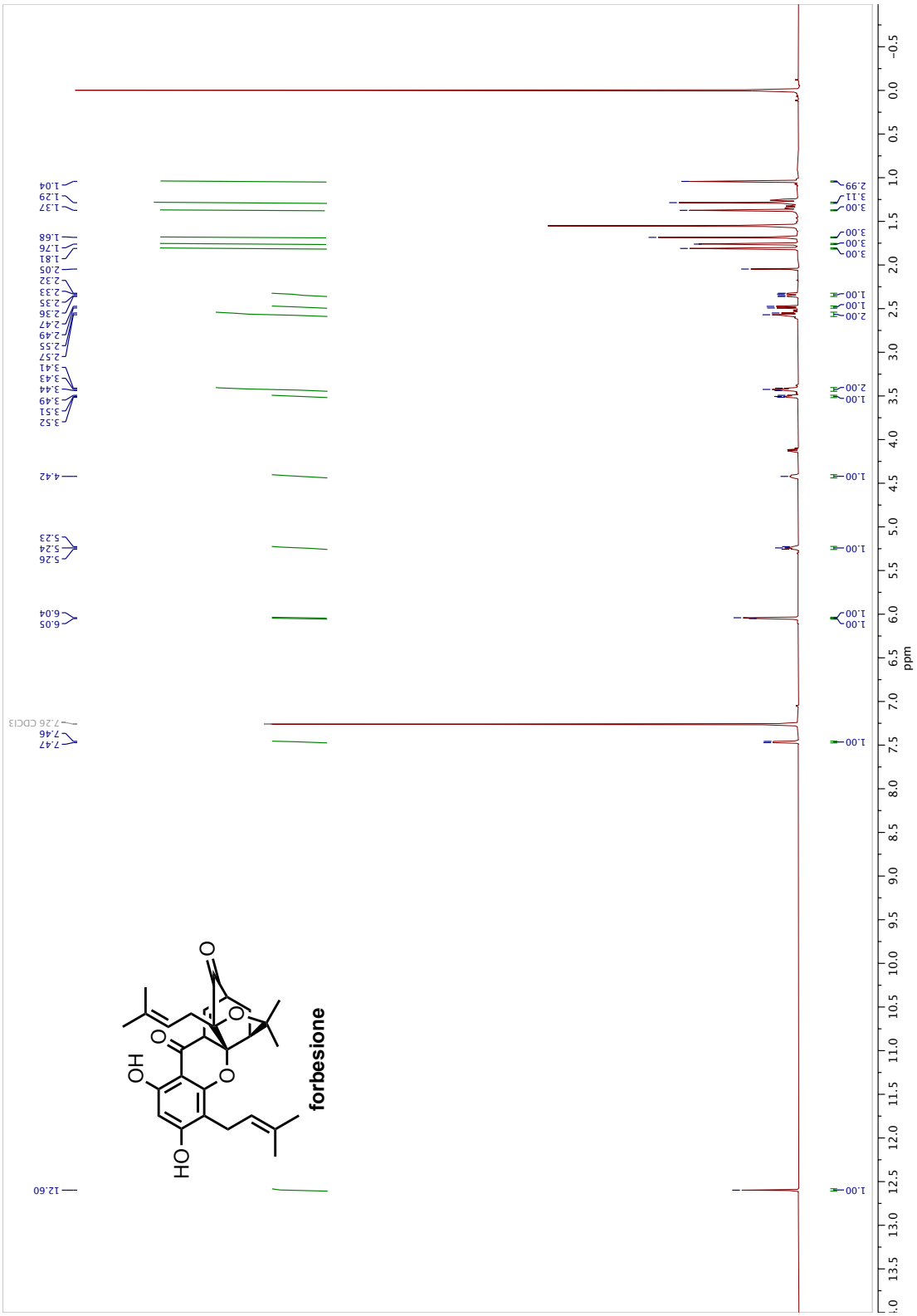
forbesione
OH
HO
O
O
O
O
ppm

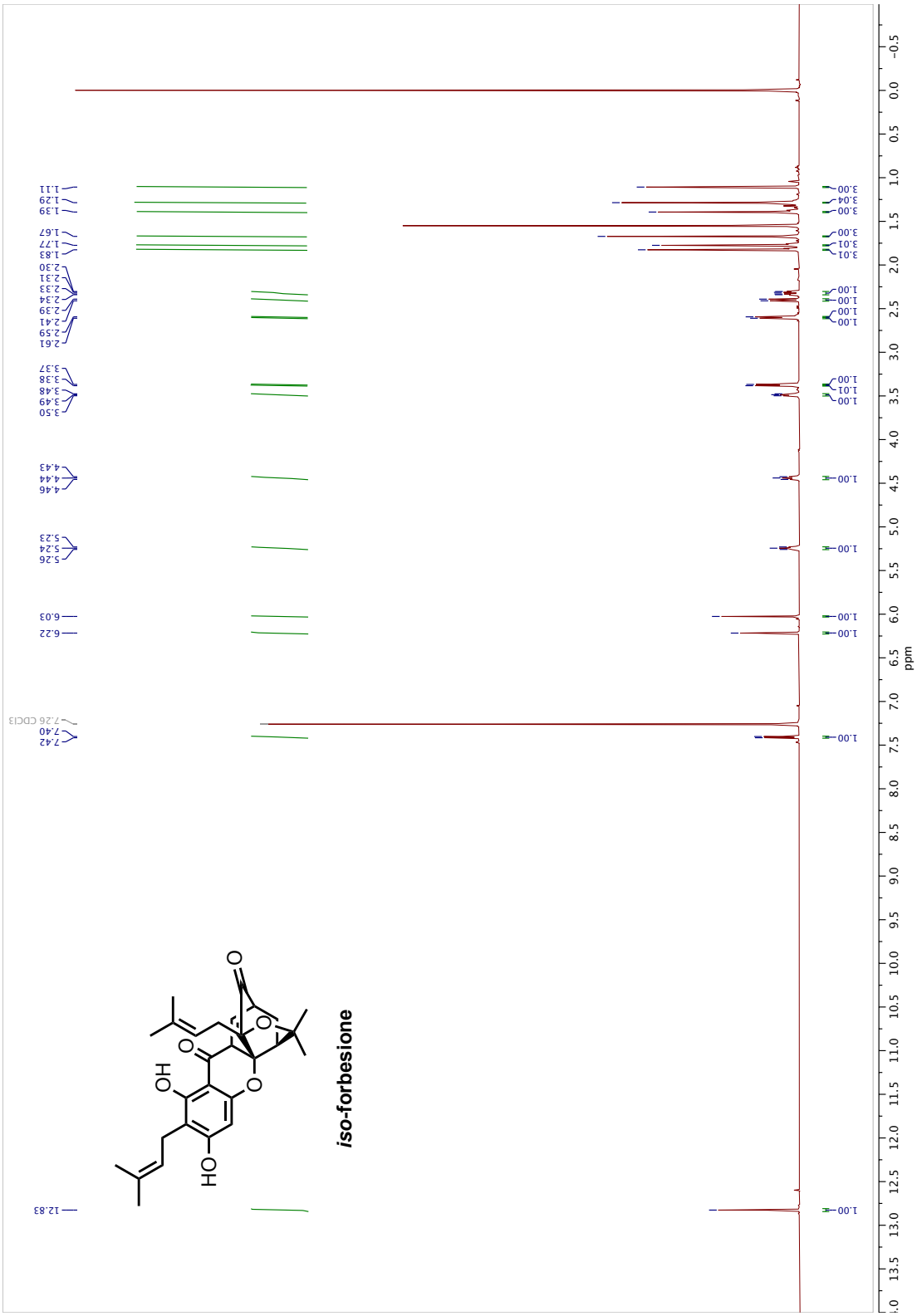
iso-forbesione
OH
HO
O
O
O
O
ppm

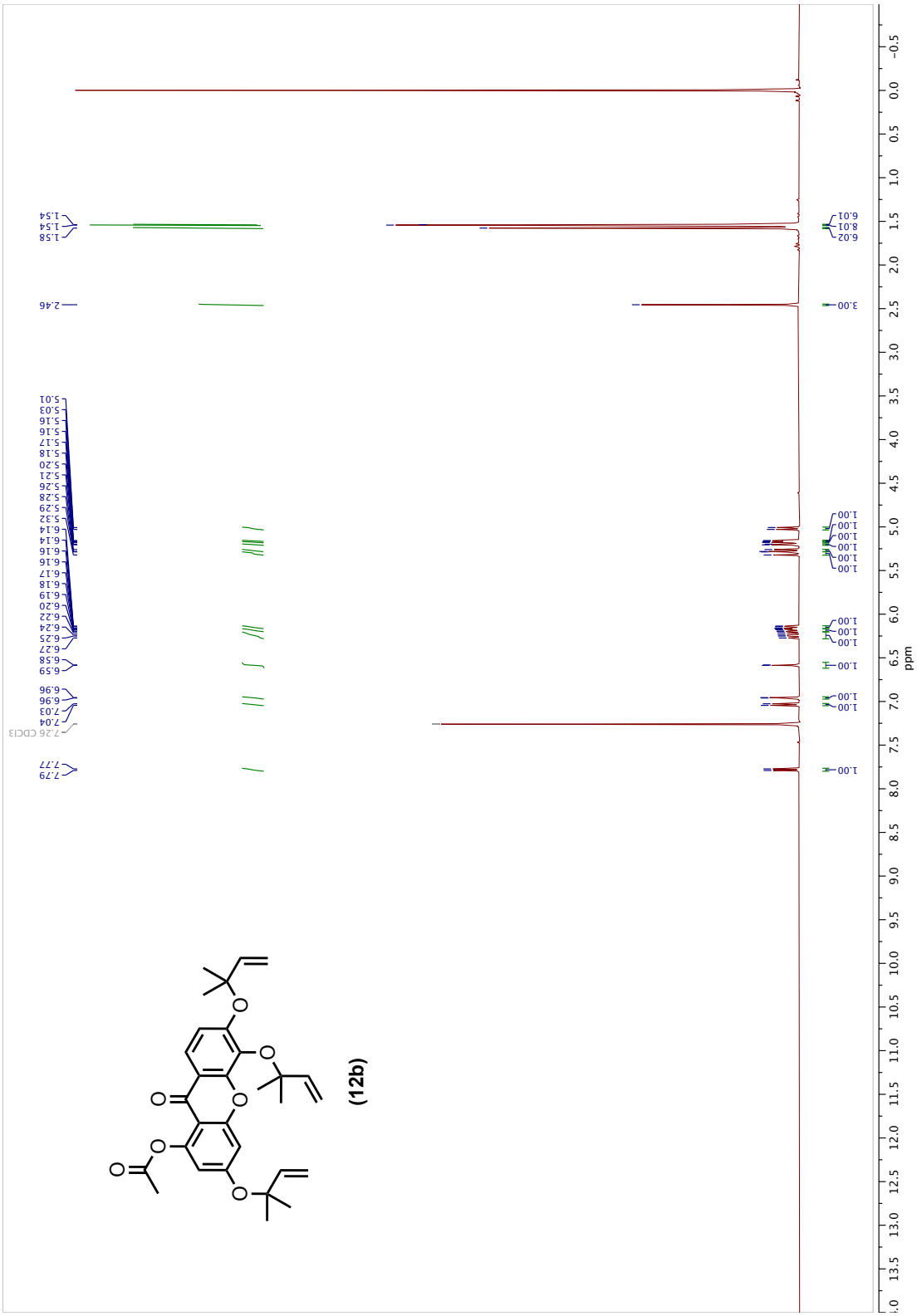
(12b)
ppm

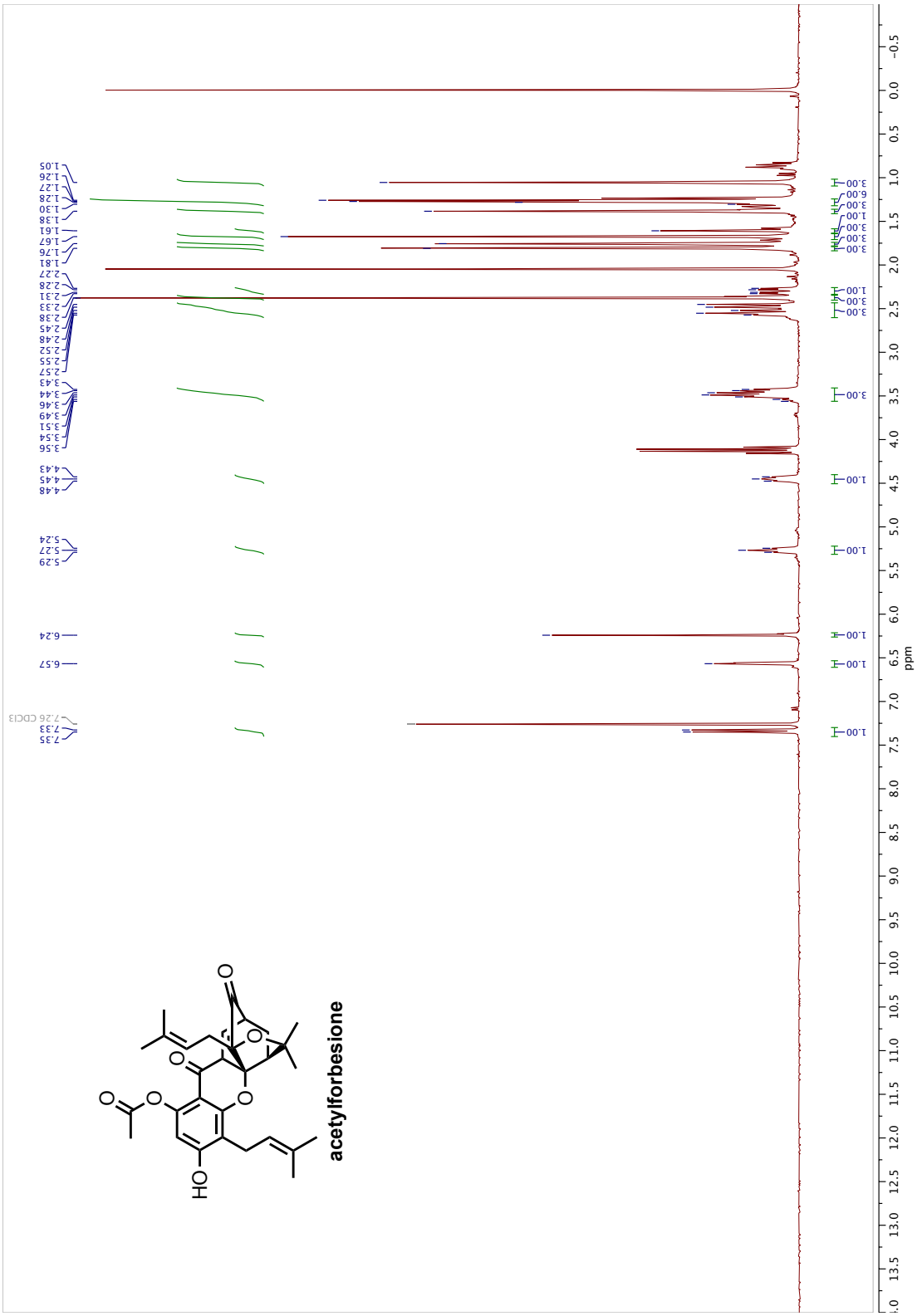
acetylforbesione
ppm

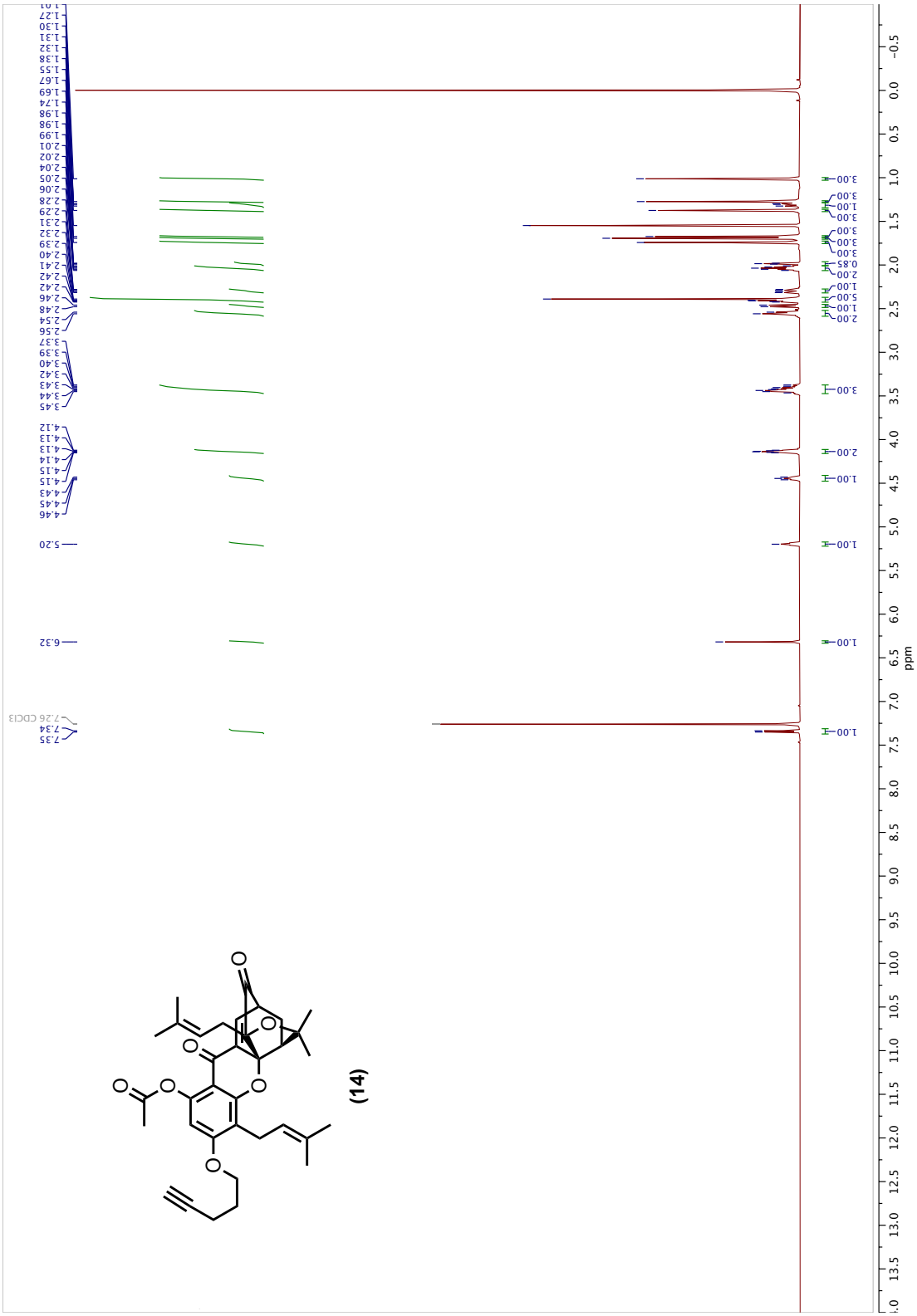
(14)
ppm

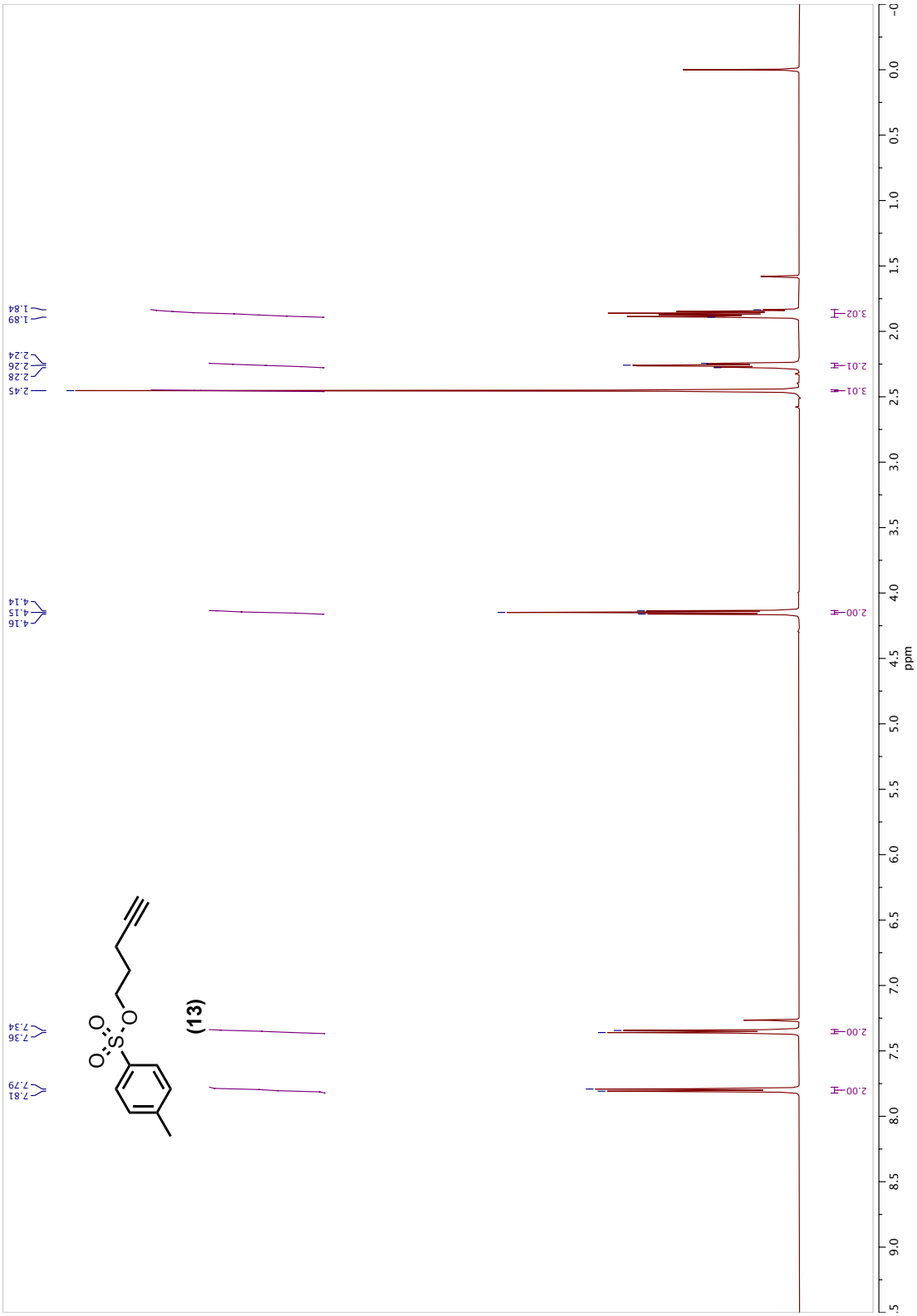
(13)
7.81
7.79
7.36
7.34
4.16
4.15
4.14
2.45
2.28
2.26
2.24
1.89
1.84
2.00
2.00
2.01
3.01
3.02
ppm

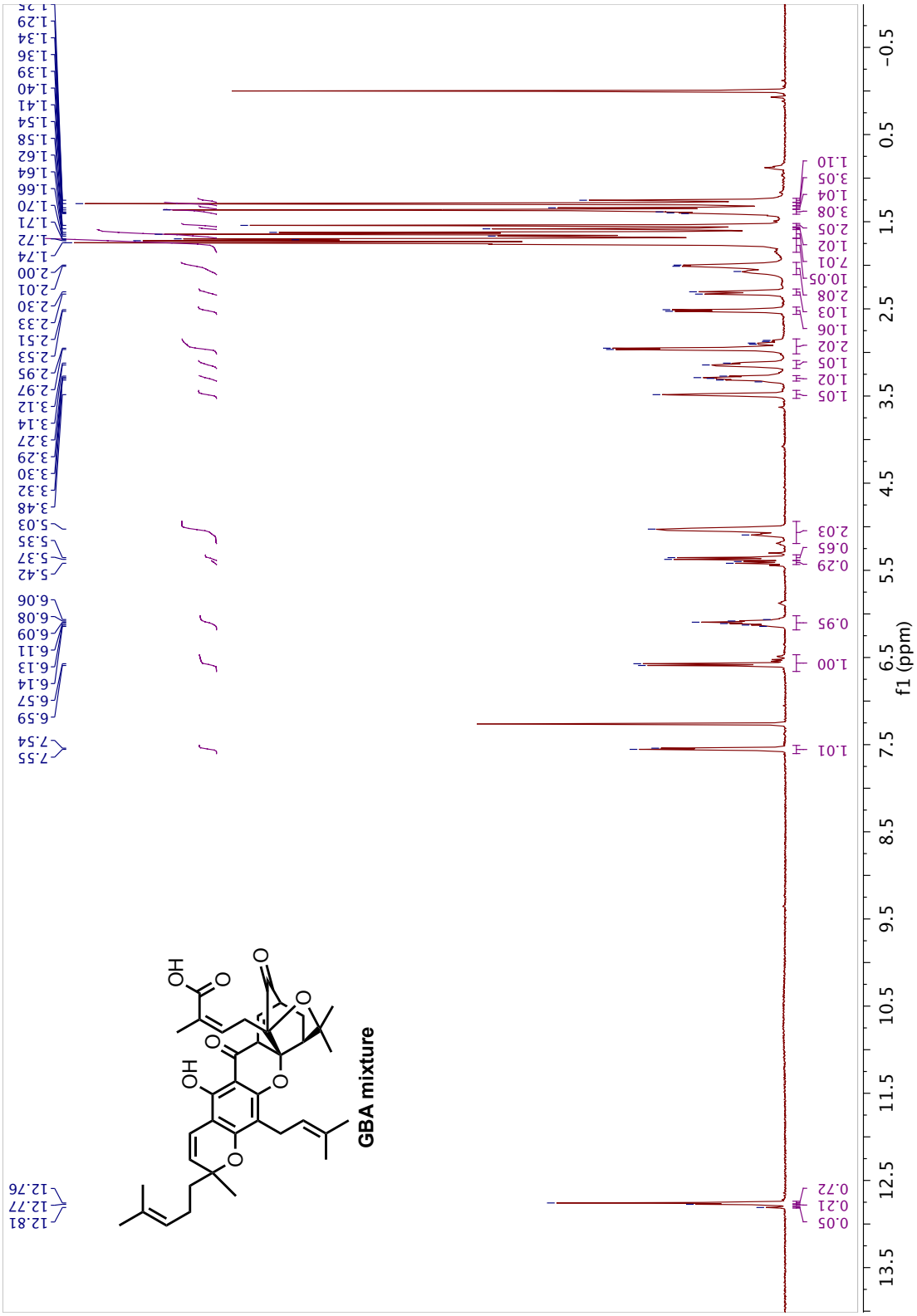
GBA mixture
f1 (ppm)

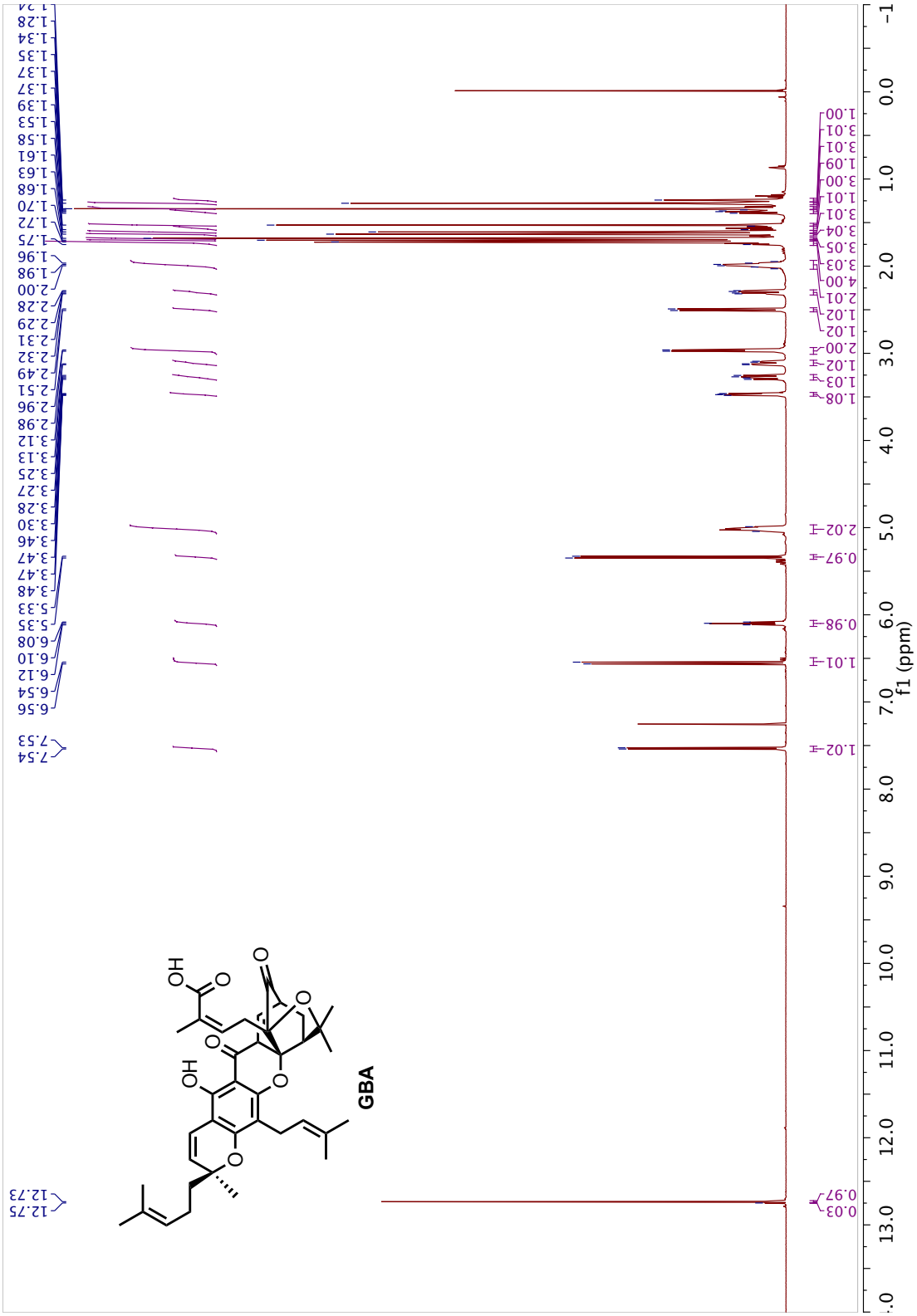
GBA
f1 (ppm)

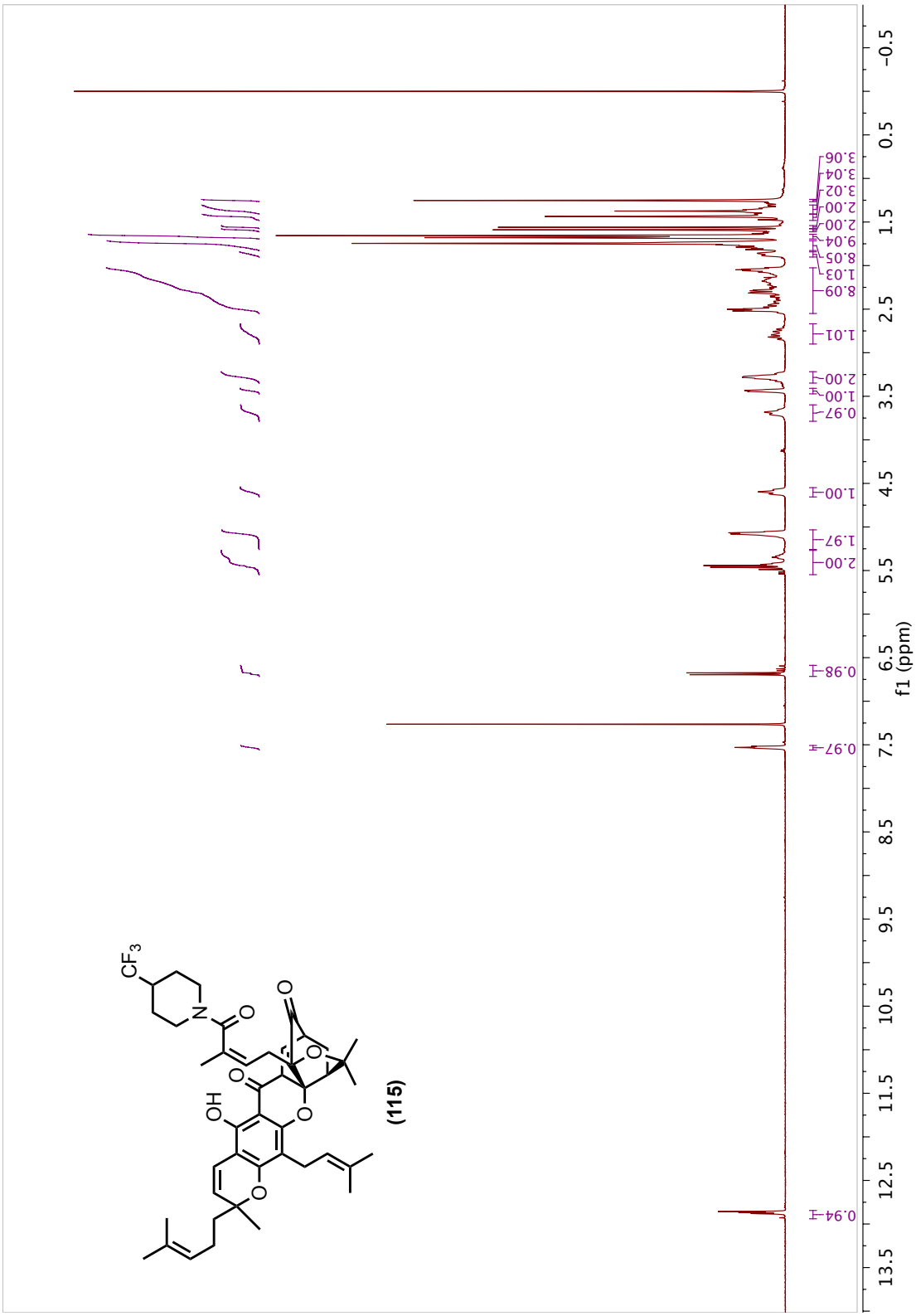
CF3
N
O
O
O
O
O
OH
O
(115)
f1 (ppm)
13.5
12.5
11.5
10.5
9.5
8.5
7.5
6.5
5.5
4.5
3.5
2.5
1.5
0.5
−0.5
0.94
0.97
0.98
2.00
1.97
1.00
0.97
2.00
1.00
1.01
8.09
1.03
8.05
9.04
2.00
2.00
3.02
3.04
3.06

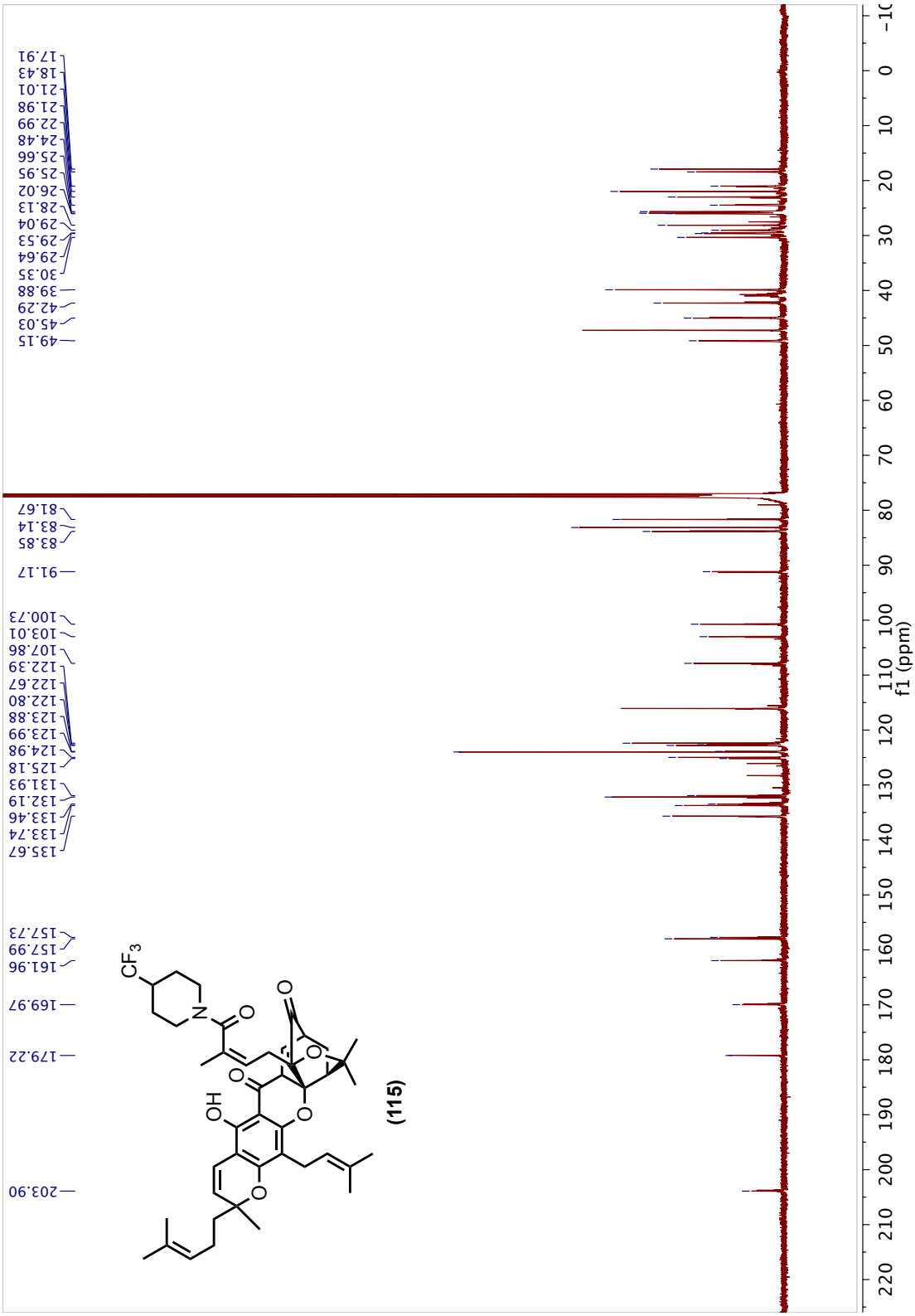
17.91
18.43
21.01
21.98
22.99
24.48
25.66
25.95
26.02
28.13
29.04
29.53
29.64
30.35
39.88
42.29
45.03
49.15
81.67
83.14
83.85
91.17
100.73
103.01
107.86
122.39
122.67
122.80
123.88
123.99
124.98
125.18
131.93
132.19
133.46
133.74
135.67
157.73
157.99
161.96
169.97
179.22
203.90
f1 (ppm)
(115)

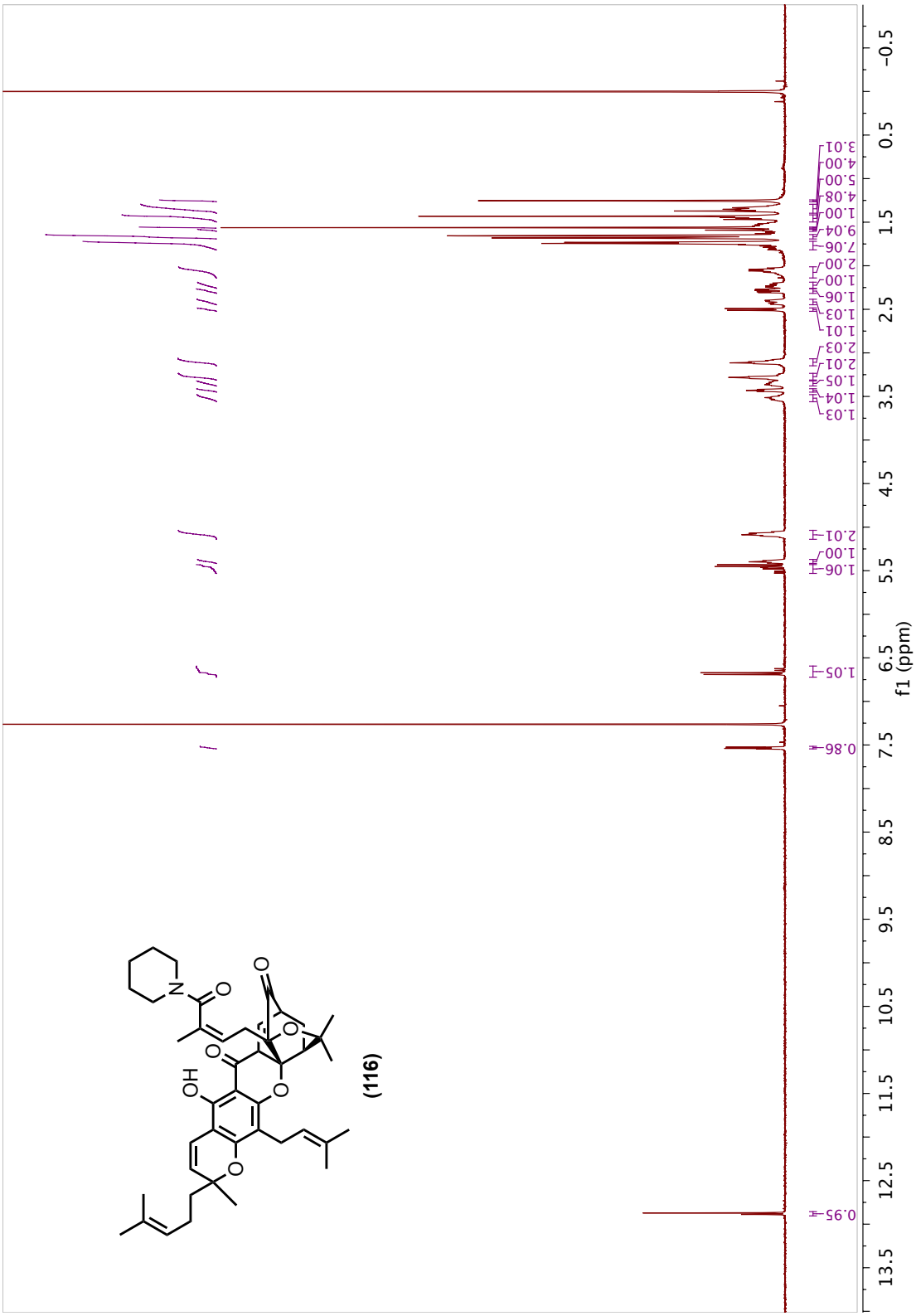
(116)
f1 (ppm)

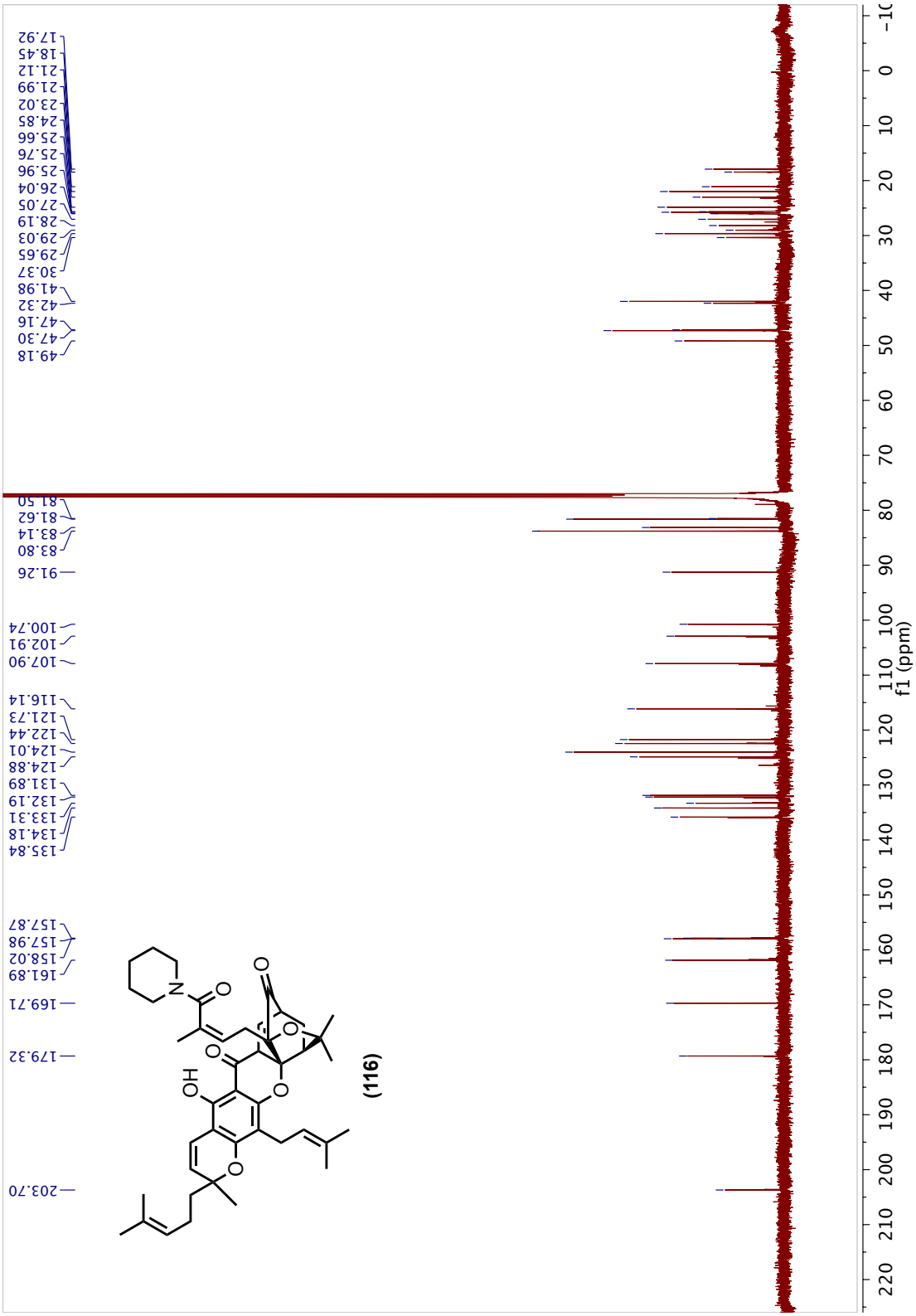
17.92
18.45
21.12
21.99
23.02
24.85
25.66
25.76
25.96
26.04
27.05
28.19
29.03
29.65
30.37
41.98
42.32
47.16
47.30
49.18
81.50
81.62
83.14
83.80
91.26
100.74
102.91
107.90
116.14
121.73
122.44
124.01
124.88
131.89
132.19
133.31
134.18
135.84
157.87
157.98
158.02
161.89
169.71
179.32
203.70
f1 (ppm)
(116)

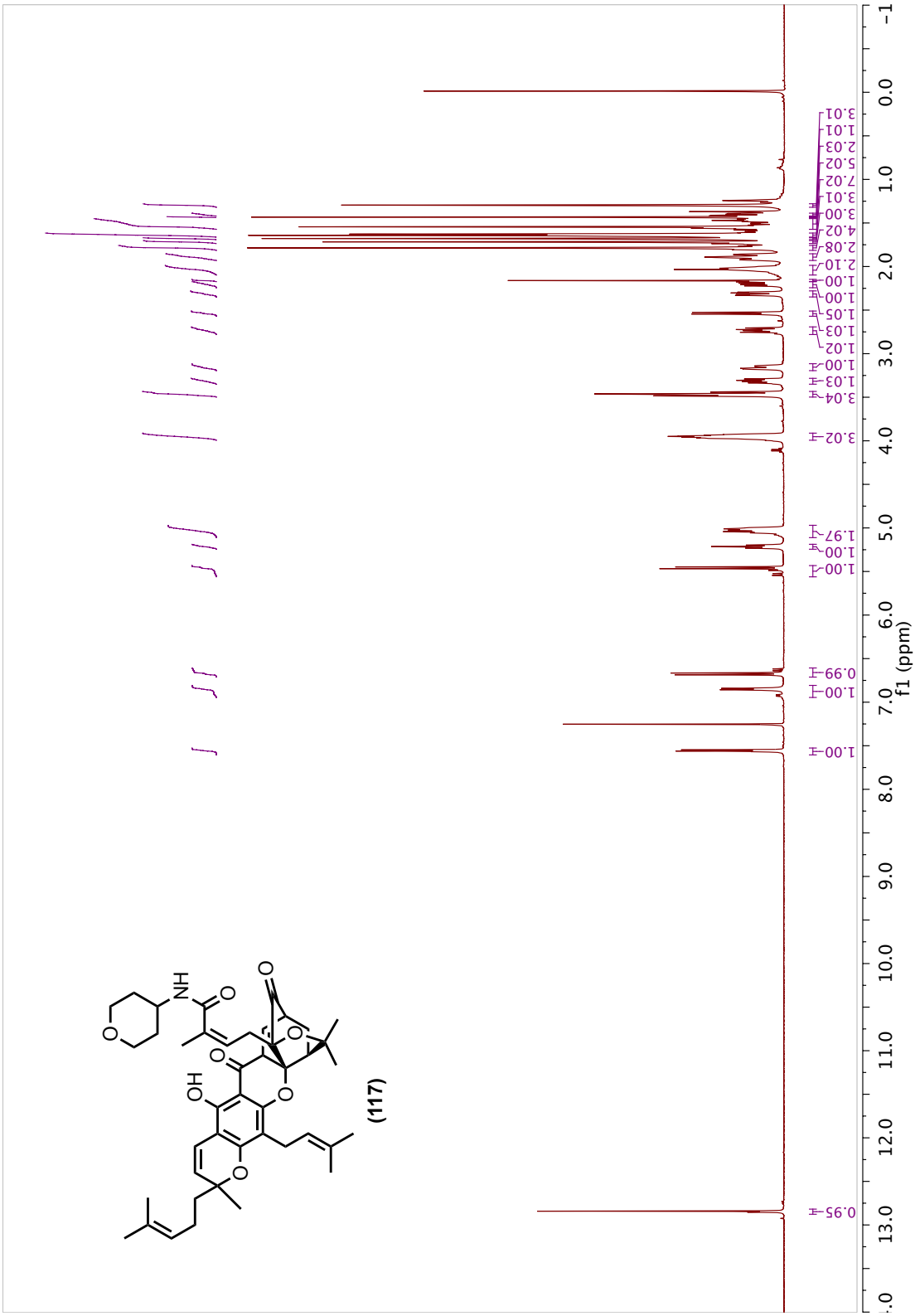
(117)
f1 (ppm)

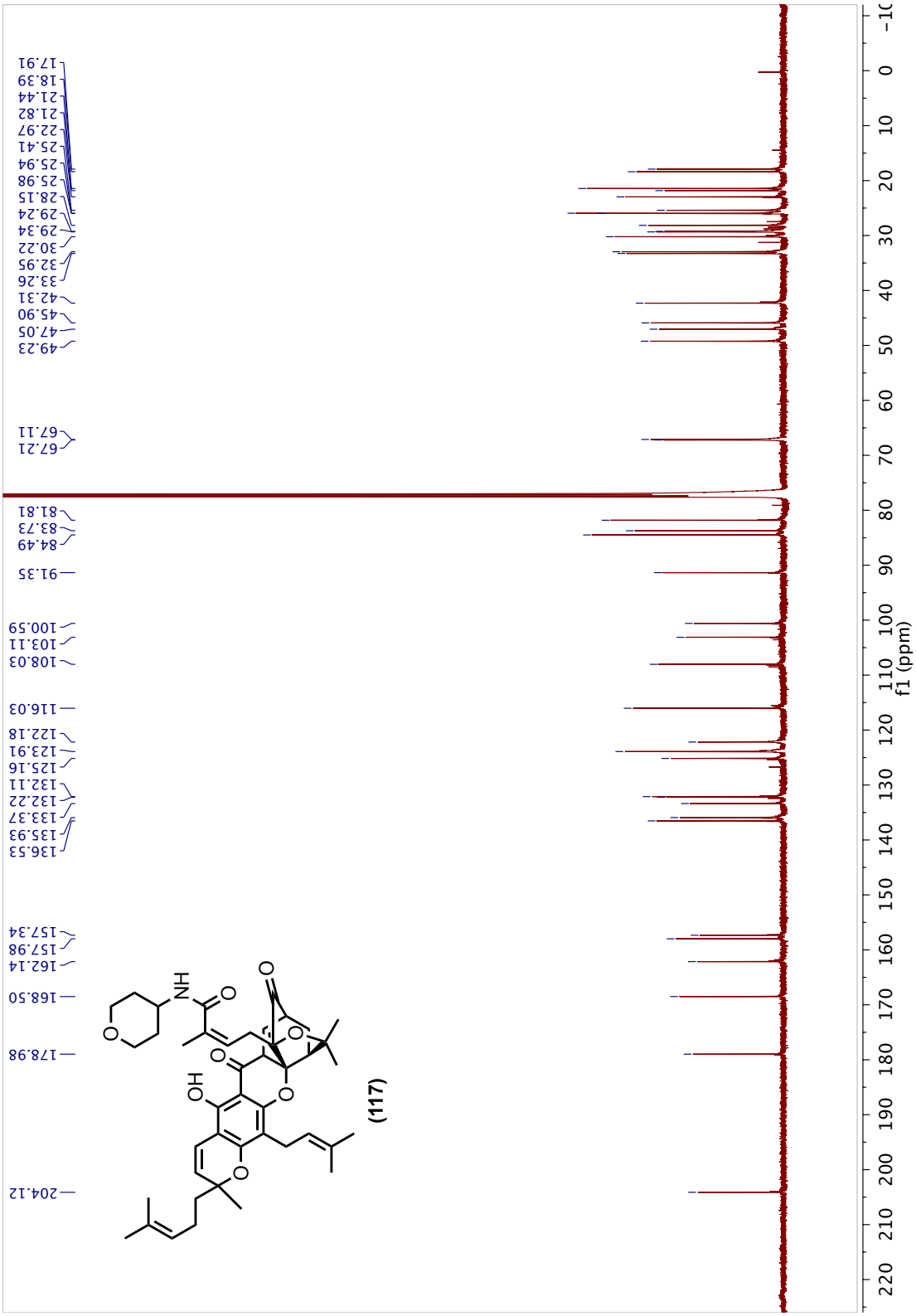
17.91
18.39
21.44
21.82
22.97
25.41
25.94
25.98
28.15
29.24
29.34
30.22
32.95
33.26
42.31
45.90
47.05
49.23
67.11
67.21
81.81
83.73
84.49
91.35
100.59
103.11
108.03
116.03
122.18
123.91
125.16
132.11
132.22
133.37
135.93
136.53
157.34
157.98
162.14
168.50
178.98
204.12
HN
O
HO
(117)
f1 (ppm)

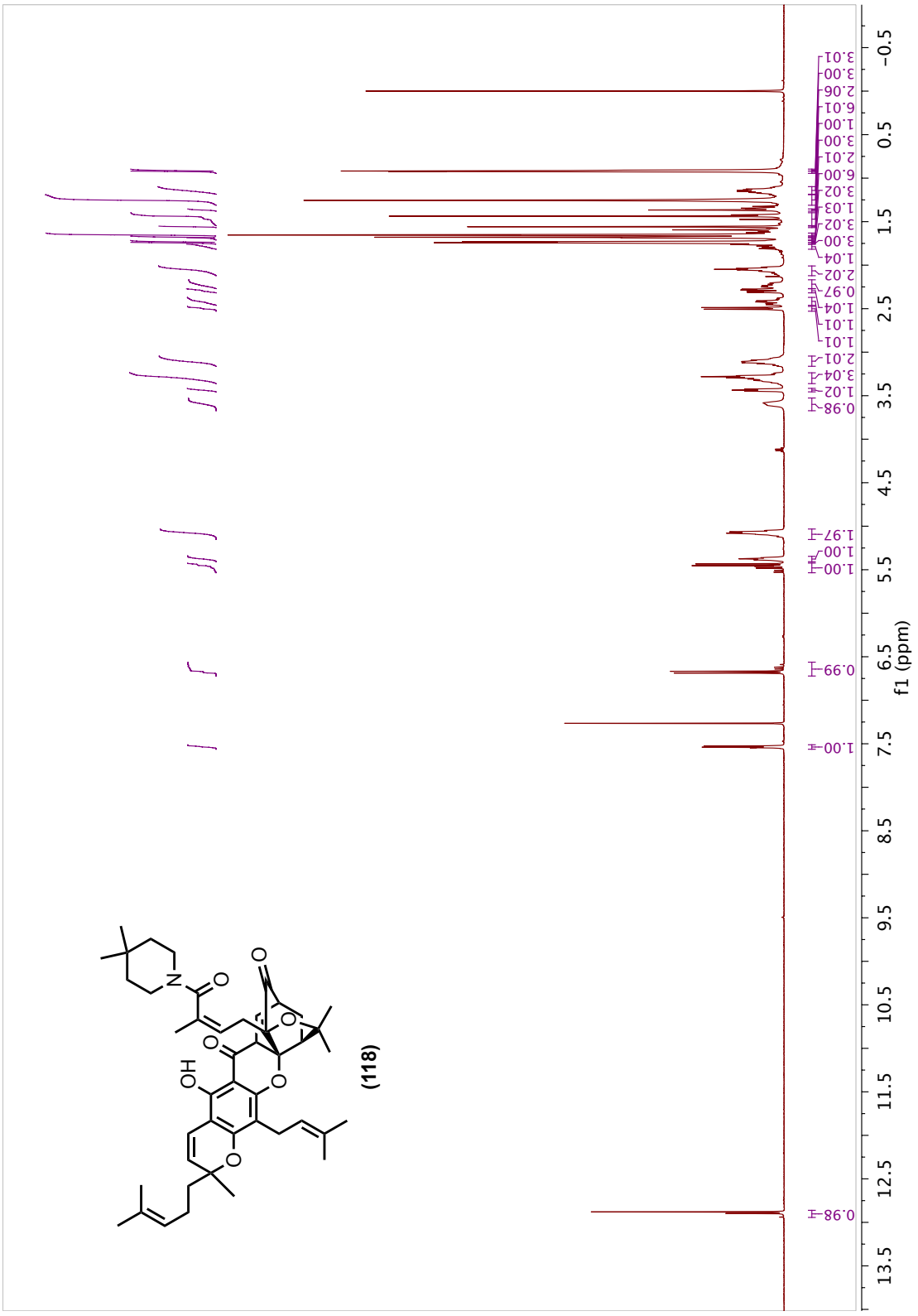
(118)
f1 (ppm)

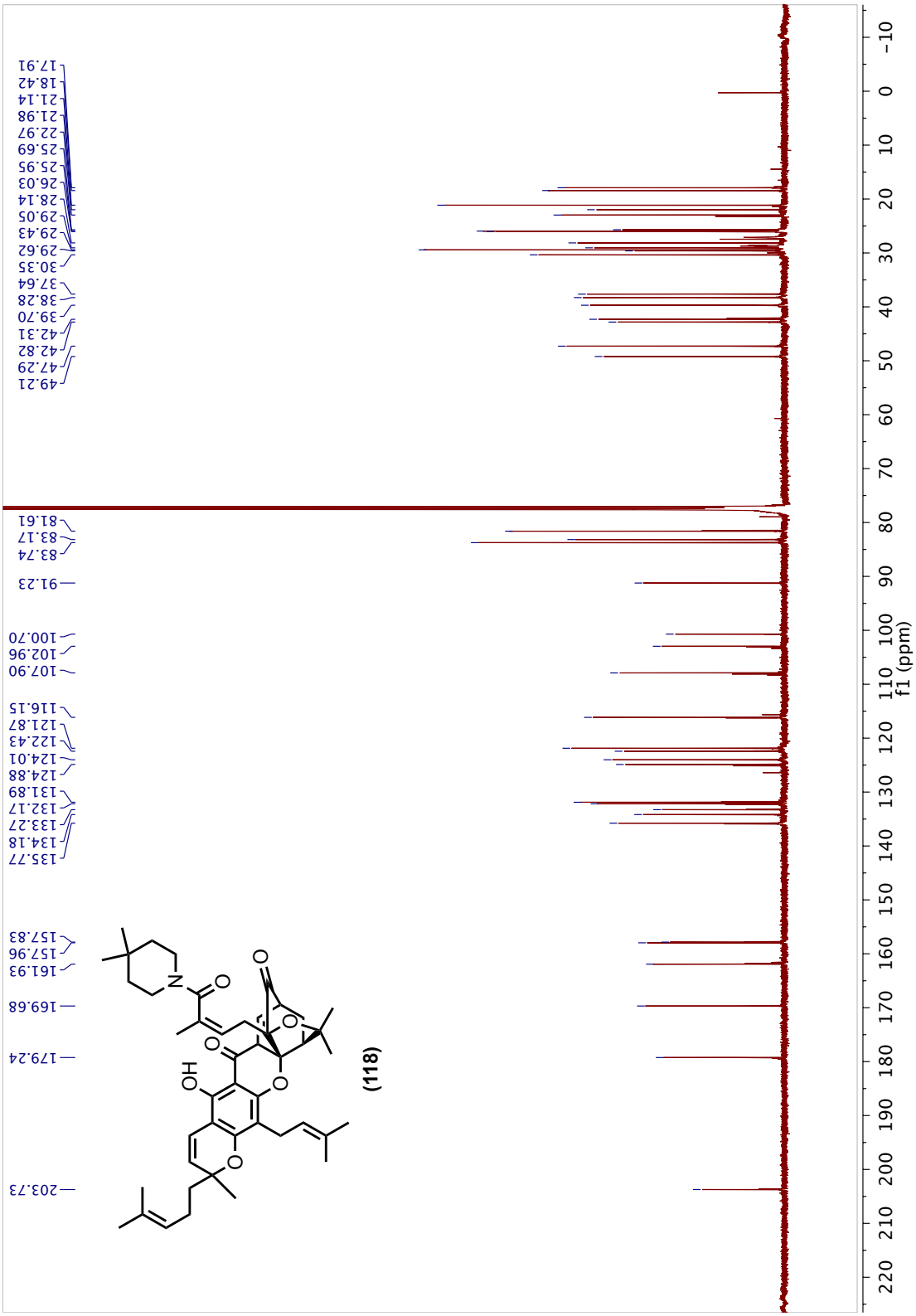
17.91
18.42
21.14
21.98
22.97
25.69
25.95
26.03
28.14
29.05
29.43
29.62
30.35
37.64
38.28
39.70
42.31
42.82
47.29
49.21
81.61
83.17
83.74
91.23
100.70
102.96
107.90
116.15
121.87
122.43
124.01
124.88
131.89
132.17
133.27
134.18
135.77
157.83
157.96
161.93
169.68
179.24
203.73
(118)
f1 (ppm)

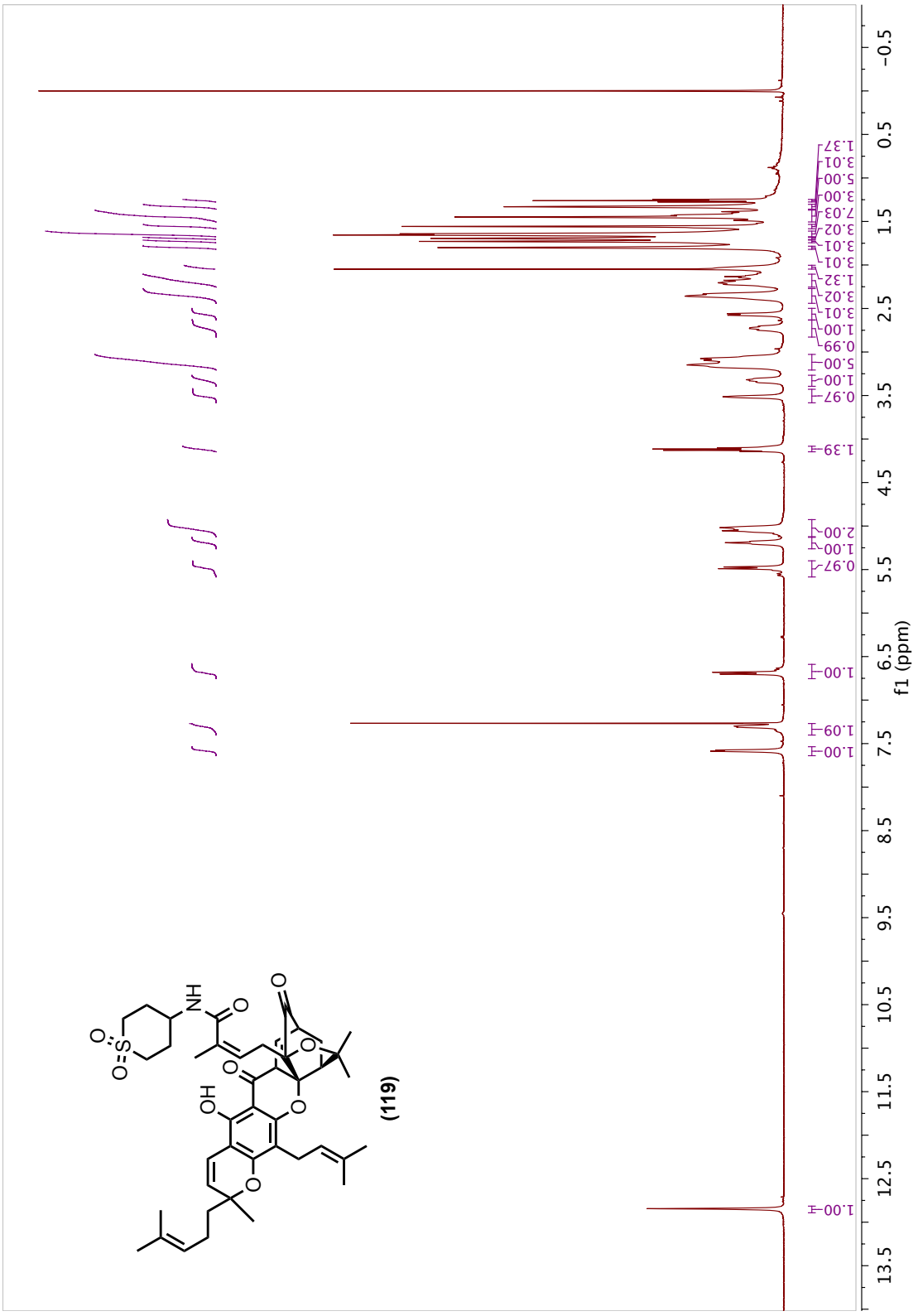
(119)
f1 (ppm)

17.91
18.40
21.35
21.37
21.81
22.95
25.43
25.94
25.98
28.16
29.30
29.41
29.50
29.97
30.20
42.31
45.03
46.95
49.19
49.68
81.90
83.87
84.85
91.20
100.58
103.20
108.02
115.98
122.08
123.87
124.17
125.27
132.21
132.26
133.35
135.92
136.59
157.20
158.02
162.23
168.72
178.86
204.75
f1 (ppm)
(119)

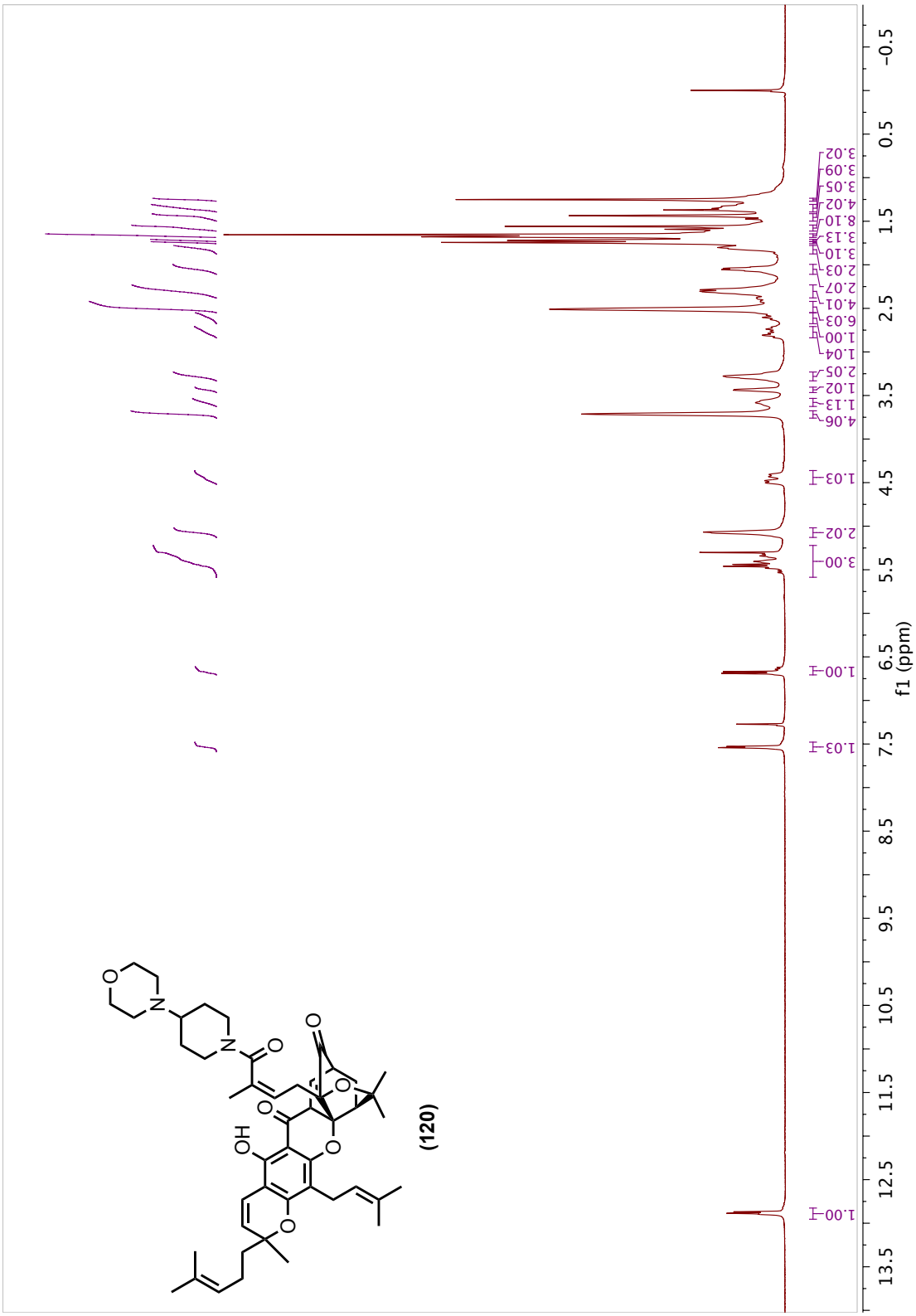
(120)
f1 (ppm)

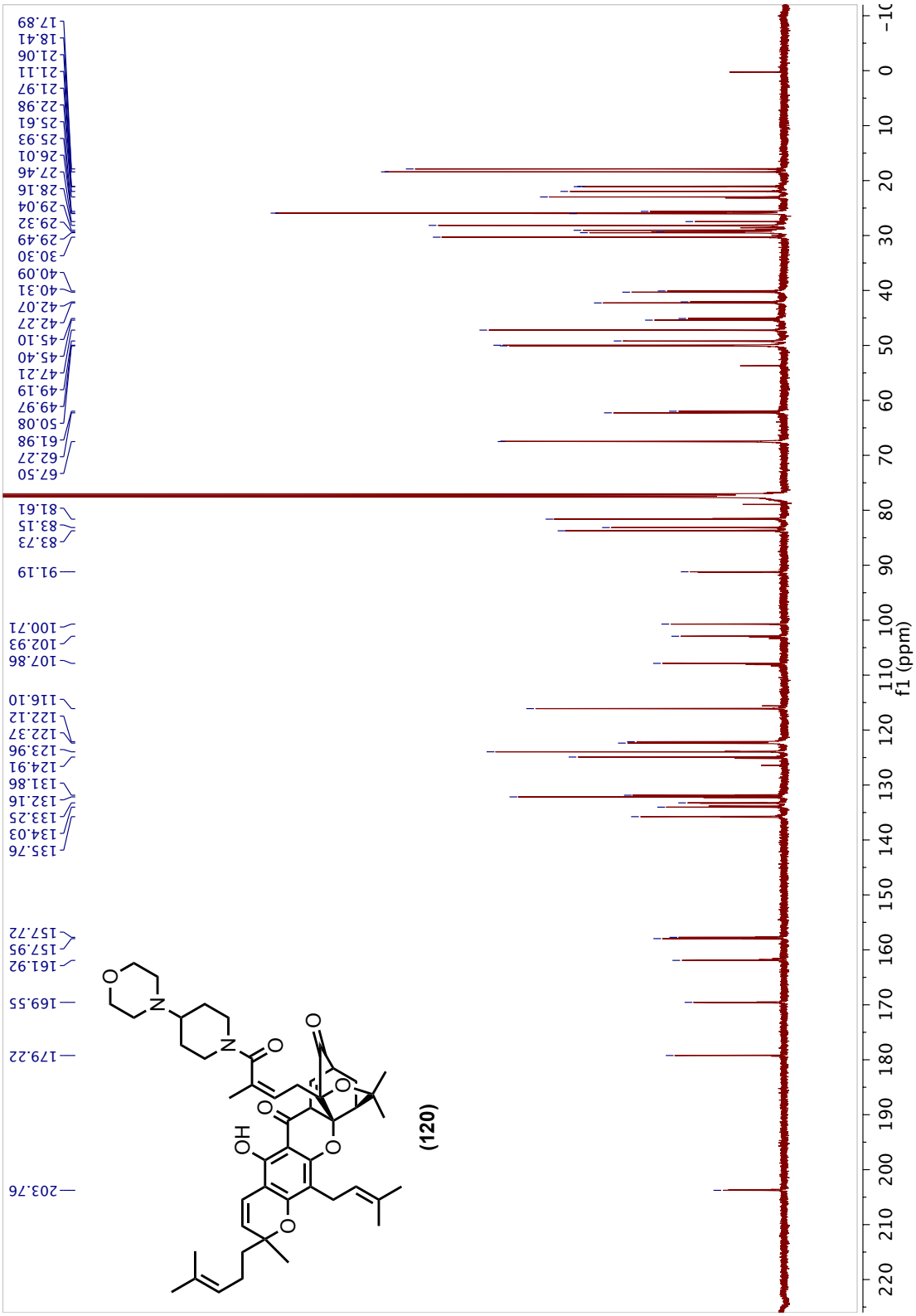
17.89
18.41
21.06
21.11
21.97
22.98
25.61
25.93
26.01
27.46
28.16
29.04
29.32
29.49
30.30
40.09
40.31
42.07
42.27
45.10
45.40
47.21
49.19
49.97
50.08
61.98
62.27
67.50
81.61
83.15
83.73
91.19
100.71
102.93
107.86
116.10
122.12
122.37
123.96
124.91
131.86
132.16
133.25
134.03
135.76
157.22
157.95
161.92
169.55
179.22
203.76
(120)
f1 (ppm)

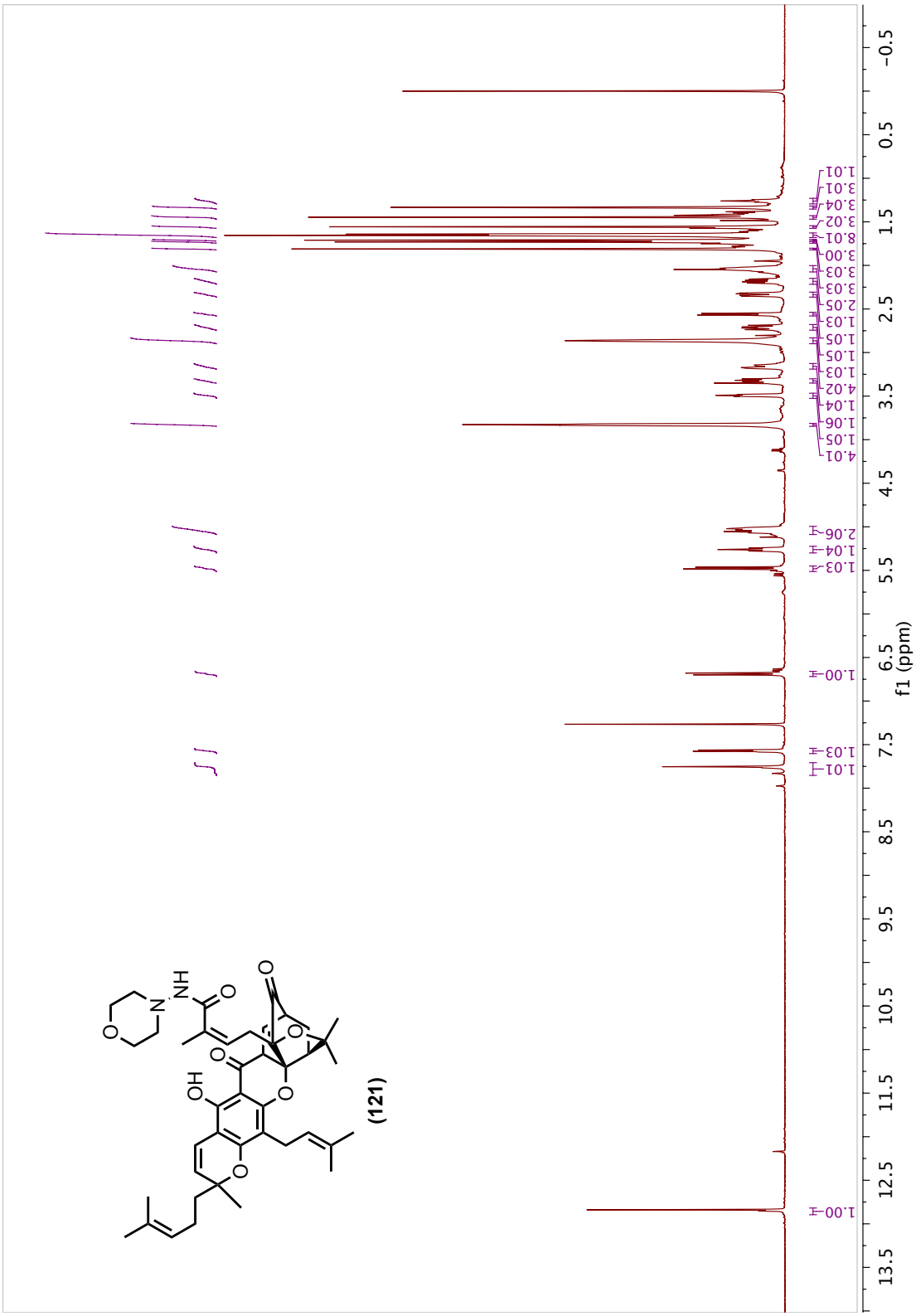
(121)
f1 (ppm)

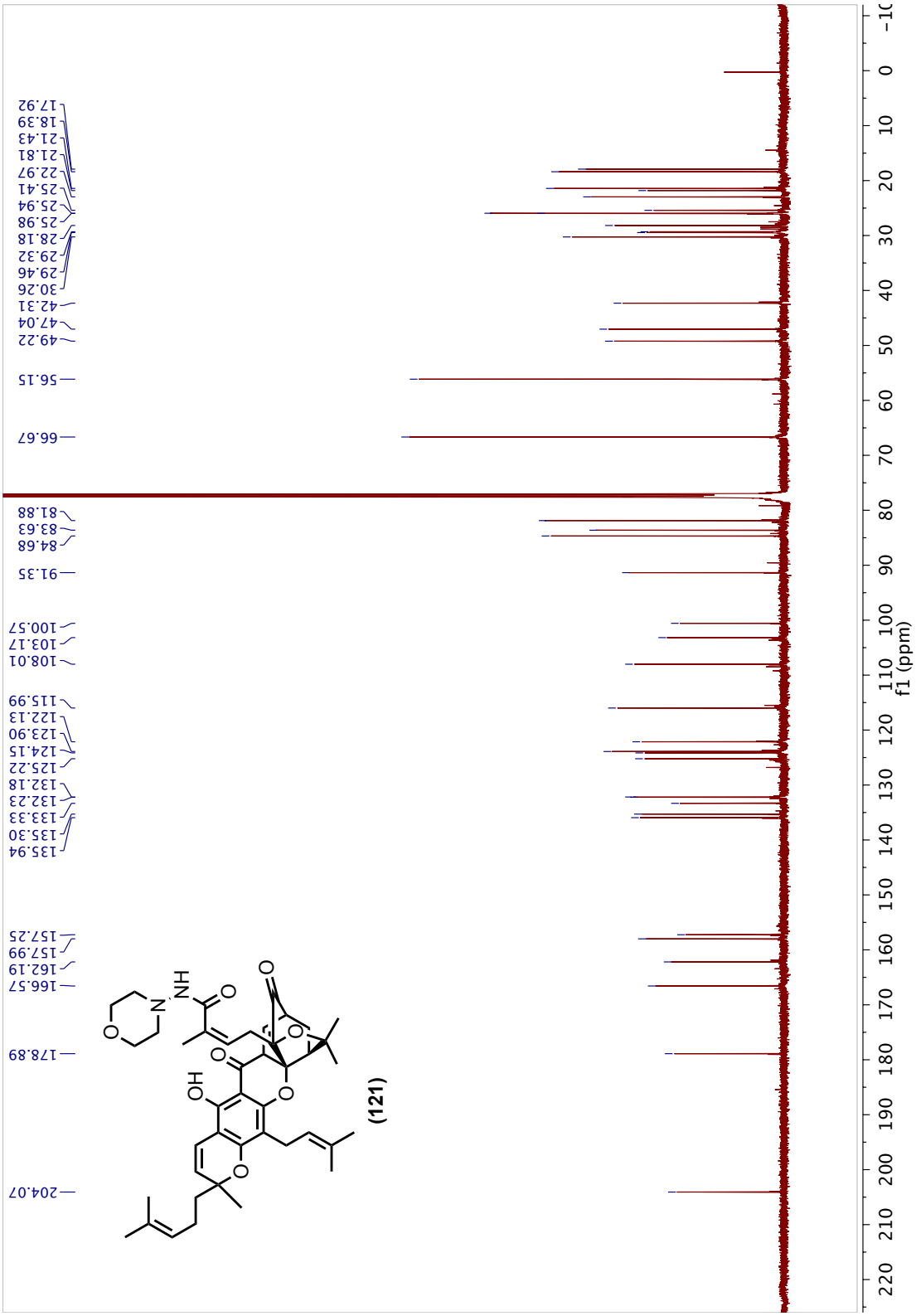
17.92
18.39
21.43
21.81
22.97
25.41
25.94
25.98
28.18
29.32
29.46
30.26
42.31
47.04
49.22
56.15
66.67
81.88
83.63
84.68
91.35
100.57
103.17
108.01
115.99
122.13
123.90
124.15
125.22
132.18
132.23
133.33
135.30
135.94
157.25
157.99
162.19
166.57
178.89
204.07
(121)
f1 (ppm)

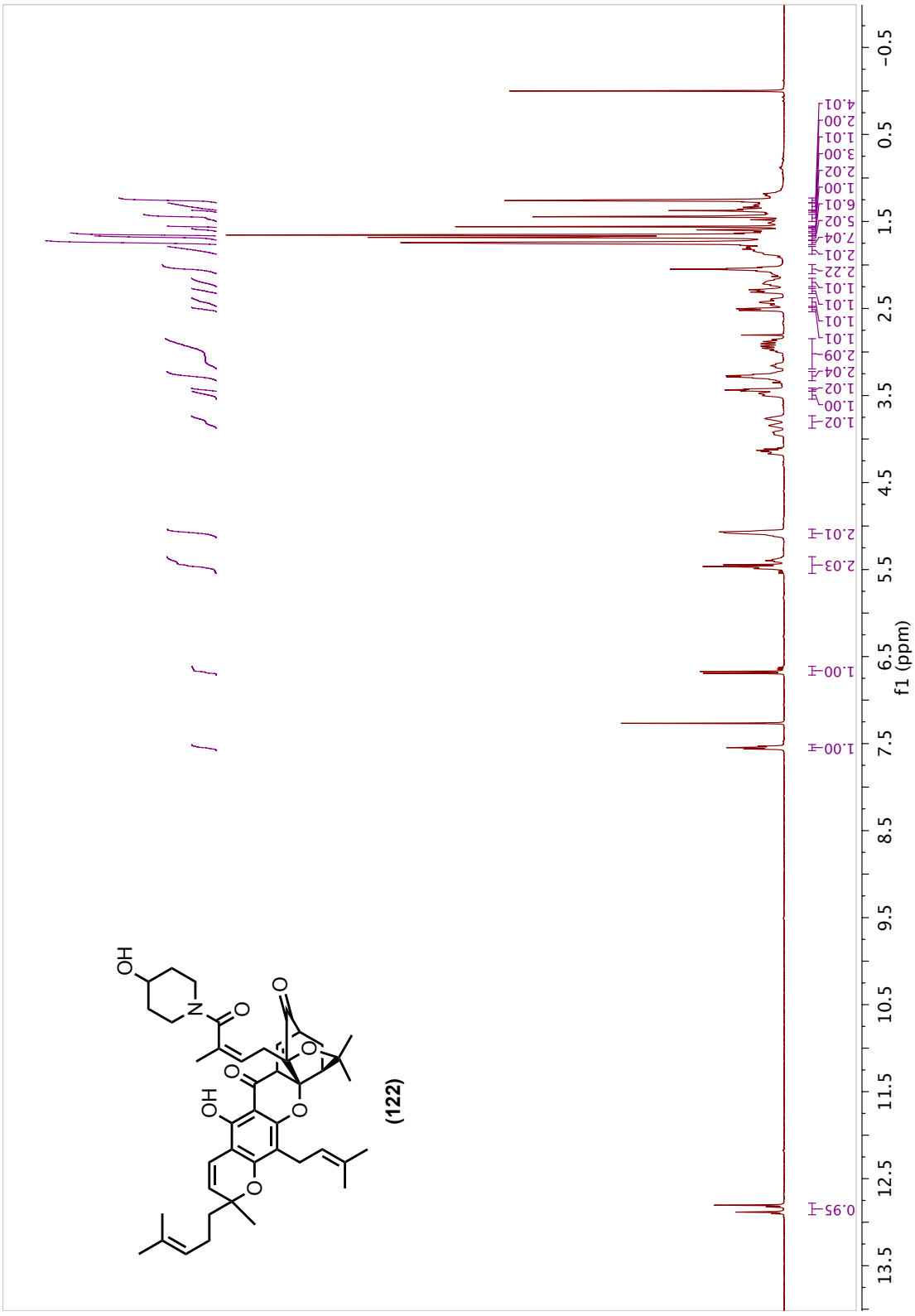
OH
N
O
O
O
O
O
O
OH
(122)
f1 (ppm)
13.5
12.5
11.5
10.5
9.5
8.5
7.5
6.5
5.5
4.5
3.5
2.5
1.5
0.5
-0.5
0.95
1.00
2.03
2.01
1.02
1.00
2.09
2.04
1.02
1.01
1.01
1.01
1.01
2.22
2.01
7.04
5.02
6.01
1.00
2.02
3.00
1.01
2.00
4.01

17.91
18.43
20.97
21.97
23.00
25.44
25.95
28.25
29.03
29.65
30.35
34.02
34.57
35.09
35.81
38.21
38.83
42.32
43.28
43.87
47.35
49.10
67.42
68.06
81.78
83.01
84.04
91.28
100.69
102.98
107.95
108.00
116.05
122.32
123.98
125.00
132.20
133.15
133.57
133.93
135.90
136.34
157.95
162.19
169.91
179.26
203.83
OH
N
O
O
O
O
O
O
OH
(122)
f1 (ppm)

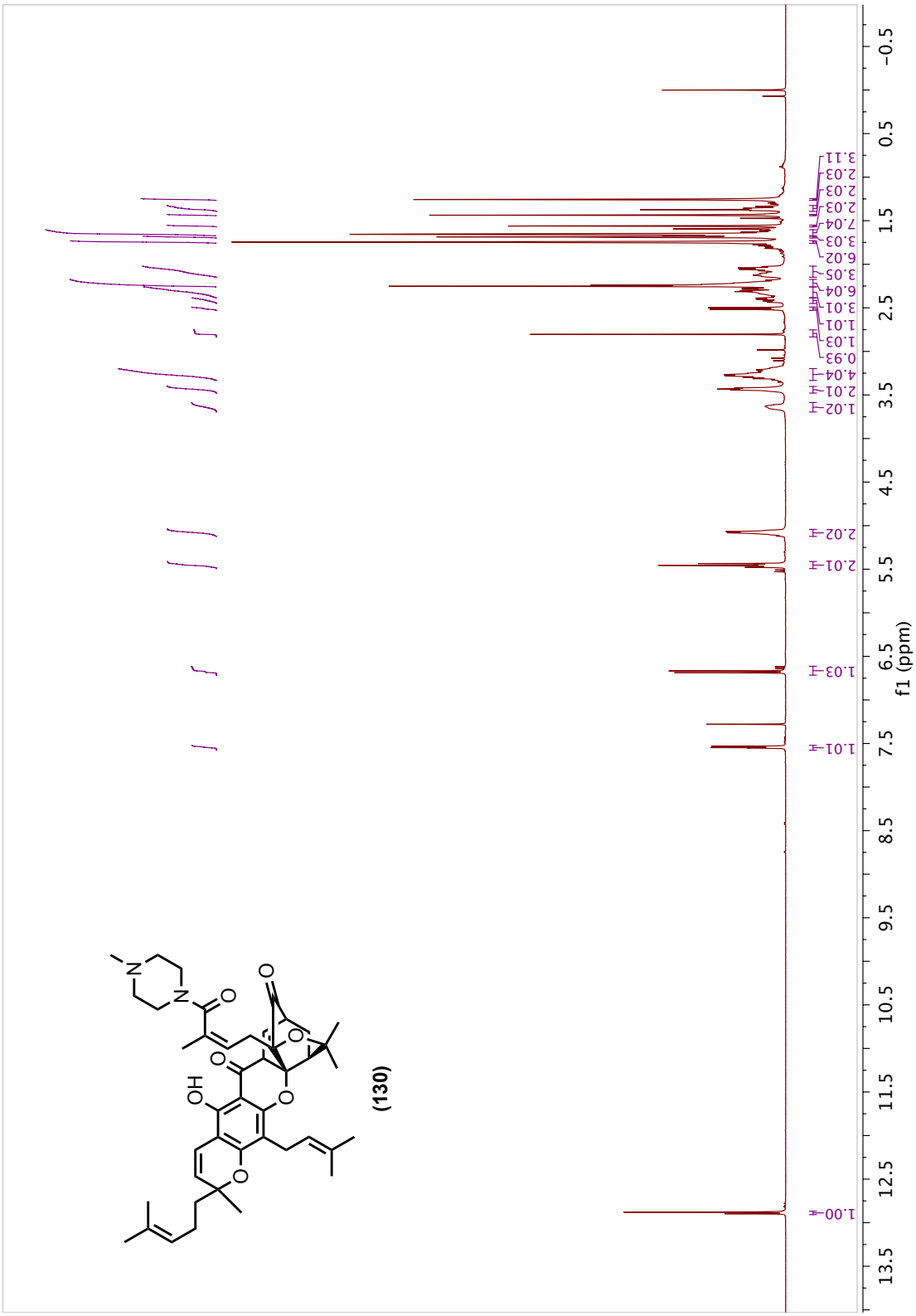
(130)
f1 (ppm)

17.87
18.40
21.04
21.95
22.97
25.61
25.92
25.99
28.14
29.00
29.68
30.33
40.97
42.27
46.02
46.25
47.25
49.12
54.86
55.83
81.60
83.02
83.83
91.24
100.65
102.92
107.87
116.09
122.38
122.46
123.96
124.86
131.86
132.13
133.23
133.49
135.79
157.76
157.93
161.89
169.82
179.14
203.75
(130)
f1 (ppm)

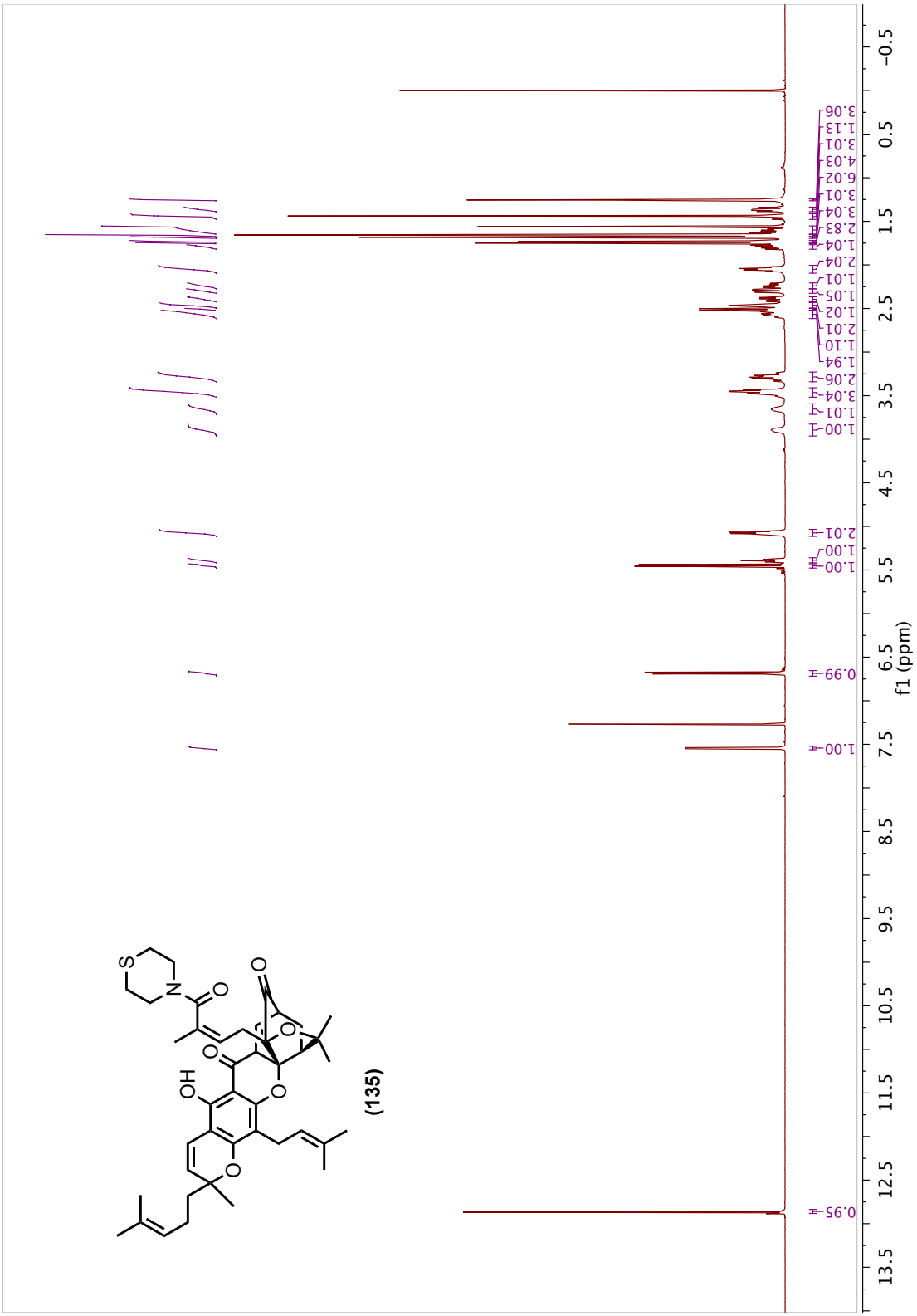
(135)
f1 (ppm)

17.89
18.43
21.13
21.99
23.00
25.65
25.93
26.01
27.74
28.18
28.62
29.05
29.66
30.36
42.33
43.40
47.27
48.70
49.22
81.69
83.16
83.84
91.24
100.73
102.99
107.89
116.12
122.45
122.63
124.02
124.94
131.94
132.17
133.38
133.69
135.75
157.77
158.01
161.95
170.12
179.23
203.74
f1 (ppm)
(135)

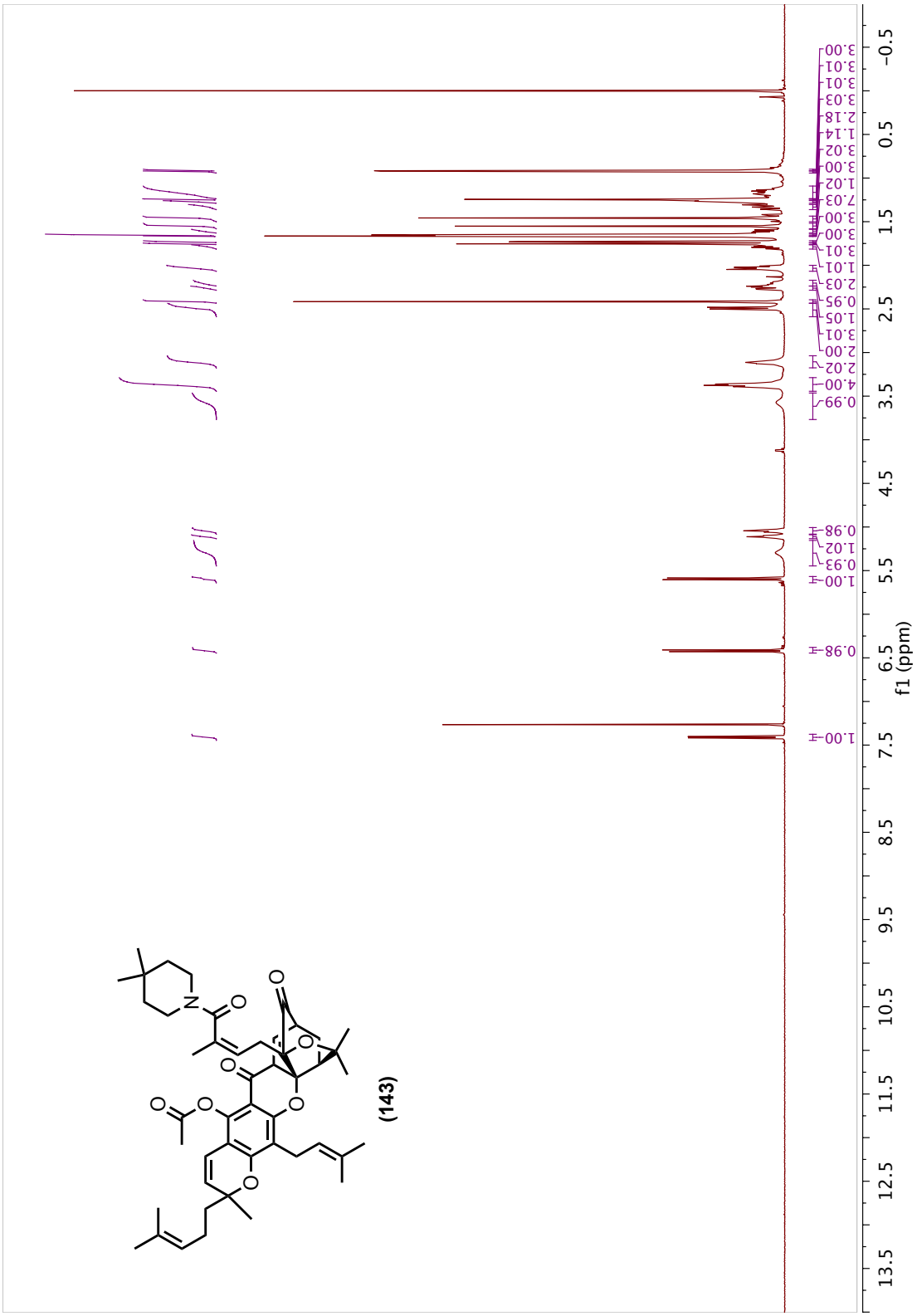
(143)
f1 (ppm)

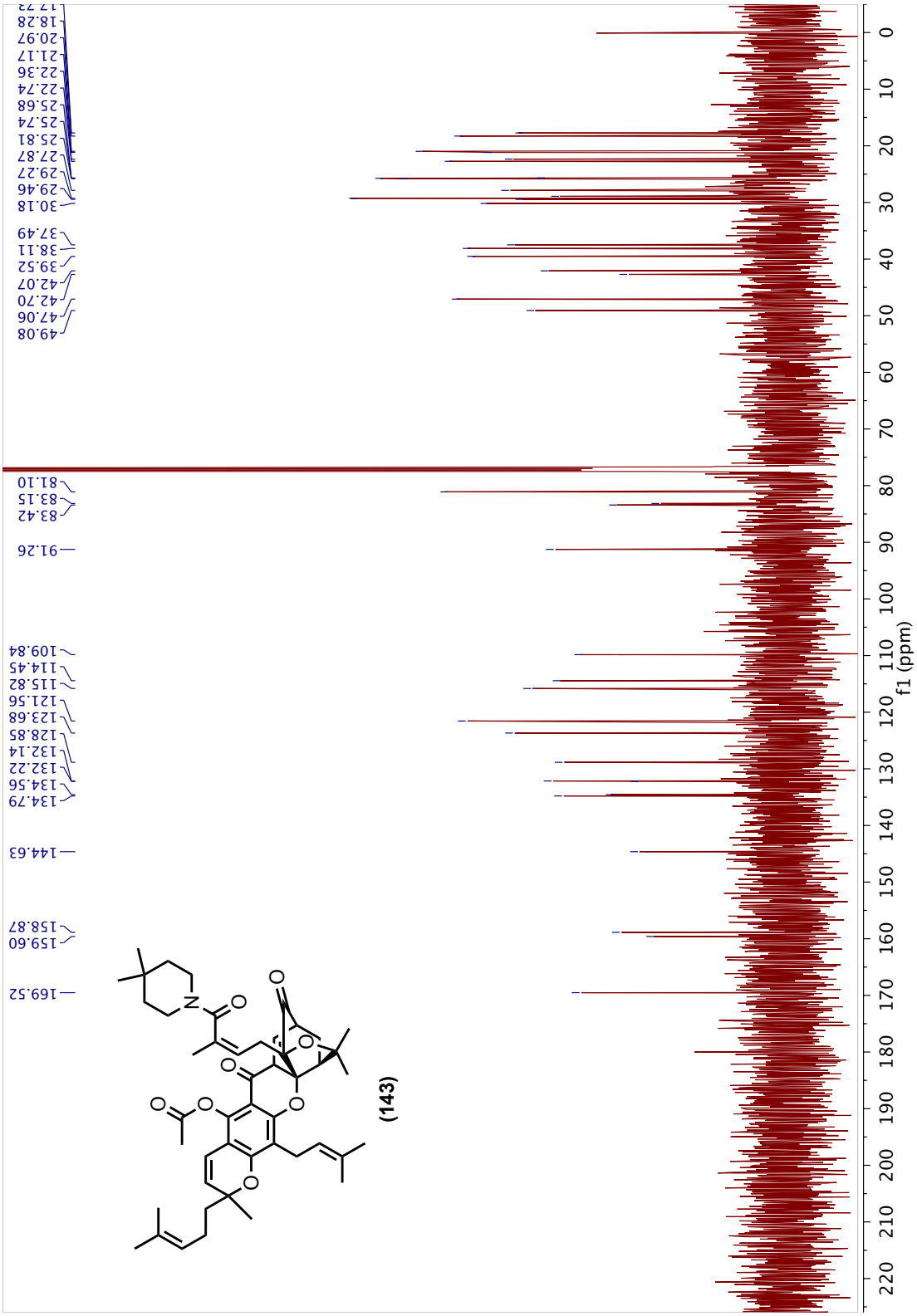
169.52
159.60
158.87
144.63
134.79
134.56
132.22
132.14
128.85
123.68
121.56
115.82
114.45
109.84
91.26
83.42
83.15
81.10
49.08
47.06
42.70
42.07
39.52
38.11
37.49
30.18
29.46
29.27
27.87
25.81
25.74
25.68
22.74
22.36
21.17
20.97
18.28
17.72
(143)
f1 (ppm)

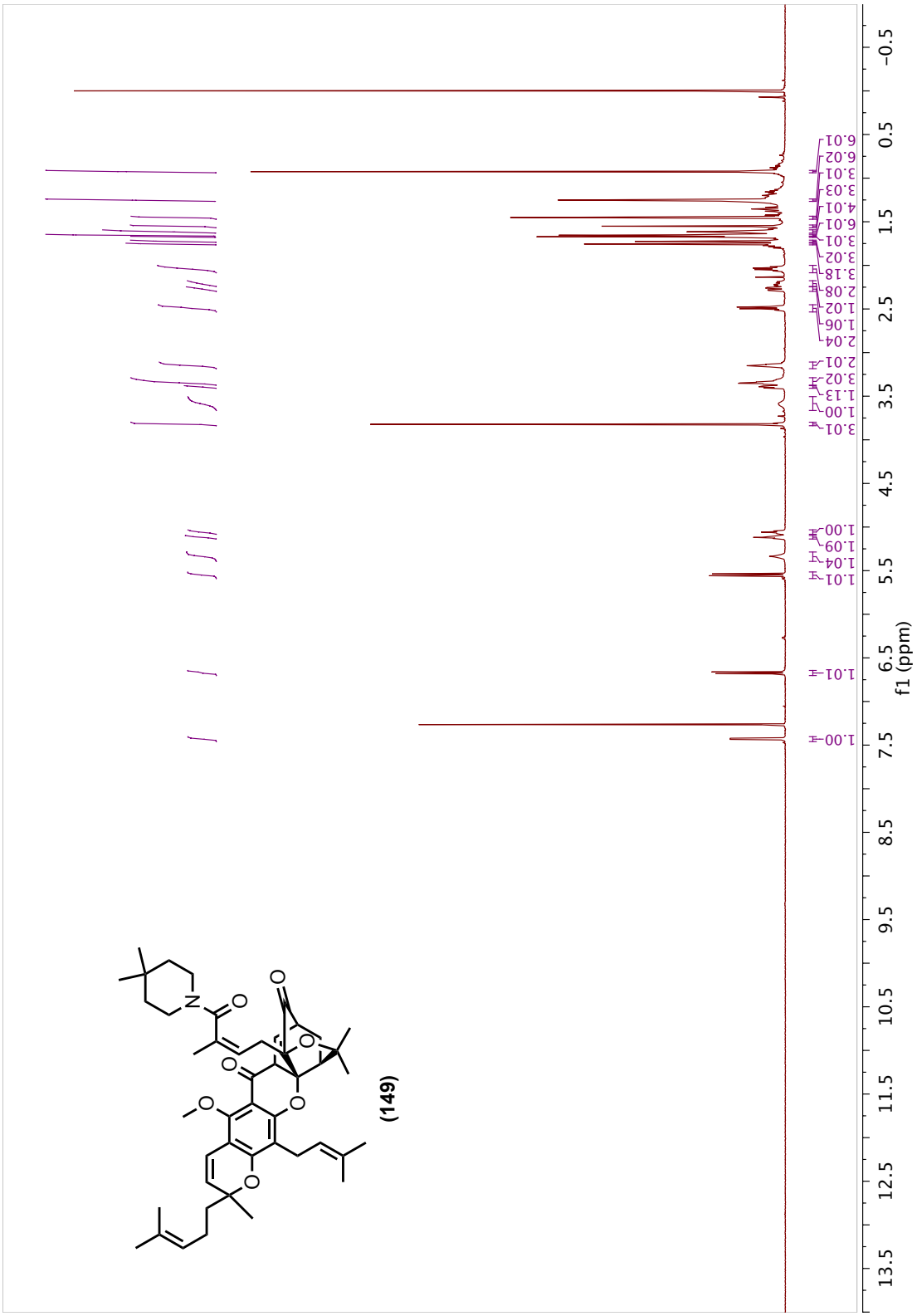
(149)
f1 (ppm)

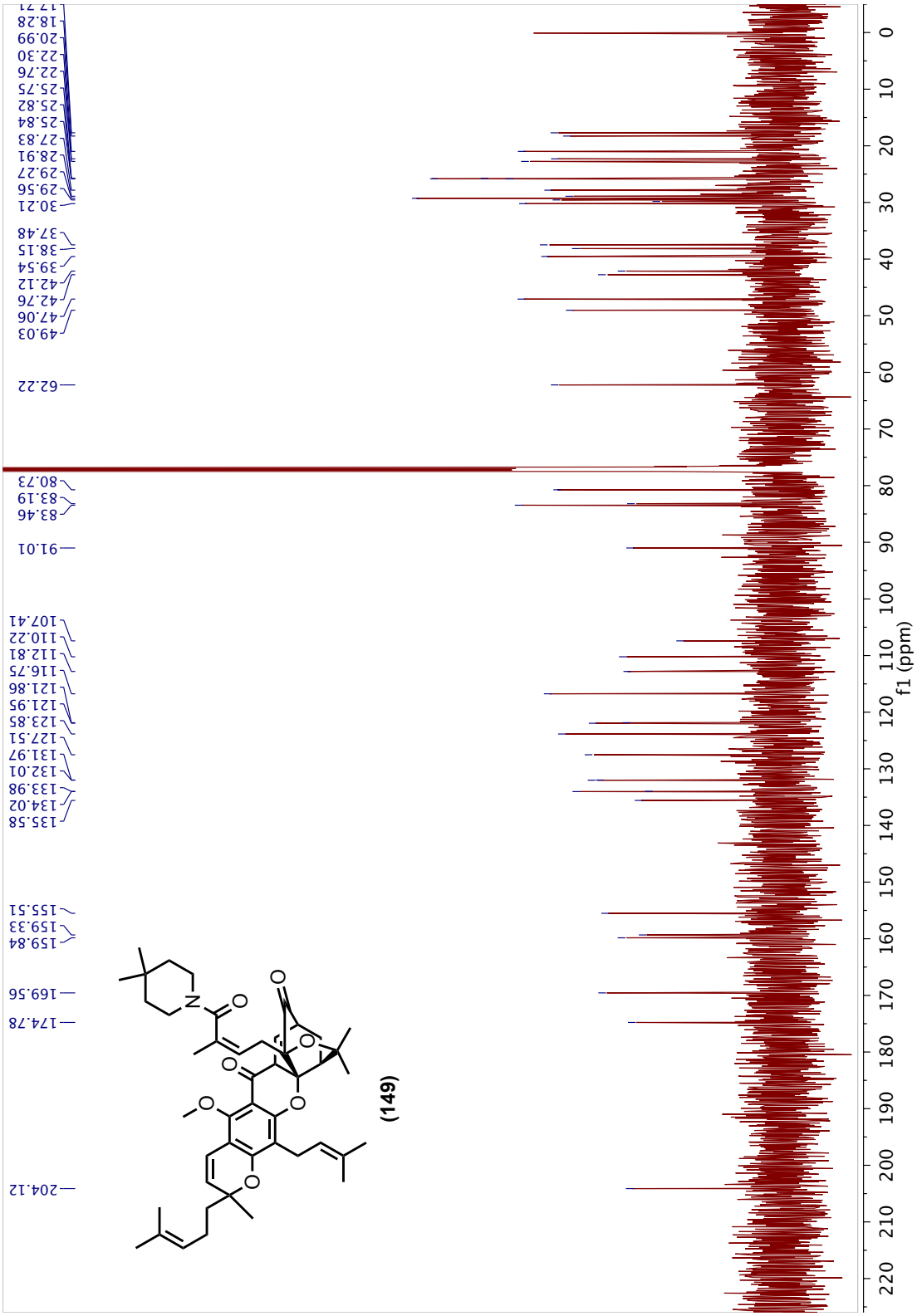
12.71
18.28
20.99
22.30
22.76
25.75
25.82
25.84
27.83
28.91
29.27
29.56
30.21
37.48
38.15
39.54
42.12
42.76
47.06
49.03
62.22
80.73
83.19
83.46
91.01
107.41
110.22
112.81
116.75
121.86
121.95
123.85
127.51
131.97
132.01
133.98
134.02
135.58
155.51
159.33
159.84
169.56
174.78
204.12
(149)
f1 (ppm)

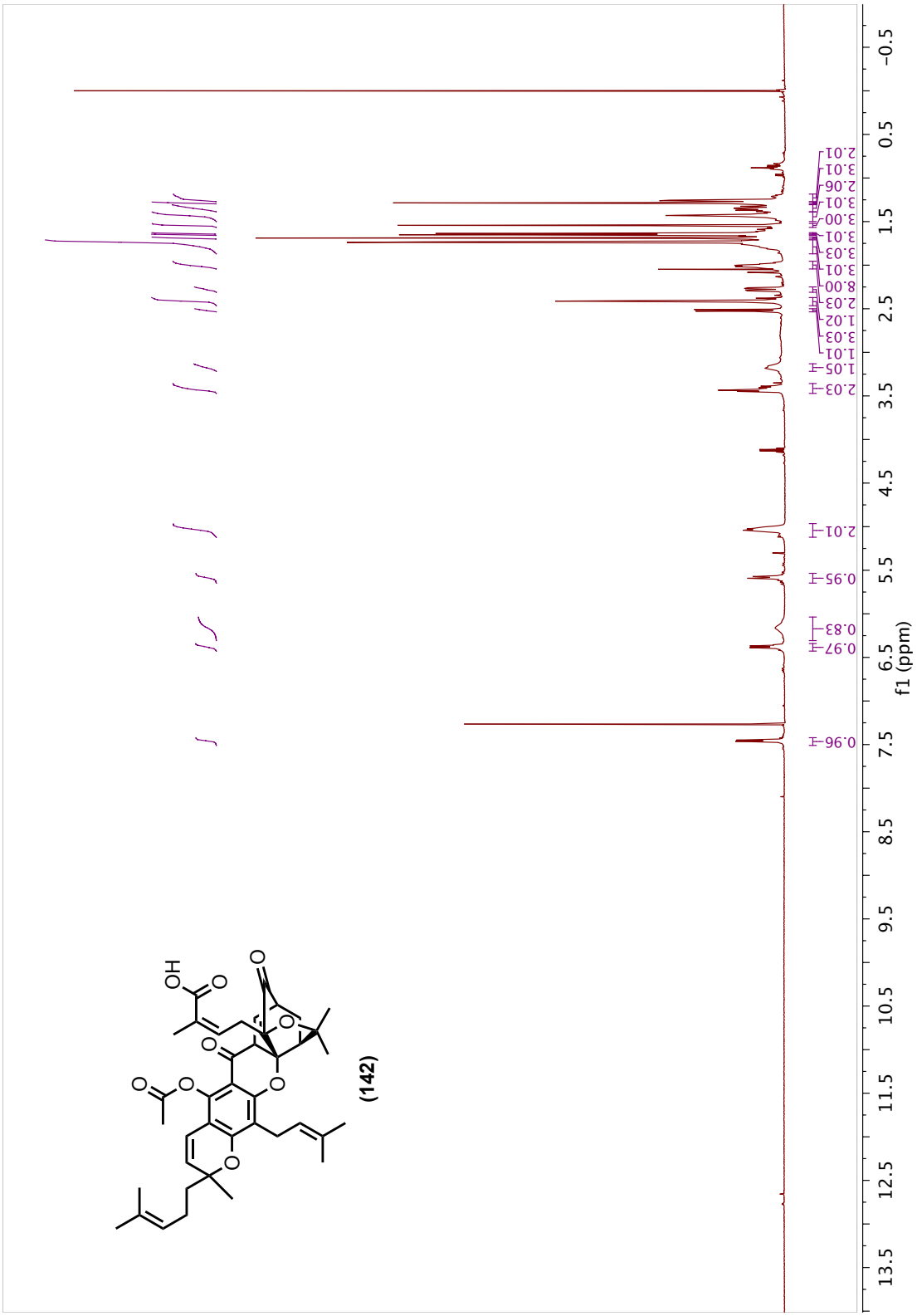
(142)
f1 (ppm)

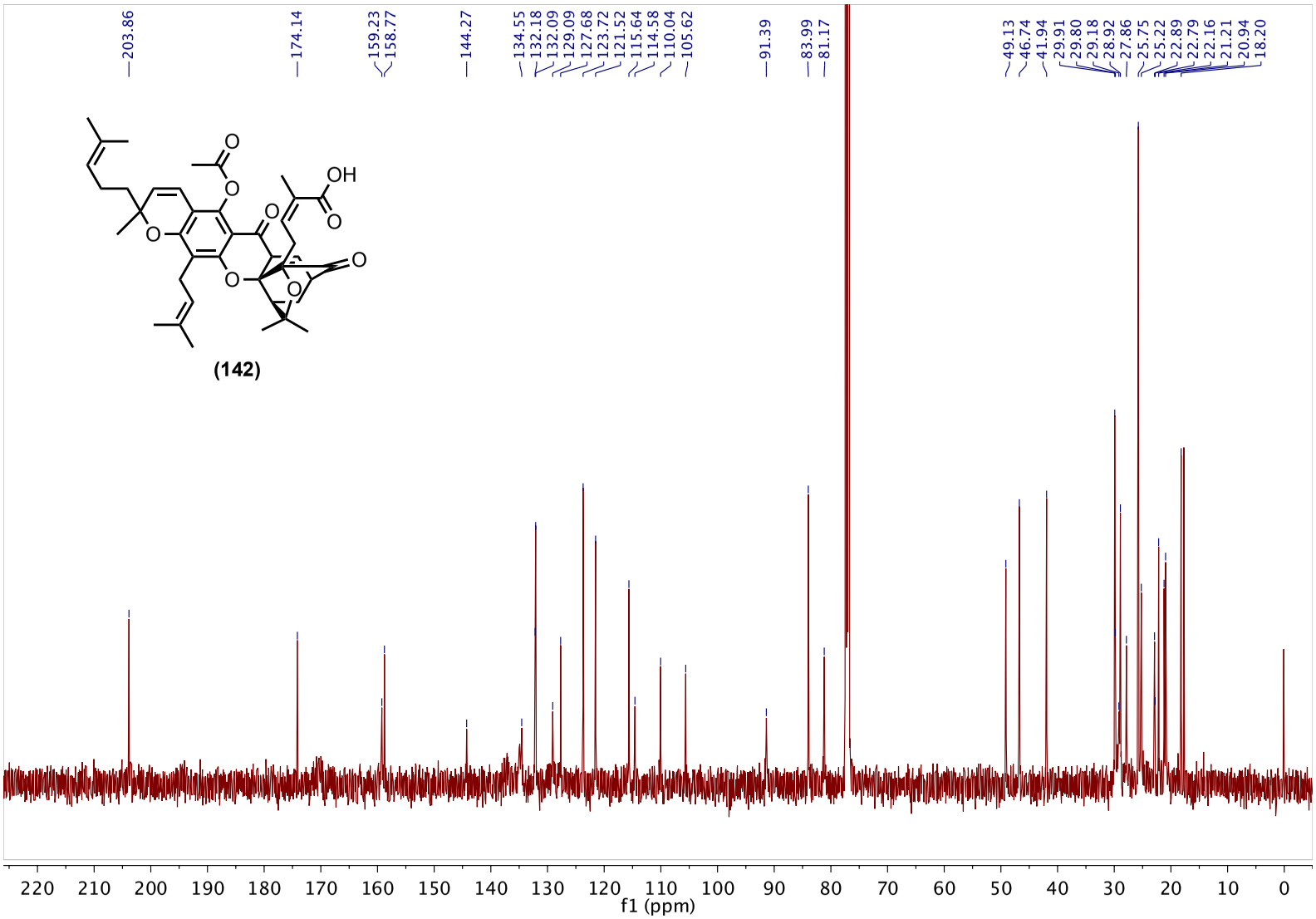
203.86
174.14
159.23
158.77
144.27
134.55
132.18
132.09
129.09
127.68
123.72
121.52
115.64
114.58
110.04
105.62
91.39
83.99
81.17
49.13
46.74
41.94
29.91
29.80
29.18
28.92
27.86
25.75
25.22
22.89
22.79
22.16
21.21
20.94
18.20
OH
O
(142)
220 210 200 190 180 170 160 150 140 130 120 110 100 90 80 70 60 50 40 30 20 10 0
f1 (ppm)

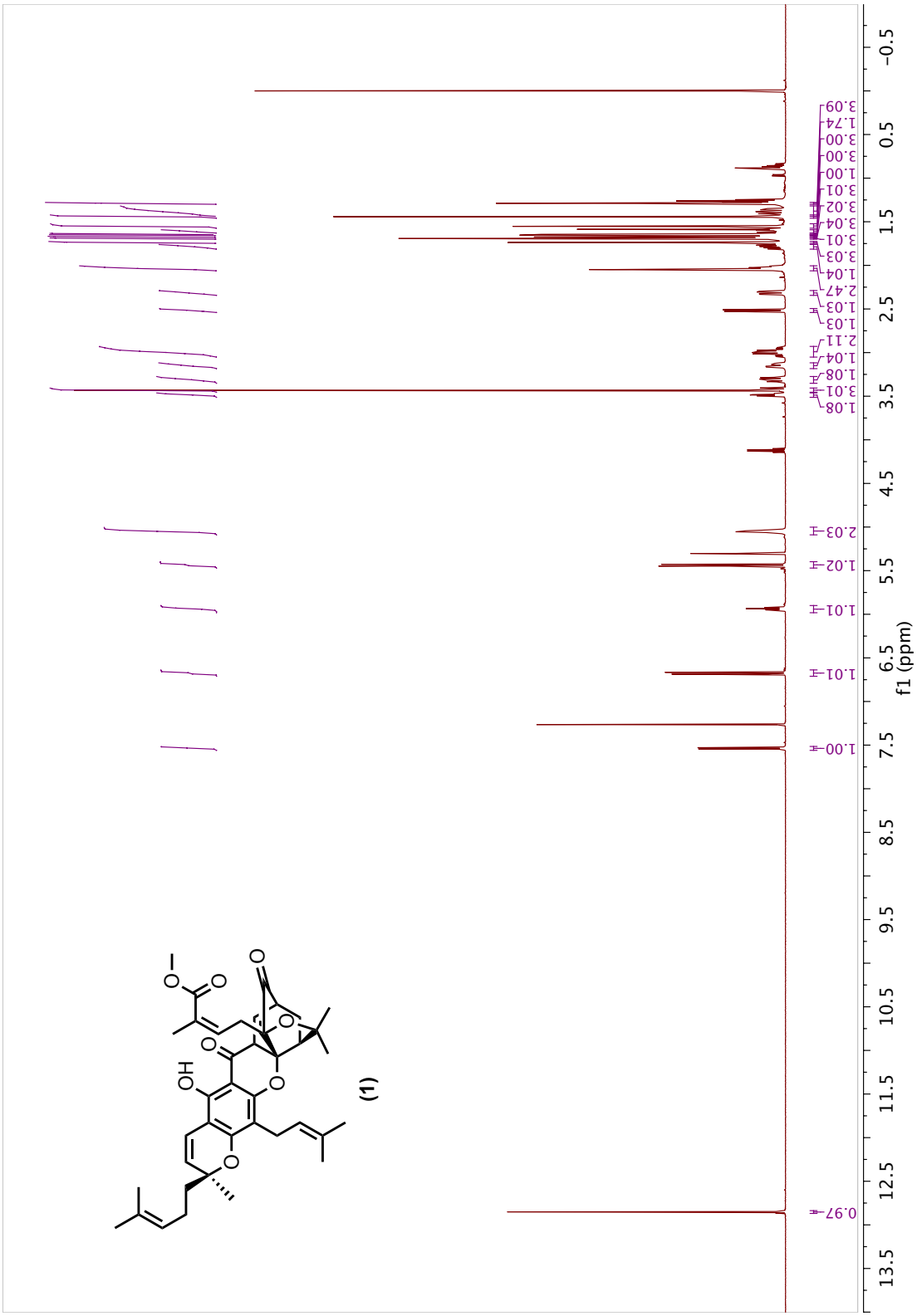
(1)
f1 (ppm)

14.22
17.72
18.18
20.96
21.70
22.76
22.83
25.19
25.75
25.78
28.12
28.93
29.22
29.98
31.69
42.15
46.92
49.14
51.21
60.51
81.37
83.81
83.97
90.99
100.54
102.56
107.61
116.00
122.27
123.85
124.58
127.89
131.65
131.99
133.65
135.13
136.17
157.65
161.40
167.44
179.12
203.68
HO
O
O
O
O
O
O
O
(1)
f1 (ppm)

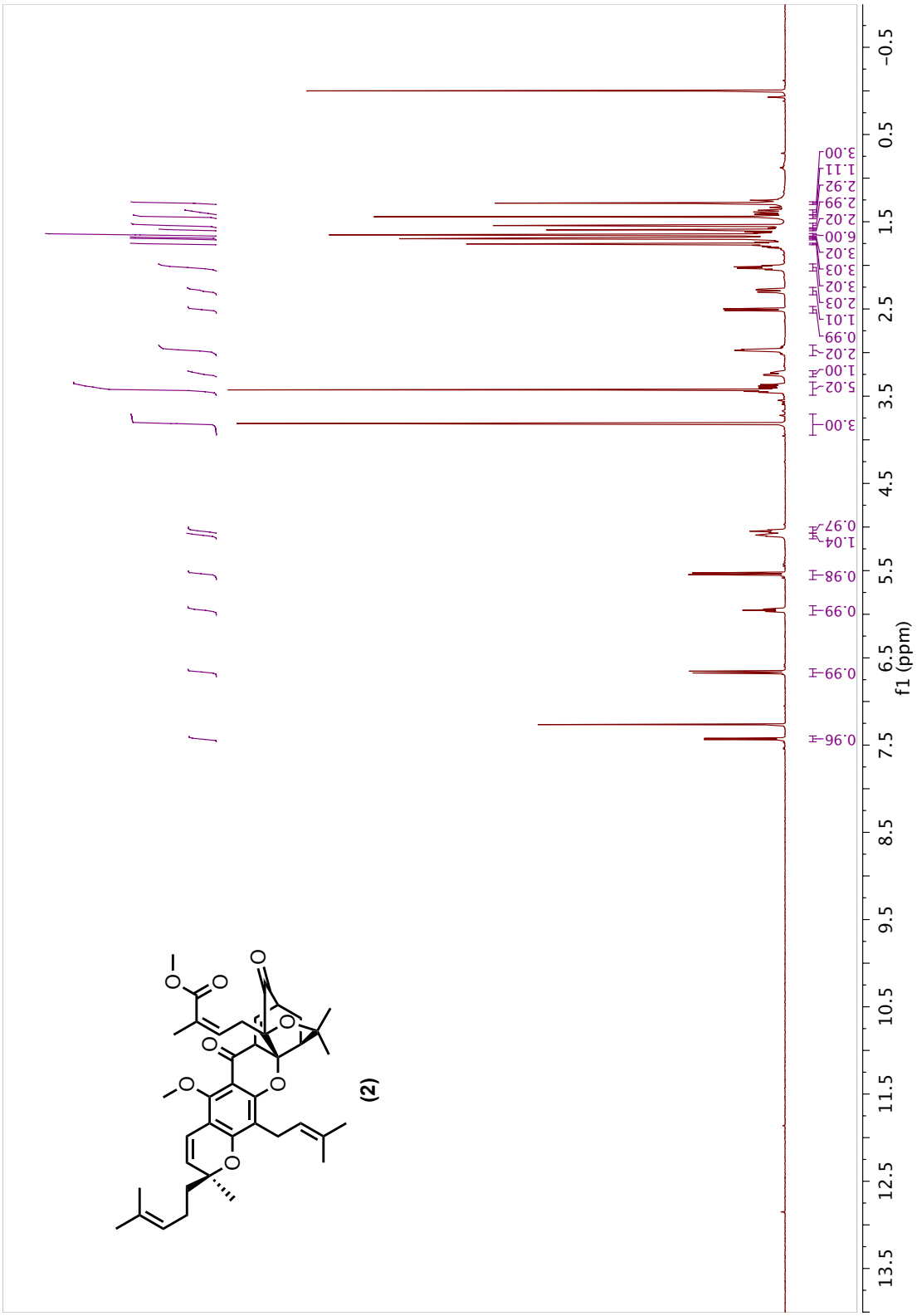
(2)
f1 (ppm)

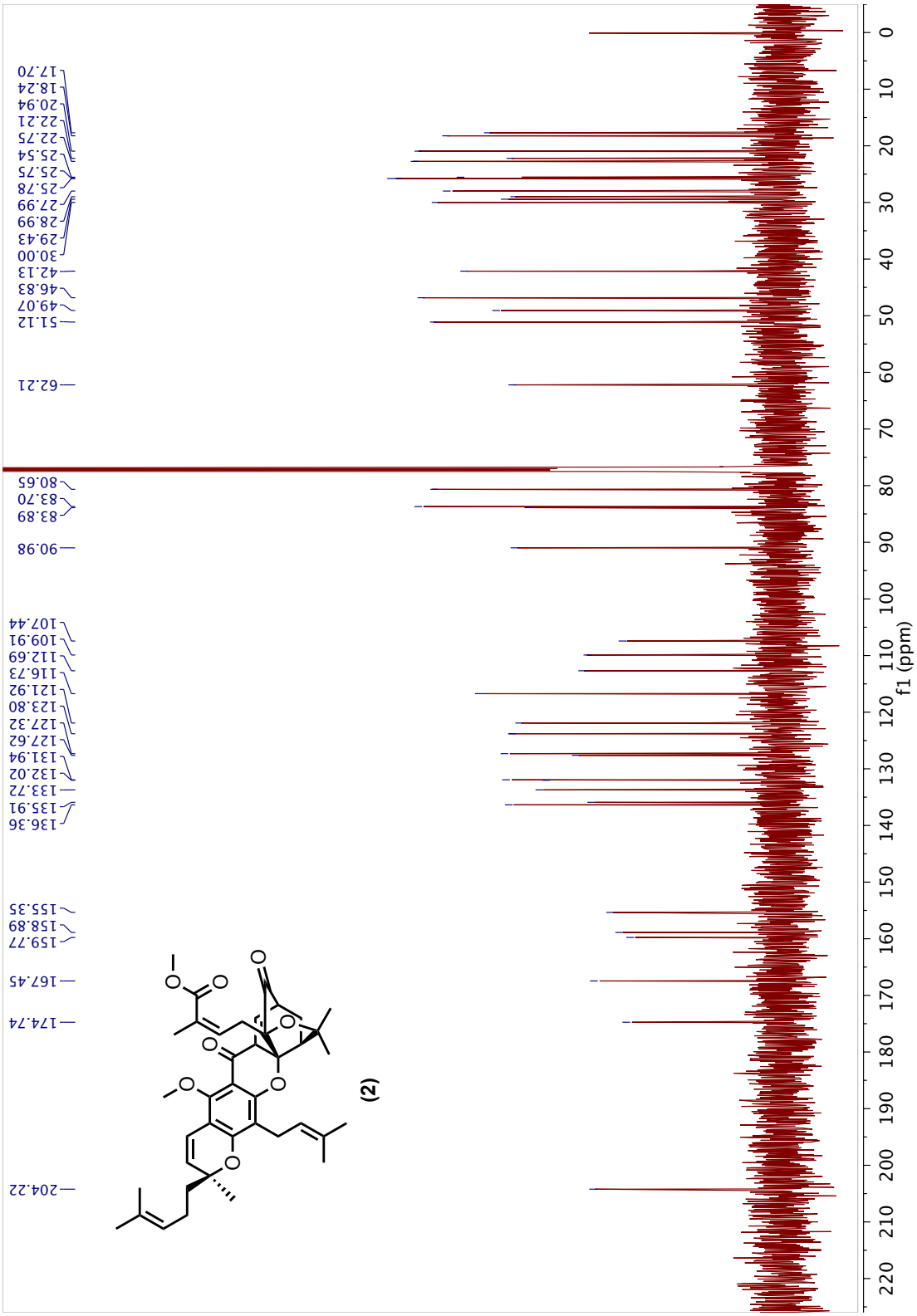
17.70
18.24
20.94
22.21
22.75
25.54
25.75
25.78
27.99
28.99
29.43
30.00
42.13
46.83
49.07
51.12
62.21
80.65
83.70
83.89
90.98
107.44
109.91
112.69
116.73
121.92
123.80
127.32
127.62
131.94
132.02
133.72
135.91
136.36
155.35
158.89
159.77
167.45
174.74
204.22
(2)
f1 (ppm)

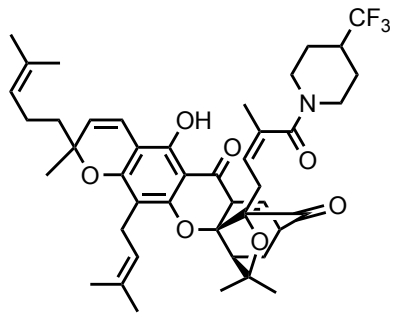

(115)

HR-ESI-TOFMS Positive Ion Mode

Mass Measured	Theoretical Mass	Delta (ppm)	Composition
764.3763	764.3769	-0.8	$[C_{44}H_{53}F_3NO_7]^+$

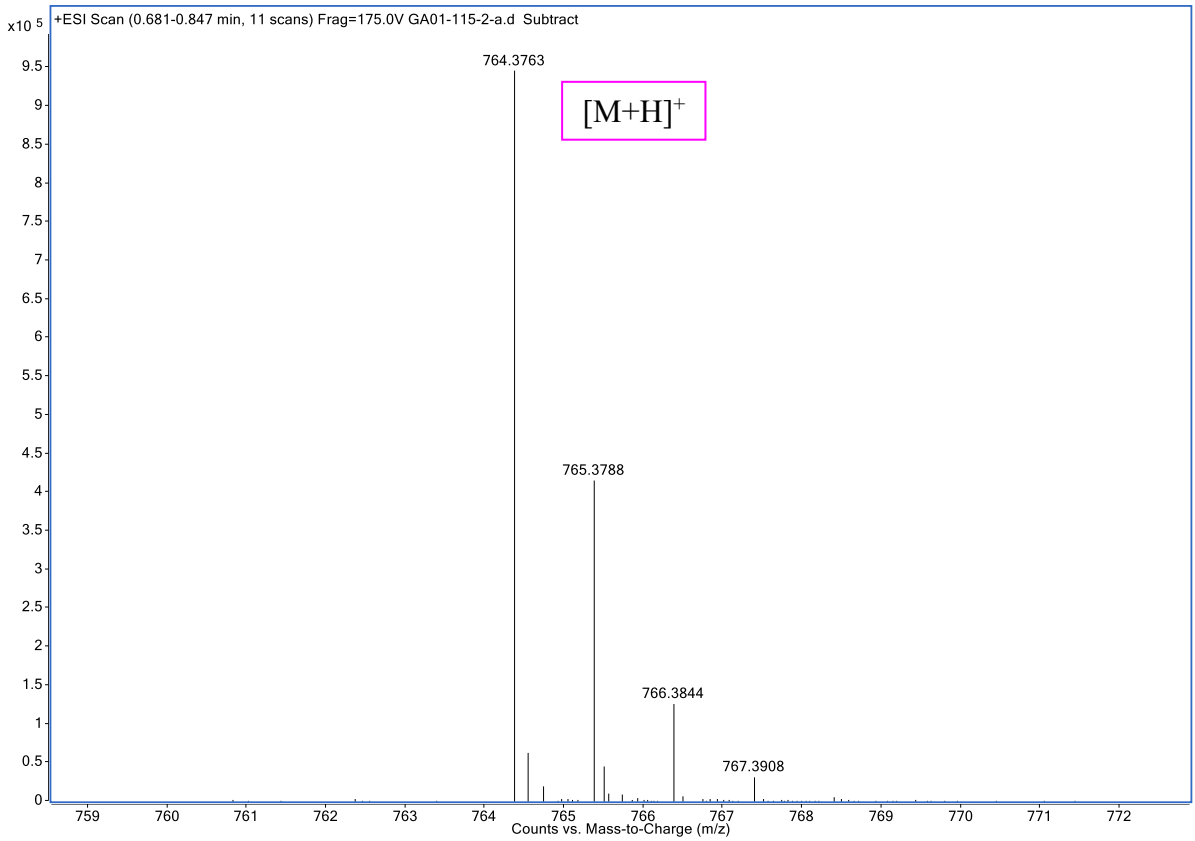

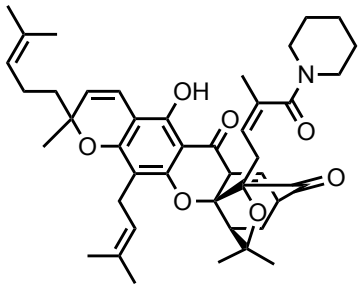

(116)

HR-ESI-TOFMS Positive Ion Mode

Mass Measured	Theoretical Mass	Delta (ppm)	Composition
696.3891	696.3895	-0.6	$[C_{43}H_{54}NO_7]^+$

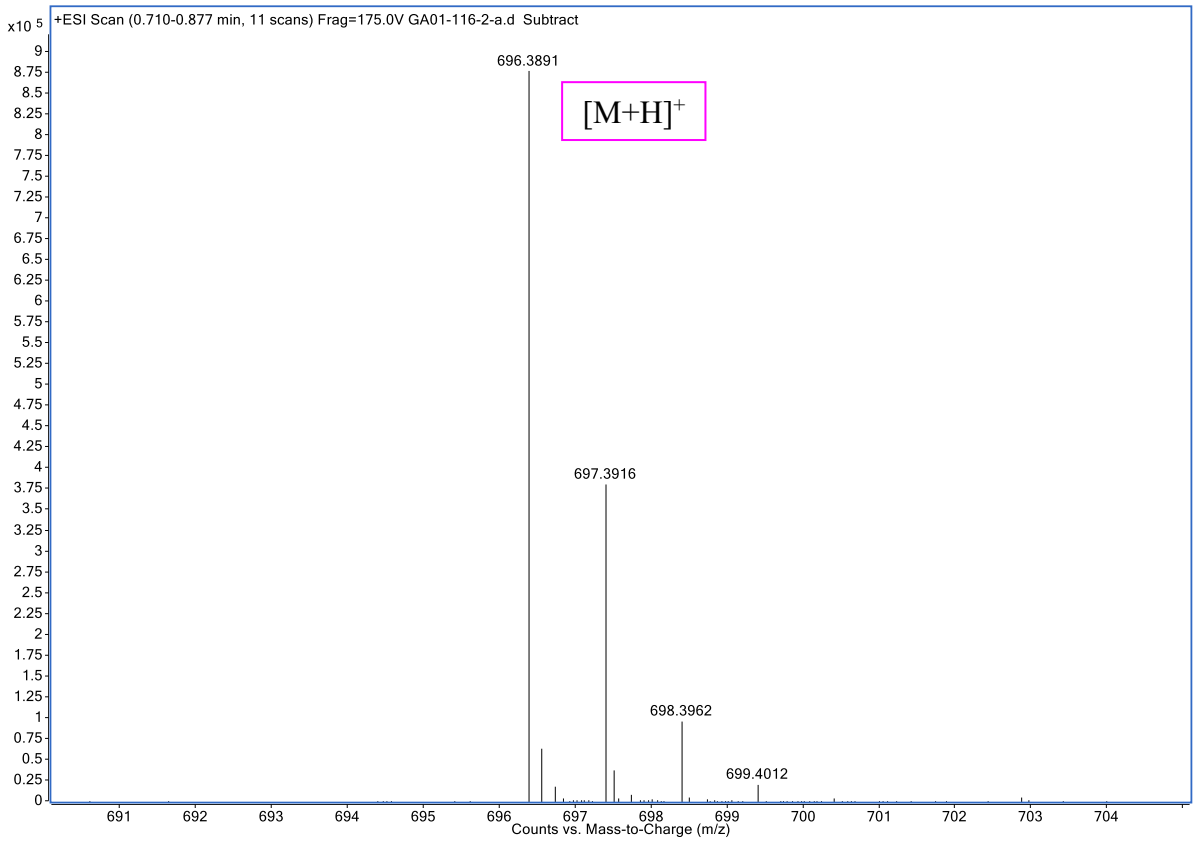

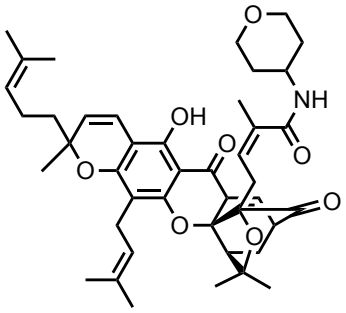

(117)

HR-ESI-TOFMS Positive Ion Mode

Mass Measured	Theoretical Mass	Delta (ppm)	Composition
712.3838	712.3844	-0.8	$[C_{43}H_{54}NO_8]^+$

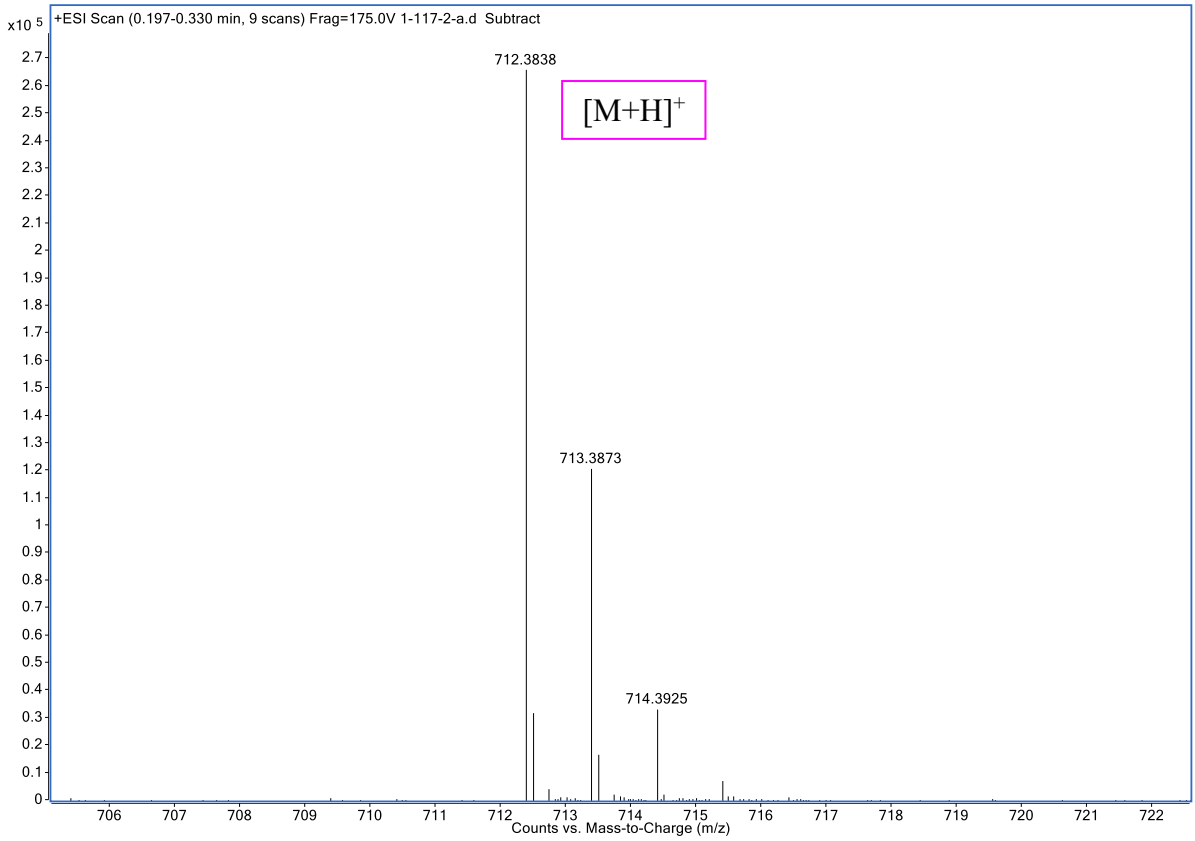

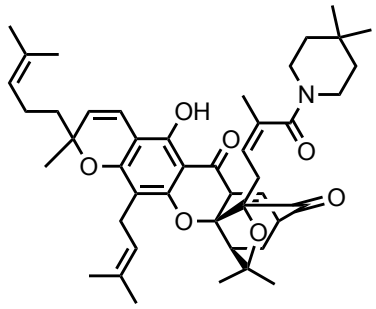

(118)

HR-ESI-TOFMS Positive Ion Mode

Mass Measured	Theoretical Mass	Delta (ppm)	Composition
724.4207	724.4208	-0.1	$[C_{45}H_{58}NO_7]^+$

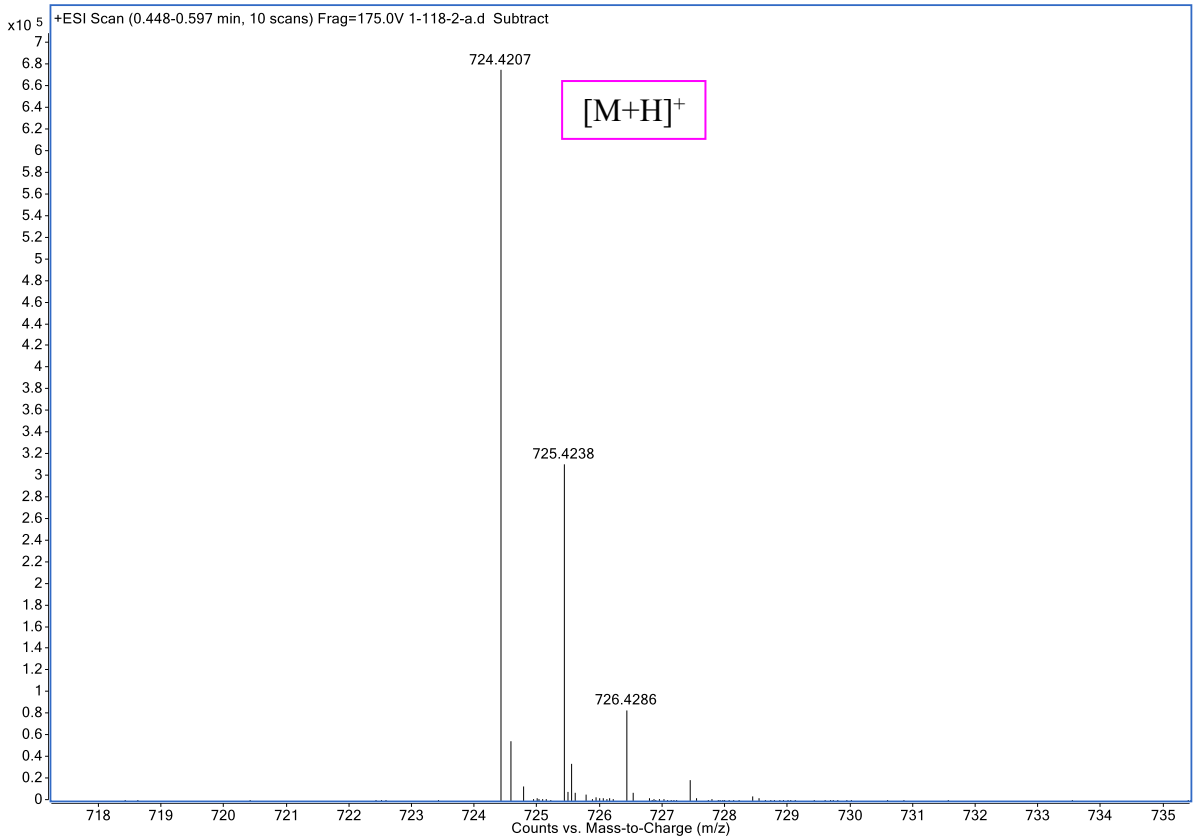

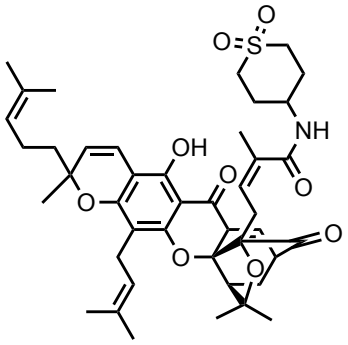

(119)

HR-ESI-TOFMS Positive Ion Mode

Mass Measured	Theoretical Mass	Delta (ppm)	Composition
760.3517	760.3514	0.4	$[C_{43}H_{54}NO_9S]^+$

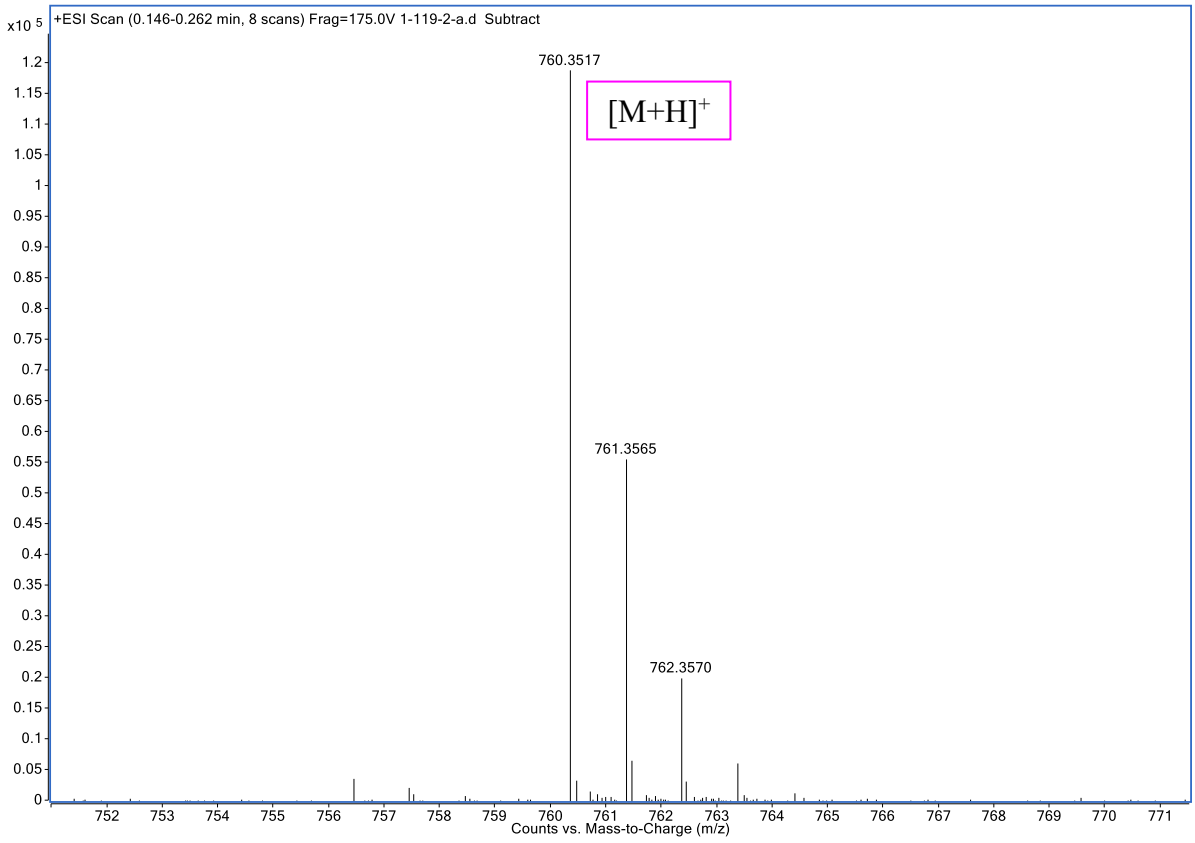

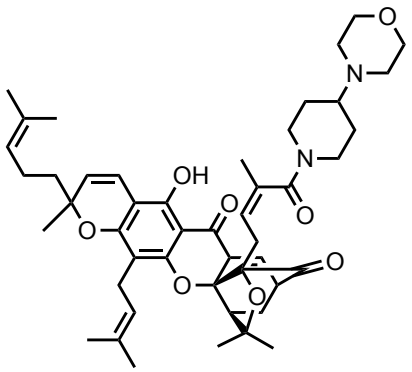

(120)

HR-ESI-TOFMS Positive Ion Mode

Mass Measured	Theoretical Mass	Delta (ppm)	Composition
781.4415	781.4422	-0.9	$[C_{47}H_{61}N_2O_8]^+$

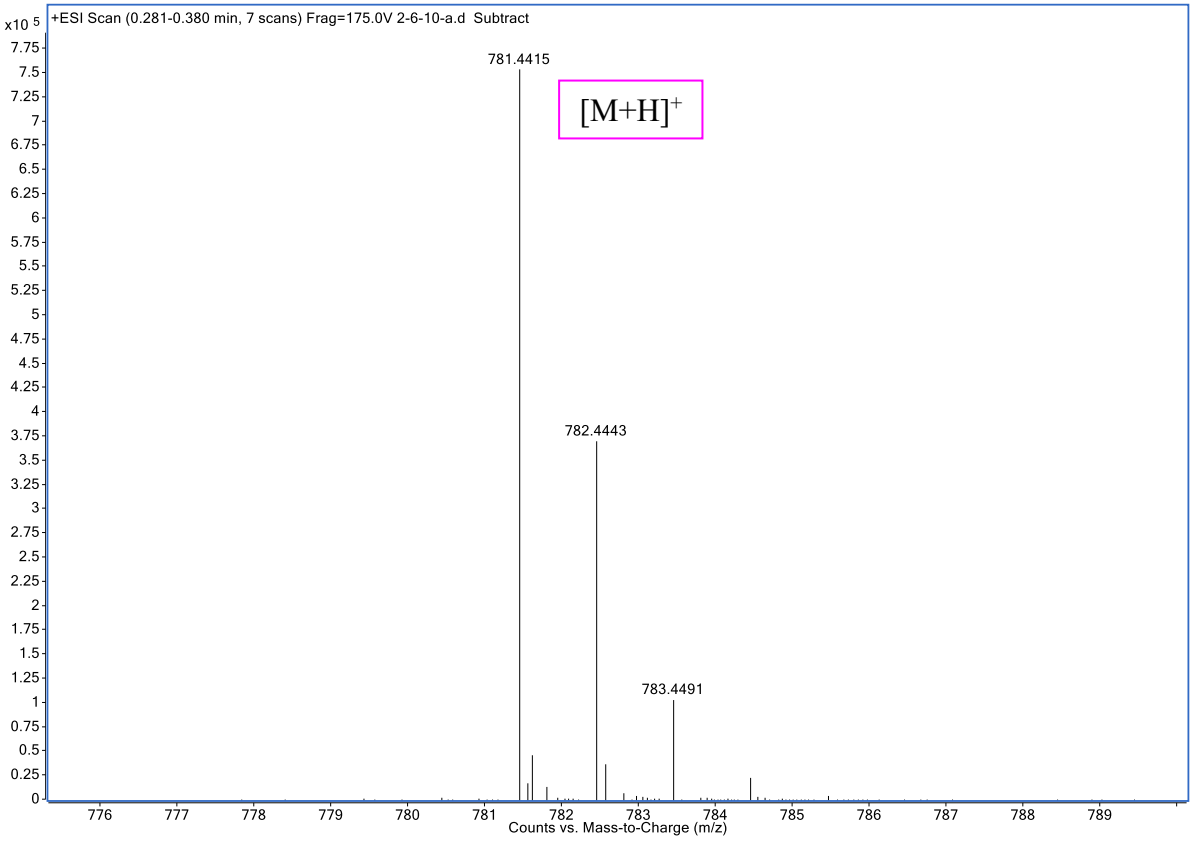

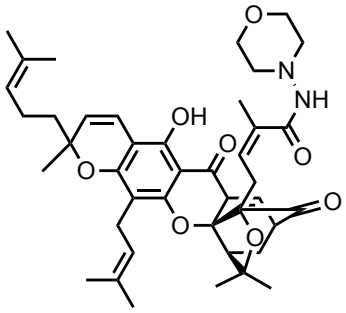

(121)

HR-ESI-TOFMS Positive Ion Mode

Mass Measured	Theoretical Mass	Delta (ppm)	Composition
713.3793	713.3796	-0.4	$[C_{42}H_{53}N_2O_8]^+$

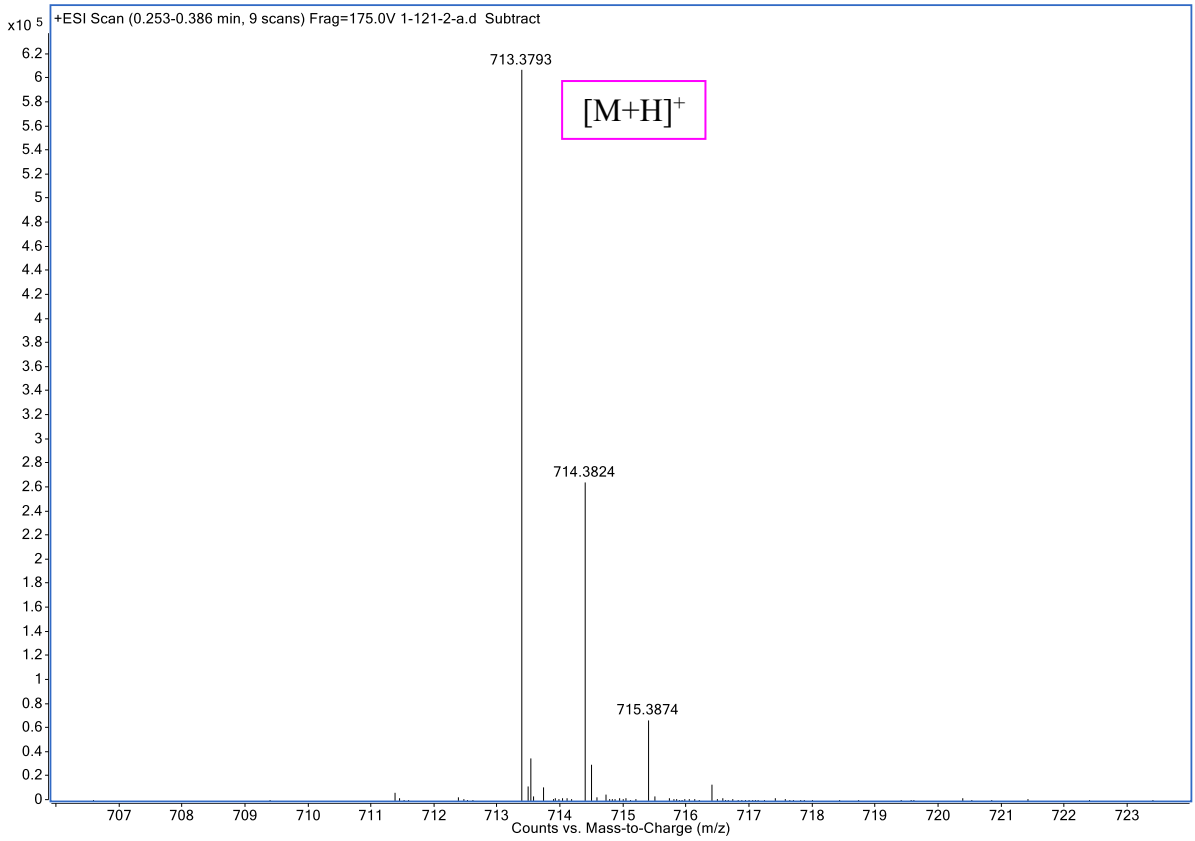

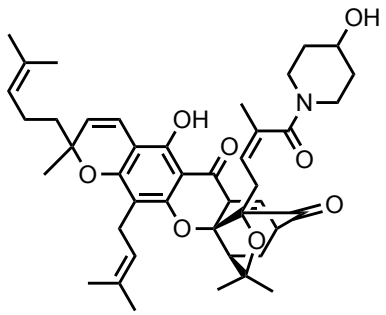

(122)

HR-ESI-TOFMS Positive Ion Mode

Mass Measured	Theoretical Mass	Delta (ppm)	Composition
712.3838	712.3844	-0.8	$[C_{43}H_{54}NO_8]^+$

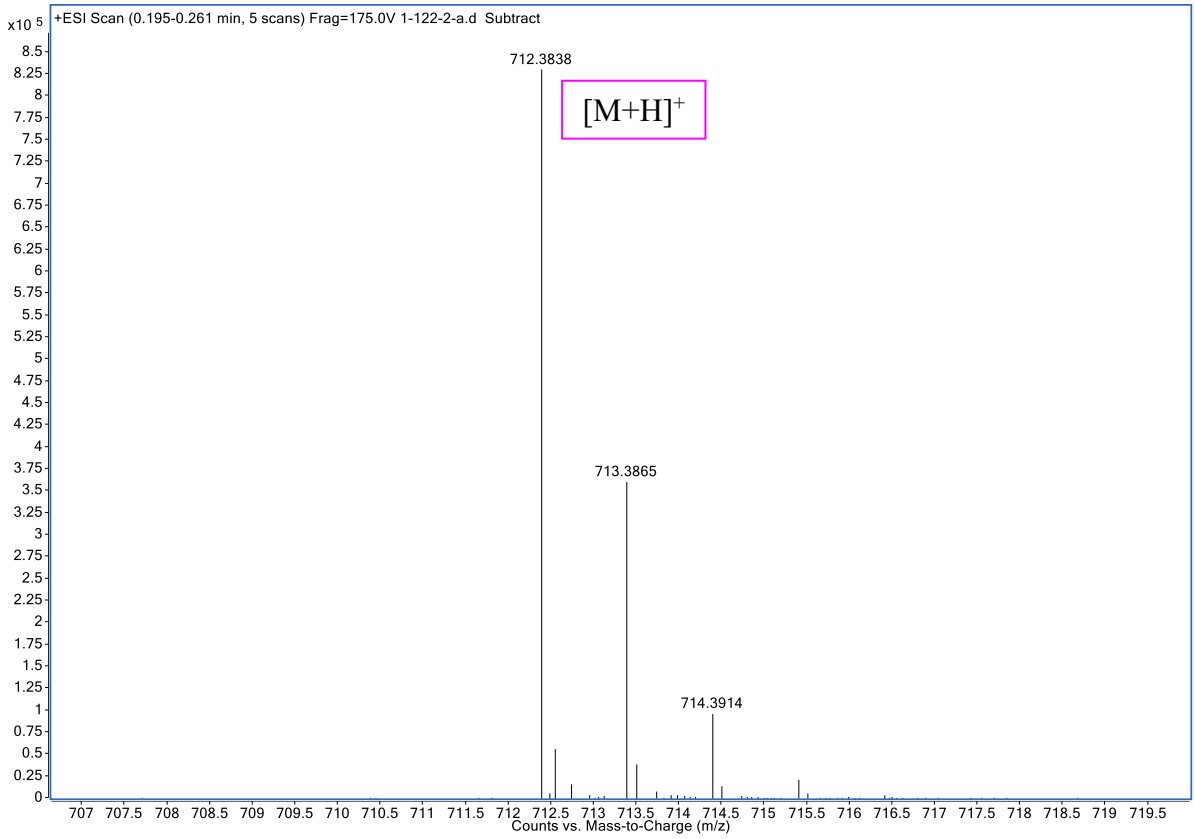

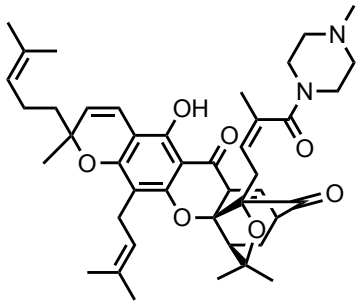

(130)

HR-ESI-TOFMS Positive Ion Mode

Mass Measured	Theoretical Mass	Delta (ppm)	Composition
711.4002	711.4004	-0.3	$[C_{43}H_{55}N_2O_7]^+$

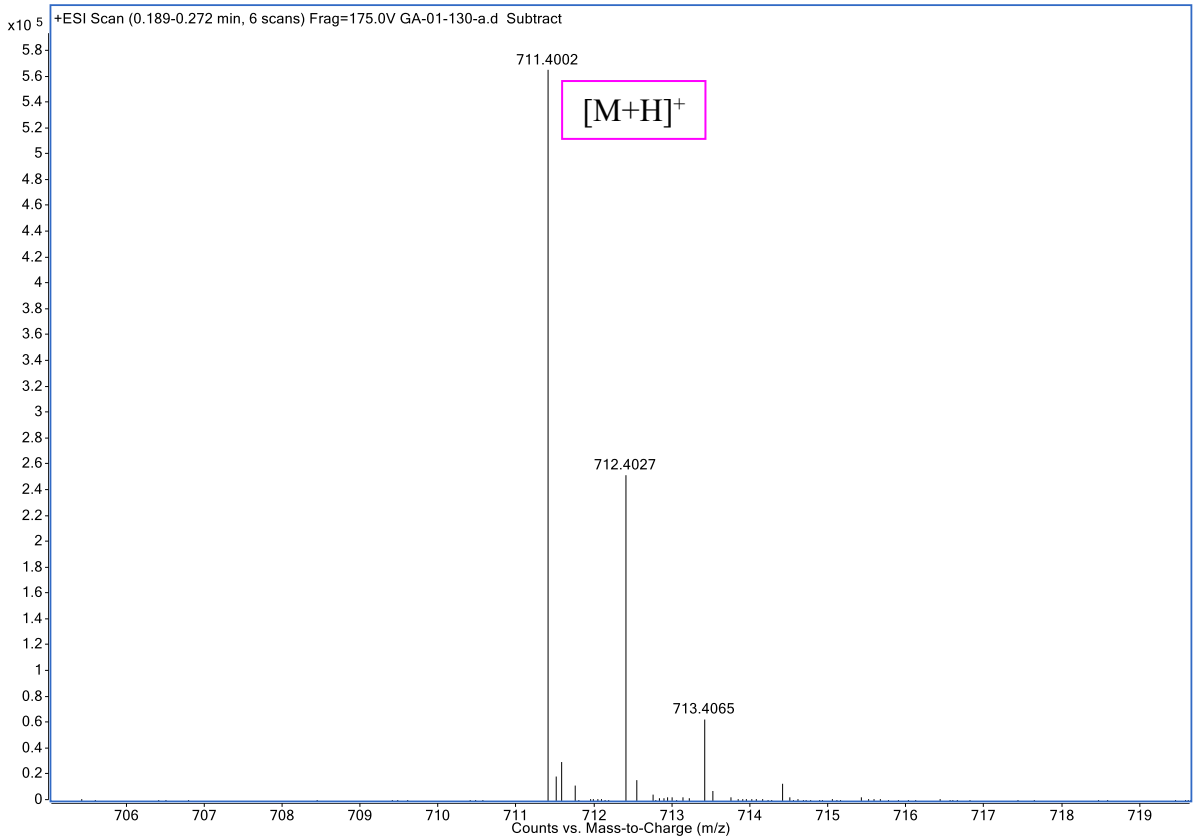

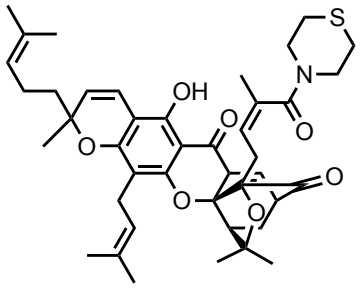

(135)

HR-ESI-TOFMS Positive Ion Mode

Mass Measured	Theoretical Mass	Delta (ppm)	Composition
714.3456	714.3459	-0.4	$[C_{42}H_{52}NO_7S]^+$

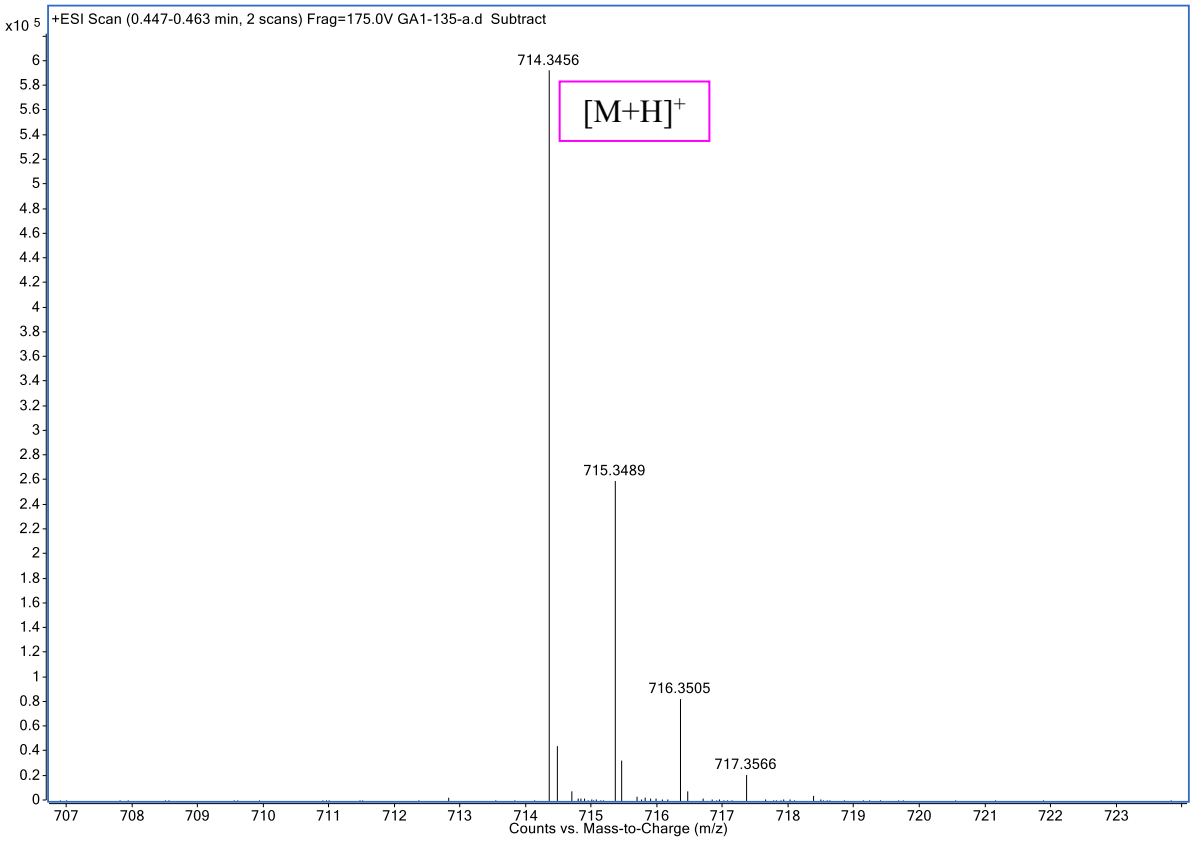

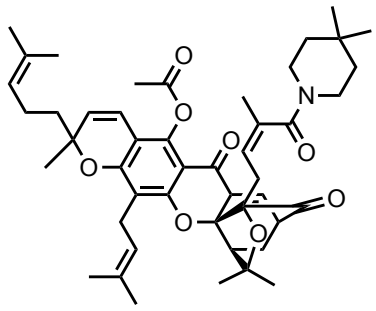

(143)

HR-ESI-TOFMS Positive Ion Mode

Mass Measured	Theoretical Mass	Delta (ppm)	Composition
766.4306	766.4313	-0.9	$[C_{47}H_{60}NO_8]^+$

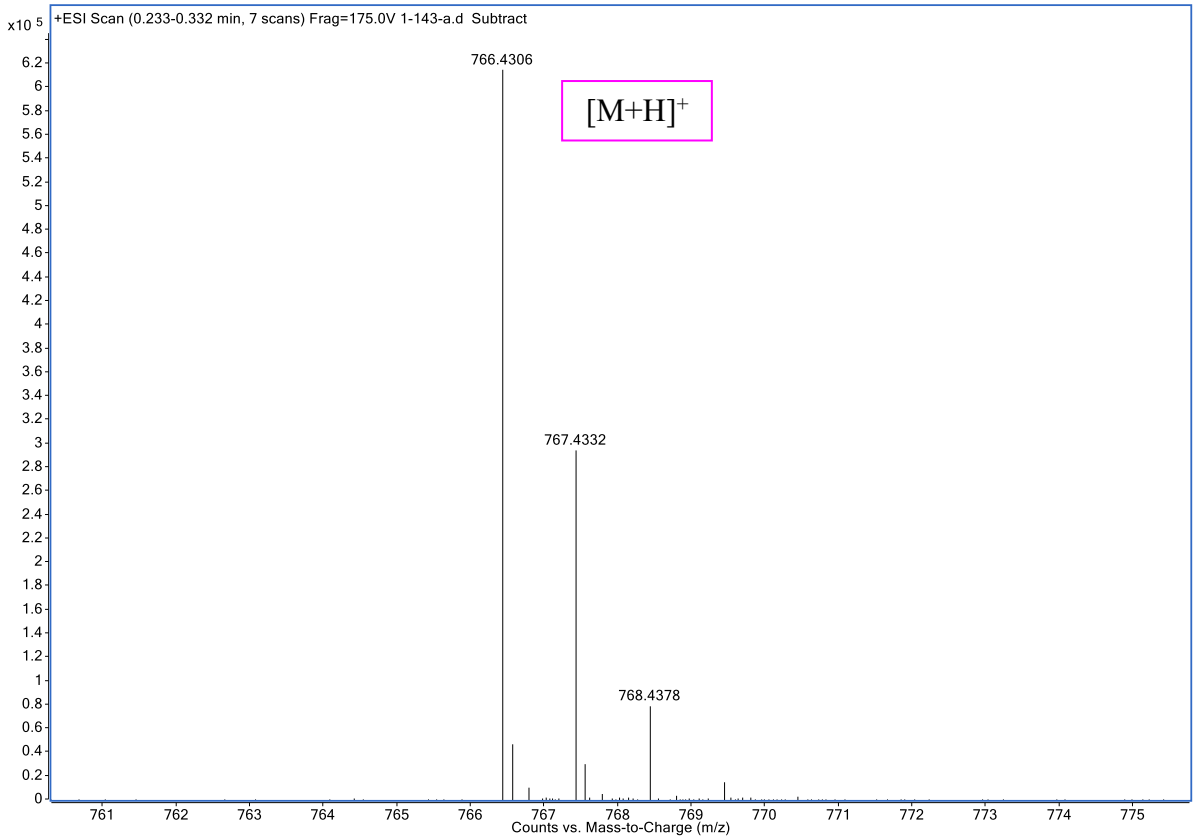

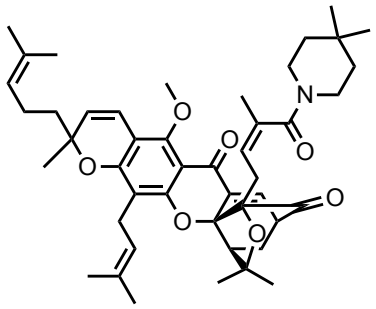

(149)

HR-ESI-TOFMS Positive Ion Mode

Mass Measured	Theoretical Mass	Delta (ppm)	Composition
766.4306	766.4313	-0.9	$[C_{47}H_{60}NO_8]^+$

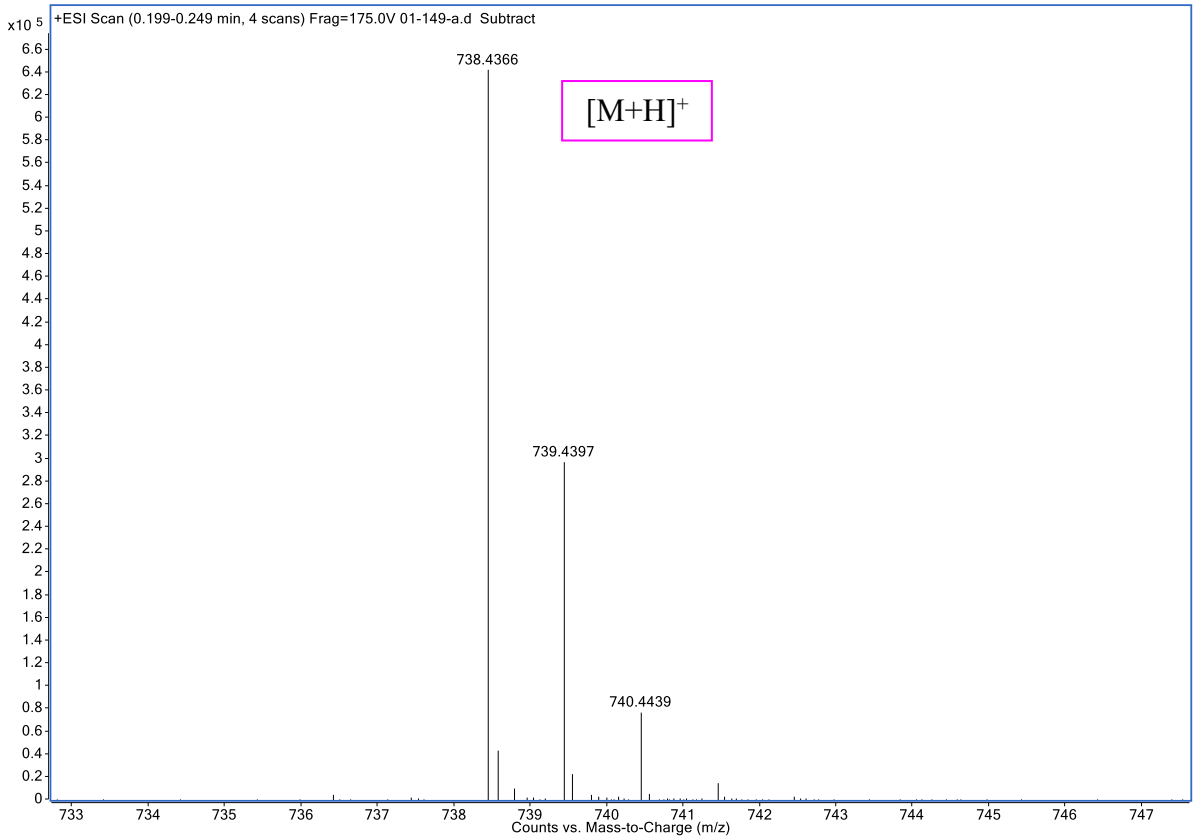

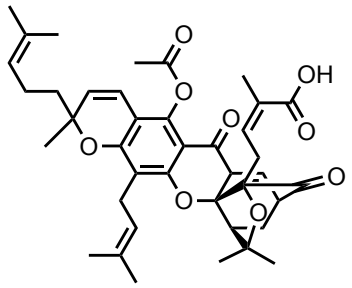

(142)

HR-ESI-TOFMS Positive Ion Mode

Mass Measured	Theoretical Mass	Delta (ppm)	Composition
671.3215	671.3215	0.0	$[C_{40}H_{47}O_9]^+$

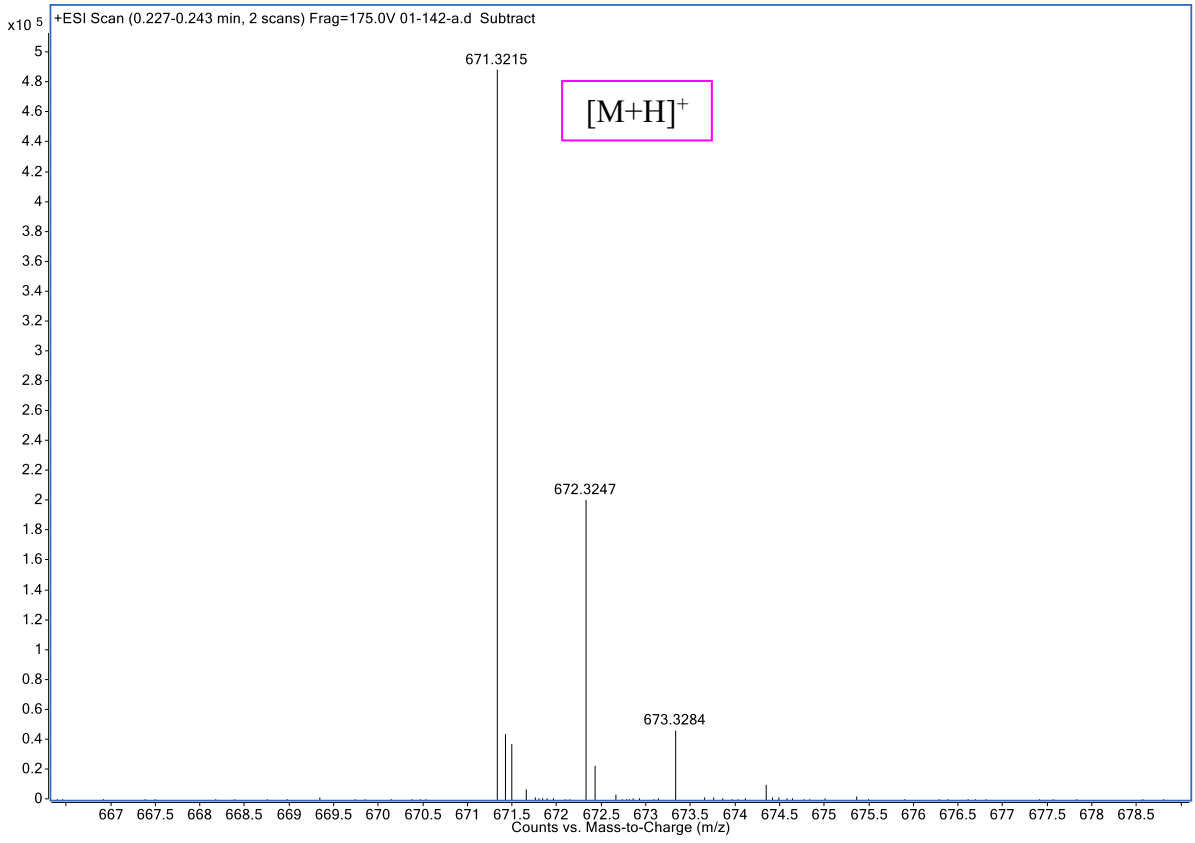

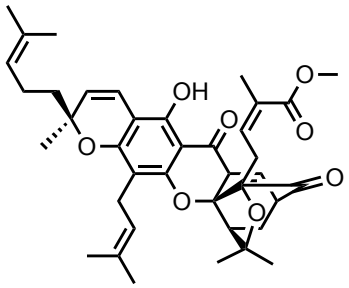

(1)

HR-ESI-TOFMS Positive Ion Mode

Mass Measured	Theoretical Mass	Delta (ppm)	Composition
643.3261	643.3265	-0.6	$[C_{39}H_{47}O_8]^+$

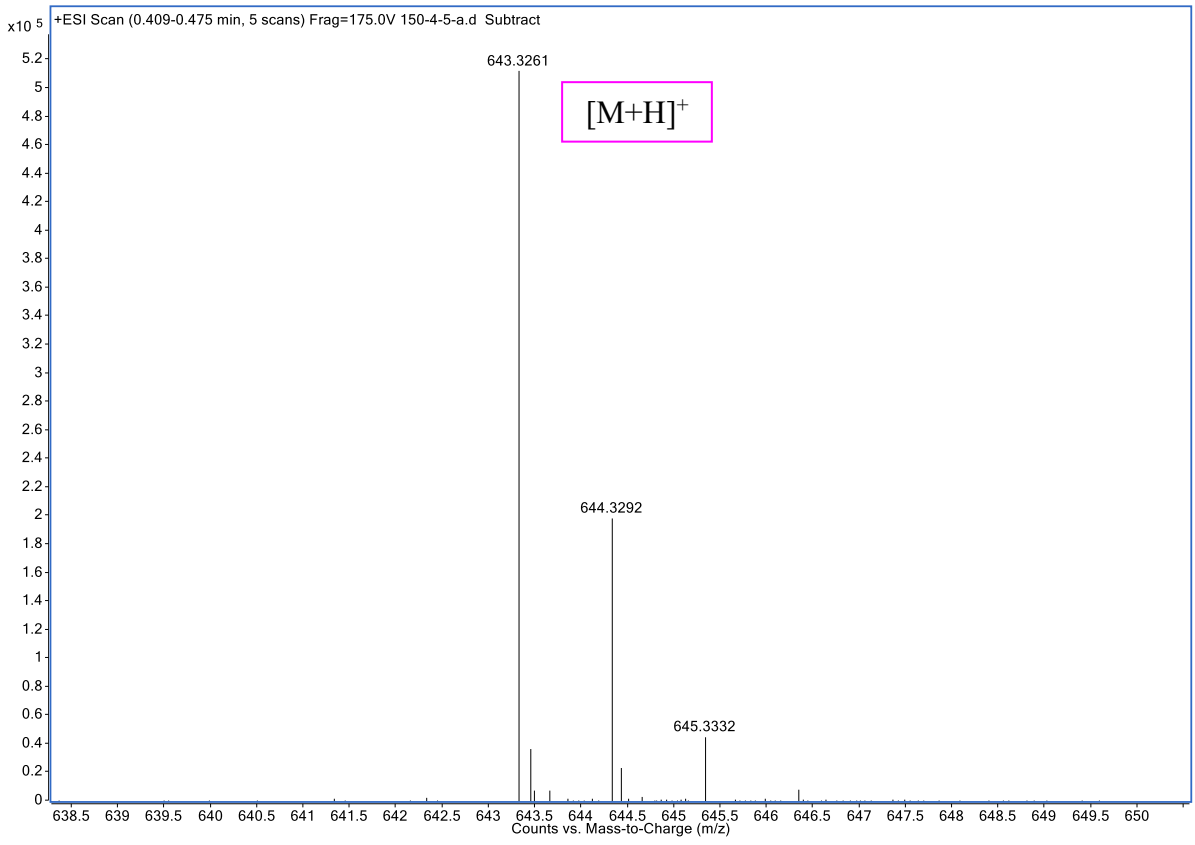

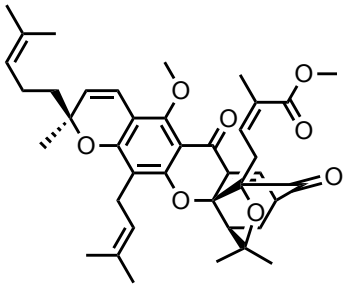

(2)

HR-ESI-TOFMS Positive Ion Mode

Mass Measured	Theoretical Mass	Delta (ppm)	Composition
657.3426	657.3422	0.6	$[C_{40}H_{49}O_8]^+$

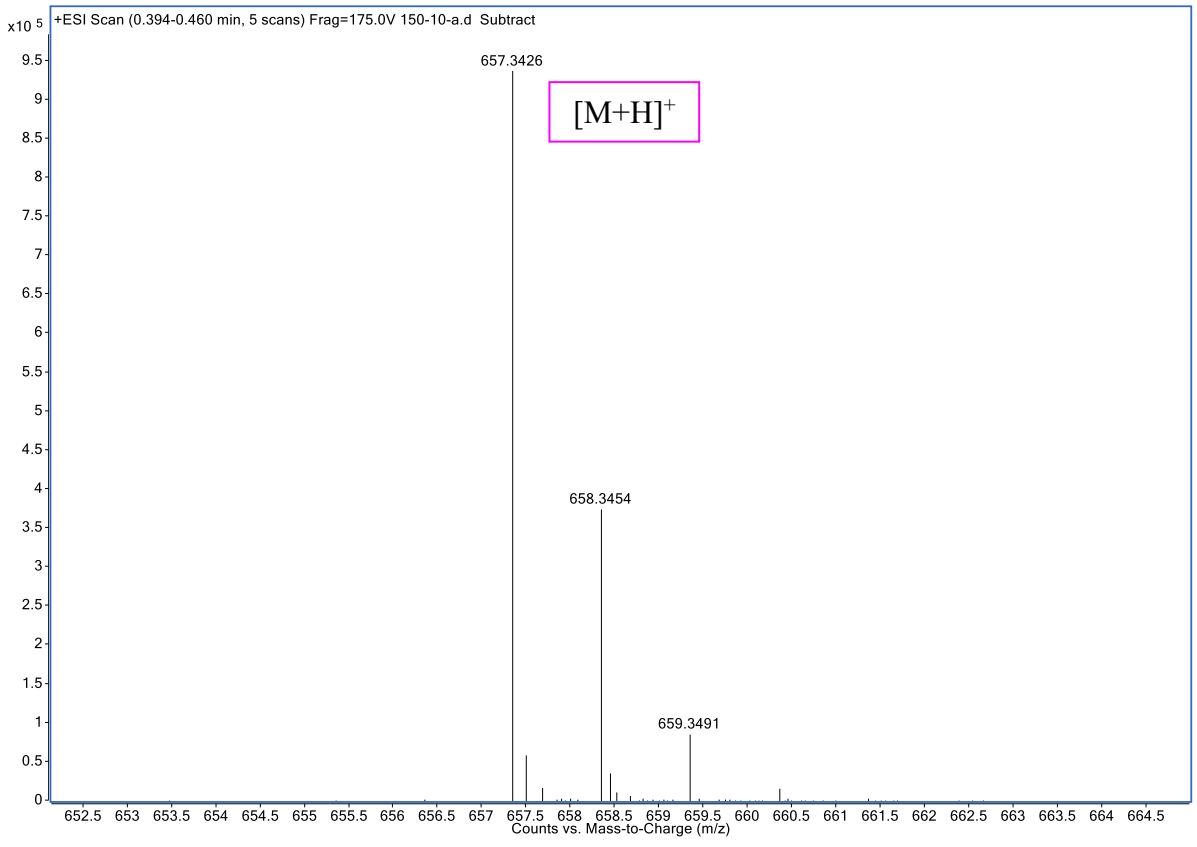

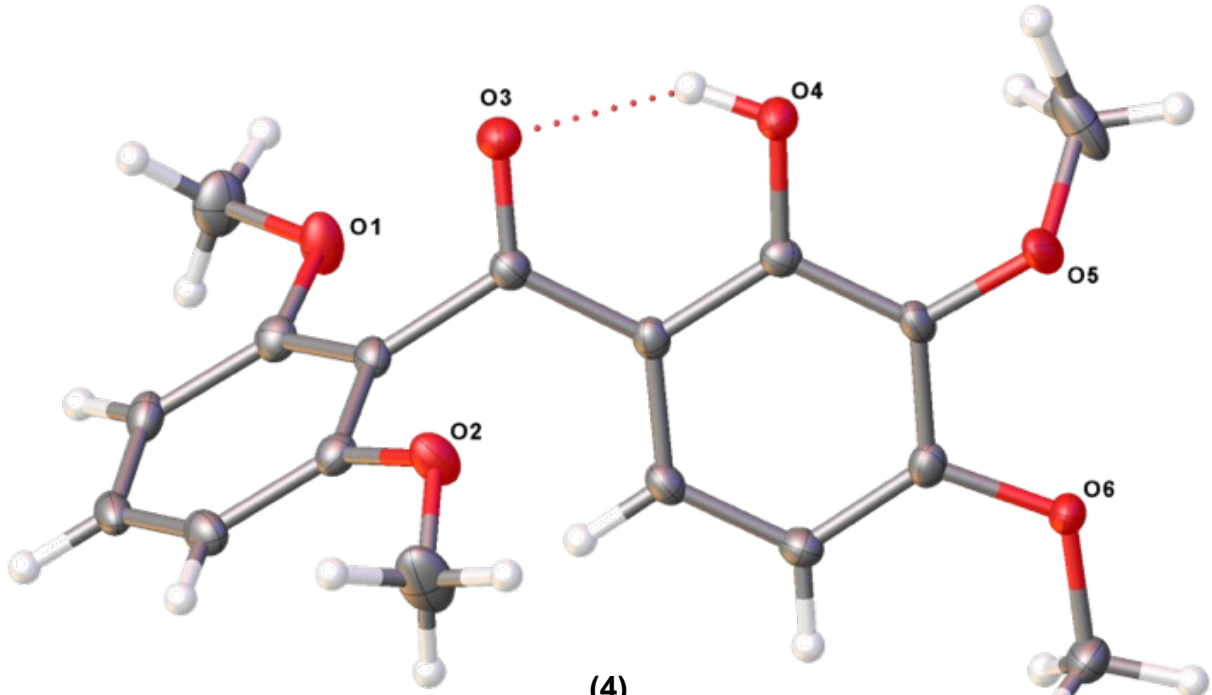

(4)

Table 1.2: Crystal data and structure refinement for **4**.

Identification code	compound **4**	
Empirical formula	$C_{17}H_{18}O_6$	
Formula weight	318.31	
Temperature	100.15 K	
Wavelength	0.71073 Å	
Crystal system	Monoclinic	
Space group	C2/c	
Unit cell dimensions	a = 18.7695(14) Å	α = 90º.
	b = 11.3506(9) Å	β = 94.269(2)º.
	c = 14.3247(10) Å	γ = 90º.
Volume	3043.3(4) $Å^3$	
Z	8	
Density (calculated)	1.389 mg/m^3	
Absorption coefficient	0.106 mm^{-1}	
F(000)	1344	
Crystal size	0.33 x 0.31 x 0.29 mm^3	
Theta range for data collection	2.098 to 28.307º.	
Index ranges	-23<=h<=24, -12<=k<=15, -19<=l<=18	
Reflections collected	11689	
Independent reflections	3778 [R(int) = 0.0482]	
Completeness to theta = 25.242º	100.0 %	

Table 1.2: Crystal data and structure refinement for **4** (continued).

Absorption correction	None
Max. and min. transmission	0.7457 and 0.6862
Refinement method	Full-matrix least-squares on F^2
Data / restraints / parameters	3778 / 7 / 225
Goodness-of-fit on F^2	1.019
Final R indices [I>2sigma(I)]	R1 = 0.0434, wR2 = 0.1139
R indices (all data)	R1 = 0.0537, wR2 = 0.1228
Extinction coefficient	N/A
Largest diff. peak and hole	0.414 and -0.297 e.$Å^{-3}$

Table 1.3: Atomic coordinates (x 10^4) and equivalent isotropic displacement parameters ($Å^2$ x 10^3) for **4**. U(eq) is defined as one third of the trace of the orthogonalized U^{ij} tensor.

	x	y	z	U(eq)
O(1)	7492(1)	8937(1)	4202(1)	23(1)
O(2)	8045(1)	7777(1)	1224(1)	22(1)
O(3)	7083(1)	9927(1)	2235(1)	21(1)
O(4)	5875(1)	9751(1)	1291(1)	20(1)
O(5)	4802(1)	8331(1)	562(1)	26(1)
O(6)	4777(1)	6079(1)	961(1)	21(1)
C(1)	7990(1)	8410(1)	3695(1)	17(1)
C(2)	8639(1)	7961(1)	4073(1)	19(1)
C(3)	9092(1)	7420(1)	3481(1)	19(1)
C(4)	8922(1)	7324(1)	2526(1)	19(1)
C(5)	8271(1)	7775(1)	2155(1)	16(1)
C(6)	7800(1)	8310(1)	2735(1)	15(1)
C(7)	7695(1)	9210(2)	5161(1)	27(1)
C(8)	8401(1)	7005(2)	627(1)	35(1)
C(9)	7118(1)	8841(1)	2309(1)	15(1)
C(10)	6524(1)	8080(1)	1979(1)	14(1)
C(11)	6537(1)	6856(1)	2111(1)	16(1)
C(12)	5969(1)	6151(1)	1786(1)	18(1)
C(13)	5370(1)	6668(1)	1306(1)	17(1)
C(14)	5354(1)	7881(1)	1133(1)	16(1)
C(15)	5921(1)	8588(1)	1476(1)	15(1)
C(16)	4750(1)	4834(1)	1103(1)	24(1)
C(17)	4359(1)	9176(2)	968(1)	36(1)

Table 1.4: Bond lengths [Å] and angles [º] for **4**.

O(1)-C(1)	1.3641(16)
O(1)-C(7)	1.4326(17)
O(2)-C(5)	1.3681(16)
O(2)-C(8)	1.4244(18)
O(3)-C(9)	1.2382(17)
O(4)-H(4)	0.8400
O(4)-C(15)	1.3472(16)
O(5)-C(14)	1.3708(15)
O(5)-C(17)	1.4228(19)
O(6)-C(13)	1.3609(16)
O(6)-C(16)	1.4292(17)
C(1)-C(2)	1.3927(19)
C(1)-C(6)	1.3993(18)
C(2)-H(2)	0.9500
C(2)-C(3)	1.389(2)
C(3)-H(3)	0.9500
C(3)-C(4)	1.387(2)
C(4)-H(4A)	0.9500
C(4)-C(5)	1.3930(19)
C(5)-C(6)	1.3952(18)
C(6)-C(9)	1.5035(17)
C(7)-H(7A)	0.9800
C(7)-H(7B)	0.9800
C(7)-H(7C)	0.9800
C(8)-H(8A)	0.9800
C(8)-H(8B)	0.9800
C(8)-H(8C)	0.9800
C(9)-C(10)	1.4606(18)
C(10)-C(11)	1.4024(19)
C(10)-C(15)	1.4187(17)
C(11)-H(11)	0.9500
C(11)-C(12)	1.3843(19)
C(12)-H(12)	0.9500
C(12)-C(13)	1.4022(18)
C(13)-C(14)	1.3983(19)
C(14)-C(15)	1.3923(19)
C(16)-H(16A)	0.9800
C(16)-H(16B)	0.9800
C(16)-H(16C)	0.9800

Table 1.4: Bond lengths [Å] and angles [º] for **4** (continued).

C(17)-H(17A)	0.921(10)
C(17)-H(17B)	0.922(11)
C(17)-H(17C)	0.923(11)
C(1)-O(1)-C(7)	117.46(11)
C(5)-O(2)-C(8)	117.34(11)
C(15)-O(4)-H(4)	109.5
C(14)-O(5)-C(17)	116.52(11)
C(13)-O(6)-C(16)	118.08(11)
O(1)-C(1)-C(2)	124.59(12)
O(1)-C(1)-C(6)	115.16(12)
C(2)-C(1)-C(6)	120.23(12)
C(1)-C(2)-H(2)	120.6
C(3)-C(2)-C(1)	118.82(13)
C(3)-C(2)-H(2)	120.6
C(2)-C(3)-H(3)	119.0
C(4)-C(3)-C(2)	122.08(13)
C(4)-C(3)-H(3)	119.0
C(3)-C(4)-H(4A)	120.7
C(3)-C(4)-C(5)	118.60(13)
C(5)-C(4)-H(4A)	120.7
O(2)-C(5)-C(4)	124.81(12)
O(2)-C(5)-C(6)	114.58(11)
C(4)-C(5)-C(6)	120.58(12)
C(1)-C(6)-C(9)	120.81(12)
C(5)-C(6)-C(1)	119.68(12)
C(5)-C(6)-C(9)	119.39(11)
O(1)-C(7)-H(7A)	109.5
O(1)-C(7)-H(7B)	109.5
O(1)-C(7)-H(7C)	109.5
H(7A)-C(7)-H(7B)	109.5
H(7A)-C(7)-H(7C)	109.5
H(7B)-C(7)-H(7C)	109.5
O(2)-C(8)-H(8A)	109.5
O(2)-C(8)-H(8B)	109.5
O(2)-C(8)-H(8C)	109.5
H(8A)-C(8)-H(8B)	109.5
H(8A)-C(8)-H(8C)	109.5
H(8B)-C(8)-H(8C)	109.5

Table 1.4: Bond lengths [Å] and angles [º] for **4** (continued).

O(3)-C(9)-C(6)	118.14(12)
O(3)-C(9)-C(10)	121.80(12)
C(10)-C(9)-C(6)	120.05(11)
C(11)-C(10)-C(9)	122.50(12)
C(11)-C(10)-C(15)	118.46(12)
C(15)-C(10)-C(9)	119.00(12)
C(10)-C(11)-H(11)	119.3
C(12)-C(11)-C(10)	121.45(12)
C(12)-C(11)-H(11)	119.3
C(11)-C(12)-H(12)	120.3
C(11)-C(12)-C(13)	119.47(12)
C(13)-C(12)-H(12)	120.3
O(6)-C(13)-C(12)	125.24(12)
O(6)-C(13)-C(14)	114.43(11)
C(14)-C(13)-C(12)	120.32(12)
O(5)-C(14)-C(13)	118.54(12)
O(5)-C(14)-C(15)	121.32(12)
C(15)-C(14)-C(13)	119.94(12)
O(4)-C(15)-C(10)	122.35(12)
O(4)-C(15)-C(14)	117.34(12)
C(14)-C(15)-C(10)	120.29(12)
O(6)-C(16)-H(16A)	109.5
O(6)-C(16)-H(16B)	109.5
O(6)-C(16)-H(16C)	109.5
H(16A)-C(16)-H(16B)	109.5
H(16A)-C(16)-H(16C)	109.5
H(16B)-C(16)-H(16C)	109.5
O(5)-C(17)-H(17A)	115.5(8)
O(5)-C(17)-H(17B)	110.9(14)
O(5)-C(17)-H(17C)	101.6(16)
H(17A)-C(17)-H(17B)	109.6(3)
H(17A)-C(17)-H(17C)	109.4(3)
H(17B)-C(17)-H(17C)	109.4(3)

Table 1.5: Anisotropic displacement parameters ($Å^2$ x 10^3) for **4**. The anisotropic displacement factor exponent takes the form: $-2\pi^2[h^2 a^{*2}U^{11} + ... + 2 h k a^* b^* U^{12}]$.

	U^{11}	U^{22}	U^{33}	U^{23}	U^{13}	U^{12}
O(1)	18(1)	34(1)	16(1)	-4(1)	-1(1)	2(1)
O(2)	22(1)	28(1)	15(1)	-2(1)	0(1)	8(1)
O(3)	19(1)	15(1)	27(1)	-1(1)	-4(1)	1(1)
O(4)	20(1)	14(1)	26(1)	2(1)	-7(1)	1(1)
O(5)	26(1)	20(1)	28(1)	-5(1)	-16(1)	8(1)
O(6)	17(1)	16(1)	30(1)	-3(1)	-8(1)	0(1)
C(1)	16(1)	17(1)	17(1)	0(1)	0(1)	-3(1)
C(2)	16(1)	19(1)	19(1)	3(1)	-5(1)	-5(1)
C(3)	14(1)	14(1)	29(1)	4(1)	-5(1)	-1(1)
C(4)	14(1)	16(1)	26(1)	0(1)	2(1)	1(1)
C(5)	17(1)	16(1)	16(1)	1(1)	-1(1)	-1(1)
C(6)	13(1)	15(1)	18(1)	1(1)	-2(1)	-1(1)
C(7)	28(1)	38(1)	16(1)	-5(1)	0(1)	-3(1)
C(8)	31(1)	49(1)	24(1)	-14(1)	0(1)	15(1)
C(9)	15(1)	17(1)	13(1)	-1(1)	1(1)	1(1)
C(10)	14(1)	16(1)	12(1)	-1(1)	0(1)	3(1)
C(11)	14(1)	18(1)	16(1)	1(1)	-1(1)	4(1)
C(12)	17(1)	13(1)	21(1)	1(1)	-1(1)	2(1)
C(13)	16(1)	18(1)	16(1)	-3(1)	-2(1)	1(1)
C(14)	15(1)	17(1)	16(1)	-1(1)	-4(1)	4(1)
C(15)	16(1)	14(1)	13(1)	0(1)	0(1)	3(1)
C(16)	22(1)	17(1)	32(1)	-1(1)	-6(1)	-2(1)
C(17)	23(1)	59(1)	27(1)	7(1)	1(1)	21(1)

Table 1.6: Hydrogen coordinates (x 10^4) and isotropic displacement parameters (Å^2 x 10^3) for **4**.

	x	y	z	U(eq)
H(4)	6218	10103	1580	30
H(2)	8769	8023	4725	22
H(3)	9533	7107	3739	23
H(4A)	9242	6958	2132	23
H(7A)	8105	9746	5195	41
H(7B)	7825	8482	5501	41
H(7C)	7294	9587	5444	41
H(8A)	8162	7031	-4	52
H(8B)	8386	6199	871	52
H(8C)	8899	7255	605	52
H(11)	6944	6502	2430	19
H(12)	5985	5324	1888	21
H(16A)	4302	4521	808	37
H(16B)	4777	4665	1776	37
H(16C)	5155	4460	824	37
H(17A)	4381(9)	9183(15)	1613(7)	87(9)
H(17B)	3890(7)	9100(20)	735(11)	72(8)
H(17C)	4541(12)	9874(16)	756(13)	170(19)

Chapter 1, in part, is currently being prepared for submission for publication of the material, Arevalo, G. E.; Frank, M. K.; Decker, K. S.; Theodoraki, M. A.; Theodorakis, E. A. The dissertation author was the primary researcher and author of this material.

Chapter 2

Mitochondrial NEET Proteins as Novel Drug Targets

2.1 Introduction: Mitochondria Give & Take Life

Mitochondria are the powerhouse of eukaryotic cells, and as such, are indispensable to cell survival and life as we know it.[138] In addition to powering cells by ATP production through oxidative phosphorylation, mitochondria are also responsible for regulating pathways that lead to cell death.[139] Proper function of mitochondria is therefore critical to human health, and their dysregulation usually has severe pathological consequences, including cancer, cardiovascular disease, diabetes, and neurodegenerative diseases.[140] For example, numerous cancers are the result of the mitochondria's inability to initiate cell death via apoptosis.[141] On the other hand, neurodegenerative diseases such as Alzheimer's dementia and Parkinson's disease, and

amyotrophic lateral sclerosis are largely the result of superfluous cell death.[142] As a result, manipulation of the mitochondria is of considerable pharmaceutical interest.[143]

2.2 General Anatomy & Physiology of the Mitochondria

Mitochondria are believed to have evolved from the phagotization of either bacteria or a prokaryotic cell precursor.[144] Rather than the normal digestive pathways taking effect, the cell likely allowed the organism to survive within itself, which explains the anatomy and physiology of the mitochondria. For example, mitochondria have an outer membrane and an inner membrane where the outer membrane is very reminiscent of eukaryotic plasma cell membrane, and the inner membrane is reminiscent of prokaryotic plasma cell membrane. This ancient symbiotic event is supported, in part, by the fact that mitochondria contain their own DNA (mtDNA), which is distinct from that of the cell containing them.[145] In addition, mitochondria replicate by fission, which is a process that occurs independently of the cell cycle and is reminiscent of bacterial division.

Mitochondria are highly dynamic structures that are composed of various compartments or regions with distinct and important roles (Figure 2.1).[146] The outer mitochondrial membrane (OMM), for example, separates the intermembrane space from the cytosol and is the barrier that controls the diffusion of metabolites into and out of the mitochondria, which communicate with the cell. The OMM also contains channel proteins called porins, which form passages that allow diffusion of ions, molecules, and small proteins between 2-6 kDa in size into the intermembrane space (IMS).[147]

The IMS, as its name suggests, is the region between the inner and outer membranes and it is the compartment where coordination of cellular activities, such as regulation of respiration and of the metabolism of amino acids, lipids, and nucleotides occur.[148] Many constituents of the

IMS (i.e., Bcl-2, cytochrome c, cytochrome c heme lyase, and Mia40) are also critical for cellular activities, including the transport of proteins, electrons, or metal ions, assembling of proteins for the inner membrane, and storage of components that activate cell death upon release.[149]

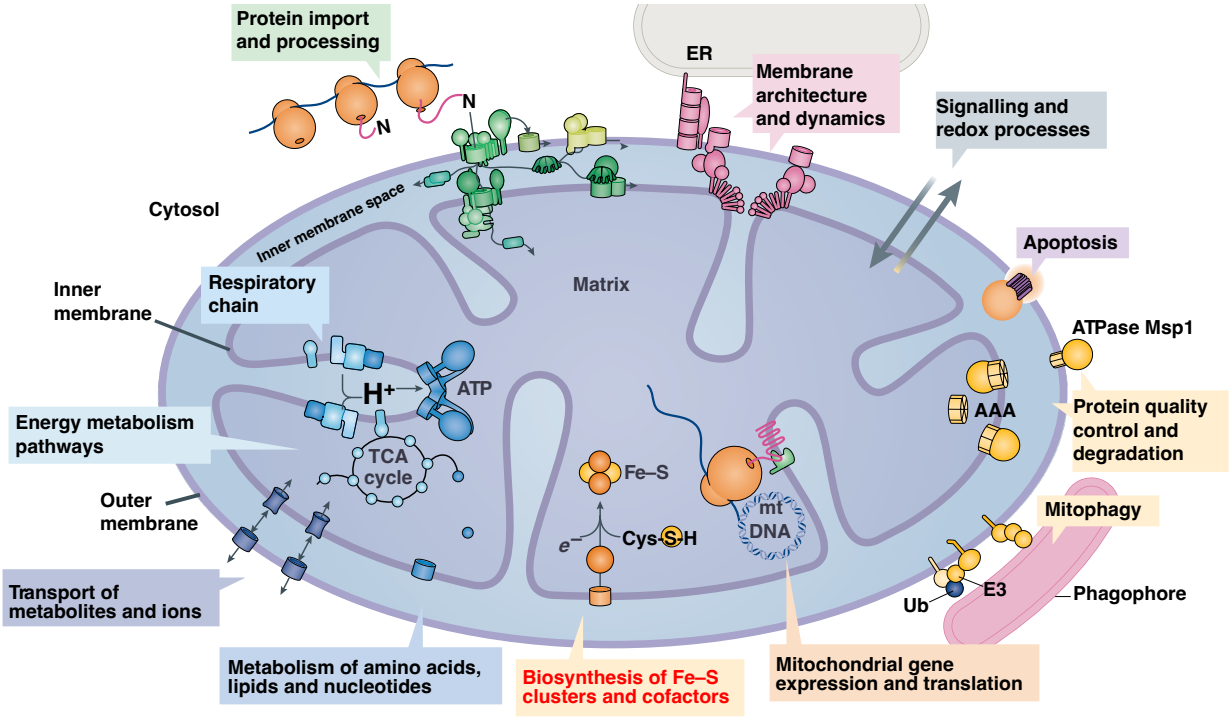

Figure 2.1: Cartoon representation of the mitochondria and its key cellular functions.

The inner mitochondrial membrane (IMM) is the mitochondrial membrane which separates the mitochondrial matrix from the intermembrane space.[150] It contains five major protein complexes where in aerobic respiration the energy of oxygen is released and enables the synthesis of ATP via chemiosmosis.

Cristae are infoldings in the inner mitochondrial membrane whose plasticity and dimensions modulate the kinetics of chemical reactions and the structure of protein complexes, and it is where energy production occurs. Their shape is maintained by the cooperation of

mitochondrial-shaping proteins and their integrity is critical for correct mitochondria functioning.[151]

The mitochondrial matrix is the innermost compartment, which is surrounded by the inner membrane and has a pH of 7.9 to 8. The high pH of the mitochondrial matrix is responsible for the trans-membrane electrochemical gradient that drives the production of ATP. The mitochondrial matrix is also where mtDNA replication, transcription, protein biosynthesis and various other enzymatic reactions occur. The biosynthetic reactions that take place in the matrix include those of the citric acid cycle and other reactions that facilitate oxidative phosphorylation, oxidation of pyruvate, and the beta oxidation of fatty acids. Since every reaction is catalyzed by its own enzyme, the mitochondrial matrix is highly dense, containing of up to 500 mg/mL of protein.[152] The matrix is where the NEET protein MiNT resides and is responsible for iron and ROS regulation within the mitochondrial matrix.[153]

2.3 Introduction to NEET Proteins & Their Relevance in Health & Disease

Iron is essential for numerous fundamental metabolic and biological processes including oxygen and electron transport, gas sensing and DNA synthesis.[154] Disruption of iron homeostasis has been shown to result in iron deficiency or iron overload, which can both contribute to various diseases including anemia, hemochromatosis and neurodegeneration.[155,156] Despite its essential role, free iron is highly toxic to cells due to its ability to catalyze the formation reactive oxygen species (ROS) via Fenton chemistry.[157] As iron readily interconverts between the reduced ferrous (Fe^{2+}) and the oxidized ferric (Fe3+) forms, it disrupts the cellular redox equilibrium and causes oxidative stress that is associated with tissue injury, disease and death.[158, 159] Thus, organisms have

developed sophisticated pathways to import, process, and export this metal. For instance, iron is transported as Fe^{2+} inside cells by diferric transferrin (Tf), which is internalized in endosomes upon binding to its receptor (TfR1) where it is then released as Fe^{3+}.[160] Moreover, in mitochondria, iron is extensively used for the synthesis of heme and [2Fe-2S] cluster-containing proteins that are involved in energy transduction and oxidative phosphorylation.[161,162]

NEET proteins are a unique class of [2Fe-2S] proteins found in the mitochondria that are involved in energy production via iron shuttling and ROS production and maintaining their homeostasis.[153] As such, NEETs are known to be key players in human health and several human diseases.[135] Mutations in NAF-1, for example, result in the autosomal recessive disorder Wolfram Syndrome Type 2 (WFS2), a disorder resulting from mitochondria dysfunction due to excessive iron accumulation in the mitochondria that results in increased cell death.[163] Moreover, studies on cardiac tissue of NEET-deficient mice were shown to have a reduced oxidative capacity, suggesting that NEETs are important iron-containing proteins involved in the control of maximal mitochondrial respiratory rates.[164,165] In addition, NEETs were found to be important for maintaining mitochondrial integrity and for regulating key cellular processes like autophagy and apoptosis, by acting as sensors or transducers of iron, and by regulating Fe/ROS trafficking between the cytosol and mitochondria.[166,167]

The NEET family of proteins consists of mitoNEET, NAF-1, and MiNT. MitoNEET and NAF-1 are found in the outer mitochondrial membrane, in addition, NAF-1 is also located in the ER of cells.[135] MiNT, however, is only found in the inner mitochondrial matrix.[153] As 3Cys:1His 2Fe-2S binding proteins, NEETs have a redox-active metal cluster that reversibly binds to the protein. NEETs are defined by a unique CDGXH amino acid sequence in their [2Fe-2S] cluster-binding domain where X can be A/S/T.[168] Previous structural studies of various NEET family

members revealed a homo-dimeric structure for the family, in which two protomers intertwine to form the unique "NEET fold" such as that seen in mitoNEET (Figure 2.1A) and the equivalent fold in NAF-1 (Figure 2.1B).[169,170] Each protomer contains a labile [2Fe-2S] cluster coordinated by the NEET cluster fingerprint ligand of 3Cys:1His (Figure 2.2 highlighted in orange). Due to their unique 3Cys:1His Fe-S coordination, however, NEETs are known to be more labile compared to other Fe-S proteins like ferredoxins.[153]

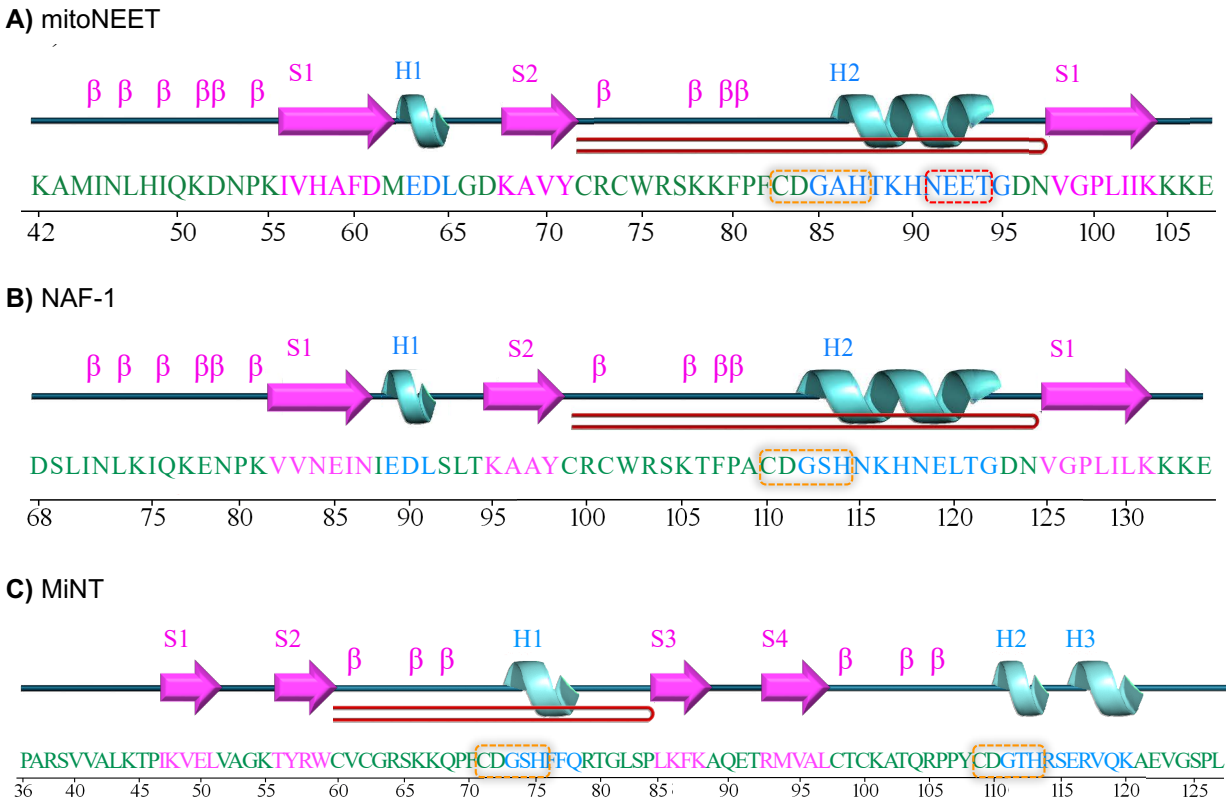

Figure 2.2: NEET Protein sequences. Shown are the amino acid sequences and secondary structure details of A) mitoNEET B) NAF-1 and C) DM MiNT. Whereas mitoNEET and NAF-1 are nearly identical homodimers, MiNT is a monomer. In green rods denote β-loops, pink arrows represent β-sheets, and in blue are α-helices.

A sequence alignment of mitoNEET, NAF-1, and MiNT revealed that mitoNEET and NAF-1 are 62% similar, whereas mitoNEET and NAF-1 each share with MiNT a 26% and 23%

identity, respectively. Whereas mitoNEET and NAF-1 are dimers, MiNT is a monomer. The monomeric nature of MiNT makes it especially dynamic and, as a result, it's 2Fe-2S clusters are especially labile compared to mitoNEET and NAF-1.

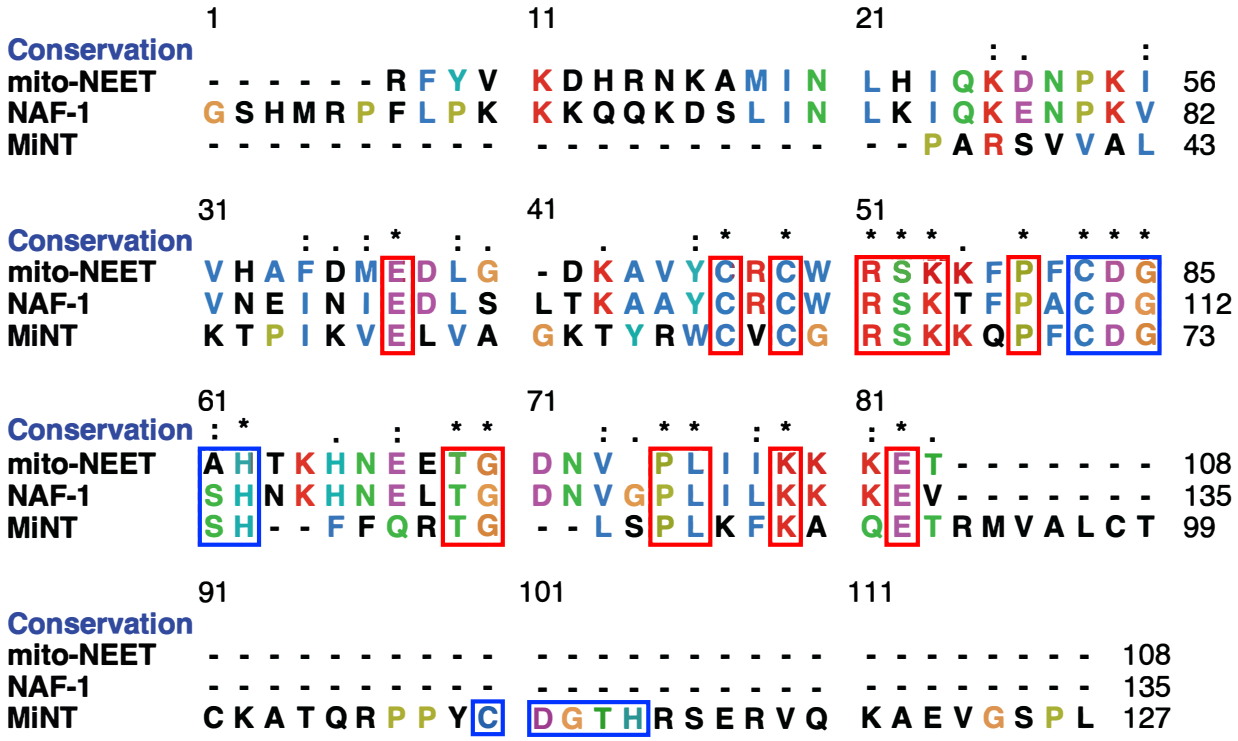

Figure 2.3: Sequence alignment of mitoNEET, NAF-1, and MiNT. Conserved residues are boxed in red or blue. Highlighted with blue are the CDG(A/S/T)H motif common to all NEET proteins.

2.4 Structure of Mitochondrial NEET Protein MiNT

NEET proteins differ from typical [2Fe-2S] metal cluster proteins due, in part, to how labile the clusters are. When metal cluster are as labile as that of NEET proteins, there can be an overaccumulation of iron in the cell.[135] It has been shown, for example, that that NAF-1 is overexpressed in breast cancer and that its ability to shuttle iron within the mitochondria of cancer cells rapidly contributes to cancer cell proliferation.[171] In this study, the wildtype NAF-1 cluster binding site consisted of 3Cys:1His. It is believed that the histidine residue is largely responsible

for the lability of its metal clusters as it is the His ligand which enables fast cluster release and tuning of its redox potential.[172,173] A NAF-1 double mutant where each metal cluster is ligated by 4Cys residues is significantly more stable than the wildtype, and when cancer cells overexpressed the NAF-1 double mutant, a significant reduction in cancer cell proliferation was observed.[174,175]

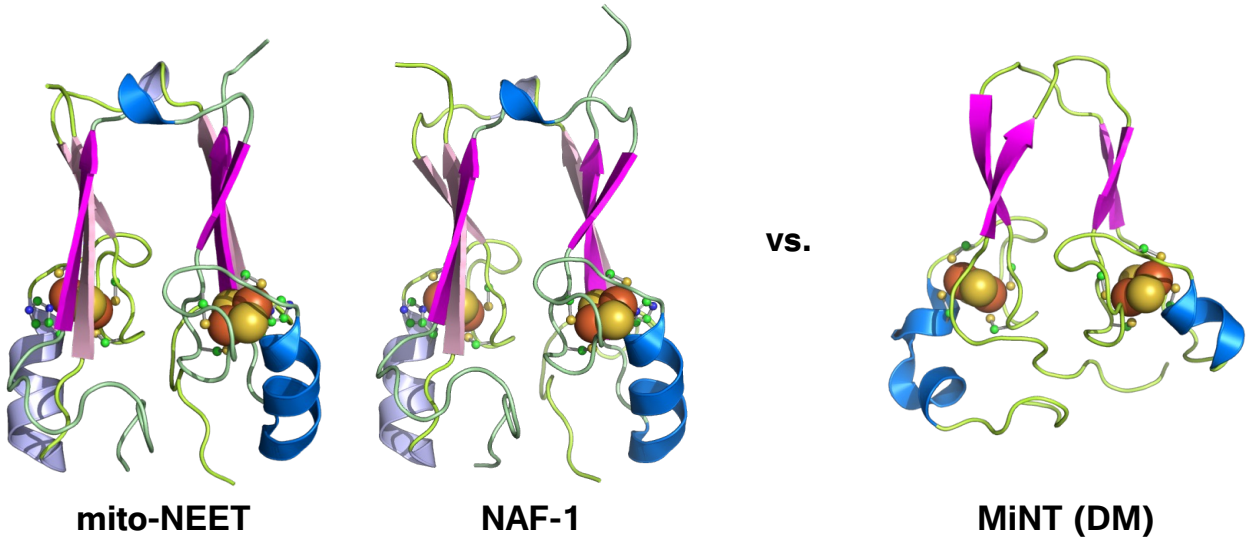

Figure 2.4: Secondary protein structures of mitoNEET and NAF-1 compared to MiNT. The secondary protein structure of A) mitoNEET (2QH7), B) NAF-1 (3FNV), and C) DM MiNT (6AVJ). mitoNEET and NAF-1 share 62% identity whereas mitoNEET and NAF-1 share a 26% and 23% identity to MiNT, respectively. Whereas mitoNEET and NAF-1 are dimers, MiNT is a monomer. Highlighted in shades of blue are α-helices and in pink are β-sheets. Loops are denoted in green.

In the family of NEET proteins, MiNT is the most unique in that it is a pseudo symmetrical monomeric protein that contains two distinct Fe-S cluster-binding motifs with especially labile Fe-S clusters.[153] Previous studies revealed that wild-type holo-MiNT is relatively short-lived ($t_{1/2}$ = 110 min). To extend its half-life, our lab previously created a double-mutant (DM) that replaced the 3Cys:1His cluster binding sites with 4Cys, which resulted in significantly more stable holo-MiNT. We therefore utilized DM MiNT to probe the interaction between MiNT and caged xanthones as it afforded us a better timescale to adequately quantify the effects of caged xanthones on the Fe-S cluster stability of MiNT. Furthermore, the integrity of DM MiNT was significantly

higher during its expression and purification, which is discussed below. We utilized UV/Vis spectroscopy to determine the decay of the Fe-S clusters of MiNT and circular dichroism to track its aromatic residues (Figure 2.5) and determine if there are any conformational change on MiNT caused by CGXs or when the clusters decay, which is the topic of chapter 3.

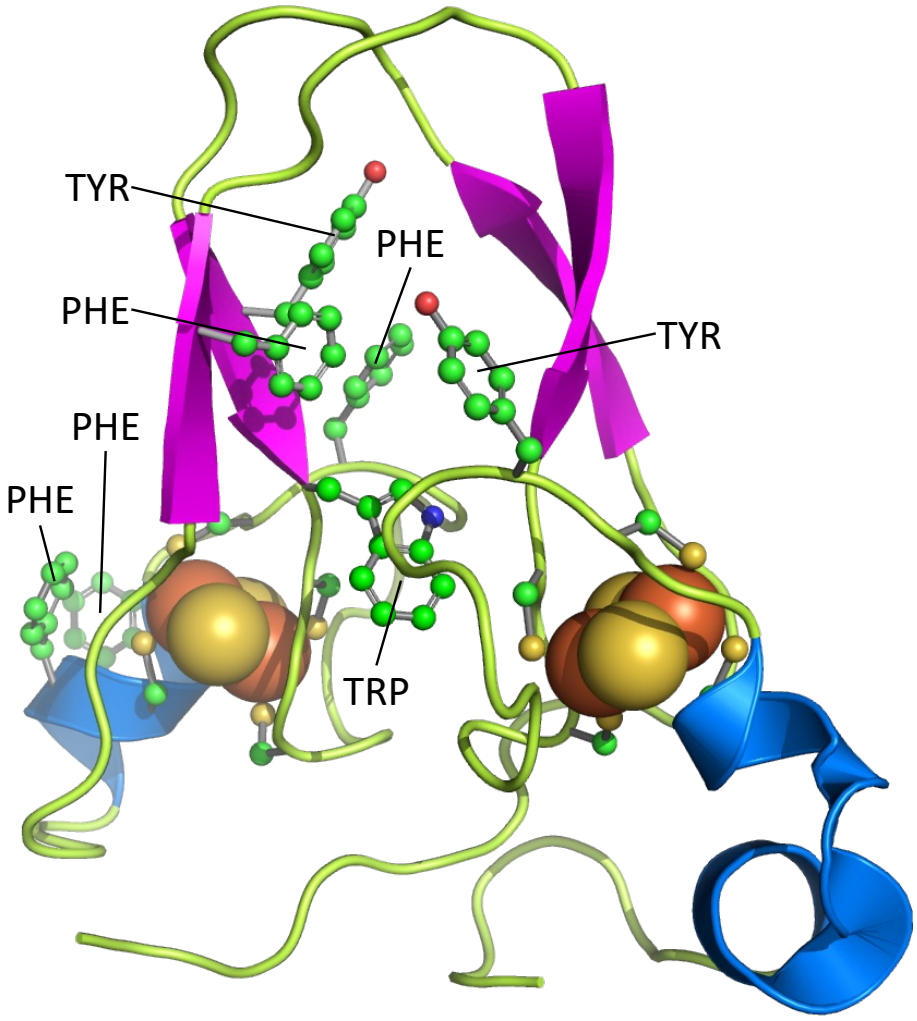

Figure 2.5: Structural representation of the asymmetry of monomeric MiNT and the location of its aromatic residues. Aromatic amino acid residues most reside on one side of the protein, which is likely the cause of the difference in stability between the two clusters.

2.5 Modulation of Iron: Making a Case for Too Much or Too Little Iron

Previous studies established that CGXs can modulate the stability of the Fe-S clusters of NEETs.[134] Upon binding to the NEET protein mitoNEET and NAF-1, for example, CGXs were shown to destabilize its Fe-S cluster, which lead to release of free iron into the mitochondria.[134] Free iron then caused excessive ROS production, lipid peroxidation, and eventually cell death (Figure 2.6).[134] Subsequent studies (not shown) demonstrated that CGXs are less effective when applied to cancer cells with suppressed levels of mitoNEET or NAF-1. In addition, CGXs were shown to be selective for cancer cells over normal cells (Figure 2.7). These studies demonstrate the potential of CGXs as less toxic alternatives for antitumor chemotherapy treatments.[1]

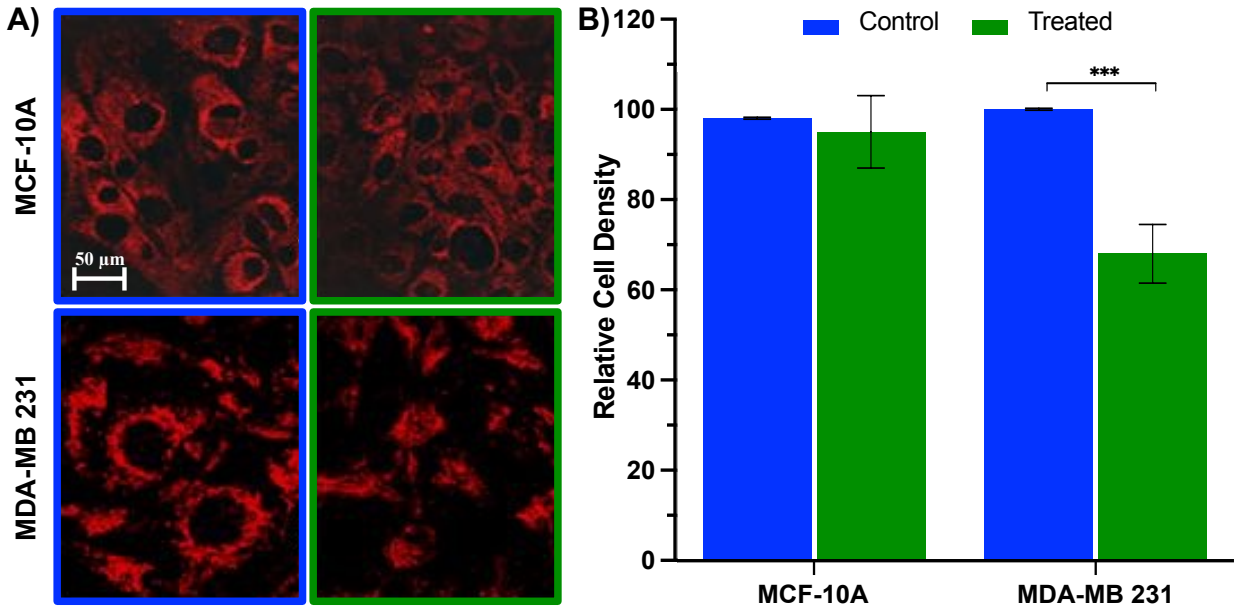

Figure 2.6: CGXs cause selective release of iron in the mitochondria of MDA-MB-231 breast cancer cells vs. MCF-10A cells as seen in A) RPA fluorescence microscopy images and B) quantification of RPA fluorescence loss (ImageJ). Control studies were performed by pretreating cells with DFP at 50-100 µM. Error bars represent SD obtained from three individual replicates, ***P < 0.001. Data for this figure was obtained from E. Theodorakis.[134]

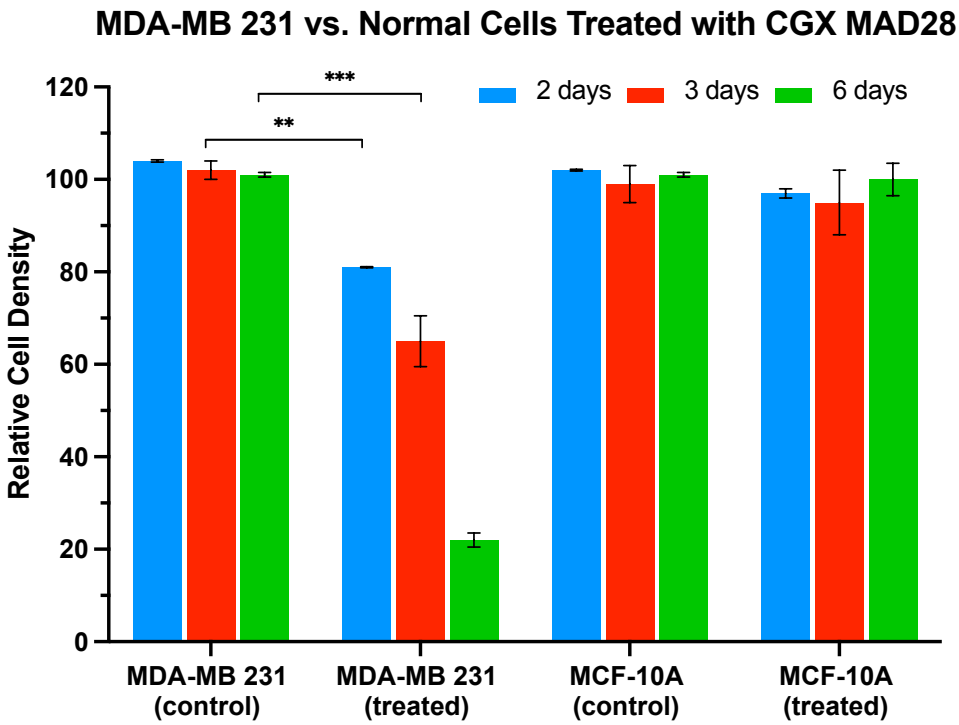

Figure 2.7: Selective cytotoxicity of CGX MAD28. The effects of MAD28 (1.25 μM) on normal human breast cells (MCF-10A) were significantly lower compared to human epithelial breast cancer cells (MDA-MB-231). Results were obtained using alamarBlue cell viability measurements at 2, 3 and 6 days of drug exposure. Error bars represent SD obtained from three individual replicates, **P<0.01, ***P<0.001. Data for this figure was obtained from E. Theodorakis.[134]

With these results in mind, we wondered whether caged xanthones can bind to the mitochondrial matrix-localized mitochondrial inner NEET protein (MiNT) as it has yet to be evaluated for its potential as a drug target. MiNT is a valuable target as it is known to be overexpressed in cancer and is only found in the inner mitochondria.[176] This prompted us to develop an in vitro model that can readily identify CGXs that can manipulate the stability of MiNT (Figure 2.8). By utilizing recombinant expression of MiNT followed by treatment of MiNT with CGXs, we measured the decay of MiNT's iron clusters using UV/Vis and circular dichroism spectroscopy, the latter which is the topic of chapter 3.

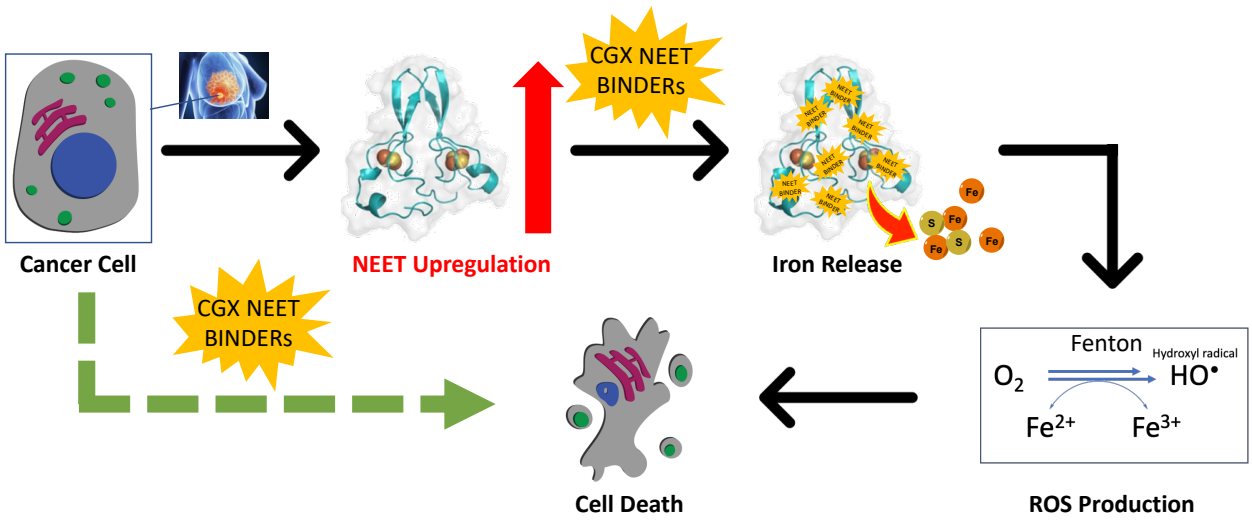

Figure 2.8: A visual representation of the potential for CGX NEET binders to cause selective cancer cell death. The green arrow process demonstrates what happens when cancer cells are treated with NEET binders and the black arrows represent the potential process by which cancer cell death occurs.

Overall, NEET proteins are valuable targets for anticancer drug discovery and development. The NEET protein MiNT is an attractive target as it is localized in the inner mitochondria and thus has the potential to be specifically targeted, specifically with CGXs.

2.6 Expression, Purification, & Spectroscopic Characterization of DM MiNT

To test our hypothesis that CGXs bind to the NEET protein MiNT, and to determine whether they stabilize, destabilize, or have no effect on MiNT, we designed an in vitro model that takes advantage of recombinant protein expression, which afforded DM MiNT in high purity, high yield, and in soluble and functional form. Our strategy for the recombinant expression of MiNT (Figure 2.9) begins with the design of a plasmid that incorporates the double mutant CISD3 gene of MiNT and can be easily incorporated into E. coli. A double mutant of MiNT was utilized due to its higher stability. After transformation, we select for cells that incorporated the CISD3-

containing plasmid and grow them in culture from a single colony. Our method is easily amenable to scale-up and, as a result, we can obtain large batch growths of transformed E. coli (6-10 L). The cultures are then centrifuged, and the resulting pellets are combined into one and lysed. After lysis, the supernatant containing DM MiNT is purified through a sequence of ion-exchange (IEX) and size-exclusion (SEC) chromatography. This results in pure MiNT, which we confirmed by gel electrophoresis.

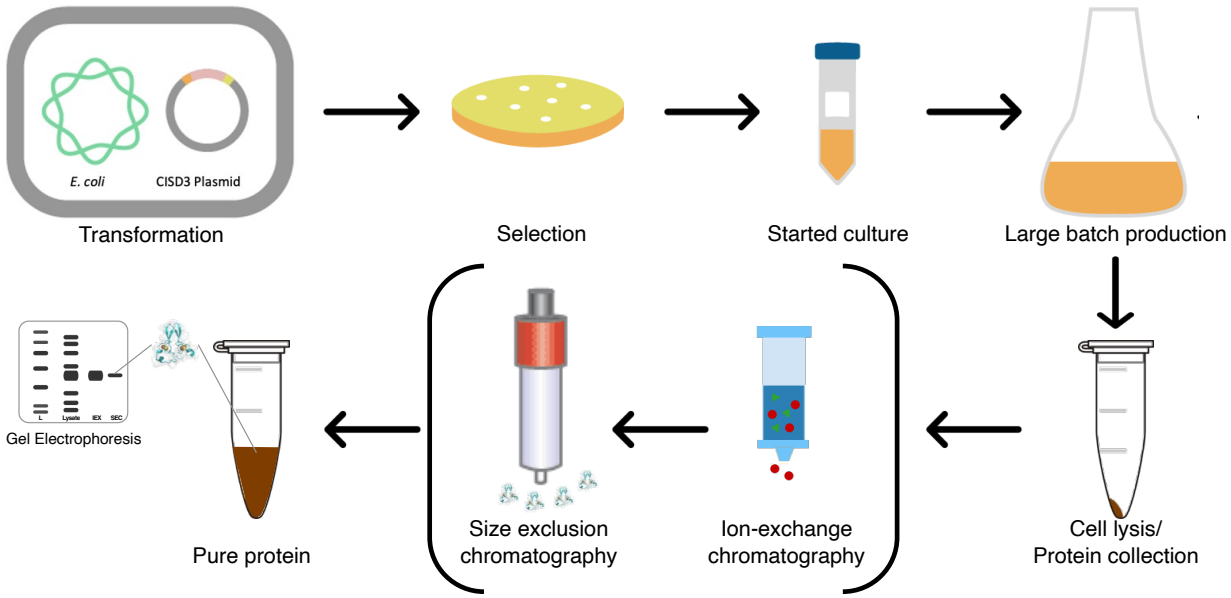

Figure 2.9: General strategy for the expression and purification of DM MiNT.

2.6.1 Transformation of Competent Cells with DM CISD3-Containing Plasmid

CISD3 (36-127) H75C/H113C (DM MiNT) gene coding for amino acids 36-127 synthesized by Integrated DNA Technologies, Inc. was subcloned into a pET24a vector with a kanamycin resistance (kanR) marker for inducible expression between the XhoI and NdeI restriction site. BL21-CodonPlus (DE3)-RIL competent *E. coli* cells (Agilent Technologies) were then transformed with the plasmids by mixing 50 µL of thawed competent cells in a 1.7 mL sterile

Eppendorf tube kept at 0 ºC with 2 µL of DM MiNT plasmid DNA. The mixture was allowed to incubate at 0 ºC for 30 min and subsequently heat-shocked at 42 ºC for 1 min. The mixture was immediately cooled to 0 ºC and the heat-shocked cells were transferred to a cell culture tube containing 500 µL of sterile Super Optimal Broth with catabolite repression (SOC) media (ThermoFisher Scientific) at 37 ºC. The transformed cells were allowed to grow at 37 ºC for one hour with shaking at 180 rpm. The mixture was then transferred to a sterile 1.7 mL Eppendorf tube and centrifuged at 5000 x g for 1 min.

The supernatant was then decanted and 20 µL of autoclaved Milli-Q water were mixed into the tube. The resulting cells were then allowed to grow on a Luria-Bertani (LB) agar plate with 50 µg/mL kanamycin (ThermoFisher Scientific) at 37 ºC overnight. Next, a single colony from the agar plate was picked using a 10 µL pipet tip, which was dropped into a cell culture tube containing 5 mL of autoclaved LB media (25 g/L) with 5 µL of kanamycin solution (300 mg/10 mL in Milli-Q water) and 5 µL chloramphenicol solution (300 mg/10 mL in EtOH). The mixture was allowed to grow at 37 ºC with shaking at 180 rpm. Glycerol stock solutions of the transformed cells were prepared from the starter culture by mixing 0.5 mL of culture with 0.5 mL of sterile 80% (v:v) glycerol solution in a 1.2 mL cryogenic vial, which was then stored at -80 ºC for up to 6 months.

2.6.2 CISD3 DNA Vector Sequence Confirmation

The sequence of the pET24a vector was verified by transforming Invitrogen MAX Efficiency DH5α Competent *E. coli* cells (ThermoFisher Scientific) in the same manner as described above. An Invitrogen PureLink HiPure Plasmid Miniprep Kit (ThermoFisher Scientific) was used to collect high-copy DNA for sequencing (Eton Bioscience, Inc). DNA concentration was measured with a NanoDrop ND-1000 UV/Vis spectrophotometer (ng/µL, λ = 260 nm).

2.6.3 DM MiNT Expression Protocol

DM MiNT was expressed by first preparing LB media. To a 500 mL Erlenmeyer flask was added 5 g of Invitrogen Miller's LB broth base (LB) powder (ThermoFisher Scientific) and 200 mL of deionized water. To each of three 4 L Erlenmeyer flasks was added 50 g of LB powder and 2 L of deionized water. The flasks were covered with foil and autoclaved for 25 min at 120 °C. Once completely cooled, the 4L flasks were set aside and to the 500 mL flask containing media was added 200 µL of kanamycin solution (300 mg/10 mL in Milli-Q water) and 200 µL chloramphenicol solution (300 mg/10 mL in EtOH). Next, a 10 µL pipette tip was quickly dipped into the frozen transformed cells in glycerol and released into the flask. The flask was allowed to stir at 37 ºC with shaking at 180 rpm overnight.

Next, to each of the 4L flasks was added 2 mL of 60 mM kanamycin (291 mg/10 mL in Milli-Q water) and 2 mL of 100 mM chloramphenicol (323 mg/10 mL of EtOH). The 200 mL cell culture was split into three by adding ~66 mL of culture to each of the 4 L flasks. Next, the flasks were stirred at 37 ºC with shaking at 180 rpm until the optical density (OD) reading reached a maximum of 0.8 at 600 nm. The OD was measured with a Bio-Rad SmartSpec Plus UV/Vis spectrophotometer. The cell cultures were then induced by adding 1 mL of 1 M IPTG solution (2.3 g/10 mL of Milli-Q water) at 18 ºC with shaking at 180 rpm for 18 h. The induced cultures were then centrifuged using a Beckman Coulter centrifuge equipped with a J-LITE JLA-8.1000 rotor at 3000 rpm for 30 min at 4 ºC. The media was then decanted, and all cell pellets were combined into one using 25 mL of lysis buffer. The combined pellets were placed into 50 mL falcon tubes and frozen overnight at 80 ºC.

To the thawed induced cell pellet kept at 0 ºC was then added an additional 25 mL of lysis buffer and 100 µL of 100 mM PMSF solution (174 mg/10 mL of IPA). The cells were lysed using

a Fisher Scientific 550 Sonic Dismembrator with a pulsar cycle of 10 seconds on and 15 seconds off for 10 minutes. The tip of the sonicator was completely submerged in the solution to prevent foaming, and the sample vessel was immersed in an ice water/NaCl bath to prevent heating of the solution throughout the sonication process. After sonication, the solution was centrifuged using a Beckman Coulter Avanti JXN-26 high-speed centrifuge equipped with a JA-25.50 rotor at 15,000 rpm and 4 ºC for 45 min. The resulting brown solution was filtered using a sterile Millex-GP 0.22 µm PES filter and kept at 0 ºC until ready for purification. If the purification was not performed immediately, the solution was stored at -80 ºC.

2.6.4 DM MiNT Purification Protocol

Preparation of Buffers

Lysis Buffer: 50 mM of Trizma base (Sigma-Aldrich) and 50 mM NaCl (Sigma-Aldrich) were combined with Milli-Q water until completely dissolved. mix until completely dissolved. The mixture was then adjusted to pH 8 with aqueous HCl then filter through a MF-Millipore membrane filter, 0.22 µm pore size type GSWP filter. The buffer was then deoxygenated by placing the buffer under mild vacuum with stirring overnight.

Buffer A: 50 mM of Trizma base was combined with milli-Q water and mixed until completely dissolved. The mixture was then adjusted to pH 8, filtered, and degassed as above.

Buffer B: 50 mM of Trizma base and 600 mM NaCl were combined with milli-Q water and mixed until completely dissolved. The mixture was then adjusted to pH 8, filtered, and degassed as above.

SEC Buffer: 50 mM of Trizma base and 150 mM NaCl were combined with milli-Q water and mixed until completely dissolved. The mixture was then adjusted to pH 8, filtered, and degassed as above.

Protein Purification

DM MiNT was purified through a sequence of ion-exchange and size exclusion chromatographies using a Bio-Rad NGC Quest 10 chromatography system (FPLC) equipped with a fraction collector. For ion-exchange chromatography, two 5 mL HiTrap SP High Performance Columns (Cytiva Life Sciences) were connected in tandem. The tandem columns were equilibrated with buffer A at 5 mL/min for 10 minutes. The protein mixture was then purified in 10 mL batches using a partial gradient method at a flow rate set to 5 mL/min (Figure 2.10A).

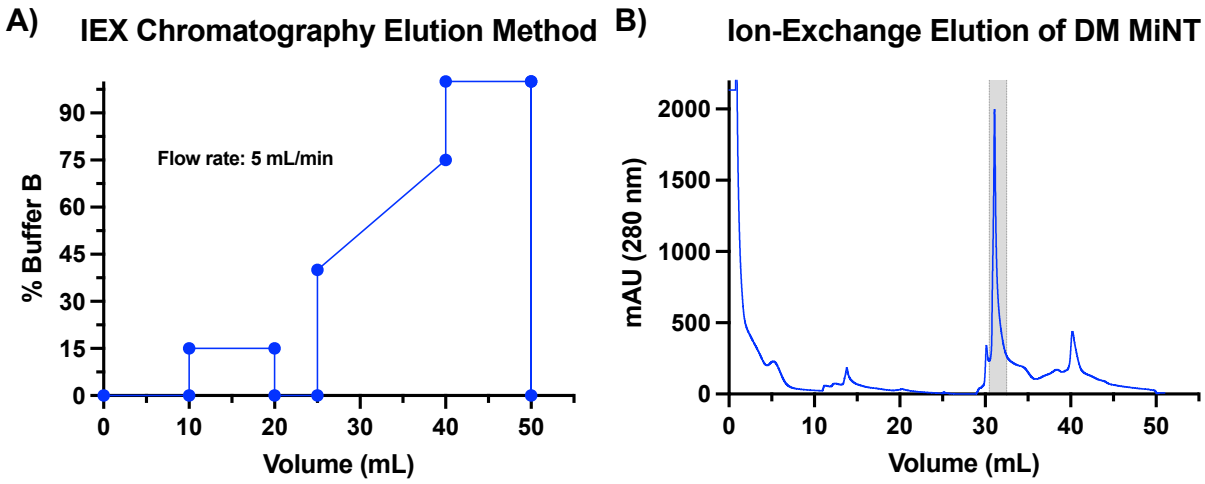

Figure 2.10: Purification of DM MiNT by ion-exchange chromatography. A) The elution method used to purify DM MiNT and B) the UV trace (280 nm) of the eluted protein appearing between 30-35 mL of column volume.

Following ion-exchange chromatography, all fractions containing DM MiNT and are red/brown in color were combined and concentrated by placing the solution in an Amicon Ultra 15 mL centrifugal unit with an Ultracel 3,000 D molecular weight cutoff filter and centrifuging at

3000 rpm until the total volume is 10 mL. The solution was then syringe-filtered using a 0.22 µm pore size GSWP syringe filter.

The filtered red/brown solution was then further purified using size-exclusion chromatography. The protein solution was injected into an FPLC instrument equipped with an equilibrated HiPrep 26/60 Sephacryl S-100 HR column (Cytiva Life Sciences). The column was equilibrated for 3 h with SEC buffer at a flow rate of 2 mL/min prior to sample injection. The method used for SEC purification was isocratic, utilizing only SEC buffer at a flow rate of 2 mL/min. DM MiNT was eluted after approximately 130 min or 260 mL of SEC buffer passed through the column (Figure 2.11A). The fractions containing pure DM MiNT were combined and concentrated until the UV/Vis signal at 458 nm was ≥ 0.4. The identity of the protein was then further confirmed by SDS-PAGE gel electrophoresis (Figure 2.11B).

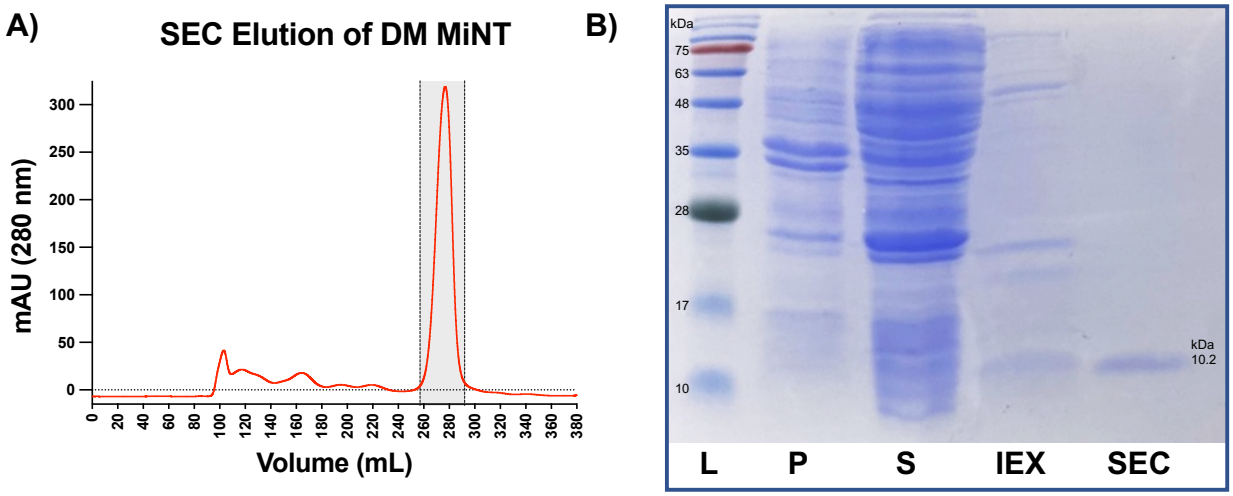

Figure 2.11: Purification of DM MiNT by size exclusion chromatography. A) The elution of DM MiNT occurs after approximately 130 min or 260 mL of column volume and B) The presence of DM MiNT was further confirmed by SDS-PAGE gel electrophoresis. 10.2 kDa corresponds to apo-DM MiNT. L = ladder, P = pellet after lysis, S = supernatant after lysis, IEX = flowthrough after ion-exchange chromatography before concentration, SEC = flowthrough after SEC purification.

SDS-PAGE Gel Electrophoresis

SDS-PAGE gels were prepared according to established protocols. Gel samples were prepared by mixing 15 μL of sample to be analyzed with 5 μL of tris-glycine SDS sample buffer (2X). Next, 1 μL of β-mercaptoethanol (Sigma Aldrich) was added to the solution and mixed by repetitive pipetting. The resulting solution was heated at 85 ºC for 5 min using a dry bath incubator. The sample(s) were allowed to cool to room temperature prior to use.

All gels were performed using a mini-protean tetra vertical electrophoresis system for handcast 0.75 mm gels (Bio-Rad Laboratories). Gels were casted by mixing the reagents and their respective quantities listed in Table 2.1. The reference used was AccuRuler prestained protein ladder G02101 (Lambda Biotech). Once the gels were set, 20 μL of sample were loaded per well and 7 μL of the ladder solution was used as a reference. The gels were resolved using 1X running buffer (preparation discussed below) as the electrophoresis buffer at 120 V for ~45 min. Gels were analyzed using a Coomassie staining solution consisting of 50% MeOH, 10% glacial acetic acid, and 0.1% Coomassie brilliant blue. The resolved gel was placed in Coomassie staining solution and placed on a gel rocker overnight. The staining solution was then removed, and the gel was destained with a solution consisting of 40% MeOH and 10% glacial acetic acid. The gel was placed into destaining solution and placed on a gel rocker for 6 h, which were then visualized on a white light box.

1X Running buffer preparation: To a 2L vessel was added 1 L of deionized water, 28.8 g of glycine, and 6.04 g of Trizma base. When the solids were completely dissolved, 2 g of sodium dodecyl sulfate were added. The mixture was then mixed with more deionized water until the total volume was 2 L.

Table 2.1: Solutions for casting SDS-PAGE electrophoresis gels.

Resolving Gel (15 mL)		**Stacking Gel (5 mL)**	
1.5 M Trizma, pH 8.8	5 mL	0.5 M Trizma, pH 6.8	620 µL
30% acrylamide	7.5 mL	30% acrylamide	833 µL
Water	2.4 mL	Water	3.8 mL
20% SDS	75 µL	20% SDS	25 µL
10% APS	75 µL	10% APS	50 µL
TEMED	25 µL	TEMED	5 µL

Chapter 2, in part, is currently being prepared for submission for publication of the material. Arevalo, G. E.; Capraro, D. T.; Lin, H. H.; Jennings, P. A.; Theodorakis, E. A. The dissertation author was the primary researcher and author of this material.

Chapter 3

Profiling the Interaction Between MiNT & CGXs

3.1 UV/Vis Spectroscopic Analysis of the Interaction Between DM MiNT & CGXs

As an Fe-S protein, DM MiNT has unique spectroscopic characteristics that make it amenable to analysis by UV/Vis and circular dichroism spectroscopies. Consequently, we opted to follow the decay of DM MiNT using both methods, which yielded valuable information of the decay rate of the 2Fe-2S clusters as well as conformational changes of the protein that occur when the metal clusters are released. The UV Vis absorption spectrum of DM MiNT clearly shows several regions where the decay of the protein can be followed (Figure 3.1A). We opted to follow changes at 458 nm since the 2Fe-2S clusters of DM MiNT are known to absorb at this wavelength (Figure 3.1B). However, no statistically significant changes were observed for DM MiNT at other

wavelengths. In addition, when DM mint was exposed to 10% DMSO, a UV/analysis showed no difference in the UV/Vis spectra between DM MiNT by itself and when mixed with 10% DMSO (Figure 3.2). Regardless of whether DMSO is present, the 458 nm half-life decay of DM Mint was measured to be ~150 min.

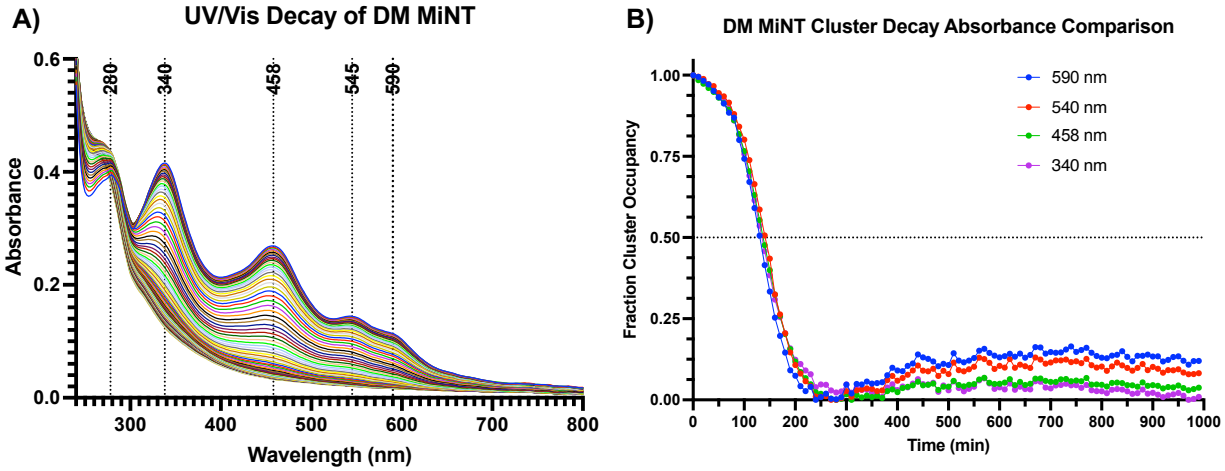

Figure 3.1: UV/Vis absorption spectrum of DM MiNT and its decay at 450 nm. A) the UV Vis spectrum of DM MiNT, which shows several regions that can be tracked for decay and B) the decay of several wavelengths, which are all nearly identical. The increase in absorbance after 300 min is likely due to apo-protein aggregation.

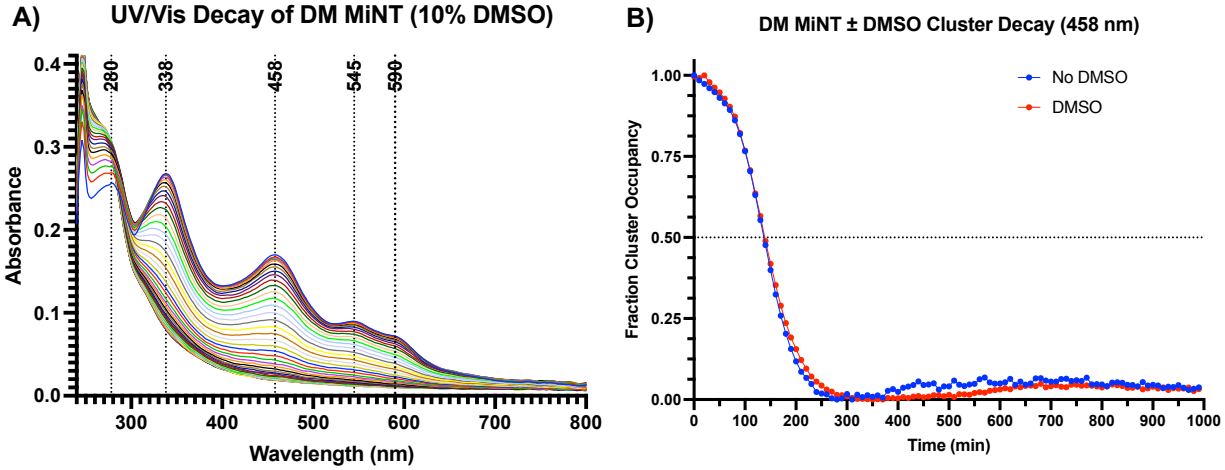

Figure 3.2: UV/Vis absorption spectrum of DM MiNT with 10% DMSO and its decay at 450 nm. A) the UV Vis spectrum of DM MiNT with 10% DMSO and B) the decay of DM MiNT with 10% DMSO at 458 nm (red), which is identical to that of the protein without DMSO (blue).

When DM MiNT was exposed to various concentrations of compound 118, an increase in the half-life of the protein was observed. This observation was consistent across all the derivatives that we tested (see chapter 3 appendix). The half-life if DM MiNT with 10% of 0.1-0.2 mg/mL solutions of 118 was extended to ~200 min. and 210-220 min for concentrations between 0.3-0.5 mg/mL (Figure 3.3). Interestingly, we observed a "tail" effect after ~220 min, which we did not observe when the protein was analyzed by itself. We speculate that this is likely the result of a difference in stability between the two clusters of DM MiNT and a difference in the way the compound interacts with each cluster. In essence, one cluster is being stabilized significantly more than the other. We measure the decay of the tail, which we refer to as the second half-life or the half-life of the more stable cluster, to be ~370 min at concentrations of 0.1, 0.4, and 0.5 mg/mL. At concentration of 0.2 and 0.3 mg/mL, we observed a longer second half-life of ~470 min and we speculate that this is the result of a concentration dependance on the stability of the second cluster.

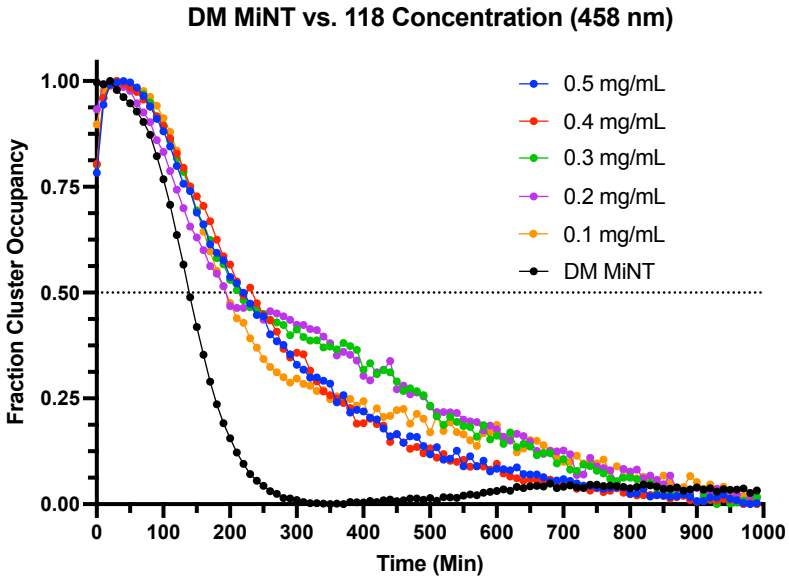

Figure 3.3: UV/Vis absorption decay at 458 nm of DM MiNT with 10% 118 in DMSO at various concentrations compared to DM MiNT with no compound.

A similar observation was made when DM MiNT was exposed to compound 130 at various concentrations. In this case, however, there is a much more cohesive interaction between compound 130 and DM MiNT regardless of concentration. At 10% of 0.1 mg/mL 130, a half-life of 200 min was observed. At every other concentration, between 0.2-0.5 mg/mL, a consistent half-life of 240 min was observed. The second half -life of 130 at 0.1 mg/mL was measured to be ~270 min, and for all other concentrations, it was determined to be ~400 min.

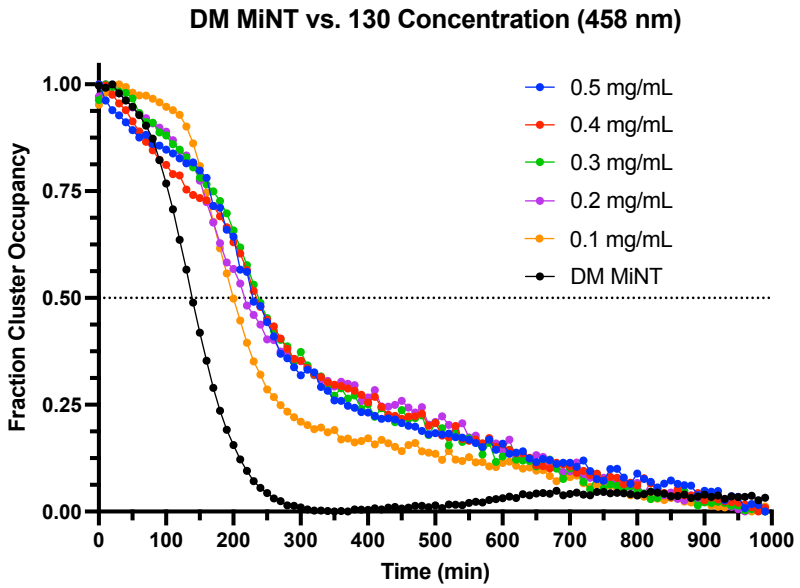

Figure 3.4: UV/Vis absorption decay at 458 nm of DM MiNT with 10% 130 in DMSO at various concentrations compared to DM MiNT with no compound.

When considering all the compounds we tested, it was apparent that there was a significant increase in first half life of MiNT with all amide derivatives compared to GBA, which showed a first half-life of and a second half-life of 170 and 222 min, respectively (Figure 3.5). Overall, our novel amide derivatives have a stabilizing effect on MiNT, which has important implications for their use as novel therapeutics. Further tests are ongoing to optimize our model for use as a predictor of small molecule biological activity in NEET proteins.

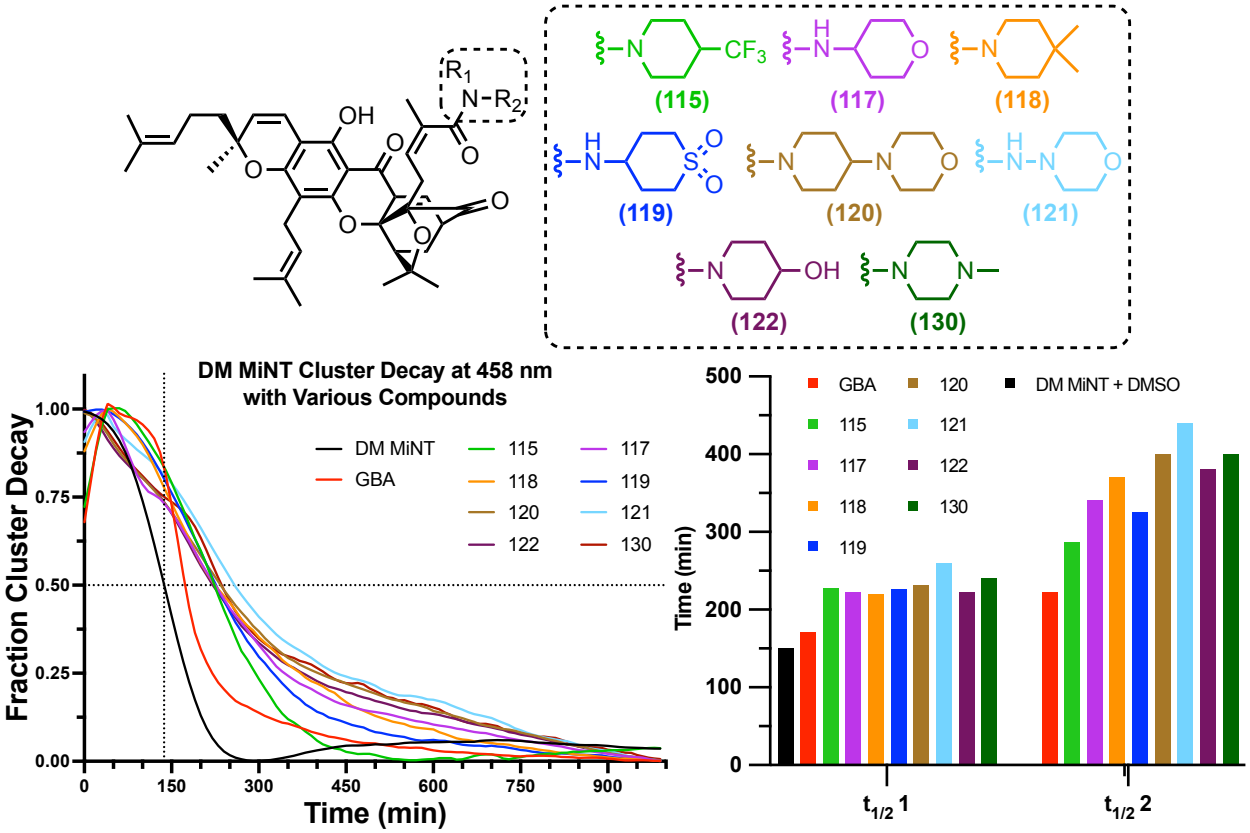

Figure 3.5: Apparent half-lives of both MiNT clusters, cluster 1 (C1) and 2 (C2), when exposed to 10% of 0.4 mg/mL solutions of various compounds. The half-lives were determined by the decay of clusters at 458 nm.

3.2 CD Spectroscopic Analysis of the Interaction Between DM MiNT & CGXs

The intrinsic CD spectrum of a protein's amide backbone is sensitive to the secondary structure of the protein.[177, 178] The amide backbone bonds absorb in the far UV, typically between 150-300 nm. CD increases in negative ellipticity between 208 and 222 nm and positive ellipticity at 193 nm are typically indicative of an increase in α-helical structure.[179] Increase in β-structure are typically observed when there is an increase in a negative band at 218 nm and positive band at 195 nm.

The CD spectrum of a protein is primary the sum of its active chromophores and secondary structure, which can be divided into three electronic transition energy wavelength categories.[180] In

the first category, the far ultraviolet region below 250 nm, circular dichroism is largely the result of n→π* electron transition of the amide bonds of the protein backbone. The second category, the near ultraviolet spectral region between 250-400 nm, circular dichroism is mainly the result of π→π* electron transition of aromatic side chains in the protein. In the third category, the UV/Vis region between 400-700 nm, circular dichroism is caused by external chromophores, such as prosthetic groups.

To study changes in the secondary structure of MiNT, we subjected the protein to analysis by CD, which were collected at wavelengths between 200-800 nm. Our initial area of interest was the helical region between 200-300 nm. However, our solvent of choice for the delivery of compounds was DMSO, which absorbs heavily in this region of the CD.[181] This precluded us from using the far UV region of the CD for analysis when DMSO was present.

However, absorption bands of proteins in the near UV, between 250-350 nm, are typically due aromatic amino acids such as phenylalanine, tyrosine, and tryptophan.[178] The absorption bands of these amino acids often have fine vibrational structure, due to the transitions between electronic states with vibrational structure.[178] Tryptophan shows a maximum around 290 nm, with fine vibrational structure between 290-305 nm. Tyrosine shows a maximum between 275-282 nm, with a shoulder at higher wavelengths, but can be overshadowed by the tryptophan bands. Phenylalanine produces bands that are narrower and less intense, with fine vibrational structure between 255-270 nm. This, in turn, allowed us to track any secondary structure changes resulting from aromatic amino acids.

Initially, when DM MiNT was subjected to CD analysis, no change in its confirmation was observed after 240 min at 37 ºC. Similarly, with 10% DMSO added, no statistically significant change was observed in the CD spectrum under the same conditions (Figure 3.6). Coupled with

our UV/Vis result of the decay of MiNT, we concluded that there is no change in the structure of the protein as it loses its clusters, which is in accordance with the role of MiNT within the mitochondria.

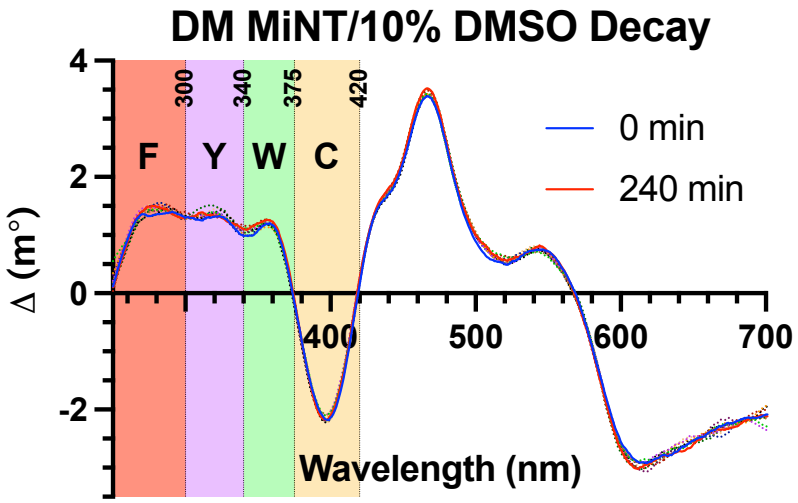

Figure 3.6: CD of DM MiNT at 37 ºC after 240 min. The blue line represents the first scan, and the red line represents the last scan at 240 min. Aromatic side chains and cysteine are labeled.

However, upon addition of CGXs to DM MiNT, we observed a notable change in the aromatic region of the CD. When 10% of a solution of GBA (0.4 mg/mL) was added to DM MiNT, there were changes that in the aromatic region of the CD (Figure 3.7A). We wondered whether this system showed additive properties, which is typical for many CD systems. To our delight, when a CD spectrum of DM MiNT with DMSO is added to a spectrum of GBA by itself and subtract a spectrum of DMSO by itself, we obtain nearly the same curve as when a CD of all three components together is taken (Figure 3.7B). We therefore subtracted a spectrum of GBA at the same concentration as our experiment of the CD decay of DM MiNT with GBA and obtained clear areas of change in the aromatic region (Figure 3.7C). Subtracting a spectrum of DM MiNT with 10% DMSO to our decay spectra, we obtained the same curve as that of GBA alone (Figure 3.7D).

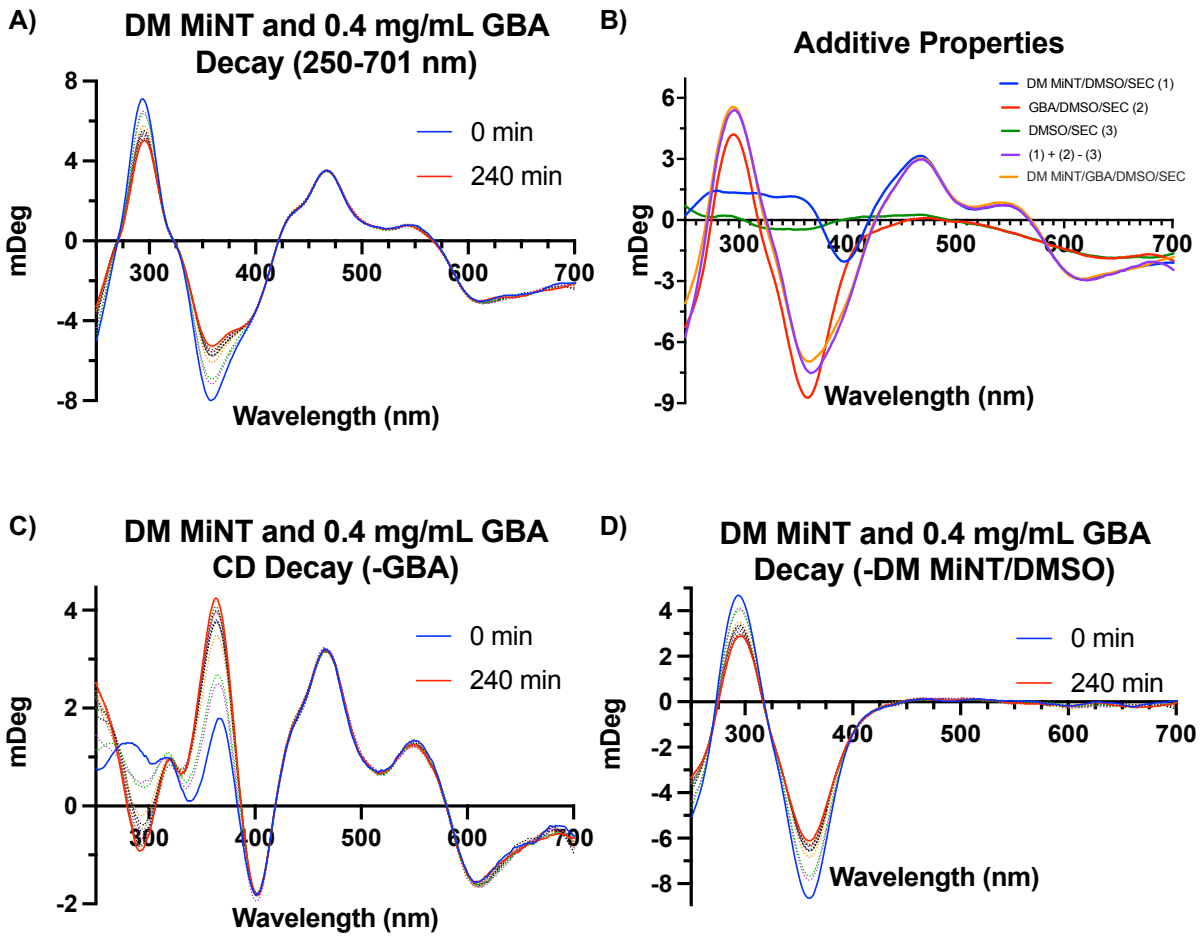

Figure 3.7: CD decay of DM MiNT with 10% GBA (0.4 mg/mL) at 37 ºC.

Upon closer examination of the CD spectrum of the decay of DM MiNT in the presence of GBA with GBA subtracted, it is event that all three aromatic side chains as well as cysteines experience a change in their environment (Figure 3.8). This process was also repeated with the data obtained for compounds 118 and 130 (Figures 3.11 and 3.12, respectively). In the GBA/MiNT CD (K_D = 32 µM, appendix Figure 3.A32), the most dramatic change is in the positive signals of the tryptophan in DM MiNT appearing between 284-305 nm and of cysteines appearing between 345-385 nm. Both the tryptophan and tyrosine residues experience a blue shift whereas the cysteine region does not.

When comparing the same region of the CD of DM MiNT/GBA to that of DM MiNT with compound 130 (K_D = 19 μM, appendix Figure 3.A37), it is event that the way the two compounds interact with the protein is different (Figure 3.9). Coincidentally, the region that changes with compound 130 is a region where GBA causes little change. Undoubtedly, GBA causes a more pronounced conformational change than compound 130. When compared to compound 118 (Figure 3.10), the conformational changes are like the changes in DM MiNT caused by GBA. In compound 118 (K_D = 47.9 μM, appendix Figure 3.A35), the most pronounced changes seem to be occurring in the tryptophan region, with a positive signal decreasing between 285-318 nm.

Overall, each of the three compounds studied by circular dichroism display different mechanisms for how they stabilize DM MiNT. For GBA, there is an apparent unfolding of the protein that occurs—and because GBA is a carboxylate at pH 8 (the pH of the buffer), it could contribute to cluster stability by donating electron density through coordination of the carboxylate to the Fe-S cluster. Neither compound 130 nor 118 possess a carboxylate as it has been replaced with an amide in both. However, both compounds stabilized DM MiNT more so than GBA. Compound 130 does not seem to cause many conformational changes and, as a result, it is possible that it binds to residues on the surface of the protein and increases the interaction between the two asymmetric sides of DM MiNT. Since compound 118 is the most hydrophobic, it is likely that it interreacts with hydrophobic pockets of DM MiNT, which expose aromatic residues and does not destabilize its cluster, but rather stabilizes them. Efforts are ongoing to conduct further tests to elucidate the mode of binding of each compound to DM MiNT.

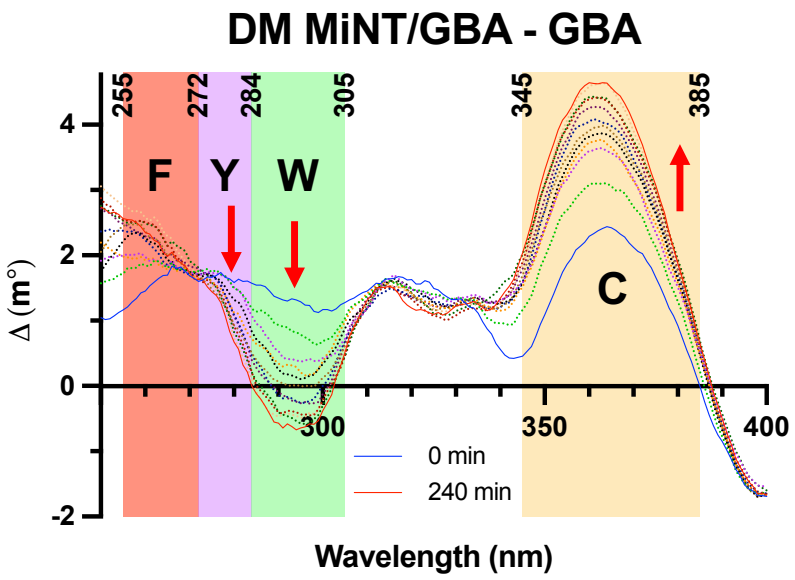

Figure 3.8: The aromatic region of the CD spectrum after DM MiNT interacts with GBA.

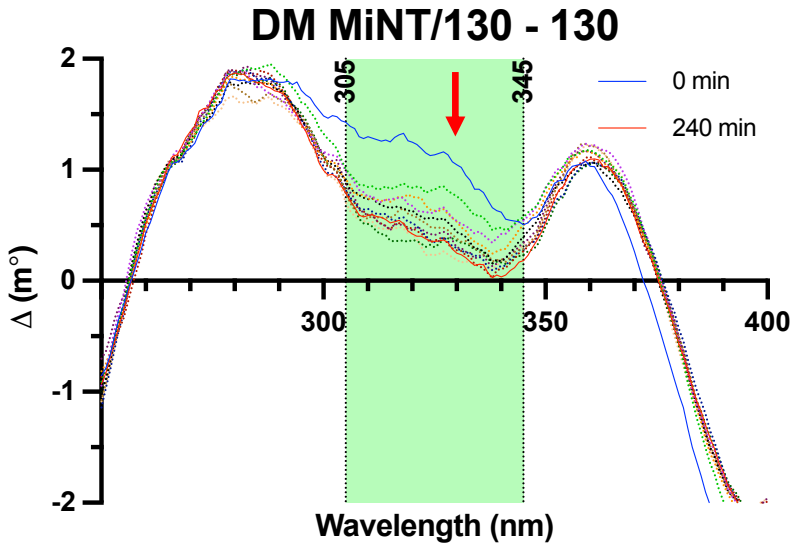

Figure 3.9: The aromatic region of the CD spectrum after DM MiNT interacts with 130.

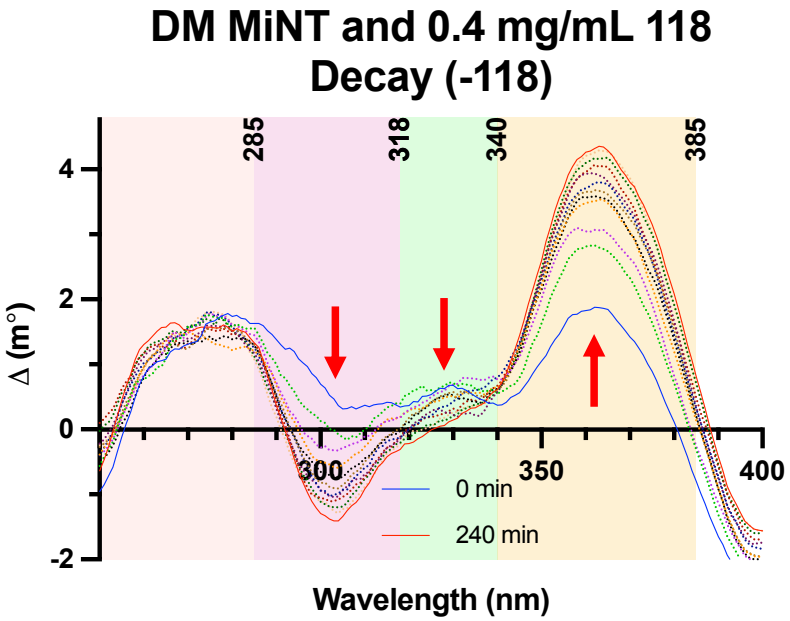

Figure 3.10: The aromatic region of the CD spectrum after DM MiNT interacts with 118.

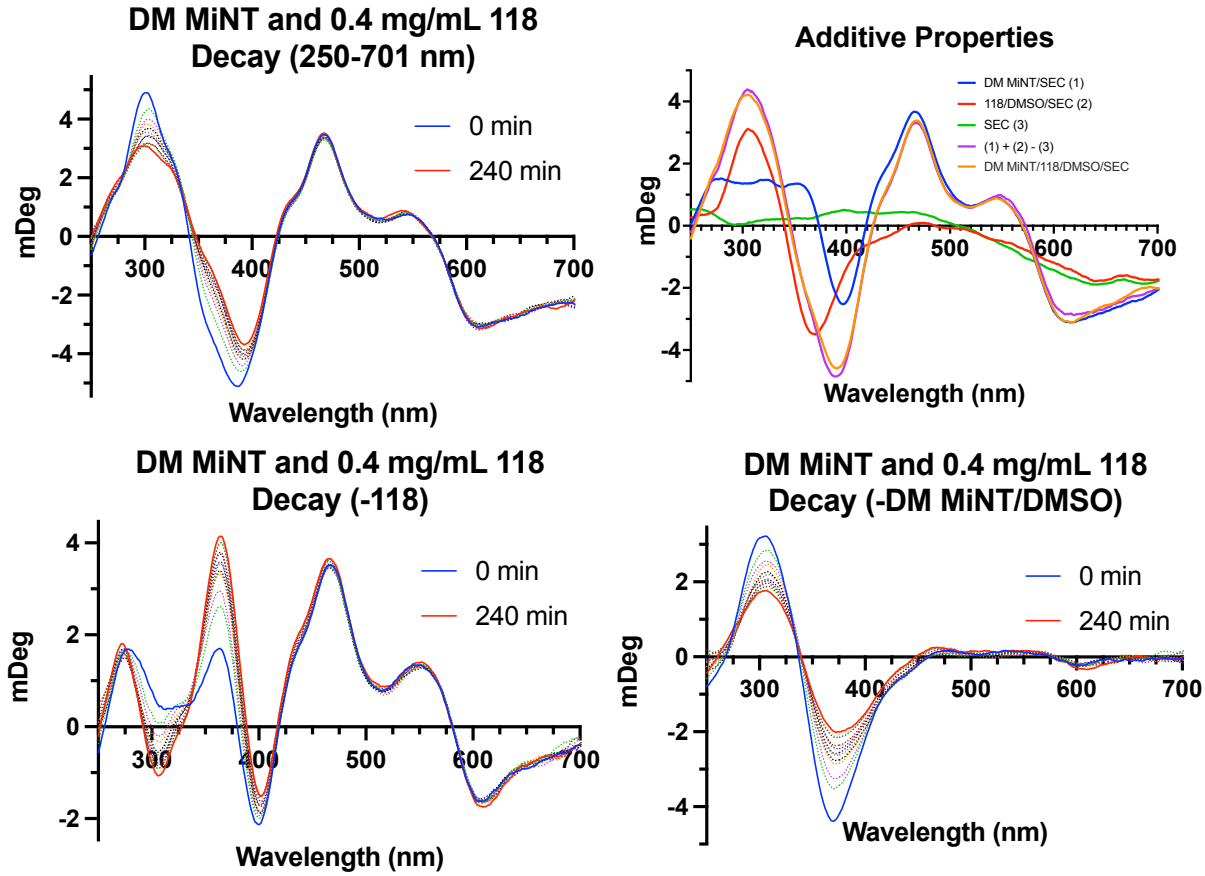

Figure 3.11: CD decay of DM MiNT with 10% 118 (0.4 mg/mL) at 37 ºC.

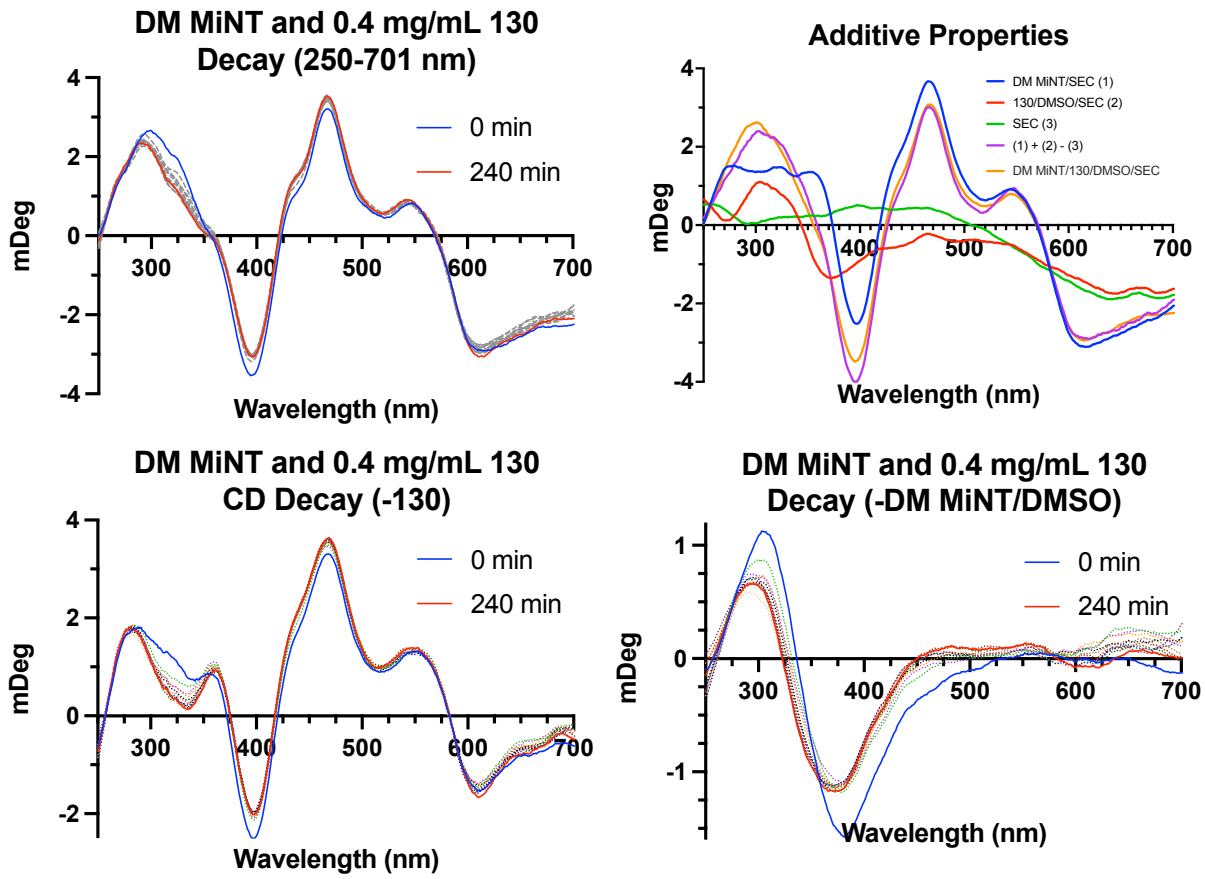

Figure 3.12: CD decay of DM MiNT with 10% 130 (0.4 mg/mL) at 37 ºC.

3.3 Appendix

UV-Vis Spectroscopy Protein Stability Assays

DM MiNT stability assays were performed using a Varian Cary 50 UV-Vis spectrophotometer equipped with a temperature-controlled cuvette holder and Varian Cary single cell Peltier accessory. The instrument was set to a wavelength collection range between 200-800 nm and a scan rate of 10 min/cycle for 100 cycles at 37 ºC. The cuvette utilized was a Hellma macro-QS 10 mm pathlength absorption cuvette equipped with a PTFE stopper. Samples were prepared by making 30 μM solutions of DM MiNT in SEC buffer and mixing with 10% DMSO or 10% of a solution of compound to be tested (dissolved in DMSO) relative to the total volume of sample. The sample was carefully, but thoroughly mixed with repetitive pipetting then topped with 50 μL of paraffin oil and placed inside the spectrophotometer for analysis. Data was processed and analyzed using GraphPad Prism 9.

Conformational Analysis by Circular Dichroism Spectroscopy

The instrument used for CD analysis was an Aviv circular dichroism spectrometer model 215. The following parameters were utilized for all CD spectra: spectral bandwidth = 1nm, scanning speed = 60 nm/min, wavelength step = 1 nm, averaging time = 0.5 sec, multi-scan wait time = 20 min, and the temperature was set to 37 ºC. All data was acquired using a Hellma QS high performance 1 mm cuvette. Samples were prepared by making 40 μM solutions of DM MiNT in SEC buffer and, if necessary, mixing with 10% DMSO or 10% of a solution of compound to be tested (dissolved in DMSO) relative to the total volume of sample (typically 300 μL). As a reference, all CD data obtained is provided here including UV/Vis data.

UV/Vis and CD Spectroscopic Data

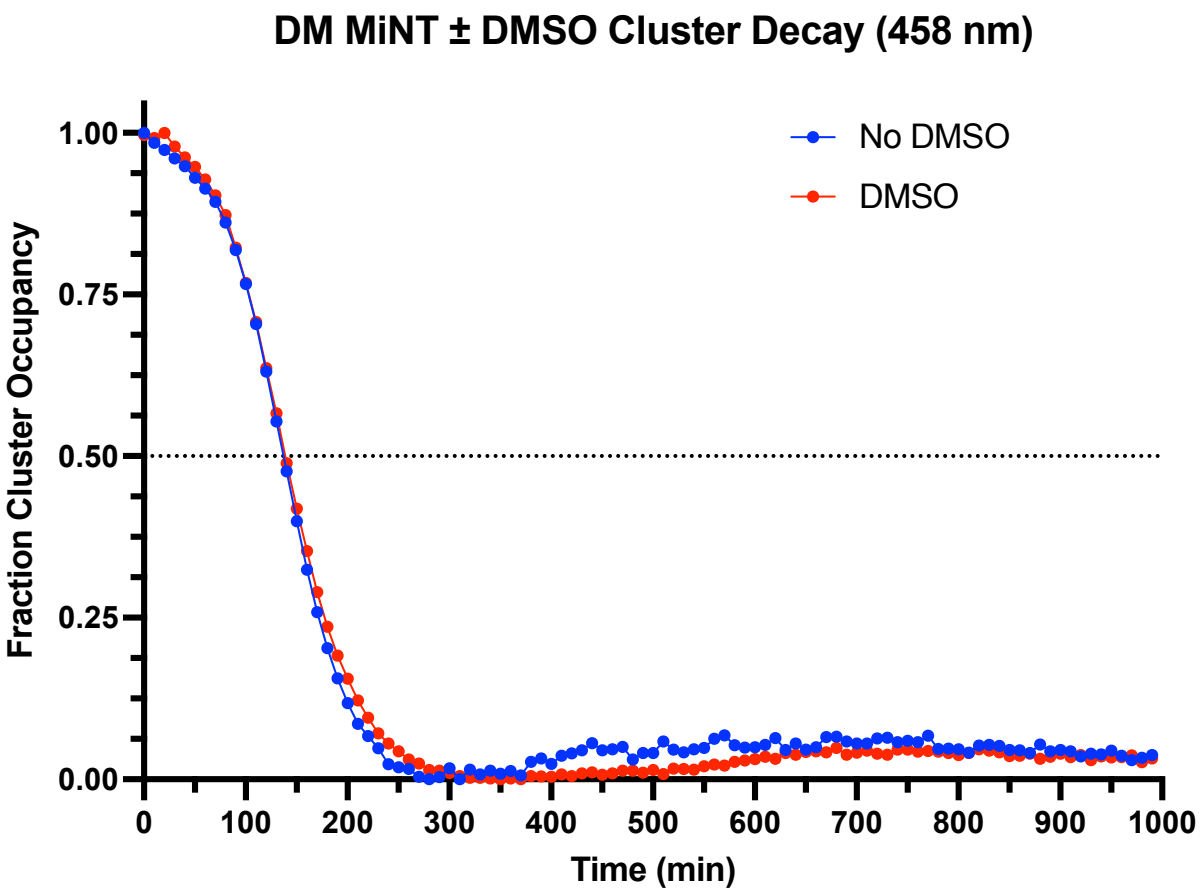

Figure 3.A1: UV/Vis decay curve of DM MiNT at 458 nm in SEC buffer without DMSO (blue) and the decay curve of DM MiNT at 458 nm with 10% DMSO (red).

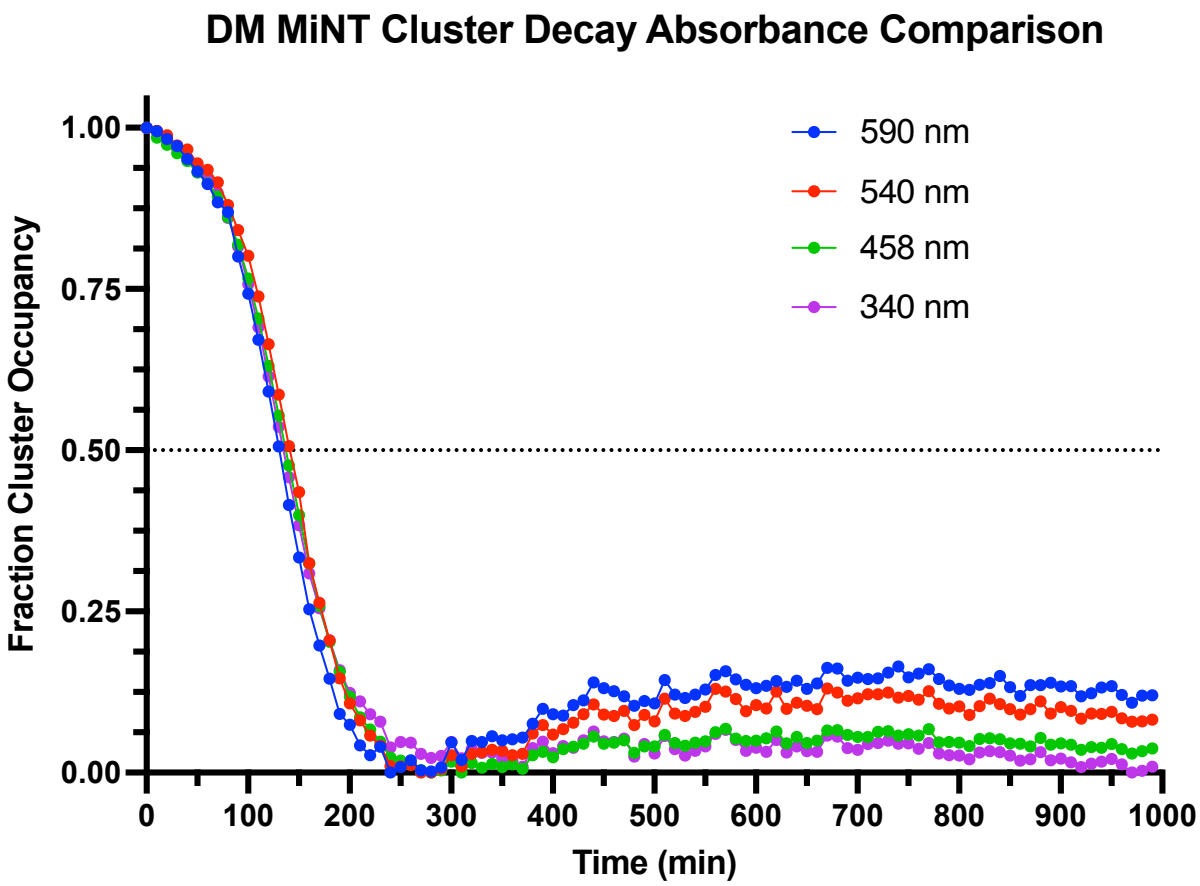

Figure 3.A2: UV/Vis decay curves of DM MiNT without DMSO at various wavelengths.

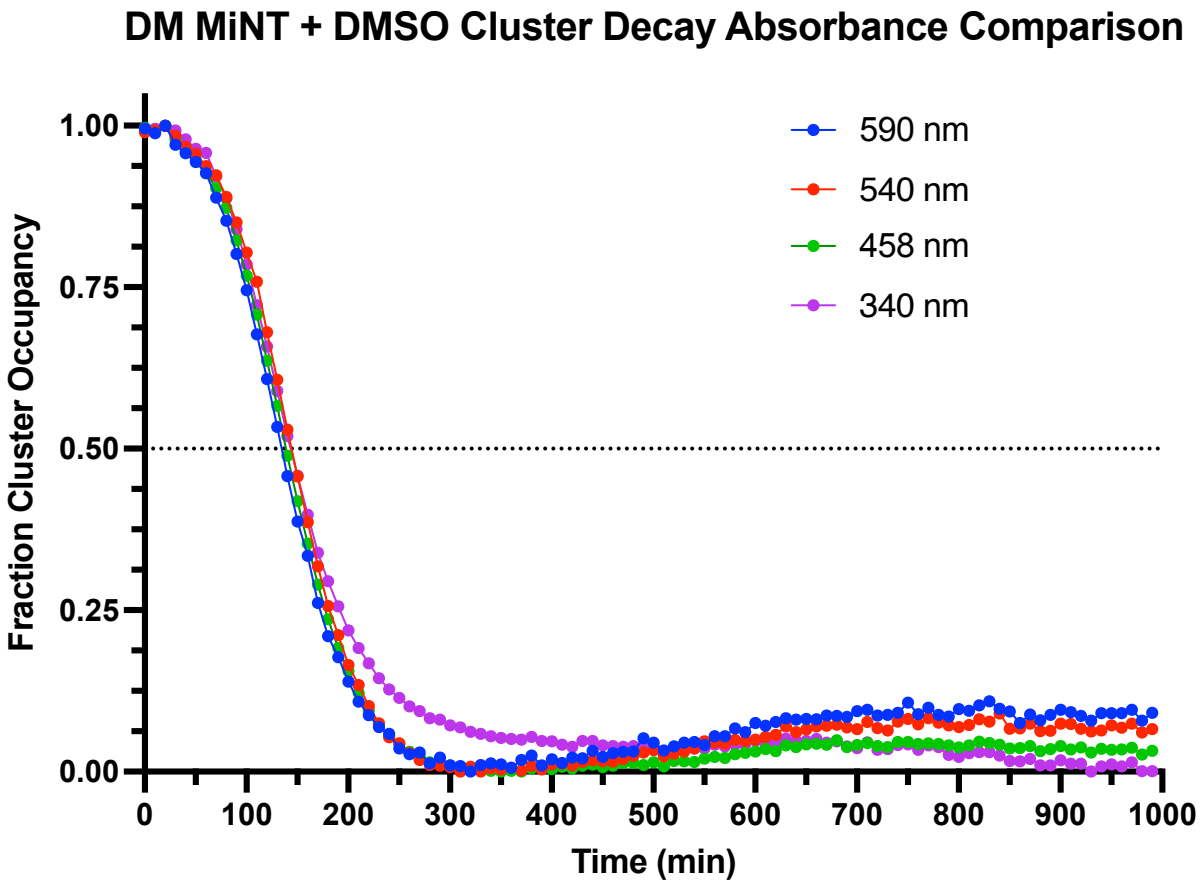

Figure 3.A3: UV/Vis decay curves of DM MiNT with 10% DMSO at various wavelengths.

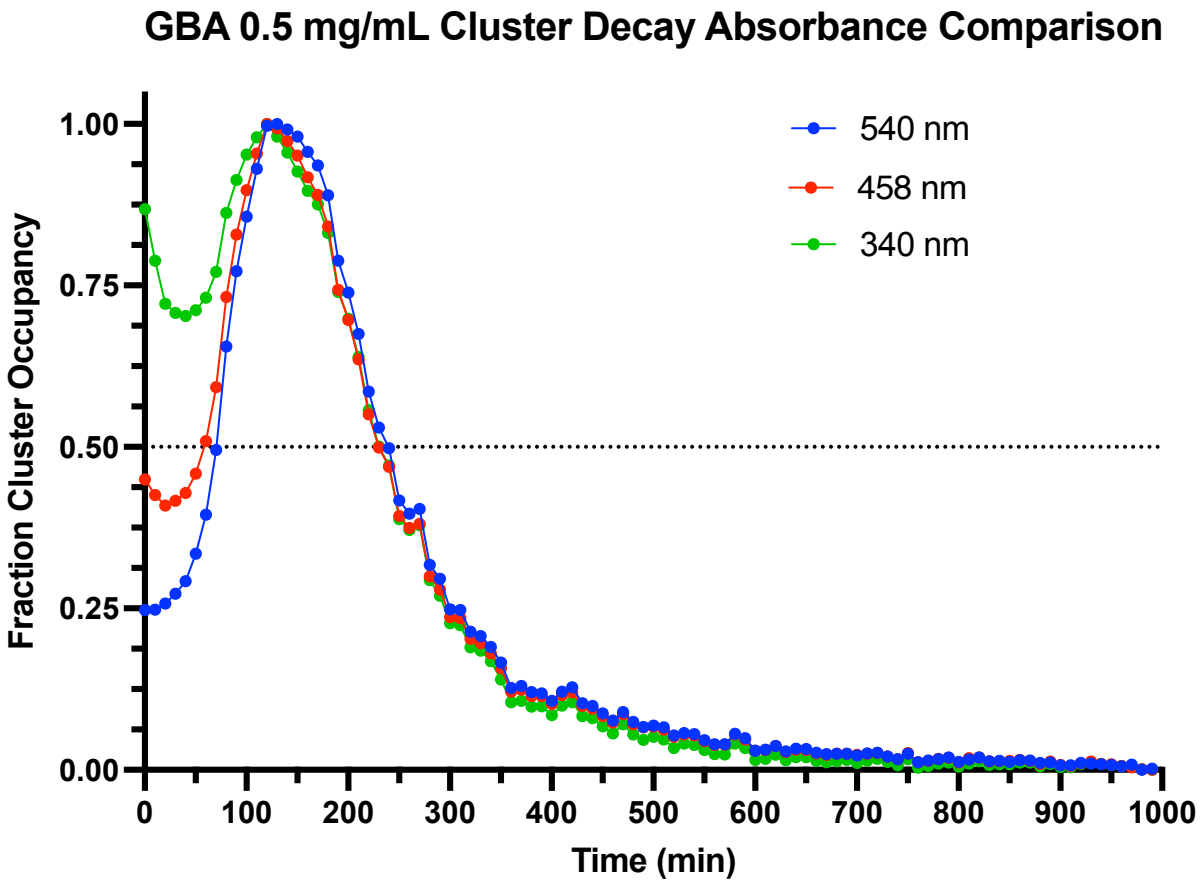

Figure 3.A4: UV/Vis decay curves of DM MiNT with 10% 0.5 mg/mL GBA at various wavelengths.

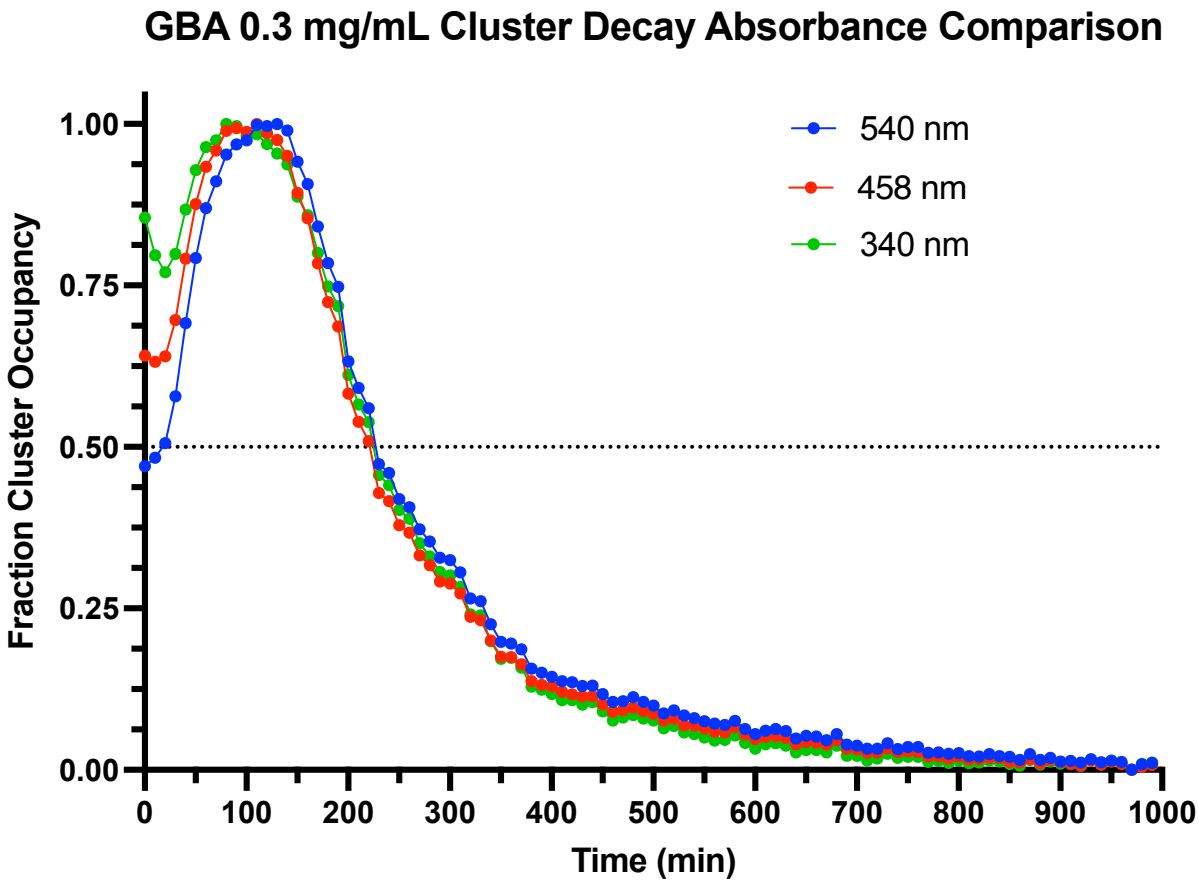

Figure 3.A5: UV/Vis decay curves of DM MiNT with 10% 0.3 mg/mL GBA at various wavelengths.

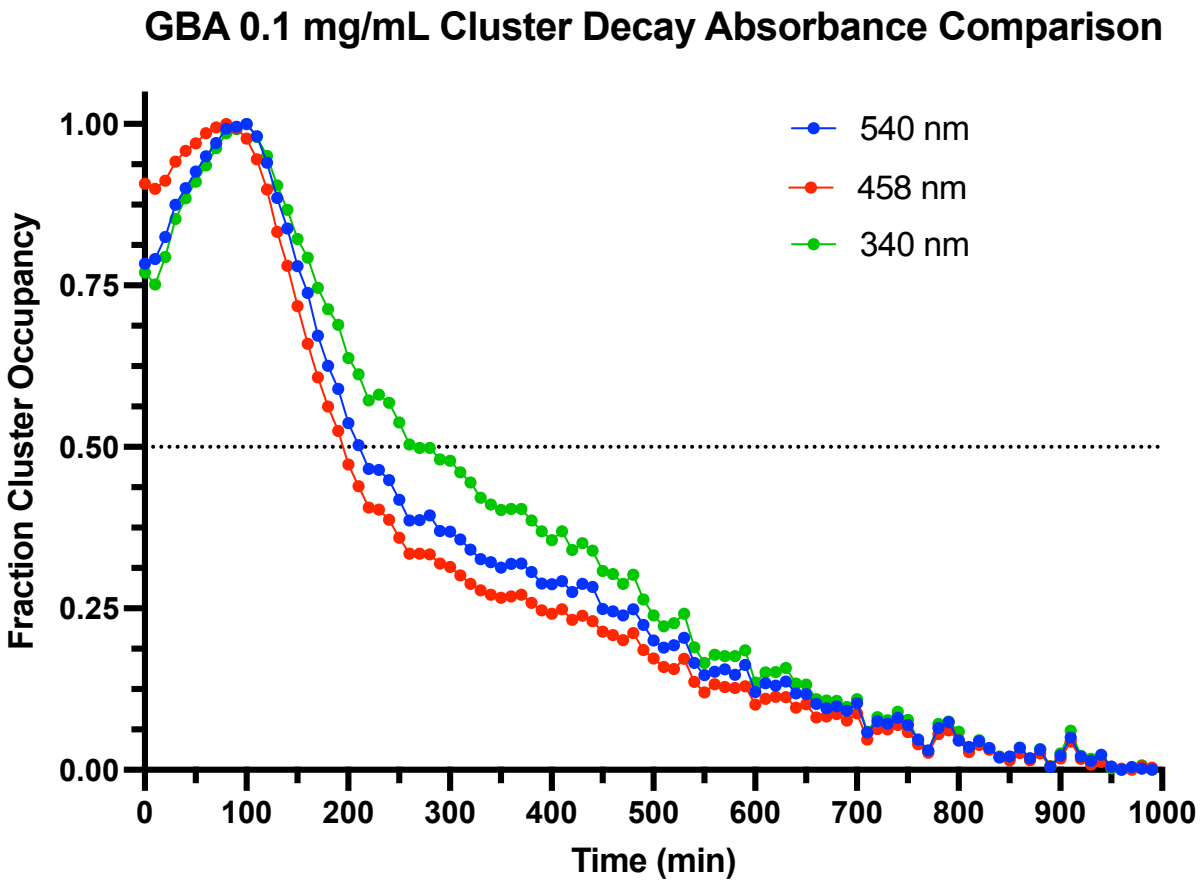

Figure 3.A6: UV/Vis decay curves of DM MiNT with 10% 0.1 mg/mL GBA at various wavelengths.

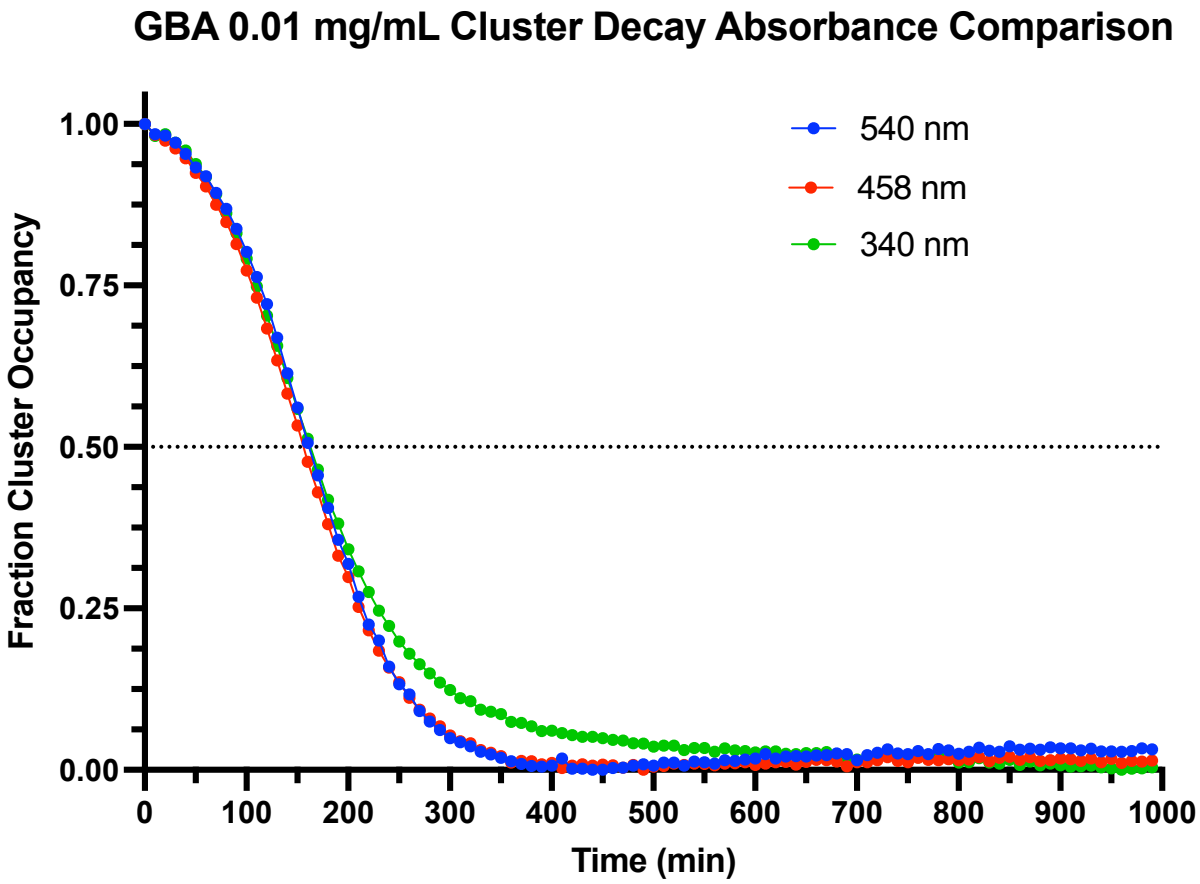

Figure 3.A7: UV/Vis decay curves of DM MiNT with 10% 0.01 mg/mL GBA at various wavelengths.

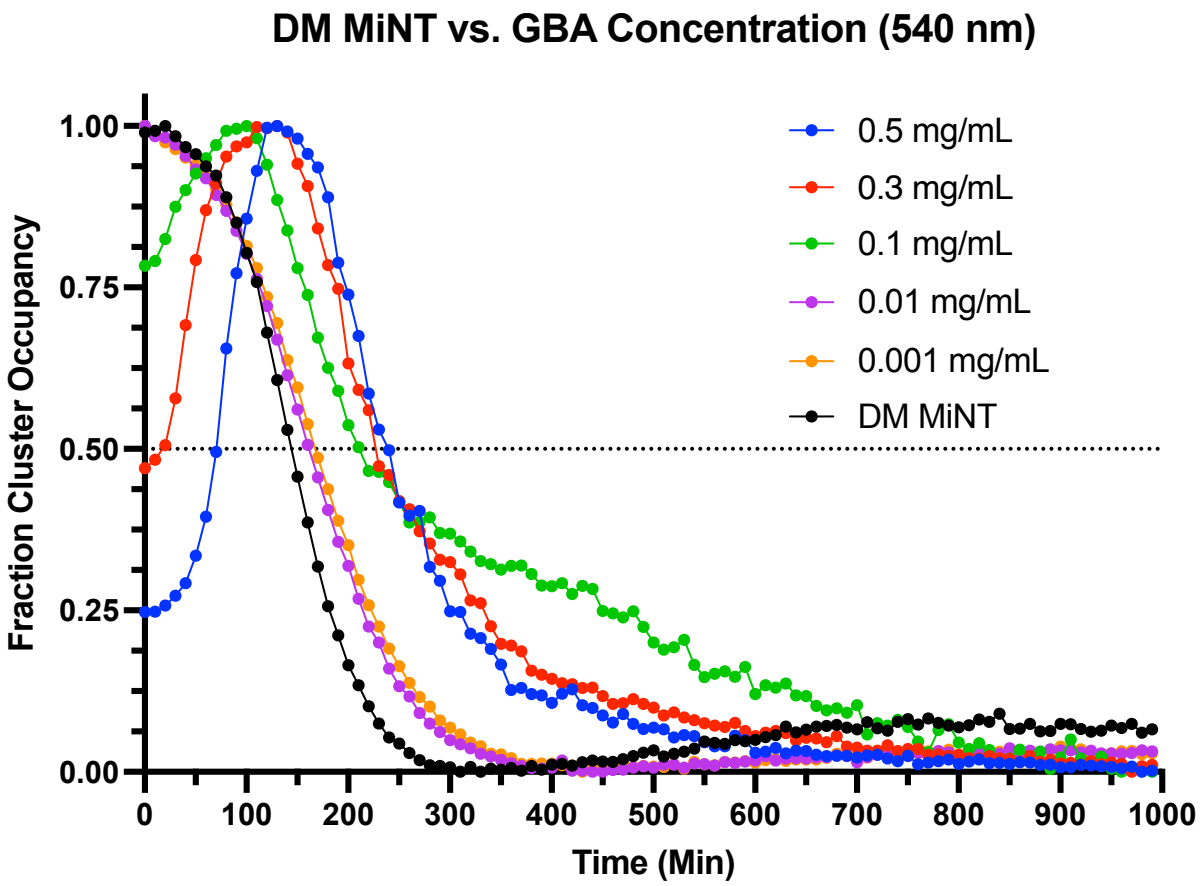

Figure 3.A8: Comparison of the UV/Vis decay curves of DM MiNT with 10% of each GBA concentration versus DM MiNT (10% DMSO) at 540 nm.

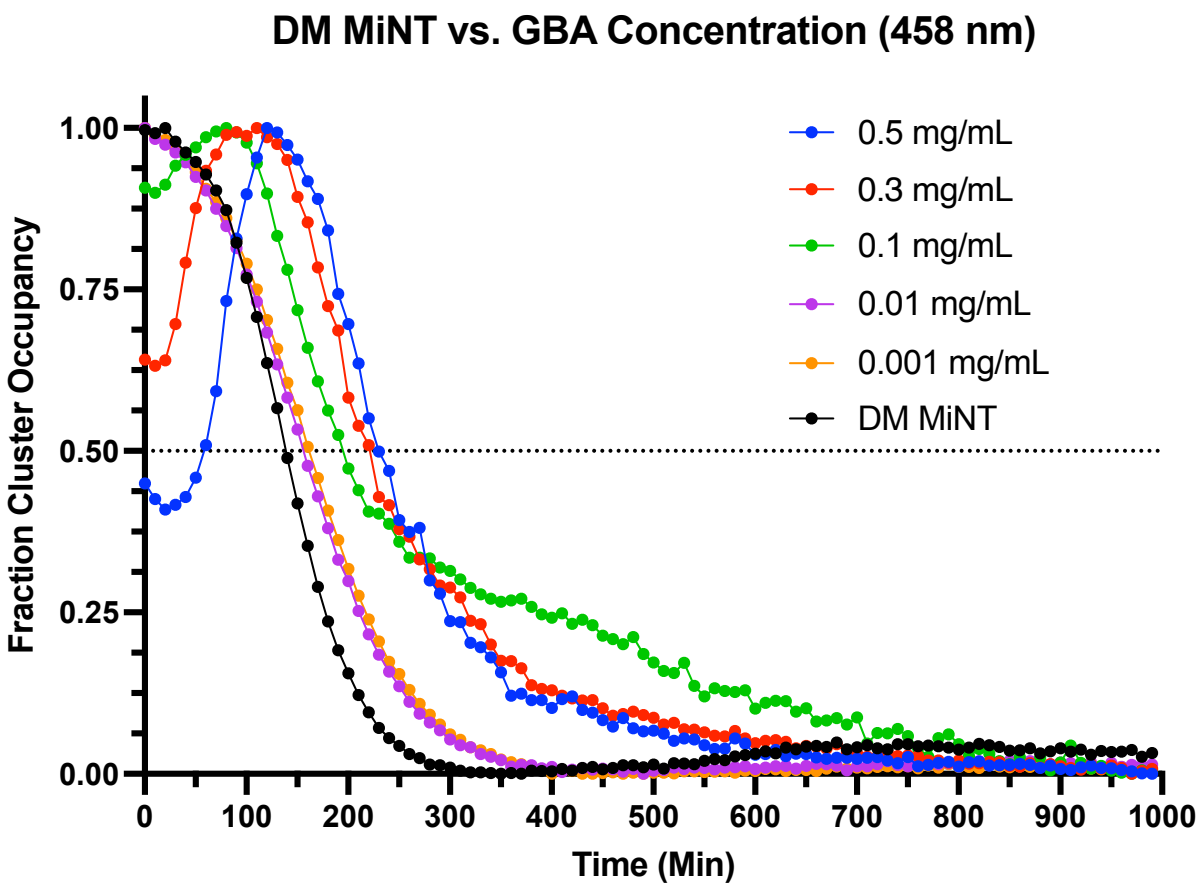

Figure 3.A9: Comparison of the UV/Vis decay curves of DM MiNT with 10% of each GBA concentration versus DM MiNT (10% DMSO) at 458 nm.

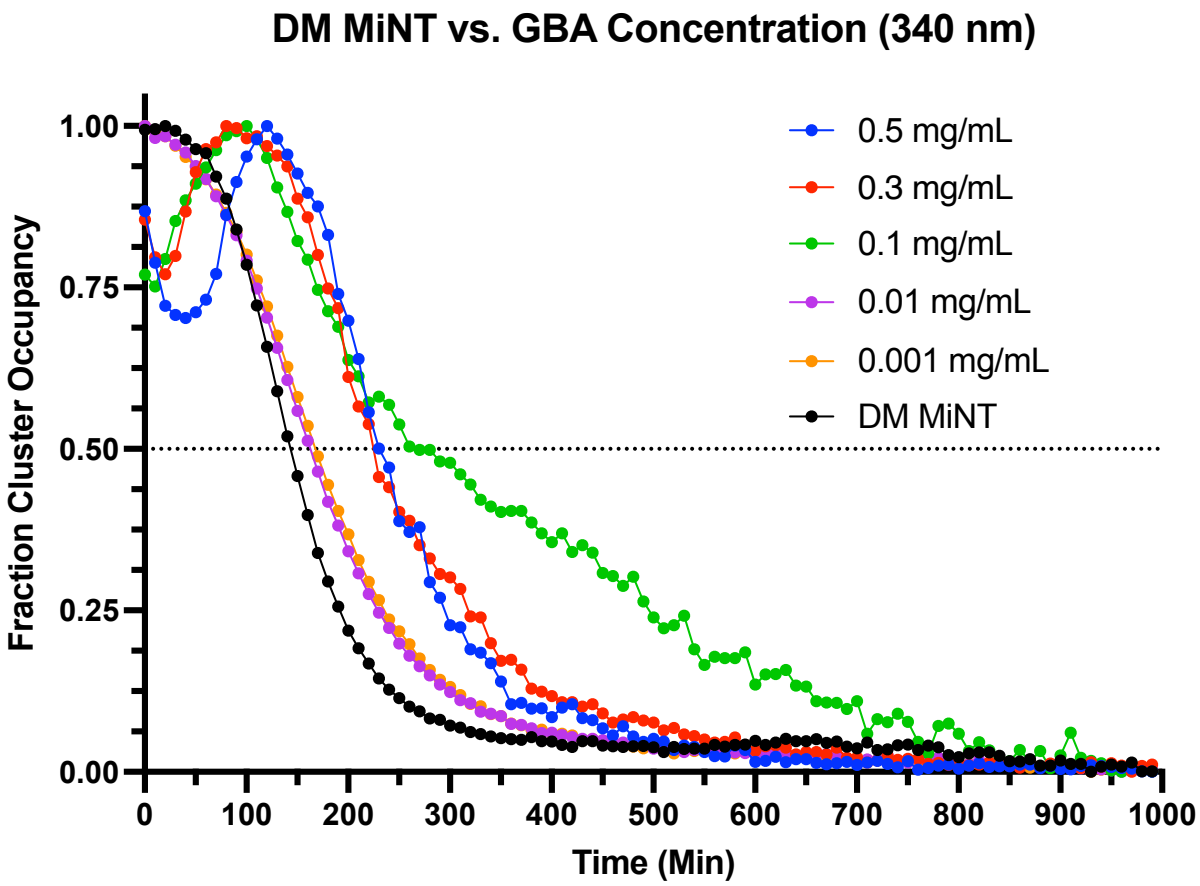

Figure 3.A10: Comparison of the UV/Vis decay curves of DM MiNT with 10% of each GBA concentration versus DM MiNT (10% DMSO) at 340 nm.

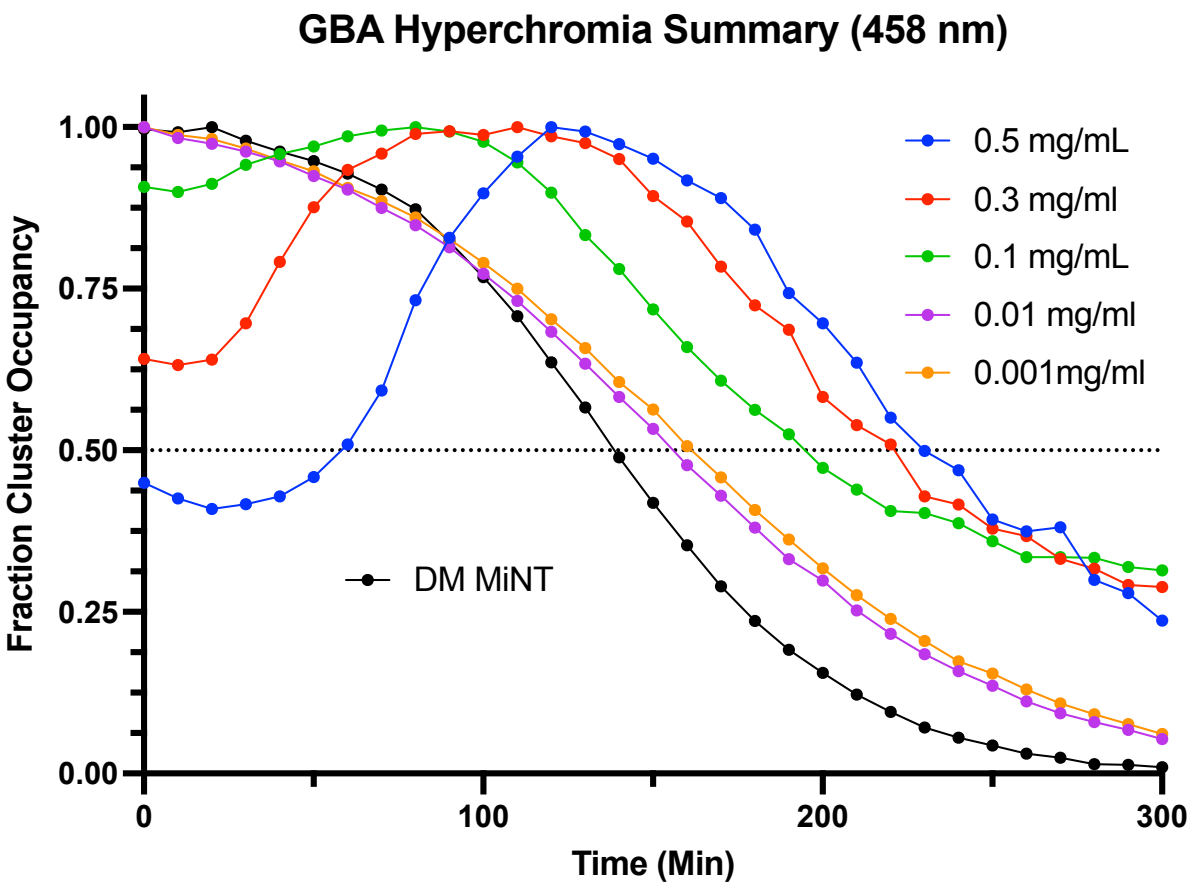

Figure 3.A11: Hyperchromicity of DM MiNT with GBA. DM MiNT exhibits a hyperchromic event as it binds to GBA, which is readily apparent in the initial increase in UV absorbance seen between 0 and 120 minutes. At lower GBA concentrations, hyperchromicity is significantly less apparent.

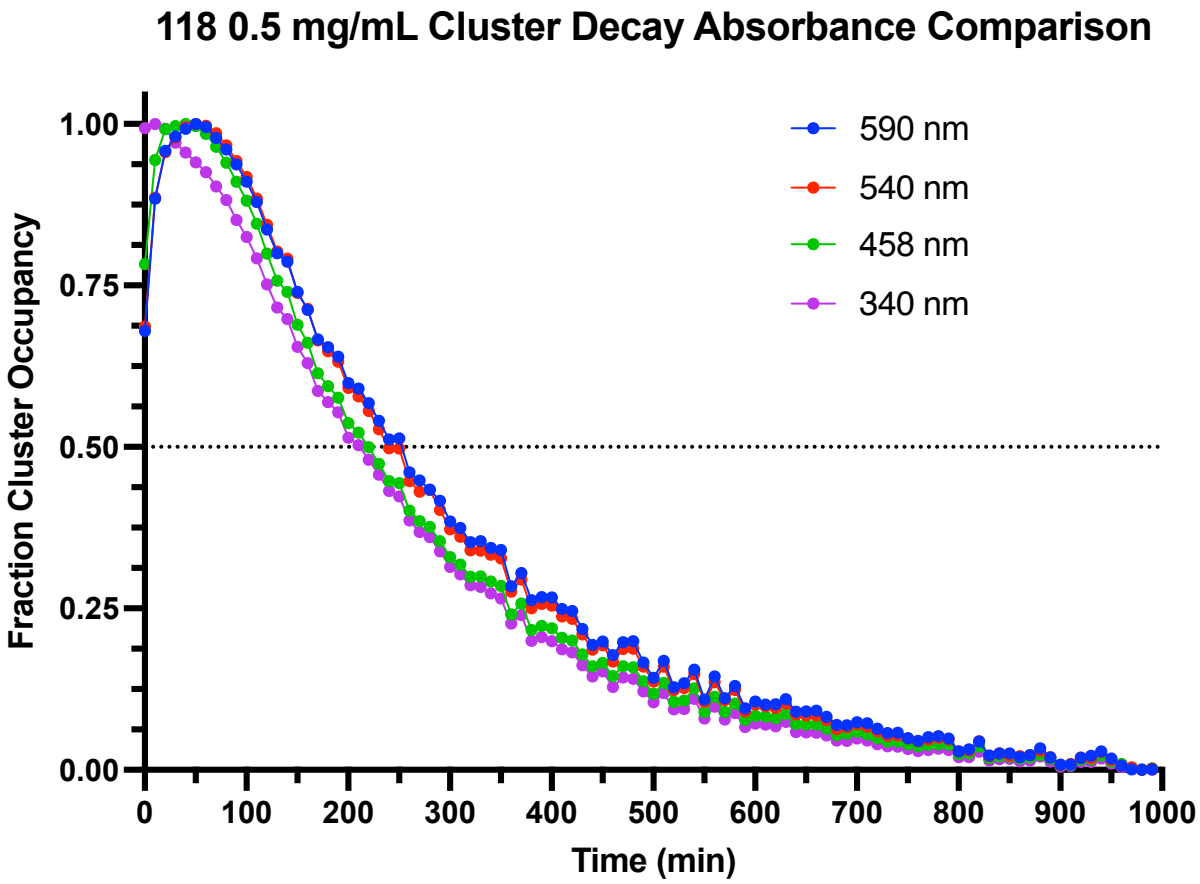

Figure 3.A12: UV/Vis decay curves of DM MiNT with 10% 0.5 mg/mL compound 118 at various wavelengths.

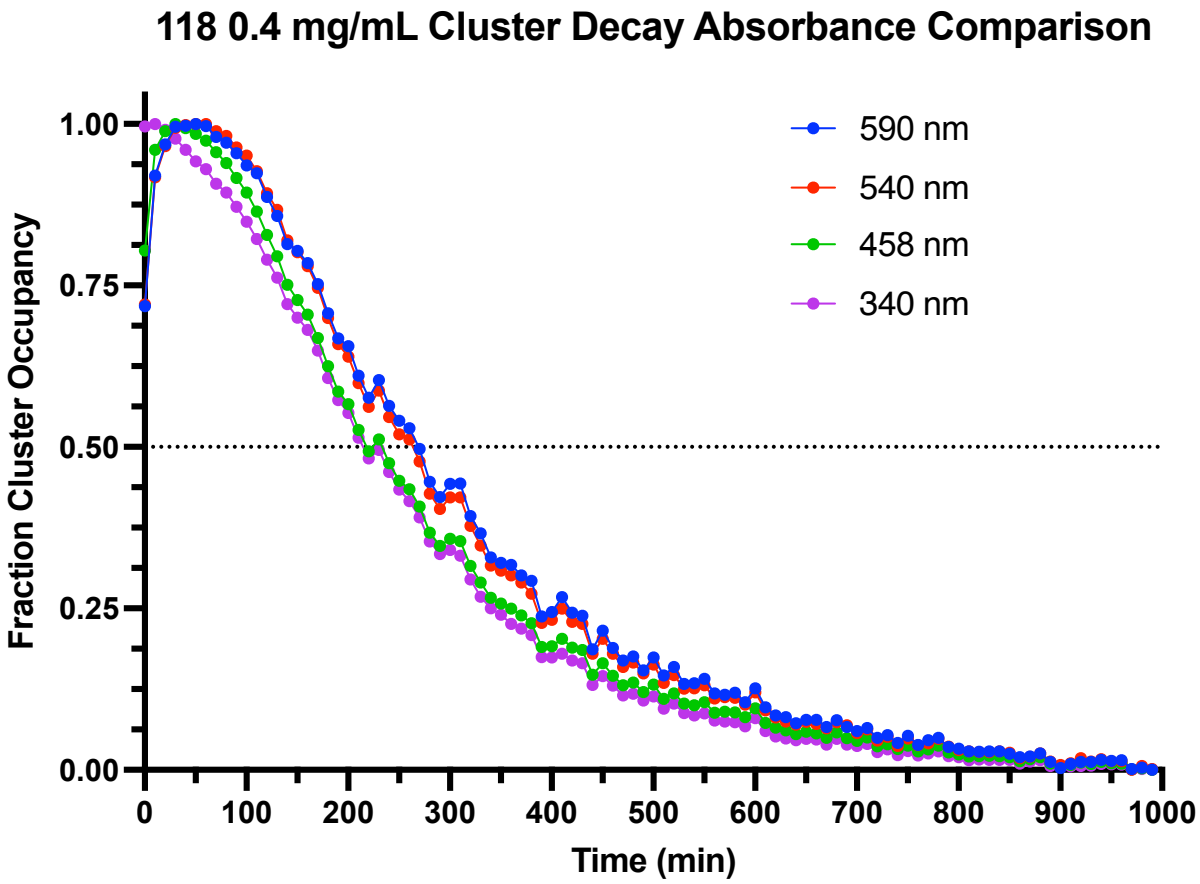

Figure 3.A13: UV/Vis decay curves of DM MiNT with 10% 0.4 mg/mL compound 118 at various wavelengths.

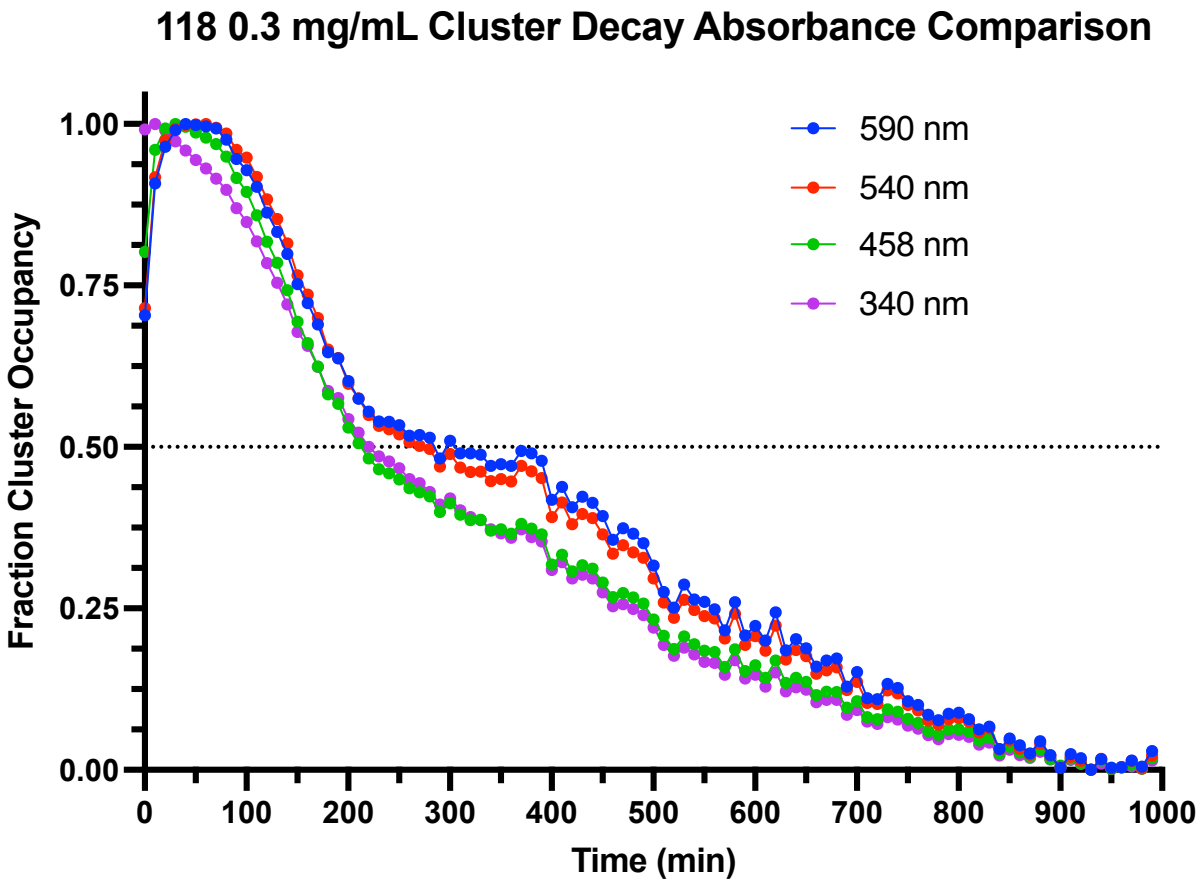

Figure 3.A14: UV/Vis decay curves of DM MiNT with 10% 0.3 mg/mL compound 118 at various wavelengths.

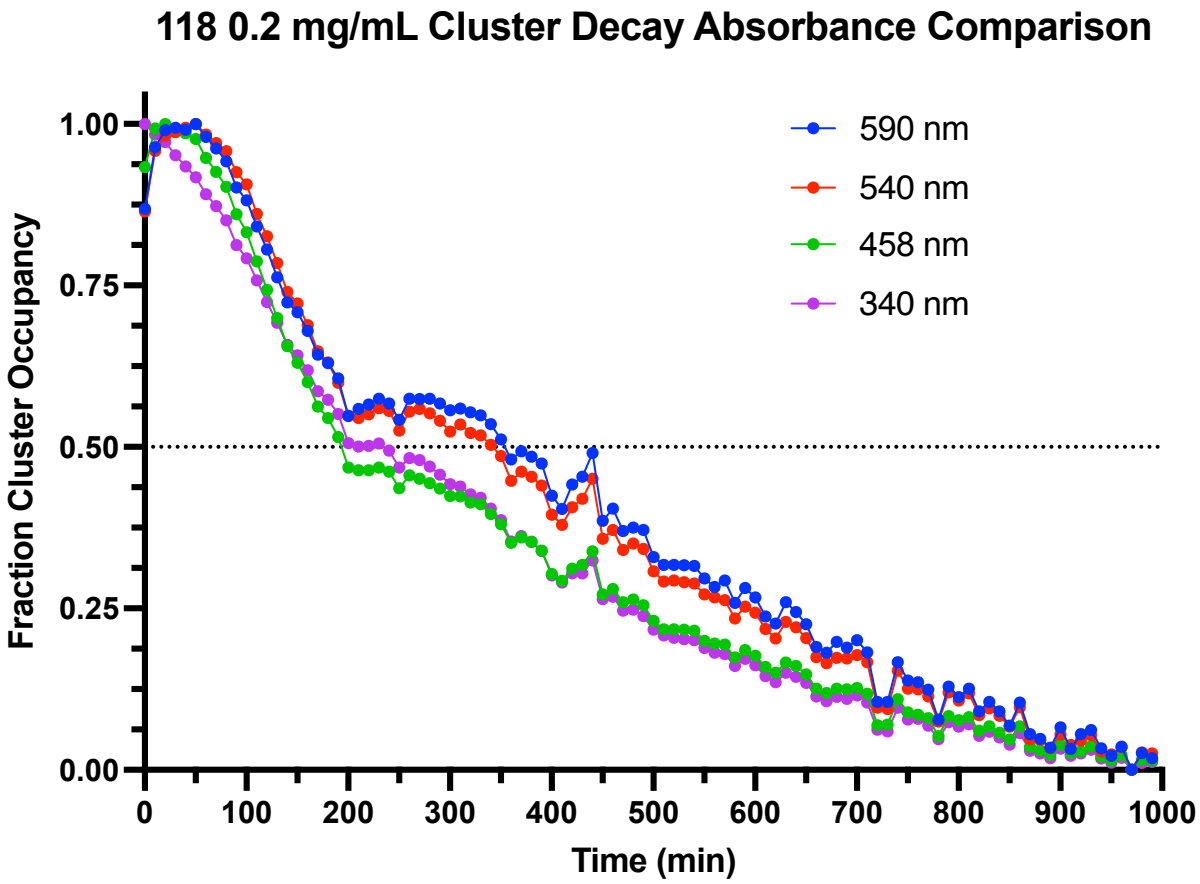

Figure 3.A15: UV/Vis decay curves of DM MiNT with 10% 0.2 mg/mL compound 118 at various wavelengths.

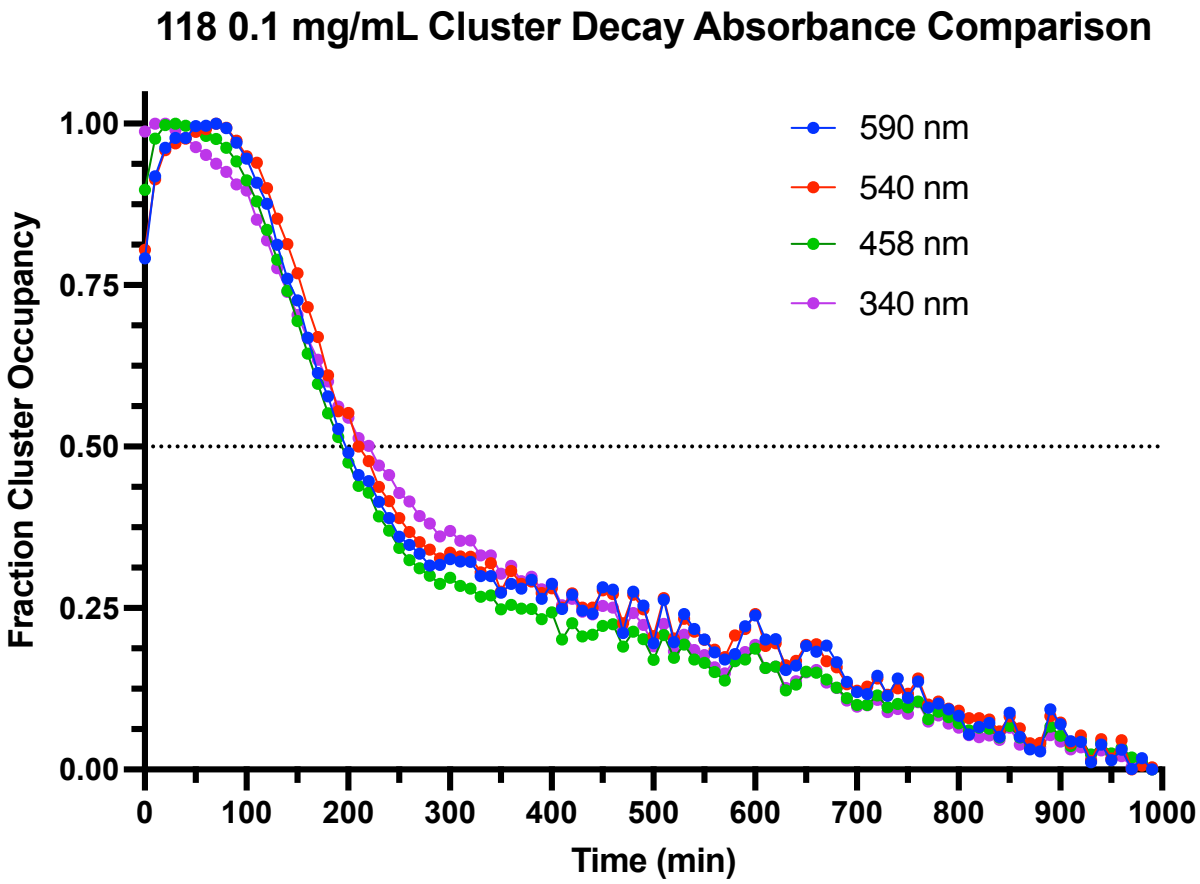

Figure 3.A16: UV/Vis decay curves of DM MiNT with 10% 0.1 mg/mL compound 118 at various wavelengths.

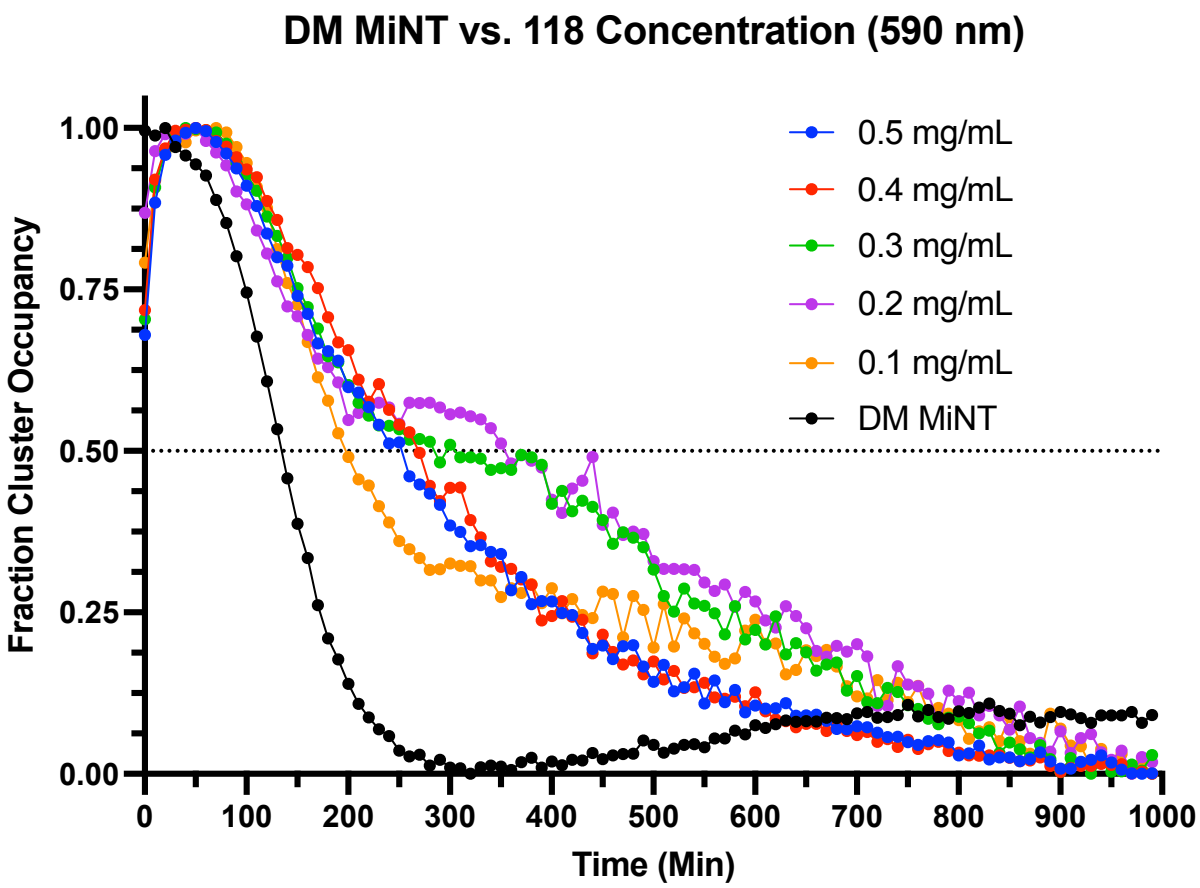

Figure 3.A17: Comparison of the UV/Vis decay curves of DM MiNT with 10% of each compound 118 concentration versus DM MiNT (10% DMSO) at 590 nm.

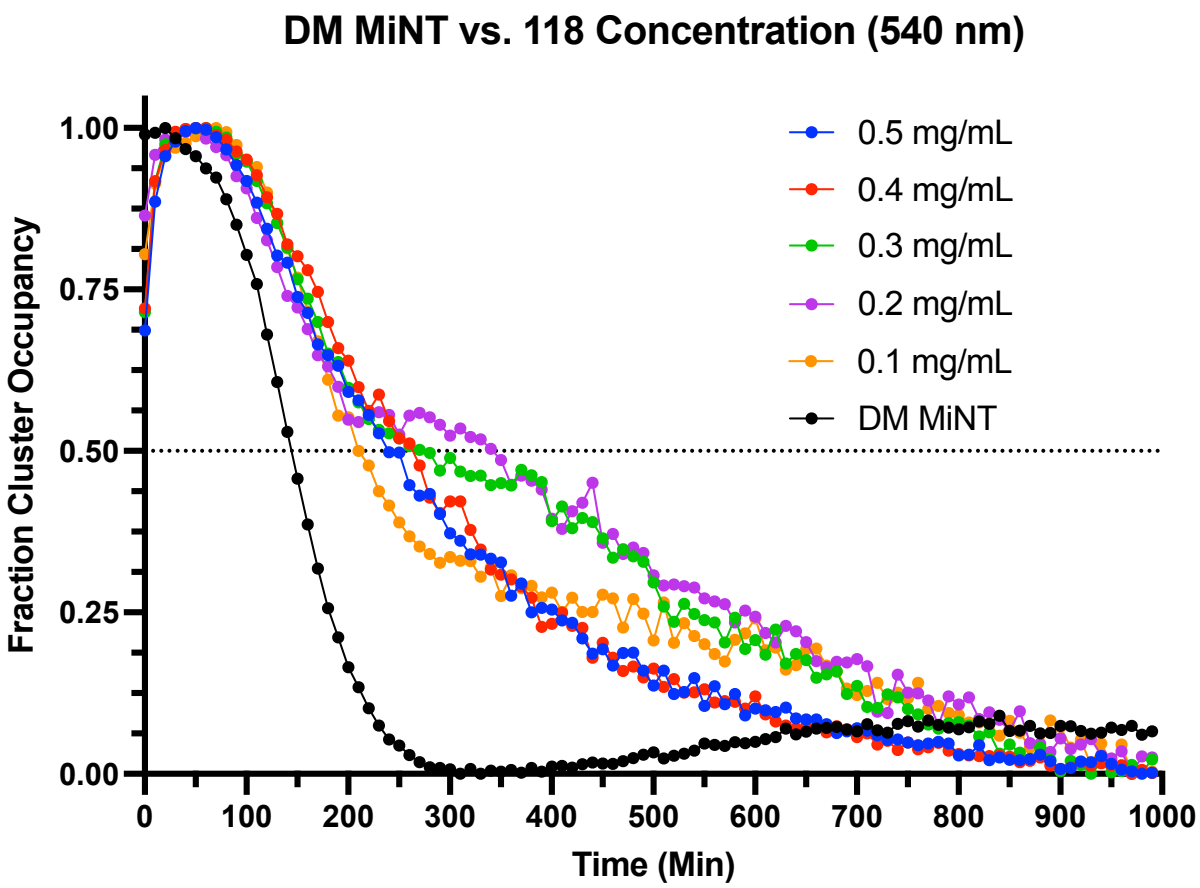

Figure 3.A18: Comparison of the UV/Vis decay curves of DM MiNT with 10% of each compound 118 concentration versus DM MiNT (10% DMSO) at 540 nm.

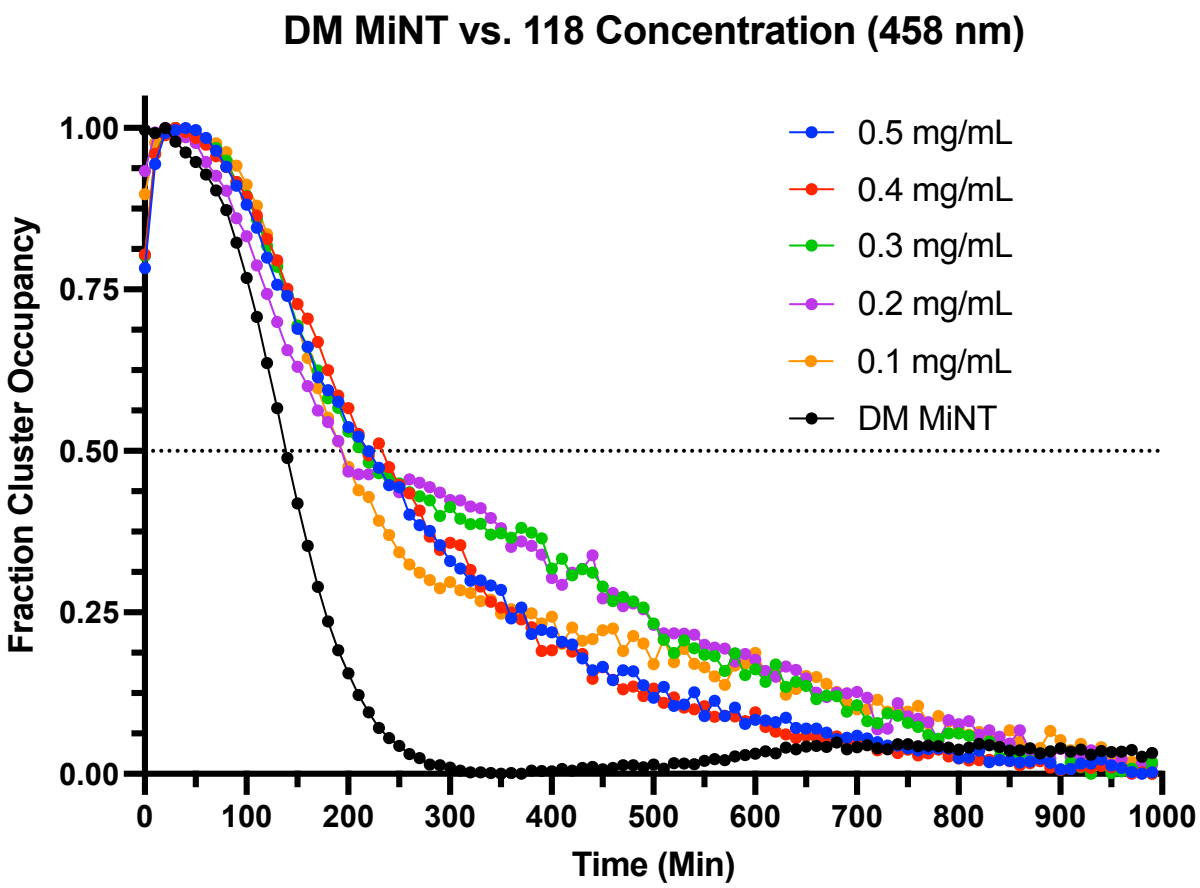

Figure 3.A19: Comparison of the UV/Vis decay curves of DM MiNT with 10% of each compound 118 concentration versus DM MiNT (10% DMSO) at 458 nm.

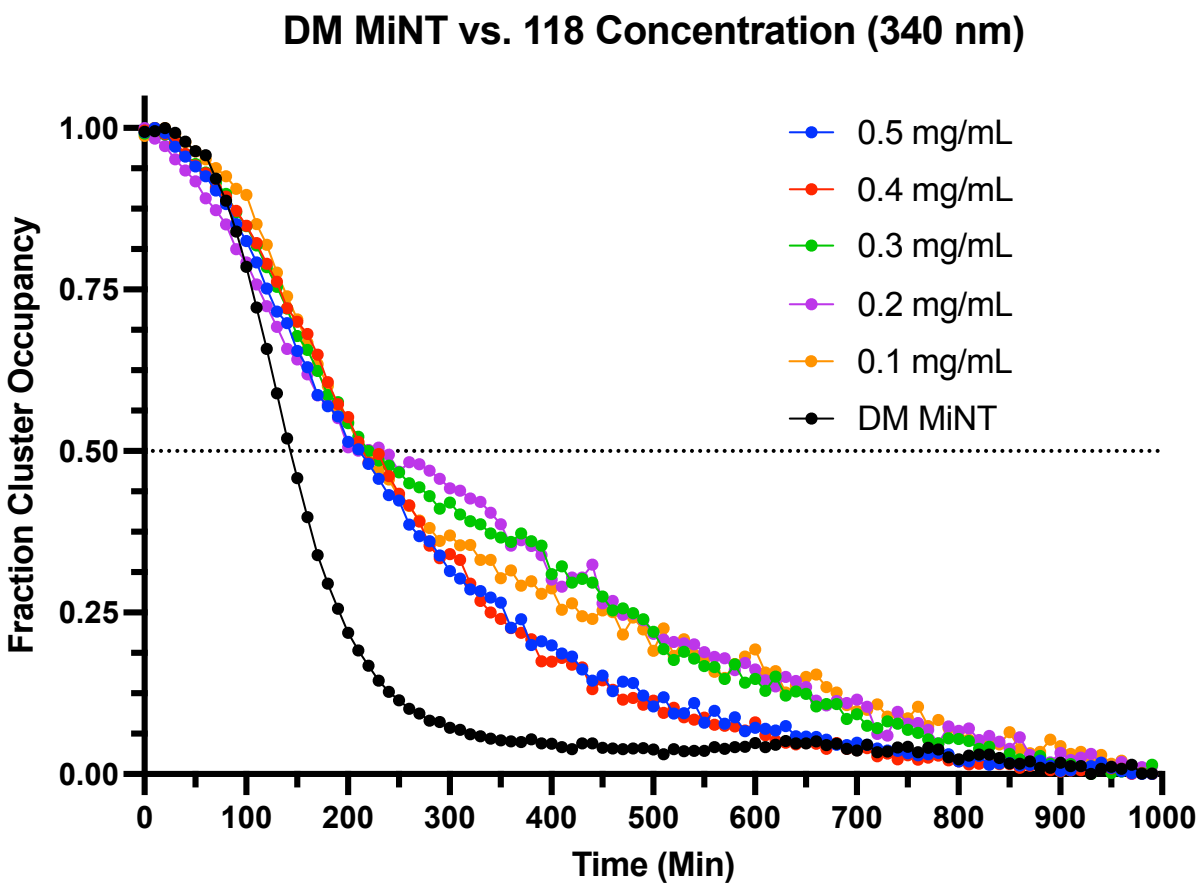

Figure 3.A20: Comparison of the UV/Vis decay curves of DM MiNT with 10% of each compound 118 concentration versus DM MiNT (10% DMSO) at 340 nm.

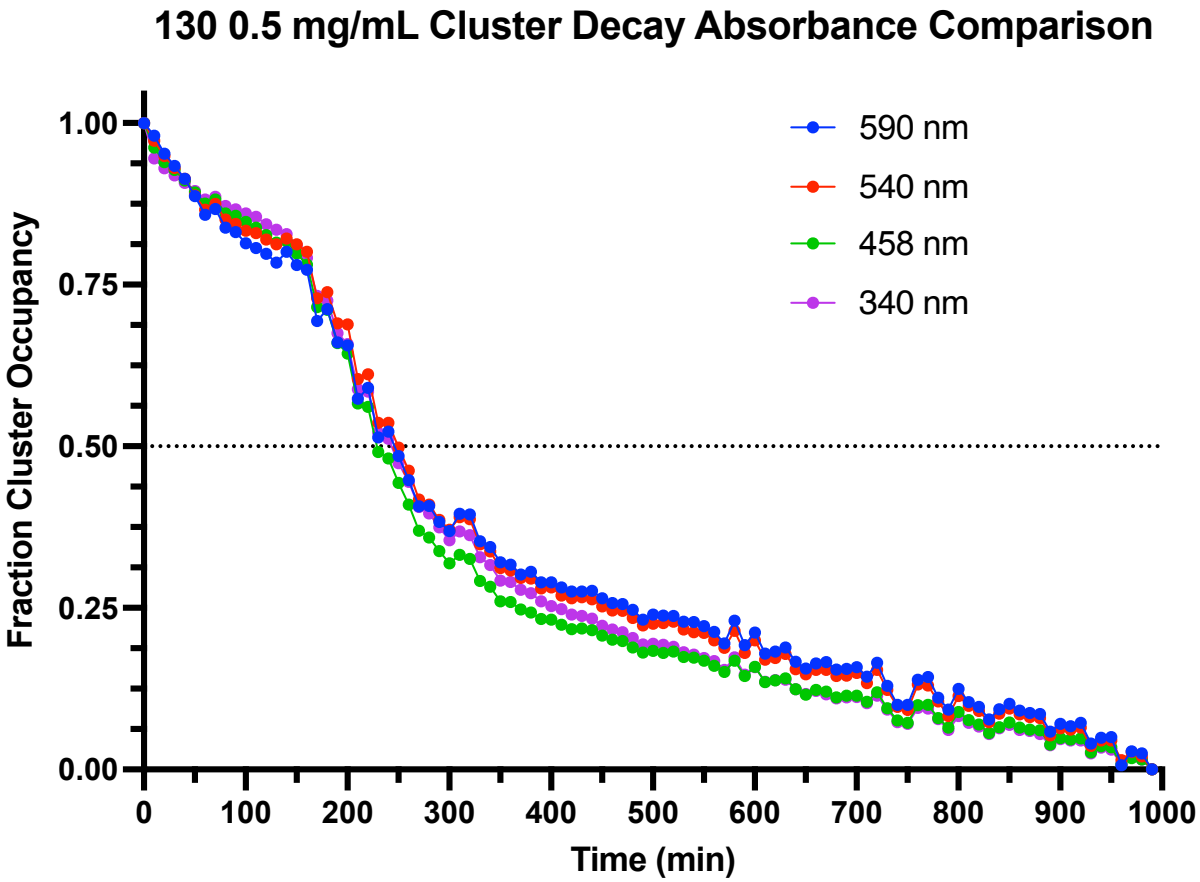

Figure 3.A21: UV/Vis decay curves of DM MiNT with 10% 0.5 mg/mL compound 130 at various wavelengths.

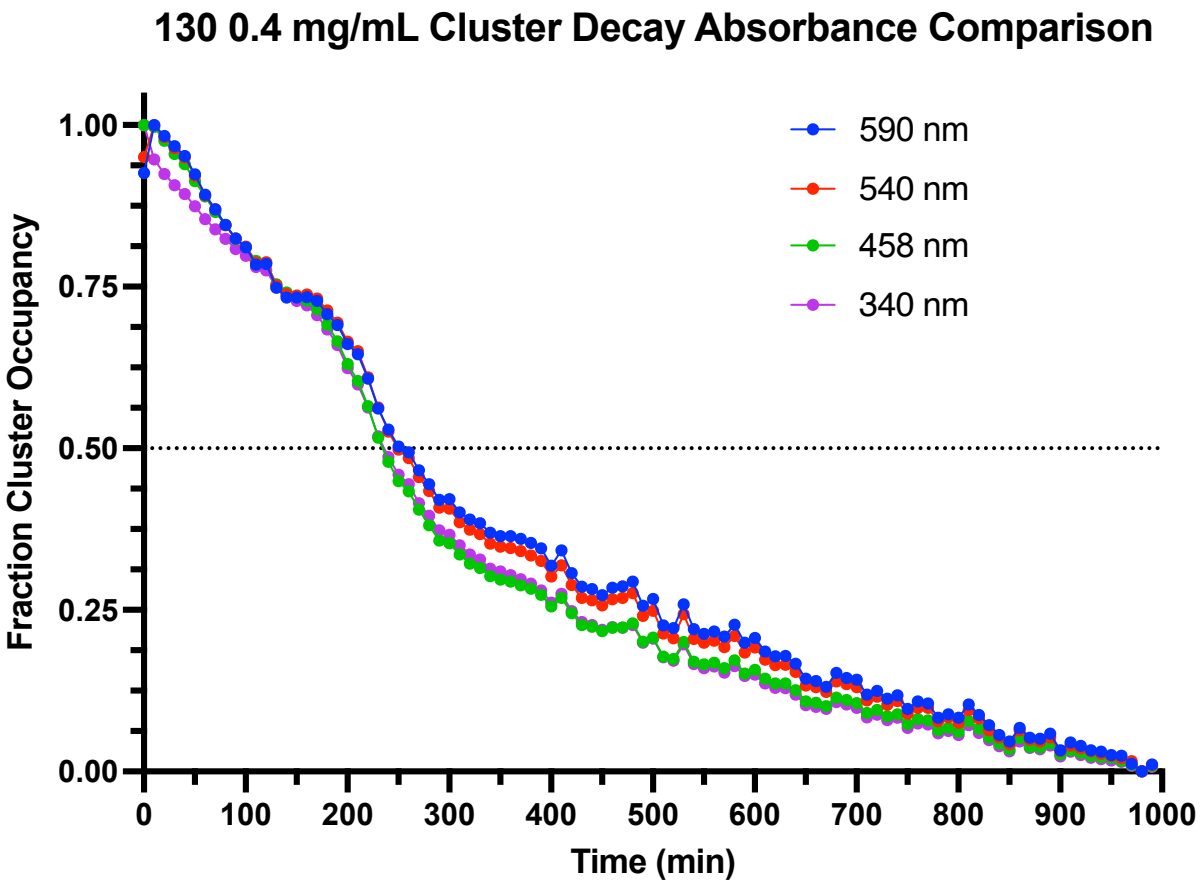

Figure 3.A22: UV/Vis decay curves of DM MiNT with 10% 0.4 mg/mL compound 130 at various wavelengths.

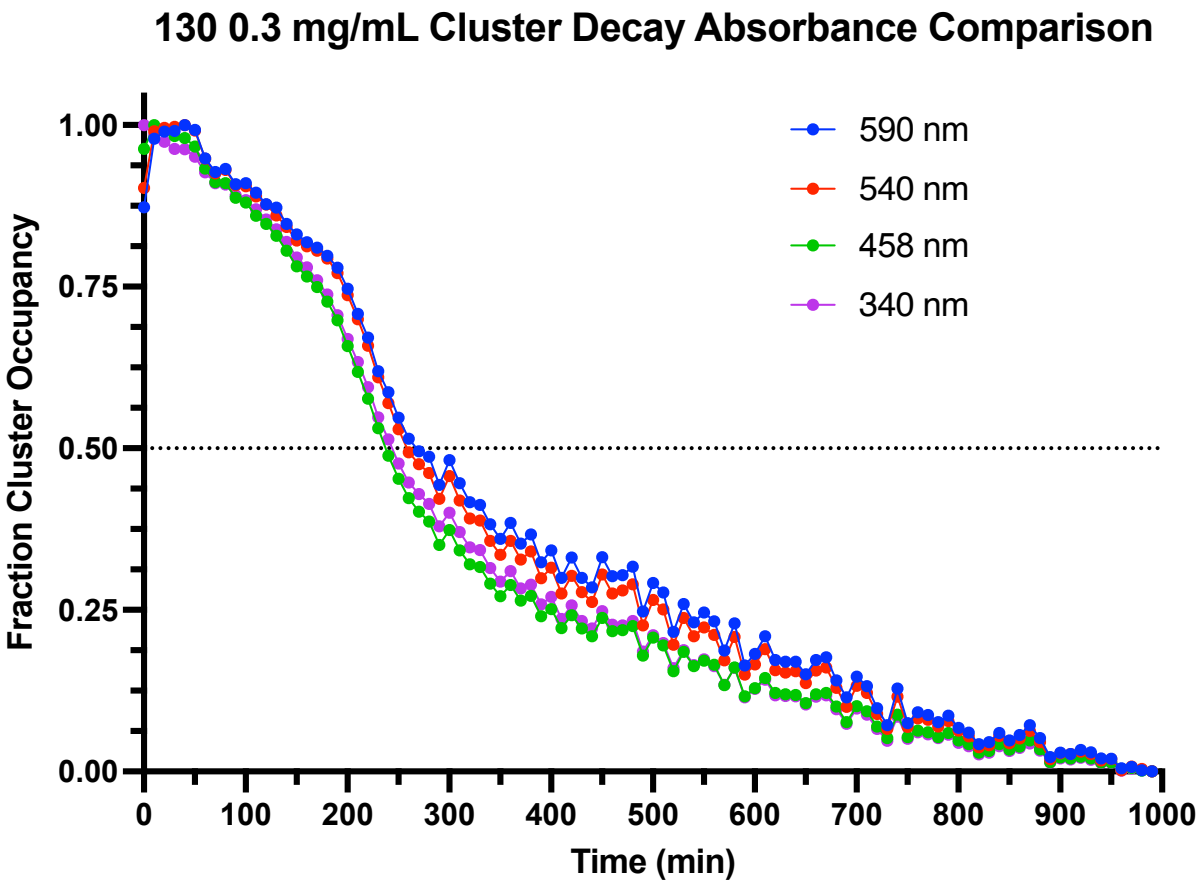

Figure 3.A23: UV/Vis decay curves of DM MiNT with 10% 0.3 mg/mL compound 130 at various wavelengths.

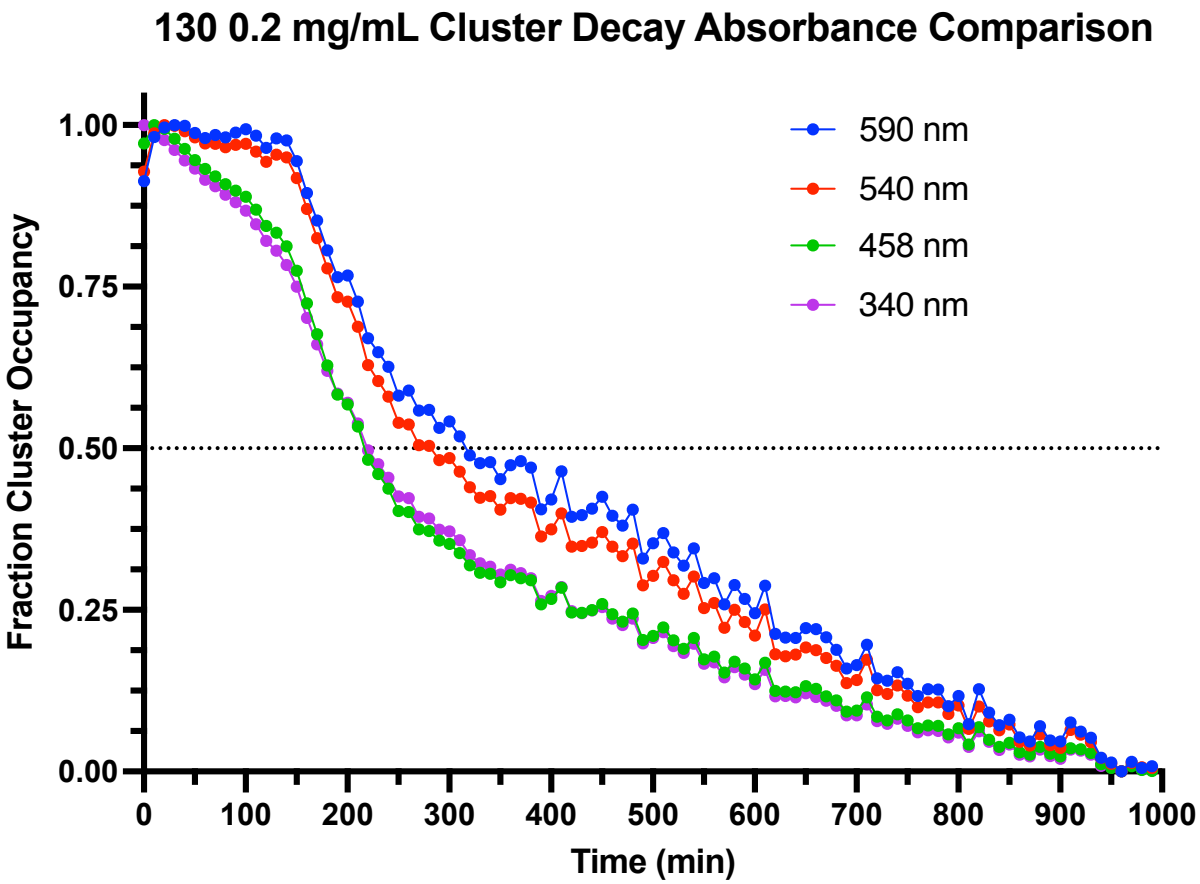

Figure 3.A24: UV/Vis decay curves of DM MiNT with 10% 0.2 mg/mL compound 130 at various wavelengths.

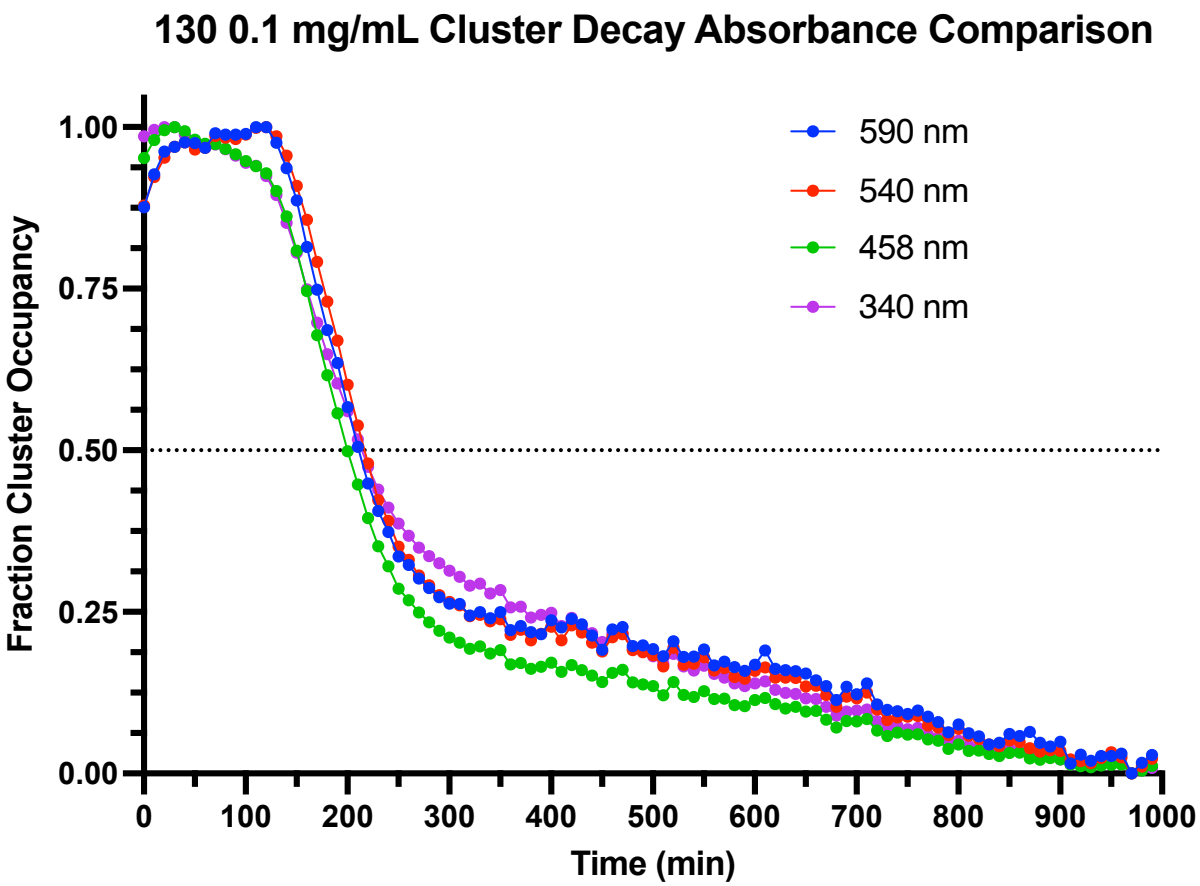

Figure 3.A25: UV/Vis decay curves of DM MiNT with 10% 0.1 mg/mL compound 130 at various wavelengths.

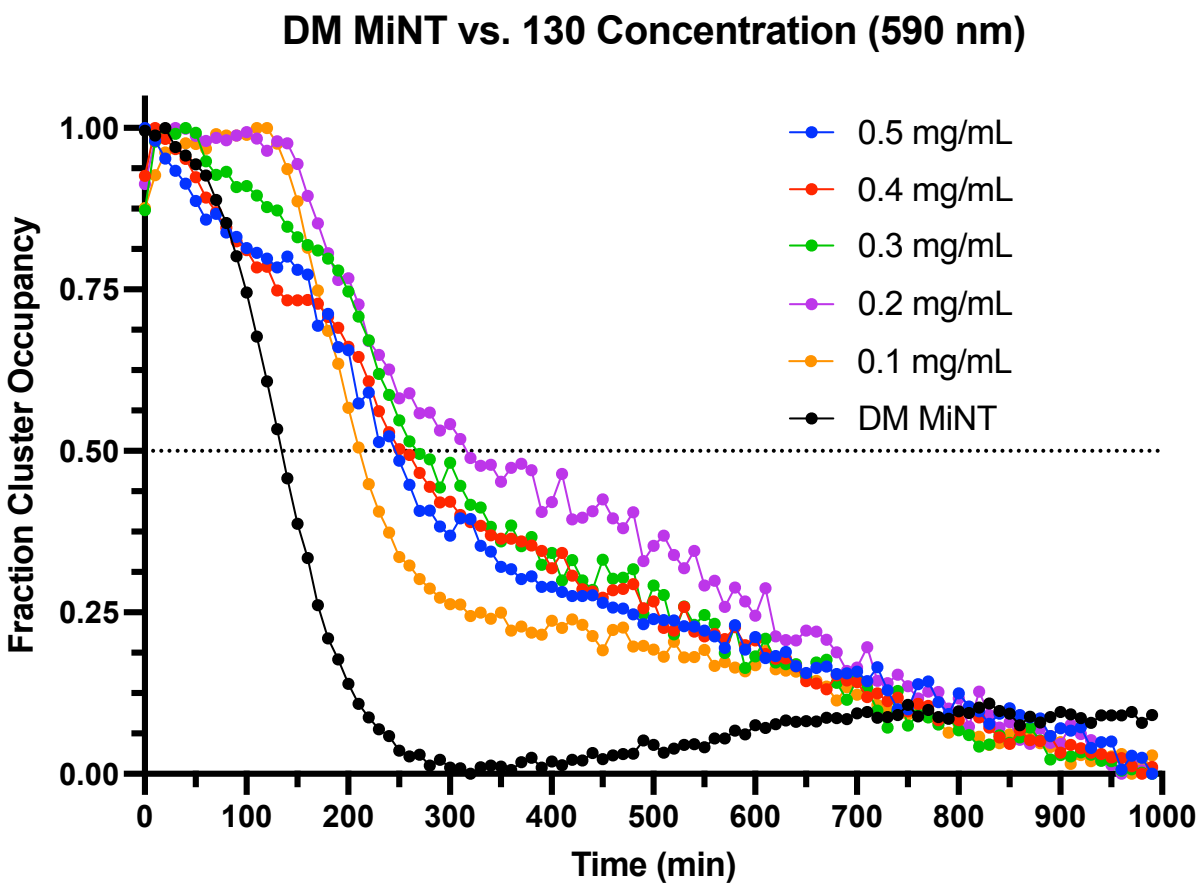

Figure 3.A26: Comparison of the UV/Vis decay curves of DM MiNT with 10% of each compound 130 concentration versus DM MiNT (10% DMSO) at 590 nm.

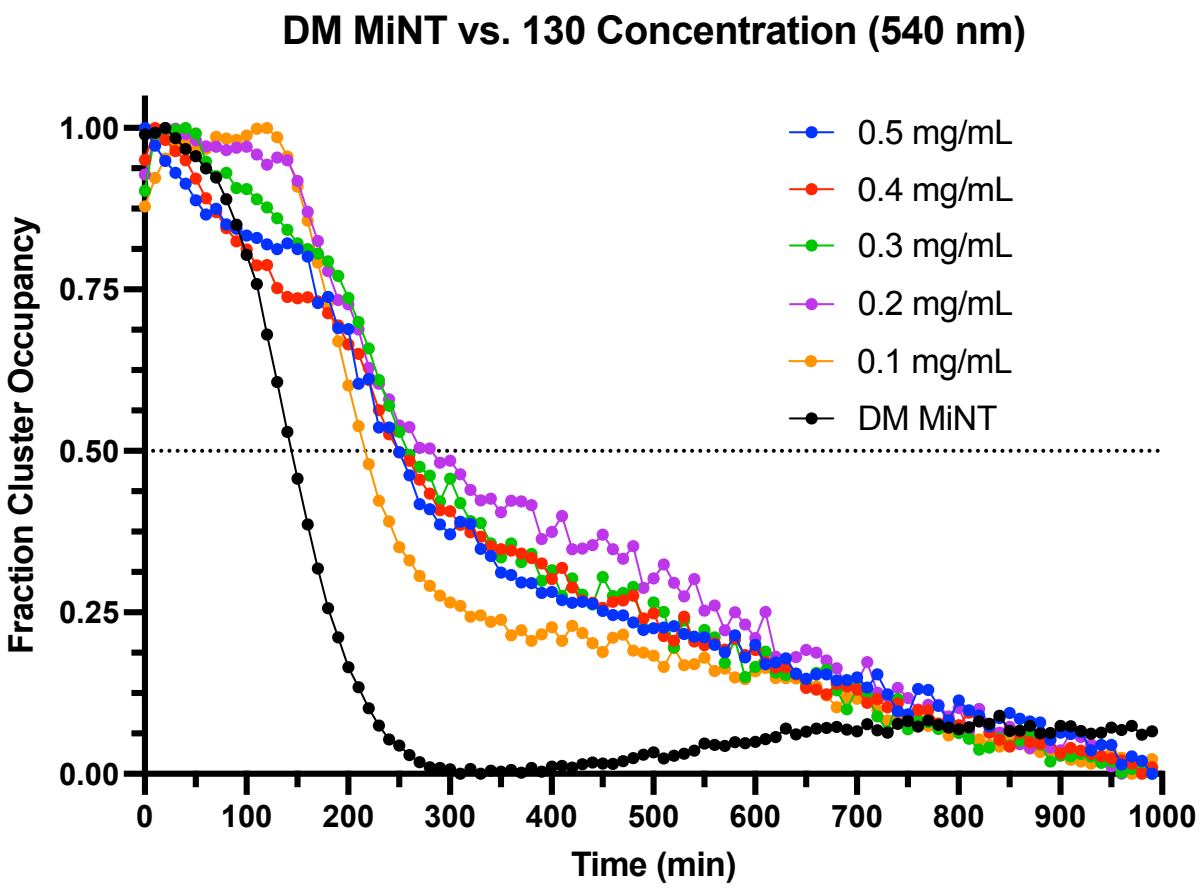

Figure 3.A27: Comparison of the UV/Vis decay curves of DM MiNT with 10% of each compound 130 concentration versus DM MiNT (10% DMSO) at 540 nm.

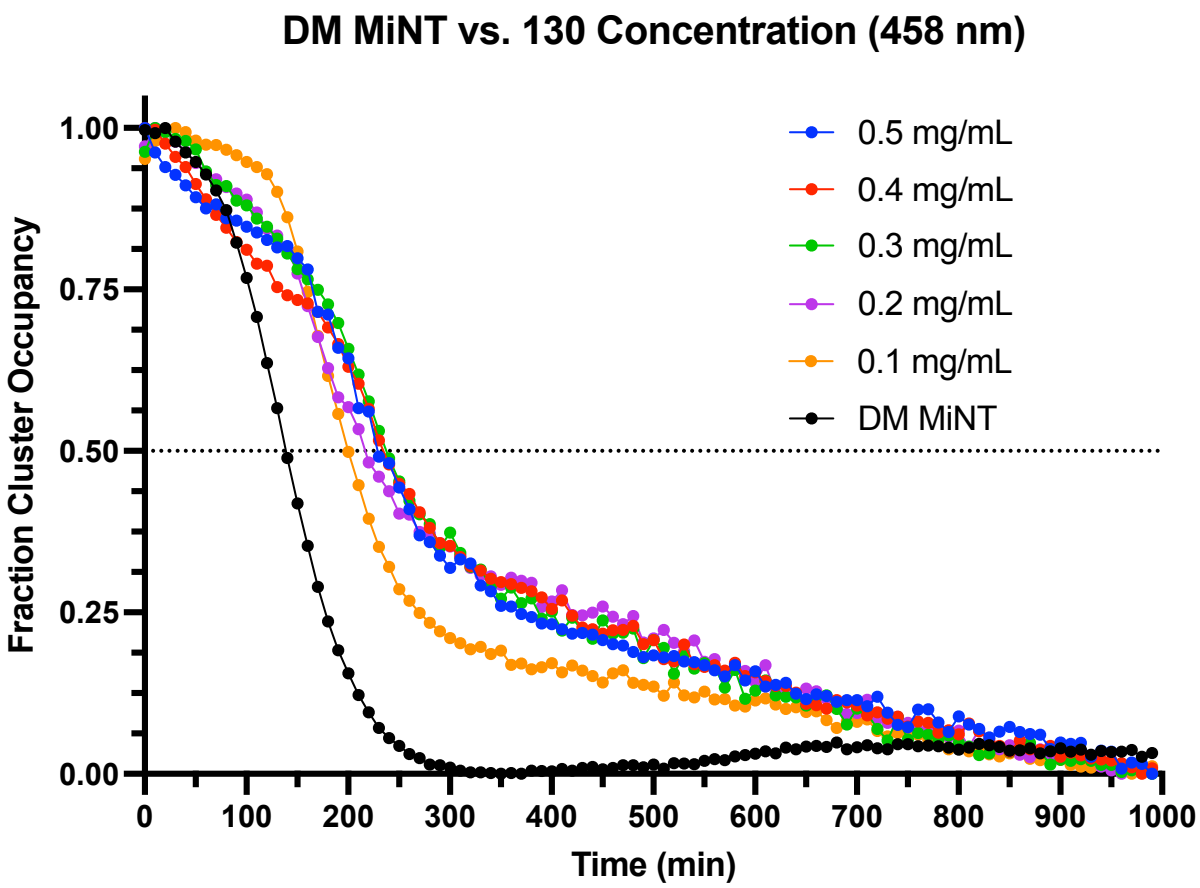

Figure 3.A28: Comparison of the UV/Vis decay curves of DM MiNT with 10% of each compound 130 concentration versus DM MiNT (10% DMSO) at 458 nm.

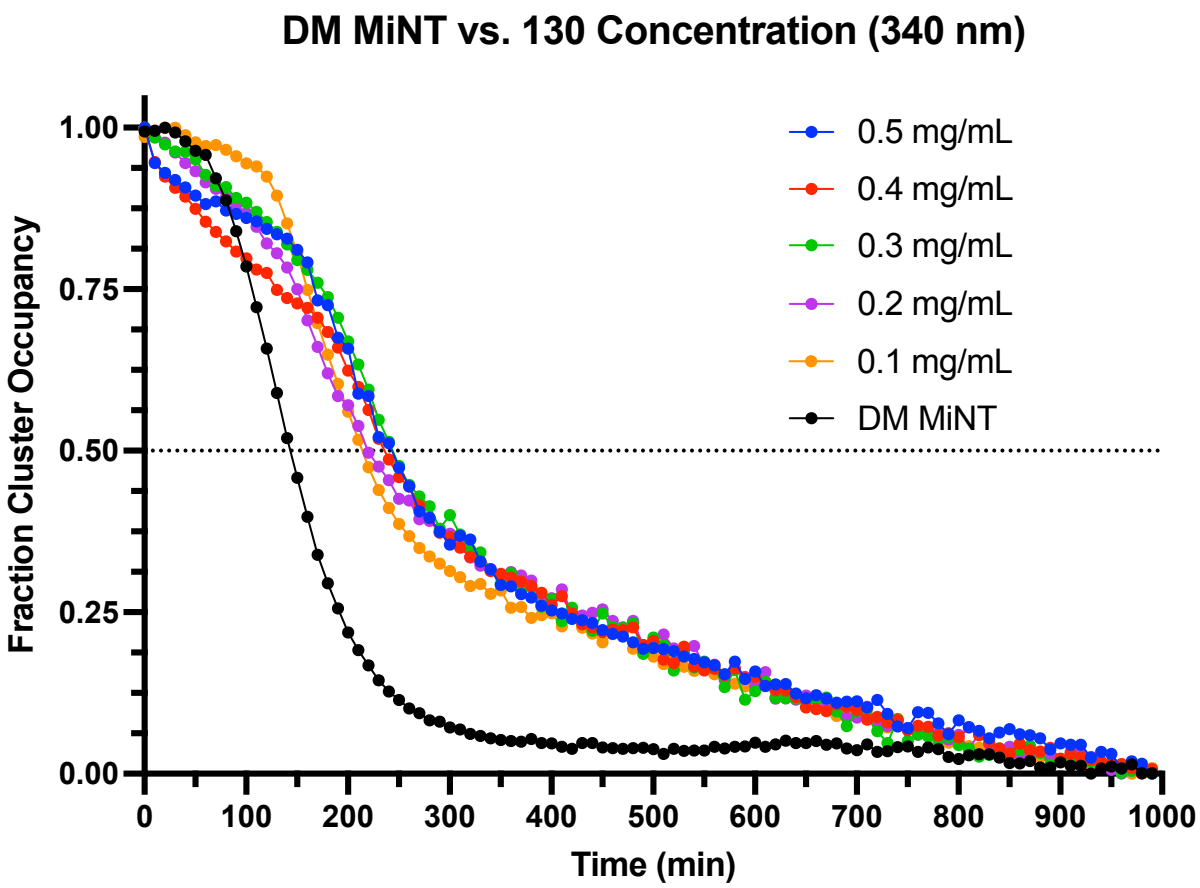

Figure 3.A29: Comparison of the UV/Vis decay curves of DM MiNT with 10% of each compound 130 concentration at 340 nm.

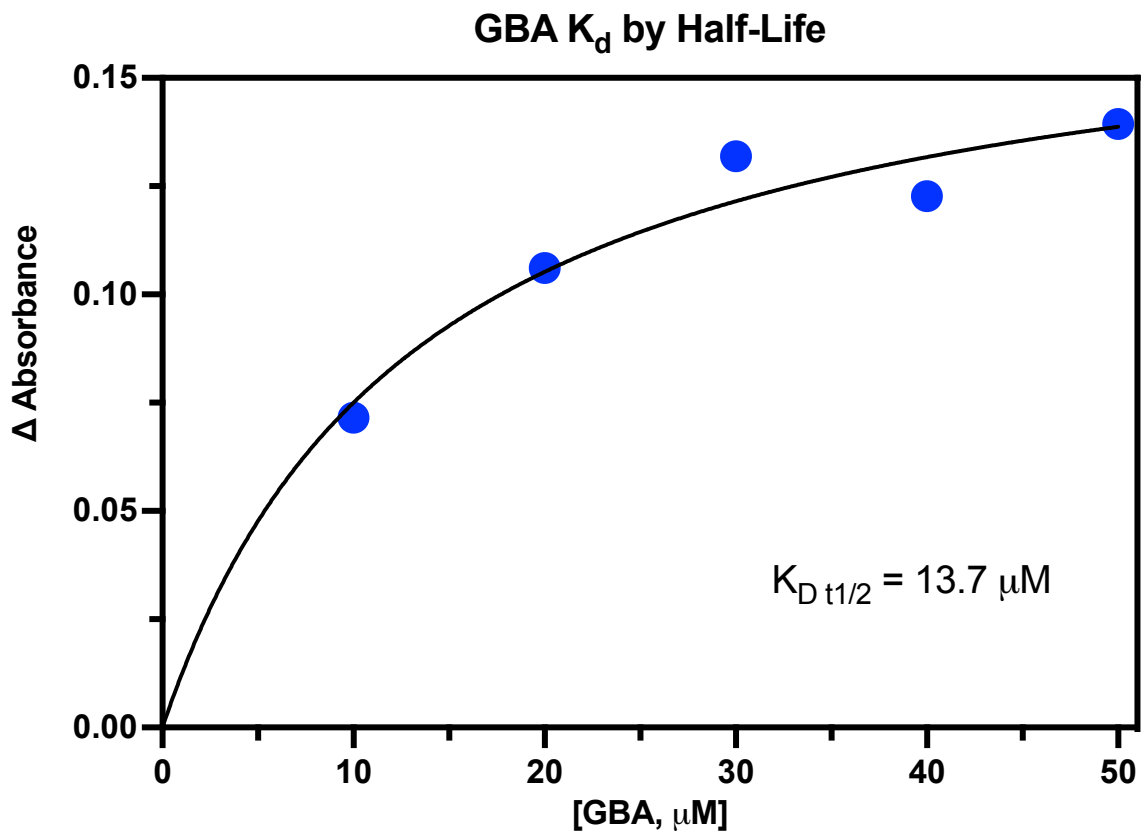

Figure 3.A30: Binding constant for GBA with DM MiNT calculated by half-life.

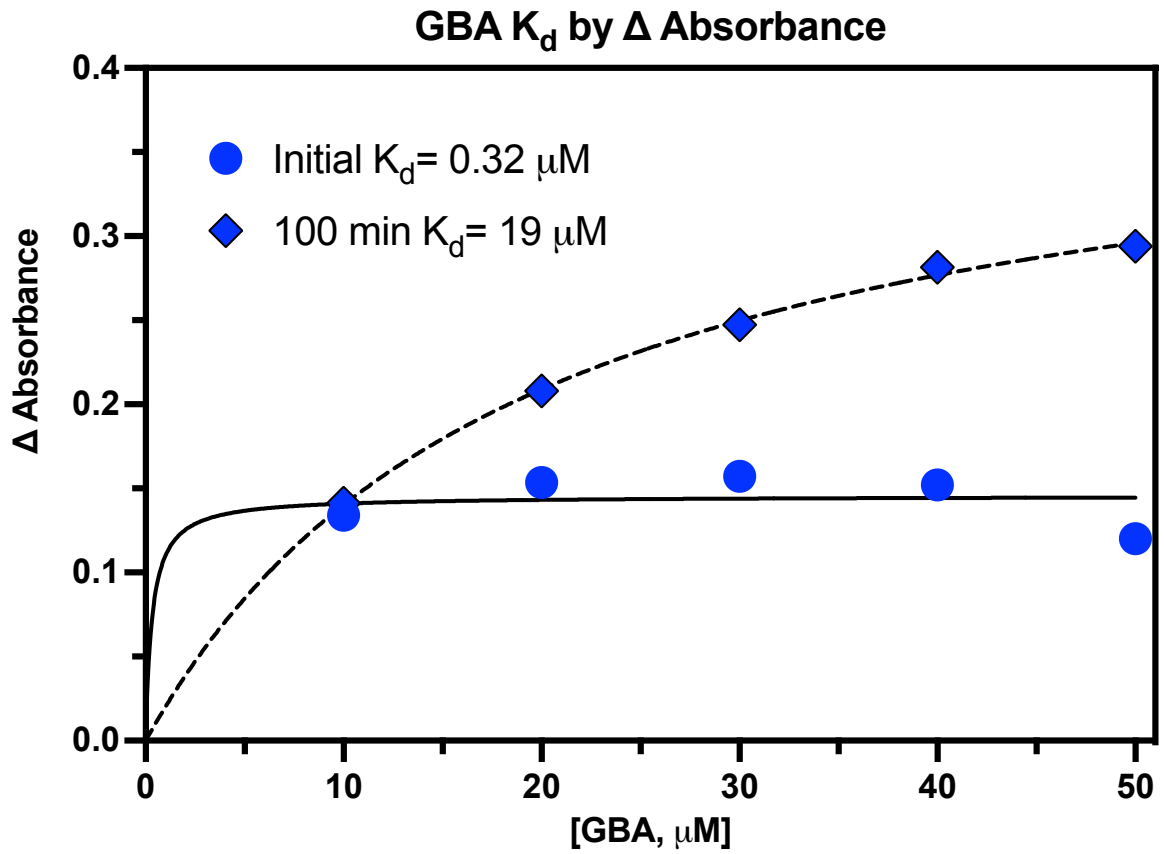

Figure 3.A31: Binding constant for GBA with DM MiNT calculated by change in absorbance.

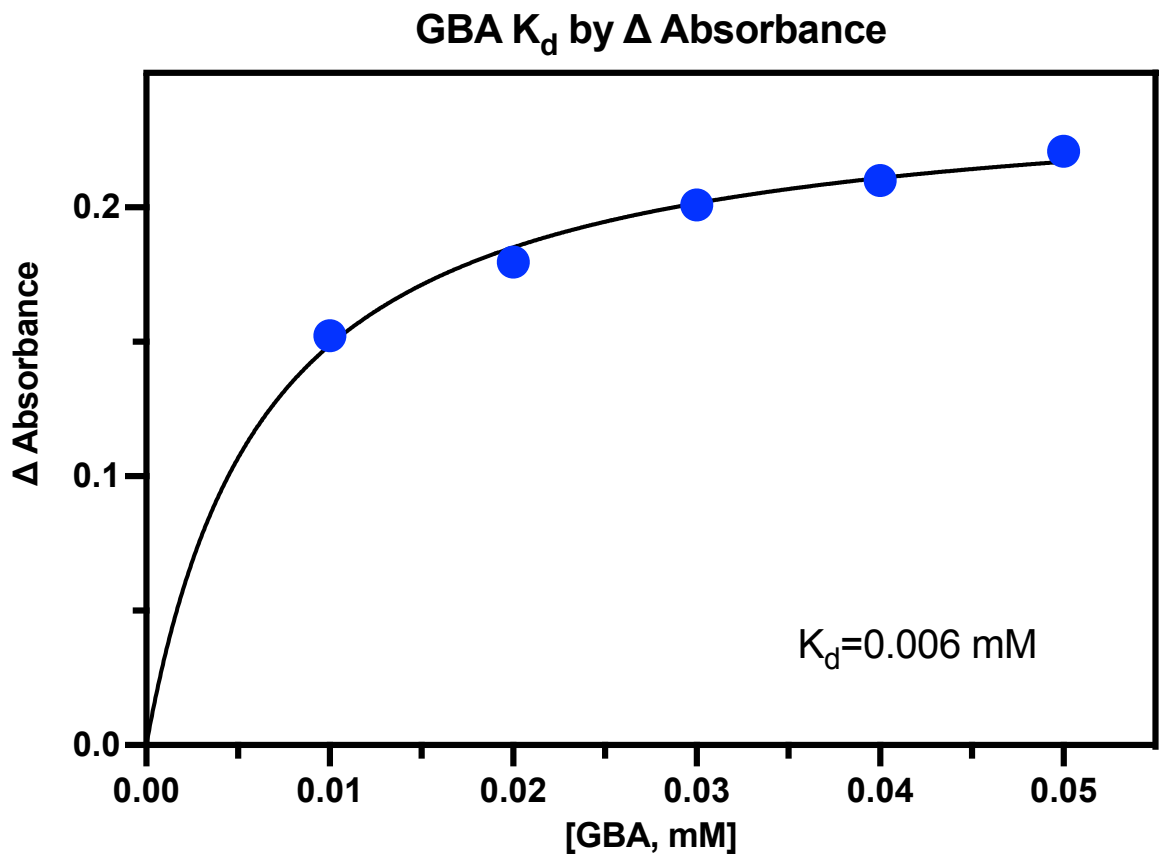

Figure 3.A32: Binding constant for GBA with DM MiNT calculated by absorbance omitting hyperchromicity.

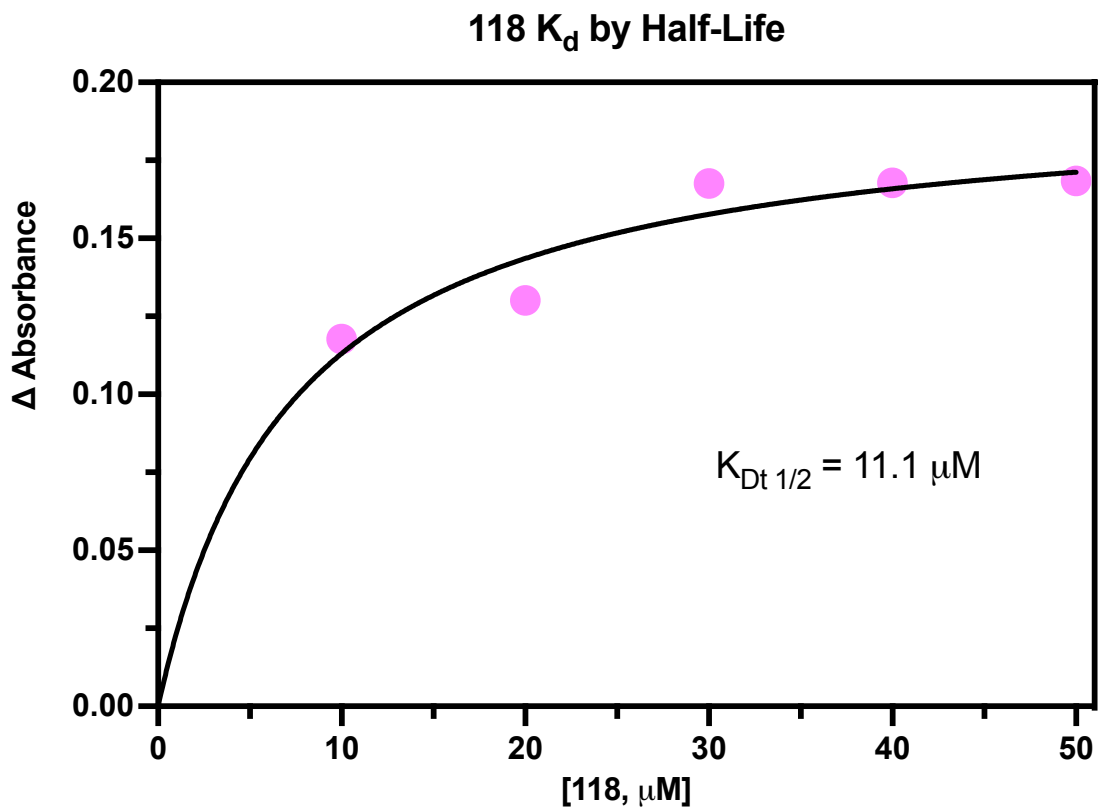

Figure 3.A33: Binding constant for 118 with DM MiNT calculated by half-life.

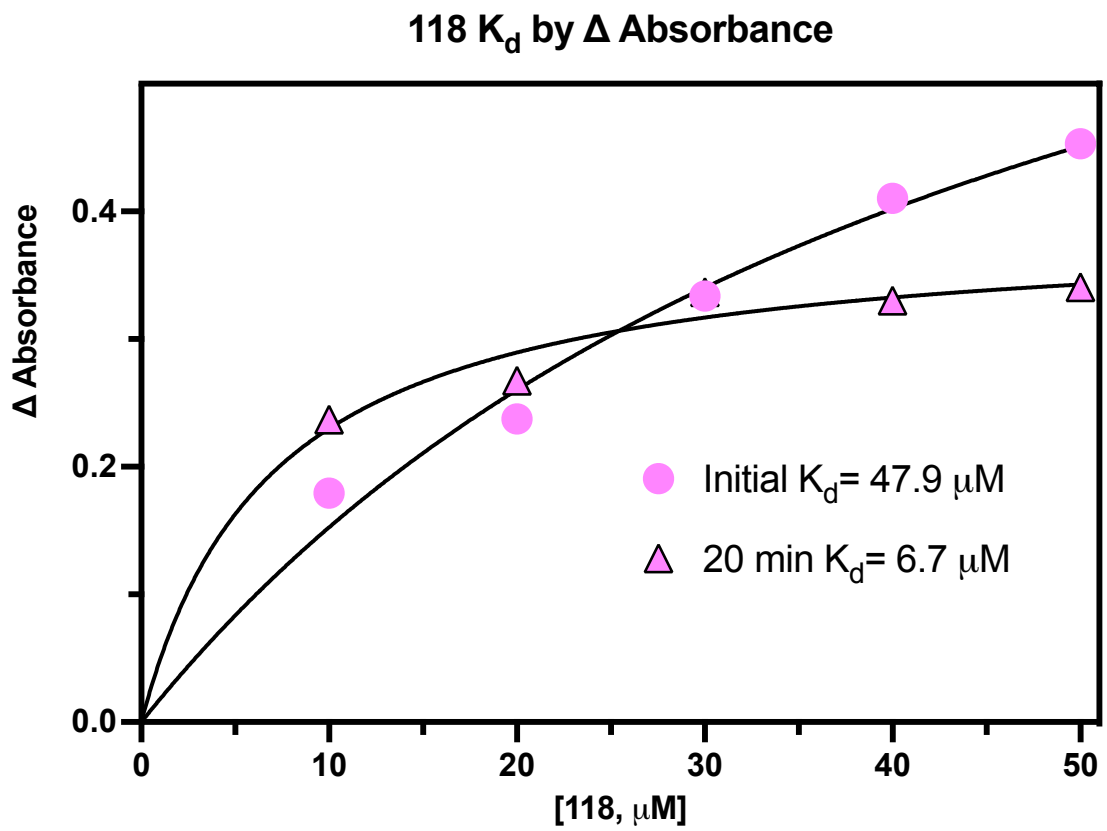

Figure 3.A34: Binding constant for 118 with DM MiNT calculated by change in absorbance.

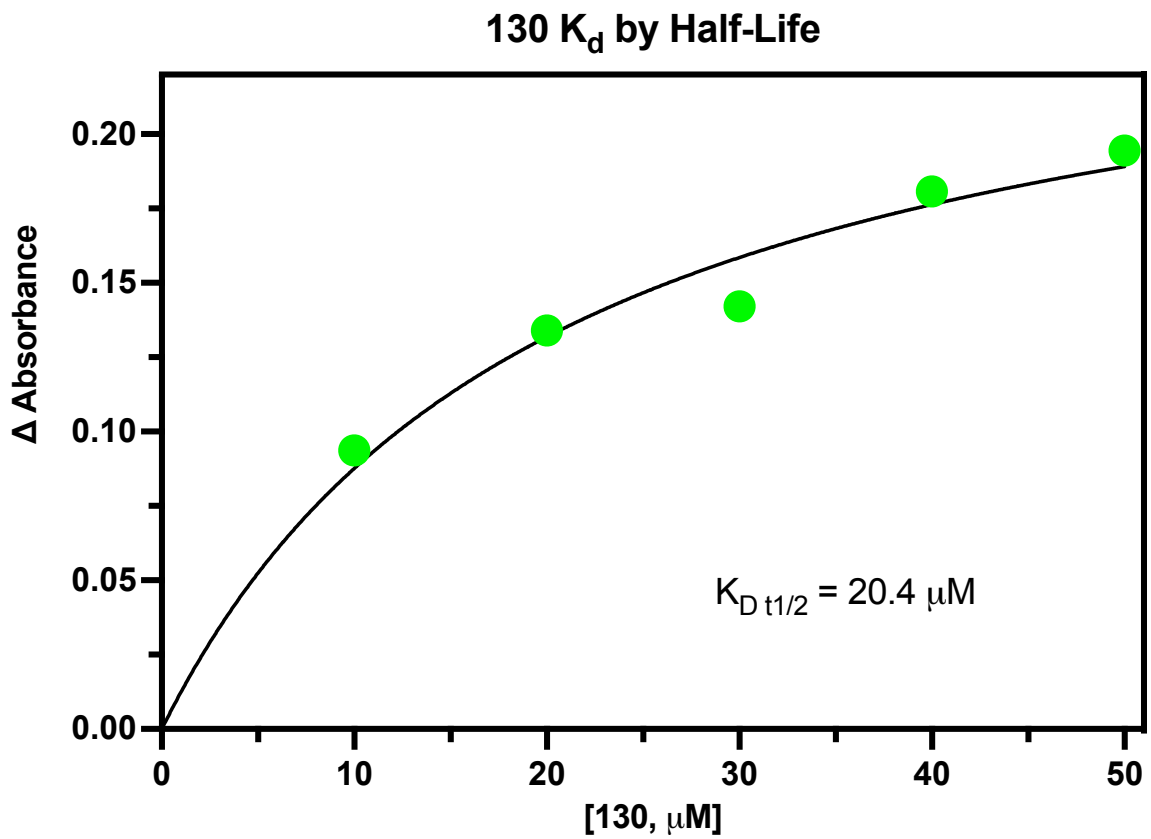

Figure 3.A35: Binding constant for 130 with DM MiNT calculated by half-life.

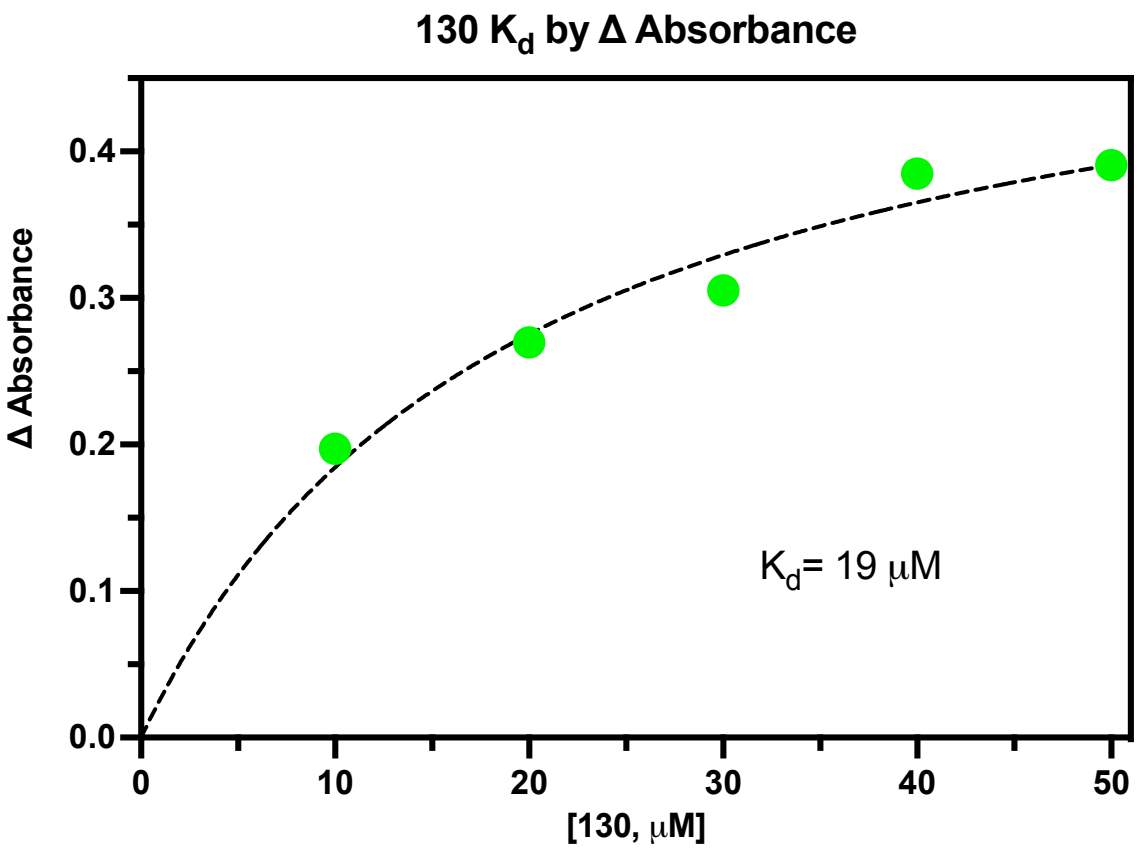

Figure 3.A36: Binding constant for 130 with DM MiNT calculated by change in absorbance.

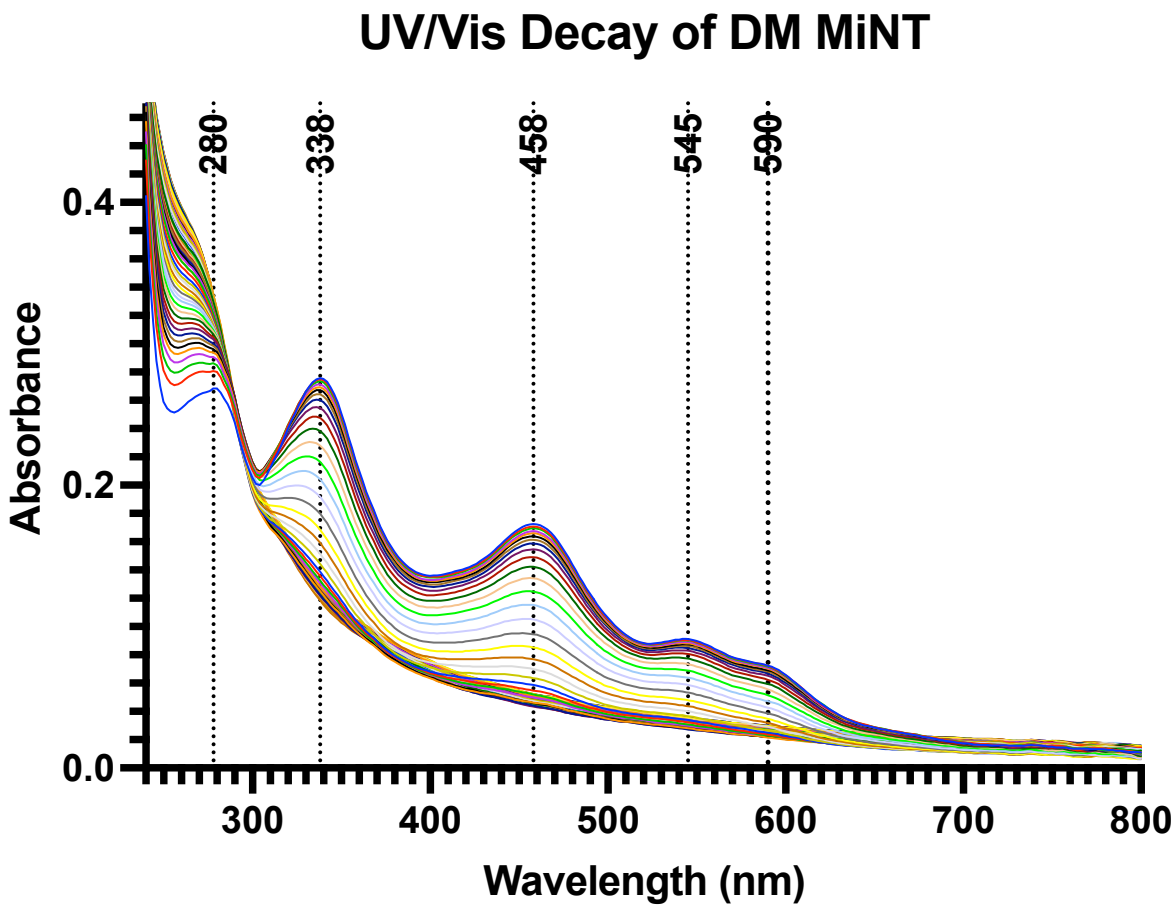

Figure 3.A37: UV/Vis decay of DM MiNT (200-800 nm).

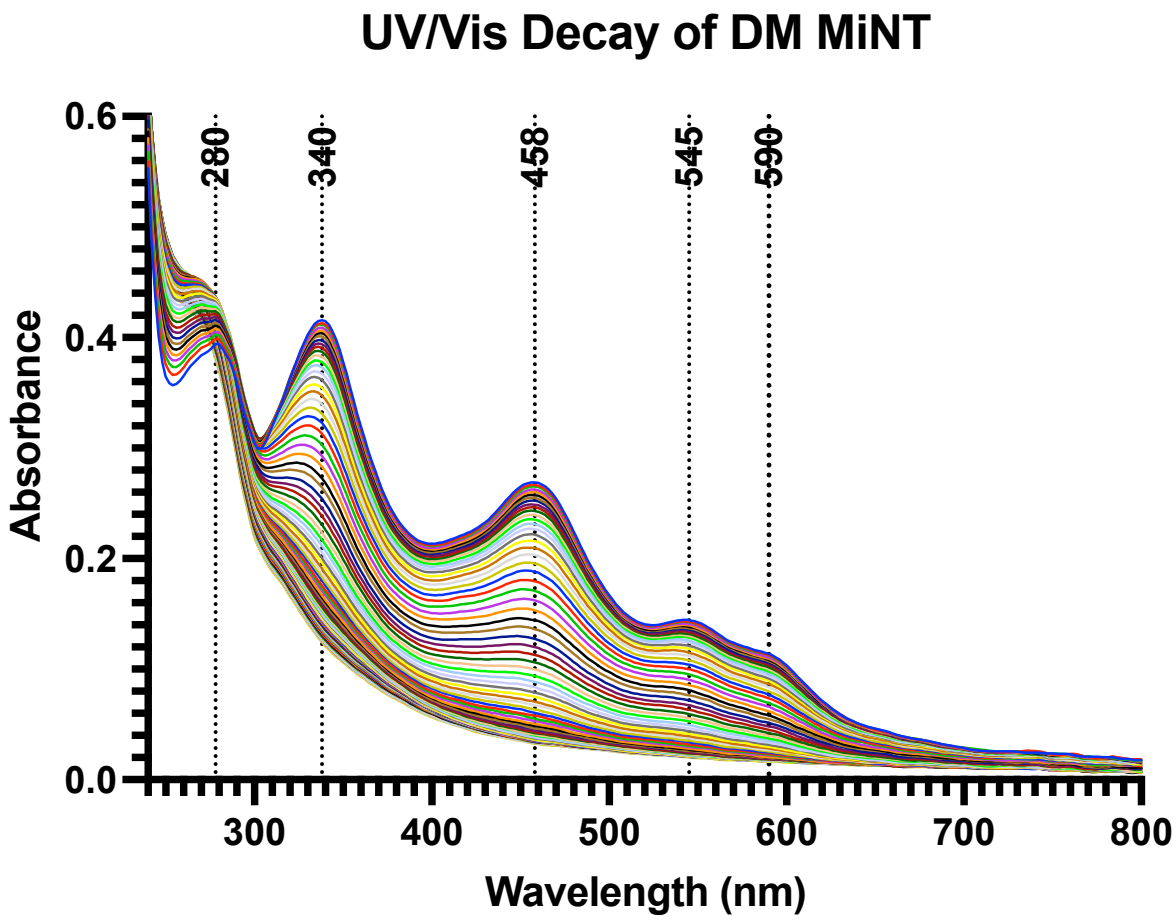

Figure 3.A38: Replicate UV/Vis decay of DM MiNT (200-800 nm).

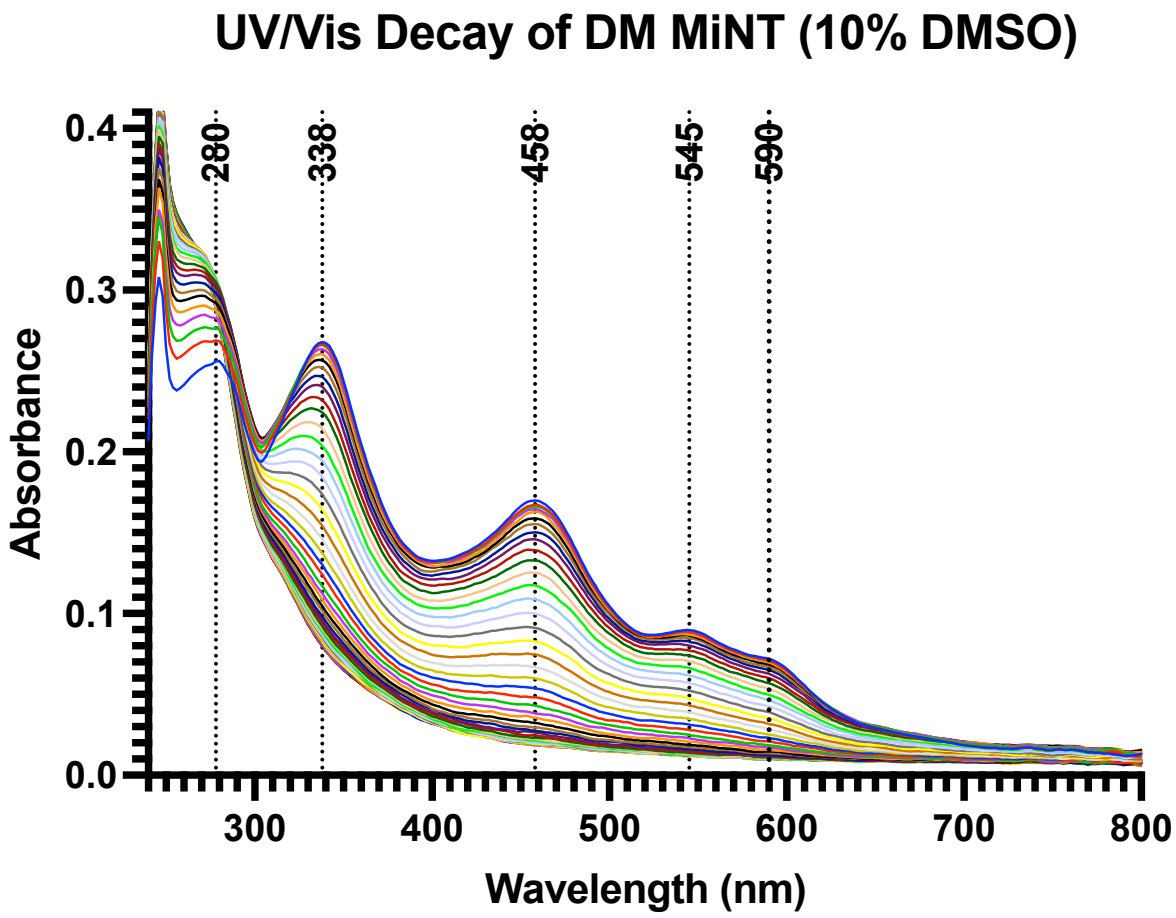

Figure 3.A39: UV/Vis decay of DM MiNT with 10% DMSO (200-800 nm).

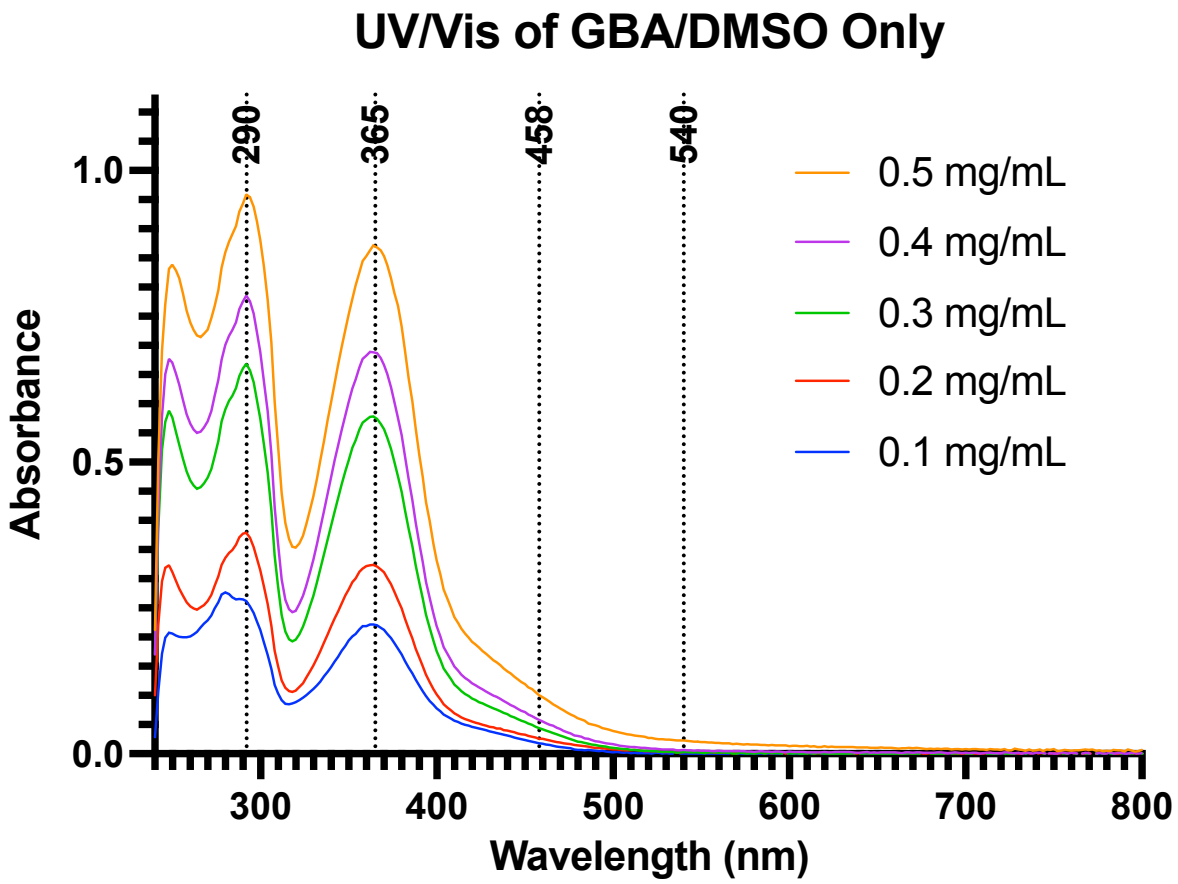

Figure 3.A40: UV/Vis of SEC buffer with 10% GBA in DMSO at various concentrations (200-800 nm).

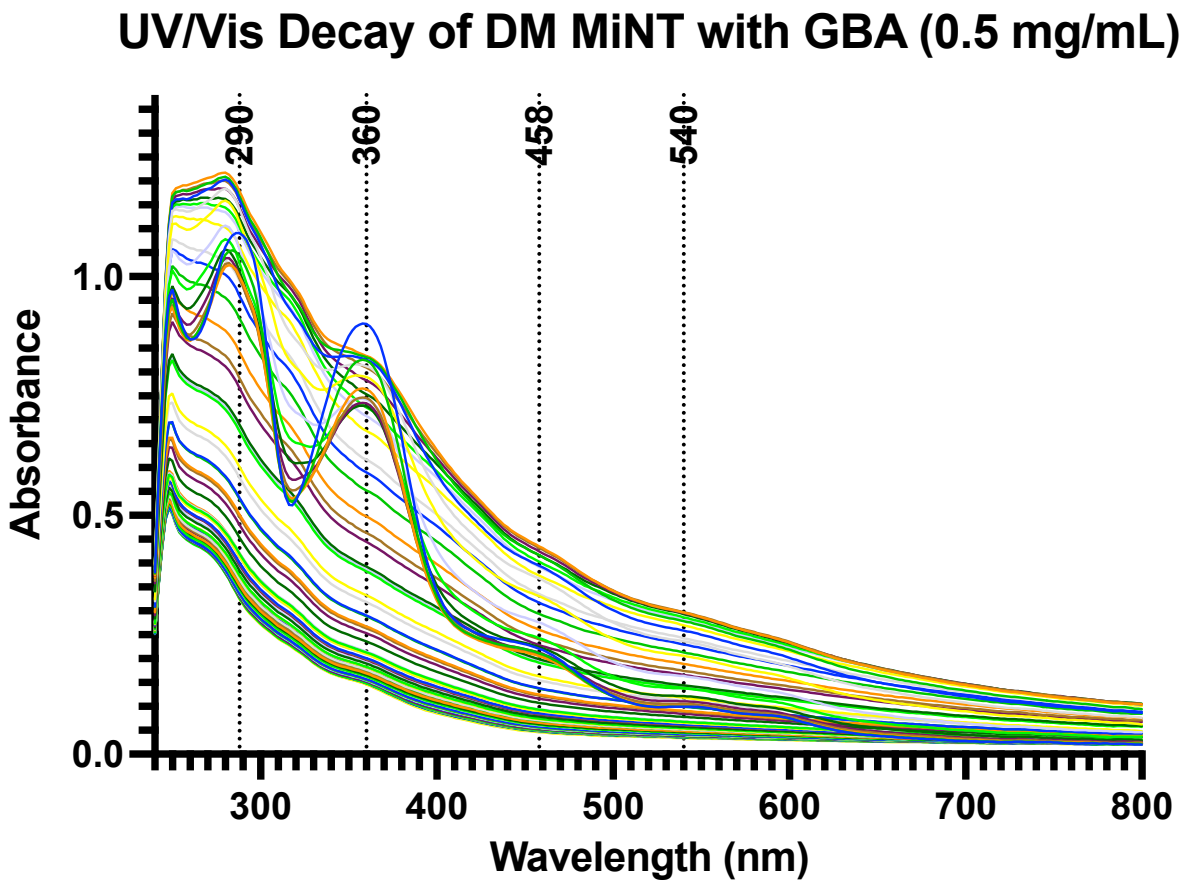

Figure 3.A41: UV/Vis decay of DM MiNT with 10% GBA in DMSO at 0.5 mg/mL (200-800 nm).

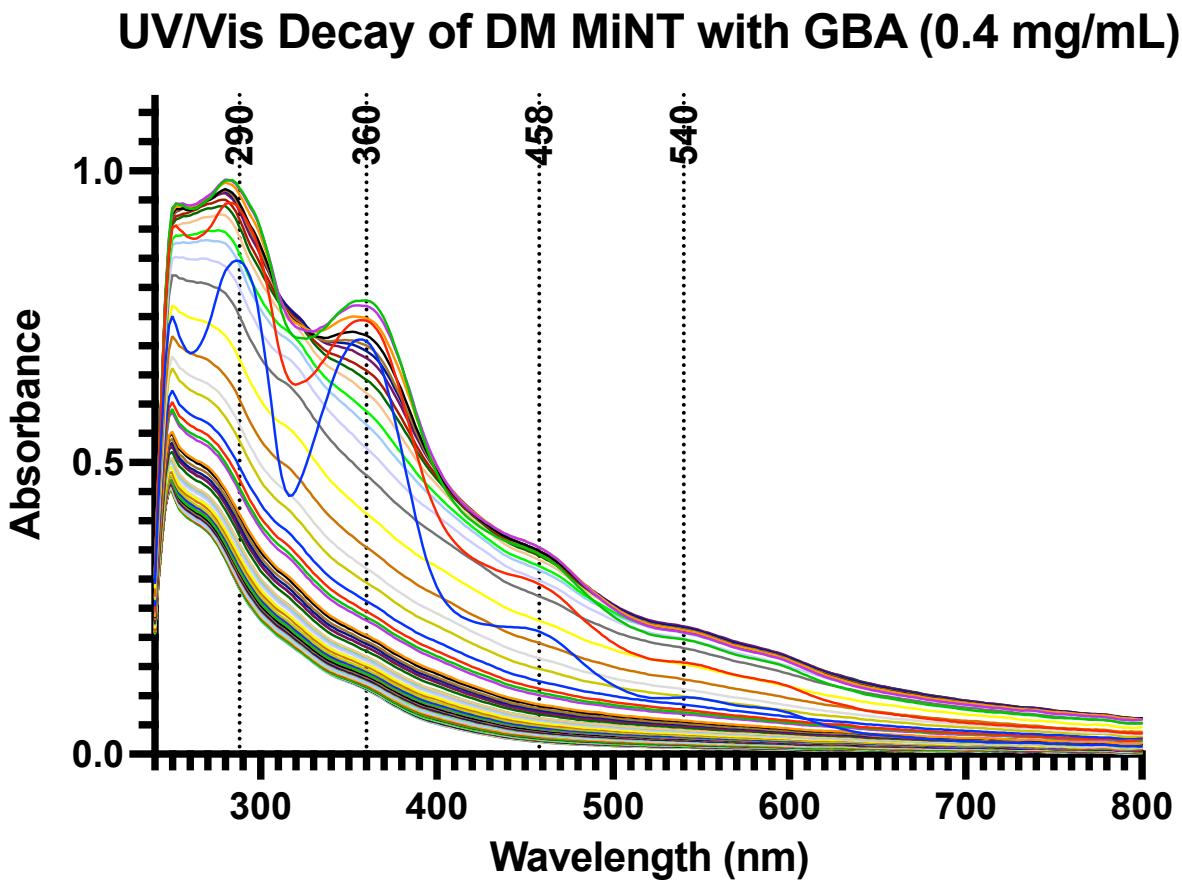

Figure 3.A42: UV/Vis decay of DM MiNT with 10% GBA in DMSO at 0.4 mg/mL (200-800 nm).

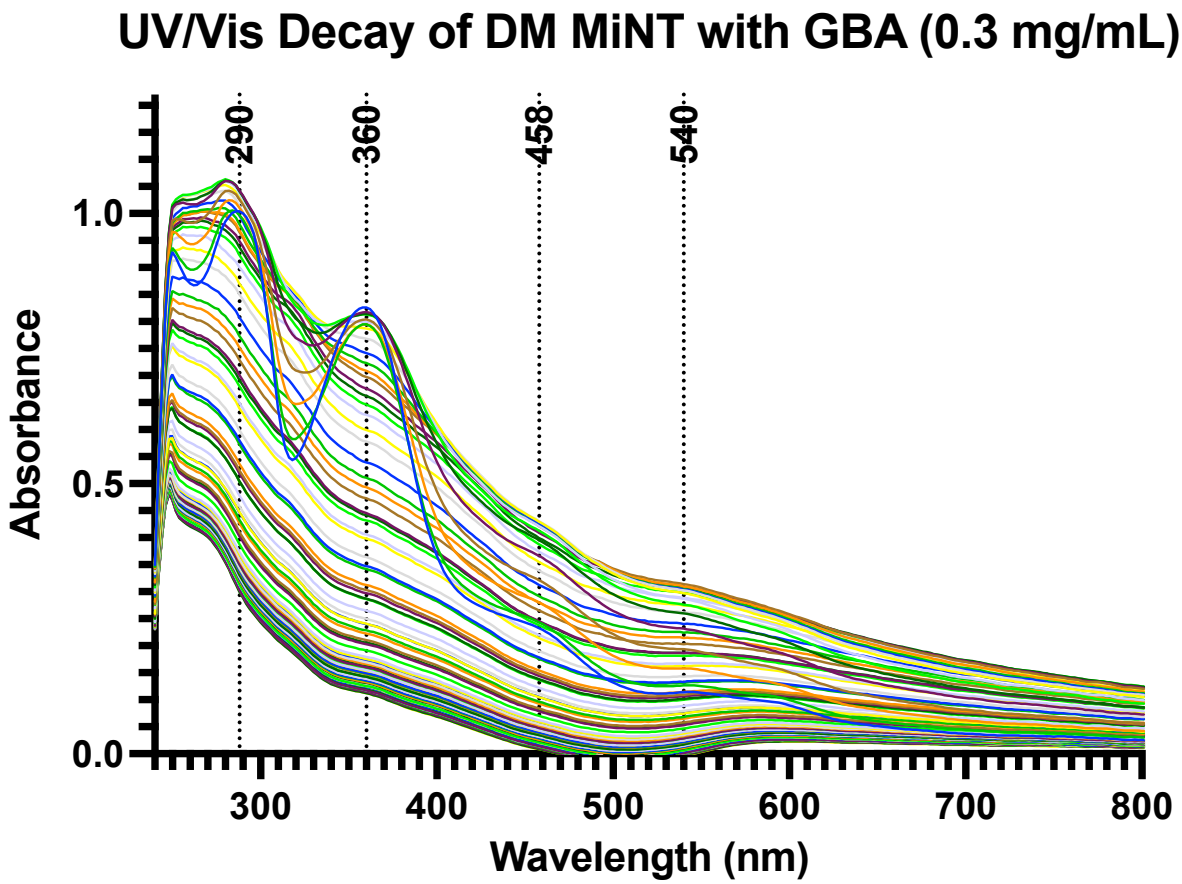

Figure 3.A43: UV/Vis decay of DM MiNT with 10% GBA in DMSO at 0.3 mg/mL (200-800 nm).

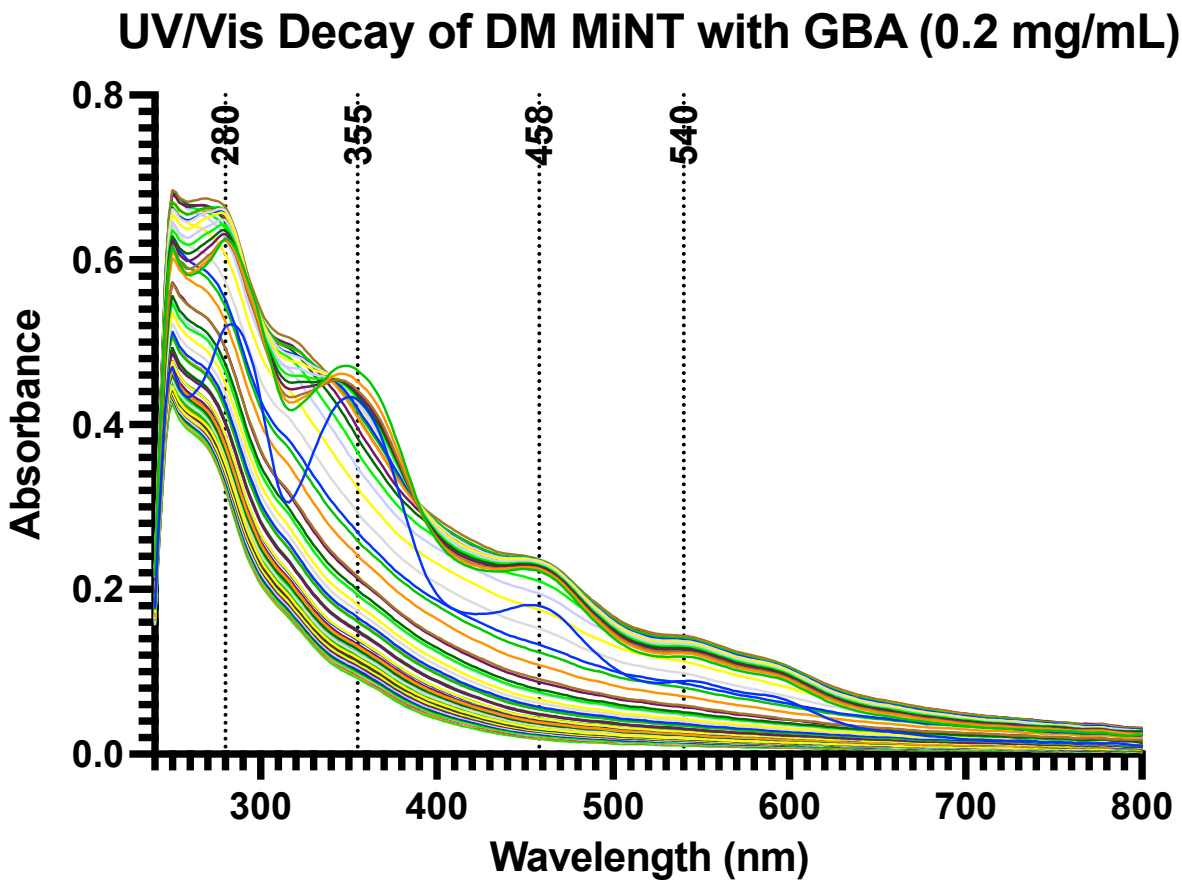

Figure 3.A44: UV/Vis decay of DM MiNT with 10% GBA in DMSO at 0.2 mg/mL (200-800 nm).

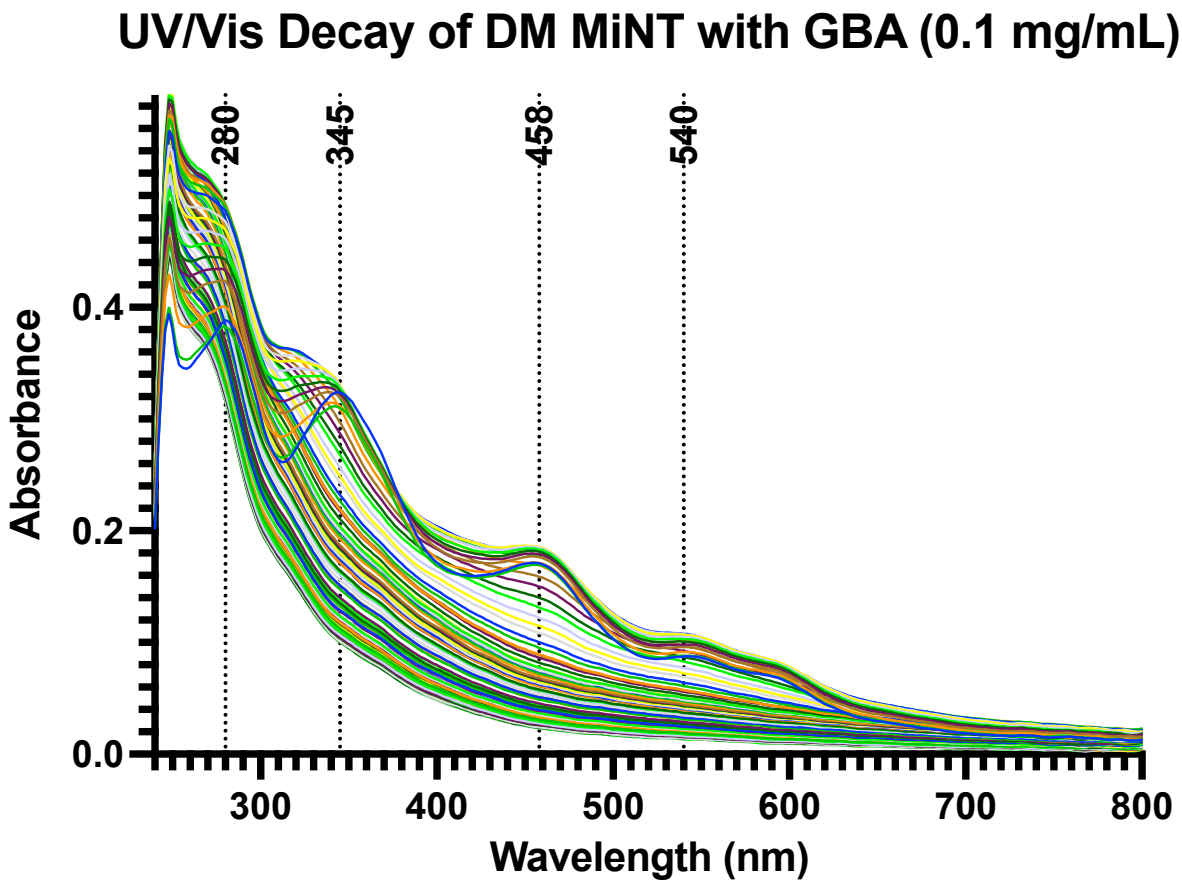

Figure 3.A45: UV/Vis decay of DM MiNT with 10% GBA in DMSO at 0.1 mg/mL (200-800 nm).

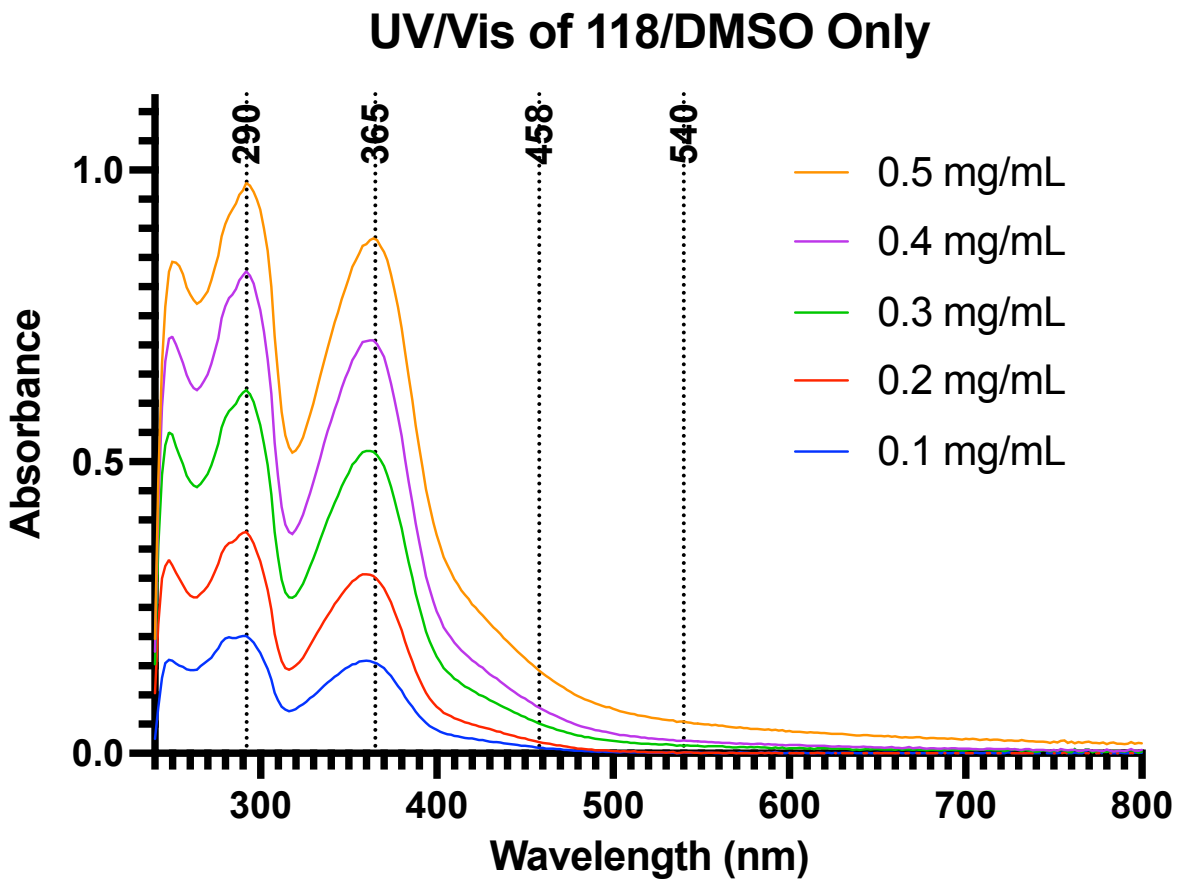

Figure 3.A46: UV/Vis of SEC buffer with 10% 118 in DMSO at various concentrations (200-800 nm).

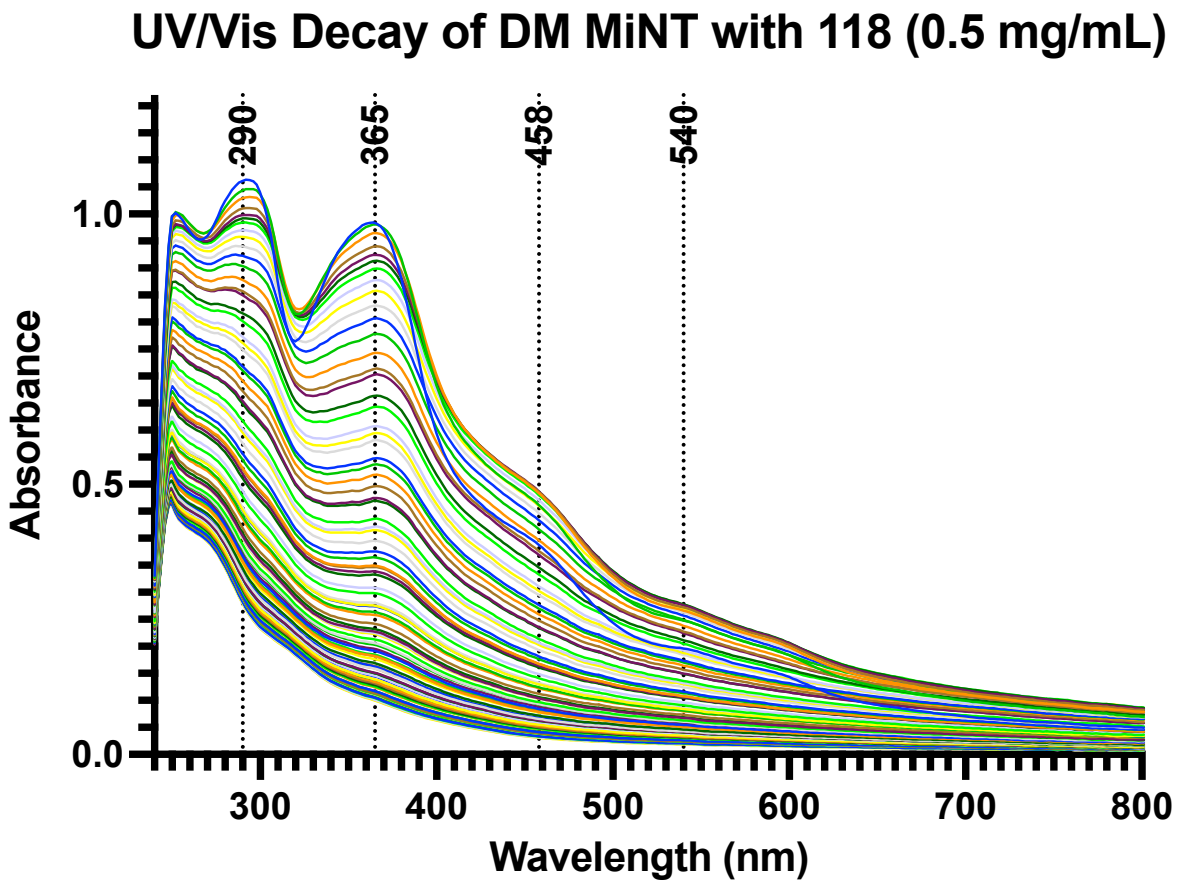

Figure 3.A47: UV/Vis decay of DM MiNT with 10% 118 in DMSO at 0.5 mg/mL (200-800 nm).

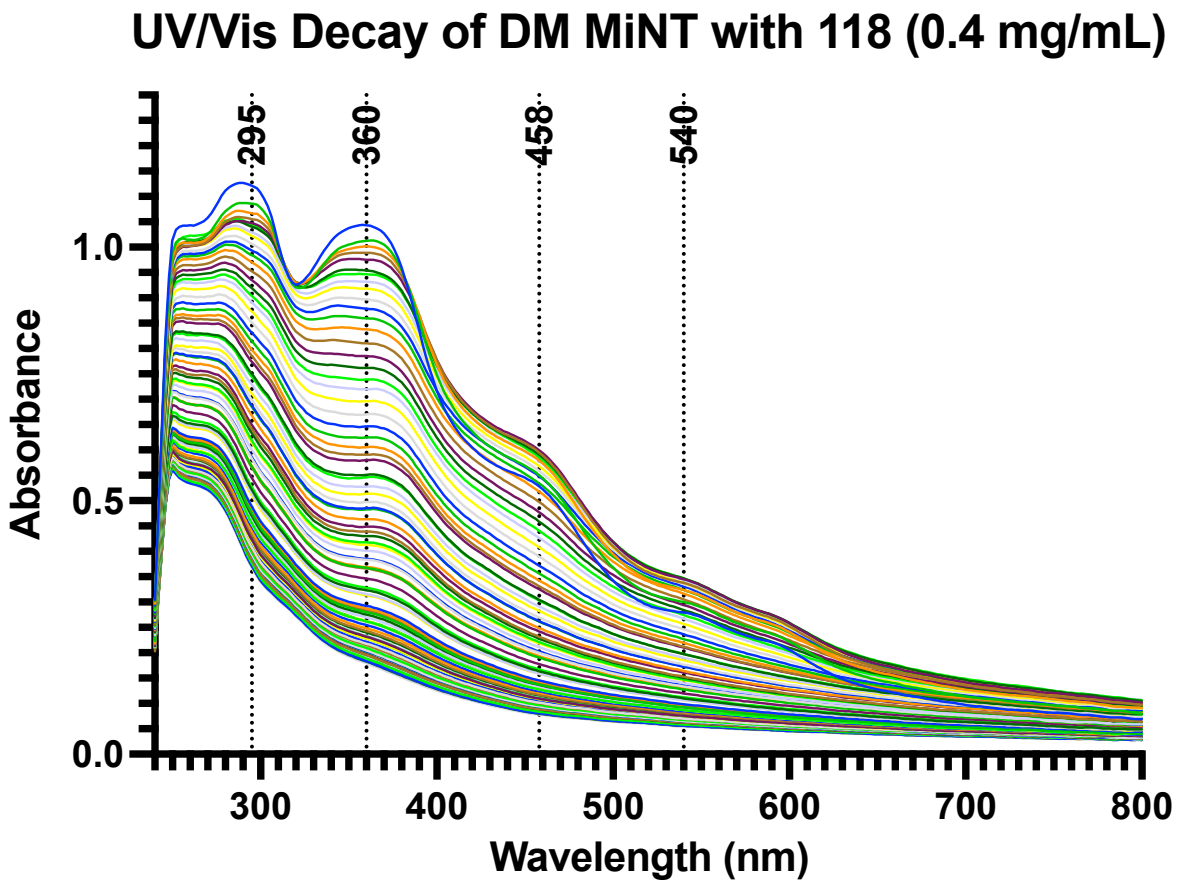

Figure 3.A48: UV/Vis decay of DM MiNT with 10% 118 in DMSO at 0.4 mg/mL (200-800 nm).

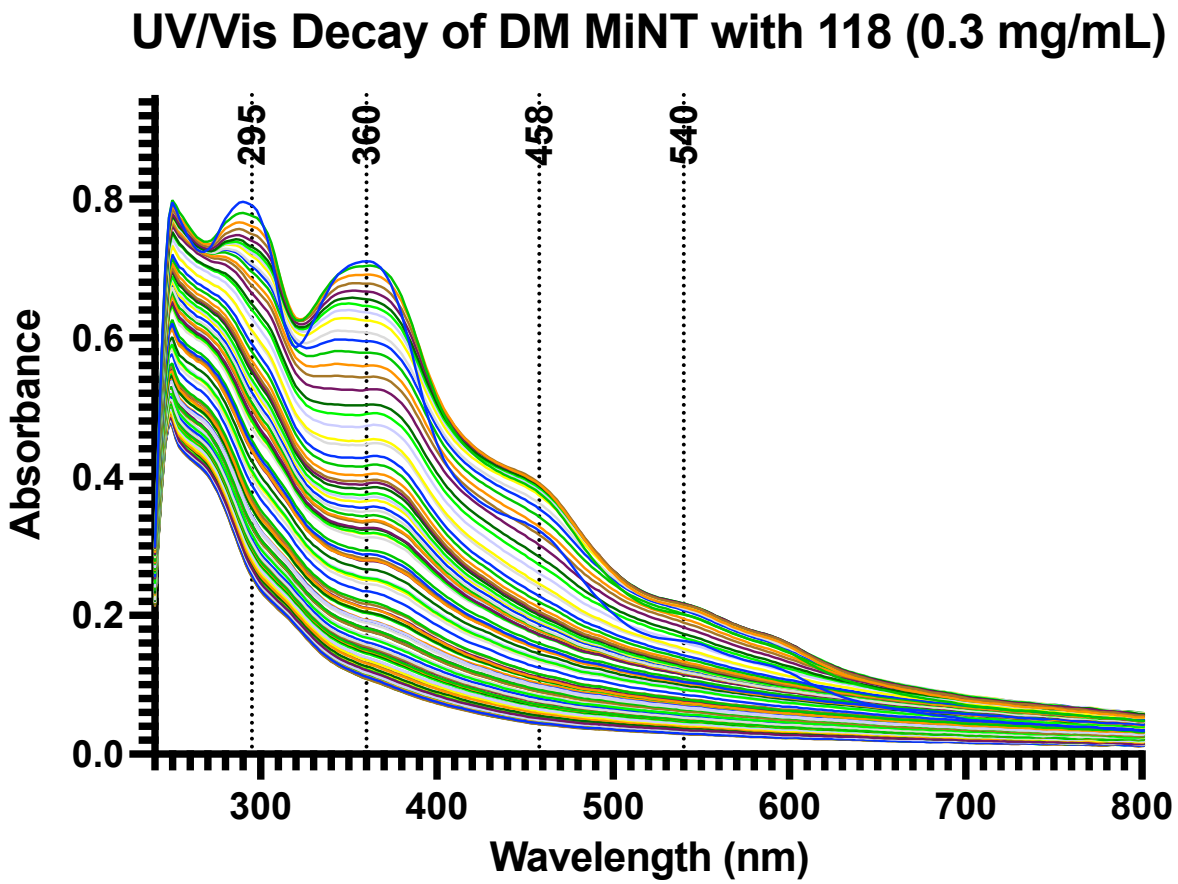

Figure 3.A49: UV/Vis decay of DM MiNT with 10% 118 in DMSO at 0.3 mg/mL (200-800 nm).

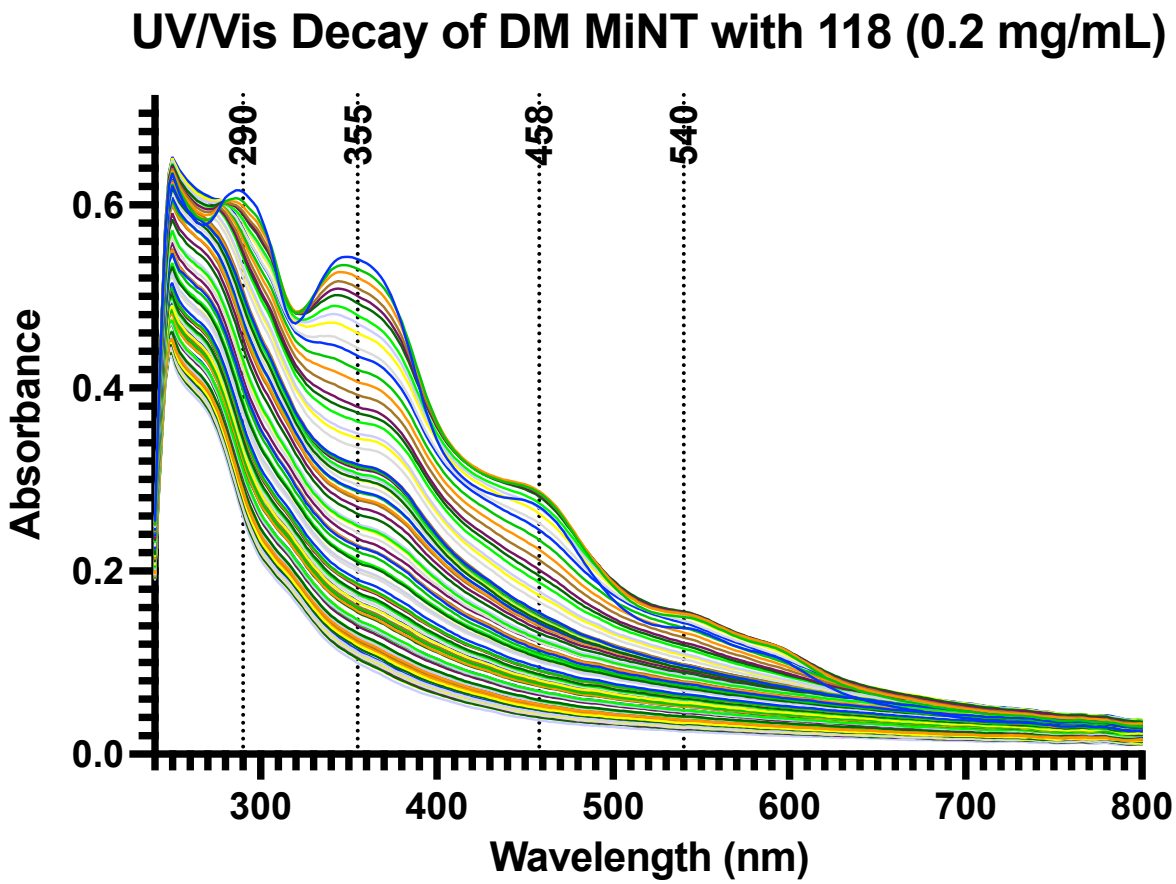

Figure 3.A50: UV/Vis decay of DM MiNT with 10% 118 in DMSO at 0.2 mg/mL (200-800 nm).

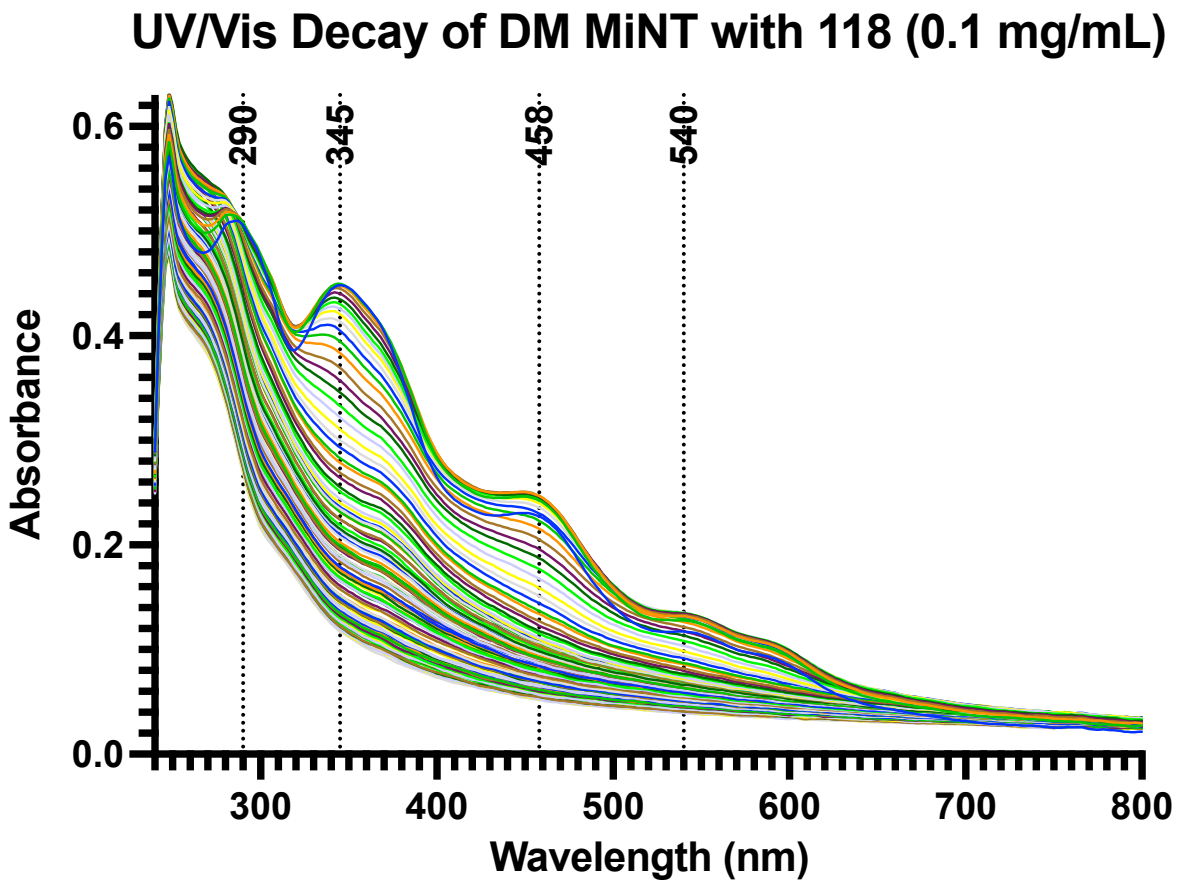

Figure 3.A51: UV/Vis decay of DM MiNT with 10% 118 in DMSO at 0.1 mg/mL (200-800 nm).

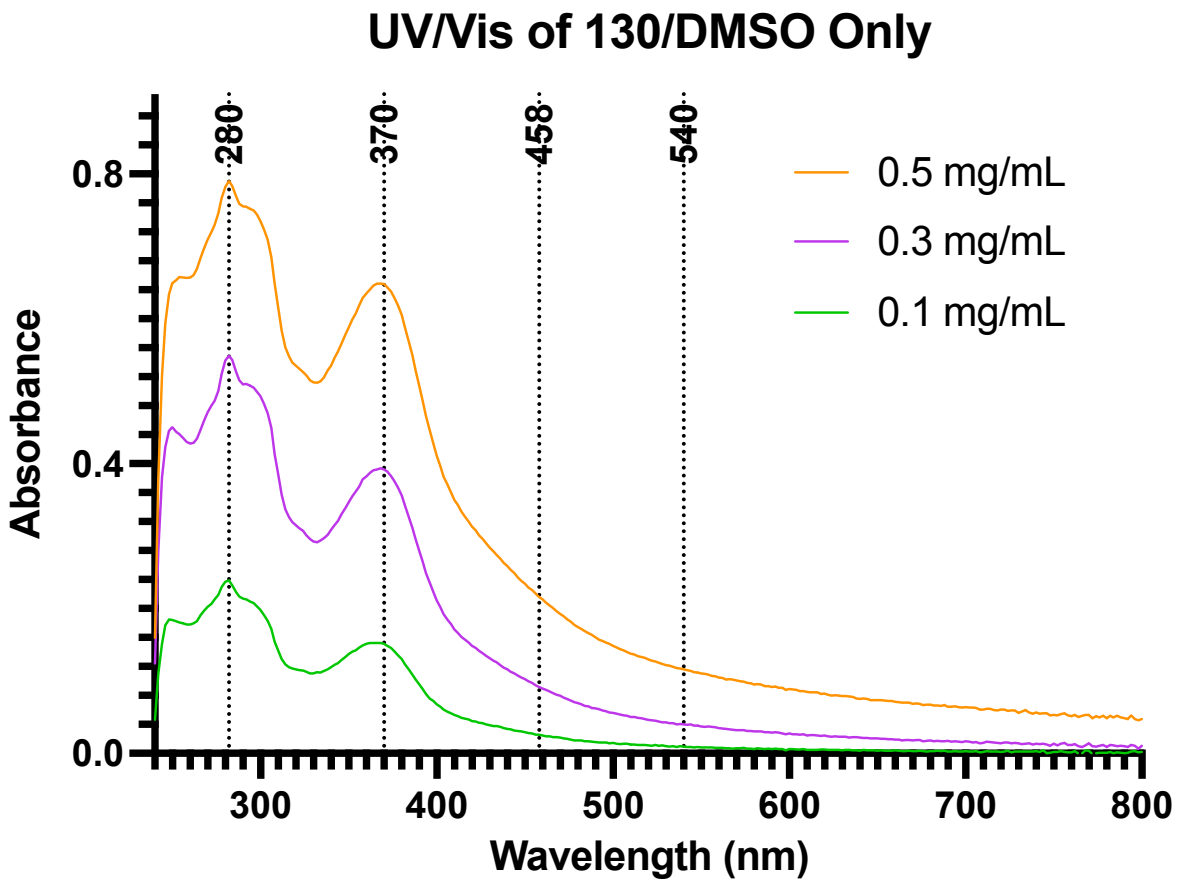

Figure 3.A52: UV/Vis of SEC buffer with 10% 130 in DMSO at various concentrations (200-800 nm).

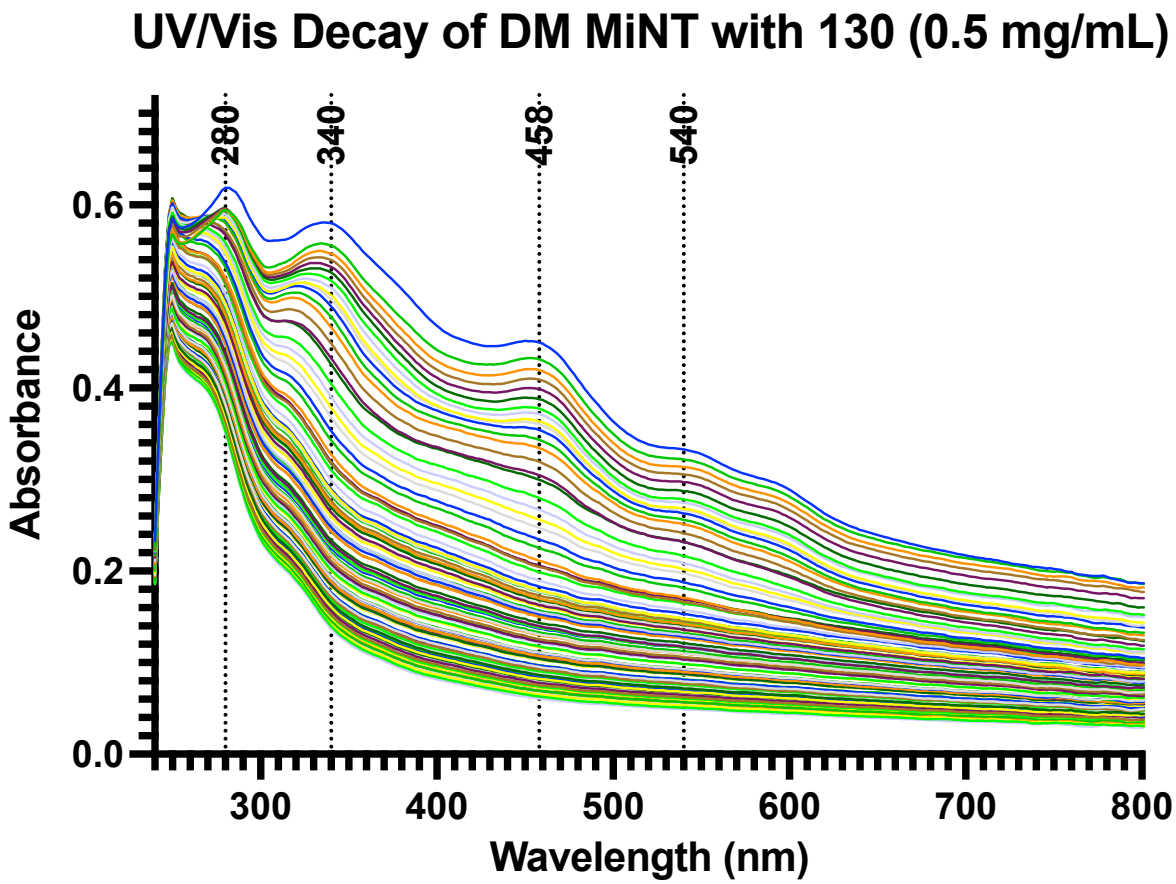

Figure 3.A53: UV/Vis decay of DM MiNT with 10% 130 in DMSO at 0.5 mg/mL (200-800 nm).

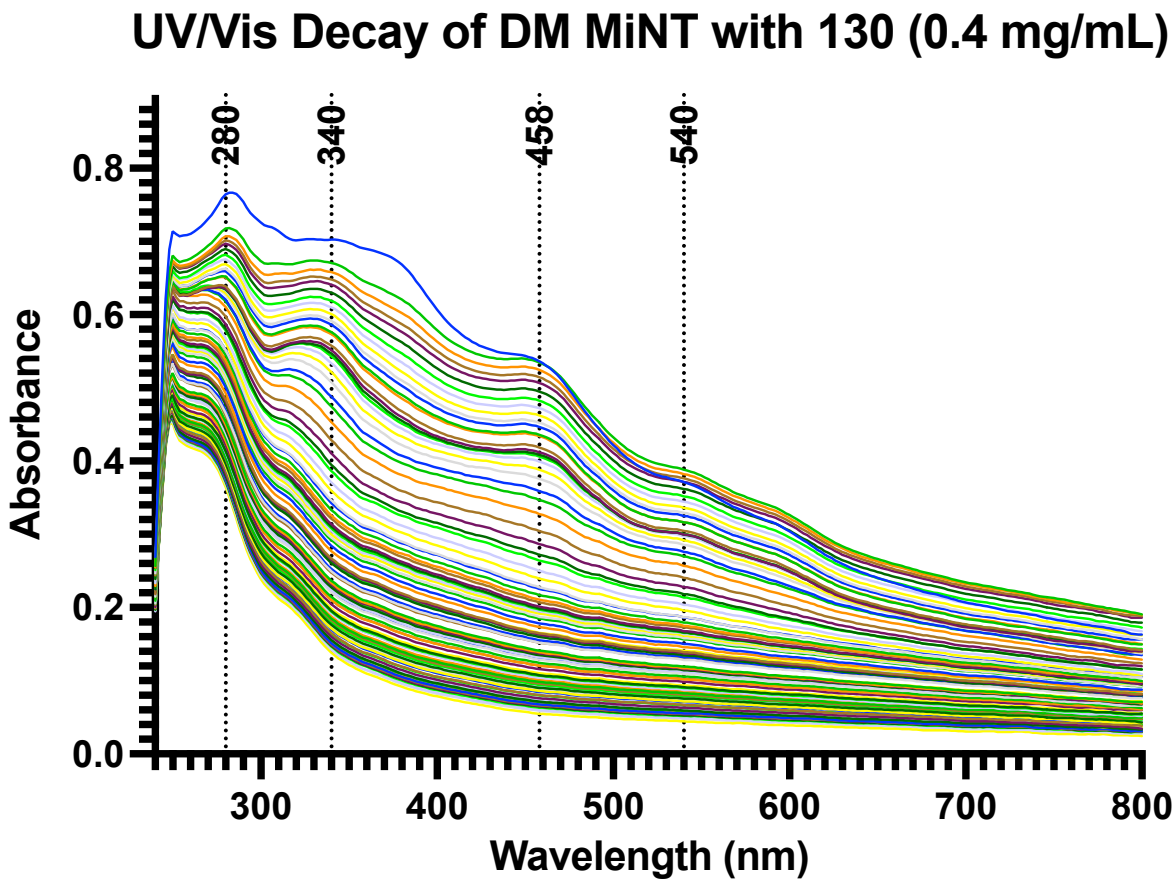

Figure 3.A54: UV/Vis decay of DM MiNT with 10% 130 in DMSO at 0.4 mg/mL (200-800 nm).

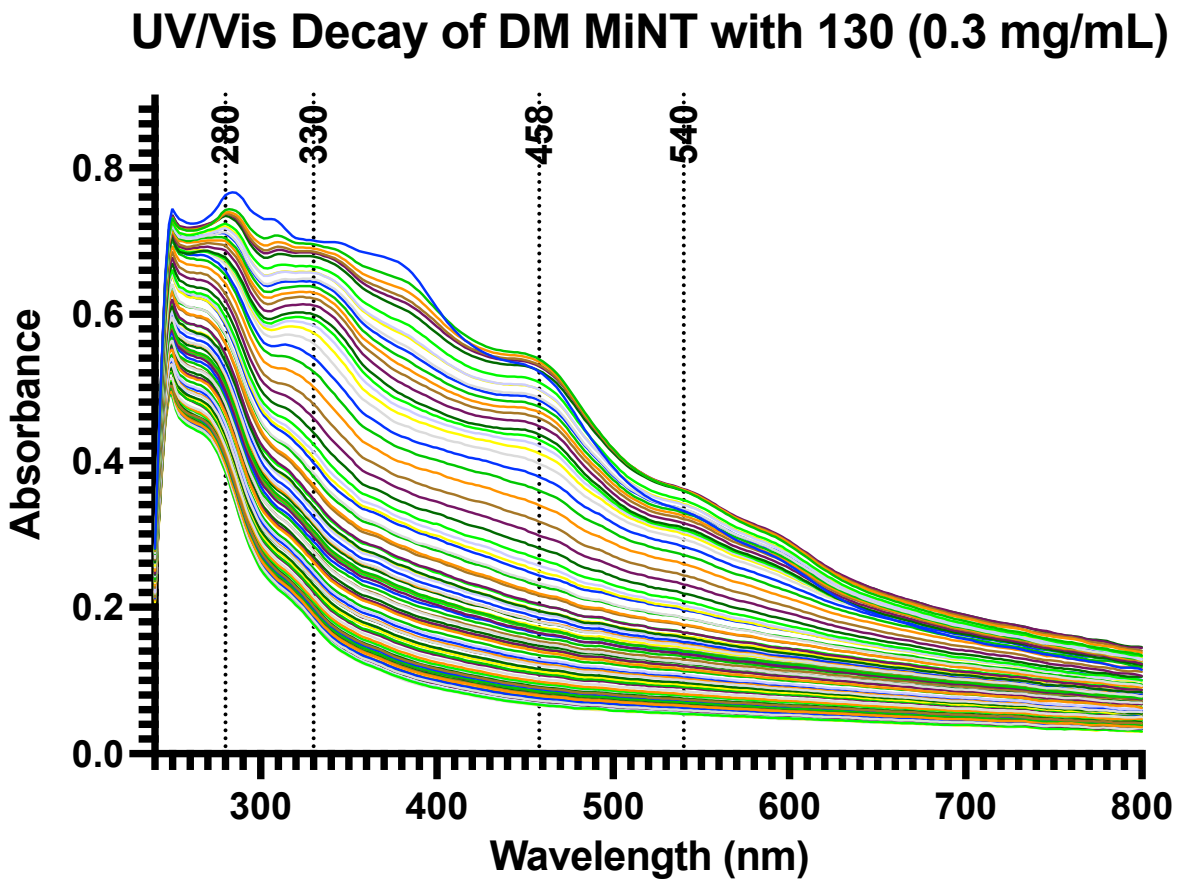

Figure 3.A55: UV/Vis decay of DM MiNT with 10% 130 in DMSO at 0.3 mg/mL (200-800 nm).

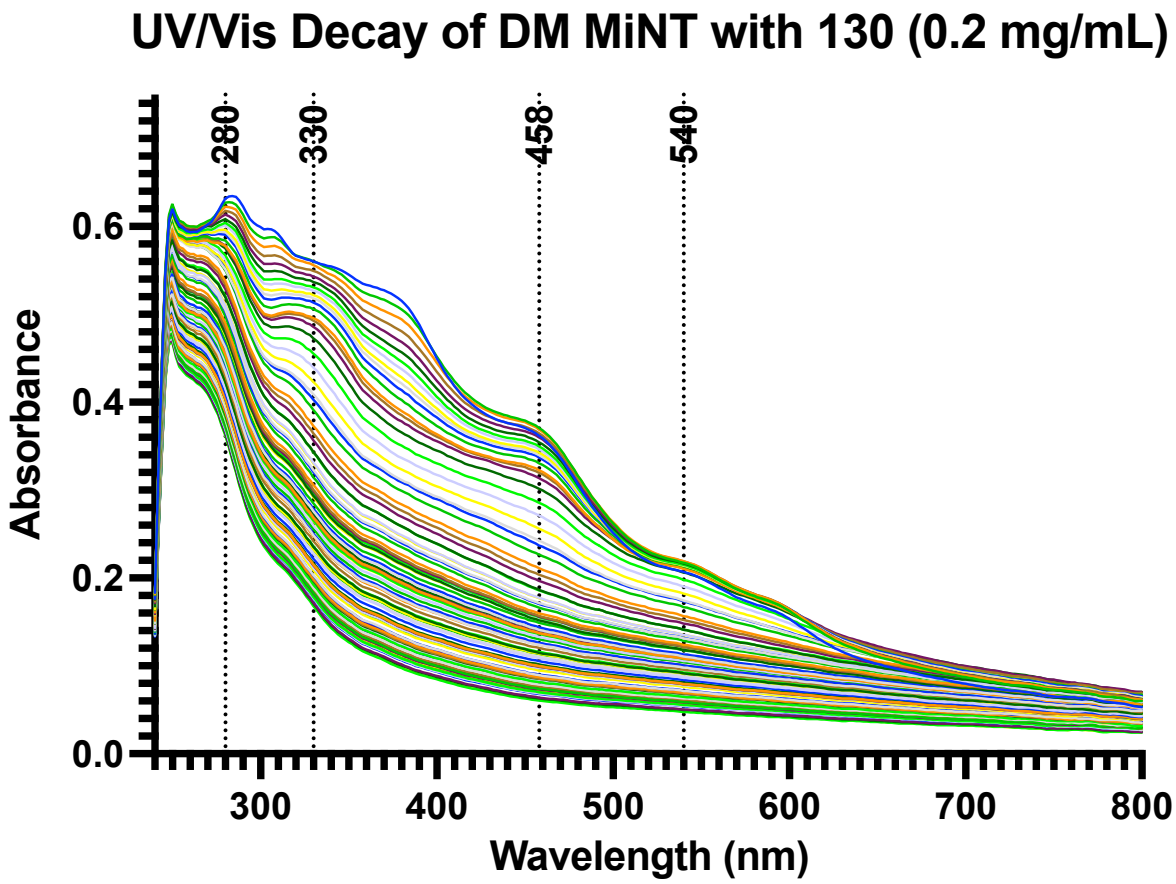

Figure 3.A56: UV/Vis decay of DM MiNT with 10% 130 in DMSO at 0.2 mg/mL (200-800 nm).

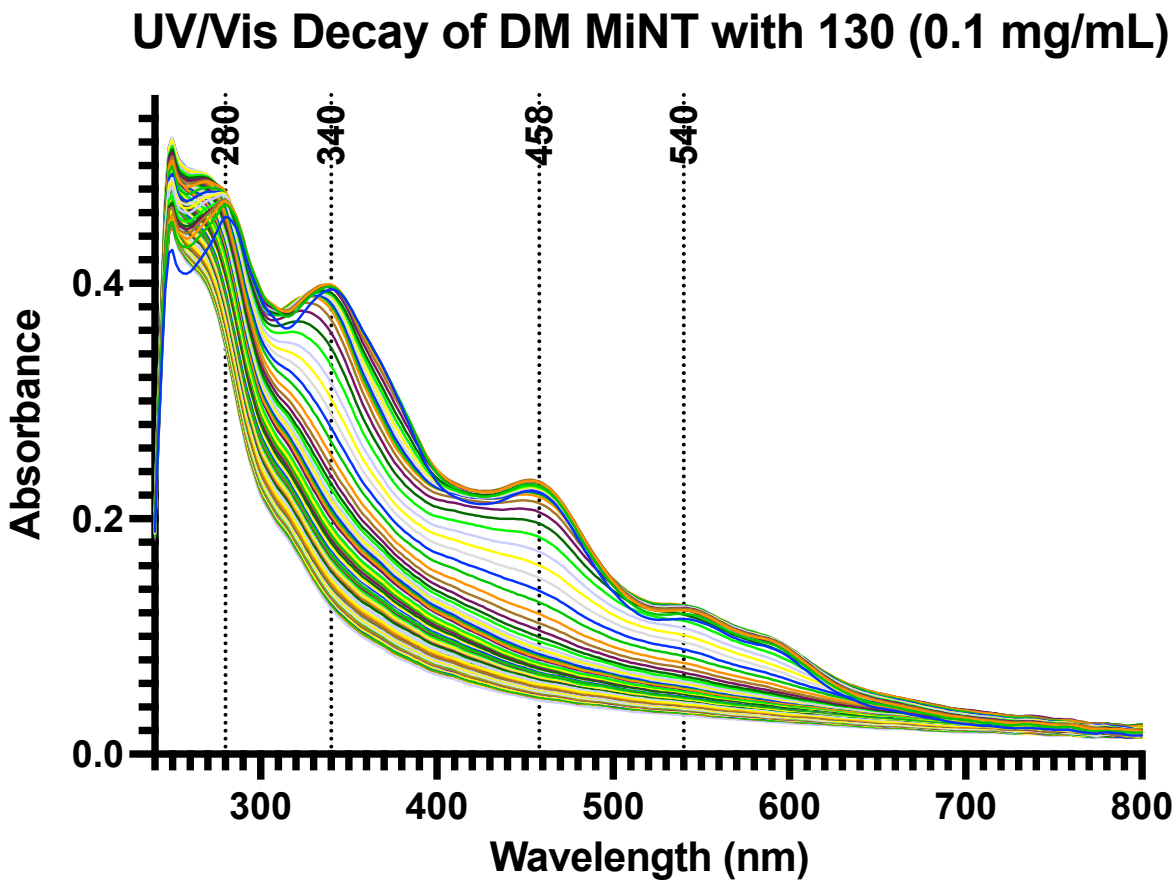

Figure 3.A57: UV/Vis decay of DM MiNT with 10% 130 in DMSO at 0.1 mg/mL (200-800 nm).

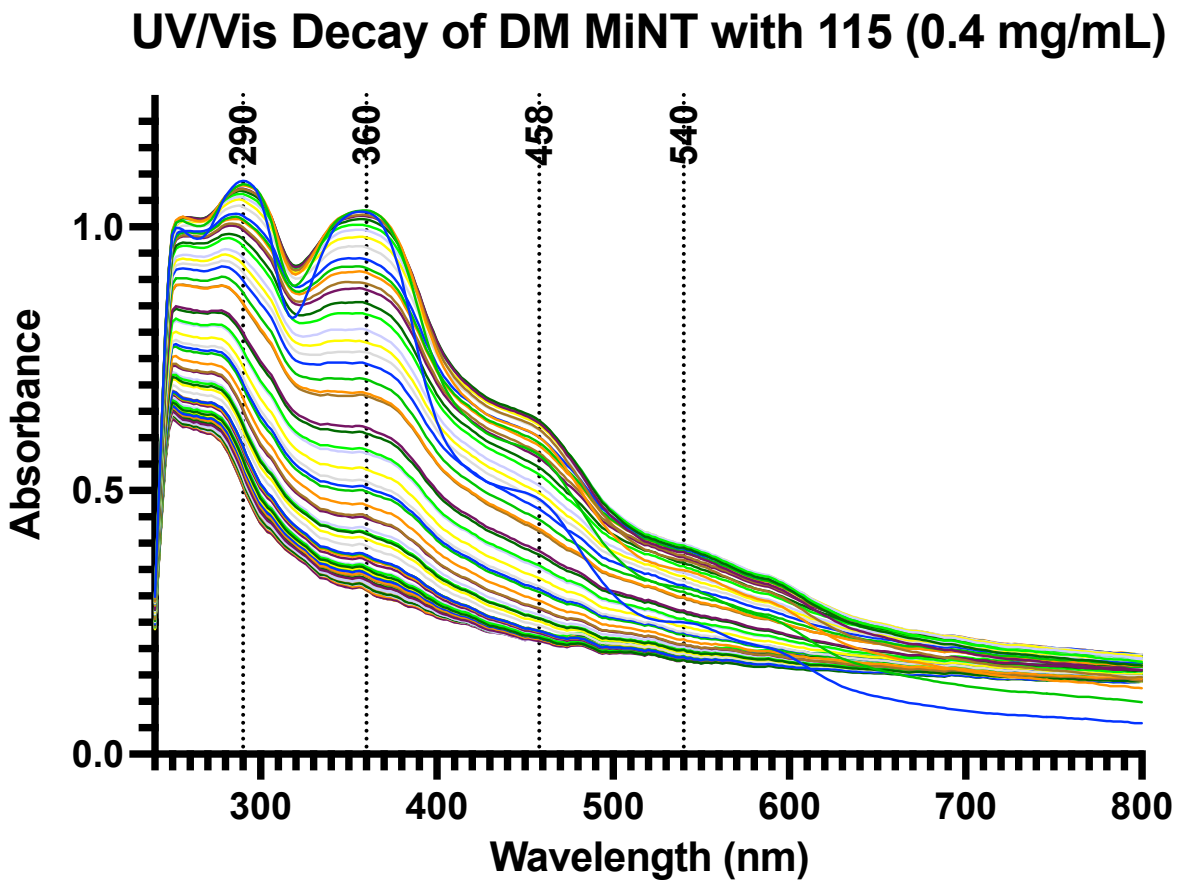

Figure 3.A58: UV/Vis decay of DM MiNT with 10% 115 in DMSO at 0.4 mg/mL (200-800 nm).

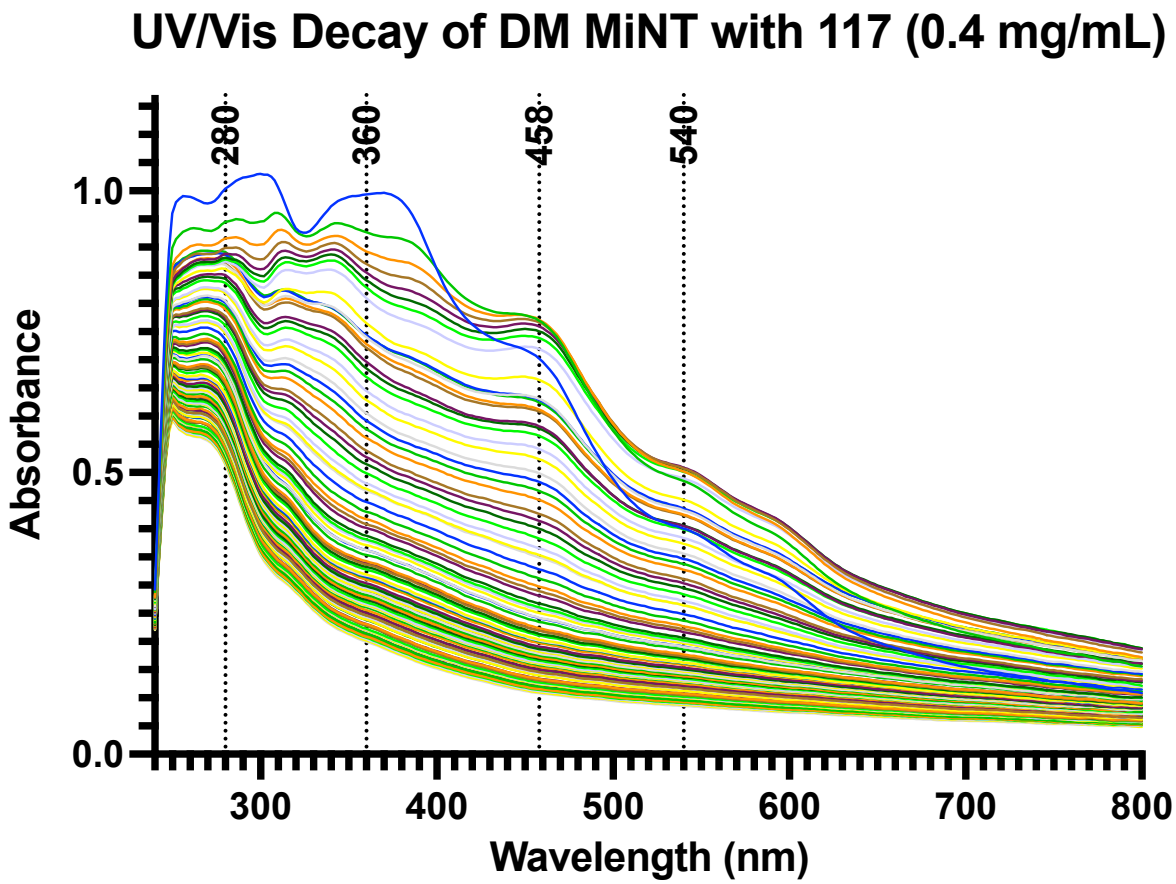

Figure 3.A59: UV/Vis decay of DM MiNT with 10% 117 in DMSO at 0.4 mg/mL (200-800 nm).

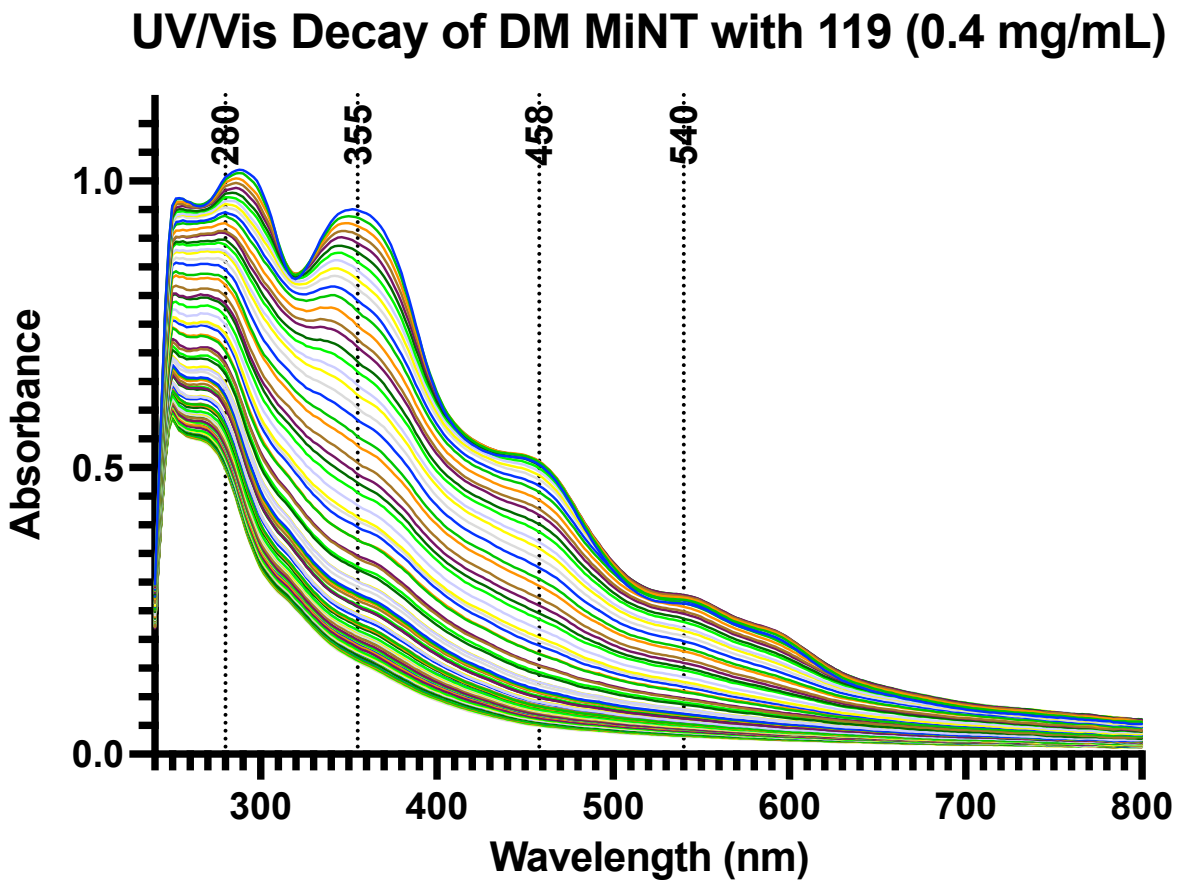

Figure 3.A60: UV/Vis decay of DM MiNT with 10% 119 in DMSO at 0.4 mg/mL (200-800 nm).

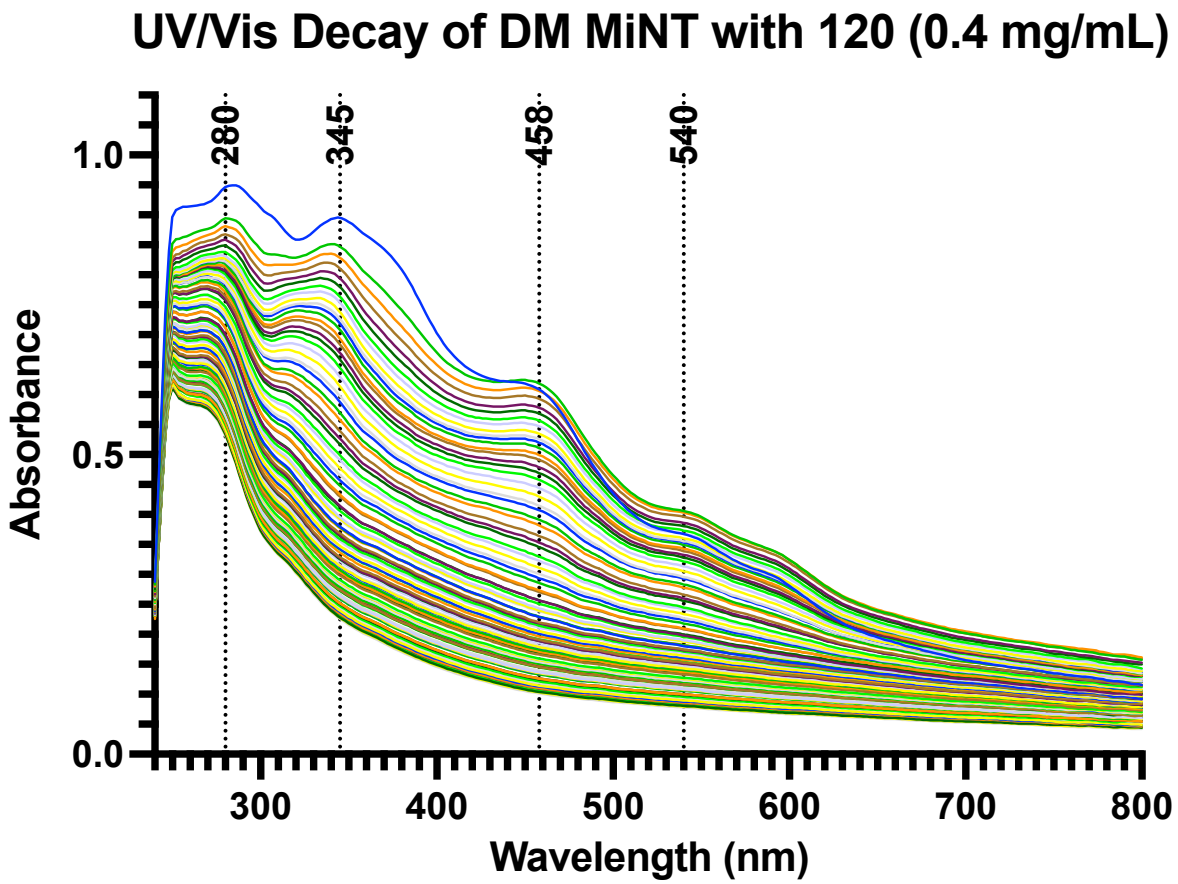

Figure 3.A61: UV/Vis decay of DM MiNT with 10% 120 in DMSO at 0.4 mg/mL (200-800 nm).

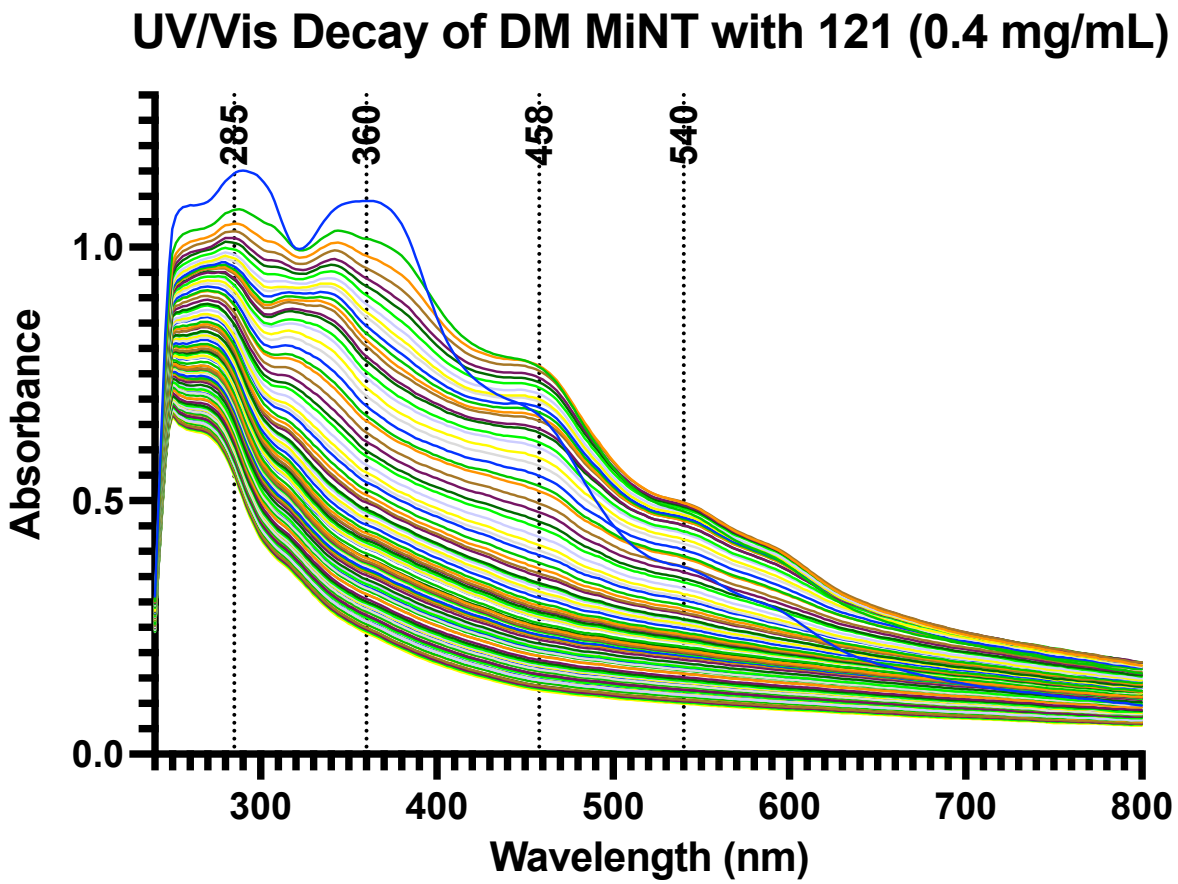

Figure 3.A62: UV/Vis decay of DM MiNT with 10% 121 in DMSO at 0.4 mg/mL (200-800 nm).

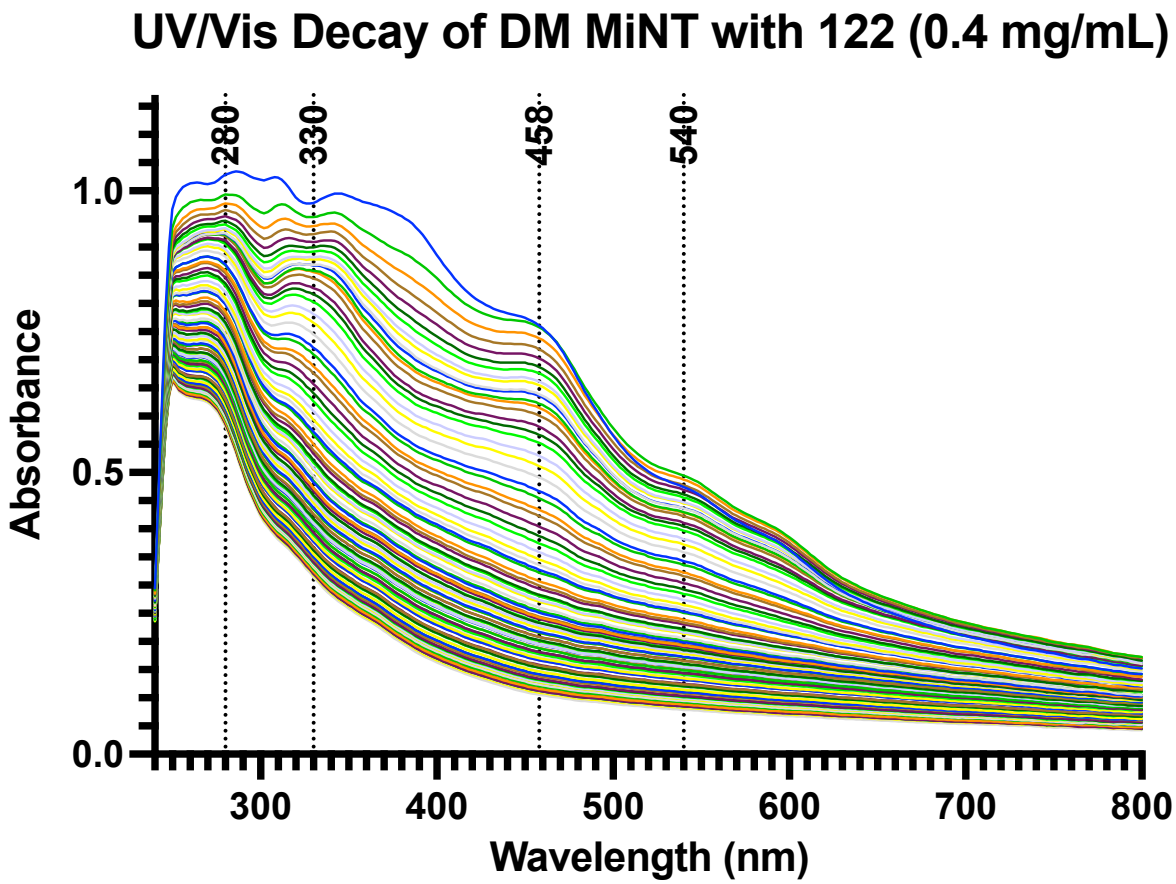

Figure 3.A63: UV/Vis decay of DM MiNT with 10% 122 in DMSO at 0.4 mg/mL (200-800 nm).

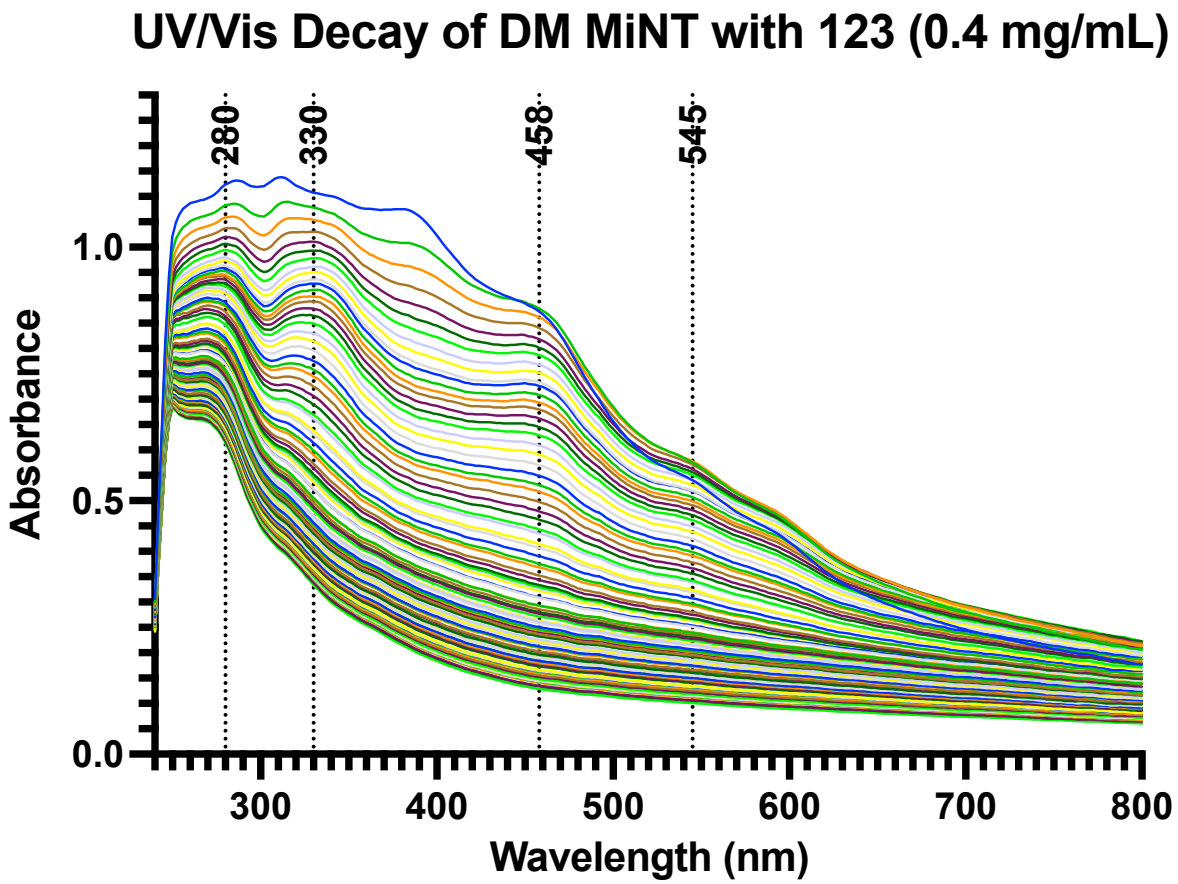

Figure 3.A64: UV/Vis decay of DM MiNT with 10% 123 in DMSO at 0.4 mg/mL (200-800 nm).

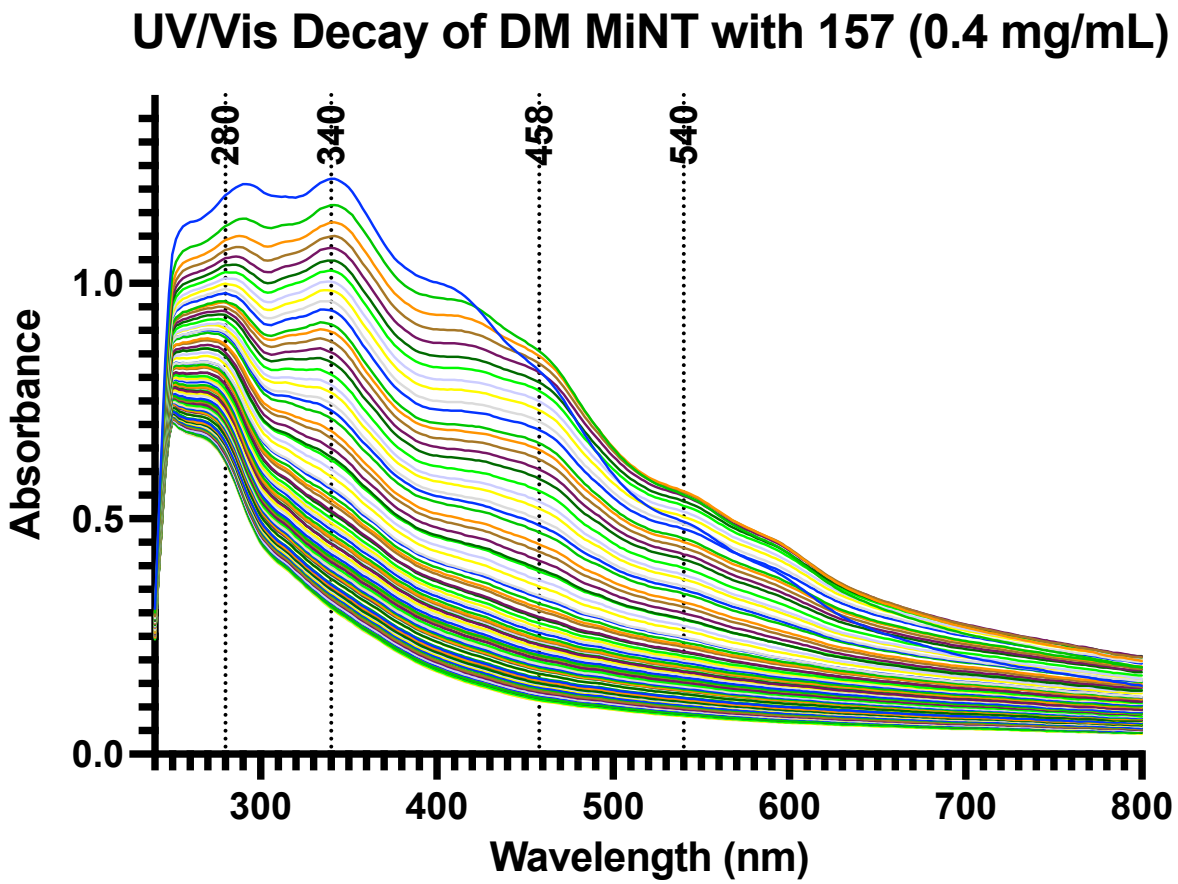

Figure 3.A65: UV/Vis decay of DM MiNT with 10% 157 in DMSO at 0.4 mg/mL (200-800 nm).

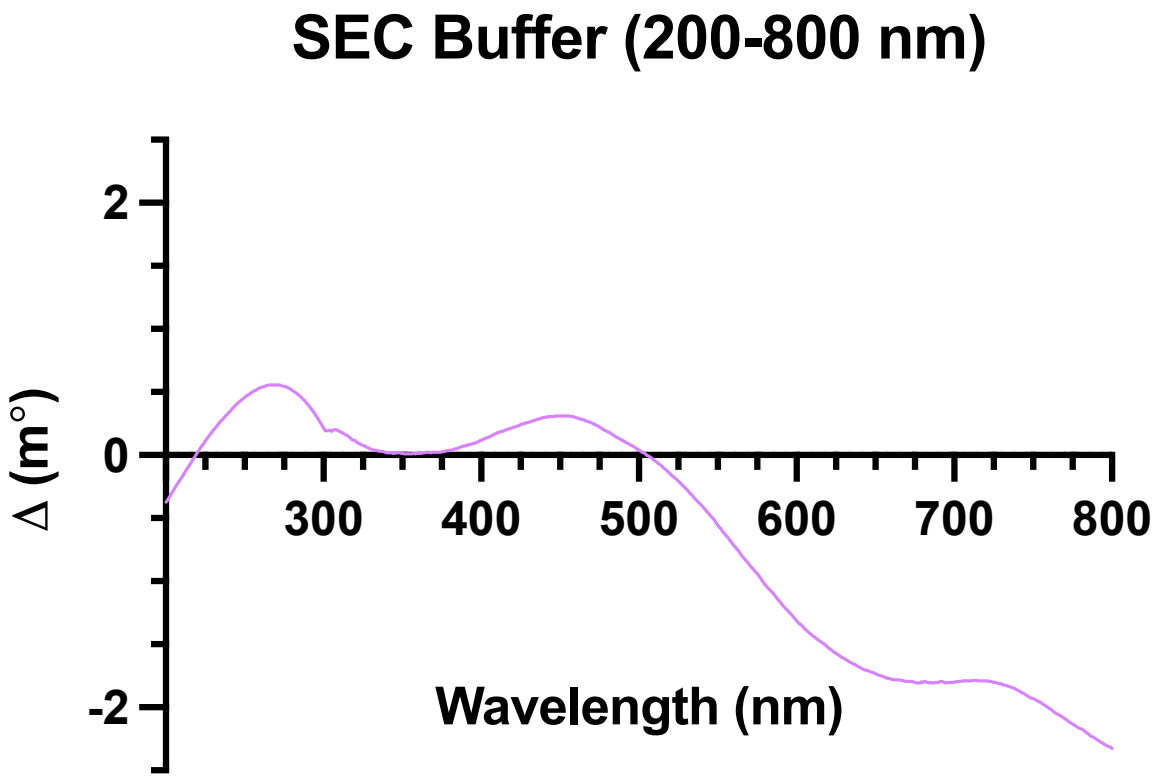

Figure 3.A66: CD spectrum of SEC buffer (200-800 nm).

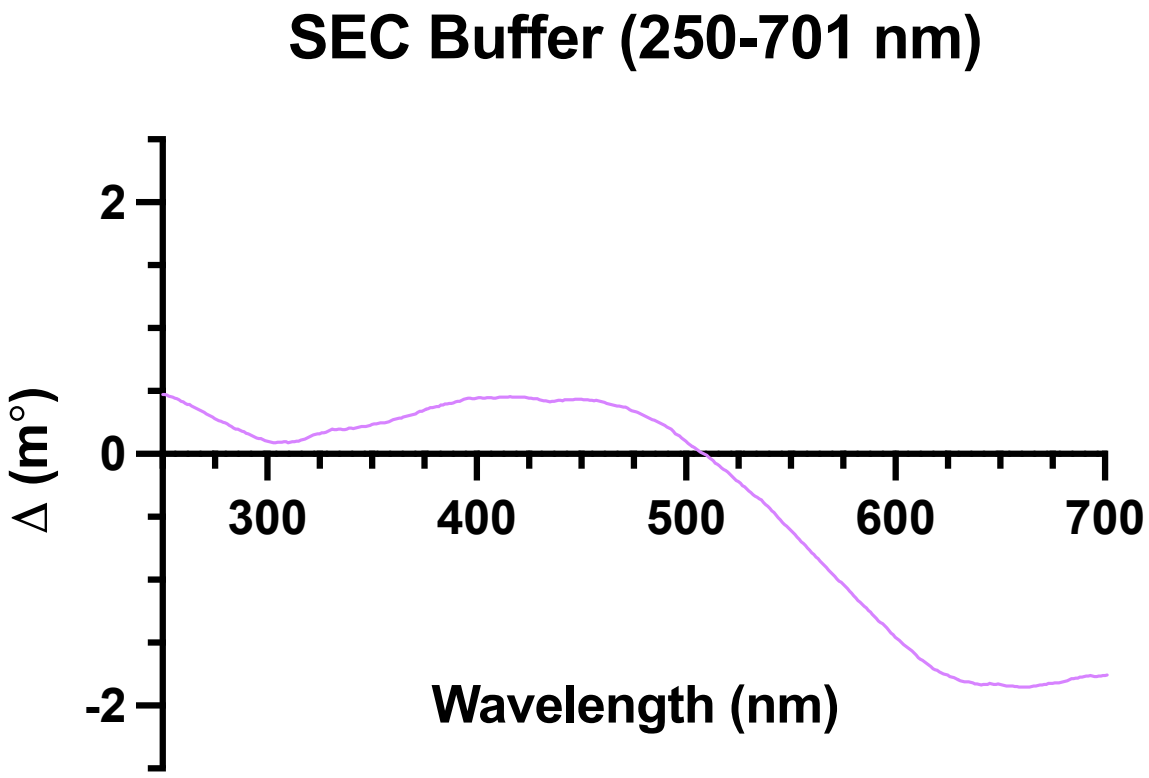

Figure 3.A67: CD spectrum of SEC buffer (250-701 nm).

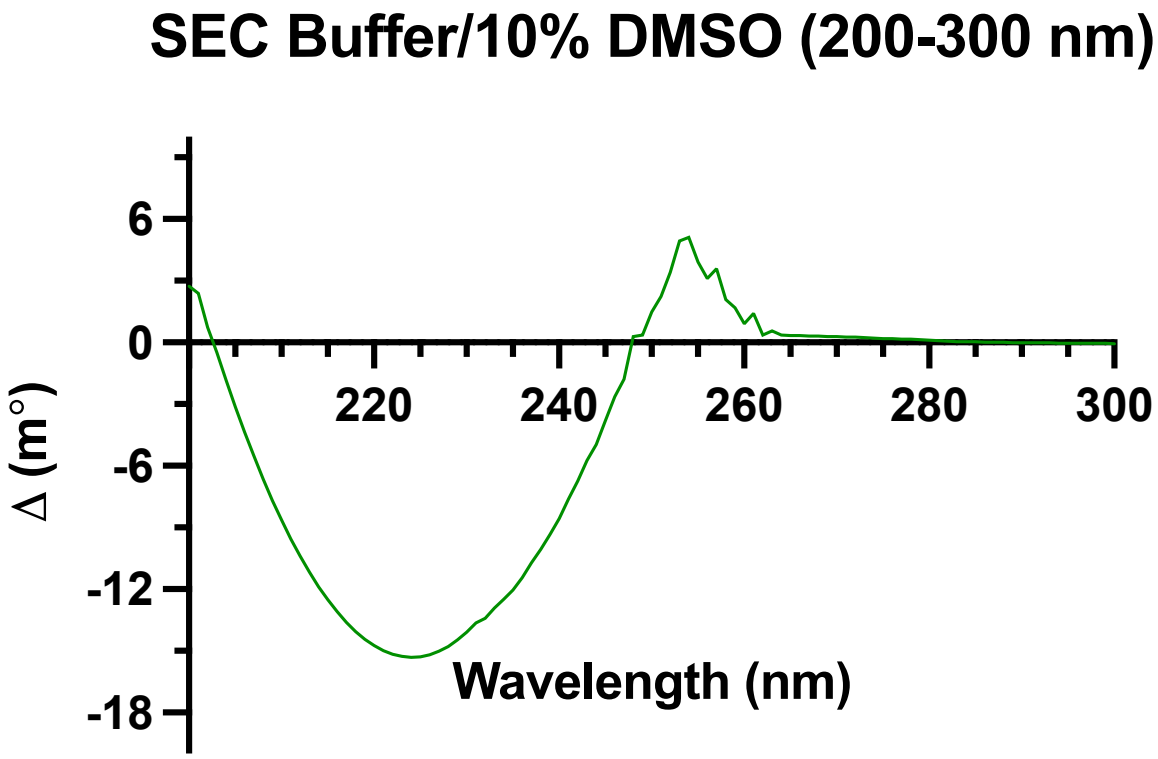

Figure 3.A68: CD spectrum of SEC buffer with 10% DMSO (200-300 nm).

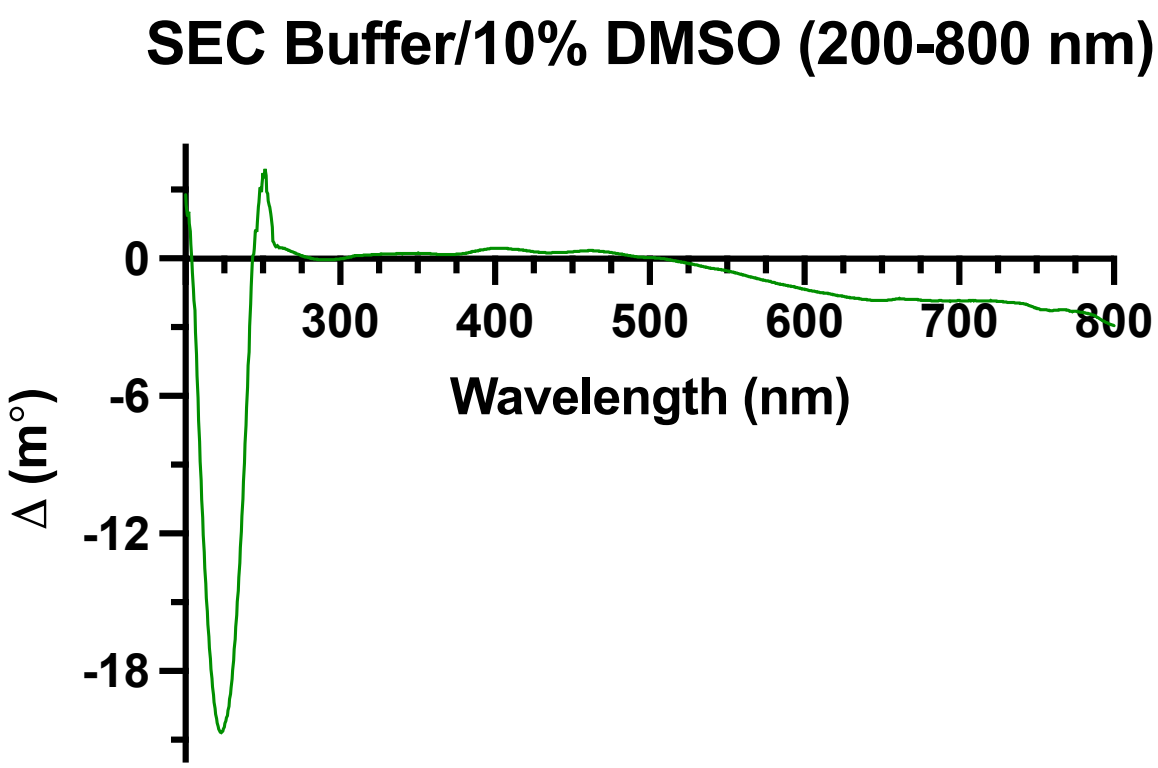

Figure 3.A69: CD spectrum of SEC buffer with 10% DMSO (200-800 nm).

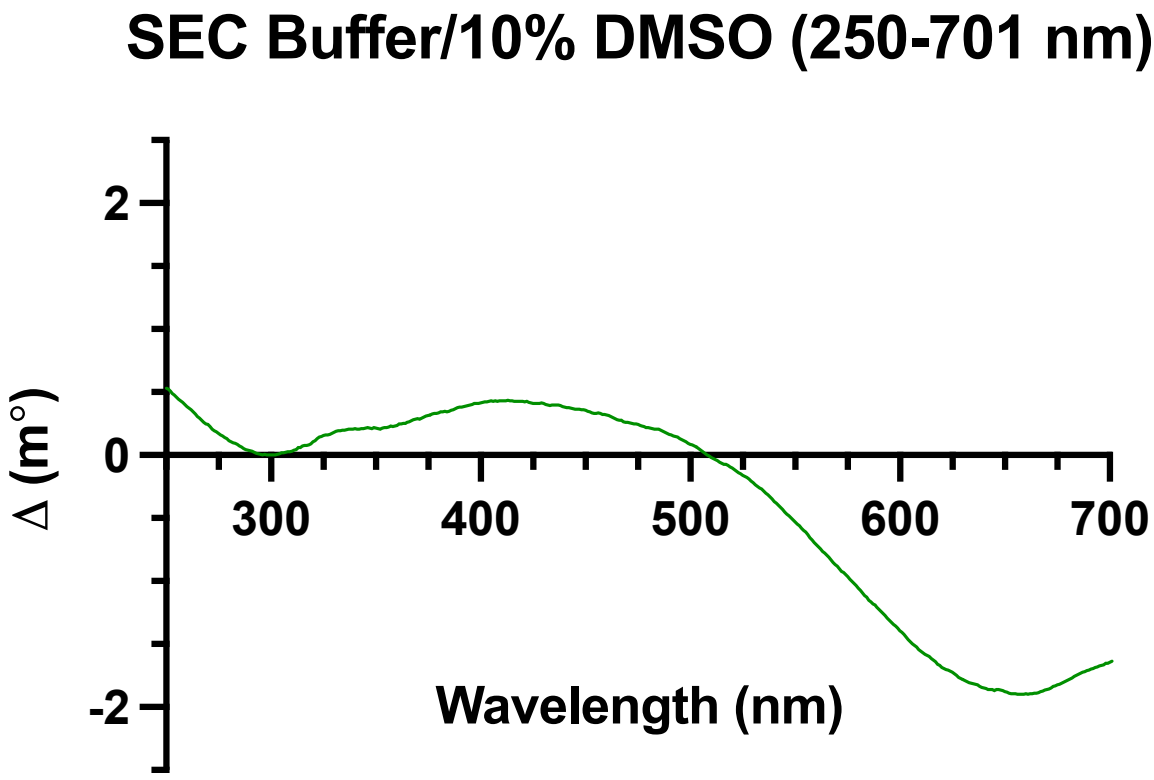

Figure 3.A70: CD spectrum of SEC buffer with 10% DMSO (250-701 nm).

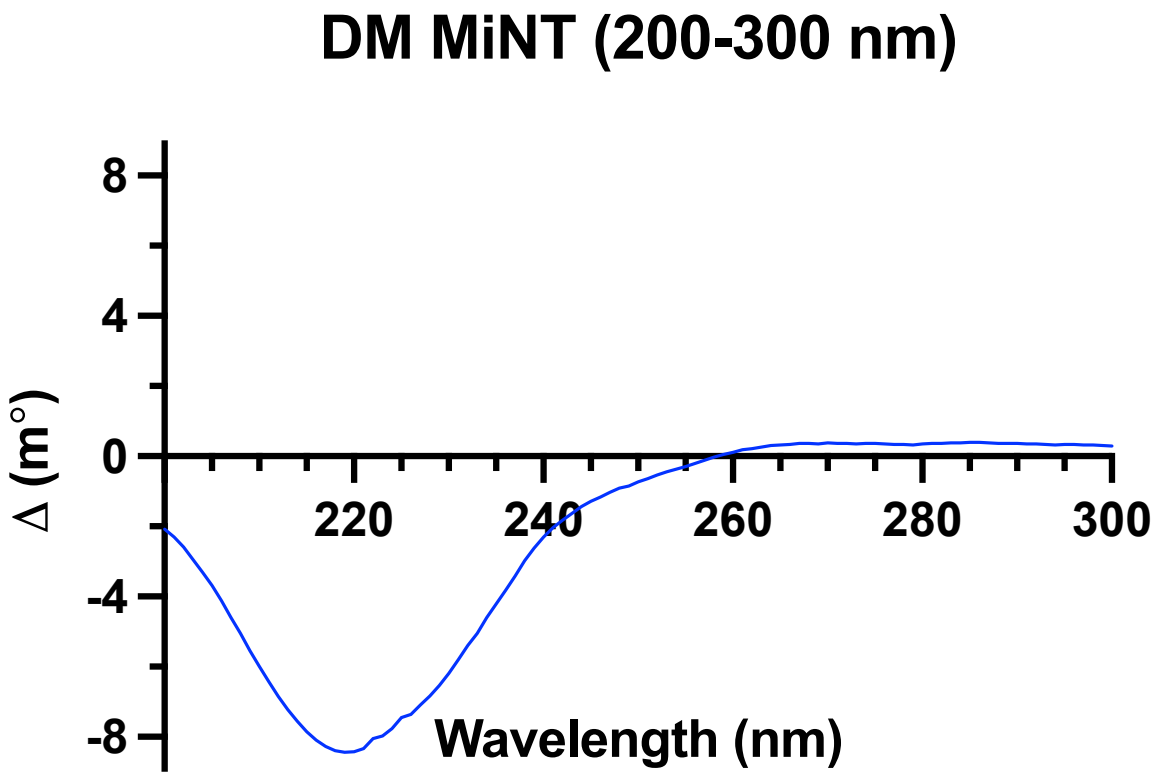

Figure 3.A71: CD spectrum of DM MiNT dissolved in SEC buffer (200-300 nm).

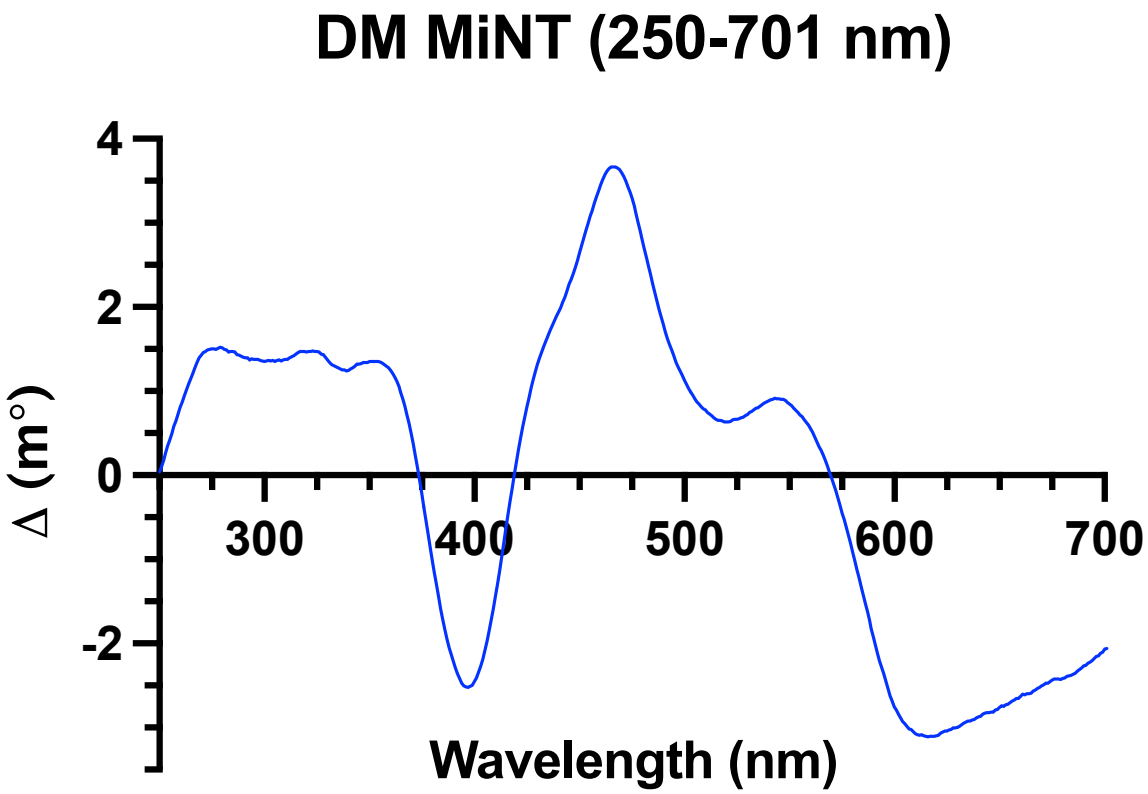

Figure 3.A72: CD spectrum of DM MiNT dissolved in SEC buffer (250-701 nm).

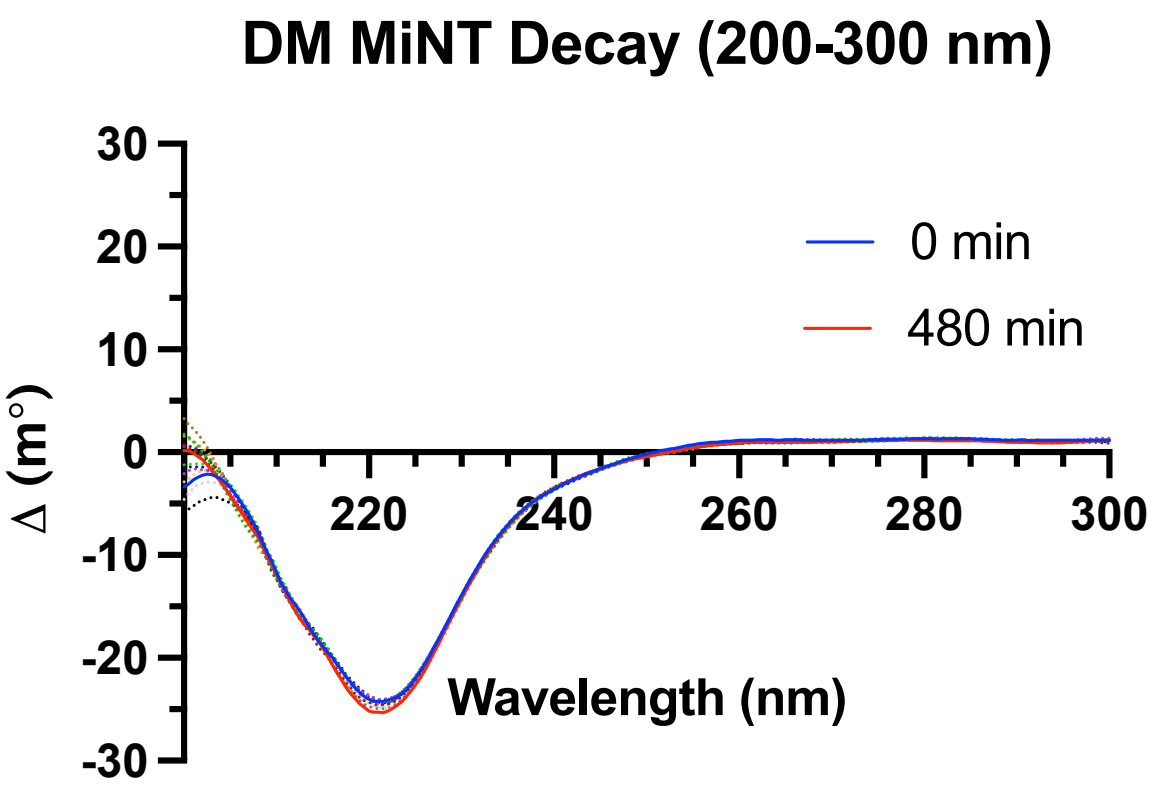

Figure 3.A73: CD spectrum of the decay of DM MiNT dissolved in SEC buffer (200-300 nm).

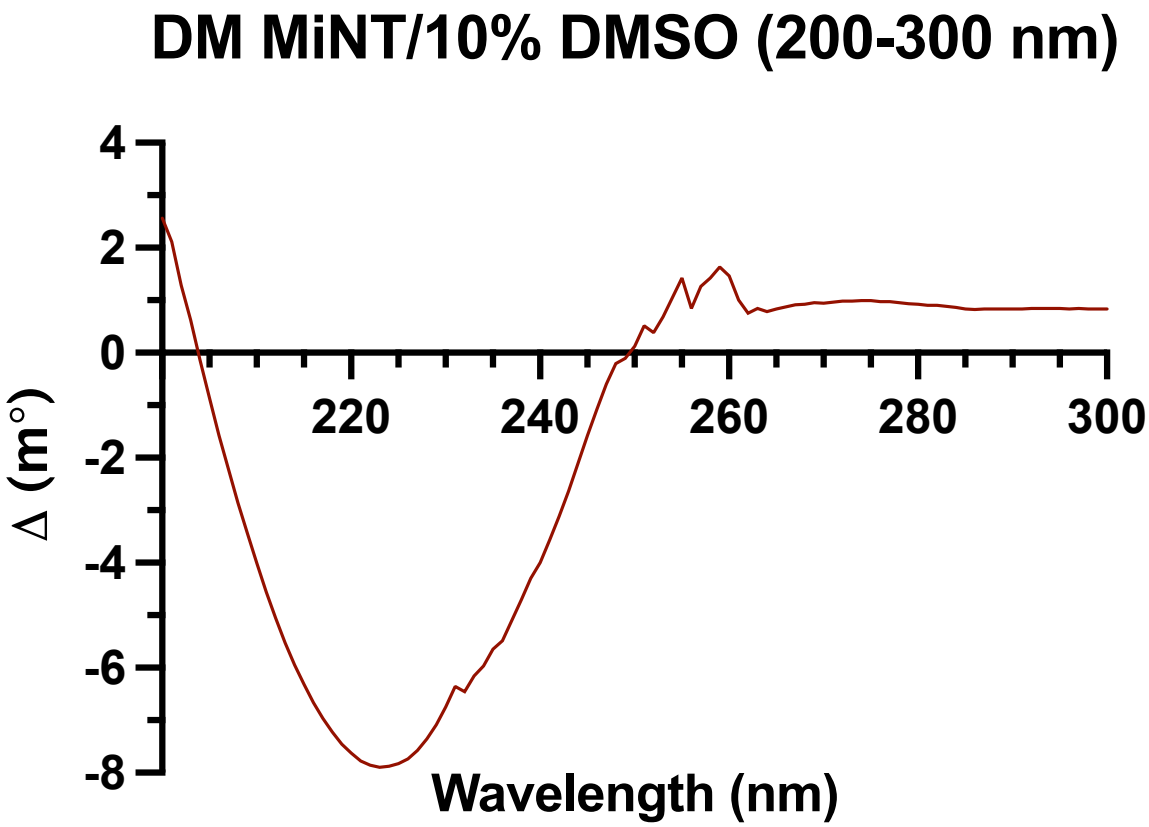

Figure 3.A74: CD spectrum of DM MiNT and 10% DMSO dissolved in SEC buffer (200-300 nm).

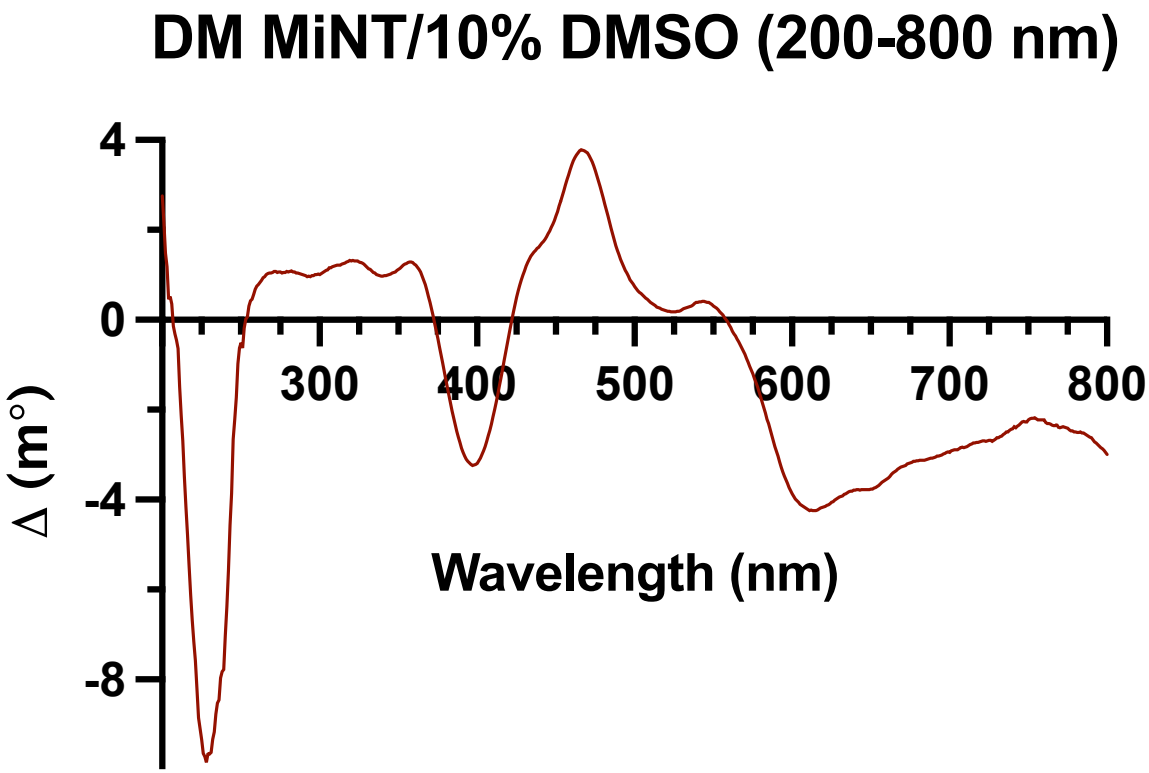

Figure 3.A75: CD spectrum of DM MiNT and 10% DMSO dissolved in SEC buffer (200-800 nm).

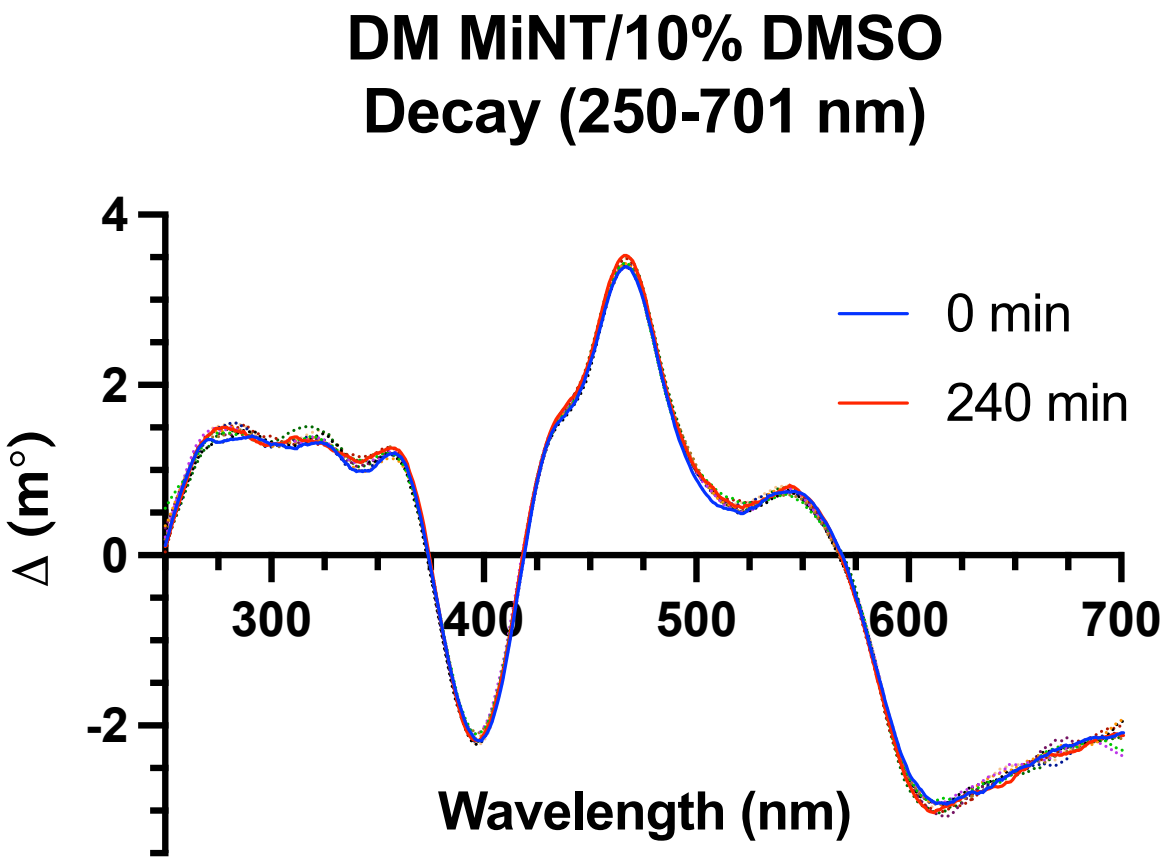

Figure 3.A76: CD spectrum of the decay of DM MiNT with 10% DMSO dissolved in SEC buffer (250-701 nm).

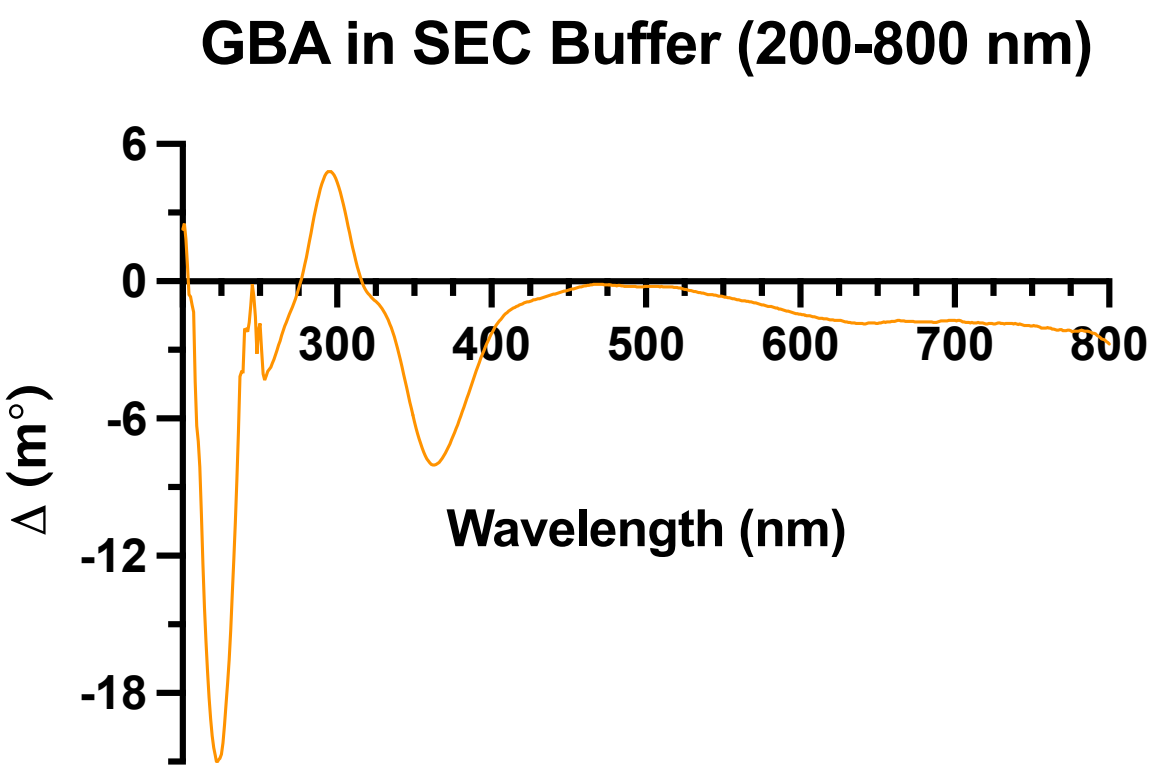

Figure 3.A77: CD spectrum of 10% GBA in DMSO (0.4 mg/mL) dissolved in SEC buffer (200-800 nm).

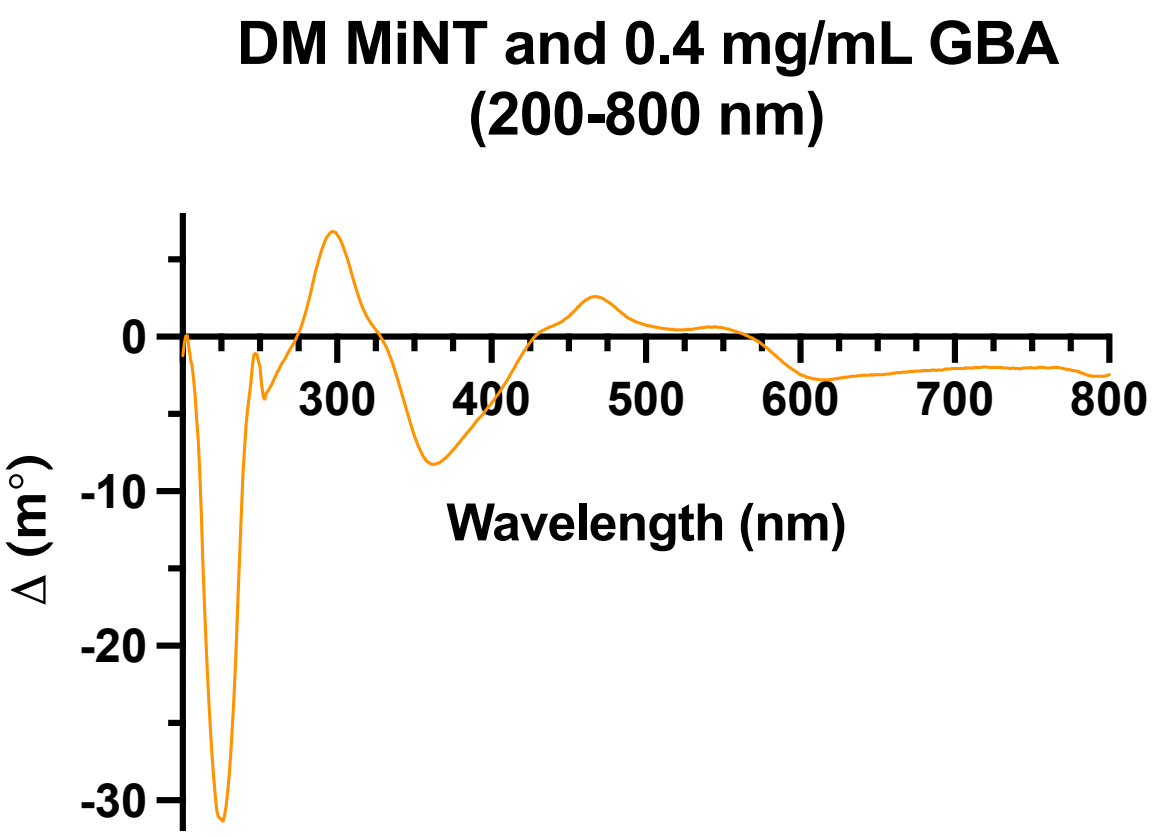

Figure 3.A78: CD spectrum of DM MiNT with 10% GBA in DMSO (0.4 mg/mL) dissolved in SEC buffer (200-800 nm).

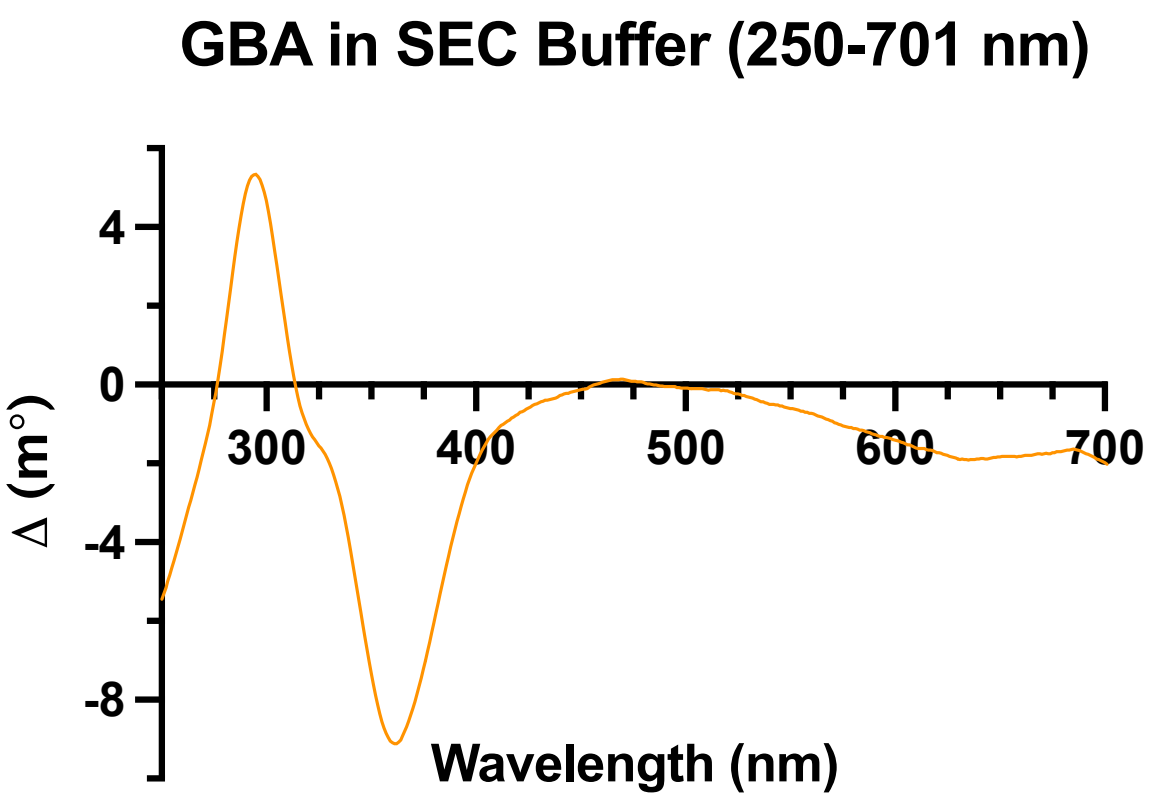

Figure 3.A79: CD spectrum of 10% GBA in DMSO (0.4 mg/mL) dissolved in SEC buffer (250-701 nm).

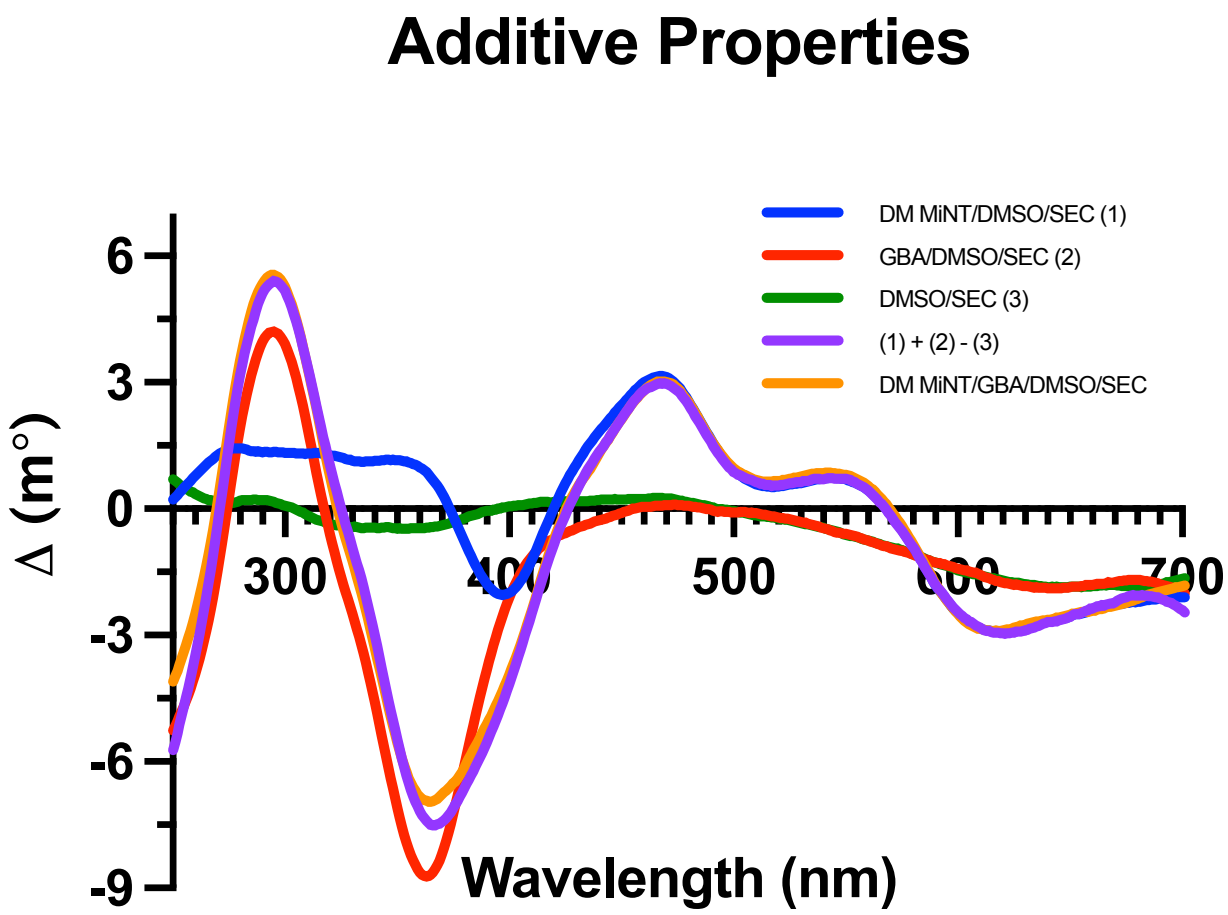

Figure 3.A80: CD spectrum showing the additive properties of DM MiNT and GBA/DMSO (250-701 nm). A spectrum of DM MiNT with 10% DMSO dissolved in SEC buffer (1, blue) can be added to a spectrum of 10% GBA in DMSO (0.4 mg/mL) dissolved in SEC buffer (2, red), which upon subtraction of a spectrum of 10% DMSO in SEC buffer (3, green) yields nearly the same spectrum (purple) as a mixture of DM MiNT with 10% GBA in DMSO (0.4 mg/mL) dissolved in SEC buffer (orange).

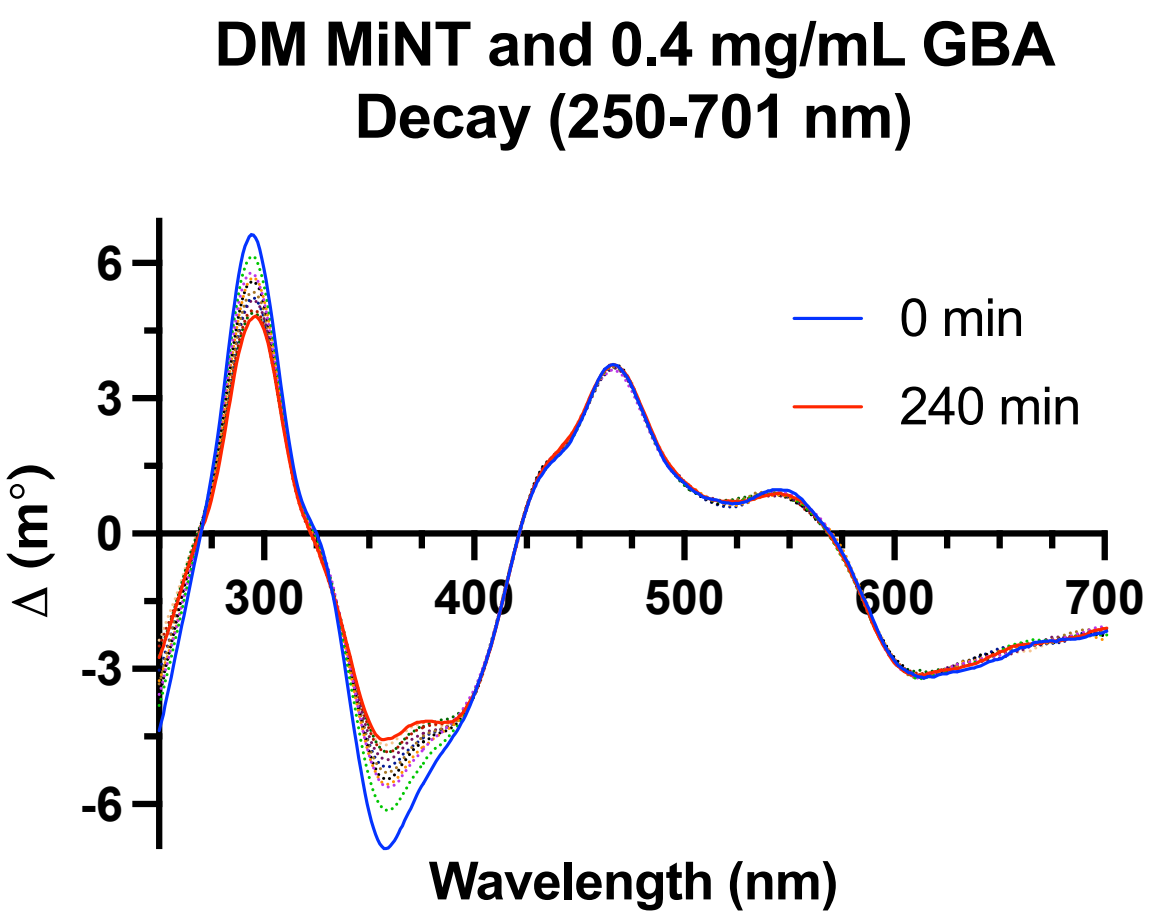

Figure 3.A81: CD spectrum of the decay of DM MiNT with 10% GBA in DMSO (0.4 mg/mL) dissolved in SEC buffer (250-701 nm).

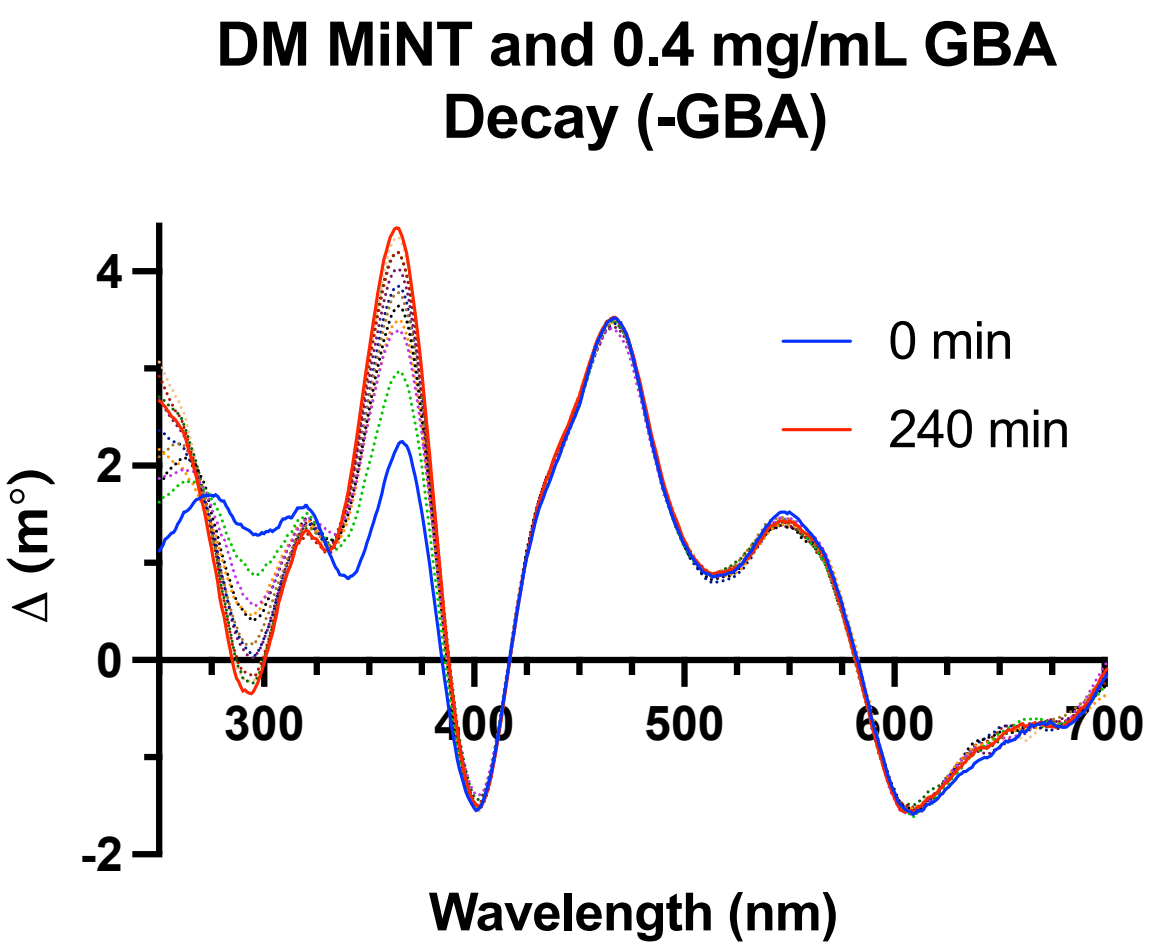

Figure 3.A82: A CD spectrum showing the result of subtracting the spectrum of 10% GBA in DMSO (0.4 mg/mL) dissolved in SEC buffer from the decay of DM MiNT with 10% GBA in DMSO (0.4 mg/mL) dissolved in SEC buffer.

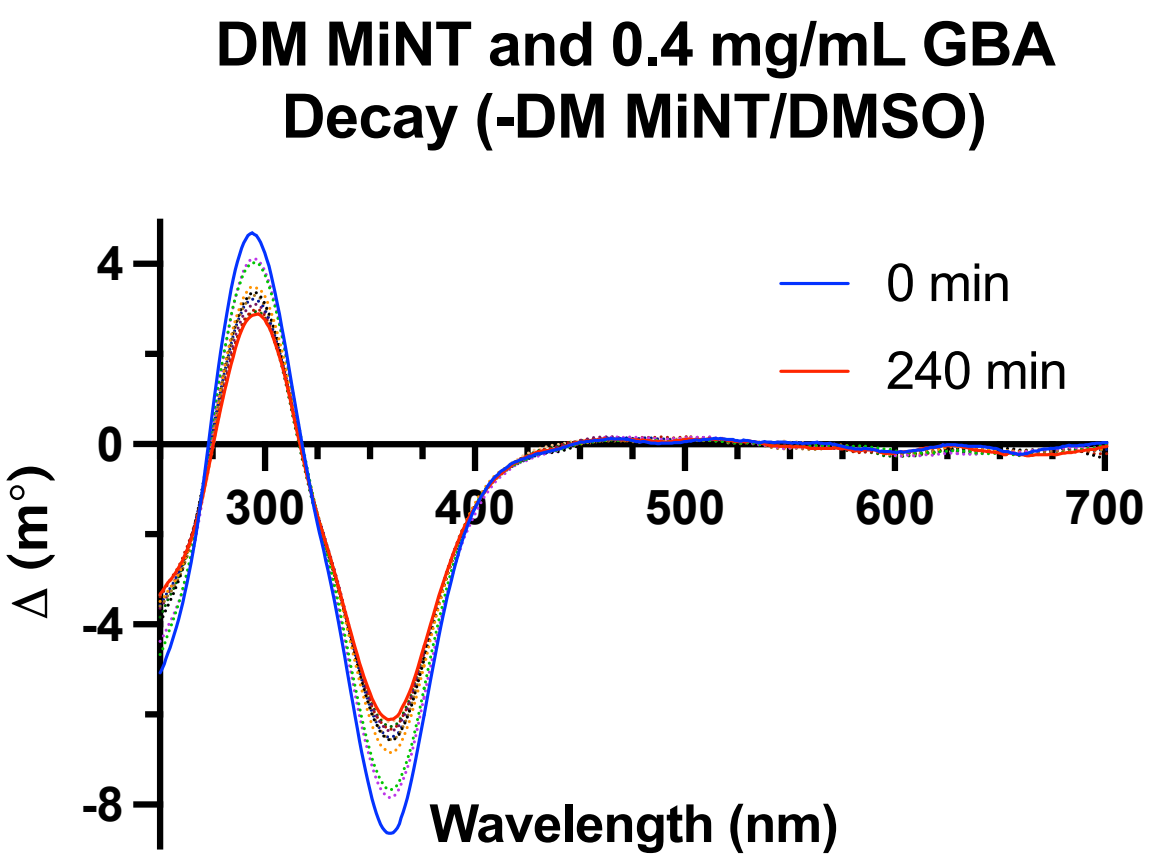

Figure 3.A83: A CD spectrum showing the result of subtracting the spectrum of DM MiNT with 10% DMSO dissolved in SEC buffer from the decay of DM MiNT with 10% GBA in DMSO (0.4 mg/mL) dissolved in SEC buffer.

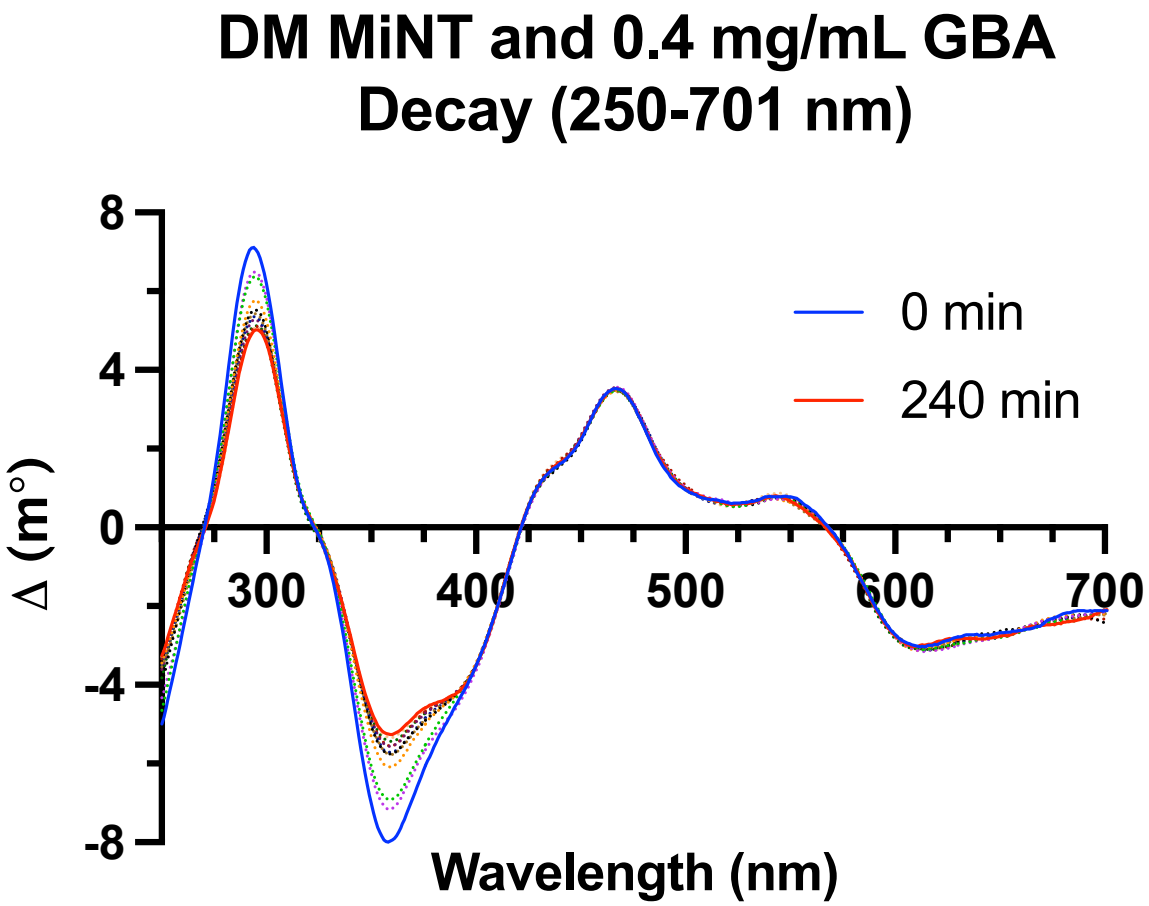

Figure 3.A84: A replicate CD spectrum of the decay of DM MiNT with 10% GBA in DMSO (0.4 mg/mL) dissolved in SEC buffer (250-701 nm).

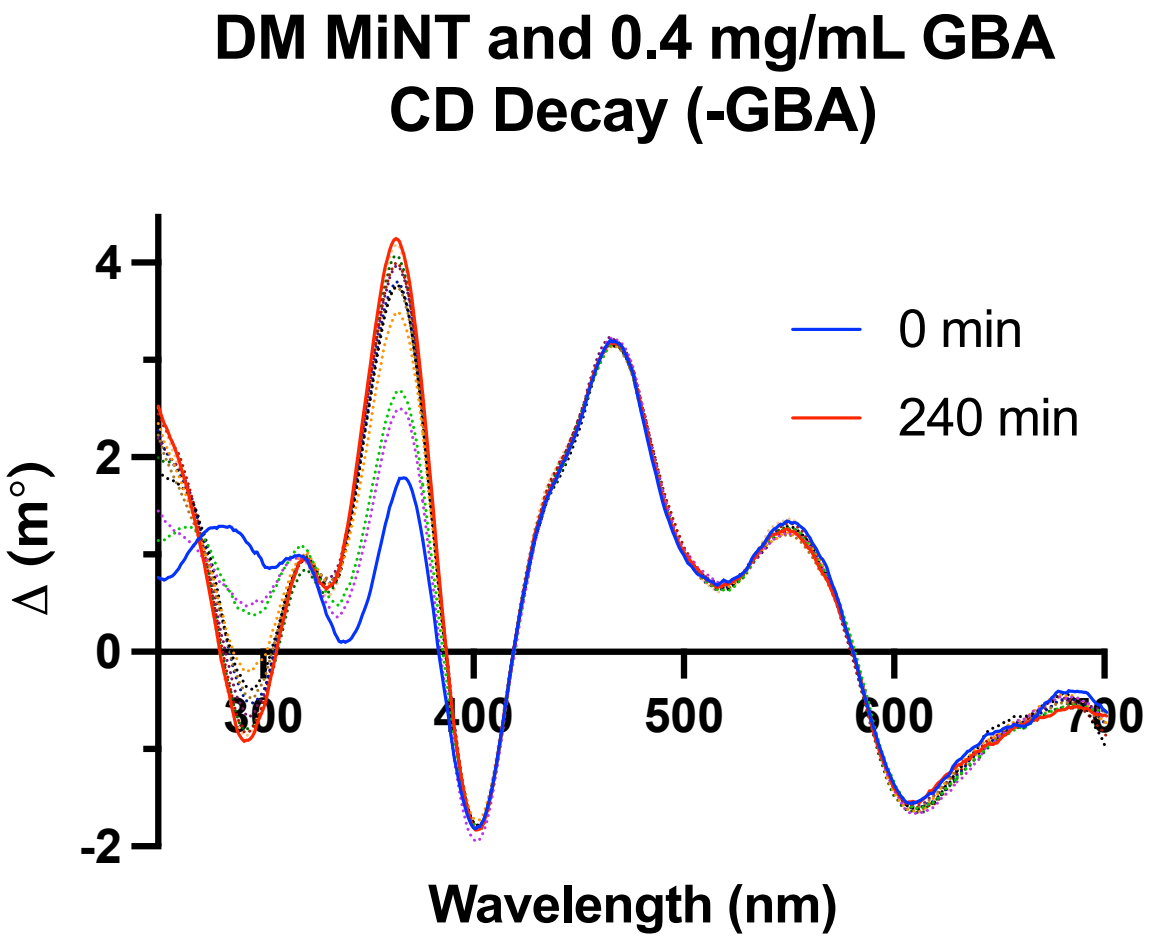

Figure 3.A85: A replicate CD spectrum showing the result of subtracting the spectrum of 10% GBA in DMSO (0.4 mg/mL) dissolved in SEC buffer from the decay of DM MiNT with 10% GBA in DMSO (0.4 mg/mL) dissolved in SEC buffer.

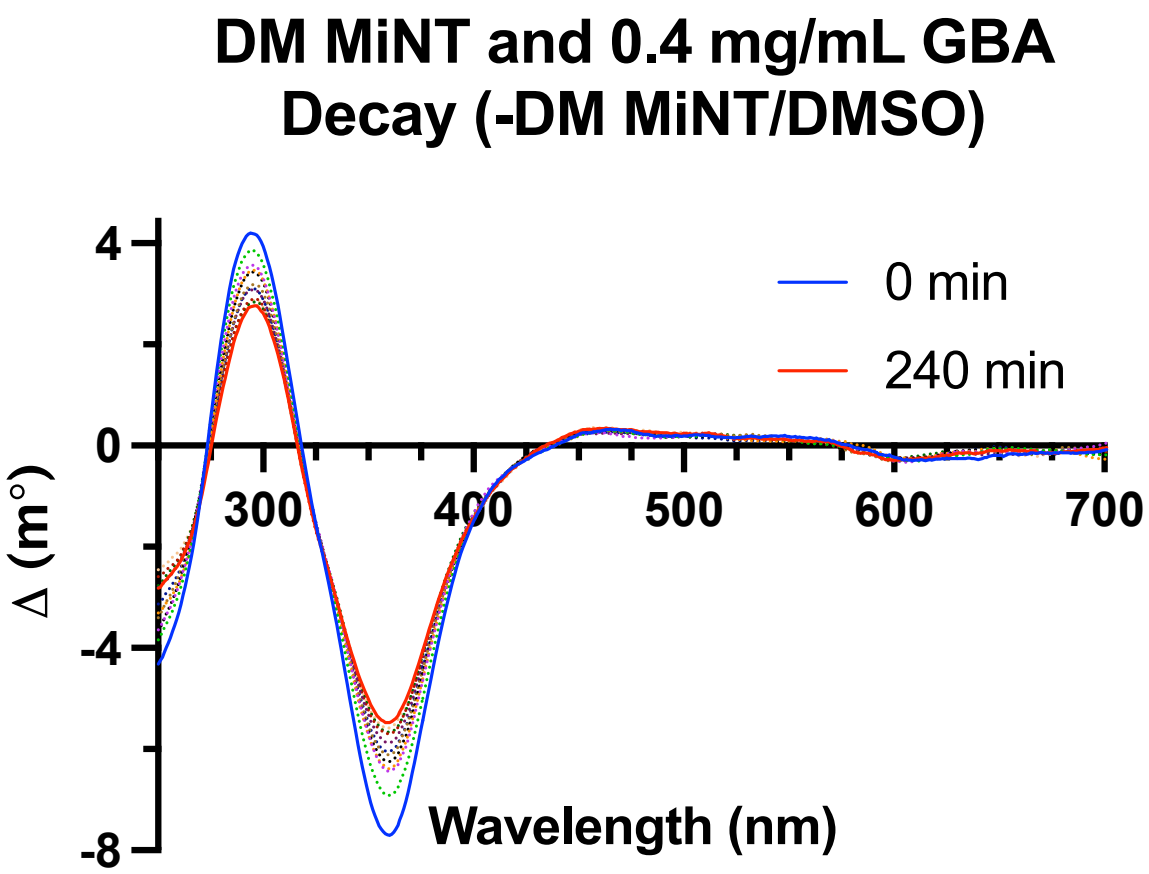

Figure 3.A86: A replicate CD spectrum showing the result of subtracting the spectrum of DM MiNT with 10% DMSO dissolved in SEC buffer from the decay of DM MiNT with 10% GBA in DMSO (0.4 mg/mL) dissolved in SEC buffer.

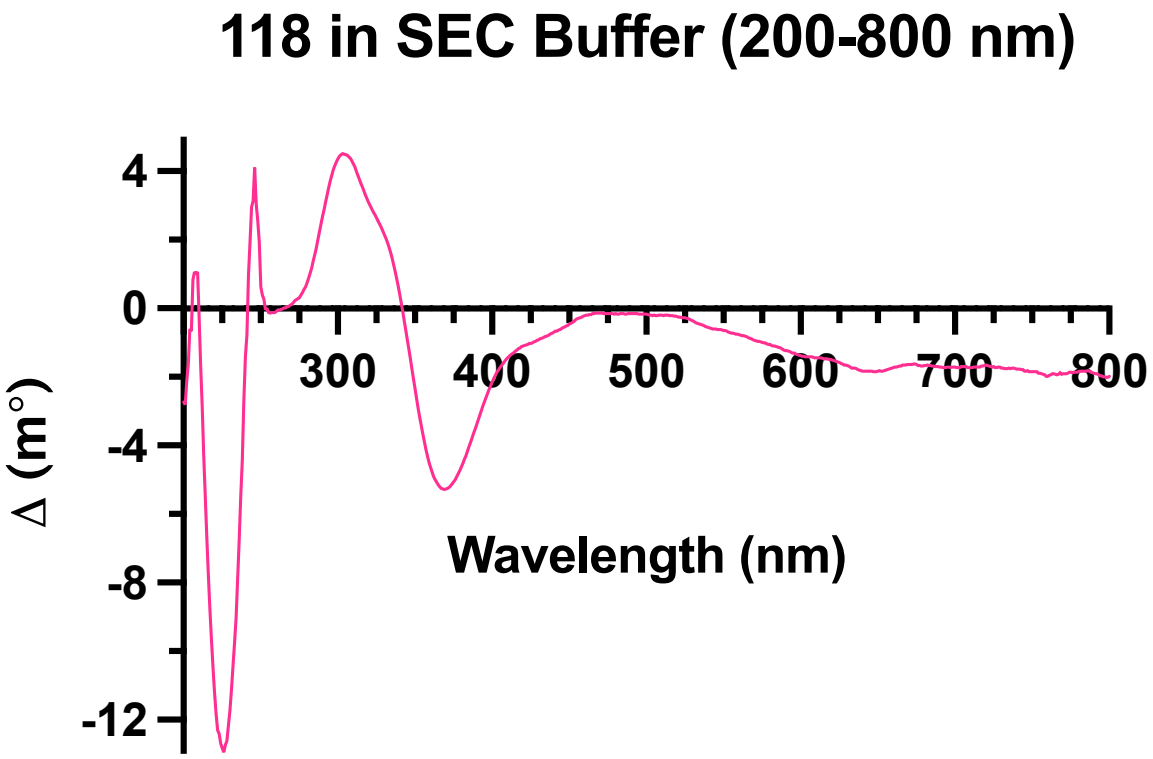

Figure 3.A87: CD spectrum of 10% 118 in DMSO (0.4 mg/mL) dissolved in SEC buffer (200-800 nm).

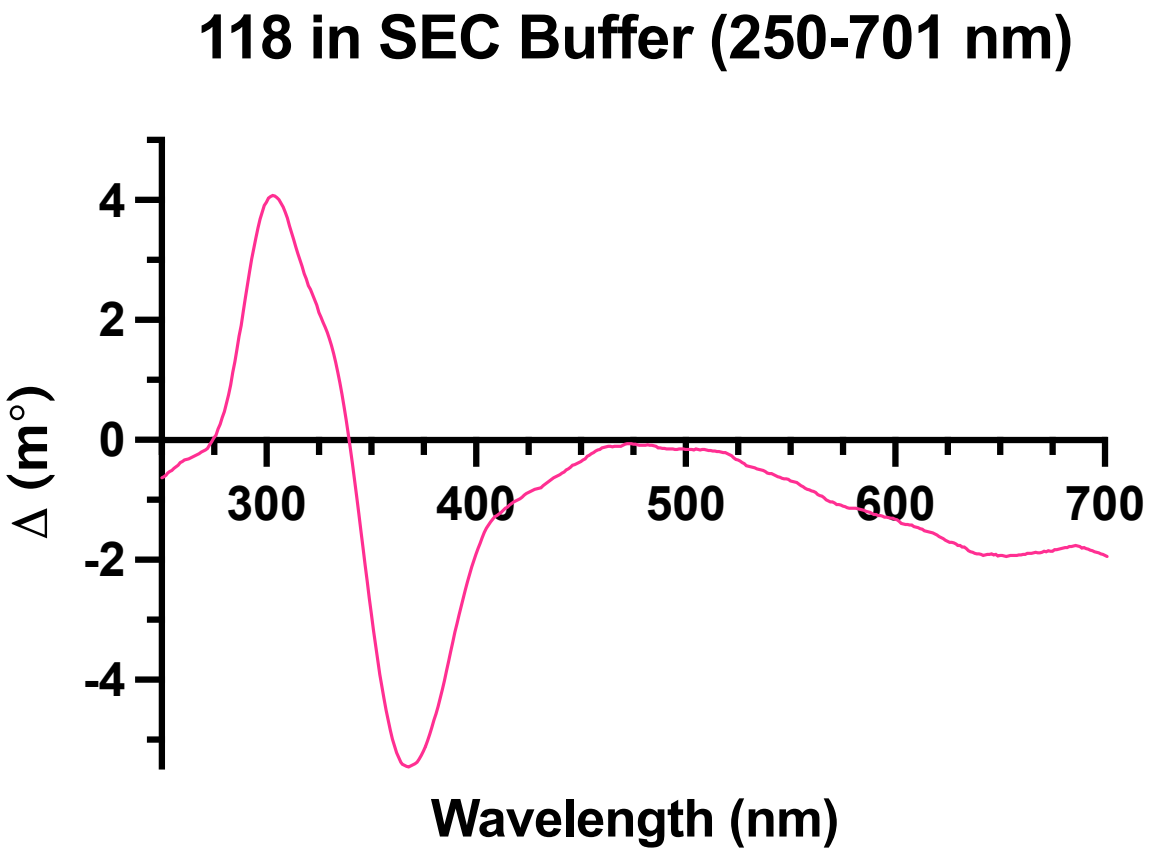

Figure 3.A88: CD spectrum of 10% 118 in DMSO (0.4 mg/mL) dissolved in SEC buffer (250-701 nm).

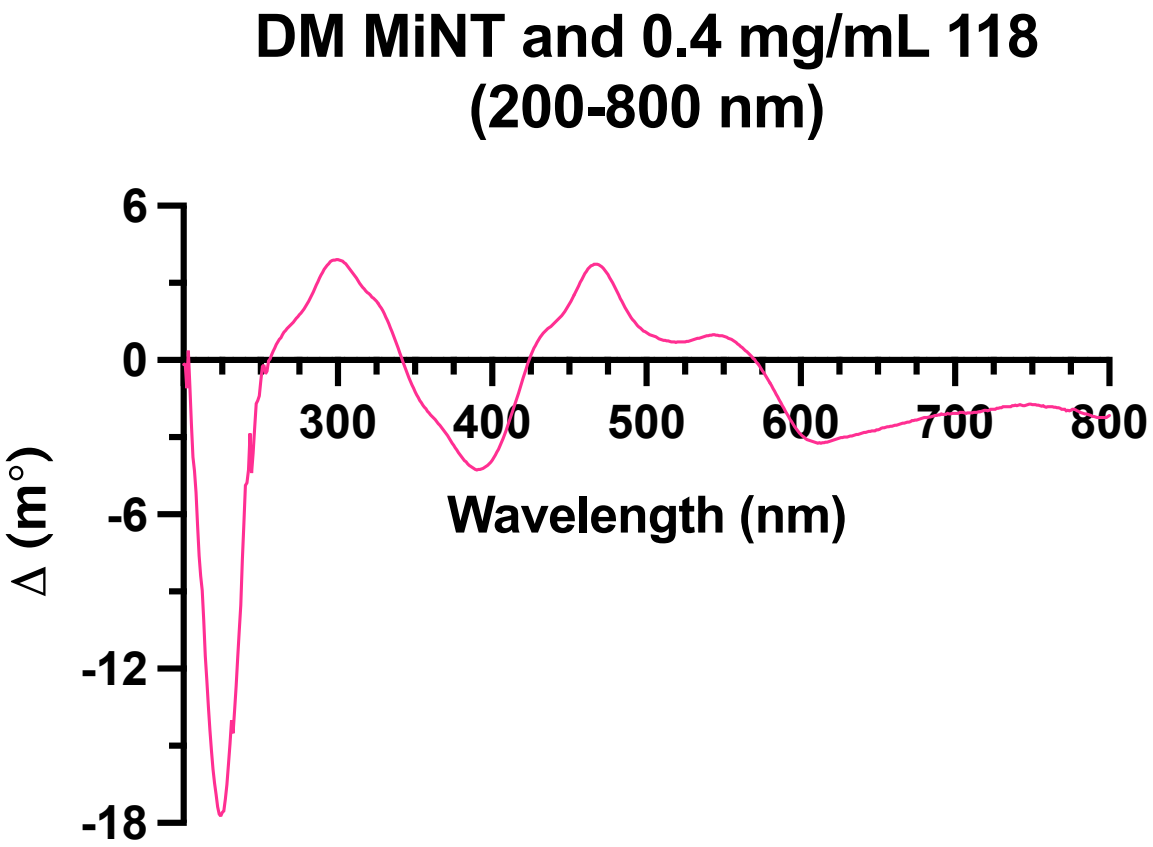

Figure 3.A89: CD spectrum of DM MiNT with 10% 118 in DMSO (0.4 mg/mL) dissolved in SEC buffer (200-800 nm).

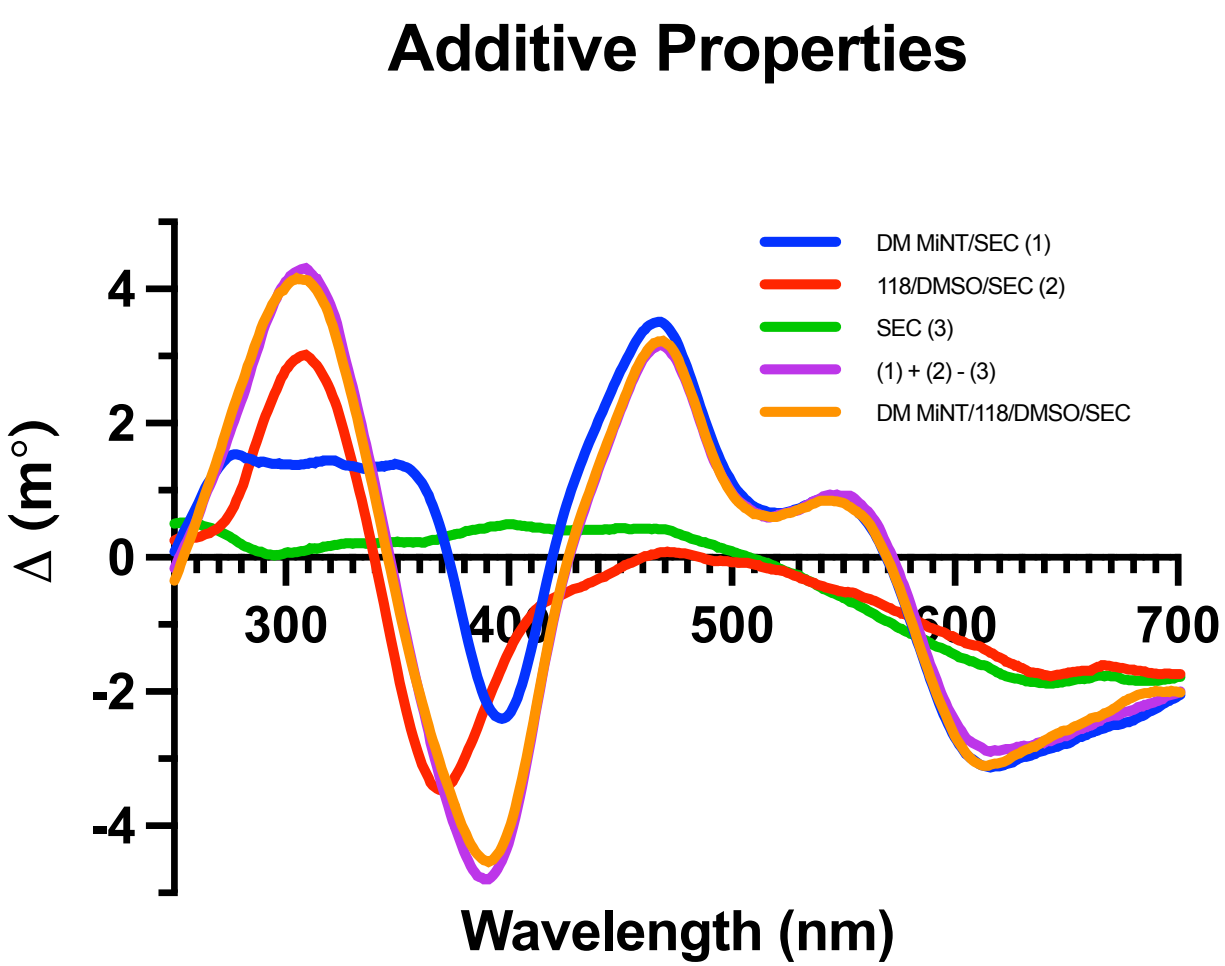

Figure 3.A90: CD spectrum showing the additive properties of DM MiNT and 118/DMSO (250-701 nm). A spectrum of DM MiNT in SEC buffer (1, blue) can be added to a spectrum of 10% 118 in DMSO (0.4 mg/mL) dissolved in SEC buffer (2, red). Subtracting a spectrum of SEC buffer (3, green) yields a nearly identical spectrum (purple) to a spectrum of a mixture of DM MiNT with 10% 118 in DMSO (0.4 mg/mL) dissolved in SEC buffer (orange).

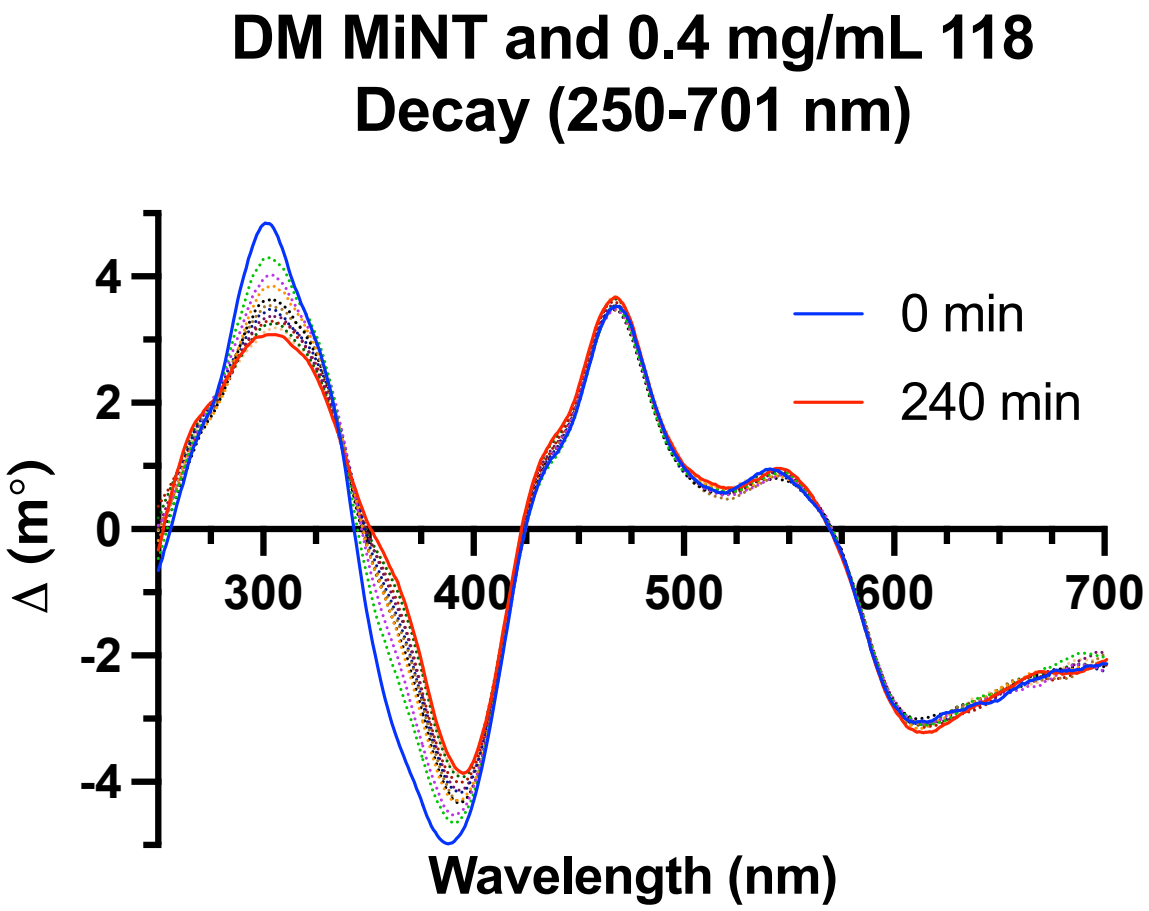

Figure 3.A91: CD spectrum of the decay of DM MiNT with 10% 118 in DMSO (0.4 mg/mL) dissolved in SEC buffer (250-701 nm).

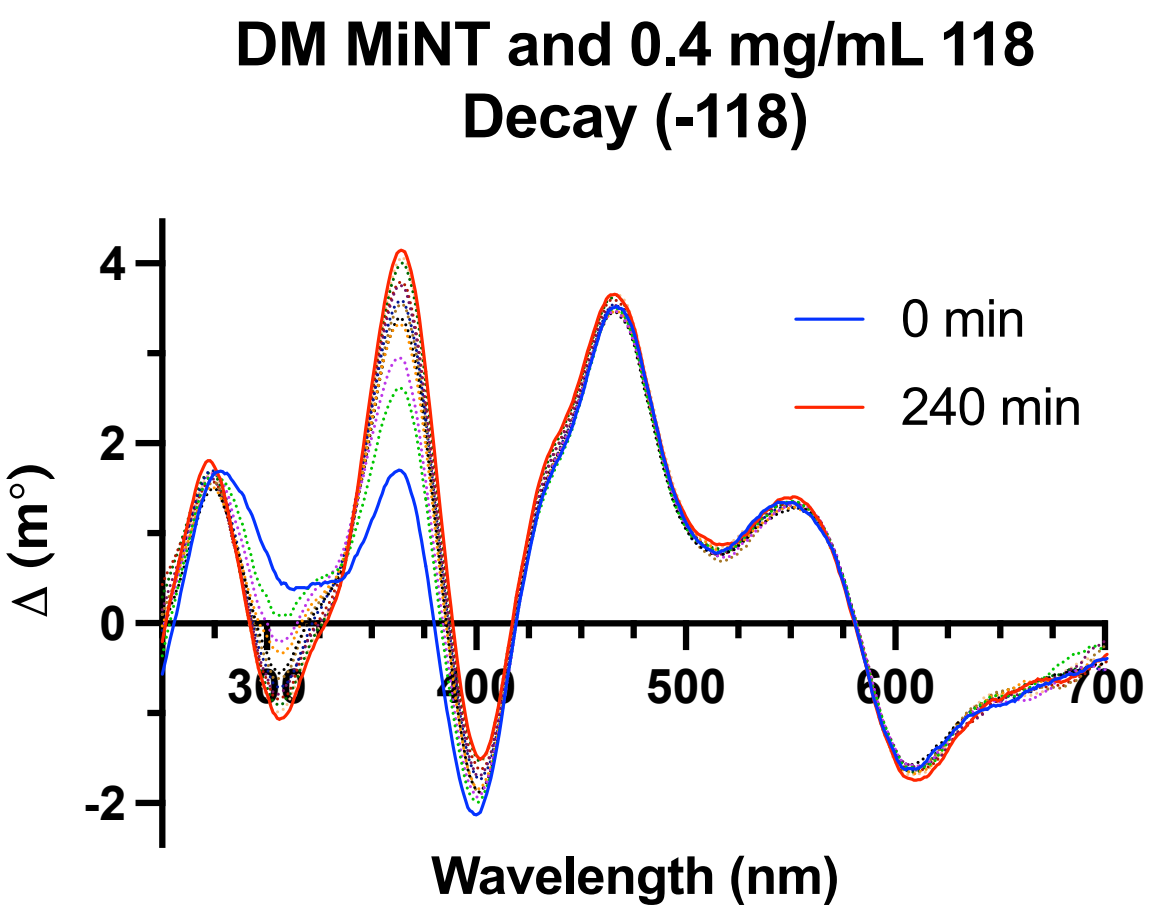

Figure 3.A92: CD spectrum showing the result of subtracting the spectrum of 10% 118 in DMSO (0.4 mg/mL) from the decay of DM MiNT with 10% 118 in DMSO (0.4 mg/mL) dissolved in SEC buffer.

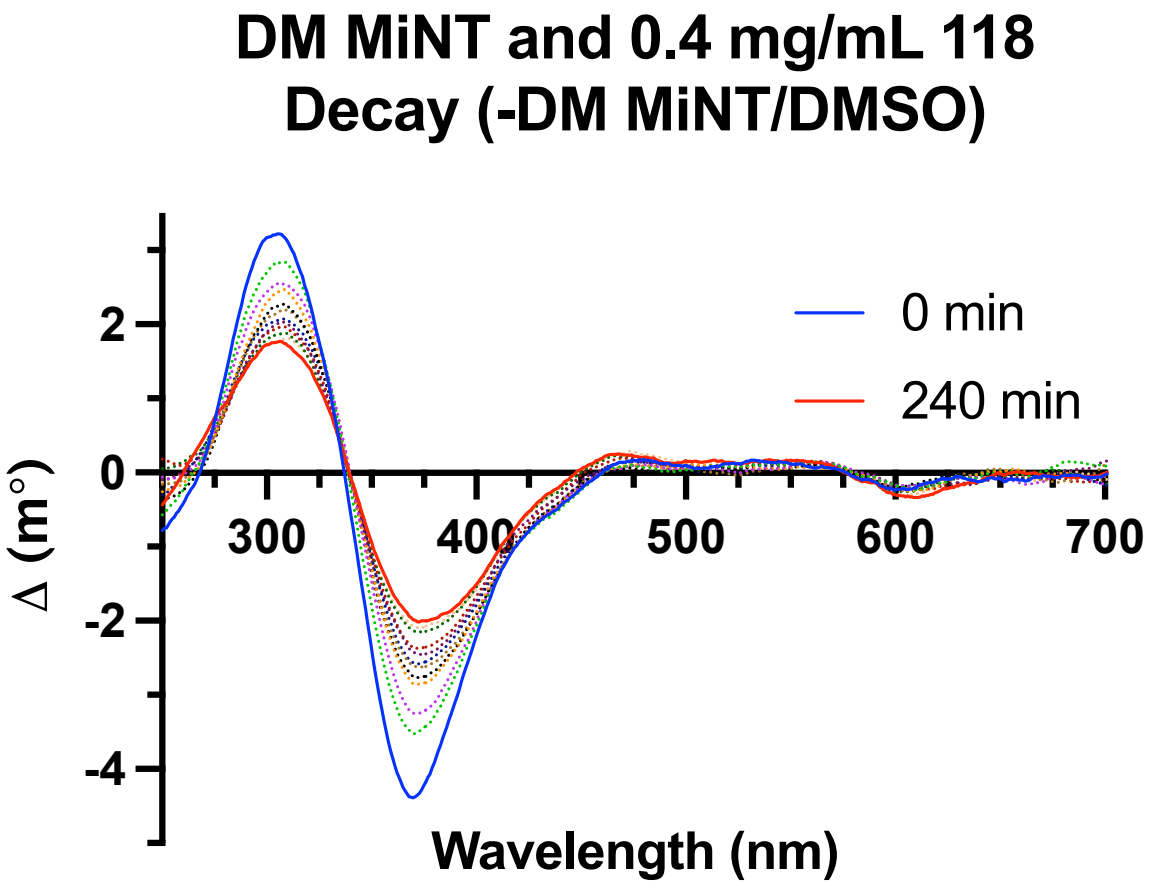

Figure 3.A93: CD spectrum showing the result of subtracting the spectrum of DM MiNT with 10% DMSO from the decay of DM MiNT with 10% 118 in DMSO (0.4 mg/mL).

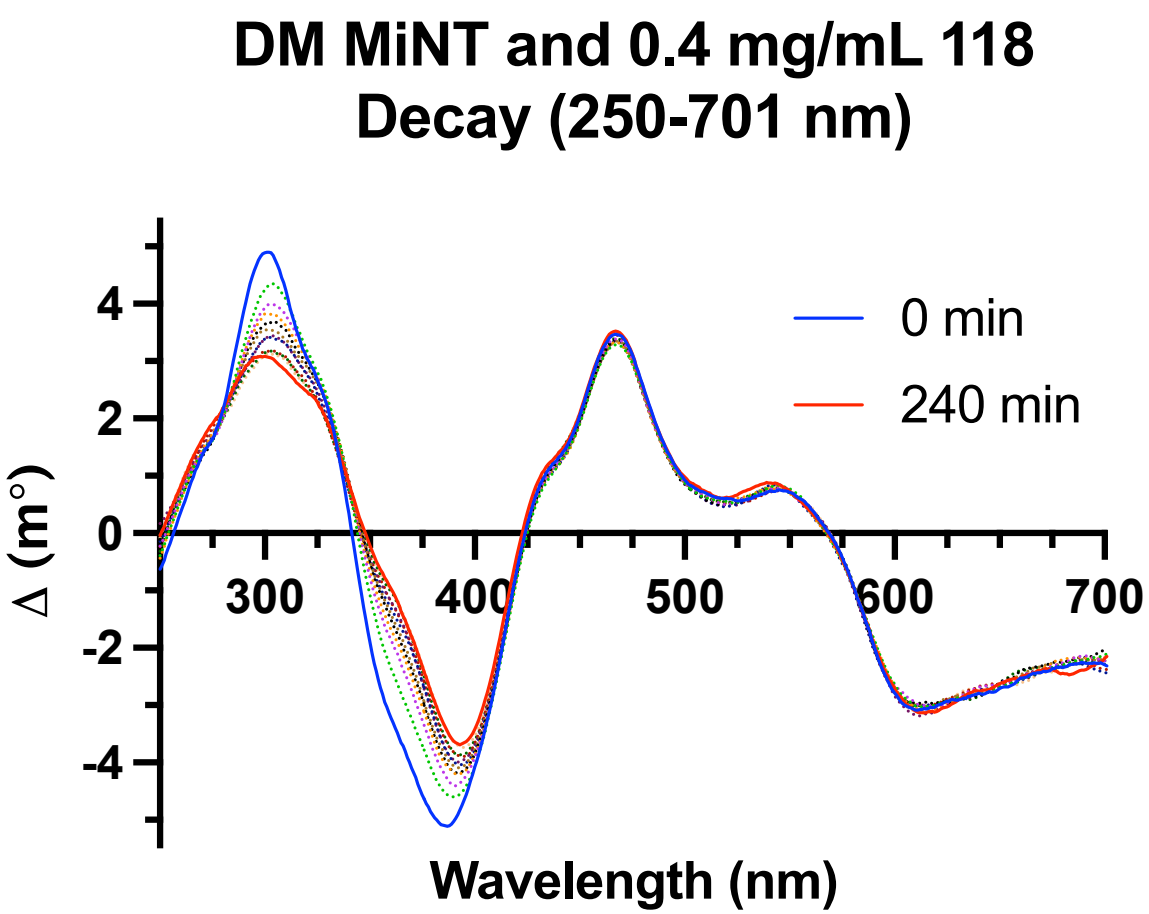

Figure 3.A94: Replicate CD spectrum of the decay of DM MiNT with 10% 118 in DMSO (0.4 mg/mL) dissolved in SEC buffer (250-701 nm).

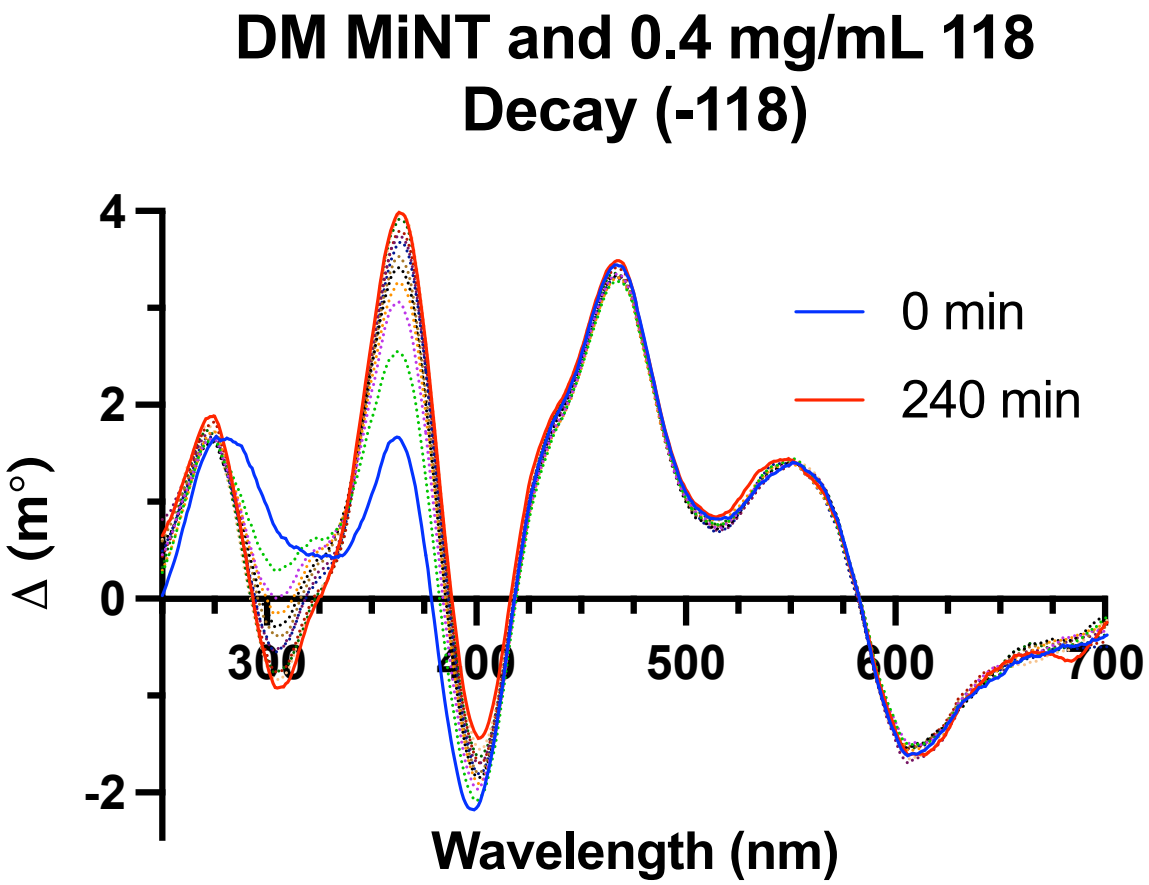

Figure 3.A95: Replicate CD spectrum showing the result of subtracting the spectrum of 10% 118 in DMSO (0.4 mg/mL) dissolved in SEC buffer from the decay of DM MiNT with 10% 118 in DMSO (0.4 mg/mL) dissolved in SEC buffer.

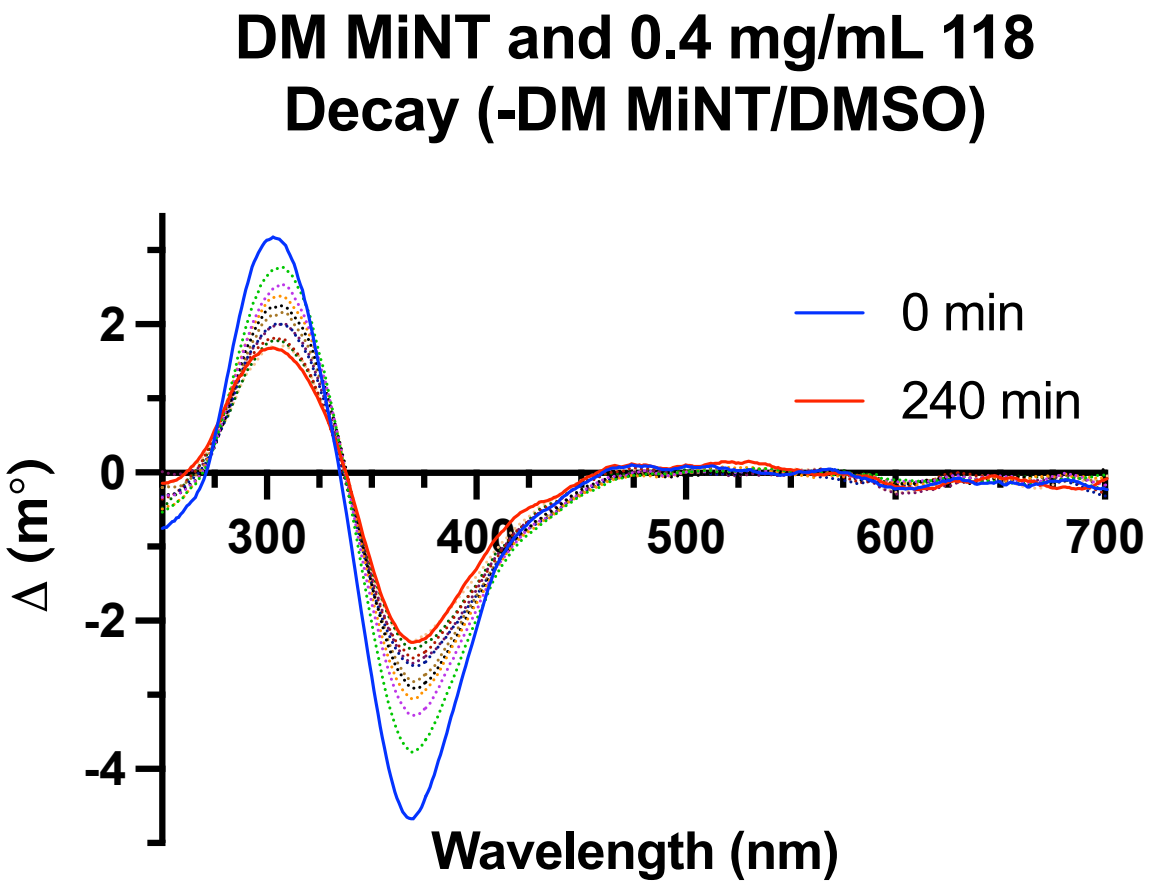

Figure 3.A96: Replicate CD spectrum showing the result of subtracting the spectrum of DM MiNT with 10% DMSO dissolved in SEC buffer from the decay of DM MiNT with 10% 118 in DMSO (0.4 mg/mL) dissolved in SEC buffer.

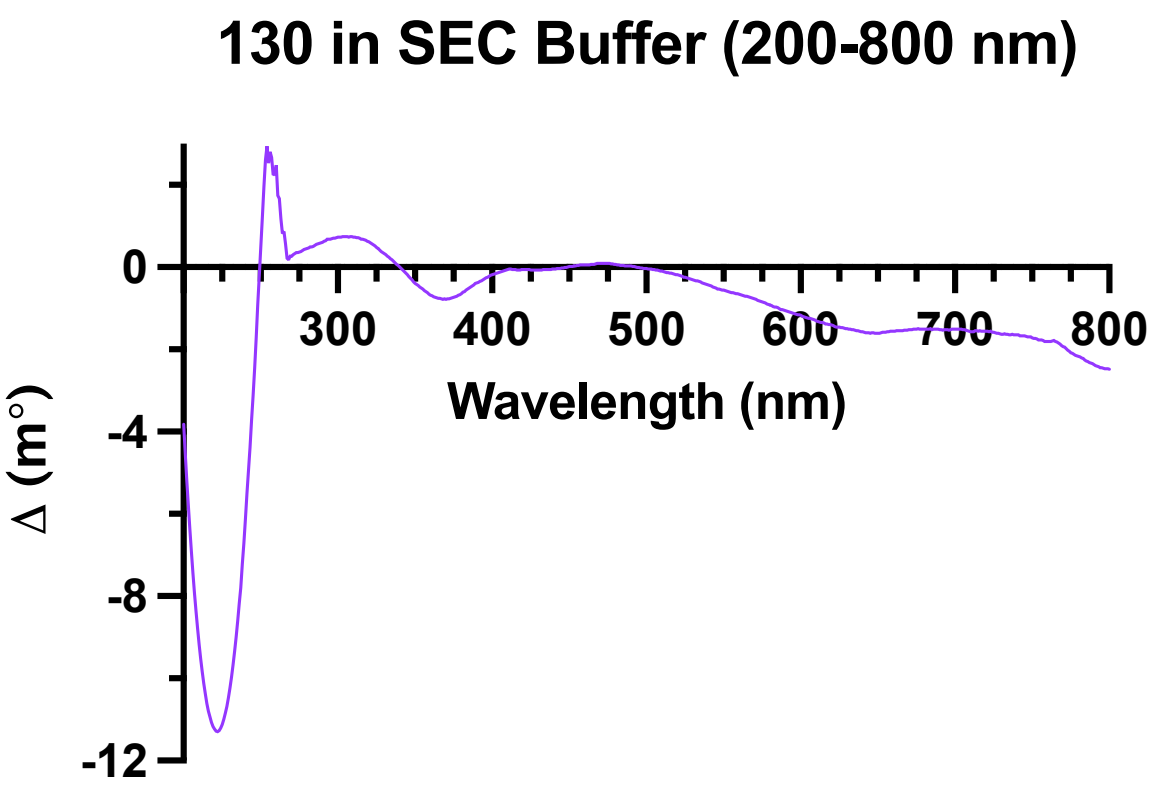

Figure 3.A97: CD spectrum of 10% 130 in DMSO (0.4 mg/mL) dissolved in SEC buffer (200-800 nm).

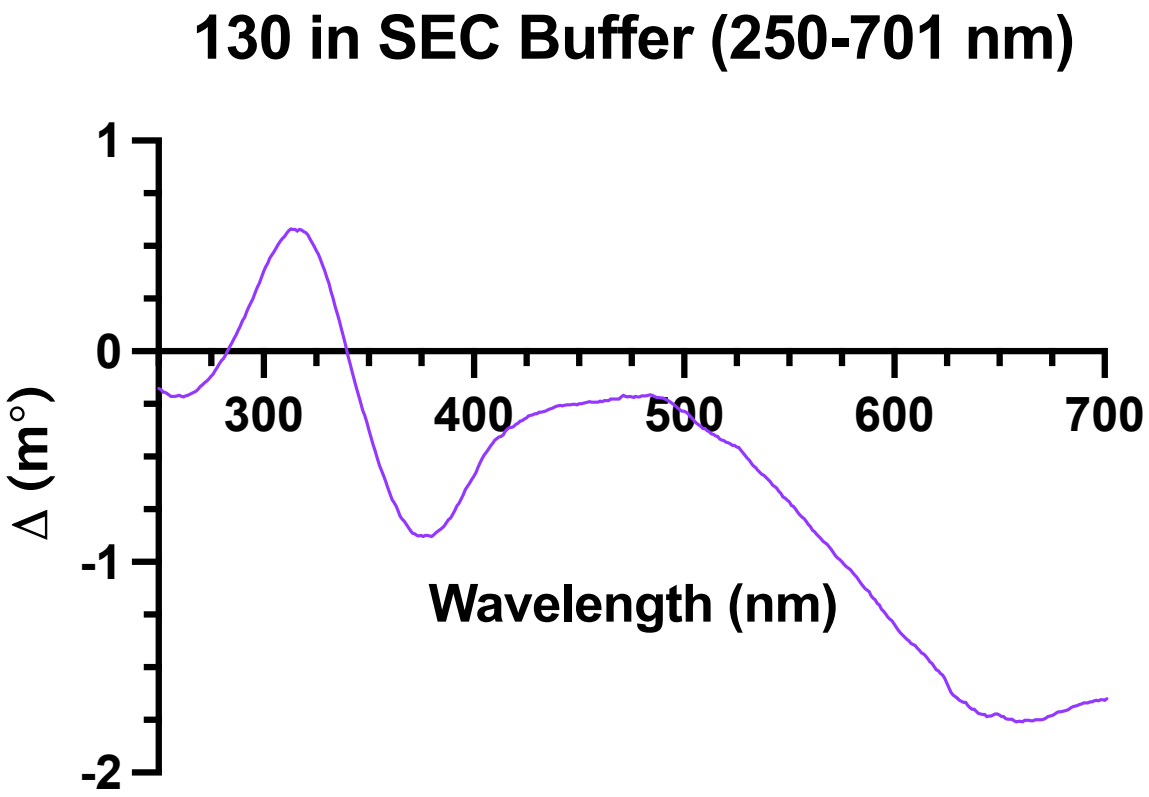

Figure 3.A98: CD spectrum of 10% 130 in DMSO (0.4 mg/mL) dissolved in SEC buffer (250-701 nm).

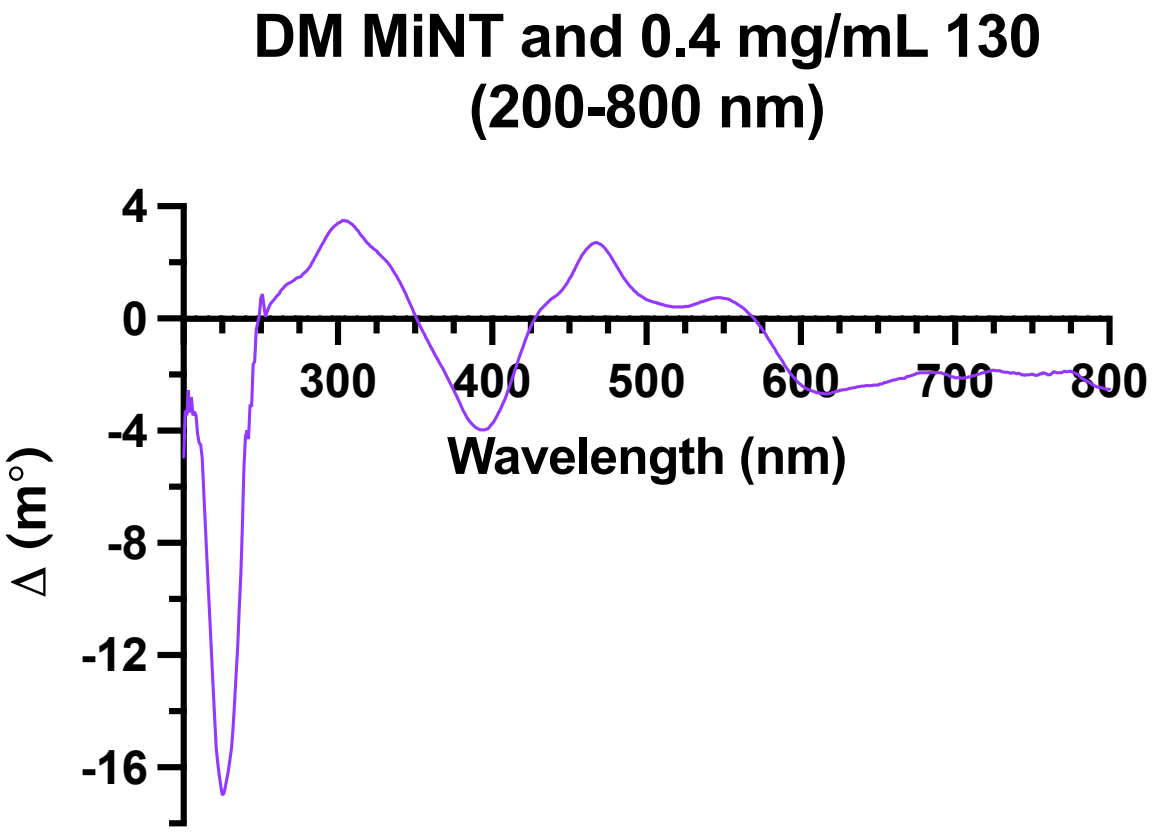

Figure 3.A99: CD spectrum of DM MiNT with 10% 130 in DMSO (0.4 mg/mL) dissolved in SEC buffer (200-800 nm).

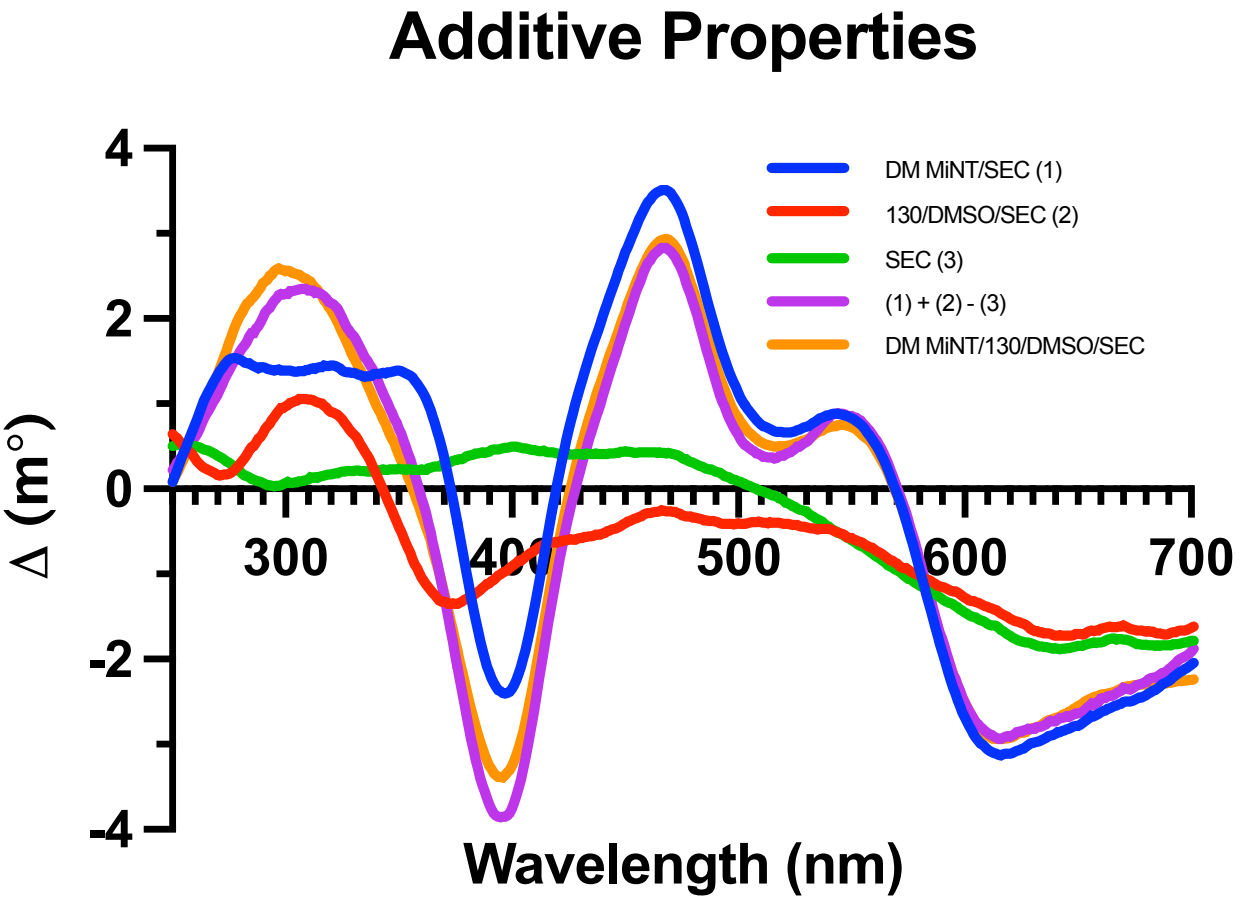

Figure 3.A100: CD spectrum showing the additive properties of DM MiNT and 130/DMSO (250-701 nm). A spectrum of DM MiNT in SEC buffer (1, blue) can be added to a spectrum of 10% 130 in DMSO (0.4 mg/mL) dissolved in SEC buffer (2, red). Subtracting a spectrum of SEC buffer (3, green) yields a nearly identical spectrum (purple) to a spectrum of a mixture of DM MiNT with 10% 130 in DMSO (0.4 mg/mL) dissolved in SEC buffer (orange).

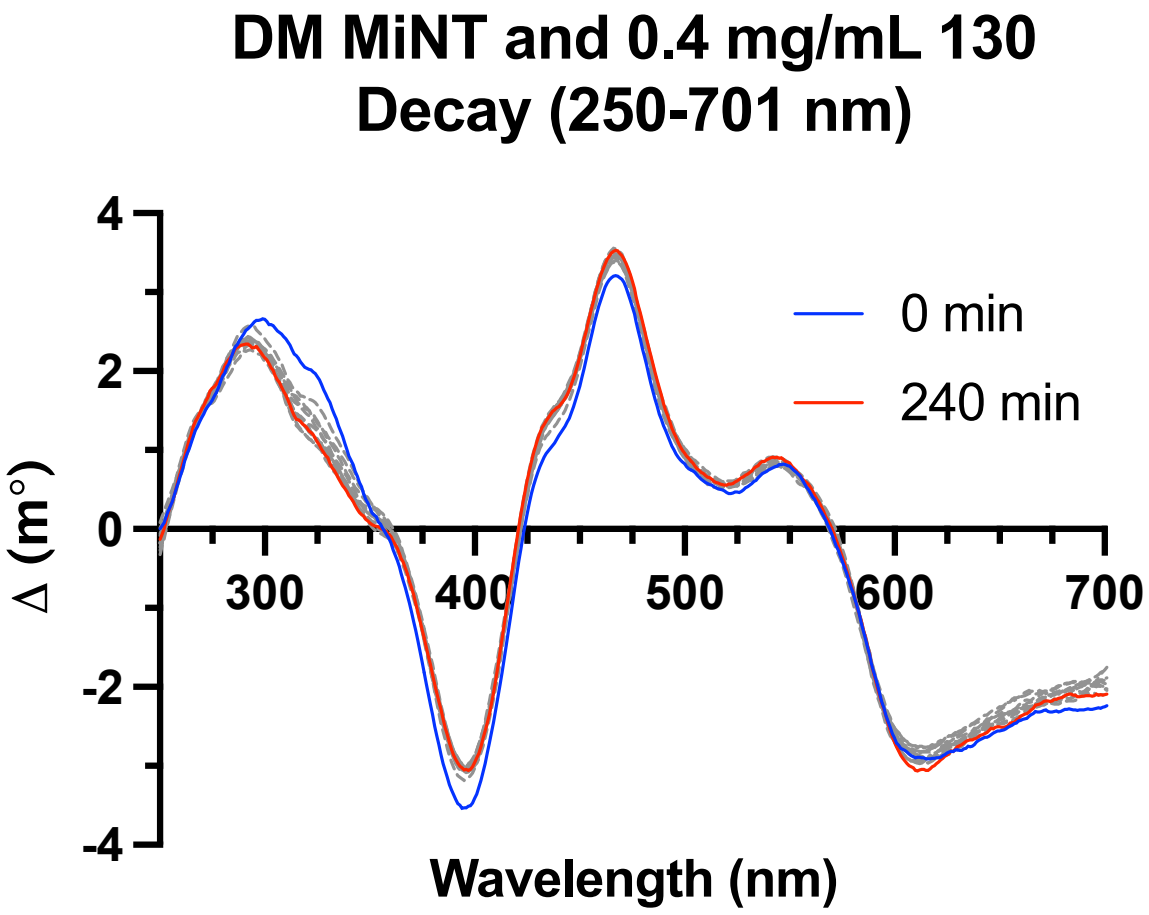

Figure 3.A101: CD spectrum of the decay of DM MiNT with 10% 130 in DMSO (0.4 mg/mL) dissolved in SEC buffer (250-701 nm).

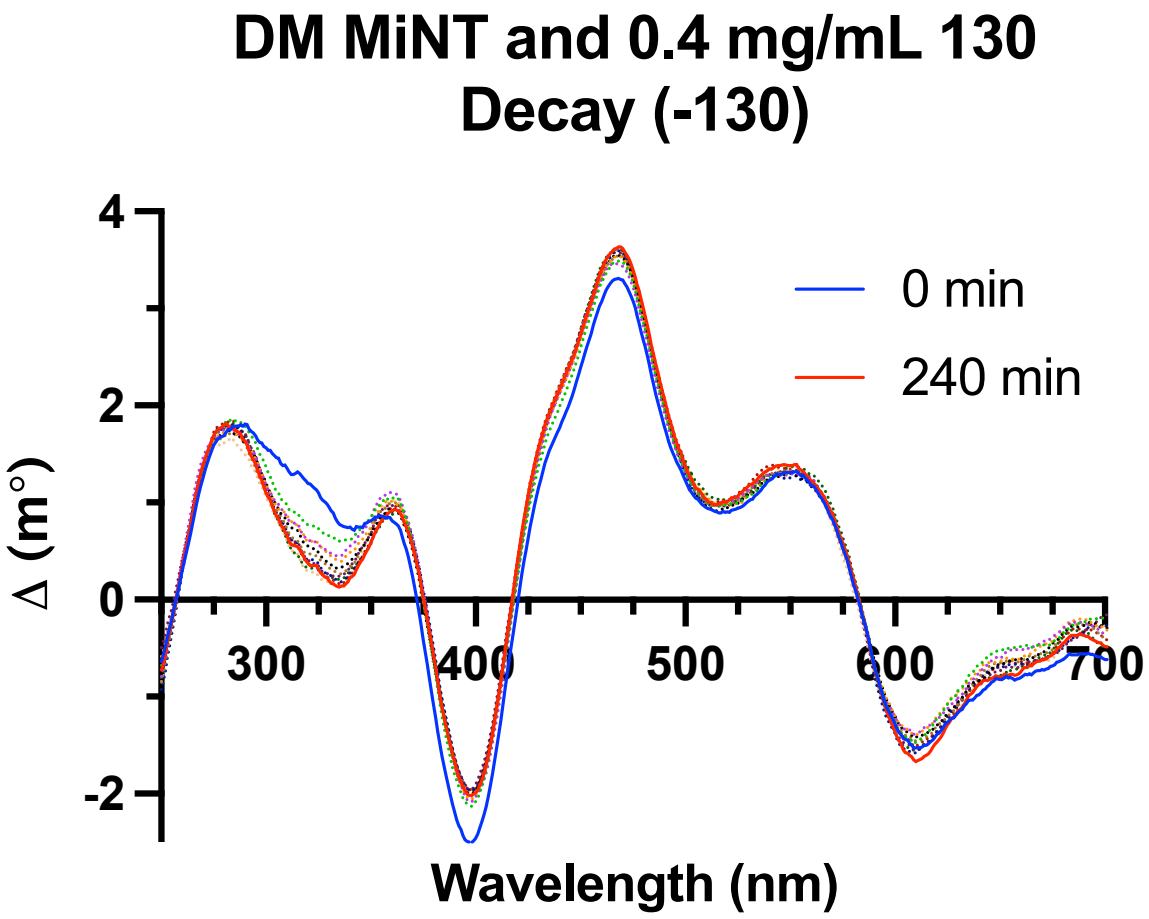

Figure 3.A102: CD spectrum showing the result of subtracting the spectrum of 10% 130 in DMSO (0.4 mg/mL) from the decay of DM MiNT with 10% 130 in DMSO (0.4 mg/mL) dissolved in SEC buffer.

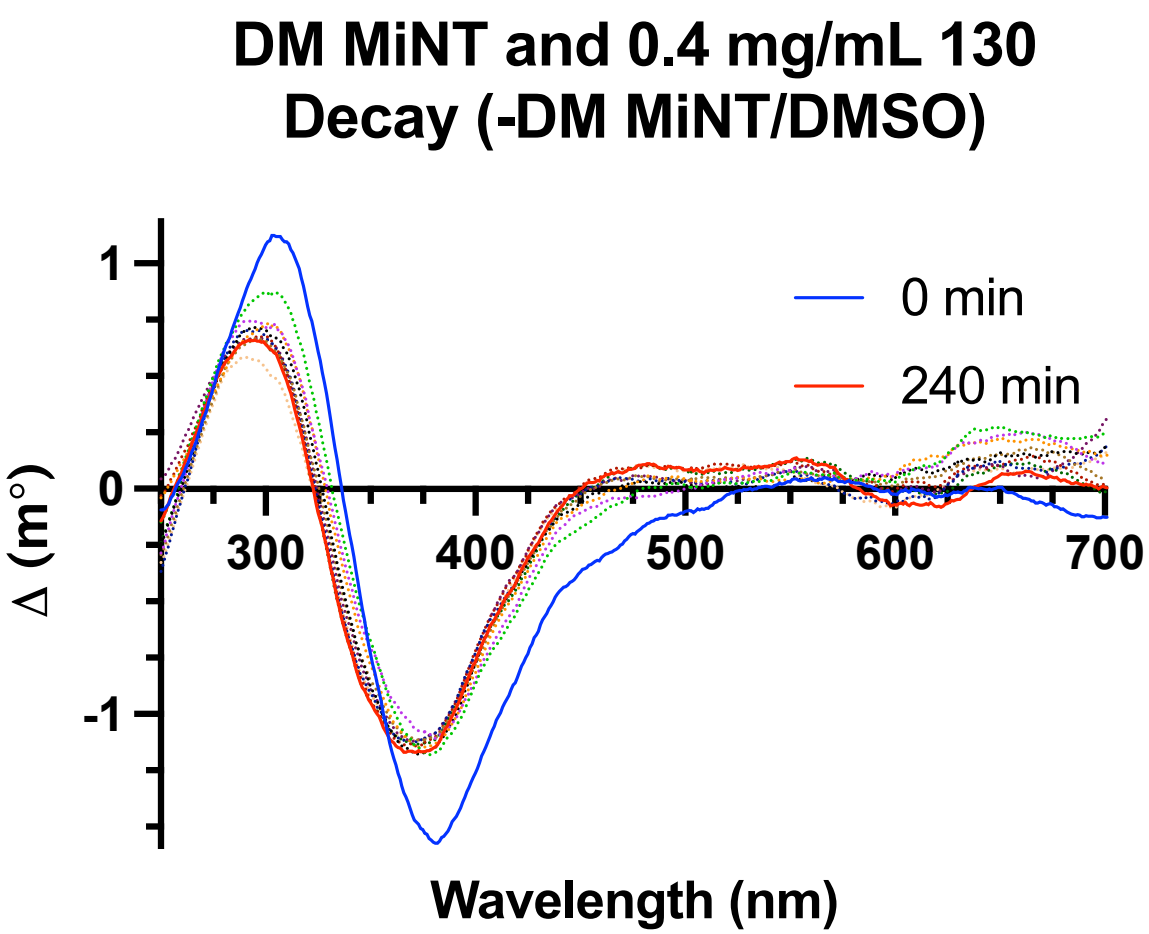

Figure 3.A103: CD spectrum showing the result of subtracting the spectrum of DM MiNT with 10% DMSO dissolved in SEC buffer from the decay of DM MiNT with 10% 130 in DMSO (0.4 mg/mL) dissolved in SEC buffer.

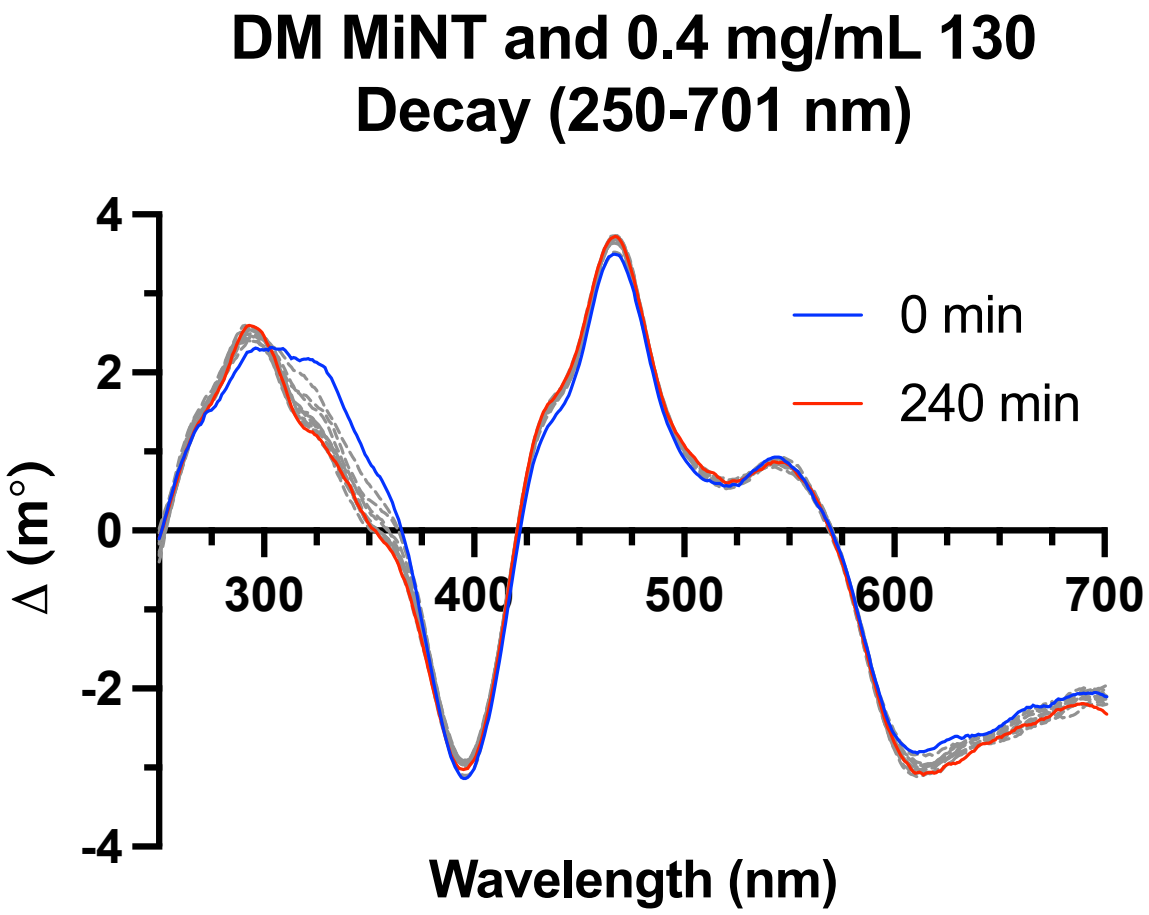

Figure 3.A104: Replicate CD spectrum of the decay of DM MiNT with 10% 130 in DMSO (0.4 mg/mL) dissolved in SEC buffer (250-701 nm).

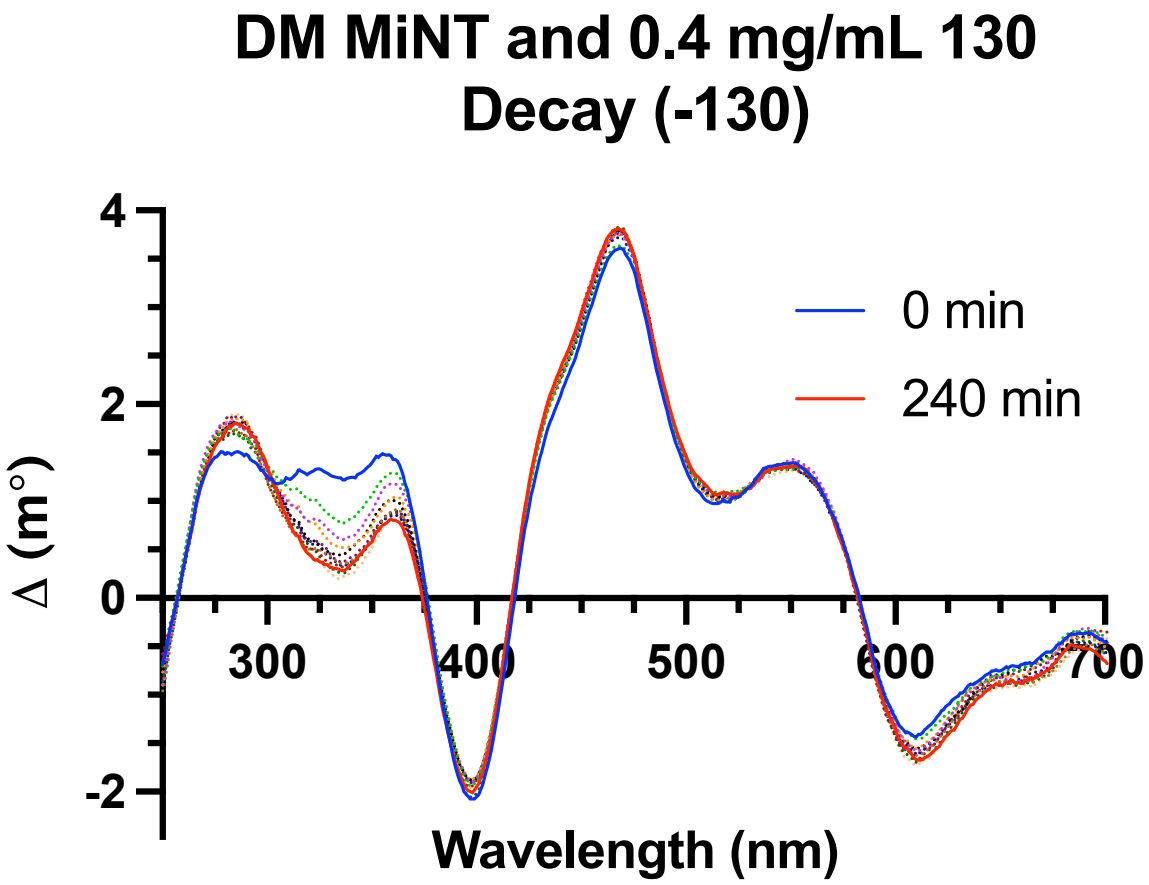

Figure 3.A105: Replicate CD spectrum showing the result of subtracting the spectrum of 10% 130 in DMSO (0.4 mg/mL) dissolved in SEC buffer from the decay of DM MiNT with 10% 130 in DMSO (0.4 mg/mL) dissolved in SEC buffer.

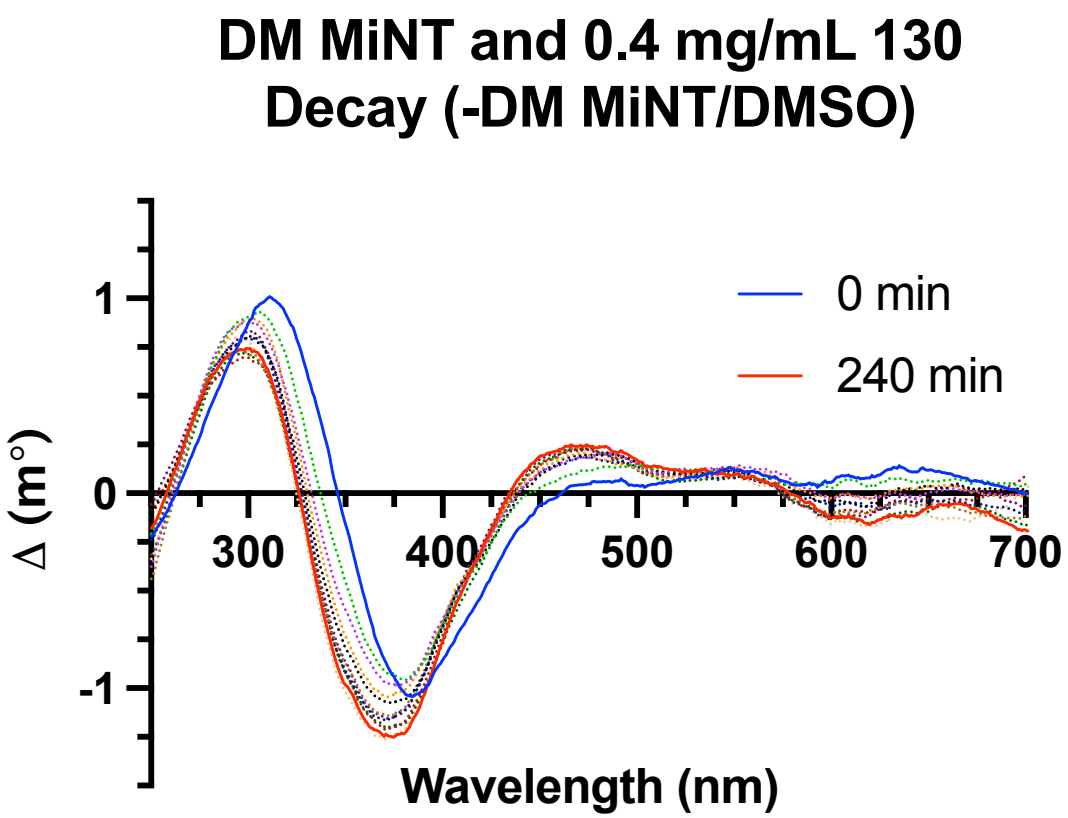

Figure 3.A106: Replicate CD spectrum showing the result of subtracting the spectrum of DM MiNT with 10% DMSO dissolved in SEC buffer from the decay of DM MiNT with 10% 130 in DMSO (0.4 mg/mL) dissolved in SEC buffer.

Chapter 3, in part, is currently being prepared for submission for publication of the material. Arevalo, G. E.; Capraro, D. T.; Lin, H. H.; Jennings, P. A.; Theodorakis, E. A. The dissertation author was the primary researcher and author of this material.

REFERENCES

(1) Chantarasriwong, O.; Batova, A.; Chavasiri, W.; Theodorakis, E. A. Chemistry and biology of the caged *Garcinia* xanthones. *Chemistry* **2010**, *16* (33), 9944-9962. DOI: 10.1002/chem.201000741

(2) Ren, Y.; Yuan, C.; Chai, H. B.; Ding, Y.; Li, X. C.; Ferreira, D.; Kinghorn, A. D. Absolute configuration of (-)-gambogic acid, an antitumor agent. *J Nat Prod* **2011**, *74* (3), 460-463. DOI: 10.1021/np100422z

(3) Qi, Q.; Lu, N.; Wang, X. T.; Gu, H. Y.; Yang, Y.; Liu, W.; Li, C.; You, Q. D.; Guo, Q. L. Anti-invasive effect of gambogic acid in MDA-MB-231 human breast carcinoma cells. *Biochem Cell Biol* **2008**, *86* (5), 386-395. DOI: 10.1139/o08-104

(4) Liu, W.; Guo, Q. L.; You, Q. D.; Zhao, L.; Gu, H. Y.; Yuan, S. T. Anticancer effect and apoptosis induction of gambogic acid in human gastric cancer line BGC-823. *World J Gastroenterol* **2005**, *11* (24), 3655-3659. DOI: 10.3748/wjg.v11.i24.3655

(5) Chen, J.; Zhou, M.; Zhang, Q.; Xu, J.; Ouyang, J. Anticancer Effect and Apoptosis Induction of Gambogic Acid in Human Leukemia Cell Line K562 In Vitro. *Med Sci Monit* **2015**, *21*, 1604-1610. DOI: 10.12659/MSM.893004

(6) Wang, Q. L.; Yang, D. Z.; Lv, C. Antiinflammatory effects of gambogic acid in murine collageninduced arthritis through PI3K/Akt signaling pathway. *Mol Med Rep* **2018**, *17* (3), 4791-4796. DOI: 10.3892/mmr.2018.8389

(7) Park, M. S.; Kim, N. H.; Kang, C. W.; Oh, C. W.; Kim, G. D. Antimetastatic effects of gambogic acid are mediated via the actin cytoskeleton and NF-κB pathways in SK-HEP1 cells. *Drug Dev Res* **2015**, *76* (3), 132-142. DOI: 10.1002/ddr.21249

(8) Lee, P. N.; Ho, W. S. Antiproliferative activity of gambogic acid isolated from *Garcinia hanburyi* in Hep3B and Huh7 cancer cells. *Oncol Rep* **2013**, *29* (5), 1744-1750. DOI: 10.3892/or.2013.2291

(9) Li, D.; Yang, H.; Li, R.; Wang, Y.; Wang, W.; Li, D.; Ma, S.; Zhang, X. Antitumor activity of gambogic acid on NCI-H1993 xenografts via MET signaling pathway downregulation. *Oncol Lett* **2015**, *10* (5), 2802-2806. DOI: 10.3892/ol.2015.3719

(10) Krajarng, A.; Imoto, M.; Tashiro, E.; Fujimaki, T.; Shinjo, S.; Watanapokasin, R. Apoptosis induction associated with the ER stress response through up-regulation of JNK in HeLa cells by gambogic acid. *BMC Complement Altern Med* **2015**, *15*, 26. DOI: 10.1186/s12906-015-0544-4

(11) Liu, W. Y.; Wu, X. U.; Liao, C. Q.; Shen, J.; Li, J. Apoptotic effect of gambogic acid in esophageal squamous cell carcinoma cells via suppression of the NF-κB pathway. *Oncol Lett* **2016**, *11* (6), 3681-3685. DOI: 10.3892/ol.2016.4437

(12) Han, Q. B.; Zhou, Y.; Feng, C.; Xu, G.; Huang, S. X.; Li, S. L.; Qiao, C. F.; Song, J. Z.; Chang, D. C.; Luo, K. Q.; Xu, H. X. Bioassay guided discovery of apoptosis inducers from gamboge by high-speed counter-current chromatography and high-pressure liquid chromatography/electrospray ionization quadrupole time-of-flight mass spectrometry. *J Chromatogr B Analyt Technol Biomed Life Sci* **2009**, *877* (4), 401-407. DOI: 10.1016/j.jchromb.2008.12.046

(13) Liu, N.; Huang, H.; Liu, S.; Li, X.; Yang, C.; Dou, Q. P.; Liu, J. Calcium channel blocker verapamil accelerates gambogic acid-induced cytotoxicity via enhancing proteasome inhibition and ROS generation. *Toxicol In Vitro* **2014**, *28* (3), 419-425. DOI: 10.1016/j.tiv.2013.12.008

(14) Chantarasriwong, O.; Dorwart, T. J.; Morales, T. H.; Maggio, S. F.; Settle, A. L.; Milcarek, A. T.; Alpaugh, M. L.; Theodoraki, M. A.; Theodorakis, E. A. Chiral resolution of a caged xanthone and evaluation across a broad spectrum of breast cancer subtypes. *Bioorg Chem* **2019**, *93*, 103303. DOI: 10.1016/j.bioorg.2019.103303

(15) Khaing, E. M.; Saenpunya, T.; Kerdklai, P.; Pangpongma, S.; Vongvijit, S.; Phaechamud, T.; Intaraphairot, T. Combination effects of gambogic acid on imatinib mesylate cytotoxicity in colon cancer cells. In *Key Engineering Materials*, **2020**; Trans Tech Publ: Vol. 859, pp 27-33.

(16) Zhang, W.; Zhou, H.; Yu, Y.; Li, J.; Li, H.; Jiang, D.; Chen, Z.; Yang, D.; Xu, Z.; Yu, Z. Combination of gambogic acid with cisplatin enhances the antitumor effects on cisplatin-resistant lung cancer cells by downregulating MRP2 and LRP expression. *Onco Targets Ther* **2016**, *9*, 3359-3368. DOI: 10.2147/OTT.S100936

(17) Hoch, D. G.; Abegg, D.; Hannich, J. T.; Pechalrieu, D.; Shuster, A.; Dwyer, B. G.; Wang, C.; Zhang, X.; You, Q.; Riezman, H.; Adibekian, A. Combined omics approach identifies gambogic acid and related xanthones as covalent inhibitors of the serine palmitoyltransferase complex. *Cell Chem Biol* **2020**, *27* (5), 586-597 e512. DOI: 10.1016/j.chembiol.2020.03.008

(18) Wang, C.; Wang, W.; Wang, C.; Tang, Y.; Tian, H. Combined therapy with EGFR TKI and gambogic acid for overcoming resistance in EGFR-T790M mutant lung cancer. *Oncol Lett* **2015**, *10* (4), 2063-2066. DOI: 10.3892/ol.2015.3599

(19) Weakley, T. J. R.; Cai, S. X.; Zhang, H.-Z.; Keana, J. F. W. Crystal structure of the pyridine salt of gambogic acid. *J Chem Crystallogr* **2001**, *31* (11/12), 501-505. DOI: 10.1023/a:1015615216439

(20) Yen, C. T.; Nakagawa-Goto, K.; Hwang, T. L.; Morris-Natschke, S. L.; Bastow, K. F.; Wu, Y. C.; Lee, K. H. Design and synthesis of gambogic acid analogs as potent cytotoxic and anti-inflammatory agents. *Bioorg Med Chem Lett* **2012**, *22* (12), 4018-4022. DOI: 10.1016/j.bmcl.2012.04.084

(21) Zhang, H. Z.; Kasibhatla, S.; Wang, Y.; Herich, J.; Guastella, J.; Tseng, B.; Drewe, J.; Cai, S. X. Discovery, characterization and SAR of gambogic acid as a potent apoptosis inducer by a HTS assay. *Bioorg Med Chem* **2004**, *12* (2), 309-317. DOI: 10.1016/j.bmc.2003.11.013

(22) Wang, X.; Li, Y.; Zhou, H.; Han, N.; Pan, L.; Yu, C. Effect of gambogic acid on miR-199a-3p expression and cell biological behavior in colorectal cancer cells. *J Oncol* **2021**, *2021*, 5140621. DOI: 10.1155/2021/5140621

(23) Yang, L. J.; Chen, Y.; He, J.; Yi, S.; Wen, L.; Zhao, S.; Cui, G. H. Effects of gambogic acid on the activation of caspase-3 and downregulation of SIRT1 in RPMI-8226 multiple myeloma cells via the accumulation of ROS. *Oncol Lett* **2012**, *3* (5), 1159-1165. DOI: 10.3892/ol.2012.634

(24) Wang, S.; Yang, Y.; Wang, Y.; Chen, M. Gambogic acid-loaded pH-sensitive mixed micelles for overcoming breast cancer. *Int J Pharm* **2015**, *495* (2), 840-848. DOI: 10.1016/j.ijpharm.2015.09.041

(25) Zou, Z. Y.; Wei, J.; Li, X. L.; Yu, L. X.; Wang, T. T.; Qian, X. P.; Liu, B. R. Enhancement of anticancer efficacy of chemotherapeutics by gambogic acid against gastric cancer cells. *Cancer Biother Radiopharm* **2012**, *27* (5), 299-306. DOI: 10.1089/cbr.2010.0943

(26) Yu, J.; Wang, W.; Yao, W.; Yang, Z.; Gao, P.; Liu, M.; Wang, H.; Chen, S.; Wang, D.; Wang, W.; Sun, G. Gambogic acid affects ESCC progression through regulation of PI3K/AKT/mTOR signal pathway. *J Cancer* **2020**, *11* (19), 5568-5577. DOI: 10.7150/jca.41115

(27) Luo, G.; Jiang, S.; Zhang, X.; Ling, Y.; Luo, H.; Zhang, Y. Gambogic acid affects ribosomal occurrence in glioma cells by downregulating the phosphoinositide kinase-3/protein kinase B/mammalian target of rapamycin signaling pathway. *J Nanosci Nanotechnol* **2020**, *20* (6), 3361-3372. DOI: 10.1166/jnn.2020.17425

(28) Tang, X.; Liu, C.; Li, T.; Lin, C.; Hao, Z.; Zhang, H.; Zhao, G.; Chen, Y.; Guo, A.; Hu, C. Gambogic acid alleviates inflammation and apoptosis and protects the blood-milk barrier in mastitis induced by LPS. *Int Immunopharmacol* **2020**, *86*, 106697. DOI: 10.1016/j.intimp.2020.106697

(29) Cui, J.; Gong, R.; Hu, S.; Cai, L.; Chen, L. Gambogic acid ameliorates diabetes-induced proliferative retinopathy through inhibition of the HIF-1α/VEGF expression via targeting PI3K/AKT pathway. *Life Sci* **2018**, *192*, 293-303. DOI: 10.1016/j.lfs.2017.11.007

(30) Chen, J.; Li, L.; Zhou, Y.; Zhang, J.; Chen, L. Gambogic acid ameliorates high glucose- and palmitic acid-induced inflammatory response in ARPE-19 cells via activating Nrf2 signaling pathway: ex vivo. *Cell Stress Chaperones* **2021**, *26* (2), 367-375. DOI: 10.1007/s12192-020-01182-1

(31) Han, Q.; Yang, L.; Liu, Y.; Wang, Y.; Qiao, C.; Song, J.; Xu, L.; Yang, D.; Chen, S.; Xu, H. Gambogic acid and *epi*-gambogic acid, C-2 epimers with novel anticancer effects from *Garcinia hanburyi*. *Planta Med* **2006**, *72* (3), 281-284. DOI: 10.1055/s-2005-916193

(32) Pesonen, L.; Svartsjo, S.; Back, V.; de Thonel, A.; Mezger, V.; Saberan-Djoneidi, D.; Roos-Mattjus, P. Gambogic acid and gambogenic acid induce a thiol-dependent heat shock response and

disrupt the interaction between Hsp90 and HSF1 or HSF2. *Cell Stress Chaperones* **2021**, *26* (5), 819-833. DOI: 10.1007/s12192-021-01222-4

(33) Pandey, M. K.; Karelia, D.; Amin, S. G. Gambogic acid and its role in chronic diseases. *Adv Exp Med Biol* **2016**, *928*, 375-395. DOI: 10.1007/978-3-319-41334-1_15

(34) Liu, Y.; Chen, Y.; Lin, L.; Li, H. Gambogic acid as a candidate for cancer therapy: a review. *Int J Nanomedicine* **2020**, *15*, 10385-10399. DOI: 10.2147/IJN.S277645

(35) Wang, X.; Deng, R.; Lu, Y.; Xu, Q.; Yan, M.; Ye, D.; Chen, W. Gambogic acid as a non-competitive inhibitor of ATP-binding cassette transporter B1 reverses the multidrug resistance of human epithelial cancers by promoting ATP-binding cassette transporter B1 protein degradation. *Basic Clin Pharmacol Toxicol* **2013**, *112* (1), 25-33. DOI: 10.1111/j.1742-7843.2012.00921.x

(36) Yu, Z.; Jv, Y.; Cai, L.; Tian, X.; Huo, X.; Wang, C.; Zhang, B.; Sun, C.; Ning, J.; Feng, L.; Zhang, H.; Ma, X. Gambogic acid attenuates liver fibrosis by inhibiting the PI3K/AKT and MAPK signaling pathways via inhibiting Hsp90. *Toxicol Appl Pharmacol* **2019**, *371*, 63-73. DOI: 10.1016/j.taap.2019.03.028

(37) Kasibhatla, S.; Jessen, K. A.; Maliartchouk, S.; Wang, J. Y.; English, N. M.; Drewe, J.; Qiu, L.; Archer, S. P.; Ponce, A. E.; Sirisoma, N.; Jiang, S.; Zhang, H.; Gehlsen, K. R.; Cai, S. X.; Green, D. R.; Tseng. B. A role for transferrin receptor in triggering apoptosis when targeted with gambogic acid. *Proc Natl Acad Sci U S A* **2005**, *102* (34), 12095-12100. DOI: 10.1073/pnas.0406731102

(38) Foggetti, G.; Ottaggio, L.; Russo, D.; Monti, P.; Degan, P.; Fronza, G.; Menichini, P. Gambogic acid counteracts mutant p53 stability by inducing autophagy. *Biochim Biophys Mol Cell Res* **2017**, *1864* (2), 382-392. DOI: 10.1016/j.bbamcr.2016.11.023

(39) Palempalli, U. D.; Gandhi, U.; Kalantari, P.; Vunta, H.; Arner, R. J.; Narayan, V.; Ravindran A.; Prabhu, K. S. Gambogic acid covalently modifies IκB-kinase-b subunit to mediate suppression of lipopolysaccharide-induced activation of NF-κB in macrophages. *Biochem. J.* **2009**, *419* (2), 401-409. DOI: 10.1042/BJ20081482

(40) Yang, J.; Li, C.; Ding, L.; Guo, Q.; You, Q.; Jin, S. Gambogic acid deactivates cytosolic and mitochondrial thioredoxins by covalent binding to the functional domain. *J Nat Prod* **2012**, *75* (6), 1108-1116. DOI: 10.1021/np300118c

(41) Lee, J. Y.; Lee, B. H.; Lee, J. Y. Gambogic acid disrupts toll-like receptor4 activation by blocking lipopolysaccharides binding to myeloid differentiation factor 2. *Toxicol Res* **2015**, *31* (1), 11-16. DOI: 10.5487/TR.2015.31.1.011

(42) Rong, J. J.; Hu, R.; Qi, Q.; Gu, H. Y.; Zhao, Q.; Wang, J.; Mu, R.; You, Q. D.; Guo, Q. L. Gambogic acid down-regulates MDM2 oncogene and induces p21(Waf1/CIP1) expression independent of p53. *Cancer Lett* **2009**, *284* (1), 102-112. DOI: 10.1016/j.canlet.2009.04.011

(43) Wei, F.; Zhang, T.; Yang, Z.; Wei, J. C.; Shen, H. F.; Xiao, D.; Wang, Q.; Yang, P.; Chen, H. C.; Hu, H.; Chen, Z. P.; Huang, Q.; Li, W. L.; Cao, J.Gambogic acid efficiently kills stem-like colorectal cancer cells by upregulating ZFP36 expression. *Cell Physiol Biochem* **2018**, *46* (2), 829-846. DOI: 10.1159/000488740

(44) Huang, H.; Chen, D.; Li, S.; Li, X.; Liu, N.; Lu, X.; Liu, S.; Zhao, K.; Zhao, C.; Guo, H.; Yang, C.; Zhou, P.; Dong, X.; Zhang, C.; Ping Dou, G. Q.; Liua, J.Gambogic acid enhances proteasome inhibitor-induced anticancer activity. *Cancer Lett* **2011**, *301* (2), 221-228. DOI: 10.1016/j.canlet.2010.12.015

(45) Yang, Y.; Sun, X.; Yang, Y.; Yang, X.; Zhu, H.; Dai, S.; Chen, X.; Zhang, H.; Guo, Q.; Song, Y.; Wang, F.; Cheng, H.; Sun, X. Gambogic acid enhances the radiosensitivity of human esophageal cancer cells by inducing reactive oxygen species via targeting Akt/mTOR pathway. *Tumour Biol* **2016**, *37* (2), 1853-1862. DOI: 10.1007/s13277-015-3974-1

(46) Na, D.; Aijie, H.; Bo, L.; Zhilin, M.; Long, Y. Gambogic acid exerts cardioprotective effects in a rat model of acute myocardial infarction through inhibition of inflammation, iNOS and NF-κB/p38 pathway. *Exp Ther Med* **2018**, *15* (2), 1742-1748. DOI: 10.3892/etm.2017.5599

(47) Li, C. Y.; Wang, Q.; Wang, X. M.; Li, G. X.; Shen, S.; Wei, X. L. Gambogic acid exhibits anti-metastatic activity on malignant melanoma mainly through inhibition of PI3K/Akt and ERK signaling pathways. *Eur J Pharmacol* **2019**, *864*, 172719. DOI: 10.1016/j.ejphar.2019.172719

(48) Wen, J.; Pei, H.; Wang, X.; Xie, C.; Li, S.; Huang, L.; Qiu, N.; Wang, W.; Cheng, X.; Chen, L. Gambogic acid exhibits anti-psoriatic efficacy through inhibition of angiogenesis and inflammation. *J Dermatol Sci* **2014**, *74* (3), 242-250. DOI: 10.1016/j.jdermsci.2014.03.001

(49) Yim, K. H.; Prince, T. L.; Qu, S.; Bai, F.; Jennings, P. A.; Onuchic, J. N.; Theodorakis, E. A.; Neckers, L. Gambogic acid identifies an isoform-specific druggable pocket in the middle domain of Hsp90β. *Proc Natl Acad Sci U S A* **2016**, *113* (33), 4801-4809. DOI: 10.1073/pnas.1606655113

(50) Wan, L.; Zhang, Q.; Wang, S.; Gao, Y.; Chen, X.; Zhao, Y.; Qian, X. Gambogic acid impairs tumor angiogenesis by targeting YAP/STAT3 signaling axis. *Phytother Res* **2019**, *33* (5), 1579-1591. DOI: 10.1002/ptr.6350

(51) Wang, Y.; Sui, Y.; Tao, Y. Gambogic acid increases the sensitivity to paclitaxel in drugresistant triplenegative breast cancer via the SHH signaling pathway. *Mol Med Rep* **2019**, *20* (5), 4515-4522. DOI: 10.3892/mmr.2019.10697

(52) Ishaq, M.; Khan, M. A.; Sharma, K.; Sharma, G.; Dutta, R. K.; Majumdar, S. Gambogic acid induced oxidative stress dependent caspase activation regulates both apoptosis and autophagy by targeting various key molecules (NF-κB, Beclin-1, p62 and NBR1) in human bladder cancer cells. *Biochim Biophys* **2014**, *1840* (12), 3374-3384. DOI: 10.1016/j.bbagen.2014.08.019

(53) Gu, H.; You, Q.; Liu, W.; Yang, Y.; Zhao, L.; Qi, Q.; Zhao, J.; Wang, J.; Lu, N.; Ling, H.; Guo, Q.; Wang, X. Gambogic acid induced tumor cell apoptosis by T lymphocyte activation in

H22 transplanted mice. *Int Immunopharmacol* **2008**, *8* (11), 1493-1502. DOI: 10.1016/j.intimp.2008.05.013

(54) Huang, G. M.; Sun, Y.; Ge, X.; Wan, X.; Li, C. B. Gambogic acid induces apoptosis and inhibits colorectal tumor growth via mitochondrial pathways. *World J Gastroenterol* **2015**, *21* (20), 6194-6205. DOI: 10.3748/wjg.v21.i20.6194

(55) Zhao, L.; Guo, Q. L.; You, Q. D.; Wu, Z. Q.; Gu, H. Y. Gambogic acid induces apoptosis and regulates expressions of Bax and Bcl-2 protein in human gastric carcinoma MGC-803 cells. *Biol Pharm Bull* **2004**, *27* (7), 998-1003. DOI: 10.1248/bpb.27.998

(56) Jang, J. H.; Kim, J. Y.; Sung, E. G.; Kim, E. A.; Lee, T. J. Gambogic acid induces apoptosis and sensitizes TRAIL-mediated apoptosis through downregulation of cFLIPL in renal carcinoma Caki cells. *Int J Oncol* **2016**, *48* (1), 376-384. DOI: 10.3892/ijo.2015.3249

(57) Xu, X.; Liu, Y.; Wang, L.; He, J.; Zhang, H.; Chen, X.; Li, Y.; Yang, J.; Tao, J. Gambogic acid induces apoptosis by regulating the expression of Bax and Bcl-2 and enhancing caspase-3 activity in human malignant melanoma A375 cells. *Int J Dermatol* **2009**, *48* (2), 186-192. DOI: 10.1111/j.1365-4632.2009.03946.x

(58) Shi, X.; Lan, X.; Chen, X.; Zhao, C.; Li, X.; Liu, S.; Huang, H.; Liu, N.; Zang, D.; Liao, Y.; Zhang, P.; Wang, X.; Liu, J. Gambogic acid induces apoptosis in diffuse large B-cell lymphoma cells via inducing proteasome inhibition. *Sci Rep* **2015**, *5*, 9694. DOI: 10.1038/srep09694

(59) Duan, D.; Zhang, B.; Yao, J.; Liu, Y.; Sun, J.; Ge, C.; Peng, S.; Fang, J. Gambogic acid induces apoptosis in hepatocellular carcinoma SMMC-7721 cells by targeting cytosolic thioredoxin reductase. *Free Radic Biol Med* **2014**, *69*, 15-25. DOI: 10.1016/j.freeradbiomed.2013.12.027

(60) Shi, X.; Chen, X.; Li, X.; Lan, X.; Zhao, C.; Liu, S.; Huang, H.; Liu, N.; Liao, S.; Song, W.; Zhou, P.; Wang, S.; Xu, L.; Wang, X.; Ping Dou, Q.; Liu, J. Gambogic acid induces apoptosis in imatinib-resistant chronic myeloid leukemia cells via inducing proteasome inhibition and caspase-dependent Bcr-Abl downregulation. *Clin Cancer Res* **2014**, *20* (1), 151-163. DOI: 10.1158/1078-0432.CCR-13-1063

(61) Zhu, M.; Wang, M.; Jiang, Y.; Wu, H.; Lu, G.; Shi, W.; Cong, D.; Song, S.; Liu, K.; Wang, H. Gambogic acid induces apoptosis of non-small cell lung cancer (NSCLC) cells by suppressing notch signaling. *Med Sci Monit* **2018**, *24*, 7146-7151. DOI: 10.12659/MSM.912563

(62) Thida, M.; Kim, D. W.; Tran, T. T. T.; Pham, M. Q.; Lee, H.; Kim, I.; Lee, J. W. Gambogic acid induces apoptotic cell death in T98G glioma cells. *Bioorg Med Chem Lett* **2016**, *26* (3), 1097-1101. DOI: 10.1016/j.bmcl.2015.11.043

(63) Wang, H.; Zhao, Z.; Lei, S.; Li, S.; Xiang, Z.; Wang, X.; Huang, X.; Xia, G.; Huang, X. Gambogic acid induces autophagy and combines synergistically with chloroquine to suppress

pancreatic cancer by increasing the accumulation of reactive oxygen species. *Cancer Cell Int* **2019**, *19*, 7. DOI: 10.1186/s12935-018-0705-x

(64) Wang, Y.; Chen, Y.; Chen, Z.; Wu, Q.; Ke, W. J.; Wu, Q. L. Gambogic acid induces death inducer-obliterator 1-mediated apoptosis in Jurkat T cells. *Pharmacol Sin* **2008**, *29* (3), 349-354. DOI: 10.1111/j.1745-7254.2008.00762.x

(65) Chen, J.; Zhou, M.; Zhang, Q.; Xu, J.; Ouyang, J. Gambogic acid induces death of K562 cells through autophagy and apoptosis mechanisms. *Leuk Lymphoma* **2015**, *56* (10), 2953-2958. DOI: 10.3109/10428194.2015.1018251

(66) He, X. Y.; Liu, X. J.; Chen, X.; Bian, L. G.; Zhao, W. G.; Shen, J. K.; Sun, Q. F. Gambogic acid induces EGFR degradation and Akt/mTORC1 inhibition through AMPK dependent-LRIG1 upregulation in cultured U87 glioma cells. *Biochem Biophys Res Commun* **2013**, *435* (3), 397-402. DOI: 10.1016/j.bbrc.2013.04.099

(67) Li, R.; Chen, Y.; Zeng, L. L.; Shu, W. X.; Zhao, F.; Wen, L.; Liu, Y. Gambogic acid induces G0/G1 arrest and apoptosis involving inhibition of SRC-3 and inactivation of Akt pathway in K562 leukemia cells. *Toxicology* **2009**, *262* (2), 98-105. DOI: 10.1016/j.tox.2009.04.059

(68) Ren, J.; Li, L.; Wang, Y.; Zhai, J.; Chen, G.; Hu, K. Gambogic acid induces heme oxygenase-1 through Nrf2 signaling pathway and inhibits NF-κB and MAPK activation to reduce inflammation in LPS-activated RAW264.7 cells. *Biomed Pharmacother* **2019**, *109*, 555-562. DOI: 10.1016/j.biopha.2018.10.112

(69) Xu, J.; Zhou, M.; Ouyang, J.; Wang, J.; Zhang, Q.; Xu, Y.; Xu, Y.; Zhang, Q.; Xu, X.; Zeng, H. Gambogic acid induces mitochondria-dependent apoptosis by modulation of Bcl-2 and Bax in mantle cell lymphoma JeKo-1 cells. *Chin J Cancer Res* **2013**, *25* (2), 183-191. DOI: 10.3978/j.issn.1000-9604.2013.02.06

(70) Yi, T.; Yi, Z.; Cho, S. G.; Luo, J.; Pandey, M. K.; Aggarwal, B. B.; Liu, M. Gambogic acid inhibits angiogenesis and prostate tumor growth by suppressing vascular endothelial growth factor receptor 2 signaling. *Cancer Res* **2008**, *68* (6), 1843-1850. DOI: 10.1158/0008-5472.CAN-07-5944

(71) Lu, N.; Hui, H.; Yang, H.; Zhao, K.; Chen, Y.; You, Q. D.; Guo, Q. L. Gambogic acid inhibits angiogenesis through inhibiting PHD2-VHL-HIF-1α pathway. *Eur J Pharm Sci* **2013**, *49* (2), 220-226. DOI: 10.1016/j.ejps.2013.02.018

(72) Lu, N.; Yang, Y.; You, Q. D.; Ling, Y.; Gao, Y.; Gu, H. Y.; Zhao, L.; Wang, X. T.; Guo, Q. L. Gambogic acid inhibits angiogenesis through suppressing vascular endothelial growth factor-induced tyrosine phosphorylation of KDR/Flk-1. *Cancer Lett* **2007**, *258* (1), 80-89. DOI: 10.1016/j.canlet.2007.08.015

(73) Wen, C.; Huang, L.; Chen, J.; Lin, M.; Li, W.; Lu, B.; Rutnam, Z. J.; Iwamoto, A.; Wang, Z.; Yang, X.; Liu, H. Gambogic acid inhibits growth, induces apoptosis, and overcomes drug

resistance in human colorectal cancer cells. *Int J Oncol* **2015**, *47* (5), 1663-1671. DOI: 10.3892/ijo.2015.3166

(74) Zhang, L.; Yi, Y.; Chen, J.; Sun, Y.; Guo, Q.; Zheng, Z.; Song, S. Gambogic acid inhibits Hsp90 and deregulates TNF-α/NF-κB in HeLa cells. *Biochem Biophys Res Commun* **2010**, *403* (3-4), 282-287. DOI: 10.1016/j.bbrc.2010.11.018

(75) Xin, Z. F.; Shen, C. C.; Tao, L. J.; Yan, S. G.; Wu, H. B. Gambogic acid inhibits invasion of osteosarcoma via upregulation of TIMP-1. *Int J Mol Med* **2013**, *31* (1), 105-112. DOI: 10.3892/ijmm.2012.1192

(76) Liang, L.; Zhang, Z.; Qin, X.; Gao, Y.; Zhao, P.; Liu, J.; Zeng, W. Gambogic acid inhibits melanoma through regulation of miR-199a-3p/ZEB1 signalling. *Basic Clin Pharmacol Toxicol* **2018**, *123* (6), 692-703. DOI: 10.1111/bcpt.13090

(77) Pandey, M. K.; Kale, V. P.; Song, C.; Sung, S. S.; Sharma, A. K.; Talamo, G.; Dovat, S.; Amin, S. G. Gambogic acid inhibits multiple myeloma mediated osteoclastogenesis through suppression of chemokine receptor CXCR4 signaling pathways. *Exp Hematol* **2014**, *42* (10), 883-896. DOI: 10.1016/j.exphem.2014.07.261

(78) Ma, J.; Ma, Y.; Liu, X.; Chen, S.; Liu, C.; Qin, A.; Fan, S. Gambogic acid inhibits osteoclast formation and ovariectomy-induced osteoporosis by suppressing the JNK, p38 and Akt signalling pathways. *Biochem J* **2015**, *469* (3), 399-408. DOI: 10.1042/BJ20150151

(79) Wang, T.; Du, J.; Kong, D.; Yang, G.; Zhou, Q.; You, F.; Lin, Y.; Wang, Y. Gambogic acid inhibits proliferation and induces apoptosis of human acute Tcell leukemia cells by inducing autophagy and downregulating betacatenin signaling pathway: mechanisms underlying the effect of gambogic acid on TALL cells. *Oncol Rep* **2020**, *44* (4), 1747-1757. DOI: 10.3892/or.2020.7726

(80) Wu, Z. Q.; Guo, Q. L.; You, Q. D.; Zhao, L.; Gu, H. Y. Gambogic acid inhibits proliferation of human lung carcinoma SPC-A1 cells in vivo and in vitro and represses telomerase activity and telomerase reverse transcriptase mRNA expression in the cells. *Biol Pharm Bull* **2004**, *27* (11), 1769-1774. DOI: 10.1248/bpb.27.1769

(81) Qin, Y.; Meng, L.; Hu, C.; Duan, W.; Zuo, Z.; Lin, L.; Zhang, X.; Ding, J. Gambogic acid inhibits the catalytic activity of human topoisomerase IIα by binding to its ATPase domain. *Mol Cancer Ther* **2007**, *6* (9), 2429-2440. DOI: 10.1158/1535-7163.MCT-07-0147

(82) Zhao, W.; Zhou, S. F.; Zhang, Z. P.; Xu, G. P.; Li, X. B.; Yan, J. L. Gambogic acid inhibits the growth of osteosarcoma cells in vitro by inducing apoptosis and cell cycle arrest. *Oncol Rep* **2011**, *25* (5), 1289-1295. DOI: 10.3892/or.2011.1189

(83) Tang, Q.; Lu, M.; Zhou, H.; Chen, D.; Liu, L. Gambogic acid inhibits the growth of ovarian cancer tumors by regulating p65 activity. *Oncol Lett* **2017**, *13* (1), 384-388. DOI: 10.3892/ol.2016.5433

(84) Lin, D.; Lin, X.; He, T.; Xie, G. Gambogic acid inhibits the progression of gastric cancer via circRNA_ASAP2/miR-33a-5p/CDK7 axis. *Cancer Manag Res* **2020**, *12*, 9221-9233. DOI: 10.2147/CMAR.S269768

(85) Pan, H.; Jansson, K. H.; Beshiri, M. L.; Yin, J.; Fang, L.; Agarwal, S.; Nguyen, H.; Corey, E.; Zhang, Y.; Liu, J.; Fan, H. T.; Lin, H. S.; Kelly, K. Gambogic acid inhibits thioredoxin activity and induces ROS-mediated cell death in castration-resistant prostate cancer. *Oncotarget* **2017**, *8* (44), 77181-77194. DOI: 10.18632/oncotarget.20424

(86) Lu, L.; Tang, D.; Wang, L.; Huang, L. Q.; Jiang, G. S.; Xiao, X. Y.; Zeng, F. Q. Gambogic acid inhibits TNF-α-induced invasion of human prostate cancer PC3 cells in vitro through PI3K/Akt and NF-κB signaling pathways. *Pharmacol Sin* **2012**, *33* (4), 531-541. DOI: 10.1038/aps.2011.180

(87) Li, C.; Lu, N.; Qi, Q.; Li, F.; Ling, Y.; Chen, Y.; Qin, Y.; Li, Z.; Zhang, H.; You, Q.; Guo, Q. Gambogic acid inhibits tumor cell adhesion by suppressing integrin β1 and membrane lipid rafts-associated integrin signaling pathway. *Biochem Pharmacol* **2011**, *82* (12), 1873-1883. DOI: 10.1016/j.bcp.2011.09.013

(88) Wang, X.; Chen, W. Gambogic acid is a novel anti-cancer agent that inhibits cell proliferation, angiogenesis and metastasis. *Anticancer Agents Med Chem* **2012**, *12* (8), 994-1000. DOI: 10.2174/187152012802650066

(89) Li, X.; Liu, S.; Huang, H.; Liu, N.; Zhao, C.; Liao, S.; Yang, C.; Liu, Y.; Zhao, C.; Li, S.; Lu, X.; Liu, C.; Guan, L.; Zhao, K.; Shi, X.; Song, W.; Zhou, P.; Dong, X.; Guo, H.; Wen, G.; Zhang, C.; Jiang, L.; Ma, N.; Li, B.; Wang, S.; Tan, H.; Wang, X.; Ping Dou, Q.; Liu, J. Gambogic acid is a tissue-specific proteasome inhibitor in vitro and in vivo. *Cell Rep* **2013**, *3* (1), 211-222. DOI: 10.1016/j.celrep.2012.11.023

(90) Gu, H.; Wang, X.; Rao, S.; Wang, J.; Zhao, J.; Ren, F. L.; Mu, R.; Yang, Y.; Qi, Q.; Liu, W.; Lu, N.; Ling, H.; You, Q.; Guo, Q. Gambogic acid mediates apoptosis as a p53 inducer through down-regulation of Mdm2 in wild-type p53-expressing cancer cells. *Mol Cancer Ther* **2008**, *7* (10), 3298-3305. DOI: 10.1158/1535-7163.MCT-08-0212

(91) Zhao, C.; Liu, S.; Yang, C.; Li, X.; Huang, H.; Liu, N.; Li, S.; Wang, X.; Liu, J. Gambogic acid moderates cardiac responses to chronic hypoxia likely by acting on the proteasome and NF-κB pathway. *Am J Cardiovasc Dis* **2013**, *3* (3), 135-145. PMID: 23991348

(92) Li, C.; Qi, Q.; Lu, N.; Dai, Q.; Li, F.; Wang, X.; You, Q.; Guo, Q. Gambogic acid promotes apoptosis and resistance to metastatic potential in MDA-MB-231 human breast carcinoma cells. *Biochem Cell Biol* **2012**, *90* (6), 718-730. DOI: 10.1139/o2012-030

(93) Geng, J.; Xiao, S.; Zheng, Z.; Song, S.; Zhang, L. Gambogic acid protects from endotoxin shock by suppressing pro-inflammatory factors in vivo and in vitro. *Inflamm Res* **2013**, *62* (2), 165-172. DOI: 10.1007/s00011-012-0563-2

(94) Gao, X.; Dai, J.; Li, G.; Dai, X. Gambogic acid protects LPS-induced apoptosis and inflammation in a cell model of neonatal pneumonia through the regulation of TrkA/Akt signaling pathway. *BMC Pharmacol Toxicol* **2021**, *22* (1), 28. DOI: 10.1186/s40360-021-00496-9

(95) Gu, H.; Rao, S.; Zhao, J.; Wang, J.; Mu, R.; Rong, J.; Tao, L.; Qi, Q.; You, Q.; Guo, Q. Gambogic acid reduced bcl-2 expression via p53 in human breast MCF-7 cancer cells. *J Cancer Res Clin Oncol* **2009**, *135* (12), 1777-1782. DOI: 10.1007/s00432-009-0624-2

(96) Zhao, K.; Zhang, S.; Song, X.; Yao, Y.; Zhou, Y.; You, Q.; Guo, Q.; Lu, N. Gambogic acid suppresses cancer invasion and migration by inhibiting TGFβ1-induced epithelial-to-mesenchymal transition. *Oncotarget* **2017**, *8* (16), 27120-27136. DOI: 10.18632/oncotarget.15449

(97) Zhou, Z.; Ma, J. Gambogic acid suppresses colon cancer cell activity in vitro. *Exp Ther Med* **2019**, *18* (4), 2917-2923. DOI: 10.3892/etm.2019.7912

(98) Liu, W.; Ning, R.; Chen, R.-N.; Hu, J.-H.; Gui, H.-Y.; Wang, Y.-W.; Liu, J.; Hu, G.; Yang, J.; Guo, Q.-L. Gambogic acid suppresses cytochrome P450 3A4 by downregulating pregnane X receptor and up-regulating DEC1 in human hepatoma HepG2 cells. *Toxicol Res* **2015**, *4* (4), 1059-1071. DOI: 10.1039/c4tx00239c

(99) Wang, F.; Zhang, W.; Guo, L.; Bao, W.; Jin, N.; Liu, R.; Liu, P.; Wang, Y.; Guo, Q.; Chen, B. Gambogic acid suppresses hypoxia-induced hypoxia-inducible factor-1α/vascular endothelial growth factor expression via inhibiting phosphatidylinositol 3-kinase/Akt/mammalian target protein of rapamycin pathway in multiple myeloma cells. *Cancer Sci* **2014**, *105* (8), 1063-1070. DOI: 10.1111/cas.12458

(100) Wu, X.; Long, L.; Liu, J.; Zhang, J.; Wu, T.; Chen, X.; Zhou, B.; Lv, T. Z. Gambogic acid suppresses inflammation in rheumatoid arthritis rats via PI3K/Akt/mTOR signaling pathway. *Mol Med Rep* **2017**, *16* (5), 7112-7118. DOI: 10.3892/mmr.2017.7459

(101) Liu, S.; Zhao, C.; Yang, C.; Li, X.; Huang, H.; Liu, N.; Li, S.; Wang, X.; Liu, J. Gambogic acid suppresses pressure overload cardiac hypertrophy in rats. *Am J Cardiovasc Dis* **2013**, *3* (4), 227-238. PMID: 24224134

(102) Ye, L.; Zhou, J.; Zhao, W.; Jiao, P.; Ren, G.; Wang, S. Gambogic acid-induced autophagy in nonsmall cell lung cancer NCI-H441 cells through a reactive oxygen species pathway. *J Cancer Res Ther* **2018**, *14* (12), 942-947. DOI: 10.4103/0973-1482.206866

(103) Wang, J.; Zhao, Q.; Qi, Q.; Gu, H. Y.; Rong, J. J.; Mu, R.; Zou, M. J.; Tao, L.; You, Q. D.; Guo, Q. L. Gambogic acid-induced degradation of mutant p53 is mediated by proteasome and related to CHIP. *J Cell Biochem* **2011**, *112* (2), 509-519. DOI: 10.1002/jcb.22941

(104) Yu, J.; Guo, Q. L.; You, Q. D.; Zhao, L.; Gu, H. Y.; Yang, Y.; Zhang, H. W.; Tan, Z.; Wang, X. Gambogic acid-induced G2/M phase cell-cycle arrest via disturbing CDK7-mediated phosphorylation of CDC2/p34 in human gastric carcinoma BGC-823 cells. *Carcinogenesis* **2007**, *28* (3), 632-638. DOI: 10.1093/carcin/bgl168

(105) Wang, J.; Zhao, Q.; Qi, Q.; Gu, H. y.; Rong, J. j.; Mu, R.; Zou, M. j.; Tao, L.; You, Q. d.; Guo, Q. l. Gambogic acid-induced degradation of mutant p53 is mediated by proteasome and related to CHIP. *J Cell Biochem* **2011**, *112* (2), 509-519 DOI: 10.1002/jcb.22941

(106) Davenport, J.; Manjarrez, J. R.; Peterson, L.; Krumm, B.; Blagg, B. S.; Matts, R. L. Gambogic acid, a natural product inhibitor of Hsp90. *J Nat Prod* **2011**, *74* (5), 1085-1092. DOI: 10.1021/np200029q

(107) Pandey, M. K.; Sung, B.; Ahn, K. S.; Kunnumakkara, A. B.; Chaturvedi, M. M.; Aggarwal, B. B. Gambogic acid, a novel ligand for transferrin receptor, potentiates TNF-induced apoptosis through modulation of the NF-κB signaling pathway. *Blood* **2007**, *110* (10), 3517-3525. DOI: 10.1182/blood-2007-03-079616

(108) Wang, T.; Wei, J.; Qian, X.; Ding, Y.; Yu, L.; Liu, B. Gambogic acid, a potent inhibitor of survivin, reverses docetaxel resistance in gastric cancer cells. *Cancer Lett* **2008**, *262* (2), 214-222. DOI: 10.1016/j.canlet.2007.12.004

(109) Hatami, E.; Jaggi, M.; Chauhan, S. C.; Yallapu, M. M. Gambogic acid: a shining natural compound to nanomedicine for cancer therapeutics. *Biochim Biophys Rev Cancer* **2020**, *1874* (1), 188381. DOI: 10.1016/j.bbcan.2020.188381

(110) Zhou, Y.; Li, W.; Zhang, X.; Zhang, H.; Xiao, Y. Global profiling of cellular targets of gambogic acid by quantitative chemical proteomics. *Chem Commun (Camb)* **2016**, *52* (97), 14035-14038. DOI: 10.1039/c6cc07581a

(111) Lupescu, A.; Jilani, K.; Zelenak, C.; Zbidah, M.; Shaik, N.; Lang, F. Induction of programmed erythrocyte death by gambogic acid. *Cell Physiol Biochem* **2012**, *30* (2), 428-438. DOI: 10.1159/000339036

(112) Qiang, L.; Yang, Y.; You, Q. D.; Ma, Y. J.; Yang, L.; Nie, F. F.; Gu, H. Y.; Zhao, L.; Lu, N.; Qi, Q.; Liu, W.; Wang, X. T.; Guo, Q. L. Inhibition of glioblastoma growth and angiogenesis by gambogic acid: an in vitro and in vivo study. *Biochem Pharmacol* **2008**, *75* (5), 1083-1092. DOI: 10.1016/j.bcp.2007.10.033

(113) Guo, Q. L.; Lin, S. S.; You, Q. D.; Gu, H. Y.; Yu, J.; Zhao, L.; Qi, Q.; Liang, F.; Tan, Z.; Wang, X. Inhibition of human telomerase reverse transcriptase gene expression by gambogic acid in human hepatoma SMMC-7721 cells. *Life Sci* **2006**, *78* (11), 1238-1245. DOI: 10.1016/j.lfs.2005.06.046

(114) Qi, Q.; Gu, H.; Yang, Y.; Lu, N.; Zhao, J.; Liu, W.; Ling, H.; You, Q. D.; Wang, X.; Guo, Q. Involvement of matrix metalloproteinase 2 and 9 in gambogic acid induced suppression of MDA-MB-435 human breast carcinoma cell lung metastasis. *J Mol Med (Berl)* **2008**, *86* (12), 1367-1377. DOI: 10.1007/s00109-008-0398-z

(115) Xu, J.; Ouyang, J.; Zhou, M.; Zhang, Q.; Zhou, R.-F. Mechanism of gambogic acid-induced apoptosis in DB cells. *Blood* **2012**, *120* (21), 4923. DOI: 10.1182/blood.V120.21.4923.4923

(116) Zhu, X.; Zhang, H.; Lin, Y.; Chen, P.; Min, J.; Wang, Z.; Xiao, W.; Chen, B. Mechanisms of gambogic acid-induced apoptosis in non-small cell lung cancer cells in relation to transferrin receptors. *J Chemother* **2009**, *21* (6), 666-672. DOI: 10.1179/joc.2009.21.6.666

(117) Wang, J.; Shen, W.; Yuan, Z.; Lan, L.; Xu, J.; Wang, C.; Ma, G.; Shi, W.; Han, L.; Zhang, Z.; Hou, L.; Shen, L.; Jiang, Z.; He, H.; Xiao, W.; Wang, Z.; Guo, Q.; Li, J.; Chen, S. Michael acceptor in gambogic acid--Its role and application for potent antitumor agents. *Bioorg Med Chem Lett* **2015**, *25* (14), 2844-2848. DOI: 10.1016/j.bmcl.2015.04.100

(118) Zhang, D.; Wang, W.; Hou, T.; Pang, Y.; Wang, C.; Wu, S.; Wang, Q. New delivery route of gambogic acid via skin for topical targeted therapy of cutaneous melanoma and reduction of systemic toxicity. *J Pharm Sci* **2021**, *110* (5), 2167-2176. DOI: 10.1016/j.xphs.2020.12.024

(119) Yang, L. J.; Chen, Y. New targets for the antitumor activity of gambogic acid in hematologic malignancies. *Pharmacol Sin* **2013**, *34* (2), 191-198. DOI: 10.1038/aps.2012.163

(120) Yue, Q.; Stahl, F.; Plettenburg, O.; Kirschning, A.; Warnecke, A.; Zeilinger, C. The noncompetitive effect of gambogic acid displaces fluorescence-labeled ATP but requires ATP for binding to Hsp90/HtpG. *Biochemistry* **2018**, *57* (18), 2601-2605. DOI: 10.1021/acs.biochem.8b00155

(121) Nie, F.; Zhang, X.; Qi, Q.; Yang, L.; Yang, Y.; Liu, W.; Lu, N.; Wu, Z.; You, Q.; Guo, Q. Reactive oxygen species accumulation contributes to gambogic acid-induced apoptosis in human hepatoma SMMC-7721 cells. *Toxicology* **2009**, *260* (1-3), 60-67. DOI: 10.1016/j.tox.2009.03.010

(122) Sun, H.; Chen, F.; Wang, X.; Liu, Z.; Yang, Q.; Zhang, X.; Zhu, J.; Qiang, L.; Guo, Q.; You, Q. Studies on gambogic acid (IV): exploring structure-activity relationship with IκB kinase-β (IKKβ). *Eur J Med Chem* **2012**, *51*, 110-123. DOI: 10.1016/j.ejmech.2012.02.029

(123) Chantarasriwong, O.; Milcarek, A. T.; Morales, T. H.; Settle, A. L.; Rezende, C. O., Jr.; Althufairi, B. D.; Theodoraki, M. A.; Alpaugh, M. L.; Theodorakis, E. A. Synthesis, structure-activity relationship and in vitro pharmacodynamics of A-ring modified caged xanthones in a preclinical model of inflammatory breast cancer. *Eur J Med Chem* **2019**, *168*, 405-413. DOI: 10.1016/j.ejmech.2019.02.047

(124) Li, D.; Song, X. Y.; Yue, Q. X.; Cui, Y. J.; Liu, M.; Feng, L. X.; Wu, W. Y.; Jiang, B. H.; Yang, M.; Qu, X. B.; Liu, X.; Guo, D. Proteomic and bioinformatic analyses of possible target-related proteins of gambogic acid in human breast carcinoma MDA-MB-231 cells. *Chin J Nat Med* **2015**, *13* (1), 41-51. DOI: 10.1016/S1875-5364(15)60005-X

(125) Hao, K.; Liu, X. Q.; Wang, G. J.; Zhao, X. P. Pharmacokinetics, tissue distribution and excretion of gambogic acid in rats. *Eur J Drug Metab Pharmacokinet* **2007**, *32* (2), 63-68. DOI: 10.1007/BF03190993

(126) Du, Q.; Lv, F.; Huang, J.; Tang, X.; Zhao, Z.; Chen, J. A multiple environment-sensitive prodrug nanomicelle strategy based on chitosan graftomer for enhanced tumor therapy of gambogic acid. *Carbohydr Polym* **2021**, *267*, 118229. DOI: 10.1016/j.carbpol.2021.118229

(127) Haw, M. D. Colloidal suspensions, Brownian motion, molecular reality: a short history. *J Phys: Condens Matter* **2002**, *14*, 7769-7779. DOI: 10.1088/0953-8984/14/33/315

(128) Mei, W.; Dong, C.; Hui, C.; Bin, L.; Fenggen, Y.; Jingjing, S.; Cheng, P.; Meiling, S.; Yawen, H.; Xiaoshan, W.; Wang, G.; Zhiwu, C.; Qinglin, L. Gambogenic acid kills lung cancer cells through aberrant autophagy. *PLoS One* **2014**, *9* (1), e83604. DOI: 10.1371/journal.pone.0083604

(129) Han, Q. B.; Cheung, S.; Tai, J.; Qiao, C. F.; Song, J. Z.; Xu, H. X. Stability and cytotoxicity of gambogic acid and its derivative, gambogoic acid. *Biol Pharm Bull* **2005**, *28* (12), 2335-2337. DOI: 10.1248/bpb.28.2335

(130) Kolc, J.; Becker, R. S. Proof of structure of the colored photoproducts of chromenes and spiropyrans. *J Phys Chem* **1967**, *71* (12), 4045-4048. DOI: 10.1021/j100871a048

(131) Reichardt, C.; Welton, T. Empirical Parameters of Solvent Polarity. In *Solvents and Solvent Effects in Organic Chemistry*, **2010**; pp 425-508. DOI:10.1002/9783527632220

(132) Beaudry, C. M.; Malerich, J. P.; Trauner, D. Biosynthetic and biomimetic electrocyclizations. *Chem Rev* **2005**, *105* (12), 4757-4778. DOI: 10.1021/cr0406110

(133) McConathy, J.; Owens, M. J. Stereochemistry in drug action. *Prim Care Companion J Clin Psychiatry* **2003**, *5* (2), 70-73. DOI: 10.4088/pcc.v05n0202

(134) Bai, F.; Morcos, F.; Sohn, Y. S.; Darash-Yahana, M.; Rezende, C. O.; Lipper, C. H.; Paddock, M. L.; Song, L.; Luo, Y.; Holt, S. H.; Tamir, S.; Theodorakis, E. A.; Jennings, P. A.; Onuchic, J. N.; Mittler, R. The Fe-S cluster-containing NEET proteins mitoNEET and NAF-1 as chemotherapeutic targets in breast cancer. *Proc Natl Acad Sci U S A* **2015**, *112* (12), 3698-3703. DOI: 10.1073/pnas.1502960112

(135) Nechushtai, R.; Karmi, O.; Zuo, K.; Marjault, H. B.; Darash-Yahana, M.; Sohn, Y. S.; King, S. D.; Zandalinas, S. I.; Carloni, P.; Mittler, R. The balancing act of NEET proteins: iron, ROS, calcium and metabolism. *Biochim Biophys Mol Cell Res* **2020**, *1867* (11), 118805. DOI: 10.1016/j.bbamcr.2020.118805

(136) Tisdale, E. J.; Slobodov, I.; Theodorakis, E. A. Biomimetic total synthesis of forbesione and desoxymorellin utilizing a tandem Claisen/Diels--Alder/Claisen rearrangement. *Org Biomol Chem* **2003**, *1* (24), 4418-4422. DOI: 10.1039/b311833a

(137) Tisdale, E. J.; Slobodov, I.; Theodorakis, E. A. Unified synthesis of caged *Garcinia* natural products based on a site-selective Claisen/Diels-Alder/Claisen rearrangement. *Proc Natl Acad Sci U S A* **2004**, *101* (33), 12030-12035. DOI: 10.1073/pnas.0401932101

(138) McBride, H. M.; Neuspiel, M.; Wasiak, S. Mitochondria: more than just a powerhouse. *Curr Biol* **2006**, *16* (14), 551-560. DOI: 10.1016/j.cub.2006.06.054

(139) Gupta, S.; Kass, G. E.; Szegezdi, E.; Joseph, B. The mitochondrial death pathway: a promising therapeutic target in diseases. *J Cell Mol Med* **2009**, *13* (6), 1004-1033. DOI: 10.1111/j.1582-4934.2009.00697.x

(140) Javadov, S.; Kozlov, A. V.; Camara, A. K. S. Mitochondria in health and diseases. *Cells* **2020**, *9* (5), 1177. DOI: 10.3390/cells9051177

(141) Vyas, S.; Zaganjor, E.; Haigis, M. C. Mitochondria and cancer. *Cell* **2016**, *166* (3), 555-566. DOI: 10.1016/j.cell.2016.07.002

(142) Lezi, E.; Swerdlow, R. H. Mitochondria in neurodegeneration. *Adv Exp Med Biol* **2012**, *942*, 269-286. DOI: 10.1007/978-94-007-2869-1_12

(143) Murphy, M. P.; Hartley, R. C. Mitochondria as a therapeutic target for common pathologies. *Nat Rev Drug Discov* **2018**, *17* (12), 865-886. DOI: 10.1038/nrd.2018.174

(144) Kutik, S.; Stroud, D. A.; Wiedemann, N.; Pfanner, N. Evolution of mitochondrial protein biogenesis. *Biochim Biophys* **2009**, *1790* (6), 409-415. DOI: 10.1016/j.bbagen.2009.04.004

(145) Wallace, D. C. Genetics: mitochondrial DNA in evolution and disease. *Nature* **2016**, *535* (7613), 498-500. DOI: 10.1038/nature18902

(146) Pfanner, N.; Warscheid, B.; Wiedemann, N. Mitochondrial proteins: from biogenesis to functional networks. *Nat Rev Mol Cell Biol* **2019**, *20* (5), 267-284. DOI: 10.1038/s41580-018-0092-0

(147) Vander Heiden, M. G.; Chandel, N. S.; Li, X. X.; Schumacker, P. T.; Colombini, M.; Thompson, C. B. Outer mitochondrial membrane permeability can regulate coupled respiration and cell survival. *Proc Natl Acad Sci U S A* **2000**, *97* (9), 4666-4671. DOI: 10.1073/pnas.090082297

(148) Backes, S.; Herrmann, J. M. Protein translocation into the intermembrane space and matrix of mitochondria: mechanisms and driving forces. *Front Mol Biosci* **2017**, *4*, 83. DOI: 10.3389/fmolb.2017.00083

(149) Garrido, C.; Galluzzi, L.; Brunet, M.; Puig, P. E.; Didelot, C.; Kroemer, G. Mechanisms of cytochrome c release from mitochondria. *Cell Death Differ* **2006**, *13* (9), 1423-1433. DOI: 10.1038/sj.cdd.4401950

(150) Giacomello, M.; Pyakurel, A.; Glytsou, C.; Scorrano, L. The cell biology of mitochondrial membrane dynamics. *Nat Rev Mol Cell Biol* **2020**, *21* (4), 204-224. DOI: 10.1038/s41580-020-0210-7

(151) Joubert, F.; Puff, N. Mitochondrial cristae architecture and functions: lessons from minimal model systems. *Membranes (Basel)* **2021**, *11* (7), 465. DOI: 10.3390/membranes11070465

(152) Kuhlbrandt, W. Structure and function of mitochondrial membrane protein complexes. *BMC Biol* **2015**, *13*, 89. DOI: 10.1186/s12915-015-0201-x

(153) Lipper, C. H.; Karmi, O.; Sohn, Y. S.; Darash-Yahana, M.; Lammert, H.; Song, L.; Liu, A.; Mittler, R.; Nechushtai, R.; Onuchic, J. N.; Jennings, P. A. Structure of the human monomeric NEET protein MiNT and its role in regulating iron and reactive oxygen species in cancer cells. *Proc Natl Acad Sci U S A* **2018**, *115* (2), 272-277. DOI: 10.1073/pnas.1715842115

(154) Ravingerova, T.; Kindernay, L.; Bartekova, M.; Ferko, M.; Adameova, A.; Zohdi, V.; Bernatova, I.; Ferenczyova, K.; Lazou, A. The molecular mechanisms of iron metabolism and its role in cardiac dysfunction and cardioprotection. *Int J Mol Sci* **2020**, *21* (21), 7889. DOI: 10.3390/ijms21217889

(155) Wessling-Resnick, M. Iron homeostasis and the inflammatory response. *Annu Rev Nutr* **2010**, *30*, 105-122. DOI: 10.1146/annurev.nutr.012809.104804

(156) Gozzelino, R.; Arosio, P. Iron homeostasis in health and disease. *Int J Mol Sci* **2016**, *17* (1), 130. DOI: 10.3390/ijms17010130

(157) Ying, J. F.; Lu, Z. B.; Fu, L. Q.; Tong, Y.; Wang, Z.; Li, W. F.; Mou, X. Z. The role of iron homeostasis and iron-mediated ROS in cancer. *Am J Cancer Res* **2021**, *11* (5), 1895-1912. PMID: 34094660

(158) Juan, C. A.; Pérez de la Lastra, J. M.; Plou, F. J.; Pérez-Lebeña, E. The chemistry of reactive oxygen species (ROS) revisited: outlining their role in biological macromolecules (DNA, lipids and proteins) and induced pathologies. *Int J Mol Sci* **2021**, *22* (9), 4642. DOI: 10.3390/ijms22094642

(159) Eid, R.; Arab, N. T.; Greenwood, M. T. Iron mediated toxicity and programmed cell death: a review and a re-examination of existing paradigms. *Biochim Biophys Mol Cell Res* **2017**, *1864* (2), 399-430. DOI: 10.1016/j.bbamcr.2016.12.002

(160) MacKenzie, E. L.; Iwasaki, K.; Tsuji, Y. Intracellular iron transport and storage: from molecular mechanisms to health implications. *Antioxid Redox Signal* **2008**, *10* (6), 997-1030. DOI: 10.1089/ars.2007.1893

(161) Ward, D. M.; Cloonan, S. M. Mitochondrial iron in human health and disease. *Annu Rev Physiol* **2019**, *81*, 453-482. DOI: 10.1146/annurev-physiol-020518-114742

(162) Dietz, J. V.; Fox, J. L.; Khalimonchuk, O. Down the iron path: mitochondrial iron homeostasis and beyond. *Cells* **2021**, *10* (9), 2198. DOI: 10.3390/cells10092198

(163) Delvecchio, M.; Iacoviello, M.; Pantaleo, A.; Resta, N. Clinical spectrum associated with Wolfram syndrome type 1 and type 2: a review on genotype-phenotype correlations. *Int J Environ Res Public Health* **2021**, *18* (9), 4796. DOI: 10.3390/ijerph18094796

(164) Wiley, S. E.; Murphy, A. N.; Ross, S. A.; van der Geer, P.; Dixon, J. E. MitoNEET is an iron-containing outer mitochondrial membrane protein that regulates oxidative capacity. *Proc Natl Acad Sci U S A* **2007**, *104* (13), 5318-5323. DOI: 10.1073/pnas.0701078104

(165) Furihata, T.; Takada, S.; Kakutani, N.; Maekawa, S.; Tsuda, M.; Matsumoto, J.; Mizushima, W.; Fukushima, A.; Yokota, T.; Enzan, N.; Matsushima, S.; Handa, H.; Fumoto, Y.; Nio-Kobayashi, J.; Iwanaga, T.; Tanaka, S.; Tsutsui, H.; Sabe, H.; Kinugawa, S. Cardiac-specific loss of mitoNEET expression is linked with age-related heart failure. *Commun Biol* **2021**, *4* (1), 138. DOI: 10.1038/s42003-021-01675-4

(166) Sohn, Y. S.; Tamir, S.; Song, L.; Michaeli, D.; Matouk, I.; Conlan, A. R.; Harir, Y.; Holt, S. H.; Shulaev, V.; Paddock, M. L.; Hochberg, A.; Cabanchick, I. Z.; Onuchic, J. N.; Jennings, P. A.; Nechushtai, R.; Mittler, R. NAF-1 and mitoNEET are central to human breast cancer proliferation by maintaining mitochondrial homeostasis and promoting tumor growth. *Proc Natl Acad Sci U S A* **2013**, *110* (36), 14676-14681. DOI: 10.1073/pnas.1313198110

(167) Lipper, C. H.; Stofleth, J. T.; Bai, F.; Sohn, Y. S.; Roy, S.; Mittler, R.; Nechushtai, R.; Onuchic, J. N.; Jennings, P. A. Redox-dependent gating of VDAC by mitoNEET. *Proc Natl Acad Sci U S A* **2019**, *116* (40), 19924-19929. DOI: 10.1073/pnas.1908271116

(168) Karmi, O.; Marjault, H. B.; Pesce, L.; Carloni, P.; Onuchic, J. N.; Jennings, P. A.; Mittler, R.; Nechushtai, R. The unique fold and lability of the [2Fe-2S] clusters of NEET proteins mediate their key functions in health and disease. *J Biol Inorg Chem* **2018**, *23* (4), 599-612. DOI: 10.1007/s00775-018-1538-8

(169) Geldenhuys, W. J.; Long, T. E.; Saralkar, P.; Iwasaki, T.; Nunez, R. A. A.; Nair, R. R.; Konkle, M. E.; Menze, M. A.; Pinti, M. V.; Hollander, J. M.; Hazlehurst, L. A.; Robart, A. R. Crystal structure of the mitochondrial protein mitoNEET bound to a benze-sulfonide ligand. *Commun Chem* **2019**, *2*, 77. DOI: 10.1038/s42004-019-0172-x

(170) Tamir, S.; Eisenberg-Domovich, Y.; Conlan, A. R.; Stofleth, J. T.; Lipper, C. H.; Paddock, M. L.; Mittler, R.; Jennings, P. A.; Livnah, O.; Nechushtai, R. A point mutation in the [2Fe-2S] cluster binding region of the NAF-1 protein (H114C) dramatically hinders the cluster donor properties. *Crystallogr D Biol Crystallogr* **2014**, *70* (6), 1572-1578. DOI: 10.1107/S1399004714005458

(171) Darash-Yahana, M.; Pozniak, Y.; Lu, M.; Sohn, Y. S.; Karmi, O.; Tamir, S.; Bai, F.; Song, L.; Jennings, P. A.; Pikarsky, E.; Geiger, T.; Onuchic, J. N.; Mittler, R.; Nechushtai, R. Breast cancer tumorigenicity is dependent on high expression levels of NAF-1 and the lability of its Fe-S clusters. *Proc Natl Acad Sci U S A* **2016**, *113* (39), 10890-10895. DOI: 10.1073/pnas.1612736113

(172) Tan, G.; Liu, D.; Pan, F.; Zhao, J.; Li, T.; Ma, Y.; Shen, B.; Lyu, J. His-87 ligand in mitoNEET is crucial for the transfer of iron sulfur clusters from mitochondria to cytosolic aconitase. *Biochem Biophys Res Commun* **2016**, *470* (1), 226-232. DOI: 10.1016/j.bbrc.2016.01.040

(173) Zuo, K.; Marjault, H. B.; Bren, K. L.; Rossetti, G.; Nechushtai, R.; Carloni, P. The two redox states of the human NEET proteins' [2Fe-2S] clusters. *J Biol Inorg Chem* **2021**, *26* (7), 763-774. DOI: 10.1007/s00775-021-01890-8

(174) Karmi, O.; Holt, S. H.; Song, L.; Tamir, S.; Luo, Y.; Bai, F.; Adenwalla, A.; Darash-Yahana, M.; Sohn, Y. S.; Jennings, P. A.; Azad, R. K.; Onuchic, J. N.; Morcos, F.; Nechushtai, R.; Mittler, R. Interactions between mitoNEET and NAF-1 in cells. *PLoS One* **2017**, *12* (4), e0175796. DOI: 10.1371/journal.pone.0175796

(175) Wei, J.; Yang, Q.; Shi, J.; Shi, B.; Ji, M.; Hou, P. Increased expression of NAF1 contributes to malignant phenotypes of glioma cells through promoting protein synthesis and associates with poor patient survival. *Oncogenesis* **2019**, *8* (4), 25. DOI: 10.1038/s41389-019-0134-2

(176) Li, Y.; Wang, X.; Huang, Z.; Zhou, Y.; Xia, J.; Hu, W.; Wang, X.; Du, J.; Tong, X.; Wang, Y. CISD3 inhibition drives cystine-deprivation induced ferroptosis. *Cell Death Dis* **2021**, *12* (9), 839. DOI: 10.1038/s41419-021-04128-2

(177) Kelly, S. M.; Jess, T. J.; Price, N. C. How to study proteins by circular dichroism. *Biochim Biophys* **2005**, *1751* (2), 119-139. DOI: 10.1016/j.bbapap.2005.06.005

(178) Kelly, S. M.; Price, N. C. The use of circular dichroism in the investigation of protein structure and function. *Curr Protein Pept Sci* **2000**, *1* (4), 349-384. DOI: 10.2174/1389203003381315

(179) Ranjbar, B.; Gill, P. Circular dichroism techniques: biomolecular and nanostructural analyses- a review. *Chem Biol Drug Des* **2009**, *74* (2), 101-120. DOI: 10.1111/j.1747-0285.2009.00847.x

(180) Martin, S. R.; Schilstra, M. J. Circular dichroism and its application to the study of biomolecules. *Methods Cell Biol* **2008**, *84*, 263-293. DOI: 10.1016/S0091-679X(07)84010-6

(181) Tjernberg, A.; Markova, N.; Griffiths, W. J.; Hallen, D. DMSO-related effects in protein characterization. *J Biomol Screen* **2006**, *11* (2), 131-137. DOI: 10.1177/1087057105284218